# DEVELOPMENT OF MAGNETORESISTIVE SENSORS FOR NANOWIRE DETECTION TARGETED AT BIOLOGICAL APPLICATIONS

NIGEL CARROLL



A thesis submitted in part-fulfilment of the requirements for the degree of

Doctor in Philosophy

Supervised by Dr. Plamen Stamenov

Co Supervised by Prof. Michael Coey

School of Physics

Trinity College Dublin

2018

*To my wife Nathalie and my three boys Joshua, Jonah and Elliott*

## DECLARATION

I have read and I understand the plagiarism provisions in the General Regulations of the University Calendar for the current year, found at http://www.tcd.ie/calendar.

I have also completed the Online Tutorial on avoiding plagiarism, 'Ready Steady Write', located at http://tcd-ie.libguides.com/plagiarism/ready-steady-write.

Nigel Carroll

## SUMMARY

This research project has focused on developing technologies for the detection of single segment and multi-segment magnetic nanowires using yoke shaped GMR sensors and TMR MgO-barrier magnetic tunnel junction sensors integrated into a microfluidic channel. The leading questions were firstly can one detect the stray field of the single-segment magnetic nanowire as it passes over the sensor and secondly can one detect the magnetic segments within a multi-segment nanowire and distinguish different signal response signatures between a single segment nanowire and multi-segmented nanowire. Over the past 20 years there has been a focus in utilizing advances in magnetoresistive sensors, nanowires and microfluidics leading to simpler and less expensive instrumentation. These technologies have been integrated into lab-on-chip biomedical platforms for applications such as magnetocardiography (MCG), magnetic cytometry (Pannetier-Lecoeur et al 2011 and Freitas et al 2012) [1, 2].

In this thesis first, the fundamentals of magnetism, magnetoresistance GMR and TMR spin valve sensors were explored. Also noise considerations in both GMR and TMR sensors and the systems that interface them. I explored the developments in electrodeposition processes towards the fabrication of magnetic nanowires using nano-porous anodic aluminium oxide (AAO) membranes and reviewed a number of studies, which investigated the detection of superparamagnetic beads using GMR sensors.

The focus of the thesis was to develop suitable magnetic nanowires for detection using magnetoresistive sensors. To achieve this goal, we first produced single segment cobalt (Co) nanowires, and single segment cobalt nickel (CoNi) nanowires. This lead to the production of two magnetic segment nanowires using CoNi segments separated by a copper (Cu) non-magnetic spacer layer (CoNi-Cu-CoNi). For the detection of the nanowire stray field, a yoke shape GMR spin-valve sensor was fabricated by sputter deposition and UV lithography processes. This provided a good linear GMR response of 7.3%, with a sensitivity of 0.8%/mT and a noise level field detectivity $13.5nT/\sqrt{Hz}$ @

10Hz. The sensor was deposited and patterned on a glass substrate to facilitate optical analysis of the nanowires. A yoke shape TMR sensor based on an MgO barrier magnetic tunnel junction was then patterned as an alternate sensor option which provided a good linear TMR response of 130% with field detectivity $4.8nT/\sqrt{Hz}$ at 10Hz. The passivation layer to protect the sensor during nanowire detection experiments into microfluidic channel was optimised using rf sputtered SiNx with a thickness of 150 nm.

To capture and analyse the signals, a number of iterations of the nanowire detection system were developed to improve the signal to noise ratio and the detection of the magnetic nanowires. The final iteration developed was a fully integrated detection system, which comprised of an interface for sensors and a microfluidic chip, low-noise pre and post-amplifiers, a data acquisition card, a microscope and camera. Software routines for capturing data were developed in Labview, and a set of Mathcad software routines provides further signal processing, resulting in improved signal-to-noise ratio. Signal detection experiments were carried out with two GMR sensors configured as a lateral gradiometer, which enabled us to detect single segment nanowires as they passed over the sensor.

# PUBLICATIONS

---

J. Y. Chen, N. Carroll, J. F. Feng, J. M. D Coey Yoke-shaped MgO-barrier magnetic tunnel junction sensors. Appl. Phys. Lett., 2012. 101(262402)

# ACKNOWLEDGEMENTS

First, I would like to thank Prof. Michael Coey who gave me the opportunity to work on this project and to be part of his research group.

I would also like to very much thank Prof. Plamen Stamenov, who supported me on so many aspects of this research. I have gained so much experience and knowledge. Working towards a PhD part time was difficult and over the course of the past several years I very much appreciate the patience and support during the more difficult times of my PhD study.

I want to thank Nathalie, my beautiful wife for her endless support, clarity and motivation. Our family grew over the course of my PhD from Joshua, to Jonah and to Elliott. Nathalie encouraged me to keep going, through all the late evenings and weekends, which was so difficult at times for all the amazing things and the tiredness that a young family brings.

To my Mum and Dad for all their support throughout my life and education.

I would like to thank the research group for their help and support during my study over the past few years. Gweneal for all the valuable discussions and scientific support as we worked through numerous technical and process issues. I would like to thank Karsten for all the scientific discussions. Junyang for his support in the development of the TMR sensors. Venky for all the SQUID measurements and valuable discussions

I would like to thank the School of Physics for supporting me throughout the PhD, and the CRANN center for all of the equipment and the facilities I used.

This work was supported by the EU FP7 NMP4-LA-2010-246479

# CONTENTS


1 INTRODUCTION 1

1.1 Introduction . . . 1

1.2 Thesis Outline . . . 6

1.3 Theory of Magnetism . . . 7

1.3.1 Atomic Magnetism . . . 12

1.3.2 Banding . . . 14

1.3.3 Magnetic materials . . . 17

1.3.4 Diamagnetism and Paramagnetism . . . 18

1.3.5 Ferromagnetism . . . 20

1.3.6 Anti-ferromagnetism . . . 25

1.3.7 Exchange bias . . . 26

1.4 Magnetoresistance . . . 28

1.4.1 Spin dependent transport in ferromagnetic transition metals . . . 28

1.5 Giant magnetoresistance . . . 30

1.5.1 GMR Current in plane & Current perpendicular to plane . . . 33

1.6 Tunneling magnetoresistance . . . 36

1.6.1 Coherent tunnelling through MgO barrier . . . 40

1.7 Magnetic sensors . . . 42

1.7.1 Giant magnetoresistance (Spin valve) sensors . . . 43

1.7.2 Tunneling magnetoresistance sensors . . . 47

1.8 Noise . . . 48

1.8.1 Frequency Space and Spectral Density . . . 50

1.8.2 Sensitivity, Signal to Noise ratio and Detectivity . . . 52

1.9 Noise sources . . . 52

1.9.1 Frequency independent noise . . . 53

1.9.2 Low Frequency noise . . . 54

1.9.3 Random telegraph noise, High Frequency noise and External noise 54
1.9.4 High Frequency noise . . . 55
1.10 Magnetoresistive noise . . . 55
1.10.1 Giant magnetoresistance noise . . . 56
1.10.2 Tunneling magnetoresistance noise . . . 56
1.10.3 Comparison of sensor characteristics . . . 57
1.11 Electrodeposition and Magnetic nanowires . . . 58
1.11.1 Electrochemistry . . . 59
1.11.2 Electrochemical Cells . . . 62
1.11.3 Magnetic nanowires using AAO membranes . . . 65
1.12 Magnetic bead detection review . . . 65
1.13 Conclusions . . . 75

2 EXPERIMENTAL TECHNIQUES 77
2.1 Introduction . . . 77
2.2 Thin film sputter deposition . . . 77
2.2.1 Physical Vapour Deposition - Thin film sputter deposition . . . 77
2.2.2 Magnetron sputtering . . . 79
2.2.3 Thin film deposition system . . . 81
2.3 Electrodeposition process for nanowire fabrication . . . 85
2.3.1 Nanowire deposition curves . . . 86
2.3.2 Removing the nanowires from the AAO membrane . . . 88
2.3.3 Nanowire magnetisation . . . 89
2.3.4 PH meter calibration . . . 89
2.3.5 Sputter coating AAO membranes . . . 90
2.4 Structural characterisation . . . 91
2.4.1 X-ray diffraction (XRD) and X-ray reflectivity (XRR) . . . 91
2.4.2 Scanning Electron Microscope (SEM) . . . 94
2.4.3 Transmission Electron Microscope (TEM) . . . 94
2.4.4 Atomic force microscope (AFM) . . . 95
2.5 Magnetic characterisation . . . 96

2.5.1 Magnetoresistance measurement . . . . . 96
2.5.2 Magnetic annealing . . . . . 97
2.5.3 Superconducting Quantum Interface Device (SQUID) Magnetometer 97
2.6 Electrical characterisation . . . . . 98
2.6.1 Noise measurements . . . . . 98
2.7 Sensor Fabrication Techniques . . . . . 99
2.7.1 Photolithography . . . . . 100
2.7.2 UV lithographic photomask mask & direct laser beam writing system 101
2.7.3 The photoresist . . . . . 102
2.7.4 UV photolithography Mask aligner . . . . . 104
2.7.5 Development . . . . . 105
2.7.6 Ion milling . . . . . 105
2.7.7 Patterning lift-off . . . . . 107
2.8 Device Fabrication . . . . . 108
2.8.1 Giant magnetoresistance sensor fabrication . . . . . 109
2.8.2 Step 1: Deposition of thin-film metal layers . . . . . 109
2.8.3 Step 2: YOKE sensor & alignment mark patterning . . . . . 110
2.8.4 Step 3: Top electrode patterning . . . . . 110
2.8.5 Tunneling magnetoresistance sensor fabrication . . . . . 111
2.8.6 Step 1: Deposition of thin-film metal layers . . . . . 112
2.8.7 Step 2: YOKE sensor bottom electrode & alignment mark patterning 112
2.8.8 Step 3: Junction area definition . . . . . 113
2.8.9 Step 4: Top electrode patterning . . . . . 113
2.8.10 Step 5: Annealing . . . . . 114

3 GIANT MAGNETORESISTANCE SENSORS & TUNNELING MAGNETORESISTANCE SENSORS 115
3.1 Introduction . . . . . 115
3.2 Giant magnetoresistance Sensors Characterisation . . . . . 115
3.2.1 Magnetoresistance response of GMR sensors . . . . . 116
3.2.2 Magnetoresistance response of GMR Gradiometer sensors . . . . . 120

3.2.3 Magnetoresistance response of GMR Gradiometer for focused flow sensors . . . 121
3.2.4 GMR sensor noise measurements . . . 122
3.2.5 GMR YOKE shape micro-magnetic simulation . . . 124
3.2.6 Conclusions . . . 125
3.3 Tunneling magnetoresistance Sensors Characterisation . . . 125
3.3.1 Tunneling magnetoresistance magnetoresistance measurement . . . 126
3.3.2 Tunneling magnetoresistance sensors 1st iteration development & characterisation . . . 127
3.4 Tunneling magnetoresistance sensors 2nd iteration characterisation . . . 130
3.4.1 TMR sensors Design 1 – Pillar . . . 131
3.4.2 TMR sensors Design 2 – YOKE . . . 132
3.4.3 TMR yoke sensor noise measurements . . . 135
3.4.4 TMR sensors Design 3 – Small YOKE . . . 137
3.4.5 TMR small yoke sensor noise measurements . . . 139
3.4.6 Final TMR sensor layout for Micro-fluidic Channel . . . 140
3.5 Summary . . . 140
3.6 Sensor passivation layer . . . 141
3.6.1 RF sputtered Silicon Nitride ($Si_3N_4$) . . . 143
3.7 Conclusions . . . 146

4 NANOWIRE FABRICATION AND CHARACTERISATION 147
4.1 Introduction . . . 147
4.2 Nanowires . . . 147
4.2.1 Estimation of nanowire per AAO membrane . . . 148
4.3 Signal magnetic segment – Cobalt (Co) nanowires . . . 150
4.3.1 Cobalt nanowire characterisation . . . 151
4.4 Two magnetic segment CoFe-Cu-CoFe nanowires . . . 153
4.4.1 CoFe-Cu-CoFe nanowire characterisation . . . 154
4.5 Signal segment CoNi & multi-segment CoNi-Cu-CoNi nanowires . . . 158
4.5.1 CoNi-Cu-CoNi nanowire characterization . . . 160

4.6 Conclusions . . . . . 162

5 DETECTION OF MAGNETIC NANOWIRES USING SINGLE SENSOR CONFIGURATION DETECTION SYSTEM 163

5.1 Introduction . . . . . 163

5.2 Magnetic nanowire detection . . . . . 163

5.3 Magnetic field calculation for Cobalt nanowires . . . . . 165

5.3.1 Stray field response of Cobalt nanowire at distances from the magnetoresistive sensor . . . . . 167

5.4 Magnetic field calculation for $Co_{50}Fe_{50}$ nanowires . . . . . 169

5.4.1 Stray field response of $Co_{50}Fe_{50}$nanowires at distances from the magnetoresistive sensor . . . . . 170

5.5 Magnetic field calculation for for $Co_{65}Ni_{35}$ nanowires . . . . . 171

5.5.1 Stray field response of $Co_{65}Ni_{35}$ nanowires at distances from the magnetoresistive sensor . . . . . 172

5.5.2 Stray field model for a uniformly magnetised $Co_{65}Ni_{35}$ cylinder . 174

5.6 Velocity of magnetic nanowires flowing in microfluidic channel . . . . . 174

5.6.1 Estimation of nanowire response time . . . . . 176

5.7 First iteration of the Nanowire detection system . . . . . 177

5.7.1 Sensor current supply . . . . . 178

5.7.2 Sensor interface & microfluidic channel . . . . . 178

5.7.3 Detection system . . . . . 179

5.7.4 Sensor and system noise calculations and measurements . . . . . 181

5.7.5 Data acquisition . . . . . 184

5.7.6 Pulse Height Amplification routine for post data analysis . . . . . 185

5.8 Nanowire detection experiments . . . . . 186

5.8.1 Sensor magnetic field Calibration . . . . . 187

5.8.2 Noise measurements . . . . . 189

5.8.3 Nanowire detection experiments - Cobalt (Co) nanowires . . . . . 189

5.9 Second iteration of the Nanowire detection system . . . . . 194

5.9.1 Sensor interface . . . . . 196

5.9.2 Low pass filter and post amplifier . . . . . 197
5.9.3 Microfluidic pump . . . . . 198
5.9.4 Microscope and camera . . . . . 198
5.10 Nanowire detection experiments - Second iteration of the detection system 198
5.10.1 Noise measurements . . . . . 199
5.10.2 Nanowire detection experiment - Cobalt (Co) nanowires . . . . . 200
5.10.3 Nanowire detection experiments using second iteration detection system - Noise measurements . . . . . 203
5.10.4 Noise measurements . . . . . 204
5.10.5 CoNi Nanowire detection experiments in single GMR sensor configuration . . . . . 204
5.11 Nanowire detection experiments using TMR sensors . . . . . 210
5.11.1 TMR current circuit . . . . . 210
5.11.2 Noise measurements using TMR sensors . . . . . 211
5.11.3 Noise measurements . . . . . 211
5.11.4 CoFe Nanowire detection experiment using TMR sensors in single sensor configuration . . . . . 212
5.12 Conclusions . . . . . 216

6 DETECTION OF MAGNETIC NANOWIRES USING GRADIOMETER SENSOR CONFIGURATION 219
6.1 Introduction . . . . . 219
6.2 Gradiometer nanowire detection system . . . . . 219
6.2.1 Gradiometer configuration . . . . . 221
6.2.2 Detection system for gradiometer . . . . . 222
6.2.3 Current circuit for graidometer . . . . . 224
6.3 Balanced Gradiometer response . . . . . 224
6.3.1 Gradiometer sensor field Calibration . . . . . 227
6.3.2 Gradiometer noise measurements . . . . . 227
6.4 Nanowire detection experiments using the Gradiometer configuration . . 228

6.4.1 CoNi Nanowire detection using the gradiometer configuration - Batch 091213-1 . . . 228
6.4.2 CoNi Nanowire detection using the gradiometer configuration - Batch SM319G9 (091213-2) . . . 234
6.4.3 CoNi-Cu-CoNi Nanowire detection using the gradiometer configuration - Batch 211013-3 . . . 238
6.4.4 CoNi-Cu-CoNi Nanowire detection using the gradiometer configuration - Batch 211013-4 . . . 243
6.4.5 Conclusions . . . 246
6.5 Final optimisation of the Gradiometer for nanowire detection . . . 247
6.5.1 Gradiometer sensor design for focused flow . . . 247
6.5.2 Detection system integration into the sensor interface . . . 248
6.5.3 Balanced optimised gradiometer response . . . 250
6.5.4 Optimised gradiometer field calibration . . . 252
6.5.5 Optimised gradiometer noise measurement . . . 252
6.6 Nanowire detection experiments using Optimised Gradiometer configuration 254
6.6.1 CoNi Nanowire detection using the optimised gradiometer - 101215-1 254
6.6.2 CoNi Nanowire detection using the optimised gradiometer - Batch 130116 . . . 258
6.6.3 CoNi-Cu-CoNi Nanowire detection using the optimised gradiometer configuration - Batch 071215 . . . 262
6.7 Conclusions . . . 266

7 CONCLUSIONS AND FUTURE WORK 269
7.1 Conclusions . . . 269
7.2 Future Work . . . 270

References 273

8 APPENDIX 285
8.1 Appendix A - Spin torque diode detector . . . 285
8.1.1 Resonant detection using Spin Torque Diodes . . . 285

8.1.2 Spin transfer torque introduction . . . . . 286
8.1.3 Spin torque nano-oscillator . . . . . 287
8.1.4 Spin-torque microwave detector – Spin-torque diode . . . . . 290
8.1.5 Literary review spin torque diodes . . . . . 292
8.1.6 Conclusions . . . . . 294
8.1.7 Electron Beam Lithography . . . . . 295
8.1.8 Elionix 7700 e-Beam lithography system . . . . . 296
8.1.9 Spin torque diode sensor fabrication . . . . . 297
8.1.10 Step 1: Expose alignment & registration marks for the overlay of each layer . . . . . 298
8.1.11 Step 2: Expose bottom electrode for Spin torque diode device . . . 299
8.1.12 Step 3: Expose junction pillars and contact pads . . . . . 300
8.1.13 Step 4: Expose top electrode . . . . . 301
8.2 Appendix B - GMR and TMR sensor fabrication procedure . . . . . 303
8.2.1 GMR sensor fabrication procedure . . . . . 303
8.2.2 TMR sensor fabrication procedure . . . . . 307
8.2.3 Shamrock Chamber A permanent magnet field measurments . . . 312
8.3 Appendix C - AAO membrane and Nanowire sample weights . . . . . 315
8.3.1 Membrane and Nanowire sample weights . . . . . 315
8.4 Appendix D - Nanowire Magnetic field calculations . . . . . 316
8.4.1 Calculated field response of Cobalt nano-wires . . . . . 316
8.4.2 Magnetic field calculation for Cobalt nano-wires . . . . . 317
8.5 Magnetic field calculation for for $Co_{50}Fe_{50}$nano-wires . . . . . 320
8.5.1 Calculated field response of $Co_{50}Fe_{50}$ nano-wires . . . . . 322
8.5.2 Magnetic field response of Cobalt nano-wires at distances from the magnetoresistive sensor . . . . . 323
8.6 Magnetic field calculation for for $Co_{65}Ni_{35}$ nano-wires . . . . . 324
8.6.1 Calculated field response of $Co_{65}Ni_{35}$ nano-wires . . . . . 326
8.6.2 Magnetic field response of $Co_{65}Ni_{35}$ nano-wires at distances from the magnetoresistive sensor . . . . . 327
8.7 Appendix E - Nanowire fabrication procedures . . . . . 328

8.7.1 Cobalt (Co) solution procedure: . . . . . 328
8.7.2 Cobalt (Co) Electrodeposition procedure: . . . . . 329
8.7.3 Cobalt (Co) nanowire removal from membrane procedure: . . . . . 330
8.7.4 CoFe & Cu solution procedure . . . . . 331
8.7.5 CoFe-Cu-CoFe nanowire electrodepositon procedure . . . . . 332
8.7.6 CoNi-Cu-CoNi solution procedure . . . . . 333
8.7.7 CoNi-Cu-CoNi electrodepositon procedure . . . . . 334
8.7.8 Growth conditions of some of the CoNi and CoNi-Cu-CoNi nanowire batches produced . . . . . 334
8.7.9 CoNi & CoNi-Cu-CoNi nanowires seperation from membrane . . 335
8.7.10 Nanowire experiment preparation procedure . . . . . 336
8.7.11 Focused flow channel was configuration . . . . . 338
8.8 Appendix F - GMR and TMR sensor magnetoresistance response . . . . 340
8.8.1 GMR sensor additional resistance measurments . . . . . 340
8.8.2 GMR sensor additional magnetoresistance measurments . . . . . 340
8.8.3 1st TMR sensor additional magnetoresistance measurments . . . . 341
8.9 Appendix G - Magneto-fluorescence Prototype System . . . . . 344

# LIST OF TABLES


Table 1.1 Advantages of magnetic sensors . . . . . 42
Table 1.2 Sensor principles and performance parameters . . . . . 43
Table 1.3 Summary of GMR and TMR sensor characteristics [1] . . . . . 57
Table 1.4 Summary of superparamagnetic bead detection . . . . . 75
Table 2.1 Summary of the deposition parameters for the metallic targets and nitride layers targets used for both GMR and TMR sensors deposited in both chamber A and B . . . . . 84
Table 2.2 CoNi-Cu-CoNi deposition conditions . . . . . 88
Table 2.3 Removing the nanowires from the AAO membrane . . . . . 88
Table 2.4 pH meter calibration procedure . . . . . 90
Table 2.5 Procedure to sputter coat AAO membrane with ~ 120 nm of Au . 91
Table 2.6 Multilayer stack configurations . . . . . 108
Table 3.1 GMR sensor two wire resistance measurements across contact pads 117
Table 3.2 TMR Sensor 280411 measured magnetoresistance response TMR% across eight YOKE sensors . . . . . 129
Table 3.3 TMR Pillar sensor detailing TMR junction product RA and measured TMR ratio (%) after 1st annealing 350 $^{o}$C . . . . . 132
Table 3.4 TMR YOKE sensors detailing TMR junction product RA and measured TMR ratio (%) after 1st annealing 350ř$C$ . . . . . 134
Table 3.5 TMR small YOKE sensors detailing TMR junction product RA and measured TMR ratio (%) after 1st annealing 350ř$C$ . . . . . 138
Table 3.6 Summary and comparison between detectivities at 10 Hz for different types of sensors . . . . . 141
Table 3.7 Summary of passivation's layers investigated . . . . . 142
Table 3.8 $Si_3N_4$ calibrations various power & gas ratio conditions . . . . . 144
Table 3.9 Optimum $Si_3N_4$calibration . . . . . 144

Table 4.1 Summary of Nanowires investigated . . . . . 148
Table 4.2 AAO membrane specifications . . . . . 148
Table 4.3 Parameters for hexagon geometry calculation of nanowires per membrane . . . . . 149
Table 4.4 Cobalt (Co) solution . . . . . 150
Table 4.5 Cobalt nanowire depositions . . . . . 151
Table 4.6 CoFe and Cu solutions . . . . . 153
Table 4.7 Process to produce two magnetic segment CoFe-Cu-CoFe nanowires 154
Table 4.8 CoNi, CoNiCu interlayer and solution Cu solution . . . . . 158
Table 4.9 Deposition sequence for CoNi-Cu-CoNi segmented nanowires . . . 159
Table 4.10 CoNi deposition conditions . . . . . 159
Table 5.1 Cobalt nanowire sample details . . . . . 166
Table 5.2 Field calculation of a Co nanowire at various heights in the microfluidic channel . . . . . 167
Table 5.3 $Co_{50}Fe_{50}$ nanowire sample details . . . . . 169
Table 5.4 Field calculation of a Co50Fe50 nanowire at various heights in the microfluidic channel. . . . . 170
Table 5.5 $Co_{65}Ni_{35}$ nanowire sample details . . . . . 171
Table 5.6 Field calculation of a $Co_{65}Ni_{35}$ nanowire at various heights in the microfluidic channel . . . . . 173
Table 5.7 Microfluidic pump parameters, channel geometries, sensor and nanowire details . . . . . 175
Table 5.8 Microfluidic pump settings with flow velocity rates for microfluidic chip height: 30 µm . . . . . 175
Table 5.9 Microfluidic pump settings with flow velocity rates for microfluidic chip height- 60 µm and 120 µm . . . . . 176
Table 5.10 Nanowire response times at different velocities for different nanowire lengths using a microfluidic chip height: 30 µm . . . . . 177
Table 5.11 Calibration conditions measured for single sensor configuration . . 188
Table 5.12 Co nanowire sample deposition conditions . . . . . 190
Table 5.13 Co nanowire sample dissolving conditions . . . . . 190

Table 5.14 Summary of initial nanowire detection experiments . . . . . 194
Table 5.15 CoNi nanowire sample deposition conditions . . . . . 204
Table 5.16 CoNi nanowire sample condition used to dissolve from membrane 205
Table 5.17 Summary of CoNi nanowire detection experiments using GMR sensor in 2nd iteration detection system . . . . . 209
Table 5.18 CoFe 111112 nanowire sample deposition conditions . . . . . 212
Table 5.19 CoFe 111112 nanowire sample condition used to dissolve from membrane . . . . . 213
Table 5.20 Summary of CoFe nanowire detection experiments using TMR sensor in 2nd iteration detection system . . . . . 216
Table 6.1 Calibration conditions measured for Gradiometer sensor configuration 227
Table 6.2 091213-1 CoNi nanowire sample deposition conditions . . . . . 229
Table 6.3 091213-1 CoNi nanowire sample condition used to dissolve from membrane . . . . . 229
Table 6.4 CoNi (SM319G4) 091213-2 deposition conditions . . . . . 234
Table 6.5 CoNi (SM319G4) 091213-2 conditions used to dissolve from membrane 234
Table 6.6 Summary of CoNi nanowire detection experiments using gradiometer 238
Table 6.7 CoNi-Cu-CoNi 210113-3 deposition conditions . . . . . 238
Table 6.8 CoNi-Cu-CoNi 210113-3 conditions used to dissolve from membrane 239
Table 6.9 CoNi-Cu-CoNi 210113-4 deposition conditions . . . . . 243
Table 6.10 CoNi-Cu-CoNi 210113-4 conditions used to dissolve from membrane 243
Table 6.11 Summary of CoNi-Cu-CoNi nanowire detection experiments using gradiometer . . . . . 246
Table 6.12 Calibration conditions measured for Gradiometer focus flow sensor configuration . . . . . 252
Table 6.13 130116 CoNi nanowire sample deposition conditions . . . . . 258
Table 6.14 130116 CoNi nanowire sample condition used to dissolve from membrane . . . . . 258
Table 6.15 Summary of CoNi nanowire detection experiments using the optimised gradiometer . . . . . 262
Table 6.16 071215 CoNi-Cu-CoNi nanowire sample deposition conditions . . . 262

Table 6.17 071215 CoNi-Cu-CoNi nanowire sample condition used to dissolve from membrane . . . 263
Table 6.18 Summary of CoNi-Cu-CoNi nanowire detection experiments using the optimised gradiometer . . . 266
Table 8.1 Summary of the development of spin-torque diodes . . . 293
Table 8.2 Main components of the Elionix system . . . 296
Table 8.3 Elionix exposure files for each of the lithography steps and the optimum exposure times for each layer . . . 298
Table 8.4 EBL exposure conditions for optical image alignment mark & registration marks . . . 299
Table 8.5 Exposure (dose) time calculations and exposure conditions for the bottom electrode . . . 300
Table 8.6 Exposure (dose) time calculations and exposure conditions for the top electrode . . . 301
Table 8.7 Shamrock Chamber A permanent magnet field measurments in detail 313
Table 8.8 Whatman Anodisc 25 details: . . . 315
Table 8.9 CoNi sample weight in complete membrane . . . 315
Table 8.10 Nanowire length to deposition charge (Q) . . . 315
Table 8.11 Nanowire sample weight per SQUID sample size . . . 316
Table 8.12 Cobalt nanowire sample details . . . 318
Table 8.13 Field calculation of a Co nanowire at various heights in the microfluidic channel . . . 319
Table 8.14 $Co_{50}Fe_{50}$ nanowire sample details . . . 321
Table 8.15 Field calculation of a Co50Fe50 nanowire at various heights in the microfluidic channel. . . . 323
Table 8.16 $Co_{65}Ni_{35}$ nanowire sample details . . . 325
Table 8.17 Field calculation of a Co65Ni35 nanowire at various heights in the microfluidic channel . . . 327
Table 8.18 CoNi, CoNiCu interlayer and solution Cu solution . . . 333
Table 8.19 Deposition sequence for CoNi-Cu-CoNi segmented nanowires . . . 334
Table 8.20 CoNi deposition conditions . . . 334

Table 8.21 CoNi-Cu-CoNi deposition conditions . . . . . 335
Table 8.22 Conditions of samples separation from membrane . . . . . 336
Table 8.23 CoNi measured sample weight after dissolving from the AAO membrane 337
Table 8.24 Nanowire estimates per volume dispensed . . . . . 338
Table 8.25 Calculations for the focused flow channel flow rates . . . . . 339
Table 8.26 GMR sensor two wire resistance measurements across contact pads for a number of sensors . . . . . 340
Table 8.27 TMR Sensor 300511 magnetoresistance response with no gaps in Yoke sensor . . . . . 342
Table 8.28 TMR Sensor 280411 measured magnetoresistance response along each juction of YOKE sensor Y5 . . . . . 343
Table 8.29 TMR Sensor 29041 TMR ratio measured across each of the eight YOKE sensors and junctions . . . . . 344

# LIST OF FIGURES


Figure 1.1 Schematic illustration of the magnetic nanowire detection concept 4

Figure 1.2 Concept design of magneto-fluorescence prototype system . . . . . 4

Figure 1.3 Block diagram detailing the design components in overall magnetic nano-wire detection scheme . . . . . 6

Figure 1.4 (a) Magnetic field line produced due to a current loop (b) Magnetic field produced due to current in a length of conductor . . . . . 7

Figure 1.5 (a) Magnetic field line created in a solenoid configuration and (b) magnetic dipole field lines from a permanent magnet . . . . . 9

Figure 1.6 Field lines B, M and H produced for a for a magnet [1] . . . . . 11

Figure 1.7 Magnetic dipole moment and angular momentum of Bohr atom and moment due to electron . . . . . 12

Figure 1.8 Formation of energy bands in solids, dependent on the separation distance between atoms . . . . . 14

Figure 1.9 DOS showing exchange splitting of spin up and spin down half bands [1] . . . . . 15

Figure 1.10 Diagram representing the occupation of allowed energy states in an electron band (a) balanced number of Spin up & spin down electrons (b) unbalanced number of spin up & spin down electrons due to exchange interaction leading to a net magnetic moment . . 16

Figure 1.11 Density of states of transition metals Fe, Co, Ni and Cu [2] . . . . 17

Figure 1.12 (a) Atomic dipole configuration for a diamagnetic material with and without a magnetic field (b) atomic dipole configuration with and without an external magnetic field for a paramagnetic material (c) Paramagnet and Diamagnet response . . . . . 19

Figure 1.13 (a) Mutual alignment of atomic dipoles for a ferromagnetic material (b) Hysteresis of a ferromagnetic material starting from a demagnetised sample, showing saturation magnetisation $M_S$, remanent magnetisation $M_r$, and coercivity $H_C$ in the easy axix [1] . . . . . 20

Figure 1.14 (a) Schematic depiction of domains in a ferromagnetic or ferrimagnetic material; arrows represent atomic magnetic dipoles. Within each domain, all dipoles are aligned, whereas the direction of alignment varies from one domain to another. (b) The gradual change in magnetic dipole orientation across a domain wall [3] . . . . . 21

Figure 1.15 The B-versus-H behaviour for a ferromagnetic or ferrimagnetic material that was initially un-magnetized. Domain configurations during several stages of magnetisation are represented. Saturation flux density magnetization and initial permeability are also indicated [4] . . . . . 22

Figure 1.16 (a) magnetisation and susceptibility curves below and above the Curie temperature. The small sketches at the top represent the distribution of classical spin directions, in zero applied field within a single domain (below $T_c$), and in a group of atoms (above $T_c$) (b) Saturation magnetisation of iron, cobalt, and nickel as a function of temperature [5] . . . . . 23

Figure 1.17 (a) Magnetisation curves for single crystals of iron and nickel [6, 7] (b) Magnetisation curves for single crystals of cobalt[8] . . . . . 24

Figure 1.18 (a) anti-ferromagnetic ordering of spins in a lattice (b) Susceptibility of an AFM material, in the parallel and perpendicular directions below TN [1] . . . . . 25

Figure 1.19 (a) Hysteresis of Co/CoO particles and (b) Schematic diagram of an exchange biased hysteresis loop . . . . . 27

Figure 1.20 Schematic of (a) stoner model: exchange splitting (b) s-d scattering rate model . . . . . 29

Figure 1.21 A Ferromagnetic material with opposite magnetisation directions showing opposite spin-polarisation polarity . . . . . 30

Figure 1.22 Schematic of GMR multilayer and results of Fert & Grunberg (1988) change in the resistance of Fe/Cr superlattices in external magnetic field H . . . . . 31
Figure 1.23 Schematic of the GMR mechanism for spin up and spin down electrons 32
Figure 1.24 Schematic of (a) GMR current in plane (CIP) (b) Current perpendicular to plane (CIP) . . . . . 33
Figure 1.25 Chemical potentials for spin-up (↑) and spin down (↓) electrons in a GMR spin valve with parallel or antiparallel alignment of the electrodes . . . . . 35
Figure 1.26 Schematic illustration of a basic spin-valve TMR sensor trilayer b) the magneto-resistance curve showing TMR ratio 250 % exchange bias field (Hex) is > 50 mT . . . . . 36
Figure 1.27 (a) The decay of electron's wave-function within the tunnelling barrier (b) the band diagram of a metal/insulator/metal structure [1] 37
Figure 1.28 Schematic of TMR multilayer and electron tunnelling band structure 39
Figure 1.29 Schematic of electron tunnelling through (a) incoherent amorphous ALOx barrier (b) coherent crystalline MgO (001) barrier [9] . . . 41
Figure 1.30 (a) DOS of electrons through an epitaxial Mg0 barrier in the parallel orientation for majority spin states (b) in the anti-parallel orientation for majority spin states . . . . . 41
Figure 1.31 (a) Schematic of spin valve configuration (b) Typical GMR multilayer stack configuration (c) Spin valve magneto response curve 44
Figure 1.32 (a) Schematic of spin valve with free layer set perpendicular to the pinned layer (b) typical GMR multilayer stack configuration (c) magnetoresistive loops for a Spin valve sensor before and pattering and properly biased . . . . . 45
Figure 1.33 (a) Schematic of GMR CIP spin valve sensor (b) Experimental transfer curve for a GMR spin valve sensor . . . . . 45
Figure 1.34 (a) Schematic of TMR spin valve sensor with free layer set perpendicular to the pinned layer (b) typical TMR multilayer in-plane stack configuration . . . . . 47

Figure 1.35 (a) Schematic of TMR CPP spin valve sensor (b) Magnetoresistive loop for a TMR Spin valve sensor . . . . . 48
Figure 1.36 Illustration of noise system . . . . . 48
Figure 1.37 (a) Plot of Debye-lorentzian spectrum (b) Contributions to the noise in a magnetoresistive sensor . . . . . 51
Figure 1.38 Noise in magnetic thin-film samples: (a) 1/f noise in a $CrO_2$ film, (b) random telegraph noise in a $La_{0.67}Ca_{0.33}MnO_3$ and , (c) 1/f and white noise in CoFeB–MgO–CoFeB MTJ [1]. . . . . 55
Figure 1.39 (a) Schematic of YOKE sensor and (b) magnetic configuration from micro-magnetic simulation [10] . . . . . 56
Figure 1.40 Oxidation and reduction half-cell reaction . . . . . 60
Figure 1.41 Oxidation and reduction reaction . . . . . 61
Figure 1.42 Schematic of the electrode-electrolyte interface formation of electrical double layer . . . . . 61
Figure 1.43 Schematic of a three electrode electrochemical cell . . . . . 63
Figure 1.44 Schematic of a potentiostat and electro-chemical cell . . . . . 65
Figure 1.45 An optical image of a 3 x12 µm$^2$ spin valve sensor strip with a single 2.8 µm diameter magnetic bead (Dynabeads M-280) [11] . . . . . 66
Figure 1.46 Resistance differences before and after depositing 16-nm $Fe_3O_4$ nanoparticles for three detection sensors (filled symbols) and two reference sensors (open symbols) [12] . . . . . 67
Figure 1.47 a) Transfer curve of a SV sensor with an average MR of 7% and a sensitivity of 5 V/T. The inset shows the simulated sensor output according to the position (x,0,z) of a flowing MP vertically magnetised by a 90 mT field [13] . . . . . 68
Figure 1.48 (a) Raw data acquired at 3 kHz, corresponding to a burst of particles flowing on top of the sensor (b) Same data as shown in (a) after digital filtering it. The exploded view shows an example of two peaks corresponding to two flowing particles, the first one having 10 points available to the reconstruction analysis and the second one 8 points [13] . . . . . 69

Figure 1.49 Signal variation with height from the sensor for cells at 10μm distance from each other along y axis . . . . . 70
Figure 1.50 Acquired signal for raw milk samples spiked with magnetically labeled Streptococcus agalactiae cells at 50 μL/min [14] . . . . . 71
Figure 1.51 (a) Simulated signals for 5 mm diameter cells, labeled with 2880 uniformly distributed nanoparticles, vertically magnetised, at different heights (5 mm, 7 mm and 11 mm) (b) Three single cell detection by a spin valve with 1 mA biasing current. The signal's amplitude is around 17–20 mV and the noise's amplitude approximately 3.54 mVrms . . . . . 72
Figure 1.52 (a) GMR sensor magnetoresistive response (b) noise spectrum . . 73
Figure 1.53 (a) shows the Magnetisation curve for 2 μm magnetic beads from Micromod (b) Simulated response of detected stray fields produced by a 2 μm magnetic bead magnetized at a field of 330 A/m . . . . 74
Figure 1.54 Response of a single half-ring GMR sensing element to various magnetic fluid weight density values . . . . . 74
Figure 2.1 (a) Basic schematic of the sputtering process and (b) schematic of the magnetron sputtering process . . . . . 78
Figure 2.2 Schematics of the S-Gun magnetron . . . . . 80
Figure 2.3 Schematic of impedance matching circuit for RF sputtering . . . . 81
Figure 2.4 High vacuum magnetron sputtering cluster tool . . . . . 81
Figure 2.5 Layout of Sputter deposition system showing three deposition chambers (A, B and D), transfer chambers (TM and Chamber C) and the load lock (CM) . . . . . 82
Figure 2.6 (a) Chamber A showing the four rotating planets and (b) one of the targets used in Chamber A . . . . . 83
Figure 2.7 Design for non-magnetic and magnetic targets used in Chamber A 83
Figure 2.8 (a) TFT target holder in chamber B and (b) CoFeB target used in the cluster gun in chamber B . . . . . 84

Figure 2.9 (a) Schematic of electrochemical cell for nanowire growth using porous AAO membrane (b) Experimental electrodeposition process setup . . . 85
Figure 2.10 Cyclic Voltammogram curve for Cu on thin film used to determine the deposition potential . . . 87
Figure 2.11 Deposition plots for each segment . . . 87
Figure 2.12 CoNi in membrane magnetised . . . 89
Figure 2.13 Calibration of pH meter JENWAY Model 3510 . . . 90
Figure 2.14 AAO membrane before & after gold sputter coating . . . 91
Figure 2.15 (a) Phillips X-Pert Pro PANalytical theta-theta diffractometer and (b) Schematic diffraction principle . . . 92
Figure 2.16 XRR measurement of the in-plane metallic target and the model fitting using WINGIXA . . . 93
Figure 2.17 Carl Zeiss Ultra Field Emission SEM . . . 94
Figure 2.18 Titan is field emission TEM . . . 95
Figure 2.19 AFM microscope and anti-vibration plate . . . 95
Figure 2.20 (a) RT rig used to measure magnetoresistance measurements and (b) Magnetoresistance scan for TMR sensor using the Labview interface . . . 96
Figure 2.21 High vacuum magnetic annealing furnace . . . 97
Figure 2.22 Quantum Design SQUID magnetometer (MPMS XL5) . . . 98
Figure 2.23 Schematic of experimental noise measurement setup for the GMR and TMR sensors . . . 99
Figure 2.24 Basic steps for GMR sensor fabrication . . . 99
Figure 2.25 Schematic of a basic lithographic exposure system . . . 100
Figure 2.26 Heidelberg DWL 66 direct writing system . . . 101
Figure 2.27 Top electrode mask for the GMR and TMR sensor . . . 102
Figure 2.28 (a) S1800 series photoresist sub-micron lines . . . 103
Figure 2.29 OAI UV mask aligner . . . 104
Figure 2.30 Millatron ion milling system . . . 106

Figure 2.31 EPD scan taken during ion-milling of (a) GMR multi-layer stack and (b) TMR GMR multi-layer stack indicating the individual layers 107
Figure 2.32 Steps for ultraviolet lithography patterning . . . . . 108
Figure 2.33 (a) 1st mask with YOKE sensors & alignment marks (b) 2nd mask sensor top electrode . . . . . 109
Figure 2.34 (a) Optical image of the YOKE sensors & alignment marks after the 1st mask pattering (b) Optical image of the top electrodes after the 2nd mask pattering . . . . . 111
Figure 2.35 (a) Optical image of the TMR sensor bottom electrode & alignment marks after the 1st mask pattering and TMR sensor junction after the 2nd mask pattering (b) TMR sensor with top electrode after the 3rd mask pattering . . . . . 114
Figure 3.1 Schematic of the GMR sensor magnetoresistance measurement technique . . . . . 116
Figure 3.2 Magnetoresistance response of GMR thin film before the sensor was patterned . . . . . 116
Figure 3.3 (a) Optical microscope image of the sensor GMR Bio-sensor pad layout and (b) contact pads along the sensors element . . . . . 117
Figure 3.4 Major loop magneto-resistance measurements GMR Bio-sensor 7245 118
Figure 3.5 Minor loop magneto-resistance measurements GMR Bio-sensor 7245 showing magnetoresistance response & sensitivity . . . . . 119
Figure 3.6 Minor loop magneto-resistance measurements for GMR Bio-sensor 7245 showing linerised response . . . . . 119
Figure 3.7 GMR sensor 290813-2 (a) exchange bias not set (b) after a post anneal at 250°C . . . . . 120
Figure 3.8 GMR Biosensor Gradiometer . . . . . 120
Figure 3.9 Major and minor loop magneto-resistance measurement GMR Bio-sensor Graiometer 220911-2 . . . . . 121
Figure 3.10 Optical image of the GMR Bio-sensor gradiometer for focus flow detailing revised YOKE gradiometer sensor pairs & top electrode 121

Figure 3.11 Major loop magneto-resistance measurement across each YOKE sensor of Gradiometer GMR Gradiometer Bio-sensor . . . . . 122
Figure 3.12 Normalized noise & GMR plotted as a function of magnetic field for GMR sensor . . . . . 123
Figure 3.13 1/f noise power spectral density as a function of frequency for the YOKE shape GMR sensor . . . . . 123
Figure 3.14 Noise dependency of the YOKE shape GMR sensor to field . . . . 124
Figure 3.15 Magnetic configuration of the YOKE sensor after the external field is decrease to zero . . . . . 125
Figure 3.16 Schematic of the TMR sensor magnetoresistance measurement technique . . . . . 126
Figure 3.17 Initial data from TMR thin film stack before pattering annealed 350°C . . . . . 127
Figure 3.18 $1^{ST}$ TMR sensor design indicating the sensor reference numbers and dimensions . . . . . 127
Figure 3.19 Optical microscope image of the TMR sensor detailing YOKE sensor, junction gaps and top contacts . . . . . 128
Figure 3.20 (a) SEM image of TMR sensor (b) AFM measurement of sensor and junction gaps . . . . . 128
Figure 3.21 (b) TMR sensor 280411 magnetoresistance response major loop (b) magnetoresistance response minor loop . . . . . 129
Figure 3.22 Normalized noise & TMR plotted as a function of magnetic field for TMR sensor 29041 . . . . . 130
Figure 3.23 (a) Schematic of TMR pillar design (b) Optical image of TMR pillar sensor showing bottom electrode, YOKE TMR junction & top electrode . . . . . 131
Figure 3.24 TMR Pillar sensor magnetoresistance measurements from two junctions after 1st anneal 350 °C . . . . . 132
Figure 3.25 (a) Schematic design of the TMR YOKE sensor (b) Optical image of TMR YOKE sensor showing bottom electrode, YOKE TMR junction & top electrode . . . . . 133

Figure 3.26 TMR YOKE sensor magnetoresistance measurements from two junctions after 1st anneal 350 ºC . . . . . 133
Figure 3.27 TMR yoke sensor magnetoresistance response result after 1st annealing at 350°C and 2nd annealing at 110°C showing linear TMR response . . . . . 135
Figure 3.28 TMR YOKE sensor junction magnetoresistance result after second anneal major & minor loops showing linear TMR response . . . . 135
Figure 3.29 TMR YOKE sensor Normalized noise & TMR plotted as a function of magnetic field . . . . . 136
Figure 3.30 TMR YOKE sensor 1/f noise power spectral density as a function of frequency . . . . . 136
Figure 3.31 Figure shows the noise dependency of the YOKE shape TMR sensor to field . . . . . 137
Figure 3.32 Schematic design of the TMR small YOKE sensor . . . . . 137
Figure 3.33 TMR small YOKE sensor magnetoresistance measurements from two junctions after 1st anneal 350 ºC . . . . . 138
Figure 3.34 TMR small YOKE sensor junction magnetoresistance result after first and second anneal showing linear TMR response . . . . . 139
Figure 3.35 TMR small YOKE sensor Normalized noise & TMR plotted as a function of magnetic field . . . . . 139
Figure 3.36 TMR small YOKE sensor 1/f noise power spectral density as a function of frequency . . . . . 140
Figure 3.37 GMR sensor passivated $SiO_2$ 600 nm failed during nanowire detection experiment . . . . . 142
Figure 3.38 RF magnetron sputtering setup for Silicon nitride ($Si_3N_4$) thin films 143
Figure 3.39 $Si_3N_4$calibration XRR fitting . . . . . 145
Figure 3.40 $Si_3N_4$ calibration XRD scan showing no crystalline structure . . . 145
Figure 3.41 (a) $Si_3N_4$ 150nm deposition GMR sensor (b) $Si_3N_4$ deposition no burn-in process . . . . . 146
Figure 4.1 Illustration nanowires per membrane using hexagon geometry . . . 148
Figure 4.2 SEM image cross section of nanowires in the membrane . . . . . 150

Figure 4.3 Cobalt magnetisation hysteresis loop measured using SQUID . . . 152
Figure 4.4 SEM image of Cobalt nanowires in membrane . . . . . 152
Figure 4.5 Cobalt wires after being dissolved from membrane . . . . . 153
Figure 4.6 Hysteresis loop of CoFe nanowires . . . . . 155
Figure 4.7 CoFe-Cu-CoFe nanowires in membrane indicating segments . . . . 155
Figure 4.8 CoFe-Cu-CoFe nanowires after being dissolved from membrane . . 156
Figure 4.9 EDX line scan plot of CoFe-Cu-CoFe nanowires showing transitions of segments . . . . . 156
Figure 4.10 Issue dissolving alumina from the CoFe segment . . . . . 157
Figure 4.11 NaOH at 45 ºC for 5mins (a) TEM of CoFe-Cu-CoFe wires showing alumina present and (b) EDX scan showing showing alumina peak 157
Figure 4.12 NaOH at 45 ºC for 8 mins (a) TEM of CoFe-Cu-CoFe wires showing no alumina present and (b) EDX scan showing no showing alumina peak . . . . . 158
Figure 4.13 CoNi magnetisation hysteresis loop measured using SQUID . . . . 160
Figure 4.14 SEM images of CoNi single segment nanowires . . . . . 161
Figure 4.15 SEM images of CoNi-Cu-CoNi segmented nanowires . . . . . 161
Figure 4.16 EDX line scan of CoNi-Cu-CoNi nanowires . . . . . 162
Figure 5.1 Schematic of nanowire at height ($z$) above the magnetoresistive sensor164
Figure 5.2 Magnetisation curve for measured for Cobalt (Co) magnetic nanowire sample . . . . . 165
Figure 5.3 Model response of Co nano-wires at different heights z above the sensor . . . . . 168
Figure 5.4 Model response of CoFe nanowire at different heights$z$ above the sensor . . . . . 171
Figure 5.5 Model response of $Co_{65}Ni_{35}$ nano-wires in membrane at different heights$z$ above the sensor . . . . . 173
Figure 5.6 Response of nanowire magnetic dipole showing field lines and magnitude . . . . . 174
Figure 5.7 Illustration of nanowire traveling across the sensor in the microfluidic channel . . . . . 174

Figure 5.8 Schematic of nanowire response time . . . . . 176
Figure 5.9 Schematic diagram highlighing design components in the first iteration nanowwire detection system . . . . . 177
Figure 5.10 First iteration of nanowire detection system showing sensor interface, pre-amplifier, SR560 post amplifier and data acquisition board . . 178
Figure 5.11 Single sensor configuration current suppy . . . . . 178
Figure 5.12 (a) Sensor & microfluidic chip interface and (b) placement under microscope . . . . . 179
Figure 5.13 Microfluidic chip single channel design . . . . . 179
Figure 5.14 Single sensor configuration pre-amplifier stage side A . . . . . 180
Figure 5.15 System noise measurements with various post-amplifier gains applied using Stanford Research amplifier type SR560 . . . . . 181
Figure 5.16 System noise considerations at various band-pass filtering using Stanford Research post-amplifier type SR560 . . . . . 182
Figure 5.17 Schematic detection system band-pass filtering on the noise power spectral density for the GMR sensor . . . . . 183
Figure 5.18 INA103 voltage and current noise spectral density . . . . . 184
Figure 5.19 Lab-view interface and block diagram . . . . . 185
Figure 5.20 Figure (a) PHA model fitting (blue line) of the captured nanowire detected responce (red dots), (c) upper and lower threshold set and (c) PHA detected events extracted a signal amplitudes . . . . . 186
Figure 5.21 (a) GMR sensor experimental single sensor configuration and (b) GMR sensor used in the experiment magnetoresistance response measurment . . . . . 187
Figure 5.22 Sensor field calibration configuration . . . . . 188
Figure 5.23 (a) background noise response recorded from GMR sensor with no deionised water flowing (b) background noise response recorded from sensor with deionised water flowing . . . . . 189
Figure 5.24 (a) SEM image of Co nanowires sample 03261108 (b) Microscope inspection image of Co nanowires prior to dispensing . . . . . 190
Figure 5.25 Response of Co nanowires sample 03261108 flowing across sensor . 191

Figure 5.26 Detected events of Co nano-wires sample 03261108 flowing across sensor . . . 192
Figure 5.27 Co nano-wires sample 03261108 model fitting to experimental data 193
Figure 5.28 Detected nanowire events during the experiment extracted as single amplitudes post PHA . . . 193
Figure 5.29 Number of detected nanowire events per field for CoNi 03261108 194
Figure 5.30 Schematic diagram highlighing design component changes in the second iteration nano-wire detection system . . . 195
Figure 5.31 (a) Second iteration nano-wire detection system (b) Detection system showing amplifier stage & Sensor interface . . . 195
Figure 5.32 Sensor interface design . . . 196
Figure 5.33 Sensor interface . . . 197
Figure 5.34 Single sensor post-amplifier side A . . . 197
Figure 5.35 (a) Mirus Venaflux software interface window and (b) Microfluidic pump connected to the sensor interface . . . 198
Figure 5.36 GMR sensor used in the experiment magnetoresistance response measurment . . . 199
Figure 5.37 2nd iteration detection system noise respnse . . . 199
Figure 5.38 (a) Response of Co nanowire using 2nd iteration detection system (b) Detected event in details from the Co nano-wires sample 03261108 200
Figure 5.39 Co nano-wires sample 03261108 PHA model fitting to experimental data using 2nd iteration detection system . . . 201
Figure 5.40 Detected nanowire events during the experiment extracted as single amplitudes from the 2nd iteration detection system . . . 201
Figure 5.41 Number of detected nanowire events per field for CoNi 03261108 in 2nd iteration detection system . . . 202
Figure 5.42 (a) Pre-amplifier high pass filter response and (b) Post-amplifier low pass filter response . . . 202
Figure 5.43 Post-amplifier low pass filter corrected response . . . 203
Figure 5.44 GMR sensor magnetoresistive curve . . . 203
Figure 5.45 Noise response of a GMR sensor in single sensor configuration . . . 204

Figure 5.46 Image of nanowire before dispensing . . . . . 205
Figure 5.47 Response of CoNi 070513 nano-wires flowing across sensor . . . . . 206
Figure 5.48 Response of CoNi 070513 wires detailing detected events . . . . . 206
Figure 5.49 Response of CoNi 070513 wires detailing detected events with longer response time . . . . . 207
Figure 5.50 Nano-wires flowing in channel . . . . . 207
Figure 5.51 CoNi nano-wires sample 070513 model fitting to experimental data 208
Figure 5.52 Detected nanowire events for CoNi batch 070513 during the experiment extracted as single amplitudes post PHA . . . . . 208
Figure 5.53 Number of detected nanowire events per field for CoNi 070513 . . 209
Figure 5.54 (a) TMR single sensor configuration and (b) TMR sensor interface connection . . . . . 210
Figure 5.55 TMR YOKE sensor junction magnetoresistance curve . . . . . 211
Figure 5.56 Background noise response recorded for TMR single sensor configuration . . . . . 212
Figure 5.57 Response of CoFe 111112 nano-wires flowing across TMR sensor . 213
Figure 5.58 Response of CoFe 111112 nano-wires detailing detected events . . 214
Figure 5.59 CoFe nano-wires sample 111112 model fitting to experimental data 215
Figure 5.60 Detected nanowire events for CoNi batch 070513 during the experiment extracted as single amplitudes post PHA . . . . . 215
Figure 5.61 Number of detected nanowire events per field for CoFe 111112 . . 216
Figure 6.1 Schematic diagram highlighing design component changes in the gradiometer nanowire detection system . . . . . 220
Figure 6.2 Illustration of the gradiometer concept . . . . . 221
Figure 6.3 Gradiometer configuration using GMR sensors . . . . . 221
Figure 6.4 Gradiometer pre amplifier stage side A . . . . . 223
Figure 6.5 Gradiometer post amplifier stage side A . . . . . 223
Figure 6.6 Gradiometer current supply side A . . . . . 224
Figure 6.7 Schematic of gradiometer balance procedure . . . . . 225
Figure 6.8 GMR-061115 magnetoresistive response of sensor 1 & 2 . . . . . 225

Figure 6.9 Measured result of balanced gradiometer; trace 1 (yellow) applied bias signal, traces 4 (green) sensor 1 & 2 response after the preamplifier stage and trace 2 (blue) the overall balanced Gradiometer output response after the post-amplifier . . . . . 226
Figure 6.10 a) background noise response recorded from balanced gradiometer sensor GMR-061115 with no deionised water flowing (b) background noise response recorded fromgradiometer sensor with deionised water flowing . . . . . 228
Figure 6.11 Microscope image of CoNi nano-wires batch: 091213-1 before dispensing . . . . . 230
Figure 6.12 Response of CoNi SM319 (091213) wires flowing across gradiometer sensor . . . . . 230
Figure 6.13 Response of CoNi SM319 wires detailing detected events . . . . . 231
Figure 6.14 CoNi single segment nanowires flowing across gradiometer in microfluidic channel . . . . . 232
Figure 6.15 CoNi nano-wires sample SM319 (091213) model fitting to experimental data . . . . . 232
Figure 6.16 Detected nanowire events for CoNi batch SM319 (091213) during the experiment extracted as single amplitudes post PHA . . . . . 233
Figure 6.17 Number of detected nanowire events per field for CoNi batch SM319 (091213) . . . . . 233
Figure 6.18 Response of CoNi SM319 (091213-2) wires flowing across gradiometer sensor . . . . . 235
Figure 6.19 Response of CoNi SM319 (091213-2) wires detailing detected events 235
Figure 6.20 CoNi single segment nanowires flowing across gradiometer in microfluidic channel . . . . . 236
Figure 6.21 CoNi nano-wires sample SM319 (091213-2) model fitting to experimental data . . . . . 236
Figure 6.22 Detected nanowire events for CoNi batch SM319 (091213-2) during the experiment extracted as single amplitudes post PHA . . . . . 237

Figure 6.23 Number of detected nanowire events per field for CoNi batch SM319 (091213-2) . . . 237
Figure 6.24 CoNiCuCoNi 211013-3 microscope image-2 . . . 239
Figure 6.25 Response of CoNi-Cu-CoNi 211013-3 nano-wires flowing across gradiometer sensor . . . 240
Figure 6.26 Response of CoNi-Cu-Coni 211013-3 nanowires detailing detected events . . . 240
Figure 6.27 CoNi-Cu-CoNi nano-wires sample 211013-3 model fitting to experimental data . . . 241
Figure 6.28 Detected nanowire events for CoNi-Cu-CoNi 211013-3 during the experiment extracted as single amplitudes post PHA . . . 242
Figure 6.29 Number of detected nanowire events per field for CoNi-Cu-CoNi 211013-3 . . . 242
Figure 6.30 Response of CoNi-Cu-CoNi 211013-4 nano-wires flowing across gradiometer sensor . . . 244
Figure 6.31 Response of CoNi-Cu-Coni 211013-4 nano-wires detailing detected events . . . 244
Figure 6.32 CoNi-Cu-CoNi nano-wires sample 211013-4 model fitting to experimental data . . . 245
Figure 6.33 Detected nanowire events for CoNi-Cu-CoNi 211013-4 during the experiment extracted as single amplitudes post PHA . . . 245
Figure 6.34 Number of detected nanowire events per field for CoNi-Cu-CoNi 211013-4 . . . 245
Figure 6.35 Schematic diagram highlighing design component changes in the optimised gradiometer nanowire detection system . . . 247
Figure 6.36 Focused Flow channel design and device . . . 248
Figure 6.37 Revised schematic for optimised gradiometer . . . 249
Figure 6.38 Revised gradiometer & fitted with shield under microscope . . . 250
Figure 6.39 GMR- magnetoresistive response of Gradiometer Sensor 1 & 2 . . . 251

Figure 6.40 Measured result of balanced optimised gradiometer; trace 1 (yellow) applied bias signal, traces 4 (green) sensor 1 & 2 response after the preamplifier stage and trace 2 (blue) the overall balanced Gradiometer output response after the post-amplifier . . . . . 251
Figure 6.41 (a) background noise response measured in optimised gradiometer sensor configuration GMR-081215 (b) background noise response measured with deionised water flowing . . . . . 253
Figure 6.42 Background noise comparison between single sensor configuration and optimised gradiometer configuration . . . . . 253
Figure 6.43 101215-1 CoNi nanowire sample deposition conditions . . . . . 254
Figure 6.44 101215-1 CoNi nanowire sample condition used to dissolve from membrane . . . . . 254
Figure 6.45 Image of nanowire batch 101215 CoNi before dispensing . . . . . 255
Figure 6.46 Detected response of the CoNi nano-wires flowing across optimised gradiometer sensor . . . . . 255
Figure 6.47 Detected events of CoNi batch 101215 wire flowing across sensor . 256
Figure 6.48 CoNi batch 101215 single segment nano-wires flowing across GMR sensor gradiometer configuration focus flow microfluidic channel . 257
Figure 6.49 CoNi batch 101215 model fitting to experimental data . . . . . 257
Figure 6.50 Detected nanowire events CoNi batch 101215 during the experiment extracted as signal amplitudes post PHA . . . . . 257
Figure 6.51 Number of detected nanowire events per field for CoNi batch 101215 258
Figure 6.52 Detected response of the CoNi 130116 nano-wires flowing across optimised gradiometer sensor . . . . . 259
Figure 6.53 Detected events of CoNi batch 130116 wire flowing across sensor . 260
Figure 6.54 CoNi batch 130116 single segment nano-wires flowing across GMR sensor gradiometer configuration focus flow microfluidic channel . 260
Figure 6.55 Detected nanowire events CoNi batch 130116 during the experiment extracted as signal amplitudes post PHA . . . . . 261
Figure 6.56 Number of detected nanowire events per field for CoNi batch 130116 261

Figure 6.57 Detected response of the CoNi-Cu-CoNi 071215 nano-wires flowing across optimised gradiometer sensor . . . . . 263
Figure 6.58 Detected events of CoNi-Cu-CoNi batch 071215 wire flowing across sensor . . . . . 264
Figure 6.59 More detected events of CoNi-Cu-CoNi batch 071215 wire flowing across sensor . . . . . 264
Figure 6.60 Detected nanowire events CoNi-Cu-CoNi batch 071215 during the experiment extracted as signal amplitudes post PHA . . . . . 265
Figure 6.61 Number of detected nanowire events per field for CoNi-Cu-CoNi batch 071215 . . . . . 265
Figure 8.1 Schematic showing two ferromagnetic layers with different direction of magnetization . . . . . 286
Figure 8.2 Illustration of the torques acting on the magnetisation during spin current injection. The spin transfer torque acts in the opposite direction to the damping and the field-like torque acts opposite the precession . . . . . 287
Figure 8.3 a) Typical nano oscillator top-contact, based on an RF GSG probe form factor (b) Nano oscillator pillar ~100 nm . . . . . 288
Figure 8.4 GMR based spin torque nano oscillator using point contact. Precession of the magnetisation of the free layer can generate frequency in the GHz range . . . . . 289
Figure 8.5 When H < Hc spin torque induces hysteretic switching between the two stable equilibrium positions . . . . . 289
Figure 8.6 When H > HC magnetisation enters a regime of spin-torque precession 290
Figure 8.7 Schematic of spin-torque diode . . . . . 290
Figure 8.8 Physical mechanism of spin torque diode and comparison to a p-n junction . . . . . 291
Figure 8.9 Schematic of Spin torque diode measurement configuration . . . . 292

Figure 8.10 Figure (a) Output signals from the resonant detector before with (green) & after the beads applied (red). (b) shows resonance frequencies as a function of external magnetic field with and without beads . . . . . 294
Figure 8.11 Elionix 7700 dedicated electron beam (e-Beam) lithography system 296
Figure 8.12 Schematic of the design of the Spin torque diode sensor detailing the bottom electrode, nano-pillar and top electrode and also an image of the Elionix process files for the respective exposure layers 297
Figure 8.13 GMR and TMR multi-layer stack configurations deposited for Spin torque diode sensors . . . . . 298
Figure 8.14 (a) shows an optical image alignment mark (b) registration marks after the 1st EBL exposure . . . . . 299
Figure 8.15 (a) SEM image of the bottom electrode at different exposure dwell times 0.1 to 0.29 µs/dot and (b) SEM image of bottom electrode after ion-milling, using optimum dwell time 0.14µs/dot . . . . . 300
Figure 8.16 SEM image of the top electrode at different exposure dwell times 0.2 to 0.3 µs/dot and (b) SEM image of top electrode after ion-milling, using optimum dwell time 0.14 µs/dot . . . . . 302
Figure 8.17 Schematic of GMR Biosensor fabrication plan . . . . . 303
Figure 8.18 Mask 1 GMR Biosensor YOKE sensors . . . . . 304
Figure 8.19 Mask 2 GMR Biosensor Top layer . . . . . 304
Figure 8.20 Substrate in Chamber A . . . . . 305
Figure 8.21 Optical image of the GMR YOKE sensors & alignment marks after the first mask pattering . . . . . 306
Figure 8.22 Image GMR YOKE sensors with top contacts . . . . . 307
Figure 8.23 TMR YOKE sensor bottom electrode and alignment marks after the first mask pattering . . . . . 310
Figure 8.24 MR YOKE sensor junction after the second mask pattering . . . . 311
Figure 8.25 TMR YOKE sensor with top contacts after the third mask pattering 311
Figure 8.26 Shamrock Chamber A permanent magnet field measurments . . . 312

Figure 8.27 Magnetisation curve for measured for Cobalt (Co) magnetic nanowire sample . . . 317
Figure 8.28 Model response of Co nano-wires at different heights z above the sensor . . . 320
Figure 8.29 Magnetisation curve $Co_{50}Fe_{50}$ . . . 321
Figure 8.30 Model response of CoFe nanowire at different heights$z$ above the sensor . . . 324
Figure 8.31 Magnetisation curve for $Co_{65}Ni_{35}$ nanowires in membrane . . . 325
Figure 8.32 Model response of $Co_{65}Ni_{35}$ nano-wires in membrane at different heights$z$ above the sensor . . . 328
Figure 8.33 Nanowire preparation . . . 337
Figure 8.34 Schematic of Focused flow cell junction . . . 339
Figure 8.35 Minor loop magneto-resistance measurement GMR Bio-sensor 7244 Pad 2 - 3 & Pad 2 - 6 . . . 340
Figure 8.36 Major loop magneto-resistance measurement across each YOKE sensor of Gradiometer GMR Gradiometer Bio-sensor 021012 . . . 341
Figure 8.37 Minor loop magneto-resistance measurements GMR Bio-sensor showing magnetoresistance response & sensitivity . . . 341
Figure 8.38 TMR Sensor 300511 magnetoresistance response with no gaps in Yoke sensor . . . 342
Figure 8.39 TMR Sensor 280411 TMR ratio measured along each juction of YOKE sensor Y5 . . . 343
Figure 8.40 TMR sensor 290411 magnetoresistance response major loop across YOKE sensor Y5 and Y6 . . . 343
Figure 8.41 Design of magneto-fluorescence prototype system . . . 345
Figure 8.42 Integrated Magneto-fluorescence prototype system . . . 345
Figure 8.43 Sensor, filter and fluorescence emission profiles . . . 346
Figure 8.44 Nanowire functionalized mechanism . . . 346
Figure 8.45 Fluorescence intensity from nanowires measured using confocal microscopy and flow cytometry. The mean fluorescence intensity was increased in the presence of the target, compared to a control 347

# 1

# INTRODUCTION

## 1.1 INTRODUCTION

Spin Electronics has become an exciting area of research and development over the last 20 years, targeting the usage of the electron spin as the active element manipulated in transport processes [1]. The magnetic properties of solids derive essentially from the magnetism of their electrons. There are two distinct sources of this magnetism; orbital motion and spin. Spin is an intrinsic property resulting from the fact that the electron behaves as if it were spinning on its own axis thereby possessing a magnetic moment. The three major phenomena used in spintronics are giant magnetoresistance, tunnel magnetoresistance and spin transfer torque. The most remarkable event in this context is the discovery of Giant Magnetoresistance (GMR) in magnetic multilayered structures in 1988 by groups A. Fert [15] and P. Grunberg [16]. They observed a significant change in the resistance of multilayer when the magnetisation of adjacent ferromagnetic layer separated by a nonmagnetic layer were brought into alignment by an applied magnetic field. They showed that the electron flow through the structure is controlled by the relative orientation of magnetisation in adjacent layers. It was not only the electron charge but also the electron spin that was used to operate the device. The discovery of this spin filtering effect generated the new field of research called spintronics [17–19].

Spin is the intrinsic angular momentum of a particle and consequence of relativistic quantum mechanics, which in the case of an electron, is characterised by a quantum number equal to $\pm\frac{1}{2}$. The magnetic moment ($m$) is $-\frac{e}{m_e}s$, where $e$ is the electron change, $m_e$ is the electron mass and $s$ is the spin angular momentum. The spin magnetic quantum number($m_s$) is $\pm\frac{1}{2}$, which indicates there are only two possible angular momentum states, spin-up ($\uparrow$) and spin-down ($\downarrow$) or “majority” and “minority”. The spin angular momentum is twice as effective as orbital angular momentum in creating a magnetic

moment. The atomic nucleus also produces angular momentum in the order $10^{-3}$ less than the electron contribution, meaning the electron is the principal contribution to the magnetic moment.

In ferromagnetic materials, the Coulomb interaction and the Pauli exclusion principle cause long-range ordering of the unpaired spin-up or spin-down electrons leading to the finite magnetic moment, $m$, per unit volume (magnetisation $M$) resulting from the difference of majority ($\uparrow$) and minority ($\downarrow$) density of states (DOS). This difference in the DOS for spin-up and spin-down at the Fermi surface leads to significantly different conductivities for the spin-up and spin-down electrons [20, 21]. Along with the existence of long range interlayer coupling between two ferromagnets separated by a nonmagnetic spacer [22], the non-magnetic material has an equal number of spin-up and spin-down electrons, and so produces no net spin polarisation. These observations were key to the discovery of GMR, and that the transport in ferromagnetic materials is spin dependent and can be considered within the two current model [23]. The advent of GMR renewed the interest in spin dependent tunnelling across semiconductors and insulators leading to demonstrations of high tunnel magnetoresistance ratios (TMR) at room temperature [24, 25] in magnetic tunnel junctions (MTJs). MTJs consist of two ferromagnetic electrodes separated by an insulating barrier. With a high sensitivity to magnetic fields, they are good candidates for applications such as hard drive read heads, logic devices and magnetic random access memories [26–28]. The spin dependent properties in MTJs such as interfaces between the ferromagnetic layer and oxide layers, the junction composition on TMR ratio and temperature dependence of the junction were investigated [29–34]. A breakthrough in the area of spin-dependent tunnelling was the prediction of extremely high tunnel magnetoresistance ratios for certain epitaxially grown magnetic tunnel junctions [35–37]. The prediction was based on a spin filtering effect that arises from the symmetry of the wave functions [38]. Experiments [39–41] confirmed the predictions made by W. H. Butler et al. [36] and J. Mahon et al. [37] for MgO based tunnel junctions. Another phenomenon which plays a role in spintronics, was proposed by J. Slonczewski [42] and Berger [43] who predicted that a spin-polarised current can induce a magnetic switching and dynamic excitation such as sustained precessions in ferromagnetic thin films. Spin transfer torque relates to the interaction of a spin polarised electronic current

with the local magnetisation, where the magnetic moment is transferred from the conduction electrons to the magnetisation, resulting in a change of the magnetisation orientation. The predictions resulted in work to understand the interactions between spin-polarised currents and ferromagnetic nanostructure. Experiments confirmed current-controlled switching and sustained magnetic precessions in magnetic nanostructure in moderate or zero applied magnetic field, finding applications in magnetic random access memories (MRAM) or magnetic oscillators.

Magnetoresistance (MR) sensors based on the Giant Magnetoresistance effect (GMR) have been incorporated into numerous industrial applications requiring magnetic sensing for speed and angle detection [44, 45]. They have found applications in the computer memory industries (hard drive storage) replacing anisotropic magnetoresistance (AMR) sensors [46]. The continuous development of GMR sensors with increased sensitivity detection in the nano tesla range, has lead to a focus in biomagnetic detection such as magnetocardiography (MCG), or for detecting magnetically-labelled biomarkers (Pannetier-Lecoeur et al 2011 and Freitas et al 2012) [47, 48]. Currently there is a focus on utilising advances in magnetoresistive sensors, both GMR, TMR and STO (Spin Torque Oscillators) into these lab-on-chip biomedical platforms, with the aim to improve current bio-sensing techniques providing higher sensitivity and less expensive instrumentation.

This research is focused on detecting the stray field of single individual magnetic nanowires and/or the magnetic segments within multi-segment nanowires as they flow across a magnetoresistive (MR) sensor. A schematic illustration of the magnetic nanowire detection concept is shown in Figure 1.1. The ferromagnetic nanowires produce a stray field indicated by the directional field lines. As the magnetic nanowires pass over the magnetoresistive sensor they change the angle of the magnetisation of the sensors free layer with respect to the pinned layer, changing the overall resistance of the sensor. Detecting single individual magnetic nanowires the device will act as a flow cytometer for counting. The final application will be the detection of molecular biomarkers, which are attached to the functionalized magnetic nanowires. By detecting the magnetic segments within a multi-segment nanowire the multi-segment nanowire will act as a magnetic barcode to a specific molecular biomarker.

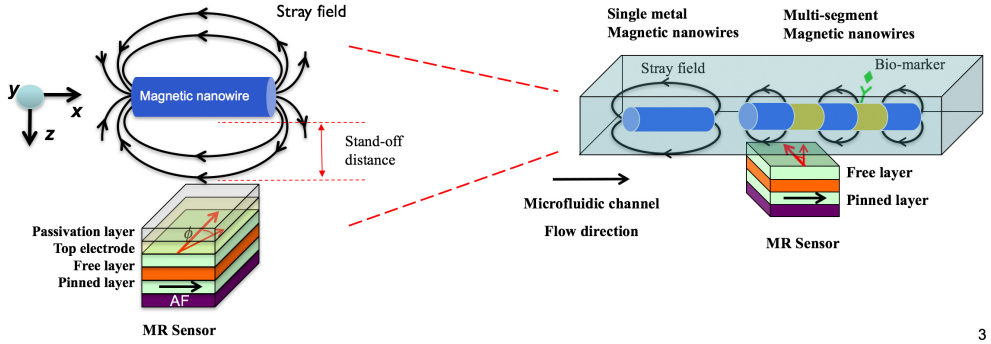



Figure 1.1: Schematic illustration of the magnetic nanowire detection concept

The magnetic nanowire detection system was part of an overall platform, which included a fluorescent sensor system. This was in collaboration with the project partner companies Cellix and Radisions as part of an Europeen FP7 project. The project aimed to investigate magnetic sensors and fluorescent sensor technologies with the aim to develop a portable and cost effective flow cytometry platform for applications such as early detection of cancer cells. Figure 1.2 shows a schematic of the project concept for the magneto-fluorescence prototype system, see Appendix 8.9 for additional information.

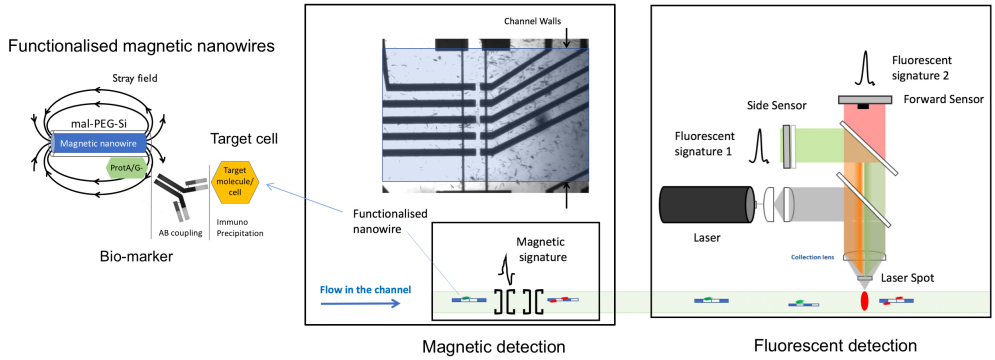



Figure 1.2: Concept design of magneto-fluorescence prototype system

Conventional Flow cytometry is a technique for counting & examining biological cells. Utilizing hydrodynamic focusing, the cells are suspended in a stream of fluid and passed via a laser light source for scatter & fluorescence detection. Optics gather & direct the light to detectors which receive the light and electronics for digital data analyses. Cells passing the laser beam scatter light at two angles, which is detected as FS (forward scatter) and SS (side scatter). FS correlates with cell size and SS is proportional to the granularity of the cells. In this manner, cell populations can often be distinguished based

on differences in their size and granularity alone. Along with counting the flow cytometry measures fluorescence intensity with up to three fluorescence's measured. These are produced by fluorescent-labeled antibodies detecting proteins, or ligands that bind to specific cell-associated molecules such as propidium iodide binding to DNA. Typically, a detection count of $10^4 \sim 10^7$ cells is required for a statistically significant detection. Before cells are dispensed into the flow cytometer for analysis, a staining procedure is used. The cells are incubated in tubes or microtiter plates with fluorochrome-labeled antibodies, typically the cells are killed during this process.

My motivation for investigating magnetic nanowire detection using magnetoresistive sensors over conventional flow cytometry detection are,

1. Counting – Magnetic detection can match single event counting detection compared to Flow Cytometry

2. Cells don't die – The process of staining cells for fluorescence detection usually kills the cells. In magnetic detection, the nanowires adhere to the cells via a functionalization process (cells live)

3. Information rate – In flow cytometry up to 3 bits of information can be detected per event, which is 8 possible outcomes per event. In comparison, a 5-segment nanowire will yield 5 bits of information per event, which is 32 possible outcomes per event

4. Cost – Flow cytometry devices cost in the order of €40K, with annual running consumable costs. Magnetic detection with regard to sensors and nanowires is a fraction of the cost

The detection of molecular biomarkers utilising magnetic beads or nanowires has led to research along a number of directions. Firstly, the synthesis of magnetic beads and nanowires with required magnetic properties for detection, which can be functionalized to molecular biomarkers. Secondly the development of magnetoresistive sensors for a quantitative detection of single magnetic beads and nanowires. Finally, development of microfluidic circuits for controllable transfer of bio-molecular beads and nanowires to the desired area on the biochip. This research will focus on the development of

magnetoresistive sensors, fabrication of magnetic nanowires and the development of the detection systems used for the detection of the magnetic nanowires. Figure 1.3 shows a block diagram detailing the various components that contribute to the overall magnetic nanowire detection scheme, which I will refer to systematically throughout this thesis as I discuss the various components and developments.

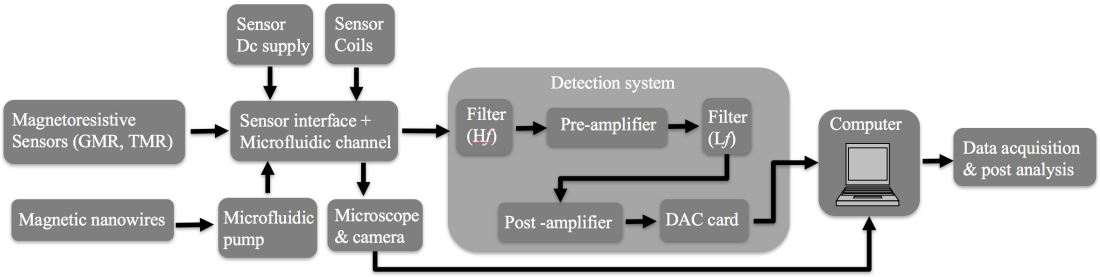



Figure 1.3: Block diagram detailing the design components in overall magnetic nano-wire detection scheme

## 1.2 THESIS OUTLINE

In this thesis, Chapter 1 discusses the theory of magnetism and magnetoresistance. The development of magnetoresistive sensors, both GMR and TMR, and sensor noise considerations. The chapter also discusses the electrodeposition process and the deposition of magnetic nanowires. Finally, I discuss a review of magnetic nanowire detection. Chapter 2 describes the experimental methods and techniques used for the deposition, fabrication and characterisation of magnetoresistive sensors and magnetic nanowires. Chapter 3 discusses the design and fabrication of the GMR and TMR Sensors, the GMR sensor characterisation results including sensor resistance measurements of junctions, magnetoresistance measurements and noise measurements; the TMR sensor characterisation results including sensor resistance measurements of junctions, magnetoresistance measurements and noise measurements. Chapter 4 discusses the fabrication of magnetic nanowires, both single magnetic nanowires and segmented nanowires that were used for investigation in my experiments for the detection of magnetic nanowires using the magnetoresistive sensors. Chapter 5 discusses the principles for magnetic nanowire detection using magnetoresistive sensors. Chapter 5 also outlines the design, development and

characterisation of the detection systems used for the detection of magnetic nano-wires using GMR sensors and TMR sensors in single sensor configuration and the results of the nanowire detection experiments of the GMR and TMR sensors in single sensor configuration. Chapter 6 discusses the development of the gradiometer configuration for noise reduction and the final optimised gradiometer configuration with integrated electronic detection system. Finally this chapter discusses the nanowire detection experiments carried out on the respective gradiometer systems and the nanowire detection experiments on two magnetic segment nanowires. Chapter 7 discusses the conclusions of the research work and forward plans.

## 1.3 THEORY OF MAGNETISM

Magnetism describes the forces exerted on an object in the presence of a magnetic dipole moment, $m$, which produces a magnetic field. A magnetic field is produced whenever there is electrical charge in motion. This could be an electrical current flowing in a conductor. The magnetic moment $m$ is equivalent to a current loop

$$m = IA \tag{1.1}$$

Where $I$ is the current and $A$ is the area of the loop, measured in units $Am^2$. This is the simplest circuit, which can generate a magnetic field as shown in Figure 1.4(a), which shows the magnetic field lines $B$, produced due to a current loop.

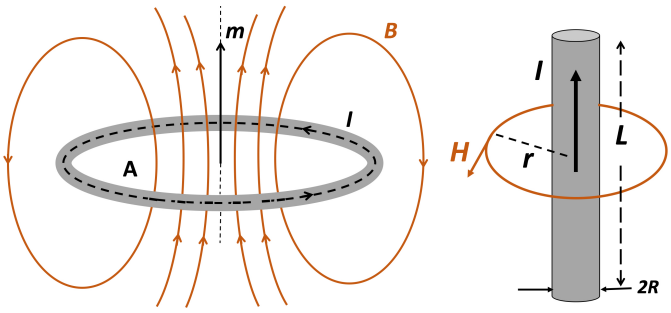



Figure 1.4: (a) Magnetic field line produced due to a current loop (b) Magnetic field produced due to current in a length of conductor

The force exerted by a magnetic field upon a charged particle is given by,

$$F = q(B \times v) \tag{1.2}$$

Where $v$ is the velocity of the particle, and $q$ is its charge. A magnetic dipole is formed by the movement of particles carrying charge, and will experience a torque $\tau$, so that the moment , $m$, is aligned with the field, $B$.

$$\tau = m \times B \tag{1.3}$$

When current flows along the length of conductor, a rotating magnetic field $H$, is induced perpendicular to the direction of current flow. Figure 1.4(b) shows the magnetic field $H$ produced along the length of conductor, the units are ampere-turns per meter, or just amperes per meter. The magnetic field $H$ generated by an electrical current, can be calculated using the Biot-Savart law, giving the field contribution generated by a current flowing in a length of conductor.

$$\delta H = \frac{1}{4\pi r^2} i\delta l \times u \tag{1.4}$$

Where $i$ is the current flowing in a length $\delta l$ of conductor, $r$ is radial distance,$u$ is the unit vector along the radial distance.

Ampere deduced that a magnetic field is produced by electrical charge in motion and is dependent on the conduction path and the current carried.

$$Ni = \int_{closedpath} H \centerdot dl \tag{1.5}$$

Where $N$, is the number of current-carrying conductors, each carrying a current $i$ amps. This is the source of the magnetic field $H$ and $l$ is a line vector. Coiling the conductor into a solenoid of $N$ closely spaced turns, having a length $L$, and carrying a current of magnitude $i$,

$$H = \frac{Ni}{L} \tag{1.6}$$

The magnetic field will form lines through the centre of the solenoid, looping back upon itself as shown in Figure 1.5(a). The field lines produced are similar to the magnetic field lines produced from a permanent magnetic dipole as illustrated in Figure 1.5(b). In a permanent magnet, it is the orbital motions and spins of electrons within the magnet, which lead to a magnetisation within the material and a magnetic field outside [1, 5, 49–51].

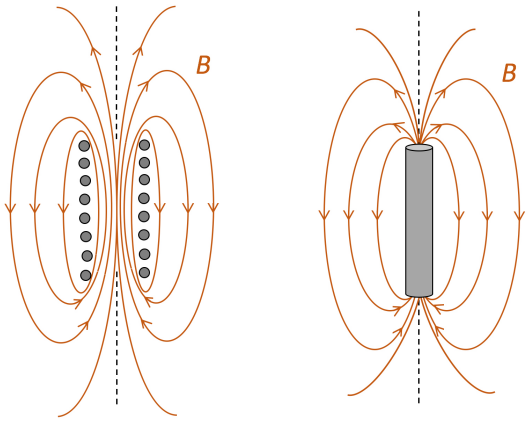



Figure 1.5: (a) Magnetic field line created in a solenoid configuration and (b) magnetic dipole field lines from a permanent magnet

When a magnetic field $H$ is generated in a medium, the response of the medium is the magnetic induction field or flux density. The units for $B$ are Tesla, and the $B$ field represents the magnitude of the internal field strength within a substance that is subjected to the $H$ field. When a magnetic field $H$ is generated in a current loop there is also a magnetic energy $E$ given by,

$$E = \frac{1}{2} i\Phi \tag{1.7}$$

Where $i$ is the current and $\Phi$ is the amount of magnetic flux generated. The magnetic flux $\Phi$, unit's Weber, and its rate of change can be measured as it generates an e.m.f in a closed circuit conductor through which the flux passes. The Weber is the amount of magnetic flux. When reduced to zero in 1 second, it produces an e.m.f of 1 volt in a one-turn coil. Linking the magnetic quantity, flux, with the energy is useful when characterising the 'strength' of a magnetic dipole $m$. The flux density in Weber per square meter is the magnetic induction $B$. One Weber per square meter is equal to

a magnetic induction of 1 Tesla. Magnetic induction $B$ is described in terms of force on a moving electric charge. Magnetic induction $B$ of 1 Tesla generates a force of 1 Newton per meter on a conductor carrying a current of 1 ampere perpendicular to the direction of the induction. The relationship between the magnetic field strength $H$ and the magnetic induction $B$ is a property called the permeability of the medium µ.

$$B = \mu H \tag{1.8}$$

The permeability is a property of the specific medium through which the $H$ field passes and in which $B$ is measured. Permeability has dimensions of webers per ampere-meter (Wb/A-m) or henries per meter (H/m). In free space or vacuum,

$$B = \mu_0 H \tag{1.9}$$

Where $\mu_0 = 4\pi \times 10^{-7}$ $\mathrm{Hm}^{-1}$ is the permeability of free space. In many media $B$ is a linear function of $H$. In permanent magnets such as ferromagnets and ferrimagnets, $B$ is not a linear function of $H$, or even a single-valued function of $H$, a plot of the $B$ versus $H$ curve will demonstrate this as shown in Figure 1.13. The relative permeability of a material is a measure of the degree to which the material can be magnetised, or the ease with which a $B$ field can be induced in the presence of an external $H$ field. It is the ratio of the permeability in a material to the permeability in a vacuum

$$\mu_r = \frac{\mu}{\mu_0} \tag{1.10}$$

There are two contributions to the magnetic induction $B$, one from the magnetic field $H$ and one for the magnetisation $M$ of the medium. The magnetisation $M$ units A $\mathrm{m}^{-1}$, of a permanent magnet is the local moment density per unit volume in the solid.

$$M = \frac{m}{V} \tag{1.11}$$

If a material has $n$ atomic magnetic dipoles per unit volume, each of which has a magnetic moment $m$, then the magnetic moment per unit volume of the material when all these moments are aligned is termed saturation magnetisation $Ms$, which is generated by

the spin and orbital angular momentum of electrons within the solid. The magnetic induction $B$ in free space is a vector sum of the magnetic field $H$ and magnetisation $M$ contributions,

$$B = \mu_0 H + \mu_0 M \tag{1.12}$$

In the presence of an $H$ field, the magnetic moments within a material tend to become aligned with the field and to reinforce it by virtue of their magnetic fields; the term $\mu_0 M$ is a measure of this contribution.

The magnetic field lines $H$ around a bar magnet have the same direction as the magnetic flux lines $B$, $B = \mu_0 H$ in free space. However inside a magnet the $B$ and $H$ fields point in opposite directions due to the magnetisation $M$ of the material as shown in Figure 1.6 which shows the quantities $B$, $H$ and $M$ for a uniformly magnetised block of material in the absence of any external field. The field lines of $B$ are continuous. $H$ is oppositely directed to $M$ inside the magnet.

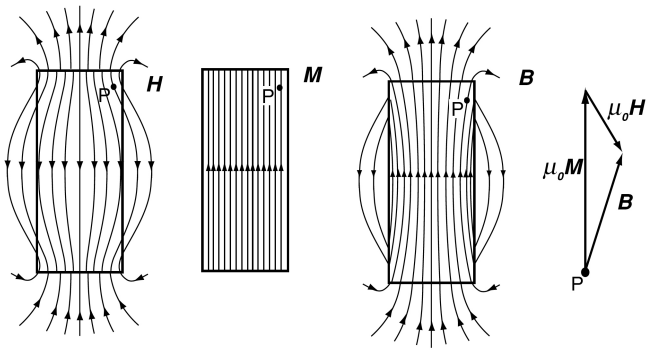



Figure 1.6: Field lines B, M and H produced for a for a magnet [1]

Magnetisation $M$ is created by aligning magnetic dipoles within a magnet, which create positive and negative magnetic charge near the ends of the magnet of finite length. This gives rise to a magnetic field that will oppose an applied field. This opposing field is called the demagnetisation field $H_d$ and its strength is dependent on the geometry and the magnetisation $M$ of the material.

The response of a magnetic material to an applied magnetic field can be represented using its susceptibility $\chi$,

$$\chi = \frac{M}{H} \tag{1.13}$$

### 1.3.1 *Atomic Magnetism*

The macroscopic magnetic properties of materials are a consequence of magnetic moments associated with individual electrons. The atom, as it is understood, consists of a nucleus of protons and neutrons, being orbited by electrons [52–54]. Since protons have a charge equal and opposite to that of an electron, there is a net zero electrical charge within a non-ionised atom. In the classical model the angular momentum of the electrons can be used to determine the magnetic moments of electrons by invoking the concept of electrical charge in motion whereby a current loop behaves as a magnetic dipole and has an associated magnetic moment. There are two contributions to the electron magnetic moment: an orbital magnetic moment due to orbital angular momentum of the electron, and a spin magnetic moment due to electron spin, which is illustrated in Figure 1.7. The spin magnetic moment is twice as effective as the orbital magnetic moment. The movement of the orbiting electron creates a magnetic dipole moment, $ml = iA$, where $i$ is the current and $A$ is the area of the loop. The electron has an orbital period, given by the ratio of its velocity to the circumference of its orbit.

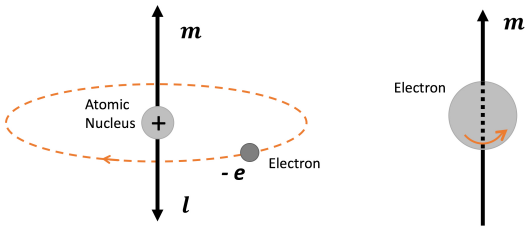



Figure 1.7: Magnetic dipole moment and angular momentum of Bohr atom and moment due to electron

Thus, the moment is given by,

$$m_l = -\frac{ev}{2\pi r} \cdot \pi r^2 = -\frac{evr}{2} \tag{1.14}$$

Since the electron has a negative charge, the dipole moment is in the opposite direction to the orbital angular momentum, $L = M_e vr$, where $M_e$ is the mass of the electron. The moment can in turn be expressed in terms of the momentum,

$$\frac{m_l}{L} = -\frac{e}{2M_e} = -\frac{\mu_B g_l}{\hbar} \tag{1.15}$$

Here, $\mu_B = eh/2M_e$ is the Bohr magneton, a natural unit of atomic magnetic dipole moments with a value $9.274 \times 10^{-24}$, and $g_l = 1$ is the orbital $g$ factor. These parameters are chosen, as the ratio of the moment and the momentum can be seen to be a constant.

The orbital momentum is quantised, as $L = \hbar\sqrt{([l(l+1)])}$, a degeneracy which allows $2l + 1$ possible energy states to be occupied in each orbit, where $l$ is the orbital quantum number. The electron also has a further intrinsic angular momentum associated with it, namely spin. Spin angular momentum is a relativistic quantum property; it is quantised similarly to orbital angular momentum, where $S = \hbar\sqrt{([s(s+1)])}$, and s is the spin quantum number. As opposed to $l$, which is an integer, $s$ can be a half-integer. For electrons, $s = \frac{1}{2}$, and therefore $2s + 1 = 2$. For each orbital state, there is an additional degeneracy, with two electrons occupying each state, one with spin $+\frac{1}{2}$ and the other $-\frac{1}{2}$. This spin angular momentum then has a magnetic dipole associated with it,

$$m_s = \frac{\mu_B g_s}{\hbar S} \tag{1.16}$$

Where $g_S = 2$ is the spin $g$ factor. Since the electron has a dipole moment, it will align with a magnetic field. The electron then has a total angular momentum given by,

$$J = L + S = \hbar\sqrt{([j(j+1)])} \tag{1.17}$$

Electrons will occupy the first spin state of each available orbital state, starting with the state with the highest $L$, before occupying the second spin state. A pair of electrons in a single orbital will have opposite spin, and therefore their magnetic moments will cancel out. Similarly, as the shell is filled, the orbital angular momenta will begin to cancel out. The net magnetic moment for an atom is the sum of the magnetic moments of each of the constituent electrons, including both orbital and spin contributions, and

taking into account moment cancellation. For an atom having completely filled electron shells there is total cancellation of both orbital and spin moments.

### 1.3.2 *Banding*

When two or more atoms come together they interact and change the magnetic moment. As the number of atoms in a solid increases, the energy levels of the electrons will spilt proportionally, forming a spread of non-discrete energy states, known as an energy band. As the distance $d$, between atoms gets smaller the energy bands can overlap [5, 52–54] as illustrated in Figure 1.8 which shows the dependence of the internuclear separation distance between atoms for the formation of energy bands. When a potential is applied to the material, the electrons energy will increase moving into higher energy states. Electrons can move between the shared bands, through available energy states and the material acts as a conductor. When there is no overlapping between a partially empty band and a filled band, electrons will have no available states through which to move and the material is an insulator. The density of states (DoS), is the number of states at a given energy $E$ per unit volume, and provides information about the electronic properties of the material, as it shows the available energy states up to and beyond the Fermi energy level. The DoS in the three-dimensional free electron model has a parabolic shape proportional to $\sqrt{E}$.

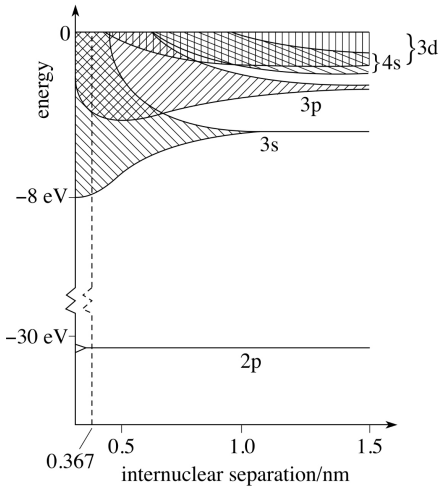



Figure 1.8: Formation of energy bands in solids, dependent on the separation distance between atoms

The bands of a material are finite in energy; meaning that the DoS are also finite and so is closed. Each of the sub-shells has a different shape due to the spread of their respective energy bands. Overlapping of bands then increases the number of available states at a given energy.

The conduction of electrons can be considered as two separate channels, one for each spin [55]. This then means that there are separate DoS for each spin as well. The electrons will fill each of the spin levels at equal rates. However, if sufficient energy is available, the spin of one or more of the electrons can be reversed, causing a spin imbalance. This imbalance can be affected by the presence of a magnetic field, and causes a shift in the DoS of the system resulting in a magnetic moment associated with them. Since magnetic moments can only arise from unpaired electrons, a filled energy band cannot contribute to a magnetic moment, since all electron spins will be paired giving $L = 0$ and $S = 0$. In a partially filled energy band, it is possible to have an imbalance of spins leading to a net magnetic moment per atom. If the half bands are exchange split as illustrated in Figure 1.9, the electrons can occupy the spin down half band before the spin up half band is full. This leads to a non-integral number of magnetic moments per atom.

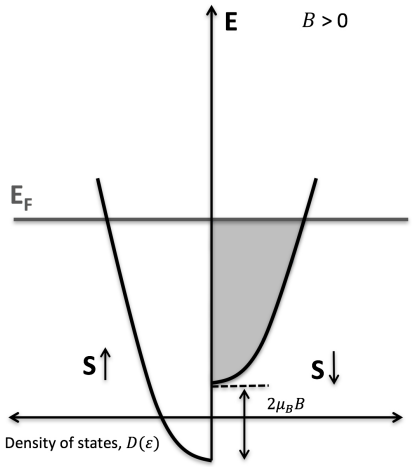



Figure 1.9: DOS showing exchange splitting of spin up and spin down half bands [1]

For example, consider a crystal with ten atoms. Each electron will have ten available levels, each with a spin up and spin down component. The first five levels will be filled equally as illustrated in Figure 1.10 (a). If the spin of one electron is reversed Figure 1.10 (b), then there will be six electrons with spin in one direction, and four with spin in

the other. This gives us an imbalance of two electrons, resulting in a magnetic moment of 0.2 µB per atom. This imbalance can be affected by the presence of a magnetic field, and causes a shift in the DoS of the system.

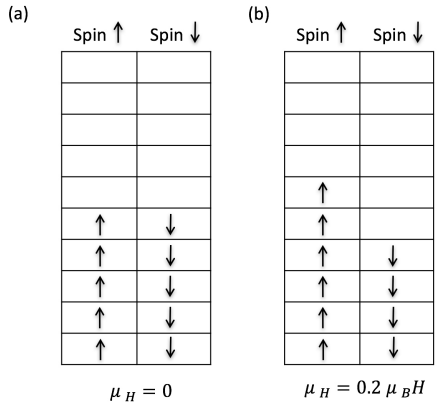



Figure 1.10: Diagram representing the occupation of allowed energy states in an electron band (a) balanced number of Spin up & spin down electrons (b) unbalanced number of spin up & spin down electrons due to exchange interaction leading to a net magnetic moment

Atoms in a solid will arrange in a parallel orientation under certain conditions. This is caused by an exchange interaction, which is dependent on interatomic spacing. The spins of the atoms are coupled in the most energetically favourable manner, leading to a large molecular magnetic field $H^i$ in the lattice, which leads to a spontaneous spin imbalance. This results in a net magnetic moment that will interact with a field. The internal molecular magnetic field $H^i$ is given as $H^i = n_w M + H$, where $n_w$ is the Weiss coefficient. If $n_w$ is large enough, the magnetisation of the material will be self-saturating, leading to spontaneous magnetisation of the material or ferromagnetism.

Spontaneous spin imbalance causes ferromagnetic materials to become spin polarised, having a higher number of electrons of one spin at the Fermi energy. This leads to conduction electrons from the Fermi surface being spin polarised. The Stoner criterion is used as a metric for determining the potential for an element to be ferromagnetic, and is defined as:

$$N_{\uparrow\downarrow}(\varepsilon_F) > \frac{1}{J} \tag{1.18}$$

$N_{\uparrow\downarrow}(\varepsilon_F)$ is the density of states at the Fermi energy per atom, for each spin, and $\jmath$ is the Stoner exchange parameter for atomic interaction. 3d DoS transition elements iron, cobalt and nickel show ferromagnetism.

In ferromagnetic metals the scattering rates of the spin up (↑) and spin down (↓) electrons are different. The band structure in a ferromagnet is exchange split, so that the density of states is not the same for spin up (↑) and spin down (↓) electrons at the Fermi level. Scattering rates are proportional to the density of states, so the scattering rates and therefore resistivities are different for electrons of different spin. This is illustrated in Figure 1.11 which shows the density of states of transition metals Fe, Co, Ni and Cu [2]. A non-magnetic metal such as Cu has an equal density of spin up (↑) and spin down (↓) electrons at the Fermi level. In the ferromagnetic metals Co and Ni, the majority (↑) d-band is fully occupied and is situated below the Fermi level, whereas the minority spin band (↓) is only partially occupied. This results in different scattering rates for spin up and down electrons at the Fermi level, as there is a difference in the density of available states into which the electrons can be scattered.

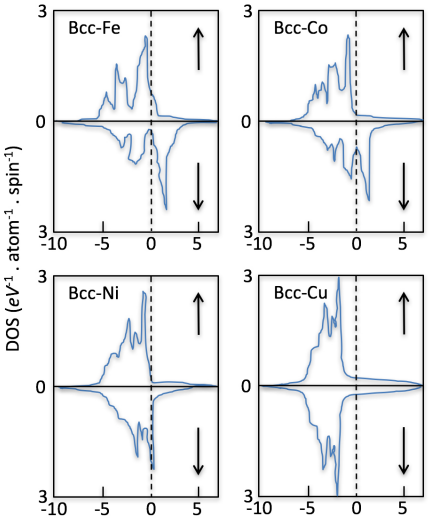



Figure 1.11: Density of states of transition metals Fe, Co, Ni and Cu [2]

### 1.3.3 *Magnetic materials*

The macroscopic behaviour of magnetic materials can be classified using a few magnetic parameters. The various different types of materials can be classified according to their

bulk susceptibility $\chi$, the first group for which the $\chi$ is small and negative $\chi \approx 10^{-5}$ are called diamagnetic, their magnetic response opposes the applied magnetic field. Examples are copper, silver and gold. The second group of materials for which the $\chi$ is small and positive and typically $\chi \approx 10^{-3} - 10^{-5}$ are paramagnets. The magnetisation is weak but aligned parallel with the direction of an applied magnetic field. Examples of paramagnets are aluminium, platinum or manganese. In ferromagnetism, the magnetic susceptibilities can be as high as $\chi \approx 10^{6}$and manifest very large and permanent magnetisations. They exhibit highly non-linear hysteretic behaviour.

### 1.3.4 *Diamagnetism and Paramagnetism*

All materials exhibit a diamagnetic response to magnetic field. The response is a very weak form of magnetism and persists only while an external field is being applied. It is induced by a change in the orbital motion of both localised electrons (Langevin) and delocalised electrons (Landau), due to an applied magnetic field. The magnitude of the induced magnetic moment is extremely small, and in a direction opposite to that of the applied field. Thus, the magnetic susceptibility is negative; that is, the magnitude of the $B$ field within a diamagnetic solid is less than that in a vacuum. The volume susceptibility for diamagnetic solid materials is in the order of $\chi \approx 10^{-5}$ . Figure 1.12 (a) shows an illustration of the atomic dipole configuration for a diamagnetic material with and without a magnetic field. In the absence of an external field, no dipoles exist; in the presence of a field, dipoles are induced that are aligned opposite to the field direction.

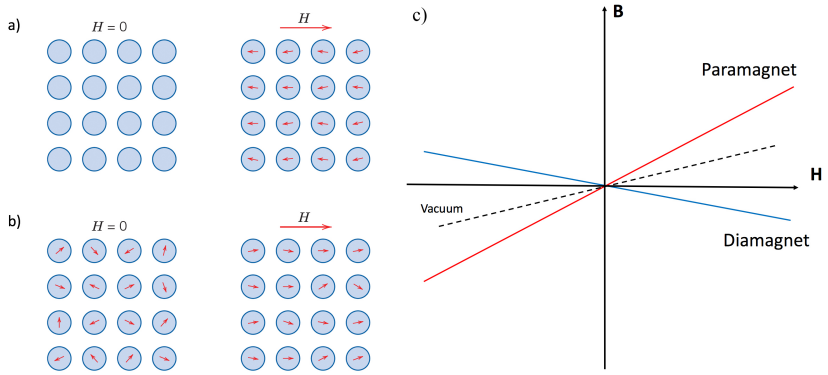



Figure 1.12: (a) Atomic dipole configuration for a diamagnetic material with and without a magnetic field (b) atomic dipole configuration with and without an external magnetic field for a paramagnetic material (c) Paramagnet and Diamagnet response

In some materials, each atom possesses a permanent dipole moment due to incomplete cancellation of electron spin and/or orbital magnetic moments. The orientations of these atomic magnetic moments are random, such that a piece of material possesses no net macroscopic magnetisation. When an external field is applied, the atomic magnetic moments align and give rise to Paramagnetism. Figure 1.12(b) shows the atomic dipole configuration with and without an external magnetic field for a paramagnetic material. The dipoles align individually with no mutual interaction between adjacent dipoles and give rise to a relative permeability that is greater than unity and a small but positive magnetic susceptibility. Susceptibilities for paramagnetic materials range from $\chi \approx 10^{-3}$ to $\chi \approx 10^{-5}$. At constant temperature and for relatively low values of magnetic field H, the magnetic $\chi$ of diamagnetic and paramagnetic materials is constant and 'linear' where $M$ is proportional to $H$.

$$M = \chi H \tag{1.19}$$

$$B = \mu_0(1+\chi)H \tag{1.20}$$

$$= \mu_0\mu_r H \tag{1.21}$$

Figure 1.12(c) shows a schematic of the $B$ versus $H$ field response for a diamagnetic and paramagnetic material.

### 1.3.5 *Ferromagnetism*

Certain metallic materials possess a permanent magnetic moment in the absence of an external magnetic applied field, as illustrated in Figure 1.13(a) which shows the mutual alignment of atomic dipoles. They manifest very large and permanent magnetisations. These are the characteristics of ferromagnetism, and are the transition metals iron (as BCC ferrite), cobalt, nickel, and some of the rare earth metals such as gadolinium (Gd). Magnetic susceptibilities as high as $\chi \approx 10^6$ are possible for ferromagnetic materials and can be expressed as,

$$B \equiv \mu_0 M \tag{1.22}$$

Due to the self-saturating nature of ferromagnetic materials they exhibit non-linear hysteretic behaviour. This is due to the strong Weiss molecular field. Figure 1.13(b) shows the hysteresis loop (Hysteresis - to lag behind) for a ferromagnetic material.

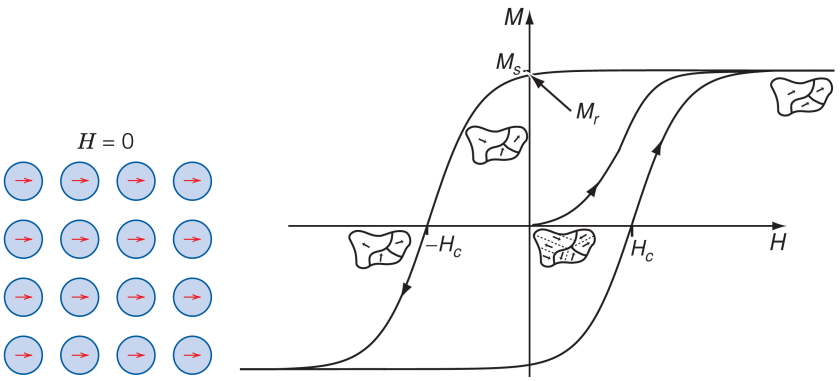



Figure 1.13: (a) Mutual alignment of atomic dipoles for a ferromagnetic material (b) Hysteresis of a ferromagnetic material starting from a demagnetised sample, showing saturation magnetisation $M_S$, remanent magnetisation $M_r$, and coercivity $H_C$ in the easy axix [1]

The hysteresis loop can define a number of magnetic properties of the material. Firstly saturation magnetisation $M_0$ gives the upper limit of the magnetisation that can be achieved, this is saturation magnetisation at 0K. At temperature below the Curie point the technical saturation $M_s$ is used. The height of the curve along the $M$ axis is the remanence $M_r$, this is the remaining magnetisation when the field is reduced to zero. The width of the loop across the $H$ axis, which is twice the coercivity $H_c$ is an independent

parameter. The coercivity $H_c$ is the field strength required to reduce the magnetisation to zero. Other properties include the slope of the curve at the coercive point and also the initial permeability $\mu_{in}$'. From this the bulk magnetic properties of the material can be characterised. The maximum possible magnetisation, or saturation magnetisation of a ferromagnetic material represents the magnetisation that results when all the magnetic dipoles in a solid piece are mutually aligned with the external field. The saturation magnetisation is equal to the product of the net magnetic moment for each atom and the number of atoms present. For each of iron, cobalt, and nickel, the net magnetic moments per atom are 2.22, 1.72, and 0.60 Bohr magnetons, respectively. Ferromagnetic or ferrimagnetic material below its Curie temperature, $T_C$, is composed of small volume regions in which there is a mutual alignment in the same direction of all magnetic dipole moments called domains as shown in Figure 1.14 (a).

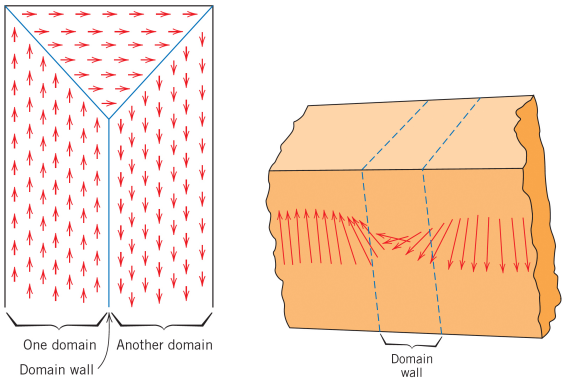



Figure 1.14: (a) Schematic depiction of domains in a ferromagnetic or ferrimagnetic material; arrows represent atomic magnetic dipoles. Within each domain, all dipoles are aligned, whereas the direction of alignment varies from one domain to another. (b) The gradual change in magnetic dipole orientation across a domain wall [3]

Each domain is magnetised to its saturation magnetisation. Adjacent domains are separated by domain boundaries or walls, across which the direction of magnetisation gradually changes Figure 1.14 (b). Domains are microscopic in size, and for a poly-crystalline specimen, each grain may consist of more than a single domain. Thus, in a macroscopic piece of material, there will be a large number of domains, and all may have different magnetisation orientations. The magnitude of the magnetisation $M$ for the entire solid is the vector sum of the magnetisations of all the domains, each domain contribution being weighted by its volume fraction. For an un-magnetised specimen,

the appropriately weighted vector sum of the magnetisations of all the domains is zero. Figure 1.15 shows the initial magnetisation curve of a ferromagnetic material, with the domain structures represented in the insets. As the $H$ field is applied, the domains change shape and size by the movement of domain boundaries.

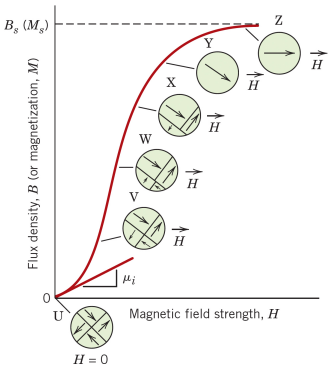



Figure 1.15: The B-versus-H behaviour for a ferromagnetic or ferrimagnetic material that was initially un-magnetized. Domain configurations during several stages of magnetisation are represented. Saturation flux density magnetization and initial permeability are also indicated [4]

Initially, the moments of the constituent domains are randomly oriented such that there is no net magnetisation. As the external field is applied, the domains that are oriented in directions favourable to the applied field grow at the expense of those that are unfavourably oriented. This process continues with increasing field strength until the macroscopic specimen becomes a single domain, which is nearly aligned with the field. Saturation is achieved when this domain, by means of rotation, becomes oriented with the $H$ field.

When a ferromagnetic material is heated to beyond its Curie temperature, $T_C$, it becomes paramagnetic. The Curie temperature is then equivalent to the temperature at which the paramagnetic susceptibility diverges $\theta$, and is dependent on the strength of the Weiss molecular field within the material. Iron exhibits a $T_C$ of 1044K and Cobalt has a $T_C$ of 1403K. As the temperature is increased up to $T_C$, the spontaneous saturation magnetisation $Ms$ decreases proportionally to the square root of the difference between the Curie temperature and the temperature of the sample:

$$M_S \alpha M_0 \sqrt{(T_C - T)} \tag{1.23}$$

Each material has a different moment per atom, and different Weiss coefficient, leading to the variation in $M_S$ and $T_C$. Figure 1.16 (a) shows the magnetisation and susceptibility curves below and above the Curie temperature and Figure 1.16 (b) the Saturation magnetisation of iron, cobalt, and nickel as a function of temperature.

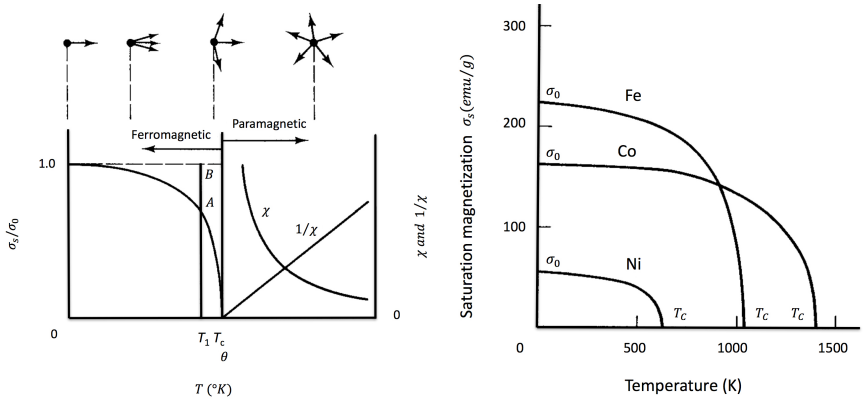



Figure 1.16: (a) magnetisation and susceptibility curves below and above the Curie temperature. The small sketches at the top represent the distribution of classical spin directions, in zero applied field within a single domain (below $T_c$), and in a group of atoms (above $T_c$) (b) Saturation magnetisation of iron, cobalt, and nickel as a function of temperature [5]

Ferromagnetic materials display anisotropic magnetisation. This means that the axis of magnetisation lies along a given direction, called the easy axis. This anisotropy, Ku, stems from three main sources:

- Shape anisotropy, wherein an internal demagnetising field is different in one axis than the others, due to the shape of the particle (spherical particles will have no shape anisotropy)
- Induced anisotropy, wherein the material is magnetically annealed or stressed. This adds additional energy into the lattice and allows the spin orientation of the atoms to take another direction
- Magneto-crystalline anisotropy, wherein the crystal structure of the material determines the favoured direction. The spins of the atoms in the lattice will be oriented in the direction that is most energetically favourable, as determined by the exchange interaction.

The tendency to form a ferromagnetic material is heavily dependent upon the crystal lattice that forms the solid. The elements iron, cobalt and nickel are transition elements,

with narrow 3d DoS that exhibit ferromagnetism. The magnetic response shown in the $M$ vs $H$ hysteresis curve for a single crystal of a ferromagnetic material depends on its crystallographic orientation relative to the direction of the applied $H$ field. This behaviour is illustrated in Figure 1.17 (a) for single crystals of nickel face-centred cubic (FCC) and iron in body-centred cubic (BCC), where the magnetising field is applied in [100], [110], and [111] crystallographic directions. Figure 1.17 (b) for cobalt hexagonal close-packed (HCP) in [0001] and [1010]/[1120] directions.

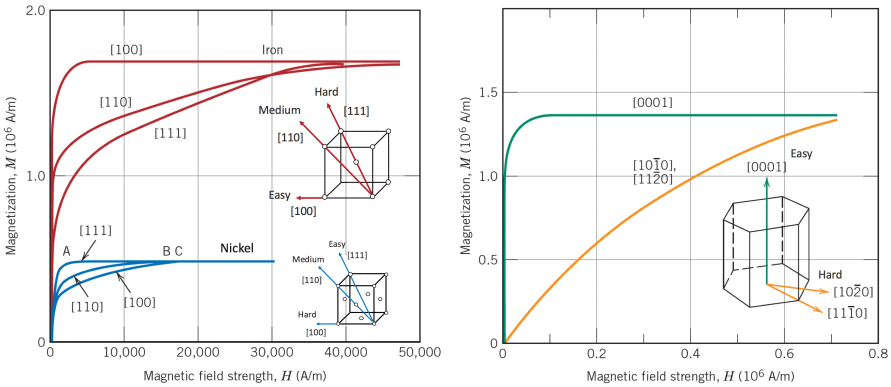



Figure 1.17: (a) Magnetisation curves for single crystals of iron and nickel [6, 7] (b) Magnetisation curves for single crystals of cobalt[8]

For each of these materials there is one crystallographic direction in which magnetisation is easiest—that is, saturation (of $M$) is achieved at the lowest $H$ field; this is termed easy axis. For example, for Ni this direction is [111] in as much as saturation occurs at point A; whereas, for [110] and [100] orientations, saturation points correspond, respectively, to points B and C. Correspondingly, easy magnetisation directions for Fe and Co are [100] and [0001], respectively. Conversely, a hard crystallographic direction is that direction for which saturation magnetisation is most difficult; hard directions for Ni, Fe, and Co are [100], [111], and [1010]-[1120].

Iron is most typically in the body-centred cubic (BCC) phase at room temperature, wherein it exhibits ferromagnetic behaviour, with a magnetic moment of 2.2 μB/atom. However, when it is in its face-centred cubic (FCC) phase, it exhibits an anti-ferromagnetic behaviour. Cobalt in the hexagonal close-packed (HCP) phase shows a ferromagnetic behaviour with a moment of 1.72 μB/atom [1, 5], and in its BCC phase has a magnetic moment of 1.53 μB/atom [56, 57].

If the anisotropy is large, then there will be a significant difference between the magnetisation in the easy and hard axes, whereas if the anisotropy is small, you will end up with little hysteresis in either direction. In this case the material would be described as being superparamagnetic, having a saturation magnetisation equivalent to a ferromagnetic material at low field, but with a linear dependance. If we consider a single domain particle, with uniaxial anisotropy, at 0K, the energy of the particle in a magnetic field is given by:

$$E_{tot} = K_u sin^2\theta - \mu_0 M_S H\, cos(\alpha - \theta) \tag{1.24}$$

Where $\theta$ is the angle between the magnetisation and the anisotropy axis, and $\alpha$ is the angle between the field and the anisotropy axis.

### 1.3.6 *Anti-ferromagnetism*

In ferromagnets the spins align parallel producing a net magnetic moment. In anti-ferromagnetic materials the spins may be aligned anti-parallel, here the magnetic moments of respective spins will cancel each other out and in the case of the anti-ferromagnetic material there will be no net magnetic moment as shown in Figure 1.18(a) .

The susceptibility of anti-ferromagnetic materials follows the Curie-Weiss law up to the critical point, the transition point between paramagnetism and anti-ferromagnetism is called the Néel temperature, $T_N$ Figure 1.18 (b), and below this point the susceptibility decreases with temperature.

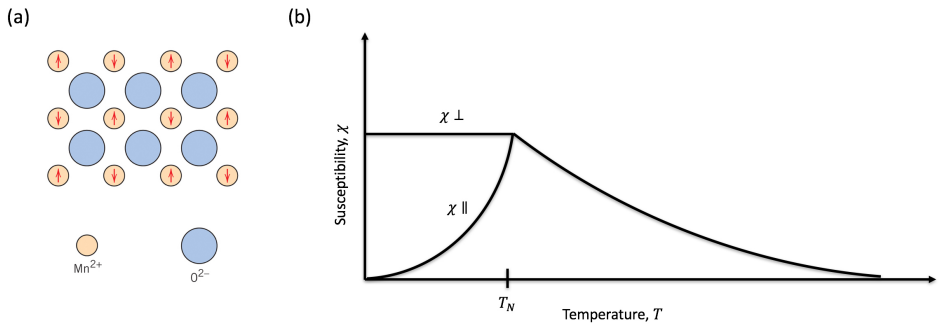



Figure 1.18: (a) anti-ferromagnetic ordering of spins in a lattice (b) Susceptibility of an AFM material, in the parallel and perpendicular directions below TN [1]

In the paramagnetic phase, the molecular field opposes the applied field, in an attempt to realign the spins antiparallel. Following to $1/\chi = 0$, the intersection is at a value of -$\theta$, which is approximately $T_C$. The Curie-Weiss law becomes,

$$\chi = \frac{C}{T + T_C} \tag{1.25}$$

Anti-ferromagnetic materials find applications in magnetoresistive sensors due to their interaction with ferromagnetic layers. Manganese alloys such as IrMn and PtMn show anti-ferromagnetic behaviour above room temperature.

### 1.3.7 *Exchange bias*

The principle interest of anti-ferromagnetic materials is their interaction with ferromagnetic materials. At the interface between an anti-ferromagnetic and ferromagnetic lattice, there will be an exchange interaction between the first couple layers of the lattice. The effect called exchange bias or anisotropy is to induce an additional torque on the ferromagnetic lattice acting against the applied field, which results in an offset in the hysteresis response of the Ferromagnet by $H_{ex}$.

The phenomenon of exchange bias was discovered in 1956 by Meiklejohn and Bean [58, 59] while studying ferromagnetic Co particles embedded in antiferromagnetic oxide CoO. A unidirectional anisotropy appeared when the particles were cooled in a magnetic field from room temperature where the CoO is paramagnetic, to 77K where it is antiferromagnetic. Figure 1.19(a) shows the hysteresis of Co/CoO particles measured at 77 K after cooling under a magnetic field of 1 T and zero field. This unidirectional anisotropy which was termed exchange “bias” anisotropy was attributed to exchange interaction between the AFM CoO particles and the FM Co core and is noted as a shift from zero field of the magnetisation hysteresis loop of the sample.

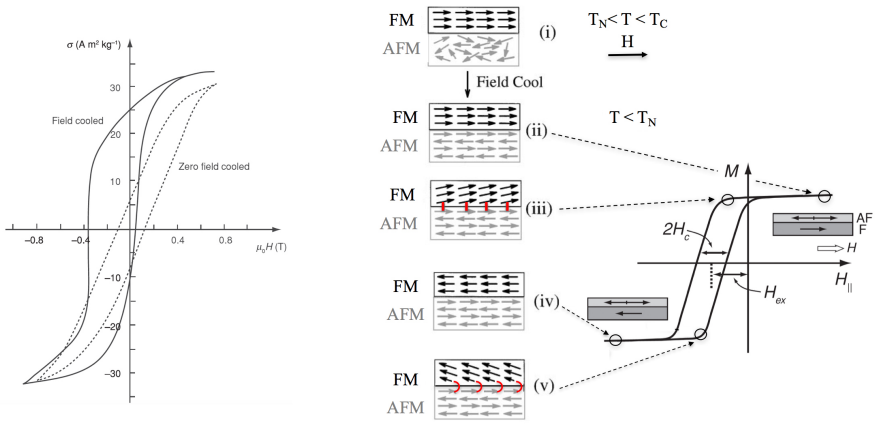



Figure 1.19: (a) Hysteresis of Co/CoO particles and (b) Schematic diagram of an exchange biased hysteresis loop

The exchange bias can be explained by looking at the FM/AFM interface as shown in Figure 1.19(b) shows a schematic diagram of the spin configuration of an FM/AFM interface at different stages (i)—(v) of an exchange biased hysteresis loop [60] . As the temperature cools down below the $T_N$ under a magnetic field (ii), the FM/AFM interface spin align ferromagnetically. This is an effective field acting on the FM layer and is more favourable from a energy point for the FM layer to be aligned along the direction of this field. As the applied field is reversed during the hysteresis cycle (iii), the FM spins start to rotate. The AFM spins remain unchanged due to a large anisotropy, and exert a microscopic torque on the FM spins at the interface keeping ferromagnetic alignment. FM spins remain aligned with the AFM until the applied field is greater than the sum of the effective field and the coercive field of the FM. During the second half of the hysteresis cycle (iv), the applied field is in the direction of the torque exerted from AFM. The FM then switches at a lower applied field (v) which is given by the difference between coercive field of the FM and the microscopic torque. Therefore the FM has only one stable configuration, as shown by unidirectional anisotropy and a shift from zero of the hysteresis cycle by a value corresponding to the exchange bias field, $H_{ex}$.

## 1.4 MAGNETORESISTANCE

Magnetoresistance (MR) is the change in the resistance of a material due to the application of an external magnetic field (Thomson et al 1857) [61]. The size of the effect is given by the MR ratio,

$$MR = \frac{\Delta\rho}{\rho} = \left(\frac{R_{max} - R_{min}}{R_{max}}\right) \tag{1.26}$$

Where $\rho$ is the material's resistivity and $R_{max}$ and $R_{min}$ are the maximum and minimum measured resistances. The anisotropic magnetoresistance (AMR) [62] is seen in bulk ferromagnetic materials, and is caused by an increased scattering of d-band conduction electrons within a ferromagnetic material, due to the shift in the DoS under the applied external field. The AMR resistance change ratio is 1-2%.

### 1.4.1 *Spin dependent transport in ferromagnetic transition metals*

All spintronic phenomena (GMR, TMR and spin transfer torque) are related by the fact that electronic transport is spin-dependent. In 1971, it was experimentally demonstrated using superconductor/ferromagnetic tunnel junctions that conduction electrons in ferromagnetic transition metals are spin polarised [63]. This was theoretically explained by considering that itinerant s-electrons are hybridised with the spin-polarised localised d-electrons [64], or the band structure showed exchange splitting between spin-up and spin-down electron bands.

As real band structure is complex, models are used as they capture most of the physics of GMR and TMR. The models state that the spin-polarised current observed in ferromagnetic transition metals is due to spin polarised free electrons. Spin-up electrons have their momentum in the same direction as the local magnetisation and are called majority electrons. Spin-down electrons have there momentum in the opposite direction to the magnetisation and are called minority electrons. Two model descriptions are mainly used, firstly the Stoner model shown in Figure1.20(a), which is typically used to explain tunnelling magneto-resistance, considers the free electron bands present exchange

splitting. Here the spin-polarised current is due to the fact that the density of state and the electron velocity at Fermi level are different for spin up and spin down electrons.

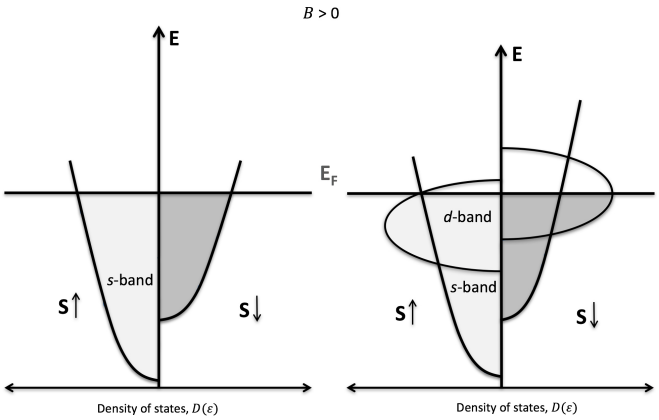



Figure 1.20: Schematic of (a) stoner model: exchange splitting (b) s-d scattering rate model

The second model considers that the spin dependent current is due to the fact that scattering rates are different for spin-up and spin-down electrons as illustrated in Figure 1.20(b). Scattering towards d-states is most frequent for spin-down electrons since the number of available states is much larger. This model is typically used for GMR description. The density of state and the velocity of conduction electrons are the same for spin-up and spin-down and the current polarisation is due to a strong difference in the diffusion constant [39].

Mott [23] introduced the concept that an electron current can be thought of as the sum of the spin-up (↑) and spin-down (↓) contributions, using the two-current model. In ferromagnetic materials a spin asymmetry exists as a result of the different density of states of spin-up and down electrons at the Fermi level resulting in a significant splitting of the DoS. If the direction of the magnetisation is switched, then the DoS shift in the opposite direction and the spin-polarisation is of the opposite polarity as illustrated in Figure 1.21.

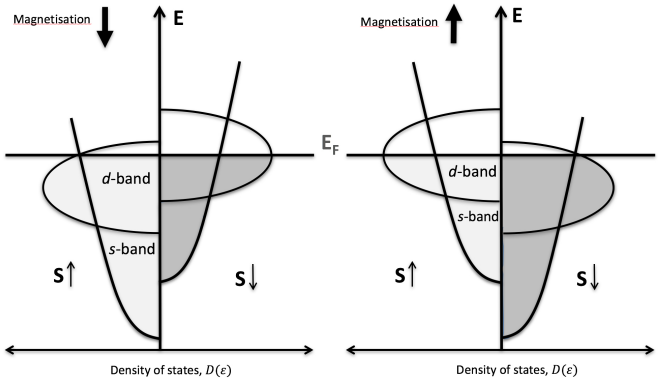



Figure 1.21: A Ferromagnetic material with opposite magnetisation directions showing opposite spin-polarisation polarity

## 1.5 GIANT MAGNETORESISTANCE

Giant magnetoresistance (GMR) is the change in electrical resistance to thin-film structures composed of alternating ferromagnetic layers separated by ultra thin non-magnetic conductive layers in response to an applied magnetic field. Figure 1.22 shows the variation in the resistance of the Fe/Cr multilayers. The change in resistance was observed using Cr spacer layers in the order of 1 nm thickness. With an applied magnetic field at zero the Fe layers are coupled antiferromagneticaly, providing an antiparallel alignment of their magnetisation and highest measured resistance. As the field is increased, the magnetic moments of the ferromagnetic layers rotate towards the applied field leading to a decrease in the multilayer resistance. When the applied field is at saturation the Fe layers align parallel with the lowest value of the resistance measured [16, 65]. The effect is due to scattering of spin-polarised electrons at the interface [66–68] of a ferromagnetic layer, and as they travel through the layer [67, 69, 70].

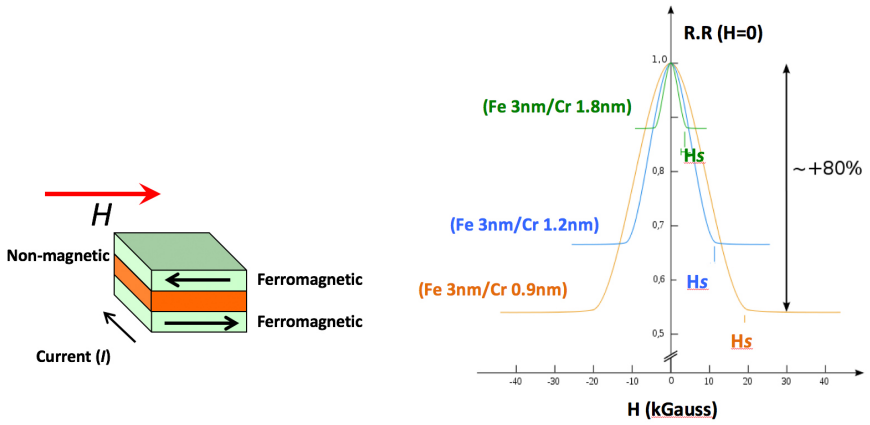



Figure 1.22: Schematic of GMR multilayer and results of Fert & Grunberg (1988) change in the resistance of Fe/Cr superlattices in external magnetic field H

Giant magnetoresistive effect has been observed in many multilayer structures comprised of ferromagnetic layers (F) using transition metals such as Fe, Co, Ni and their alloys and non-magnetic (NM) metal Cu, Ag, Ir, Au. In these magnetic multilayers the thickness of each layer is typically in the nanometer range and the thickness of the non-magnetic layer is selected to get spontaneous antiparallel alignment of magnetisations in successive ferromagnetic layers. Therefore the zero field resistance is high and decreases when a large applied magnetic field aligns the magnetisations of all layers. The measured magnetoresistance is larger than the anisotropic magnetoresistance and called giant magnetoresistance (GMR) with values to more than a 100 % in Fe/Cr [71] or Co/Cu [72] multilayers.

GMR can be in part explained using both the two-current model introduced by Mott [23] and considering the band structure of the ferromagnetic transition metals. In Mott's two-current model electrical conductivity in metals can be described in terms of two independent conducting channels, which correspond to the spin-up and spin-down electrons. The probability of spin-flip scattering processes in metals is normally small as compared to the probability of the scattering processes in which the spin is conserved. This means that the spin up ( $\uparrow$) and spin down ( $\downarrow$ ) electrons do not mix over long distances and, therefore, the electrical conduction occurs in parallel for the two spin channels.

If we take two thin ferromagnetic layers separated by a non-magnetic spacer layer as illustrated in Figure 1.23, when the magnetisation of the multilayer is aligned parallel

the spin-up electrons pass through the structure with little scattering, as their spin is parallel to the magnetisation of the layers. The spin-down electrons are scattered strongly within both ferromagnetic layers, because their spin is antiparallel to the magnetisation of the layers. As both spin-up and spin-down channels conduction occurs in parallel, a low resistance state is determined by the low resistivity of the spin up channel. When the magnetisation of the multilayer is aligned antiparallel, the spin-up and spin-down electrons are scattered strongly within one of the ferromagnetic layers respectively as the spin is antiparallel to the magnetisation direction and so the resistance of the multilayer is high.

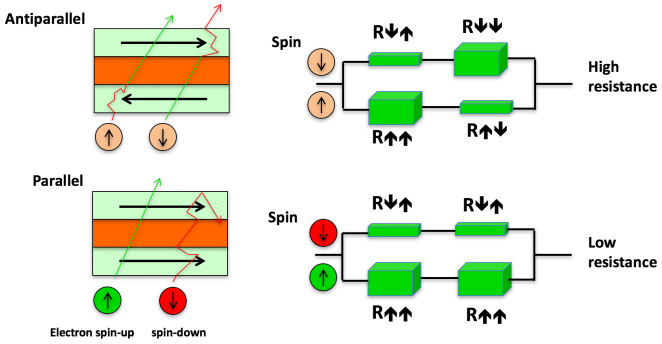



Figure 1.23: Schematic of the GMR mechanism for spin up and spin down electrons

The amplitude of the GMR can be characterised by the ratio,

$$\delta H = \frac{R(0) - R(H)}{R(H)} \tag{1.27}$$

Where $R(H)$ is the resistance of the sample in a magnetic field $H$ and $R(0)$ corresponds to the resistance when $H = 0$. In a parallel configuration the resistivity is given by: $R_P = \frac{R\uparrow R\downarrow}{R\uparrow + R\downarrow}$ and in an antiparallel configuration it is described by: $R_{AP} = \frac{R\uparrow R\downarrow}{4}$. The GMR ratio is then given by,

$$\frac{\Delta R}{R} = \frac{R_{AP} - R_P}{R_P} \tag{1.28}$$

### 1.5.1 *GMR Current in plane & Current perpendicular to plane*

The two methods to measure the GMR effect through the multi-thin film stack configuration are current in plane (CIP) and current perpendicular to plane (CPP) as illustrated in Figure 1.24 (a) and (b).

In CIP the configuration Figure 1.24 (a), the electrical connections are placed in parallel along the top surface, so current flows parallel with the thin film layers.

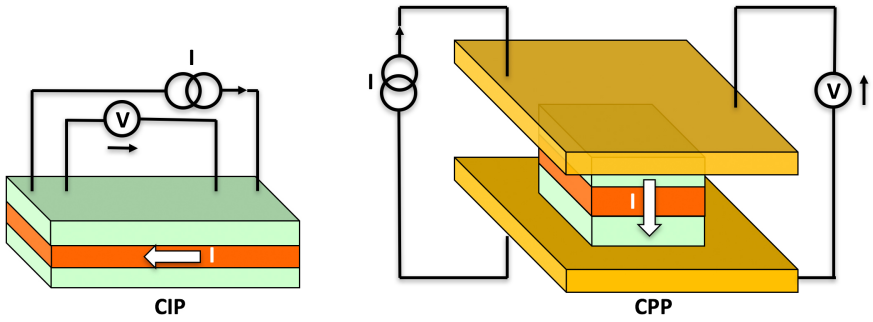



Figure 1.24: Schematic of (a) GMR current in plane (CIP) (b) Current perpendicular to plane (CIP)

The CIP GMR magnetoresistance can be in part explained using the two-current model introduced by Mott [23], considering the band structure of the ferromagnetic transition metals, also the finite size effect of the non-magnetic spacer layer between adjacent ferromagnetic layers, the ferromagnetic layer thickness and the probability $p$ of specular reflection and transmission at the interface or the interfacial scattering [67, 68].

Good matching of the band structures of the ferromagnetic and non-magnetic layers and near the interfaces is a factor in obtaining a large GMR effect. It explains in part the high GMR ratios for Fe/Cr multilayers which show good matching for the spin down ($\downarrow$) electrons and for the Co/Cu multilayers which show good matching for the spin up ($\uparrow$) electrons [73].

The non-magnetic spacer layer between the adjacent ferromagnetic layers needs to be thin enough or smaller than the elastic mean free path $\lambda$ to allow the electrons successively travel in both layers, alternatively probing the two respective layers. If the non-magnetic spacer layer thickness is larger than the elastic mean free path $\lambda$, the GMR disappears. However, if the spacer layer is too thin, the parallel coupling between

ferromagnetic layers increases. Therefore a compromise is found between the GMR amplitude and the coupling with a non-magnetic spacer layer thickness between 1.8 nm and 2.2 nm.

The magnetoresistance can be optimised depending on the ferromagnetic layer thickness and interface. Consider no specular reflection at the interfaces i.e. a rough interface where the probability $p$ of specular reflection is 0. If the ferromagnetic layer is thin, there will be little scattering contrast between the spin up ($\uparrow$) electrons spin down ($\downarrow$) electrons. If the ferromagnetic layer thickness is increased to the order of the majority spin up ($\uparrow$) electron mean free path, the minority spin down ($\downarrow$) electrons are mostly scattered, ensuring an optimum scattering contrast. If the interface is smooth, with a specular reflection probability $p$ of 1. This optimum magnetoresistance is achieved when the ferromagnetic layer thickness is of the order of the minority spin down ($\downarrow$) electron mean free path.

In the current perpendicular to plane (CPP) configuration as shown in Figure 1.24(b), the electrical connections are placed perpendicular to the thin-film layer stack configuration and the current flows perpendicular to the plane. The transport properties can be described in the two-channel resistor model.

Current flowing perpendicular to the plane causes a build-up of spin polarization near the interface between the ferromagnetic and non-magnetic layers, which is known as spin accumulation. In a ferromagnetic material, the two spin channels do not carry the same amount of current due to the difference in the scattering rates, as the spin up ($\uparrow$) current density is larger than the spin down ($\downarrow$). In contrast, in the non-magnetic layer the two spin currents are equal. At the interface between a ferromagnetic material and non-magnetic material, there is a diffusion of the spin-polarised electrons into the non-magnetic layer, and a diffusion of unpolarised electrons into the ferromagnetic layer. When a current is applied there is an accumulation of spin-up ($\uparrow$) electrons that will fill empty states above the Fermi level, increasing their chemical potential $\mu^{\uparrow}$. And conversely a loss of spin-down electrons ($\downarrow$), leading to a chemical potential $\mu^{\downarrow}$ below the Fermi level. This causes a change in the local DOS between the two layers and creates a potential across the interface [1, 70, 74]. Figure illustrates the chemical potentials for

spin-up (↑) and spin down (↓) electrons in a GMR spin valve with parallel or antiparallel alignment of the electrodes.

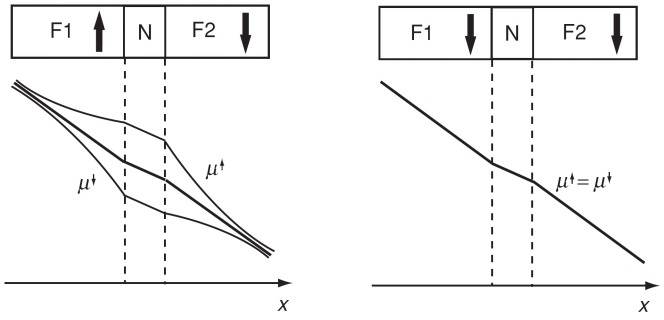



Figure 1.25: Chemical potentials for spin-up (↑) and spin down (↓) electrons in a GMR spin valve with parallel or antiparallel alignment of the electrodes

The accumulated spins will diffuse from the interface, which is given by the spin diffusion length

$$l_S = \sqrt{D_e \tau_S} \tag{1.29}$$

Where $D_e$ is the electron mean diffusion constant, and $\tau_S$ is the spin relaxation time of the material. The spin diffusion length $l_S$ is longer in non-magnetic metals than in ferromagnets. Therefore for a thin nonmagnetic interface layer, there is a spin accumulation potential at each interface. So in CPP the characteristic length scale $l_S$, the spin diffusion length, is much longer than the CIP length scale $\lambda$ , which is the elastic mean free path. The GMR in CPP has a dependence on the spin diffusion length.

$$GMR = \frac{(\alpha - 1)^2}{4\alpha} \frac{l_S}{t_F} \tag{1.30}$$

Where, $\alpha$ is the spin polarisation of the ferromagnetic material, $l_S$ is the spin diffusion lenght and $t_F$ is the thickness of the ferromagnetic material. GMR CPP is larger than the equivalent GMR CIP [67, 70, 74].

## 1.6 TUNNELING MAGNETORESISTANCE

Following the discovery of GMR, the effect of tunneling magnetoresistance was realised. Similar to GMR the tunneling magnetoresistance (TMR), based on magnetic tunnel junctions (MTJ) consists of two ferromagnetic layers, which are now separated using an ultra-thin insulating tunnel barrier as illustrated in Figure 1.26 (a). Since the discovery of TMR at room temperature in 1995 using amorphous aluminium oxide (Al-O) with TMR ratio's of up to 70%, development has continued with TMR ratios of 500% using epitaxial CoFeB/MgO/CoFeB with crystalline MgO (001).

When the current is applied perpendicular to plane (CPP), spin-polarized electrons of specific symmetry can tunnel through the insulating barrier. The resistance change of the device depends on the relative magnetic alignment (parallel or antiparallel) of the ferromagnetic layers. The size of the resistance change, which is the TMR ratio is determined by the resistance change between a parallel and anti-parallel state and is calculated by the formula,

$$TMR = \left(\frac{Rap - Rp}{Rp}\right) \times 100 \tag{1.31}$$

Where Rap and Rp are the anti-parallel alignment resistance and parallel alignment resistance values of the multilayer. Compared to GMR the magnetoresistance change in TMR is much higher.

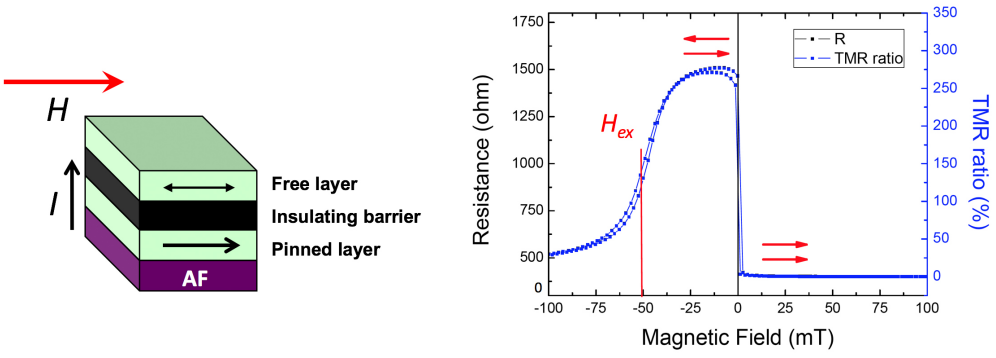



Figure 1.26: Schematic illustration of a basic spin-valve TMR sensor trilayer b) the magnetoresistance curve showing TMR ratio 250 % exchange bias field (Hex) is $>$ 50 mT

Figure 1.26 (b) shows a magnetoresistance curve for a spin-valve TMR sensor with TMR ratio of TMR ratio 250 %. There is a sharp change of resistance around the zero field, which is due to the switching of free layer. The parallel (P) and antiparallel (AP) magnetisation states are indicated with red arrows.

The basic principle of tunneling can be explained looking at Figure 1.27 (a), which shows the decay of the electron's wave-function while tunneling through an insulating barrier [18, 75]. Although most of the electron wave function is reflected back from the barrier due to electrons not having sufficient energy to pass through the barrier, under quantum mechanics there is a probability that some electrons will tunnel through the barrier [76]. The amplitude of the wave function is attenuated exponentially in the barrier.

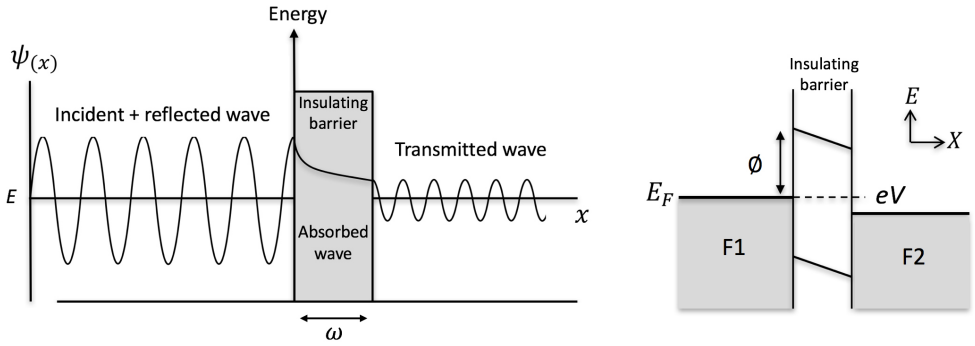



Figure 1.27: (a) The decay of electron's wave-function within the tunnelling barrier (b) the band diagram of a metal/insulator/metal structure [1]

Figure 1.27 (b) shows the energy band diagram for a tunneling barrier in a TMR metal/insulator/metal structure. The proability of a electron tunneling between two metals seperated by an insulating barrier of height $\phi$ and width $\omega$ is

$$\tau = a \exp\left(-b\omega\phi^{1/2}\right) \tag{1.32}$$

Where, $a$ and $b$ are constants. The formula for the tunnelling between similar electrodes through a thin insulating barrier was proposed by Simmons [77] shows the expotential dependance on the barrier thickness.

$$G = \left(3e^2/2\omega\hbar^2\right)(2me\phi)^{1/2} \exp\left\{-(4\pi\omega/\hbar)(2me\phi)^{1/2}\right\} \tag{1.33}$$

Where, $e$ is the electron charge, $m$ is the mass of the electron. The TMR is dependent on the barrier height, thickness and applied voltage bias, with a low bias producing a constant TMR.

The tunneling current in TMR metal/insulator/metal structure, which is given by,

$$I_l \rightarrow r\,(V) = \; = \int_{-\infty}^{+\infty} D_l \cdot (E) \cdot D_r\,(E + eV) \cdot \mid M \mid^2 \cdot f(E) \cdot [1 - f\,(E + eV)]\, dE \tag{1.34}$$

Which, describes the tunneling current from the left electrode to the right electrode in the metal/insulator/metal structure. $D_l\,(E)$ is the density of states in the left electrode and $D_r\,(E + eV)$ is the density of states in the right electrode. $V$ is the bias voltage and $\mid M \mid^2$ is the square of the matrix element, which is the tunneling probability. $f(E)$ is the probability that the states in the left electrode are occupied and $[1 - f\,(E + eV)]$is the probability that the states in the right electrode are empty where $f(E)$ is the Fermi-Dirac distribution function. The total current is given by $I_{l \rightarrow r} - I_{r \rightarrow l}$.

The origin of TMR comes from the difference in the electronic band structure for spin-up and spin-down electrons. As electrons preserve their spin orientation during tunneling, they can only tunnel into the sub-band of the same spin orientation. Figure 1.28 shows the band structure for the electrons involved in the tunneling process in a parallel and antiparallel configuration.

The tunneling conductance is proportional to the product of the Fermi level density of states values of the two electrodes for the same spin orientation. A change from parallel to antiparallel configuration of two ferromagnetic layers will result in an exchange between the two spin sub-bands.

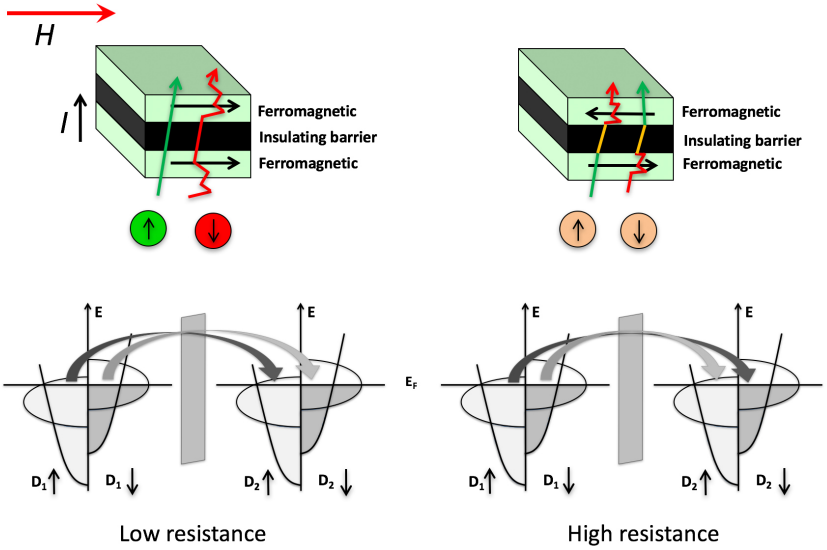



Figure 1.28: Schematic of TMR multilayer and electron tunnelling band structure

TMR effect was discovered by M. Julliere in 1975 using a Co/Ge-O/Fe junctions [78], where he observed a change in the tunneling magnetoresistance (TMR) of 14% at 4.2K. Jullière proposed a model that the probability of an electron tunneling through the barrier was dependent on the DoS for each ferromagnetic layer and the TMR effect is due to this spin-dependent electron tunneling.

Here $D_{1\uparrow,2\uparrow}$ are the DoS for the spin ($\uparrow$) majority electrons and $D_{1\downarrow,\,2\downarrow}$ are the DoS for the spin ($\downarrow$) minority electrons of the ferromagnetic electrodes at the fermi energy ($E_F$), the TMR can be given in terms of the of the conductance in both parallel and anti-parallel configuration [12], [86]–[88]

$$TMR = \frac{G_P}{G_{AP}} = \frac{D_{1,2\uparrow} - D_{1,2\downarrow}}{D_{1,2\uparrow} + D_{1,2\downarrow}} - 1 \tag{1.35}$$

If we define the spin polarisation of a layer as,

$$P = \frac{D_\uparrow - D_\downarrow}{D_\uparrow + D_\downarrow} - 1 \tag{1.36}$$

The tunneling magnetoresistance of the junction is proportional to the product of both ferromagnetic electrode polarisations $P$ as shown in Julière formula for TMR ratio,

$$TMR = \frac{2 \times P_1 \cdot P_2}{1 - P_1 \cdot P_2} \tag{1.37}$$

Following Jullière's early experiments, TMR at room temperature was demonstrated by Moodera et al. [79] in 1995, using CoFe / AlOx / Co junctions achieving a TMR of 11 %. Further improvements using alumina based junctions Miyazaki et al. [25] and Gao et al. [80] achieved a TMR of up to 70% using amorphous ALOx barrier. Figure 1.29(a) shows an illustration of incoherent tunneling transport using amorphous ALOx barrier for Fe (001)/ AlOx / Fe (001). The three tunnelling (evanescent) states, $\Delta 1$, $\Delta 5$ and $\Delta 2$ in the Fe (001) couple with the AlO evanescent states. The AlO is amorphous with no Crystallographic symmetry and so provides incoherent tunneling.

In 2004 Parkin et al [81] reported very high TMR ratio's using crystalline magnesium oxide (MgO) as a barrier layer. Using CoFe/Fe electrodes they achieved TMR ratios of 160 % at room temperature. Independently, Yuasa et al. [40] achieved TMR ratios of 180 % at RT and 247 % at 20 K using Fe (001) / MgO (001) / Fe (001). TMR ratios above 500 % at RT were reported using MgO barriers with CoFeB electrodes, Lee et al, Ikeda et al and Jiang et al. [82][41][83].

### 1.6.1 *Coherent tunnelling through MgO barrier*

Epitaxial Fe (001) / MgO (001) / Fe (001) magnetic tunnel junctions using a crystalline magnesium oxide (MgO) tunnel barrier was predicted to have TMR ratios of over 1000%. The effect was independently predicted by Butler et al. [36]and Mathon & Umerski [37] in 2001. Subsequently Zhang and Butler further predicted even greater ratios in such junctions using Co or ordered CoFe electrodes instead of Fe [84].

Crystalline MgO (001) barrier layer can be epitaxially grown on a bcc Fe (001) layer with a relatively small lattice mismatch. In MgO, there are three tunnelling (evanescent) states, $\Delta_1$, $\Delta_5$ and $\Delta_2$. The Fe (001) majority electrons, which have a $\Delta_1$, s-like symmetery are theoretically expected to dominantly tunnel through the MgO (001) $\Delta_1$ state, which has a much slower decay rate or less attenuation than the minority-spin electrons, which have a $\Delta_5$, d-like symmetery. The thin crystalline insulator barrier acts as a spin filter, producing a spin-polarized tunnelling current. Figure 1.29(b) shows an illustration of coherent tunneling transport in epitaxial Fe (001) / MgO (001) / Fe (001).

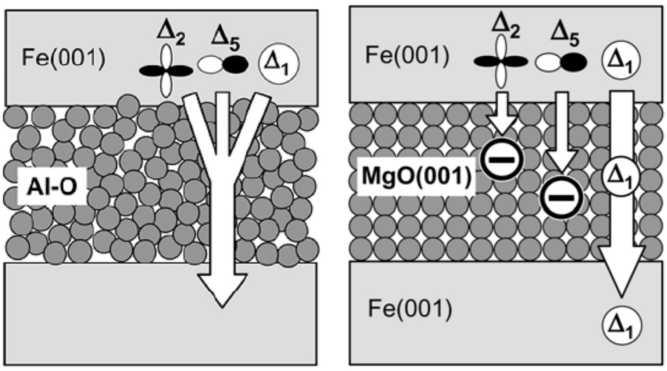



Figure 1.29: Schematic of electron tunnelling through (a) incoherent amorphous ALOx barrier (b) coherent crystalline MgO (001) barrier [9]

The wavefunction of certain electron modes decay slower than others [37][36]. At the interface, bands can match with the evanesent (tunnelling) component of the electron waveform from the adjecent layer and complex bands can form. In MgO (001) the $\Delta_1$ band decays slower than $\Delta_5$ or $\Delta_2$ bands. The spin-polarised $\Delta_1$ majority electrons in the Fe ferromagnetic electrode couples with the MgO $\Delta_1$ band, and so a higher conductance through the barrier. Figure 1.30(a) shows the DOS of electrons through an epitaxial MgO barrier in the parallel orientation for the majority spin states. In the anti-parallel orientation the $\Delta_1$ band is orders of magnitude lower as shown in Figure 1.30(b). To insure the $\Delta_1$ band is present and has a low decay rate a high crystal quality of the MgO barrier is essential.

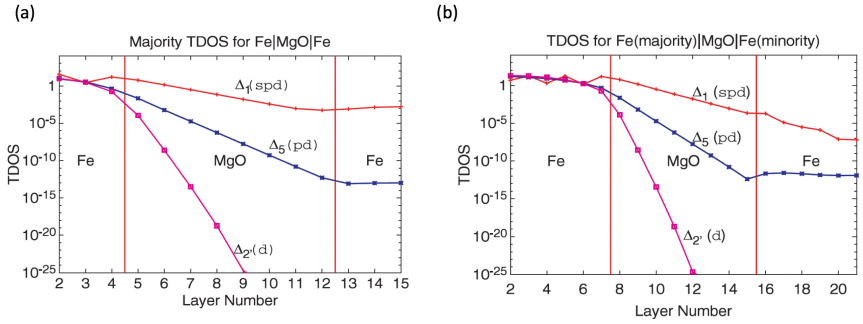



Figure 1.30: (a) DOS of electrons through an epitaxial Mg0 barrier in the parallel orientation for majority spin states (b) in the anti-parallel orientation for majority spin states

The $\Delta_1$ states are highly spin-polarized not only in bcc Fe (001) but also in many other bcc ferromagnetic metals and alloys based on Fe and Co. Amorphous CoFeB electrodes have been grown on MgO (001). Using post annealing above 300 $^{o}$C, resulted

in the crystallization of the CoFeB in a (001) direction. This allows the thickness of the barrier to be reduced to the order of 1.2 nm, while still remaining crystalline and also achieving very high TMR values [85][86].

## 1.7 MAGNETIC SENSORS

A variety of different physical effects are exploited in magnetic sensors, which are passive devices that detect the presence of a magnetic field. Proximity of a magnet or magnetised object is detected via its stray field. Magnetic sensors offer a number of advantages as outlined in Table 1.1,

| **Advantages of magnetic sensors** |
|---|
| Contactless sensing |
| Deliver an electrical response that is monotonic and often linear in field |
| Can detect one component of the field, or sometimes the scalar magnitude |
| Can measure fields in the range fT to 100 T |
| Sense magnetic field, electric current or proximity (with external magnet) |
| Detecting *B, H,* Φ or dΦ/dt |
| Manufactured in huge quantities, a few billion sensors every year market ~ €7B |

Table 1.1: Advantages of magnetic sensors

The sensors can be magnetoresistive structures, hall bars, magneto-impedance or sensors based on NMR. The great advantage of magnetic sensing is that it avoids the need for direct contact between the sensor and the object sensed. Several billion magnetic field sensors are manufactured each year, about a billion of them destined for hard-disc drives. Most of the rest are low-cost proximity sensors. A car may contain as many as 100 of them, mostly integrated silicon Hall chips. If a thin-film sensor, which depends for its operation on the direction of magnetisation of a responsive ferromagnetic layer, is to deliver a magnetoresistive signal that is monotonic in field, the magnetisation has to be able to respond continuously, rather than flip between bistable configurations ('high' and 'low' resistance states). Table 1.2 lists some of the magnetic sensors and the magnetic principle they are based on. The most optimum magnetic sensor for the specific

application can be selected from a number of parameters including magneto-resistive sensor performance and noise spectroscopy also detailed in Table 1.2.

| **Sensor type & magnetic principle** | |
|---|---|
| AMR | Spin-orbit scattering |
| GMR | Spin accumulation |
| TMR | Spin-dependent tunnelling |
| **Sensor performance parameters** | |
| Magneto-resistive transfer response | Linear response, non-hysteretic |
| Sensitivity (V/mT) | High MR ratio and soft magnetic free layers |
| Intrinsic noise (V/√Hz) | $1/f$ noise |
| Detectivity (T/ √Hz) | Noise/Sensitivity approximates minimum detectable field |
| Other parameters | Drift, dynamic range |

Table 1.2: Sensor principles and performance parameters

### 1.7.1 *Giant magnetoresistance (Spin valve) sensors*

For sensor applications requiring low field switching and high GMR% ratio a structure called a spin valve was developed [87]. The spin valve consists of two ferromagnetic layers separated by a non-magnetic spacer layer. The magnetisation of one of the layers is pinned by exchange interaction with an adjacent antiferromagnetic layer, while the magnetisation of the second ferromagnetic layer is free to rotate in an applied field as illustrated in Figure 1.31 (a). Figure 1.31 (b) shows a typical GMR multilayer stack configuration for a GMR spin valve sensor. The two ferromagnetic layers are weakly coupled and so the change from a parallel to antiparallel magnetic configuration can occur in small fields giving these systems a large sensitivity. As a magnetic field is applied, when close to zero field the magnetisation of the free layer switches while the pinned layer remains fixed. As the applied magnetic field is increased greater than the exchange anisotropy field $H_{ex}$ , the exchange interaction of the ferromagnetic layer with the antiferromagnet is overcome and switches its magnetisation direction. One of the advantages of exchange biased spin valves is the sharp switching and high field sensitivity at near-zero fields as shown in Figure 1.31 (c) which shows the magnetoresistive response curve. This makes them ideal for sensor applications or example in a memory MRAM device, were the spin valve is used as a bistabe state device with two states, parallel

alignment leading to a low resistance state or anti-parallel alignment leading to a high resistance state.

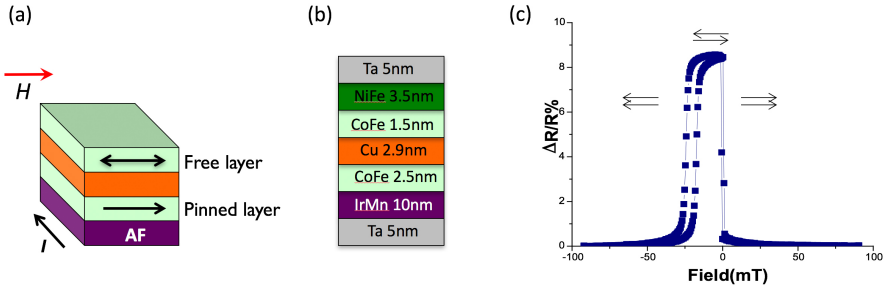



Figure 1.31: (a) Schematic of spin valve configuration (b) Typical GMR multilayer stack configuration (c) Spin valve magneto response curve

The development of uncoupled ferromagnetic/non-magnetic/ferromagnetic thin films by Dieny et al. in 1991 [87] lead too much of the research into the optimisation of GMR multilayer exchange-biased spin valves. The typical GMR multilayer stack configuration for a spin valve as shown in Figure 1.31 (b) is composed of six layers: buffer layer, free layer, spacer layer, pinned layer, antiferromagnetic layer and capping layer. The buffer layer is usually 2-5 nm of Ta and is used to increase the quality of the subsequent layers and reduce roughness. The capping layer is also usually Ta and protects the structure from oxidation and corrosion. The free layer consists of two ferromagnetically coupled layers, a typical combination is $Ni_{80}Fe_{20}/Co_{90}Fe_{10}$. The NiFe layer is used to reduce the coercivity, while the CoFe gives a higher MR ratio due to the larger scattering potential for minority electrons at the CoFe/Cu interface. The anti-ferromagnetic layer are Mn based alloys such as IrMn.

For field sensor applications the spin valve can be used where the resistance varies continuosly as the free layer turns relative to the pinned layer. The output must be linearised and have maximum sensitivity. This is achieved firstly by setting the free layer magnetisation perpendicular to the pinned layer as shown in Figure 1.32(a). This can be done by either controlling the magnetic field direction during the deposition process or by using a post annealing process (induced magnetic anisotropy).

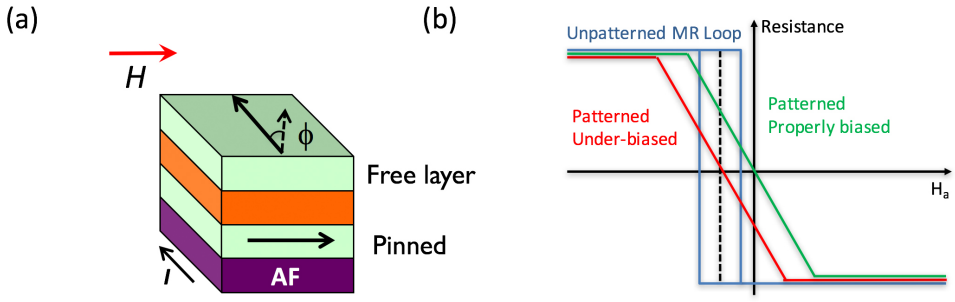



Figure 1.32: (a) Schematic of spin valve with free layer set perpendicular to the pinned layer (b) typical GMR multilayer stack configuration (c) magnetoresistive loops for a Spin valve sensor before and pattering and properly biased

Secondly by patterning the sensor into a shape (shape magnetic anisotropy). Figure 1.32(b) shows a schematic of the magnetoresistive curve for a spin valve sensor in an un-patterned state, patterned but under-biased state and properly-biased centred state. Figure 1.33 (a) shows a schematic of a spin valve sensor with the free layer set at 90ř to the pinned layer. Figure 1.33 (b) shows the experimental magnetoresistive curve for a GMR spin valve sensor [88].

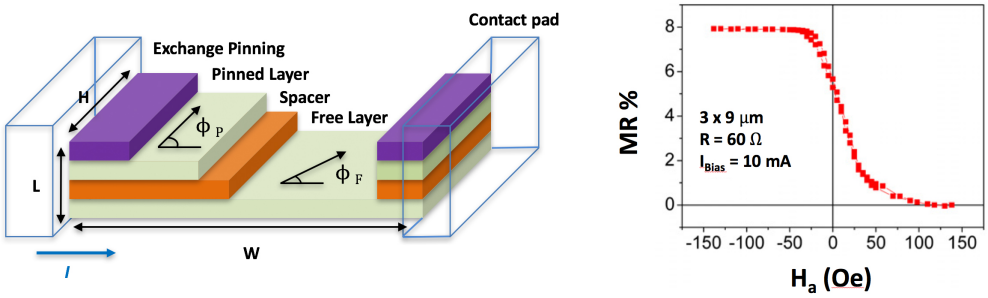



Figure 1.33: (a) Schematic of GMR CIP spin valve sensor (b) Experimental transfer curve for a GMR spin valve sensor

The sensor output voltage is given by,

$$V = \frac{1}{2}\left(\frac{\Delta R}{R}\right) Rsq \times I \left(\frac{W}{h}\right) [\cos(\phi f - \phi p)] \tag{1.38}$$

Were $\frac{\Delta R}{R}$ is the maximum MR, $Rsq$ is the sensor square resistance ($Rsq = \rho/t$), $\rho$ is the sensor resistivity, $t$ is the thickness. $h$ is the sensor height. $I$ is the current supplied to the sensor, $W$ is the width. $\phi f$ Is the angle between the free layer magnetisation and

the longitudinal direction, and $\phi p$ is the angle between the pinned layer magnetisation and the longitudinal direction. For a linearised output $\phi p = \pi/2$ and $\phi f \sim 0$.

Assuming uniform magnetisation for the free and pinned layers, for a case where $W > h$, the free layer $(\sin \phi f) = (H_a + H_{bias} + H_{coupling}) / H_{keff}$. Where $H_a$ is the external applied field, $H_{bias}$ is the bias field used to centre the transfer curve and $H$ coupling corresponds to the sum of the ferromagnetic Neel coupling between the free and pinned layers. $H_{keff}$ is the effective anisotropy field, incorporating the free layer shape anisotropy field ($H_{demag}$) and its uniaxial anisotropy field $H_k$. Equation 4 can then be rewritten as,

$$V = \frac{1}{2}\left(\frac{\Delta R}{R}\right) Rsq \times I \left(\frac{W}{h}\right) (H_a + H_{bias} + H_{coupling}) / 2H_{keff} \tag{1.39}$$

In a crossed anisotrpoy configuration, the response of the sensor is proportional to the cosine. An applied field (in my application this is the stray field of the nanowire $H_a$) will exert a torque $\tau$ on the free layer of the sensor as it passes.

$$\tau = m \cos\theta \, H_a \tag{1.40}$$

Where,

$$\theta = \frac{H_a}{H_{demag}} = \frac{\pi}{2} \tag{1.41}$$

The sensors free layer switches by coherent rotation, which provides linear variation of resistance to the appplied field. The sensitivity is optimised for a crossed anisotropy where $\theta = \frac{\pi}{2}$. It is known that magnetisation reversal, in the case of uniaxial anisotropy takes place by coherent rotation when the field is applied perpendicular to the anisotropy axis. The effect of the applied field $H_a$ from a passing nanowire on the sensor free layer demagnetiation field $H_{demag}$ will result in small angle changes to the free layer. which is seen a small resistance changes.

### 1.7.2 *Tunneling magnetoresistance sensors*

Tunneling magnetoresistive spin valve sensors based on linear MTJs (Magnetic tunnel junctions) have a magnetic behavior similar to GMR spin valve sensors, but with higher MR ratios, and higher noise levels. Similar to the GMR spin valve sensor field sensor application, the pinned is set perpendicular to the free layer. This is achieved using a post annealing process, which sets the sensors exchange bias, as illustrated in Figure 1.34 (a) [88].

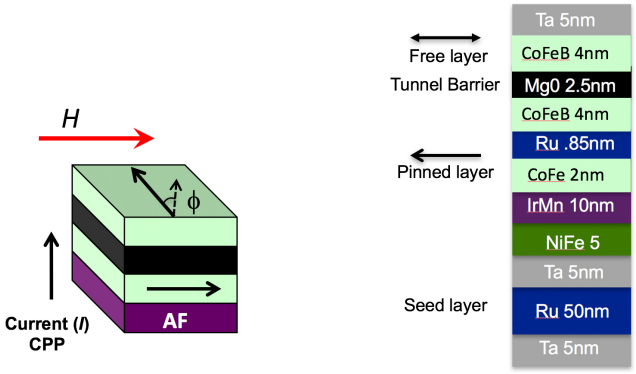



Figure 1.34: (a) Schematic of TMR spin valve sensor with free layer set perpendicular to the pinned layer (b) typical TMR multilayer in-plane stack configuration

The typical TMR multilayer stack configuration for an in-plane TMR spin valve sensor is shown in Figure 1.34 (b). The seed or bottom electrode is Ta/Ru/Ta is used to increase the quality of the subsequent layers and reduce roughness. The capping layer again is Ta. The pinned layer is formed using an anti-ferromagnetic layer IrMn placed beside the CoFe layer. The Ru layer, which is antiferromagnetic in the 0.5 – 1.0 nm range [89], forms a synthetic anti-ferromagnet (SAF) between the two ferromagnetic layers and enhances the pinning and also reduces the stray field created by the pinned layer on the sensing layer [90]. The tunnel junction is formed using epitaxial crystalline CoFeB/MgO/CoFeB. The post annealing process induces the crystallisation of CoFeB at the MgO interfaces, which is necessary for a high TMR ratio. Figure 1.35 (a) shows a schematic of a TMR CPP spin valve sensor.

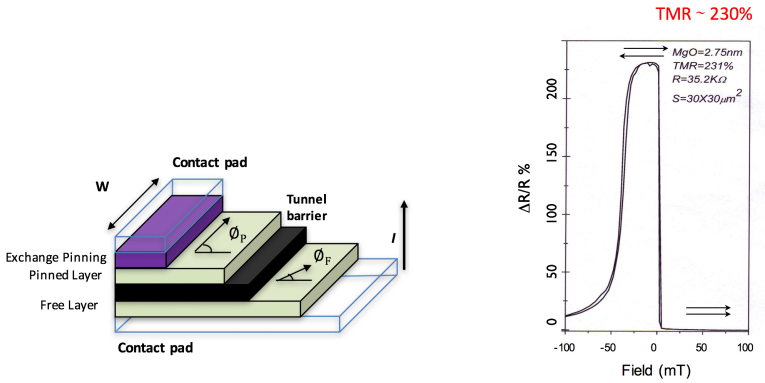



Figure 1.35: (a) Schematic of TMR CPP spin valve sensor (b) Magnetoresistive loop for a TMR Spin valve sensor

Figure 1.35 (b) shows a magnetoresistive loop for a TMR Spin valve sensor. The sensor linearisation depends not only on shape anisotropy but also on a bias in the longitudinal direction with the expense of a decrease in sensitivity. The TMR sensor output is given by,

$$V = \frac{1}{2} TMR \times \left( I \frac{RA}{W_h} \right) [\cos(\phi f - \phi p)] \tag{1.42}$$

## 1.8 NOISE

The critical figure of merit for any sensor is the signal/noise ratio. Optimum performance of a GMR or TMR sensor can only be estimated with respect to the sources of noise. In this section I give some bases on noise theory and sources of noise in GMR and TMR sensors.

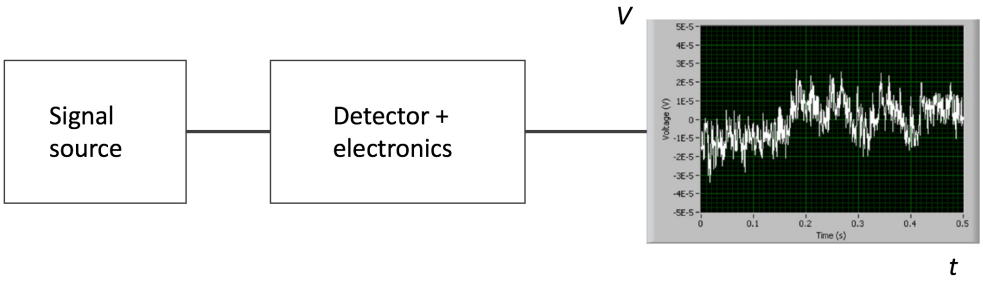



Figure 1.36: Illustration of noise system

Noise in a magnetic sensor can be electrical or magnetic in origin. It is manifest as uncontrolled random fluctuations of the voltage $V(t)$ across the device as illustrated Figure 1.36. In an experiment the sensor response $V(t)$ is measured at discrete time t1,... tn by the acquisition system. A number of quantities can be derived from the measurement such as the average fluctuation $V(t)$, variance $\sigma$ and correlation [91]. If $V(t)$ is a random variable the average can be defined as,

$$\bar{V} = \lim_{T\to\infty} \frac{1}{T} \int_0^T V\,(t)\,dt \tag{1.43}$$

Where $T$ is the duration of the experiment. The average is also the fluctuating quantity on a time scale $T$ corresponding to the total acquisition time. The variance $\sigma$ of V, is defined as,

$$\sigma^2 = \lim_{T\to\infty} \frac{1}{T} \int_0^T \left(V\,(t) - \bar{V}\right)^2 dt \tag{1.44}$$

The variance measures the exploration in amplitude of $V$ and can be used as a comparison of different signals. Knowledge of $\sigma$ and $V$ is sufficient to know the distribution function $\rho$ of the voltage measurement $V$. This is achieved using the central limit theorem, which shows that a sum of n random identical quantities tends to a normal (Gaussian) distribution.

$$\rho(V) = \frac{1}{\sqrt{2\pi\sigma^2}} \exp\left(-\frac{(V-\bar{V})^2}{2\sigma^2}\right) \tag{1.45}$$

Analysis of the signal distribution may help distinguish the presence of discrete levels for example Random telegraph Noise (RTN). In the time domain, correlations are important as they give measure of the similarities between two functions (cross-correlations) or for the same function but a different time (auto-correlation). The general form of the correlation of two functions $X$ and $Y$ is defined as the average of the functions at a time difference $\tau$.

$$C_{xy}(\tau) = \lim_{T\to\infty} \frac{1}{T} \int_0^T X\,(t)\,Y(t-\tau)dt \tag{1.46}$$

For the auto-correlation function is,

$$g_x(\tau) = \lim_{T\to\infty} \frac{1}{T} \int_0^T X\,(t)\, X(t-\tau) dt \tag{1.47}$$

### 1.8.1 *Frequency Space and Spectral Density*

The spectral analysis gives the frequency dependence of the noise, which is essential for separating and understanding noise sources. The frequency spectrum of the fluctuations $V(\omega)$ is the Fourier transform of the time series $V(t)$. The Fourier transform is used to switch from the time domain to the frequency domain.

$$V(\omega) = \frac{1}{2\pi} \int_0^T V\,(t)\, e^{i\omega t} dt \tag{1.48}$$

Typically we wish to find the energy and power distribution of $x(t)$ as a function of frequency. The total energy of the signal is given by,

$$E = \int_0^T \mid V\,(t)\mid^2 dt \tag{1.49}$$

Which can be expressed through the Parseval theorem by

$$E = 2\pi \int \mid V(\omega)\mid^2 d\omega \tag{1.50}$$

For communications signals, the energy is effectively infinite (the signals are of unlimited duration), so we usually work with power quantities. We find the average power by averaging over time. Therefore the average power associated to the fluctuations can be defined as,

$$P = \lim_{T\to\infty} \frac{1}{T} \int_0^T \mid V\,(T)\mid^2 dt = \lim_{T\to\infty} \int_0^\infty \frac{2 \mid V_T(\omega)\mid^2}{T} d\omega \tag{1.51}$$

The power spectral density (PSD) is defined as,

$$S_V(\omega) = \lim_{T\to\infty} \frac{\mid V_T(\omega)\mid^2}{T} \tag{1.52}$$

The power spectral density for a signal is a measure of its power distribution as a function of frequency. It is a useful concept, which allows us to determine the bandwidth required of the system. The power spectral density is given for voltage fluctuations in $V^2/Hz$. The voltage spectrum can be measured directly in a spectrum analyser. It is important to note the relation between the power spectrum density and the auto-correlation function which is the Wiener-Khintchine theorem.

$$S_v(\omega) = 2\pi \int g(\tau) cos(\omega\tau) d\tau \tag{1.53}$$

Using the Wiener-Khintchine Theorem it can be shown that the PSD is also given by the FT of the autocorrelation function, which gives us information about the time variation. An example is an exponentially decreasing auto-correlation function, which decreases with a characteristic time $\tau_c$ similar to the response of a low pass filter,

$$g(\tau) = g(0) \exp\left(-\frac{\tau}{\tau_c}\right) \tag{1.54}$$

This is similar to the response from the low pass filter. The PSD is,

$$S_V(\omega) = 4g(0) - \frac{\tau_c}{1 + \tau_c^2 \omega^2} \tag{1.55}$$

The spectrum is called Debye-lorentzian spectrum and presents a flat response at low frequencies and a $1/f^2$decrease at high frequencies with a corner at $1/\tau_c$ as shown in Figure 1.37(a).

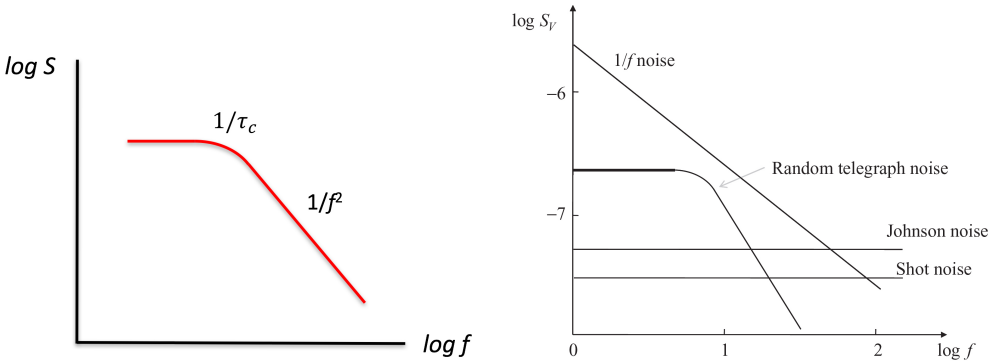



Figure 1.37: (a) Plot of Debye-lorentzian spectrum (b) Contributions to the noise in a magnetoresistive sensor

### 1.8.2 *Sensitivity, Signal to Noise ratio and Detectivity*

Noise PSD is given in $V^2/Hz$ but it is more convenient to compare a signal given in V to the square root of the PSD, which is in $V/\sqrt{Hz}$.

To allow calibration of a sensor and evaluate the signal-to-noise ratio, a reference signal at a known frequency is used. When the acquisition system sees the signal $V_0 \cos(\omega t)$, the PSD is the power associated to this signal taken on a bandwidth of 1Hz, so 1 second and this corresponds to $V_0^2/2$.

The sensitivity for a magnetoresistive signal $\beta$, is given in V/T. Values of GMR sensors are typically of the order 20-40V/T or 2-4%/mT. For a linearised and offset centred magnetoresistive sensor the output voltage can be written as

$$V_{out} = \left( R_0 + \frac{\delta R}{\delta H}.H \right) I \tag{1.56}$$

Where $\frac{\delta R}{\delta H}$ is given in Ohms/Tesla. The sensitivity is given by $\frac{\delta R}{\delta H}/R_0$. In order to compare different sensors, it is convenient to use the field equivalent noise power spectral density, also called detectivity, which is the PSD divided by the sensitivity. For example if a sensor shows a thermal noise of $1nV/\sqrt{Hz}$ and a sensitivity of 20V/T, the detectivity will be 50pT for 1V of bias voltage.

## 1.9 NOISE SOURCES

There are various sources of noise existing in both GMR and TMR magnetoresistive sensors as shown in Figure 1.37(b). Noise can be frequency independent or dependent and has four main types, thermal (Johnson-Nyquist) noise, shot noise, $1/f$ (flicker) noise and random telegraph noise (RTN). Noise sources may also be magnetic field dependent. Magnetic field dependent noise appears when an external field is applied and can be separated by measuring the sensor noise in its whole range of operation.

### 1.9.1 *Frequency independent noise*

Frequency independent noise is called Thermal or Johnson-Nyquist noise and appears flat in the range of measurement. The noise is approximately white, meaning that its power spectral density is nearly equal throughout the frequency spectrum. Thermal noise is directly related to the resistance of the sensor and the temperature. The spectrum is frequency independent and the PSD is,

$$Sv(\omega) = 4k_BTR \tag{1.57}$$

Where $k_B = 1.3806 \centerdot 10^{-23}\text{J.K}^{-1}$ is the Boltzmann constant and the energy available for a dipole of resistance is $k_BT/2$. Thermal noise cannot be reduced except by reducing the temperature or resistance. But is independent on the voltage applied to the sensor. The impact on the signal-to-noise ratio is related to the working bandwidth and the noise will increase as the square root of the bandwidth. Hence the incentive is to make electrical measurements in as narrow a bandwidth as possible at the frequency of the signal of interest, in order to improve the signal-to-noise ratio.

Shot noise is due to the fact that electric current is not continuous due to the discrete nature of electrons. The noise is detectable only if there is a barrier to cross such as a TMR sensor. It is less observable in GMR CIP sensors. This is due to the fact that in metals the electrons inelastic scattering length is very small a few nm at room temperature, the GMR sensor comprises of a number of individual layers a few nm in series, therefore the shot noise is divided by the square root of this number. In TMR magnetic tunnel junctions shot noise can be observed at low temperature when sufficient current passes through the junction for the shot noise to exceed the equilibrium Johnson noise. In magnetic tunnel junctions the electrons are following a Poisson law when they pass through a barrier and so it is possible to calculate the PSD of the shot noise. The PSD is flat in frequency and is given as,

$$S_I(f) = 2eI \tag{1.58}$$

At high frequency, the noise contributions that limit performance are Johnson noise and shot noise, varying as $\sqrt{R}$ and $\sqrt{I}$ respectively. Both are known as white noise on account of their flat frequency spectrum.

### 1.9.2 *Low Frequency noise*

1/f noise is a general term referring to a frequency decreasing noise, where the power spectral density SV varies as $1/f^{\alpha}$where $\alpha$ is an exponent typically with a value $\alpha \approx 1$. This noise is observed in nearly all fluctuating systems including biological and geological fluctuations, ranging from the human heartbeat ($1/f$ below 0.3 Hz) to the water level of rivers and the musical output of radio stations. The square of the voltage fluctuations $S_V$(t) varies as $I^2$, which allows the $1/f$ noise coming from a sample to be distinguished from white noise. In magnetoresistive sensors, there is also a magnetic contribution to $1/f$ noise that is associated with domain walls. There is a formula proposed by Hooge which allows the comparison of $1/f$ resistance fluctuations on various sensors

$$S_V(f) = \gamma_H \frac{V^2}{N_C f} \tag{1.59}$$

where V is the applied voltage, $N_C$ is the number of charge in the volume. $\gamma_H$ is a dimensionless number known as the Hooge coefficient, which allows a normalised comparison of different systems. Values of $\gamma_H \sim 10^{-3}$ are found for well-crystallised metal films, and for semiconductors.

### 1.9.3 *Random telegraph noise, High Frequency noise and External noise*

Random telegraph noise is a noise, which arises from the fluctuations of a specific source between two different levels with comparable energies and barrier height able to give a characteristic time in the measurement range. In magnetoresistive sensors it appears in devices with junctions small enough to let individual defects to become dominant, such as TMR sensors.

### 1.9.4 *High Frequency noise*

At high frequencies noise is dominated by thermal or shot noise. In the GHz range noise peaks can be detected in magnetoresistive sensors due to the fact that thin magnetic films present ferromagnetic resonances with frequencies dependent on the material and on the shape of the sensor. With magnetic sensors it is important to take care of external inductive noise sources. Within a laboratory these sources can be frequency related, such as power supply line (50 Hz) and higher frequencies (MHz) from lights. These correspond to AC magnetic fields and are proportional to the bias current in the magnetoresistive sensor. For $1/f$ noise, which exists everywhere a good magnetic shield room with passive and active shielding can reduce this noise from 100 nT at 1 Hz to 100 fT V.

## 1.10 MAGNETORESISTIVE NOISE

Figure 1.38 shows some of the noise contributions in magnetic thin-film samples (a) the 1/f noise in a $CrO_2$ film, (b) the random telegraph noise in a $La_{0.67}Ca_{0.33}MnO_3$ film and (c) the 1/f and white noise in a CoFeB–MgO–CoFeB magnetic tunnel junction. GMR and TMR magnetoresistive sensors exhibit common noise features, which are thermal noise, the $1/f$ noise and the magnetic noise. The noise measurement is expressed as the PSD in $V/\sqrt{Hz}$, also a good comparison of sensor performance is the detectivity or the field equivalent noise given in $nT/\sqrt{Hz}$.

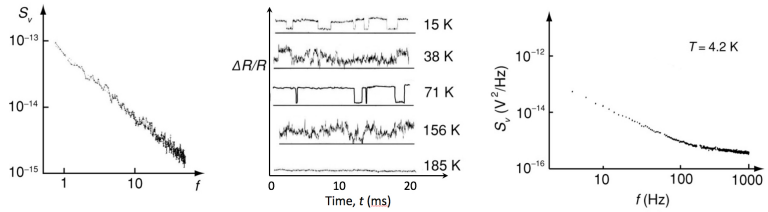



Figure 1.38: Noise in magnetic thin-film samples: (a) 1/f noise in a $CrO_2$ film, (b) random telegraph noise in a $La_{0.67}Ca_{0.33}MnO_3$ and , (c) 1/f and white noise in CoFeB–MgO–CoFeB MTJ [1].

### 1.10.1 *Giant magnetoresistance noise*

The main noise contributions in GMR sensors are thermal noise, the $1/f$ noise and the magnetic noise. The thermal noise depends on the resistance of the device, which is related to its size. The lower the resistance the lower the noise, but for applications this is limited by the noise contribution of the preamplifier that are to interface the GMR device. The low frequency $1/f$ noise is dominant. It scales as the square root of the volume of the device, but for practical applications size may be a consideration. Magnetic noise is typically due to magnetic domain formation and motion in the soft layer. The magnetic noise contribution can be suppressed by patterning the sensor into a YOKE shape as shown in Figure 1.39. The magnetic domains are confined to the edges, providing a stable magnetic domain structure in the sensor long arm of the YOKE, reducing the noise associated with macroscopic domain wall motion reported by Pannetier et al in 2004 [10].

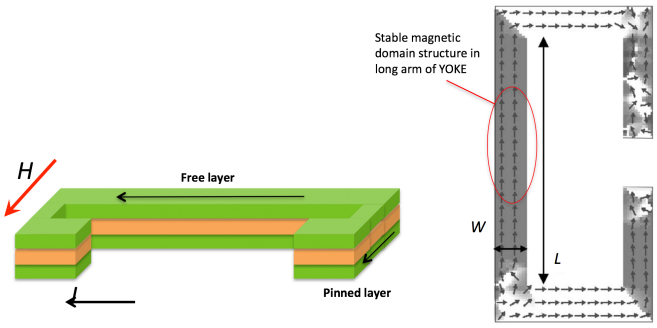



Figure 1.39: (a) Schematic of YOKE sensor and (b) magnetic configuration from micro-magnetic simulation [10]

### 1.10.2 *Tunneling magnetoresistance noise*

TMR sensors exhibit common noise features to GMR, which are thermal noise, $1/f$ noise and magnetic noise. Also they exhibit shot noise. At room temperature, the shot noise is small compared to thermal noise. The $1/f$ noise dominates at low frequencies and is very large compared to the GMR CIP sensors. The 1/f noise arises from the spin-independent resistance fluctuation within the tunneling barrier due to pinholes

within the tunneling barrier. It is larger in the TMR sensor due to the fact that the TMR CPP junction is small or smaller compared to the GMR CIP lateral junction. There is a proability of a larger number of fluctuations or less averaging compared to the GMR CIP junction, were there is fluctuations and they average out [92, 93].

Reducing the magnetic noise is of importance for the improvement of the field detectivity in TMR sensor. The $1/f$ noise can be separated into magnetic $1/f$ noise and electronic $1/f$ noise. The electronic $1/f$ noise is described by the modified Hooge formula,

$$S_V(f) = \alpha \frac{V^2}{Af} \tag{1.60}$$

Where $A$ is the active surface of the device and $\alpha$ is then a parameter with the dimension of a surface. It can be reduced by ensuring that thin films and barrier are of excellent crystalline quality.

The magnetic noise is typically due to the magnetic domain formation and motion in the soft layer and can be suppressed by patterning the sensor into a YOKE shape. This is more difficult to fabricate due to the specific lithographic processes required for the bottom electrode, barrier junction and the top electrode.

### 1.10.3 *Comparison of sensor characteristics*

GMR and TMR sensors are very sensitive and have been incorporated into numerous applications. The low frequency noise is the main limitation of the performance. Table 1.3 shows a summary of GMR and TMR sensor characteristics.

| Sensor | Field (T) | Noise/√Hz | Freq Range | Detects | Type |
|---|---|---|---|---|---|
| GMR | $10^{-9} - 10^{-3}$ | 10nT | $0 - 10^{9}$ | $H$ | Thin-film |
| TMR | $10^{-9} - 10^{-3}$ | 1nT | $0 - 10^{8}$ | $H$ | Thin-film |

Table 1.3: Summary of GMR and TMR sensor characteristics [1]

Despite the advantages of TMR sensors, not many groups have adapted them for biological related applications. This is primarily due to difficulties in fabrication for CPP operation and using the sensors in biocompatible liquids. Producing high quality ultra thin oxide layers for the tunnelling barrier is also a constraint.

## 1.11 ELECTRODEPOSITION AND MAGNETIC NANOWIRES

Electrodeposition refers to deposition of a metal or an alloy from an electrolyte by passing a charge, applied current or voltage potential between the two electrodes located in the electrolyte [77, 78]. It is a widely implemented technique, in both industry and research for applications such as fabricating magnetic recording devices, integrated circuits as well as nano fabrication [79, 80], and enables a control of the length of the nanostructure by the duration of the electrochemical process. The technique is versatile, inexpensive and does not require vacuum equipment. The electrodeposition methods used for the production of nano materials are typically a bottom up or a top down approach. The bottom up electrodeposition approach is more commonly used in the fabrication of nanowires, where the starting materials are atoms or molecules, which then form nano materials into conducting substrates or into nanoporous templates. The bottom up approach allows for the precise fabrication of nanostructures with small diameters, less defects and more homogeneous chemical compositions. Several parameters influence the kinetics of the electrodeposition reaction, namely:

1. The electro-deposition potential determines the species and the corresponding quantity that will be deposited onto the substrate

2. The electrolyte composition, typically metallic and magnetic single element nanostructures

3. Electrolyte temperature affects the ions diffusion velocity and the diffusion of already reduced atoms on the substrate surface

4. The electron diffusion can be enhanced by stirring and enables the removal of $H_2$ gas, which can inhibit the process, keeping the electrolyte concentration and the electrolyte/substrate interface pH constant

The properties of the metal depositions such as hardness, stress depend on a number of factors including the electrolyte solution characteristics and the deposition process [77]. The electrodeposition of single metal nanostructures is achieved using a electrochemical cell, which is connected to a potentiostat via a working electrode, reference electrode and counter electrode. The electrochemical cell contains the electrolyte solution, and the metallic multilayers are formed on the electrode by periodically varying either the deposition potential voltage (potentiostatic control) or deposition current (galvanostatic control) between two suitable potential values [81, 82].

### 1.11.1 *Electrochemistry*

Electrochemistry investigates chemical reactions, which occur at the interface of an electrode, typically a solid metal and an ionic conductor called electrolyte. The electro-deposition technique was originally developed to create a decorative or protective layers on conducting materials [94][95][95]. It is a process were cations in the electrolyte are reduced to the surface of a conducting electrode by using either potential or current to form a layer on the surface of the electrode.

The electro-deposition reactions involve transfer of electrons between electrode and electrolyte. The electrochemical cell, which facilitates the chemical reaction such as an oxidation-reduction reaction, consists of a cathode, an anode and an electrolyte. Reactions can occur spontaneously or by using an external potential. A common example of an oxidation-reduction reaction is when a piece of zinc metal is placed in a solution of copper ions. The zinc metal slowly "dissolves" as its oxidation produces zinc ions, which enter into solution. At the same time, the copper ions gain electrons and are converted into copper atoms, which coats the zinc metal. The reaction is described by the ionic equation,

$$Cu^{+2}(aq) + Zn(s) \longrightarrow Cu(s) + Zn^{+2}(aq) \tag{1.61}$$

To understand the reaction mechanisms, it is common to design an electrochemical cell that is composed to two compartments or half-cells. Each half-cell contains an electrode, which is placed in a solution of electrolyte. The half-cells are designed to contain the oxidation half-reaction and reduction half-reaction separately as shown in Figure 1.40.

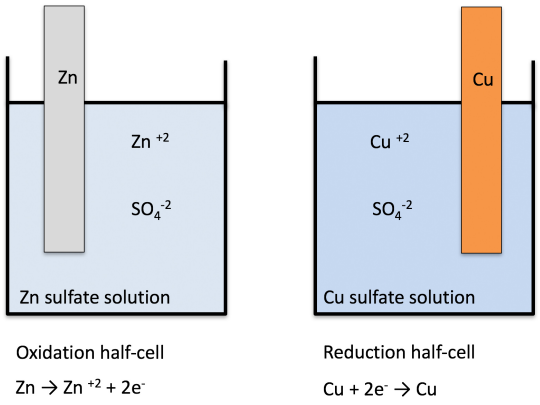



Figure 1.40: Oxidation and reduction half-cell reaction

During the oxidation of zinc, the zinc electrode will slowly dissolve to produce zinc ions ($Zn^{+2}$), which enter into the solution containing $Zn^{+2}(aq)$ and $SO4^{-2}(aq)$ ions. This is the anode. The reaction is given by,

$$Zn(s) \longrightarrow Zn^{+2}(aq) + 2e^{-} \tag{1.62}$$

When the reduction of copper ions ($Cu^{+2}$) occurs, copper atoms accumulate on the surface of the solid copper electrode. This is the cathode. The reaction is give by,

$$Cu^{+2}(aq) + 2e^{-} \longrightarrow Cu(s) \tag{1.63}$$

The oxidation-reduction reaction occurs when the two half-cells are connected via a salt bridge, as shown in Figure 1.41 . A salt bridge is a porous barrier, which allows the migration of ions in both directions to maintain electrical neutrality. As the oxidation-reduction reaction occurs, $Zn^{+2}$ (cations) from the anode migrate via the salt bridge to

the cathode, while the, $SO4^{-2}$ (anion) migrates in the opposite direction to maintain electrical neutrality.

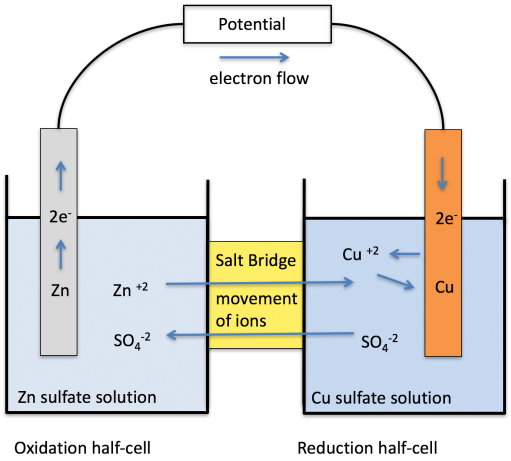



Figure 1.41: Oxidation and reduction reaction

Using an external potential, electrons provided by the oxidation reaction are forced to travel via an external circuit to the site of the reduction reaction. The fact that the reaction occurs spontaneously once the half-cells are connected indicates that there is a difference in potential energy. This difference in potential energy is called an electro-motive force (emf) measured in volts.

When an electrode (solid metal) is placed into an electrolyte solution, an electron exchange between the electrode and the ions in solution will take place. This leads to a potential difference over the metal-electrolyte interface i.e. an electrical field is generated. This field leads to the redistribution of mobile ions and electrolyte water dipole molecules in the region near the surface of the electrode forming a layer as illustrated in Figure 1.42 .

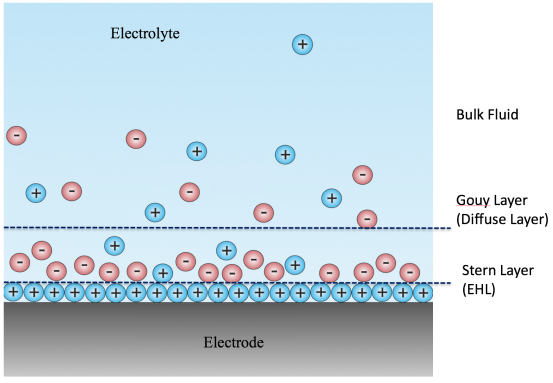



Figure 1.42: Schematic of the electrode-electrolyte interface formation of electrical double layer

Helmholtz proposed [96] [97], that the redistribution at the surface interface will lead to absorption of one layer of water molecules, followed by a positive or negative layer of solvated ions, depending on the charge on the electrode. The layer of ions forms the so called exterior Helmholtz layer (EHL). In the most simple case the charge densities on the electrode and EHL are equal and different in sign. Therefore, the interface can be approximated to a planar capacitor (double layer), one plate being the EHL and the second one the electrode. Thus, according to the Helmholtz model, the potential over the metal-electrolyte interface is considered to change linearly, as for a planar capacitor. The Helmholtz model sometimes does not properly reflect the experimental results, especially for diluted solutions. Gouy and Chapman proposed a new model [98]. They assumed that the electrical field at the interface decreases exponentially with the distance from the electrode. This way the double layer becomes a diffuse one. Although more realistic, the issue was the capacity of a diffuse double layer is not equal to the capacity of a planar capacitor. This model did not explain all experimental results. Stern [99] proposed a combination of the two models, here the diffuse distribution of the ions does not start immediately on the surface of the electrode, but starts from the EHL defined in the Helmholtz model. As a consequence the interface capacity in this model is composed of two capacitors connected in serial: the Helmholtz capacity and the Gouy-Chapman capacity. The Gouy-Chapman capacity increases as the concentration of the electrolyte increases, whereas the Helmholtz capacity stays constant. This way at high concentrations the Gouy-Chapman capacity becomes negligible as compared with the Helmholtz capacity. The Stern model describes satisfactorily nearly all experimental results.

### 1.11.2 *Electrochemical Cells*

Through advancements and development, the electrochemical cell now consists of three of electrodes as shown in Figure 1.43 . A working electrode (WE), which is the electrode where the electrochemical reaction should take place. A counter electrode (CE), which is used to close the circuit and enable the reaction. The third electrode called the reference

electrode (RE), is used to measure the voltage between the electrolyte and the working electrode (WE). Figure 1.43 shows a schematic of a basic three electrode electrochemical cell.

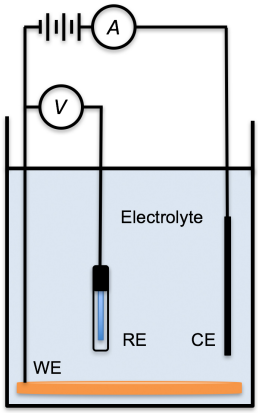



Figure 1.43: Schematic of a three electrode electrochemical cell

When a current is flowing thought a solid-electrolyte interface, chemical reactions will occur at the interface. Electrons leaving the solid will reduce species in solution, whereas electrons moving into the solid lead to the oxidation of species in solution. Due to the chemical reactions at the interface the composition of the electrolyte near the surface of the solid will change continuously and thus the distribution of the voltage across the solid-electrolyte interface will vary as well. For this reason, in order to maintain a constant composition of the solution near the surface of the sample, i.e. the working electrode, continuous pumping of the electrolyte is necessary. The electrochemical cell shown in Figure 1.43 contains a WE/electrolyte junction and a CE/electrolyte junction. The potential U across the electrochemical cell will be,

$$U = U_{WE} + U_{CE} \tag{1.64}$$

Where $U_{WE}$ and $U_{CE}$ are the voltages across the WE/electrolyte and CE/electrolyte junctions respectively. This means that not all the voltage supplied will be applied to the junction of interest, i.e. WE/electrolyte. The voltage ($U_{WE}$) between the sample and solution needs to be controlled, and resulting current change monitored.

As the current supply will stimulate electrochemical reactions at the CE/electrolyte interface, so the potential of the counter electrode $U_{CE}$ will vary over time and influence

the value of $U_{WE}$, due to the fact that their sum should be equal to the voltage supplied. Therefore using a constant supply does not ensure that the voltage measured between the sample and the reference electrode UWE, will stay constant as well. One solution is to decrease the value of $U_{CE}$, so it will have a negligible influence on $U_{WE}$. One method to achieve this is by choosing a counter electrode, which has a large area, so that the resistance of CE will be much smaller than the resistance of WE. In this case,

$$U = U_{WE} \tag{1.65}$$

This would allow $U$ to control $U_{WE}$. However a CE with a large area is not always the most optimum solution with regard to increased current densities, which will cause $U_{CE}$ too effect $U_{WE}$. To solve this issue we now use a device called a potentiostat, which allows the voltage between the working electrode and the reference electrode to be controlled directly. Figure 1.44 shows a schematic of a three-electrode potentiostat with electro-chemical cell. In the potentiostat the electrometer circuit measures the voltage difference between the reference (RE) and working (WE) electrodes using a differential amplifier providing a cell voltage. The Control amplifier (second differential amplifier) compares the measured cell voltage with the desired input voltage and drives current into the cell to force the voltages to be the same. In the event there is a difference between the input voltage and the WE-RE cell voltage the controlling amplifier will increase/decrease the voltage to the cell until the actual and the input voltages are equal. The I/U converter measures the cell current and forces it to flow through the resistor $Rm$. The voltage drop across $Rm$ is a measure of the cell current. During an anodisation experiment the current in the electro-chemical cell can vary, so a number of different $Rm$ resistor values are switched in automatically during the process.

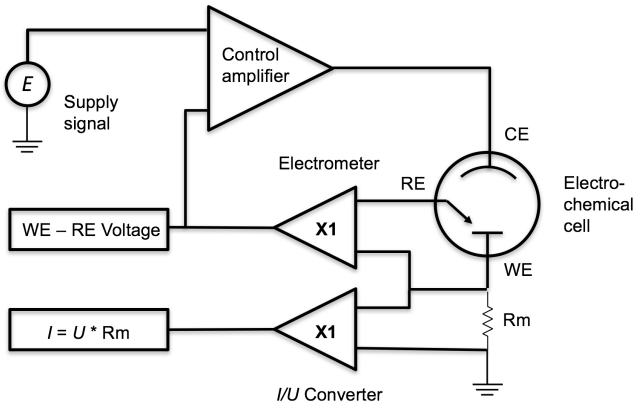



Figure 1.44: Schematic of a potentiostat and electro-chemical cell

### 1.11.3 *Magnetic nanowires using AAO membranes*

Ordered nano-porous anodic aluminium oxide (AAO) was first fabricated by Masuda and Fukuda in oxalic acid in 1995 [100] and has since been the subject of research and commercial applications interests.

Various magnetic and non-magnetic single element and alloy nanowires e.g. Fe, Co, Ni, Cu, Ag, Au, CoFe, CoNi, FeNi, and CoPd have been electrodeposited into the nano-pores of ordered array of alumina for various purposes [101][102][103][104][105][106][106][107] and their fabrication parameters and physio-chemical properties have been optimised.

## 1.12 MAGNETIC BEAD DETECTION REVIEW

There have been numerous studies investigating the detection of superparamagnetic beads or particles using magnetoresistive sensors towards bio-medical applications such as magnetic flow cytometry.

In 2002 L. Guanxiong et al [11] demonstrated detection of a single superparamagnetic bead using a GMR sensor. The sensor was bottom pinned with a crossed anisotropy and had a stack configuration in nm's of Ta 3/seed layer 4/PtMn 15/$Co_{90}Fe_{10}$ 2/Ru 0.85/$Co_{90}Fe_{10}$ 2/Cu 2.3/$Co_{90}Fe_{10}$ 2/Cu 1/Ta 4. The seed layer type was not listed. The sensor measured a GMR ratio of 10.3 %. Two principle sensors GMR sensor designs

were patterned into a bar shape of width 3 µm by length 12 µm and width 2.5 µm by length 10 µm respectively. The top electrode was Al thickness 300 nm. To protect the sensor during the microfluidic detection experiments the sensor was passivated with 1 µm of photoresist layer that was then hard baked. Figure 1.45 shows an optical image of a 3 x 12 $\mu m^2$ spin valve sensor strip with a single 2.8 µm diameter magnetic bead (Dynabeads M-280).

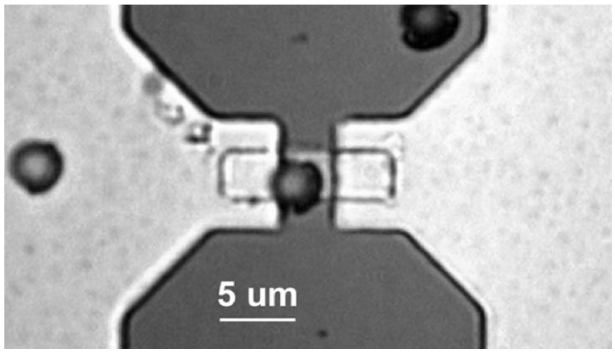



Figure 1.45: An optical image of a 3 x12 $\mu m^2$ spin valve sensor strip with a single 2.8 µm diameter magnetic bead (Dynabeads M-280) [11]

The beads were filled with paramagnetic $Fe_3O_4$ nanoparticles, magnetised with a vertical external field to induce a magnetic moment during the experimental detection experiments, and placed on the sensing area. They observed a reduction in the sensor's magnetoresistance response, caused by the magnetic dipole field from the bead that partially cancelled the applied fields to the spin valve. A lock-in amplifier technique was used to measure a voltage signal due to the reduction in magnetoresistance. The gain was set at 100 and the noise measured 0.1 mV. The 3 µm x 12 µm sensor showed a reduction in signal of 1.2 mV rms or 5.2 mΩ of resistance and the 5 µm x 10 µm sensor showed a reduction in signal of 3.8 mV rms or 11.9 m Ω.

In 2006 the same group [12] demonstrated detection of ∼23 mono-dispersed 16 nm superparamagnetic $Fe_3O_4$ nanoparticles using a GMR sensor. Using the same sensor stack configuration. The sensor measured a GMR ratio of 11.3 %. The GMR sensor design was patterned into a bar shape of width 0.2 µm by length 1 µm. The top electrode was Al thickness 300 nm.

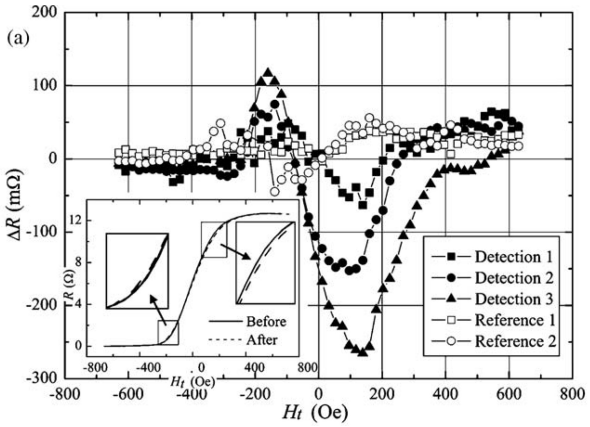



Figure 1.46: Resistance differences before and after depositing 16-nm $Fe_3O_4$ nanoparticles for three detection sensors (filled symbols) and two reference sensors (open symbols) [12]

$Fe_3O_4$ nanoparticles with a diameter of 16 nm, were placed on the sensing area, which were magnetised with a vertical external field to induce a magnetic moment during the experimental detection experiments. They observed a change in the sensor's magnetoresistance response as shown in Figure 1.46 , which shows resistance differences before and after depositing 16 nm $Fe_3O_4$ nanoparticles for three detection sensors (filled symbols) and two reference sensors (open symbols). The inset shows the MR transfer curves measured before (solid line) and after (dashed line) the nanoparticle deposition for the detection sensor 3. The three detection sensors have different numbers of the $Fe_3O_4$ nanoparticles.

J. loureirgo group in 2009 [13] reported detection of magnetic beads flowing in a microfluidic channel using a GMR sensor. The sensor was top pinned with a crossed anisotropy and had a stack configuration in nm's of Ta 2/ $Ni_{80}Fe_{20}$ 2.5/ $Co_{80}Fe_{20}$ 2.5/ Cu2/$Co_{80}Fe_{20}$ 2.5/ $Mn_{76}Ir_{24}$ 6/ Ta 2. The sensor measured a GMR ratio of 7 % with a sensitivity of 5 V/T. The sensor was patterned into a YOKE shape of width 2.5 µm and length 40 µm. To protect the sensor during the microfluidic detection experiments the sensor was passivated with 100 nm $Al_20_3$ and 700 nm $SiO_2$. The 2 µm magnetic beads where filled with paramagnetic $Fe_3O_4$ nanoparticles, which where magnetised using a 90 mT vertical external field to induce a magnetic moment during the experimental detection experiments. Figure 1.47 shows the transfer curve of the SV sensor with an average MR of 7% and a sensitivity of 5 V/T. The inset shows the simulated sensor

output according to the position (x,0,z) of a flowing MP vertically magnetised by a 90 mT field. Maximum signals of 6 V pk-pk are expected for MPs at z = 10 µm and 40 µV pk-pk at z = 3 µm.

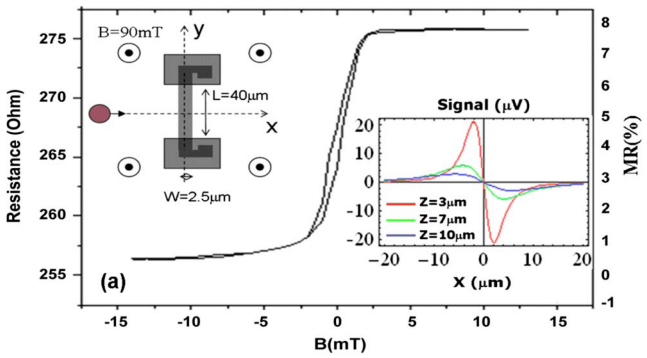



Figure 1.47: a) Transfer curve of a SV sensor with an average MR of 7% and a sensitivity of 5 V/T. The inset shows the simulated sensor output according to the position (x,0,z) of a flowing MP vertically magnetised by a 90 mT field [13]

To measure the detected signals the overall amplification gain was set at 2000 (70 dB) which incorporated a narrow band filter 3 Hz to 3 KHz, this comprised of a custom made low noise preamplifier 1.2 $nV/\sqrt{Hz}$ incorporating a high pass filter at 3 Hz, a low pass filter at 6 kHz, and a gain of 56 dB followed by a commercial Stanford amplifier SR560 set with a high pass filter at 100 Hz, a low pass filter at 3 kHz, and a gain of 14 dB. This connected to a commercial 16 bit DAC digital to analog conversion board that allows continuous acquisition up to a sample rate of 20 kHz. With this setup, the total rms noise of the measurement is 1 µV for a bandwidth of 3 kHz and a sensor biasing current of 1 mA. This corresponds to field equivalent rms noise of 215 nT. The device was sensitive enough to detect, and count micro-sized beads flowing at velocities of 8 – 35mm/s. Figure 1.48 (a) shows the data acquired at 3 kHz, corresponding to a burst of particles flowing on top of the sensor Figure 1.48 (b) the same data as shown in (a) after digital filtering. The exploded view shows an example of two peaks corresponding to two flowing particles, the first one having 10 points available to the reconstruction analysis and the second one 8 points. The maximum signals detected were of 6 µV pk-pk at a height of 10 µm and 40 µV pk-pk at 3 µm above the sensor. Sensor signals of 3 µV to 100 µV pk-pk correspond to bead moments at different directions indicating a physical rotation of the beads.

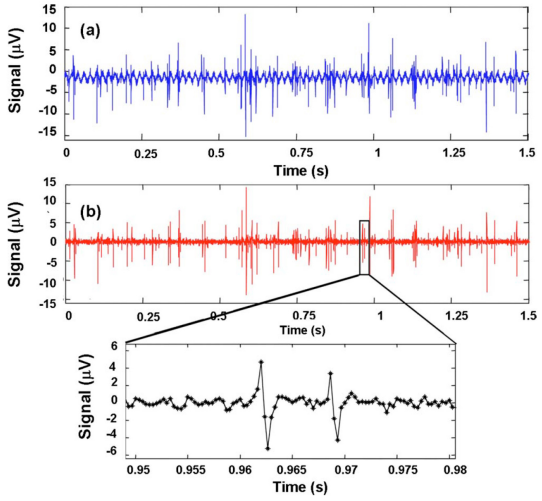



Figure 1.48: (a) Raw data acquired at 3 kHz, corresponding to a burst of particles flowing on top of the sensor (b) Same data as shown in (a) after digital filtering it. The exploded view shows an example of two peaks corresponding to two flowing particles, the first one having 10 points available to the reconstruction analysis and the second one 8 points [13]

A. Fernandes et al group in 2014 [14]reported detection of magnetic beads flowing in a microfluidic channel using a GMR sensor. The sensor was top pinned with a crossed anisotropy and had a stack configuration in nm's of Ta 2/$Ni_{80}Fe_{20}$2.5/$Co_{80}Fe_{20}$2.3/Cu 2.2/$Co_{80}Fe_{20}$3.3/$Mn_{76}Ir_{24}$7/Ta 10. The sensor measured a GMR ratio of 7.5 % and sensitivity 0.24 %/Oe. A number of sensors were patterned into a rectangle bar shape of width 3 µm and lengths varying from 20 µm to 100 µm. To protect the sensor during the microfluidic detection experiments the sensor was passivation with 300 nm $Si_3N_4$ using thermal evaporation. The microfluidic channel was custom fabricated using poly (dimethylsiloxane) (PDMS) of width 100 µm width and height 100 µm. The 1 µm biological cells were coated with 1600 superparamagnetic $Fe_3O_4$ beads (Nanomag®-D-spio) diameter 50 nm. A permanent magnet was used to induce a magnetic moment in the beads during the experimental detection experiments. To measure the detected signals the overall amplification gain was set at 10,000 (80 dB) which incorporated a band filter 100 Hz to 100 KHz using a Stanford Research amplifier SR560. This connected to a commercial 16 bit DAC digital to analog conversion board that allows continuous acquisition up to a sample rate of 20 kHz. With this setup, the total rms noise of the measurement is 10 µV and a sensor biasing current of 3 mA. This corresponds to field equivalent noise of 2 µT. From simulations of the expected detection response of the

magnetic bead surface coated cells, bipolar peak amplitudes of 15 μV correspond to cells traveling at a height of 10 μm above the sensor. As the sensor noise is 10 to 15 μV, they conclude that cells passing at a height above 10 μm are unable to be detected. Figure 1.49 shows the simulation of signal variation with height from the sensor for cells at 10 μm distance from each other along y axis.

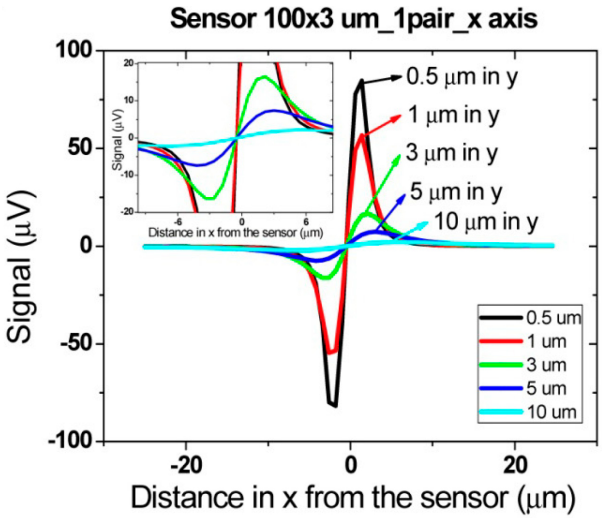



Figure 1.49: Signal variation with height from the sensor for cells at 10μm distance from each other along y axis

The biological cells and nanoparticles suspended in a milk solution were dispensed across the channel at a flow rate of 50 μL/min. The concentration milk sample was 200 μL of functionalised nanoparticles (6.4 x $10^9$particles/μL for $10^4$ cells/μL) and 4.6 μL of Streptococcus agalactiae cells suspension (1.28 x $10^6$ cells/μL). During experimental detection the device measured a noise of 30 μV pk – pk. The cell detection was sporadic with a low cell detection yield detected, which varied from 40 μV to 325 μV in respective experiments. Figure 1.50 shows the acquired signal for raw milk samples spiked with magnetically labeled Streptococcus agalactiae cells at 50 μL/min

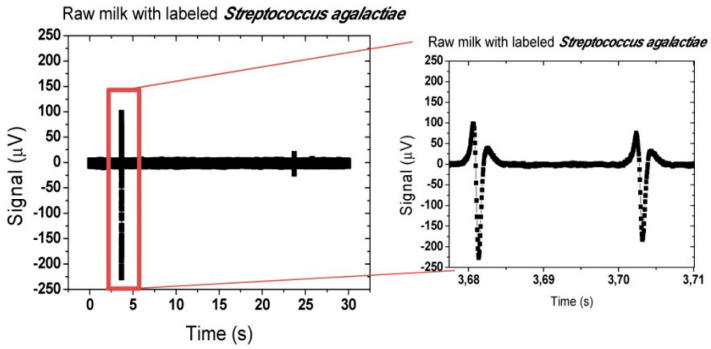



Figure 1.50: Acquired signal for raw milk samples spiked with magnetically labeled Streptococcus agalactiae cells at 50 µL/min [14]

In 2011 J. loureirgo et al group using a similar scheme as in 2009 reported detection of magnetic beads flowing in a microfluidic channel using a GMR sensor. The sensor was top pinned with a crossed anisotropy and had a stack configuration in nm's of Ta 2/$Ni_{80}Fe_{20}$2.5/$Co_{80}Fe_{20}$2.5/Cu 2/$Co_{80}F_{e20}$2.5/$Mn_{76}Ir_{24}$ 6/Ta 2/ TiW($N_2$) 15. The sensor measured a GMR ratio of 7.69 % with a sensitivity of 4.8 V/T using 1 mA bias current. The sensor was patterned into a YOKE shape of width 2.5 µm and length 40 µm. To protect the sensor during the microfluidic detection experiments the sensor was passivated with 100 nm $Al_2O_3$ & 700 nm $SiO_2$. The microfluidic channel was custom fabricated using poly (dimethylsiloxane) (PDMS) of width 150 µm width and height 14 µm. The cells used in the experiments have an average diameter of 5 µm , and were coated with paramagnetic $Fe_3O_4$ nanoparticles diameter 50 nm. The average total number of nanoparticles per cell was estimated to be 2880 +/- 500. The nanoparticles have a magnetic content equivalent to a 10 nm magnetite core, coated with dextran (a complex branched glucan), and have an overall diameter of about 50 nm. The magnetic moment of these particles was measured for a 10 µl sample with a concentration of 3.3 x $10^{12}$particles/ml using a vibrating sample magnetometer (VSM). The individual nanoparticle saturation moment was 1.96 x $10^{-17}$ $Am^2$ (for fields higher than 100 mT). The nanoparticles were magnetised using a 190 mT vertical external field to induce a magnetic moment during the experimental detection experiments. Figure 1.51 (a) Simulated signals for 5 µm diameter cells, labelled with 2880 uniformly distributed nanoparticles, vertically magnetized, at different heights (5 µm, 7 µm and 11 µm).

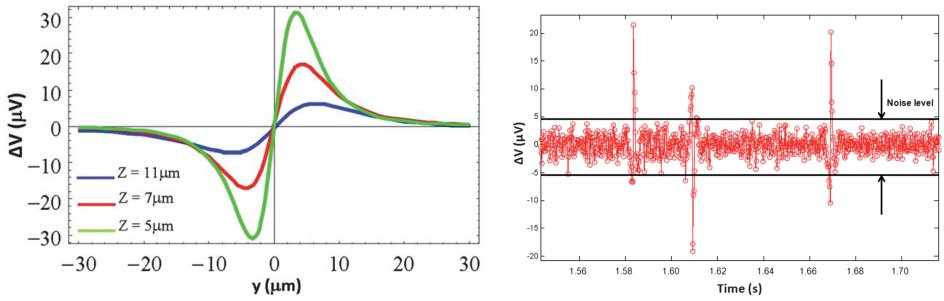



Figure 1.51: (a) Simulated signals for 5 mm diameter cells, labeled with 2880 uniformly distributed nanoparticles, vertically magnetised, at different heights (5 mm, 7 mm and 11 mm) (b) Three single cell detection by a spin valve with 1 mA biasing current. The signal's amplitude is around 17–20 mV and the noise's amplitude approximately 3.54 mVrms

The simulation shows a background noise below 5 μv, indicating that cells can be detected at the top of the channel. To measure the detected signals the overall amplification gain was set at 20,000 (86 dB), which incorporated a band filter 100 Hz to 3 KHz using a Stanford Research amplifier SR560. This was connected to a commercial 16 bit DAC digital to analog conversion board that allows continuous acquisition up to a sample rate of 20 kHz. With this setup, the total rms noise of the measurement is 4.5 μV for a bandwidth of 5 kHz and a sensor biasing current of 1 mA. After the acquisition, the data is filtered (using a digital high pass filter) and the RMS noise reduced to approximately 3.5 μV, which corresponds to a field equivalent RMS noise of 0.7 μT. The detection experiment used a concentration of 4.76 x $10^3$ cells/μL, which were dispensed using a syringe pump flowing inside the micro-channel at speeds of 10 mm/s. For this experiment, signal amplitudes varied between 5 and 20 μV as shown in Figure (b), which highlights the detection of three single cells. Using a hemocytometer, the estimated number of detected cells was 14119 with an error of +/- 1272 cells. The cell detection experiments using the GMR sensor showed an average of 4492 cell counts per run. Taking into consideration the number of data points acquired in 3 min with an acquisition rate of 5 kHz, given that the GMR sensor length is 40 μm and the channel width 150 μm, assuming a uniform distribution of cells across the channel width, the SV sensor is able to detect approximately 27% of the total number of cells flowing inside the channel. This means that in order to compare the SV result with the one given by the hemocytometer, the first must be multiplied by (1/0.27), leading to an average

of 14274 cells, which is within the error bar of the number of cells measured with the hemocytometer.

P. Gooneratne et al group in 2011 [108] reported concentrating and detecting superparamagnetic beads (SPBs) using an array of ring-type structures for the GMR sensor. The beads could be manipulated toward the inner GMR sensing area where they attached and are detected. The sensor was bottom pinned with a crossed anisotropy and had a stack configuration in nm's of Si / $SiO_2$ 50/ MgO 10/ $Ni_{80}Fe_{20}$ 2.5/ $Mn_{83}Ir_{17}$15/ $Co_{70}Fe_{30}$4.5/ Ru 0.8/ $Co_{70}Fe_{30}$ 1.0/$Ni_{80}Fe_{20}$4/ $Co_{70}Fe_{30}$ 1.5/ Cu 3 / $Co_{70}Fe_{30}$1.5/ $Ni_{80}Fe_{20}$5/ Ru 1. The sensor was patterned into a circular ring shape of width 4 µm and diameter 10 µm. To protect the sensor during the detection experiments the sensor was passivated with 100 nm $Si_3N_4$ using a thermal evaporator and a 500 nm Al conducting ring placed on top. The sensor measured a GMR ratio of 5.9 % using a dc bias current of 5 mA. The linear region of sensitivity was between 1 and 3 mT is 1.3 mV/mT Figure 1.52 (a). Figure 1.52 (b) shows the noise spectrum of a single half-ring GMR element. fc was found to be 30 Hz, which is the lowest frequency measurements should be performed at, if a high signal to noise ratio is supposed to be obtained. The noise value at fc is approximately $6nV/\sqrt{Hz}$. Figure 1.52 shows the GMR sensor magnetoresistive response and noise spectrum.

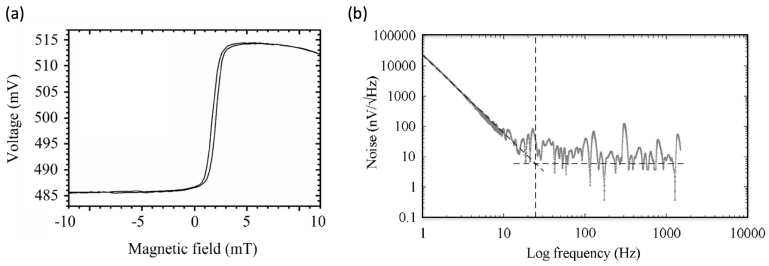



Figure 1.52: (a) GMR sensor magnetoresistive response (b) noise spectrum

Iron oxide ($Fe_3O_4$) diameter 2 µm beads were placed over the sensor, which were magnetised during the experiment using an applied field of 2 mT. Figure 1.53 (a) shows the magnetisation curve for 2 µm magnetic beads from Micromod.

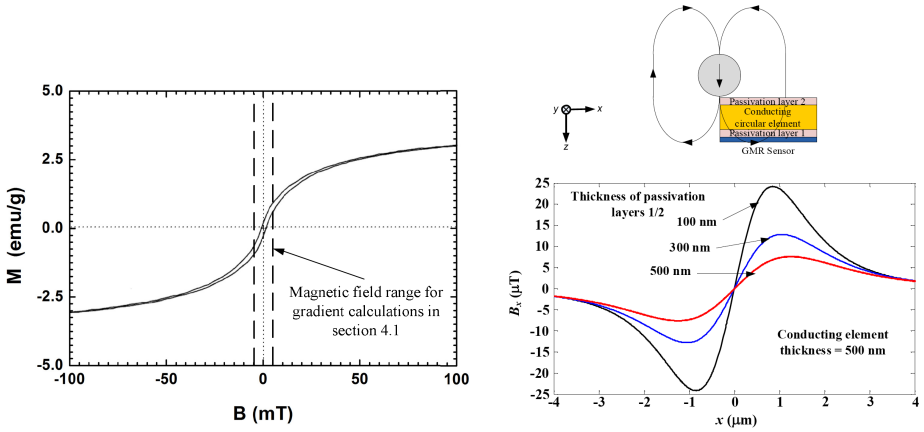



Figure 1.53: (a) shows the Magnetisation curve for 2 μm magnetic beads from Micromod (b) Simulated response of detected stray fields produced by a 2 μm magnetic bead magnetized at a field of 330 A/m

Figure 1.53 (b) shows the simulated response of detected stray fields produced by a 2 μm magnetic bead magnetised at a field of 330 A/m at various heights z above the GMR sensor. The field response is inversely proportional to $t$, which is the thickness of the passivation layers and the conducting layer. The magnetic stray fields decrease by approximately 70 % when the passivation layer thickness is increased from 100 to 500 nm.

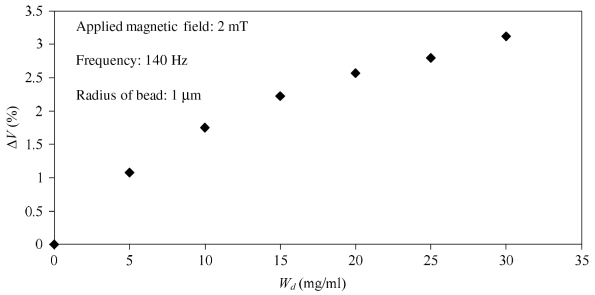



Figure 1.54: Response of a single half-ring GMR sensing element to various magnetic fluid weight density values

Figure 1.54 shows the output signal of the sensor is a function of $Wd$ ranging from 5 to 30 mg/ml. $Wd$ refers to the ratio of the weight of MBs to the total weight of a 1 ml solution of beads and water.

A summary for magnetic bead detection is shown in Table 1.4.

| Ref. | Detection | Sensor GMR | Sensor Area (μm) | Gain dB | Bandwidth | Noise μV | Noise μT | Detection | Velocity (mm/s) |
|---|---|---|---|---|---|---|---|---|---|
| L. Guanxiong *et al* 2002 | Micro beads 2.8 μm $FeO_x$ Passivation 1 μm photoresist | 10.3 % Strip | 3 x 12 5 x 10 | 40 | | 100 | | 1.2 mV reduction 3.8 mV reduction | MB placed No flow |
| L. Guanxiong *et al* 2006 | Nano particles ~23 16 nm $FeO_x$ Passivation 1 μm photoresist | 11.3 % Strip | 0.2 x 1 | 40 | | 100 | | 50 to 200 mΩ | MB placed No flow |
| J. Loureiro *et al* 2009 | Micro beads 2 μm $FeO_x$ Passivation $SiO_2$ 700nm & $Al_2O_3$ 100 nm Ch Height 14 μm | 7% YOKE | 2.5 x 40 | 70 | 3 Hz – 3 KHz | 1 | 0.212 | 6 μV @ 10 μm 40 μV @ 3 μm | 8 – 35 |
| A.Fernandes *et al 2011* | Cells 1 μm coated $FeO_x$ particles Passivation $Si_3N_4$ 300 nm Ch Height 100 μm | 7.5% Strip | 3 x 20 to 100 | 80 | 100 Hz – 100 KHz | 30 | 6 | 40 μV - 325 μV | 6 – 30 |
| J. Loureiro *et al* 2012 | Cells 2 μm coated $FeO_x$ particles Passivation $SiO_2$ 700nm & $Al_2O_3$ 100 nm Ch Height 14 μm | 7% YOKE | 2.5 x 40 | 86 | 100 Hz – 3 KHz | 10 | 1.25 | 15 μV @ 9 μm 25 μV @ 6 μm | 8 - 10 |
| P.Goneratne *et al* 2012 | Micro beads 2 μm $FeO_x$ | 5.9 % Ring | 0.2 x 1 | 80 | 100 Hz – 100 KHz | 10 | | | MB placed No flow |

Table 1.4: Summary of superparamagnetic bead detection

## 1.13 CONCLUSIONS

GMR and TMR sensors are very sensitive devices that have been incorporated into numerous applications. Specifically YOKE shaped GMR sensors have been incorporated into biomagnetic applications such as magnetocardiography (MCG) [48], and detection of magnetically-labelled biomarkers [109]. A summary of the detection of superparamagnetic beads is shown in Table 1.4. Advances in the electrodeposition processes of magnetic nanowire deposition using nano-porous anodic aluminium oxide (AAO) membranes has been the subject of research and commercial applications interests. There are no reports of ferromagnetic nanowire detection using either GMR or TMR sensors. In this research I want to explore the use of YOKE GMR and TMR sensors for the detection of ferromagnetic nanowires flowing in a microfluidic channel towards application such as the detection of molecular biomarkers using functionalized magnetic nanowires.

# 2

# EXPERIMENTAL TECHNIQUES

## 2.1 INTRODUCTION

This chapter describes the experimental methods used for the deposition and characterisation of magnetic thin film devices. These devices include GMR sensors and TMR (magnetic tunnel junctions) sensors. The fabrication of the devices uses a number of processes including magnetron sputter deposition, UV lithography, Argon ion milling and annealing. This chapter also describes the experimental methods used for the electro deposition and characterisation of magnetic nanowires. The thin film devices were characterised using several analysis techniques like X-ray diffraction, X-ray reflection, SQUID magnetometer, Scanning Electron Microscope (SEM) and magneto-transport measurements and noise measurements. Magnetic nanowires were characterised using several analysis techniques including SEM, TEM and SQUID magnetometer.

## 2.2 THIN FILM SPUTTER DEPOSITION

GMR and TMR sensors are structures composed by multilayer engineered structures based on nanometric thick layers of metals and insulators. Deposition techniques using ultra-high vacuum systems and providing control of the thickness of the deposited layers are essential for the correct functionality of the magnetoresistive devices.

### 2.2.1 *Physical Vapour Deposition - Thin film sputter deposition*

Sputtering [65] is one of the most widely used physical vapour deposition techniques. This method is applicable both in industry and in the research laboratories. The advantages

of sputtering can be stated as moderately low cost, high deposition rate, reproducibility and large area fabrication ability. The sputtering process occurs when an accelerated ion collides with a solid target material. When the ion kinetic energy is sufficient, ejection of an atom from the target takes place due to momentum of transfer. In the following sections, the sputter deposition process is described in more detail.

The basic thin film deposition requires pumping the reaction chamber to a low enough pressure ($10^{-7}$Torr), so that the water and oxygen absorbed at the walls is reduced. The deposition requires an inert gas (Argon) in order to produce a plasma (mTorr). A high voltage is then applied to the target producing an electrical discharge that allows the ionisation of the gas and leads to the plasma as illustrated in the schematic of the sputtering process shown in Figure 2.1(a). The ions are then attracted toward the cathode hitting the target. The ions with energy above the threshold can extract atoms from the target material. The atoms are deposited onto the substrate, which is facing the target, and so forming a layer of material. During the collision process, secondary electrons are produced, promoting a sustainable plasma at lower pressures.

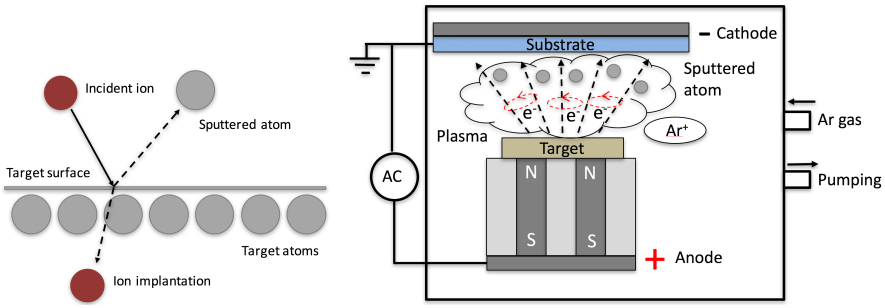



Figure 2.1: (a) Basic schematic of the sputtering process and (b) schematic of the magnetron sputtering process

The plasma is a partially ionised, neutral, gas containing ions, and electrons, with high enough concentrations of charged particles for significant Coulomb interaction to occur [67]. Plasma has a positive potential relative to the surface in contact with it, which is due to the higher velocities of the electrons in the plasma compared to the ions. This results in a negative charge on the surface of the target, the negative charge repels electrons and attracts positive ions from the plasma until equilibrium is reached at a certain negative potential, relative to the plasma potential. The plasma is ignited by applying a negative voltage (few hundred volts) to the target, which causes ions in the plasma to

be accelerated toward the target [66]. The resulting collisions give rise to sputtering of target atoms and emission of secondary electrons. The electrons are accelerated toward the anode to ionise (by direct impact) more gas atoms, which bombard the target and produce more sputtered atoms and secondary electrons. When equilibrium is reached, a steady-state discharge is sustained and the ejected target atoms/molecules are deposited on the substrate. With the use of a magnetron placed near the target, as illustrated in the schematic shown in Figure 2.1(b), the ionisation yield increases. Overall, sputtering is an efficient process since the incident ions and sputtering atoms can retain most of their energy and directionality due to their mean free paths inside the chamber. This is achieved by use of low base pressure ($<10^{-7}$Torr) and working pressures ($10^{-3}$Torr). Terminal energy is used by the deposited atom to diffuse a more stable position on the substrate or on the growing film at the later stage. Cooling of the substrate holder provides a good control of the temperature of the deposition process. The advantage of the sputtering method over the evaporation method is the ability to deposit from a target composed of different materials (alloys) [66]. As a result of this, sputtering is the preferred technique to deposit metallic and magnetic layers in GMR and TMR devices and insulators.

### 2.2.2 *Magnetron sputtering*

Magnetron sputtering is a physical vapour deposition technique used to deposit thin films of material under vacuum [68], [69-71]. The basic principle in magnetron sputtering is the use of permanent magnets behind the target to create a magnetic field between the outer and inner parts of the target. The principle of operation is positive ions strike a negatively biased target, which sits on the cathode. Material is ablated from the target surface and is deposited on a substrate, which is placed over the target. The positive ions are released through the plasma. The plasma is ignited by applying a voltage between the anode and cathode of the magnetron through a process gas, typically Argon, which ionises the gas. The magnetic fields from the permanent magnets in the magnetron confine the electrons to a circular path close to the target increasing the rate of ionisation

and creating a higher density plasma close to the target, improving the sputter process [70]. The Shamrock sputter deposition chamber that is used for the depositions uses S-Gun geometries for the magnetron sputtering [68] as illustrated in the schematic of the S-Gun magnetron shown in Figure 2.2. The S-Gun magnetron uses a conical shaped target, which sits on the cathode and the permanent magnet. The anode connects to the chamber and protrudes through the centre of the target. This geometry provides a uniform sputter track over the surface area of the target, increasing the target efficiency and sputter rate. The planar magnetron uses a flat circular target, which is attached to the cathode. The outer body of the magnetron connects the anode and sample holder to chamber ground, creating a potential between the substrate and the target.

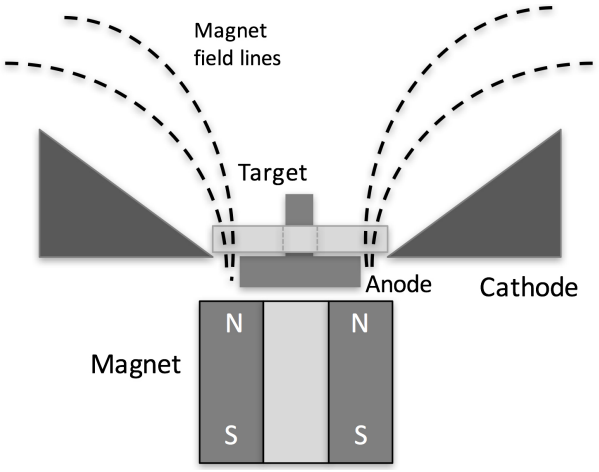



Figure 2.2: Schematics of the S-Gun magnetron

There are three main modes of operation for magnetron sputtering – direct current (DC), pulsed DC, and radio frequency (RF). Direct current (DC) operation uses a constant voltage and current polarity. It is most commonly used for sputtering of metallic, conducting films. In pulsed DC operation a modulated DC supply produces a square wave (20 – 100 kHz) and is used for both sputtering of metal films and reactive sputtering. During each cycle the signal switches on and off. This method promotes electrons bombarding the target and also assists in the cleaning off the thin reactive compound film that may have formed on the target surface during the off cycle [72]. The Radio Frequency (RF) operation [68] is typically used to deposit insulating material as illustrated in the schematic of the impedance matching circuit used for RF sputtering shown in Figure 2.3. It uses a RF supply with frequencies oscillating at 13.56 MHz, which

creates a plasma in the space between the target and the substrate. An RF generator power supply is connected through a capacitor to the magnetron. When the target is coupled to the plasma, a charge builds up on the surface of the target, which then negatively self-biases to produce a net current of zero. It is this self-bias which creates the potential required for sputtering. RF sputtering uses a matching circuit, to balance the impedance difference between the chamber and the RF generator.

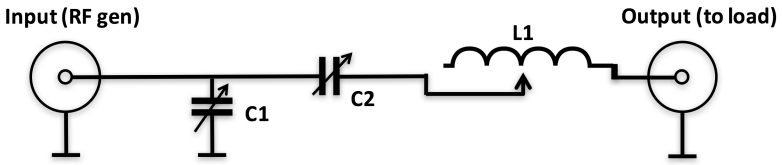



Figure 2.3: Schematic of impedance matching circuit for RF sputtering

### 2.2.3 *Thin film deposition system*

The thin films multilayer depositions in this study were all carried out in our high vacuum magnetron sputtering/evaporation cluster tool, which is located in the CRANN Class 10000 clean room, as shown in Figure 2.4.

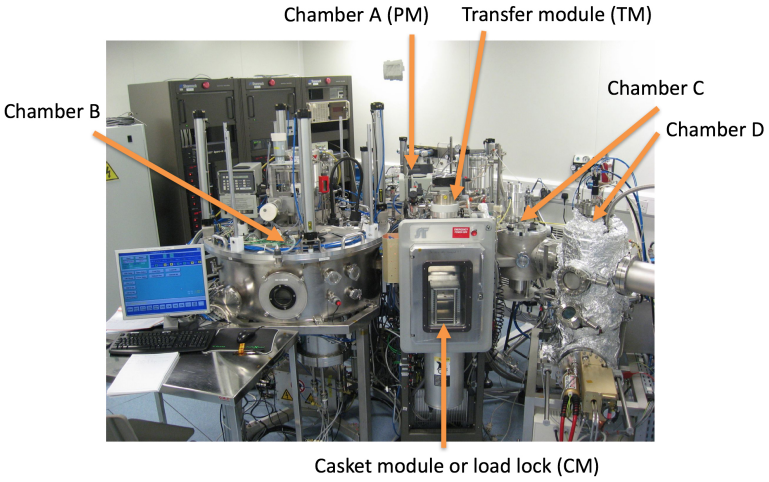



Figure 2.4: High vacuum magnetron sputtering cluster tool

The overall system, which allows for the deposition of metals and insulators, comprises of two high vacuum, and one ultra high vacuum process chambers. Chamber A is a high vacuum Shamrock sputtering deposition system, Chamber B is a Plassys MP900 sputter deposition system and Chamber D is a custom-built ultra high vacuum (UHV) e-beam

evaporation/sputter deposition system. These are an interconnected system through a high vacuum transport module chamber (TM) containing a computer controlled robot for movement of wafers directly between process chambers with or without returning wafers to the load-lock casket module (CM). The high vacuum CM module allows loading up to 15 wafer or substrates for deposition. This allows for multiple sputtering on multiple wafers without having to break the vacuum. Figure 2.5 shows the layout of Sputter deposition system showing three deposition chambers (A, B and D), transfer chambers (TM and Chamber C) and the load lock (CM).

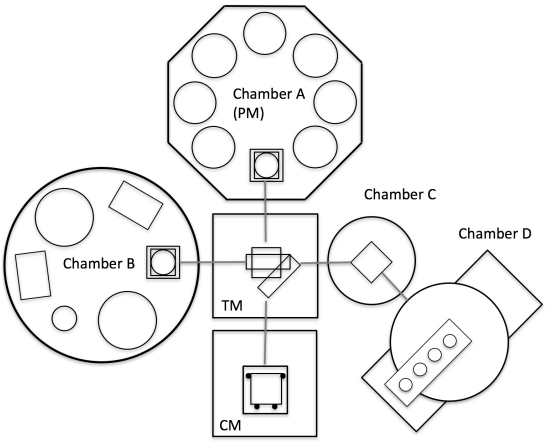



Figure 2.5: Layout of Sputter deposition system showing three deposition chambers (A, B and D), transfer chambers (TM and Chamber C) and the load lock (CM)

Chamber A, referred to as the Process Module (PM) is a high vacuum chamber for magnetron sputtering. The chamber holds six 3" Series III magnetron guns and an ion-milling gun. The magnetron guns can operate in DC mode. The cathode bias voltage for each gun is controlled by six 1.5 kW (Advanced Energy- MDX 1.5K) power supplies. Two power supplies control the anode bias on guns 1-3 and 4-6 respectively. A pulsed DC supply can be used on guns 2 & 6. The chamber is pumped using an Agilent turbo molecular pump and Oxford water pump. The chamber can reach base pressure of $< 8$ x $10^{-8}$ Torr, with typical pressure during deposition 5 x $10^{-3}$ Torr. The system use both 4" and 6" wafers, with up to 4 wafers processed at the same time. The deposition is fully automated and computer controlled. The chamber has four rotating planets on a motorised turntable, which sit above the guns. Figure 2.6 (a) shows the four rotating planets in Chamber A.

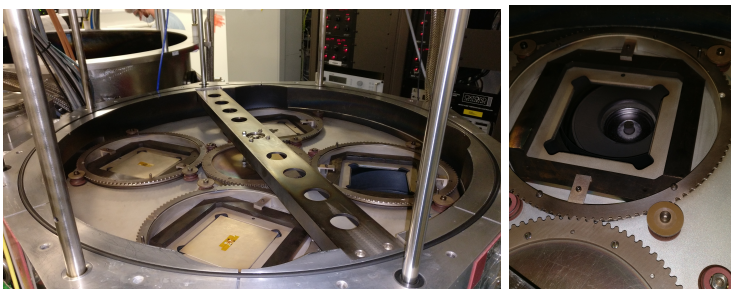


Figure 2.6: (a) Chamber A showing the four rotating planets and (b) one of the targets used in Chamber A

This enables uniform deposition up to 6" wafers from only 3" targets and allocates time for the cooling of the substrate during growth which results in smoother films. Each planet has permanent magnets, which produce a field of 10 mT. The field produced by the permanent magnet, is used during deposition of the GMR sensor to set the easy axis of the free layer and setting the exchange bias. The targets used in chamber A as shown in Figure 2.6 (b) are 3" in diameter and have a different design for magnetic and non-magnetic materials as show in Figure 2.7. Chamber A was used for the deposition of all the metal layers in the GMR stacks and most of the metal layers in the TMR (MTJ) stack configuration. Chamber A was also used for the nitride depositions AlN and RF SiN nitride layers, which were used for the protective passivation layer on the sensor.

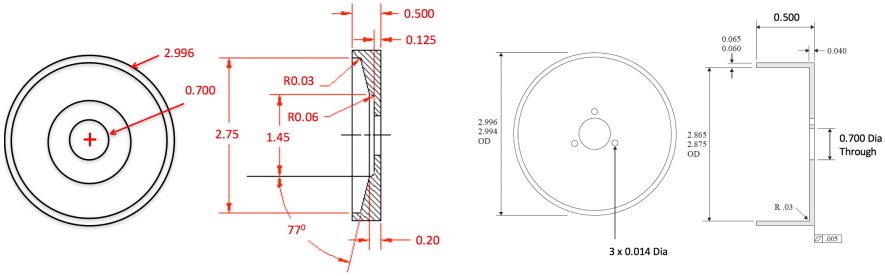



Figure 2.7: Design for non-magnetic and magnetic targets used in Chamber A

Chamber B comprises of eight sputtering guns and one ion gun. These are arranged as two Target Facing Target (TFT) guns, which are supplied using 300W RF power supply (Huttinger PFG 300 RF) with a matching RF circuit. Two cluster guns, which have three guns each. These are supplied using three 0.5 kW DC power supplies (Advanced Energy-MDX 500). The TFT targets are used to grow high quality oxide materials including MgO for the MTJ barrier layer in the TMR sensors. Figure 2.8 (a) shows the

TFT target holder in chamber B . The cluster guns are used for metal depositions of alloys including CoFeB for MTJ growth. Figure 2.8(b) shows one of the CoFeB target used in the cluster gun in chamber B.

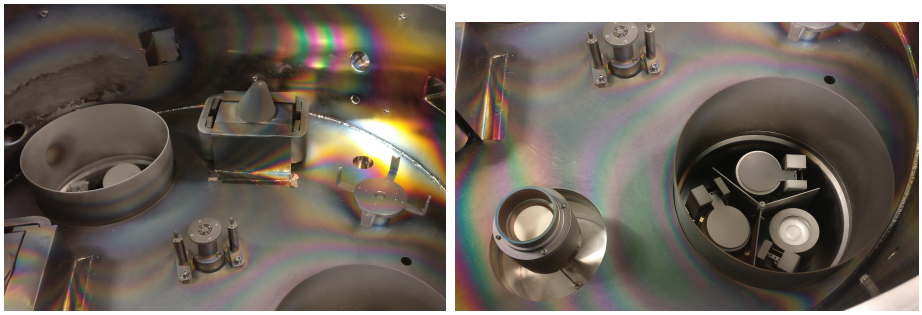


Figure 2.8: (a) TFT target holder in chamber B and (b) CoFeB target used in the cluster gun in chamber B

A Turbo Molecular Pump and a CTI water pump are used to achieve a base pressure $< 3 \times 10^{-8}$ Torr. The partial pressure of water vapour is $< 3 \times 10^{-9}$ Torr. This is critical for the deposition of high quality MgO layers. The chamber can heat the substrates up to 750 °C. Table 2.1 shows a summary of the deposition parameters for the in-plane metallic targets and nitride layers targets used for both GMR and TMR sensors deposited in both chamber A and B.

| Material | Chamber | Power (W) | Gas flow (sccm) | Pressure ($10^{-3}$ Torr) | Rate (nm/s) |
|---|---|---|---|---|---|
| Ta | A | 100 | Ar: 40 | 2.0 | 0.01 |
| $Co_{90}Fe_{10}$ | A | 100 | Ar: 25 | 1.4 | 0.01 |
| $Ni_{80}Fe_{20}$ | A | 100 | Ar: 25 | 1.4 | 0.01 |
| Cu | A | 100 | Ar: 25 | 1.4 | |
| $Ir_{22}Mn_{78}$ | A | 100 | Ar: 25 | 1.4 | 0.02 |
| Ru | A | 100 | Ar: 25 | 1.4 | 0.016 |
| AlN | A | 250 | Ar: 10<br>$N_2$: 40 | 1.4 | 0.003 |
| SiNx | A | 150 | Ar: 7<br>$N_2$: 25 | 1.4 | 0.005 |
| $Co_{40}Fe_{40}B_{20}$ | B | 100/30/40 | Ar: 25/20/25 | 1.4/4.7/1.0 | 0.009 |
| MgO | B | 100 | Ar: 7 | 1.4 | 0.017 |

Table 2.1: Summary of the deposition parameters for the metallic targets and nitride layers targets used for both GMR and TMR sensors deposited in both chamber A and B

## 2.3 ELECTRODEPOSITION PROCESS FOR NANOWIRE FABRICATION

In my research I use an electrochemical cell with three electrodes connected to a potentiostat for the growth of nanowires using a porous anodic aluminium oxide (AAO) membrane template. Figure 2.9 (a) shows a schematic of my electrochemical cell set-up, which is a bottom up electrodeposition technique that is more commonly used in the fabrication of nanowires. For my application the working electrode is a porous AAO membrane, which has been sputter coated on the bottom surface with gold thickness 100 nm using a Balzers SCD 004 sputter coater, but other "inert" material can be used such as platinum. The working electrode (WE), which is the cathode, is the electrode where the potential is controlled and where the current is measured and serves as a surface on which the electrochemical reaction takes place.

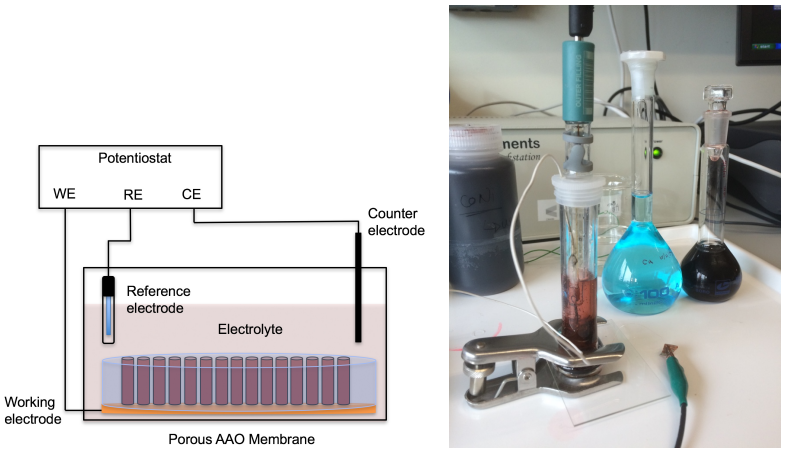



Figure 2.9: (a) Schematic of electrochemical cell for nanowire growth using porous AAO membrane (b) Experimental electrodeposition process setup

The reference electrode, which is used to measure the working electrode potential, is a saturated silver/silver chloride (Ag/AgCl) electrode. The counter electrode (CE) completes the cell circuit, is an inert conductor like platinum or graphite. The electrodes are immersed in an electrolyte (the electrically conductive solution). The porous anodic aluminium oxide (AAO) membrane used in my application is a commercial product from a company called Whatman. Figure 2.9 (b) shows the experimental electrodeposition setup used the in research project. The electrodeposition cell comprises of a small glass cell, which is designed to hold one sputtered membrane, and is sealed against an

O-ring. The glass cell is filled with the solution required for deposition (electrolyte). A potentiostat type Solatron SI 1280B is connected to the electrochemical cell via the reference electrode and counter electrode (anode), which are immersed in the electrolyte solution and the AAO membrane working electrode via a silver wire. The potentiostat provides a current for fixed time duration. The Solatron potentiostat software CoreWare allows the deposition parameters to be configured, by selecting potentiostatic mode, setting the potential voltage required, selecting electrode type and finally setting the time duration for the deposition. While assembling the glass cell with the AAO membrane, care needs to be taken to ensure there is a good seal to the O-ring to prevent the solution leaking while also not damaging or cracking the fragile AAO membrane. Both the calibrated Ag/AgCl reference electrode and the platinum counter electrode are washed with DI water before it is placed into the electrolyte solution. When not in use the reference electrode is stored in just slightly less than saturated KCl solution. Keeping the solution just below saturation allows enough ionic flow to prevent salt crystals from forming in the glass pores. The electrode must be kept wet at all times to ensure the impedance of the electrode remains low.

### 2.3.1 *Nanowire deposition curves*

Before each nanowire deposition is started the open-circuit potential (OCP) is plotted using the CoreWare software. The OCP ensures that the electrodeposition cell is correctly connected to the potentiostat.

To determine the deposition over-potential for each of the nanowire solutions the Cyclic Voltammogram plot is used. From the Cyclic Voltammogram curve we can determine the optimum deposition potential to be applied. The deposition voltage potentials were determined from Cyclic Voltammogram curves on thinfilm, for each of the nanowire solutions produced. Figure 2.10 shows the Cyclic Voltammogram curve for Cu deposition.

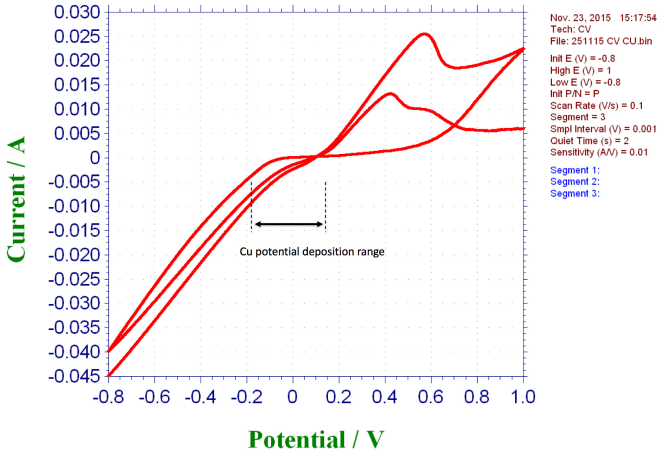



Figure 2.10: Cyclic Voltammogram curve for Cu on thin film used to determine the deposition potential

Nanowires are potentio-statically electrodeposited. The deposition is monitored using the the current vs time dependence plots, which are set using the potentiostats multi-potential step function. Here the deposition parameters are set for the nanowire deposition, such as applied potential and time duration. We can also monitor the Coulomb charge during the deposition. Figure 2.11 shows the typical deposition plots that are recorded for a two magnetic segment nanowire separated by a non-magnetic segment with interlayer step. After deposition the plots are saved to file.

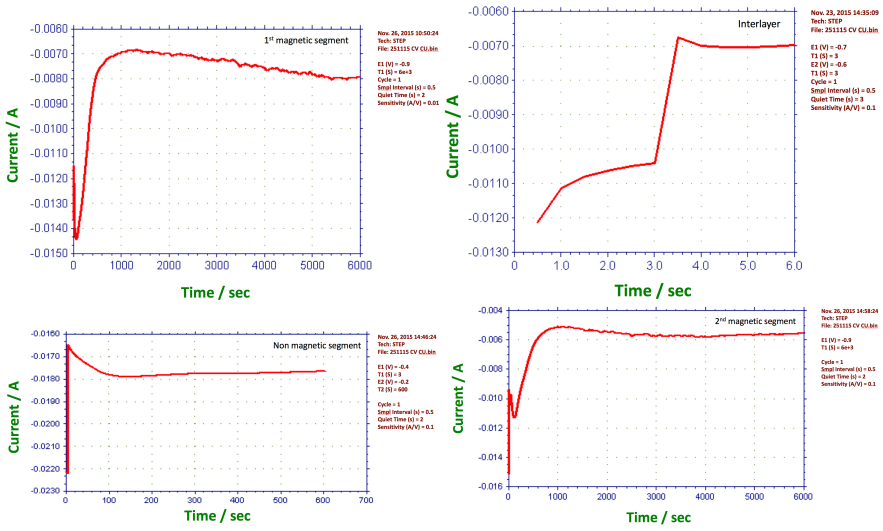



Figure 2.11: Deposition plots for each segment

Figure 2.2 shows the deposition conditions that are monitored for a two magnetic segment nanowire separated by a non-magnetic segment with interlayer.

| Sample | Segment | Type | Pot (V) | Time (Sec) | I (mA) | Charge (Q) | Length (µm) | OCP (V) | Mag (T) |
|---|---|---|---|---|---|---|---|---|---|
| 211013-4 | CoNi | 1st mag seg | -0.9 | 2500 | 6.3 | 15 | 3.3 | 0.14 | 1.2 |
| CoNiCuCoNi | CoNiCu | Interlayer | -0.7 | 3 | 40 | | | | |
| | | | -0.6 | 3 | 20 | | | | |
| | Cu | Spacer | -0.4 | 3 | 15 | | | | |
| | | | -0.2 | 600 | 11 | 20 | 4 | | |
| | CoNi | 2nd mag seg | -0.9 | 2500 | 6.2 | 15 | 3.4 | | |

Table 2.2: CoNi-Cu-CoNi deposition conditions

The single segment nanowires and two segmented nanowires were produced using this process.

### 2.3.2 *Removing the nanowires from the AAO membrane*

When the deposition process is complete the excess solution is removed, the glass cell is disassembled and the membrane is removed and washed in Di water. After deposition, wires are then released from the membrane. The sputtered gold layer (Au) is removed from the AAO membrane using a polishing process. The membrane is then dissolved to remove the alumina thus releasing the wires using sodium hydroxide (NaOH) at a set temperature for a period of time ~ 10 minuets. NaOH 1 molar was prepared by dissolving 4g of NaOH into 100ml of DI water. The AAO membrane is placed into a beaker of 10ml of the NaOH solution at 70$^{o}$C. A process of sonication and inspection every 2 – 3 minuets as detailed in Table 2.3 is used to remove the alumina from the membrane. When complete the NaOH solution is removed to stop the reaction by using a magnet to hold the nanowires and the NaOH removed. The NaOH is removed by rinsing the nanowires in DI water. This is repeated six times. This process is critical to produce wires with good surface structure producing wires that are well dispersed and requires constant visual inspection for each respective nanowire batch produced.

| Sample | Type | Solution (1molar) | Temp ($^{0}$C) | Method | Weight (g) |
|---|---|---|---|---|---|
| 211013-3 | CoNi-Cu-CoNi | NaOH | 70 | Min 4/sonication 10sec, Min 8/ sonication 10sec, Min 10 stop, Rinse in DI water x 6 using magnet | 0.09200 |

Table 2.3: Removing the nanowires from the AAO membrane

The full procedures for the preparation of the nanowire solutions, electrodeposition process and dissolving the nanowies from the AAO membrane for each of the nanowires produced is detailed in Appendix D.

### 2.3.3 *Nanowire magnetisation*

Nanowires were magnetised in membrane using a Bouhnik power supply and electromagnet, which is set at a field of 1.2 Tesla. The Bouhnik system is powered on and the required voltage and current is set. The water supply is switched on, which is required to cool the electromagnet. A RFL 912 Gaussmeter was used to measure the field at 1.2 Tesla. The nanowires, which are in membrane, are placed into the electromagnet as shown in Figure 2.12. This magnetises the nanowires in the parallel direction along the length of the nanowire.



Figure 2.12: CoNi in membrane magnetised

### 2.3.4 *PH meter calibration*

Before calibration of the Ag/AgCl reference electrode, the pH meter must first be calibrated. The pH is a JENWAY model 3510 shown in Figure 2.13

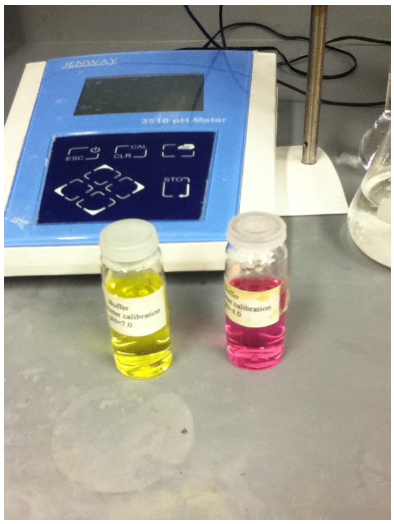


Figure 2.13: Calibration of pH meter JENWAY Model 3510

The calibration procedure is detailed in Table 2.4.

| Step | Calibration procedure for the JENWAY Model 3510 |
|---|---|
| 1 | Remove electrode from Kcl solution and rinse in Di water |
| 2 | Turn the PH meter on and place electrode in Buffer Meter Calibrating Solution PH 4. Keep the electrode held into position |
| 3 | Press CAL button on the PH meter. CAL 1 will appear at the bottom of the monitor. Give a few seconds for the measurement to stabilize |
| 4 | When the PH is stable, a small arrow will appear at the bottom of the monitor. Press CAL button. CAL OK will appear on the monitor |
| 5 | The monitor will now say CAL 2 in the bottom of the monitor |
| 6 | Remove the electrode from the solution and rinse in Di water |
| 7 | Place electrode in buffer meter calibration solution PH 7, and Allow to stabilize as before |
| 8 | The PH meter is now calibrated |

Table 2.4: pH meter calibration procedure

### 2.3.5 *Sputter coating AAO membranes*

To act as a working electrode the porous anodic aluminium oxide (AAO) membrane first needs to be sputter coated with Au with a thickness of ~ 120 nm. The commercial porous membrane from the company Whatman has a nominal pore size of 200 nm, an external diameter 25 mm and internal diameter 16 mm. The lip side of the membrane is coated with a layer of gold to provide electrical contact for the working electrode using a Balzers SCD 004 sputter coater. Figure 2.14 shows the AAO membrane before & after gold sputter coating.

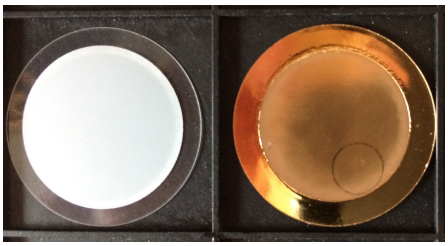


Figure 2.14: AAO membrane before & after gold sputter coating

The procedure to sputter coat the membrane using the Balzers SCD 004 sputter coater is detailed in Table 2.5.

| Step | Calibration procedure for the JENWAY Model 3510 |
|---|---|
| 1. Vent Balzers Unit | • Switch unit off & switch main air line on<br>• Open gas valve on Balzer unit, when vented, close gas valve |
| 2. Place Target & Sample | • Place target under lid, ensure it is secure<br>• Place sample (lip side up) in chamber |
| 3. Pressurise Chamber | • Hold lid down and switch unit on & ensure the gas valve is closed<br>• Flush chamber 8 times |
| 4. Flush Chamber | • Unit on under pressure & open A gas valve until vacuum is completely over to right-hand side<br>• Close gas valve until vacuum bar & repeat 3 times |
| 5. Run | • Set time 700 sec, set current 20 mA & pressure @ 2 x $10^{-2}$<br>• Start |

Table 2.5: Procedure to sputter coat AAO membrane with ~ 120 nm of Au

## 2.4 STRUCTURAL CHARACTERISATION

The structural characterisations of thin films used in the GMR and TMR sensors are performed by X-ray diffraction and X-ray reflectivity. The Scanning Electron Microscope (SEM) is also used for thin films and magnetic nanowire characterisations. These methods are described in the following sections.

### 2.4.1 *X-ray diffraction (XRD) and X-ray reflectivity (XRR)*

The X-Ray diffraction and reflectivity measurements in this study were performed using a Phillips X-Pert Pro PANalytical theta-theta diffractometer shown in Figure 2.15 (a).

X-ray diffraction (XRD) is the standard technique for crystal structure determination. In this technique, the diffraction of the X-rays occurs within the sample according to the Bragg's Law;

$$m\lambda = 2d \sin\theta \tag{2.1}$$

Where $\lambda$ is the X-ray wavelength, $d$ is the layer separation, $m$ is the diffraction order and $\theta$ is the angle of incidence with the sample surface. This allows a diffraction pattern to be built up as the angle is varied around the normal of the reflecting planes.

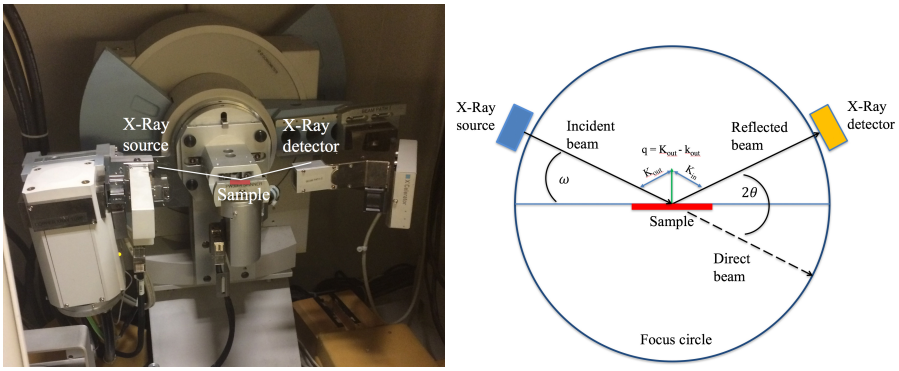



Figure 2.15: (a) Phillips X-Pert Pro PANalytical theta-theta diffractometer and (b) Schematic diffraction principle

The Phillips X-Pert Pro system has a Cu-Ka radiation of wavelength λ =1.5418 °A, which is in the order of the interatomic distance. Figure 2.15 (b) shows a schematic diffraction principle. $q$ is half the angle between the transmitted x-ray beam and the reflected beam [ref]. We align the diffractometer to the substrate diffraction peak, which is Si 69.13°. As we vary the angle $2q$ we will obtain a diffraction pattern from the lattice planes perpendicular to the substrate normal. The peaks obtained in the diffraction pattern will contain information about the texture or growth direction of the thin film on crystalline systems.

X-ray reflectivity (XRR) is used to determine the thin-film thickness, density, and surface roughness. This is used to calibrate the growth rates of the thin-film sputter depositions in the Shamrock deposition tool. At low angles, above the critical angle (where total external reflectivity occurs) we will have constructive interference pattern based on the distance between the air/film interface and the film/substrate interface.

Since there is a change of refractive index and electronic density at the film/air interface and the film/substrate interfaces we will have a change in reflection/ transmission at theses interfaces. This will form two coherent sources of reflected beams. These coherent sources will interfere constructively and create an oscillatory pattern based on the Fourier transform of the vertical distance between the two sources. The oscillations are modelled using WinGixa software. Figure 2.16 shows the XRR measurement from some of the in-plane metallic thin-film depositions (blue trace) and the model fitting using WINGIXA (red trace).

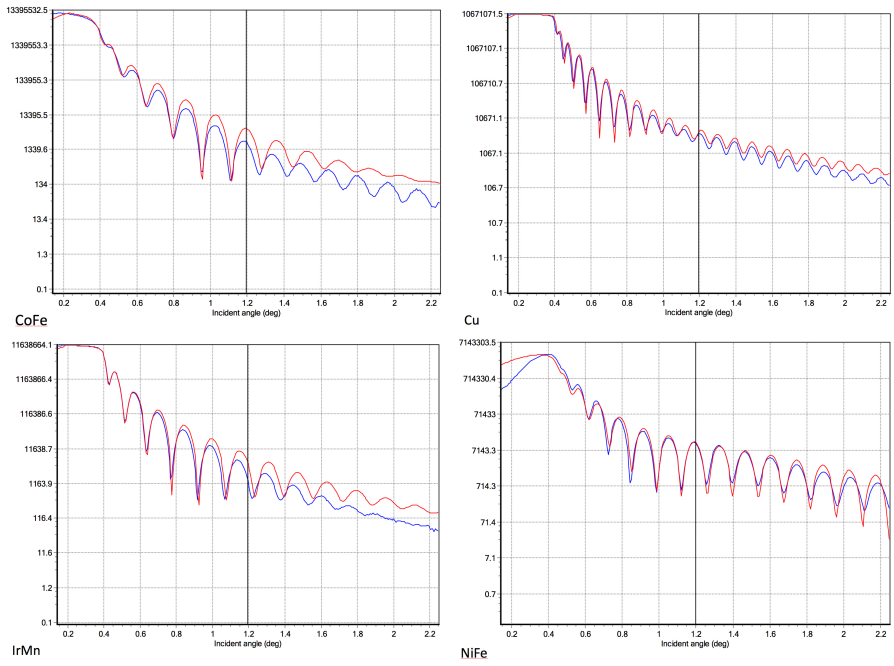



Figure 2.16: XRR measurement of the in-plane metallic target and the model fitting using WINGIXA

The materials density, which determines the critical angle for total external reflection; the layer thickness, which gives rise to the oscillation frequency as the scanning angle is increased; the layer roughness, which determines the drop in amplitude as a function of angle.

### 2.4.2 *Scanning Electron Microscope (SEM)*

The Carl Zeiss Ultra is a high resolution (< 1nm) Field Emission SEM with a Gemini column is installed for imaging, and analytics as shown in Figure 2.17. It was used for some of the structure characterisation of the magnetoresistive sensors and analysis and characterisation of the nanowires to ensure that the they had good separation and morphology. The SEM has an imaging resolution of 1 nm. Accelerating voltages between 100 V and 30 kV. EDX (energy dispersive X-ray analysis) elemental analysis, imaging and mapping using an Oxford Instruments INCA system. Extensive electron detection system including, an Energy Selected Backscattered detector, a Secondary Electron detector and an In lens detector.

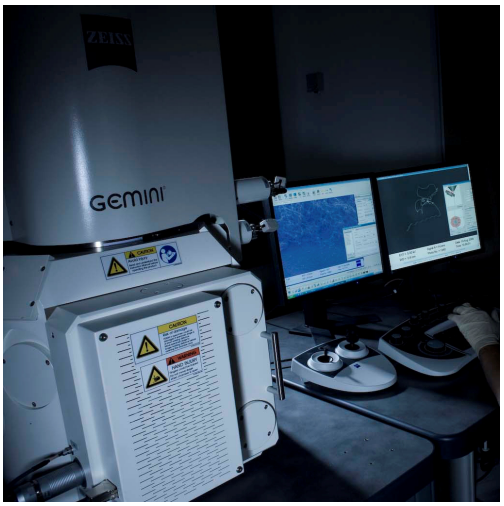



Figure 2.17: Carl Zeiss Ultra Field Emission SEM

### 2.4.3 *Transmission Electron Microscope (TEM)*

The Titan is field emission Transmission Electron Microscope (TEM) with accelerating voltages between 80 kV and 300 kV as shown in Figure 2.18. It is capable of sub-angstrom imaging, and select area electron diffraction, [SAED] for locally measuring the crystallographic properties of materials. It was mainly used for analysis and characterisation of the nanowires to ensure they had good morphology.

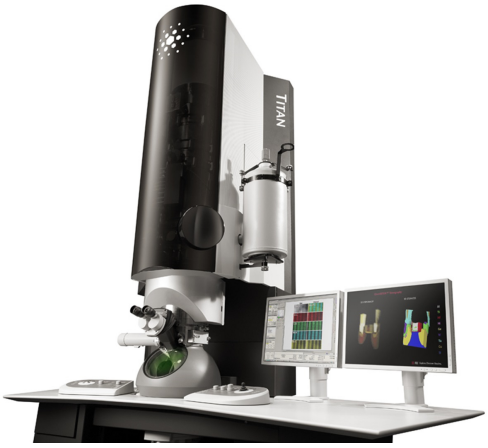



Figure 2.18: Titan is field emission TEM

### 2.4.4 *Atomic force microscope (AFM)*

The atomic force microscope (AFM) type MultiMode, which is supplied by Digital Instruments is a high resolution scanning probe microscope. It consists of a cantilever with a sharp tip that is used to scan the surface of a sample mounted on an anti-vibration plate, which was supplied by Ambios Technology as shown in Figure . The atomic force microscope was used for some of the structure characterisation of the magnetoresistive sensors and the passivation layer thickness.



Figure 2.19: AFM microscope and anti-vibration plate

## 2.5 MAGNETIC CHARACTERISATION

### 2.5.1 *Magnetoresistance measurement*

Magneto-resistance (MR) measurements were carried out on both un-patterned and patterned multi-thin film GMR and TMR samples using a four-point and two-point probe techniques. This is computer controlled using a Labview interface, Keithley 2400 source meter, power supply and electro-magnet shown in Figure 2.20(a). The electromagnet provides a variable field, which is supplied by a Kepco 10 amp bi-polar power supply. The maximum field attainable using this power supply is 180 mT. The field is applied parallel to the easy axis of the sample and is measured by reading out the voltage from a Hall sensor attached to one of the pole pieces of the magnet. Indium is used to connect to the sample, which is connected to the Keithley using BNC connectors.

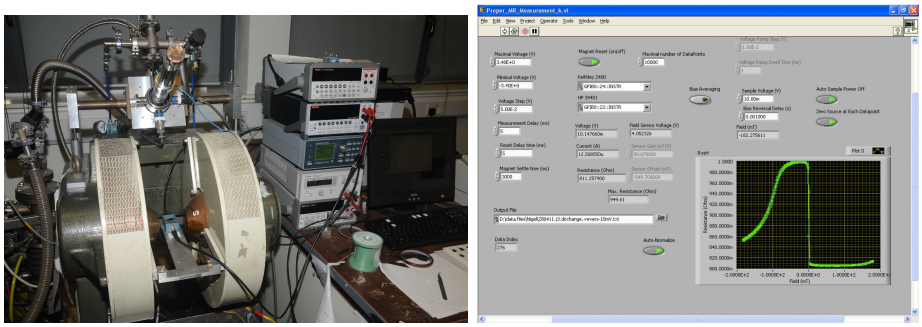


Figure 2.20: (a) RT rig used to measure magnetoresistance measurements and (b) Magnetoresistance scan for TMR sensor using the Labview interface

The magnetoresistive measurements for GMR and TMR sensors is achieved by applying a constant current to the device and measuring the voltage response simultaneously while sweeping the magnetic field. The resistance is obtained by dividing the current to the measured voltage. The magnetoresistance ratios of the junctions are calculated from the parallel and anti-parallel resistance values. Figure 2.20 (b) shows a magnetoresistance measurement scan taken from the Labview interface for a TMR sensor.

### 2.5.2 *Magnetic annealing*

Magnetic annealing is used to set the exchange bias in the TMR sensors. It also assists in the crystallisation of the CoFeB/MgO/CoFeB layers, which is necessary for high TMR ratios. The annealing furnace shown in Figure 2.21 comprises of a permanent magnet, which has a magnetic field of 0.8 Tesla. A quartz tube with a heater wrapped around is fixed inside a permanent magnet. The quartz tube size allows up to three samples 30 x 30 $mm^2$ to be placed inside. The tube is pumped using a turbo molecular pump to $10^{-6}$ Torr. A Eurotherm 2416 temperature controller is used to monitor and control the temperature. The furnace can anneal samples up to 500 °C and water is circulated during the process to prevent overheating of the permanent magnet. The samples are inserted with their easy axis aligned with the field direction of the permanent magnet.

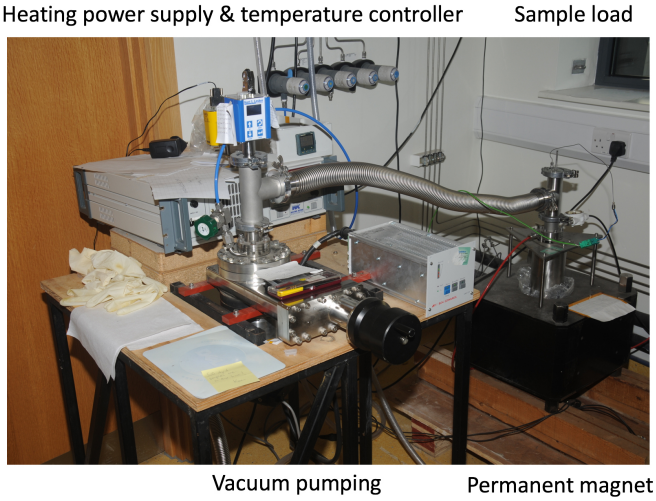



Figure 2.21: High vacuum magnetic annealing furnace

### 2.5.3 *Superconducting Quantum Interface Device (SQUID) Magnetometer*

To characterise the magnetic properties of magnetic nanowires in membrane a Superconducting Quantum Interference Device (SQUID) Magnetometer, type Quantum Design MPMS 5XL was used. The system comprises of a high-field superconducting magnet, which is cooled using liquid helium, a temperature control unit and computer operating system. The SQUID can monitor very small changes in magnetic flux, detect and

measure the magnetic moment of the sample. From this the magnetisation and magnetic properties can be determined. Nanowire samples are cut or diced into typically 3 x 2.5 $mm^2$ sample sizes, which are placed into a sample holder (plastic straw) and mounted into the system. Quantum Design SQUID magnetometer (MPMS XL5)



Figure 2.22: Quantum Design SQUID magnetometer (MPMS XL5)

## 2.6 ELECTRICAL CHARACTERISATION

### 2.6.1 *Noise measurements*

Noise measurements were carried out on the GMR and TMR sensors in a variable controlled electromagnet using the experimental noise measurement setup shown in Figure 2.23. The setup comprises of a low noise current source, which is powered using batteries, and a variable ballast resistor network. Sensor is connected to both the current source and ballast resistor and is placed in a PC controlled variable electromagnet. The noise spectrum of the sensor response is amplified using a Stanford Research SR560 and SR552 preamplifier, and is filtered using a Krohn-Hite 3362 filter to provide an overall gain of $1 * 10^4$. The sensor response is then fed into a NI 24 bit data acquisition card for PC control via a labview interface.

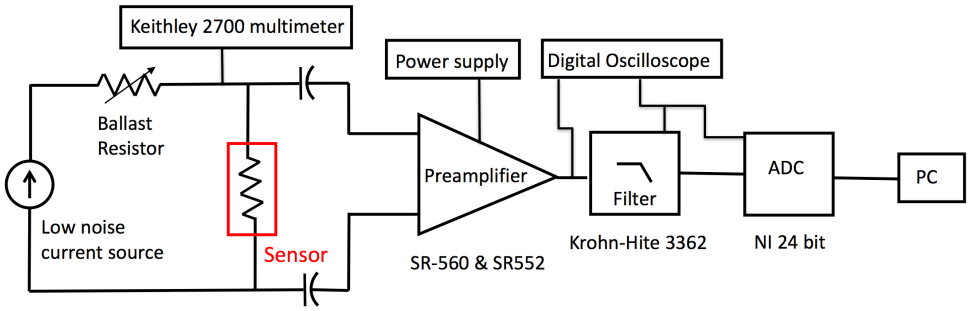



Figure 2.23: Schematic of experimental noise measurement setup for the GMR and TMR sensors

## 2.7 SENSOR FABRICATION TECHNIQUES

The micro-fabrication process and nano-fabrication process used for the fabrication of GMR and TMR sensors use ultraviolet lithography of masks, combined with physical/chemical etching processes to realise the final device. Patterned on Si wafer or glass substrates, devices require several levels of lithography with intricate patterns. Figure 2.24 shows a schematic of the patterning process to define a GMR sensor element. This requires a lithographic step in order to imprint the photosensitive polymer (resist) with a certain pattern (mask) and a further step where the pattern is transferred to the GMR thin films. This section discusses the photolithography process, argon ion milling and lift-off processes. The last section discusses the fabrication procedures used to produce the GMR and TMR devices in my work.

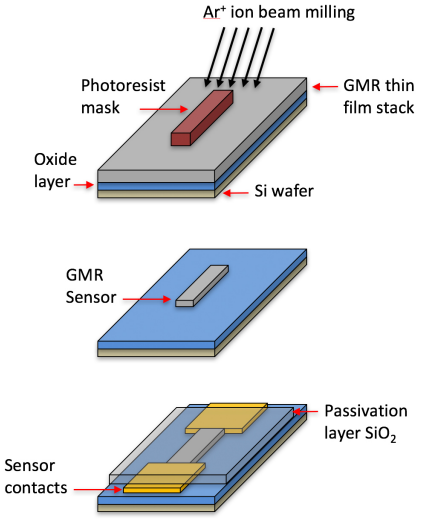



Figure 2.24: Basic steps for GMR sensor fabrication

### 2.7.1 *Photolithography*

The photolithography process is used to produce accurate micron size features on a sample substrate using photoresist, which is a photosensitive material. A photo-mask containing a master pattern is used to created identical copies of the design feature. The masks are made of quartz glass with a patterned layer of chromium [110]. An ultraviolet (UV) source typically a mercury arc lamp is used in a mask aligner system to expose the design feature onto the substrate. The UV typical wavelengths used are 436 nm, 405nm and 365 nm. Figure 2.25 shows a schematic of the photolithography system. The mask aligner system has to reproduce the image of the mask design feature onto the substrate and also it must align the mask pattern to the previous one. The GMR and TMR devices involve several lithography steps and alignment is critical for reproducibility. The process involves exposing the photoresist-coated substrate with the mask design from the UV source. The image on the mask is transferred to the wafer via exposure of the resist. The areas exposed depend on the type resist used. In a positive resist the exposed area is dissolved, and in a negative resist the unexposed area is dissolved. A developer solution in a process called developing is used to dissolve the exposed area.

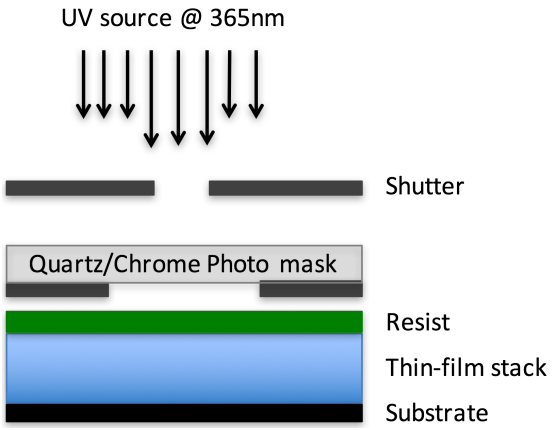



Figure 2.25: Schematic of a basic lithographic exposure system

The minimum feature that can be exposed is determined by the resolution of lithography. This can be affected by a number of parameters; the exposure system, photoresist, substrate and the mask.

### 2.7.2 *UV lithographic photomask mask & direct laser beam writing system*

The lithographic photomasks used to pattern the sensors in my work are UV transparent fused quartz blanks covered with a chrome metal-absorbing Cr/CrO2 thin film. The photo-mask design for the sensor pattern was done using CleWin 4.0, which is a layout editor software. Photo-masks can be fabricated using either e-beam lithography or direct laser beam writing systems. For my work the photo-masks sets for each sensor were fabricated using the Heidelberg DWL 66 direct laser beam writer system as shown in Figure 2.26 (a). Each mask is chrome glass 4" x 4" x 1.5 mm, the Heidelberg writes the sensor pattern onto the chrome glass and through development process the area of the chrome layer containing the sensor pattern is removed. When the design pattern is complete, the mask is developed using AZ3000MIF developer.

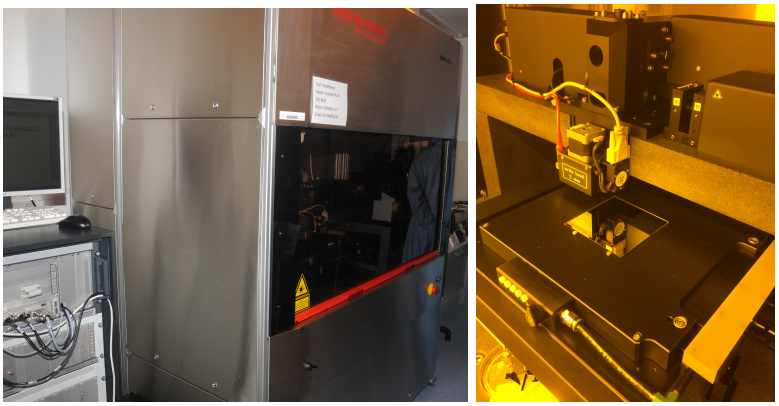


Figure 2.26: Heidelberg DWL 66 direct writing system

The Heidelberg DWL 66 is a high resolution pattern generator for mask making and direct writing. The system has three computers, one for converting user patterns to LIC files (Linux PC); one for setting up the writing job (Windows PC); and one for executing the job (OS9, on board of the tool). The system uses acousto-optic modulators to adjust the laser intensity, and acousto-optic deflectors to scan the beam. During an exposure, only the stage moves. The substrate is held down on the stage by vacuum and moves in the x-y plane. It's position is constantly monitored by an interferometer system with a resolution of 10 nm. The optical setup utilises a diode laser ($\lambda = 405nm$) as its light source. It can expose both 2D and 3D structures, e.g. grey scale lithography with thick photoresists. There are two write heads available: 4 mm & 20 mm. Both

heads use an air-gauge to monitor N2 pressure change, which is then fed back to the lens piezo actuators for auto focus. During a scan, user patterns are divided into stripes along Y-axis, each stripe contains 100 pixels. The stage moves along Y-axis to finish exposing one stripe then steps in X-axis to start exposing the next stripe. The user patterns are then stitched together. In terms of resolution, the 4 mm write head can achieve a minimum feature size of ~800 nm, the 20 mm head can achieve a minimum feature size of $\sim 4\mu m$. The 20 mm head writes about 12 times faster than the 4 mm head. Figure 2.26 (b) shows the mask setup in the stage with the 4 mm head configured. The system uses two CCD cameras for top side metrology and alignment, with two additional cameras for back side alignment. Standard crosses, squares or even arbitrary structures can all be used as alignment marks. The alignment accuracy is ~ 250 nm with 4 mm write head, and ~1 μm when using the 20 mm head. Figure 2.27 shows the completed top electrode mask for the GMR and TMR sensor design, the dark areas on the mask are the Cr/CrO2 coated regions which will block the UV light during exposure.

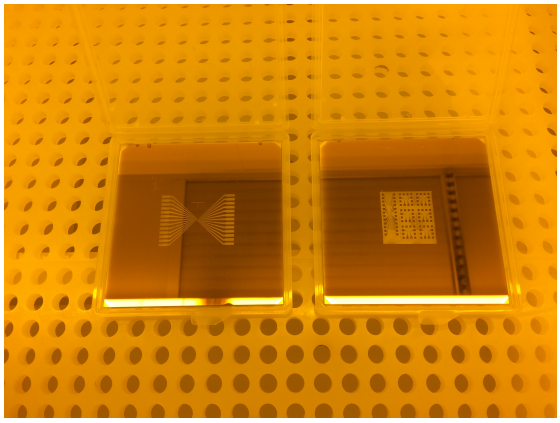


Figure 2.27: Top electrode mask for the GMR and TMR sensor

### 2.7.3 *The photoresist*

Two principle types of photoresist are used during device fabrication are positive and negative. A positive resist is a type of photoresist in which the portion of the photoresist that is exposed to light becomes soluble to the photoresist developer. The unexposed portion of the photoresist remains insoluble to the photoresist developer. A negative photoresist is a type of photoresist in which the portion of the photoresist that is exposed

to light becomes insoluble to the photoresist developer. The unexposed portion of the photoresist is dissolved by the photoresist developer. The photoresist solution includes a resin, base material and a photoactive compound (PAC) [74]. After exposure, the PAC becomes sensitiser due to a chemical process and increases the dissolution rate of the resist. In positive resists, PAC acts as an inhibitor before exposure, slowing the dissolution rate of the resist in developer. After exposure, the PAC becomes sensitiser due to a chemical process and increases the dissolution rate of the resist. Opposite effects happen in the case of a negative resist. Two important parameters are resolution and sensitivity. The resolution is given by the size of the polymer molecule used in the resist. The sensitivity is the amount of light energy that is needed to start the chemical process. The more sensitive a resist, the faster the chemical process will be and the exposure time

S1813 positive photoresist is used in the fabrication for both GMR and TMR sensors in my work. It is a high-resolution positive resist designed for 436 nm wavelength g-line exposure. It has very good adhesion and coating uniformity, with different viscosities available for different resist thickness ranging from 0.5 μm - 3 μm. The resolution is below 1 μm and the sensitivity is 90-150 mJ/cm$^2$. It can be removed using either Acetone or Microposit 1165 remover. Figure 2.28 (a) shows the sub-micron lines that can be achieved using the S1800 series photoresist.

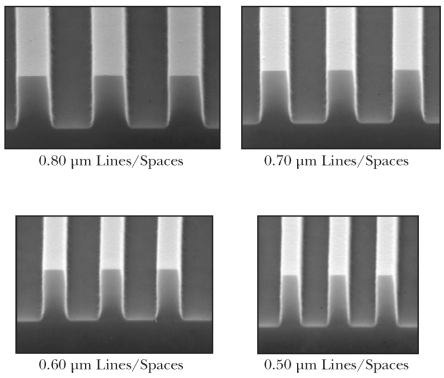



Figure 2.28: (a) S1800 series photoresist sub-micron lines

The ma-N1420 negative photoresist is used to expose the sensor junctions in the TMR sensors. It is a high-resolution negative resist designed for 405nm (h-line) and 365 nm (i-line) exposure. Good adhesion and coating uniformity, and again with different viscosities available for different resist thickness ranging from 0.5 μm - 4 μm. The resolution is below

1 µm and the sensitivity is 300-700 mJ/cm2. It can be removed using either Acetone or Microposit 1165 remover. Figure 2.28 (b) shows the ma-N 400 & 1400 series photoresist patterns at various development times.

### 2.7.4 *UV photolithography Mask aligner*

The OAI Model 800 CE mask aligner was used to carry out photolithography on the GMR and TMR sensors in my study. The OAI Model 800 CE is a semi-automated contact printing tool with four-camera, optical front and backside. It has an alignment accuracy of 1µm - 2µm. A resolution of $< 2$ µm can be obtained by vacuum contact with optimisation of exposure dose and development time of the resist. The exposure wavelength from the UV light source can be varied from 365 nm to 220-260 nm. The exposure is performed at ~ 20 mW/cm2. The mask aligner tooling can accommodate substrates up to 8-inch square, and the wafer chuck is positioned to allow for easy loading and unloading. There are three exposure modes: soft contact, hard contact and the vacuum contact.




Figure 2.29: OAI UV mask aligner

### 2.7.5 *Development*

After lithography, the exposed pattern is developed. First the sample undergoes a post-bake at 80°C to stop uncompleted resist reactions and remove stress. The sample is then placed into developer solution. If it is a positive resist, the exposed regions are rendered soluble and will be removed. In contrast if the resist is negative, the exposed regions will harden and remain after developing. When complete the sample is washed to stop the process, dried, and the pattern is printed onto the resist layer.

### 2.7.6 *Ion milling*

Ion milling or ion beam etching is similar to the sputtering process whereby target atoms are ejected when a highly energetic noble gas ion hits the surface, but in this case noble gas ions are created in an ion gun and accelerated towards the sample surface. The advantages are good directionality due to the fact that ions in the beam are accelerated by a strong electric field and the chamber pressure is low enough to minimise the atomic collisions, and also ion milling can be used to etch wide range of materials. There are different types of sources for ion milling, our Millatron system uses the electron cyclotron resonance controlled plasma reactor (COPRA). The advantages this ion source are low pressure operation 0.3 to 3 x $10^{-3}$ Torr, high ion current density 3 mA/cm$^2$ and high plasma density 1 x $10^{12}$ cm$^3$. It operates using an inductively coupled RF (13.6 MHz) discharge with a transverse magnetic field. Process gas (Argon) is fed into the excitation cavity of the source and plasma is ignited by the creation of a pressure pulse. The resonant excitation of the plasma is achieved by applying a weak DC transverse magnetic field (~ 2 mT), which generated by Helmholtz coils. The field strength is controlled by a power supply.




Figure 2.30: Millatron ion milling system

The Millatron ion milling system used for the ion milling of all GMR and TMR sensor substrates comprises of a vacuum chamber and cryogenic pump, the chamber can reach a base pressure of 2 x $10^{-7}$ Torr and operates at 0.5 – 1.0 x $10^{-4}$ Torr. A mass flow controller (MFC) supplies high purity Ar into the system. Substrate samples are loaded onto a rotational water-cooled sample stage. The sample stage can be tilted 0 - 90° with respect to the ion beam during milling. The plasma beam source is a CCR Technology COPRA DN250 with an RF power supply (1.2kW) and a DC supply controls Helmholtz coils in the ion gun. The RF power is typically 300 - 400 W with a current of 2.5 A.

The Millatron system also has a Hiden End-Point Detector (EPD) installed. This provides monitoring of metallic layers as they are etched from the multi-layer stacks and allows precise control in stopping the process at a certain layer. It is used in both GMR and TMR fabrication and more critical in the TMR sensor fabrication, where I needed to stop the milling just below the MgO layer to realise the sensor junction. The Hiden EPD consists of ion milling probe, which contains a quadrupole mass spectrometer, energy filter and a secondary electron multiplier detector. There is an RF head and this is controlled via a PC running MASsoft software. As ions are deflected from their original trajectory as they enter the quadrupole field. The ion deflection is related to its mass: charge (m/e) ratio. During an RF scan one ion species m/e ratio resonates with the field allowing the ion to pass, while other species are deflected. The ion signal is then collected and displayed using the MASsoft software. An EPD scan taken during

ion milling for both a GMR sensor and TMR sensor indicating individual metallic layers is shown in Figure 2.31.

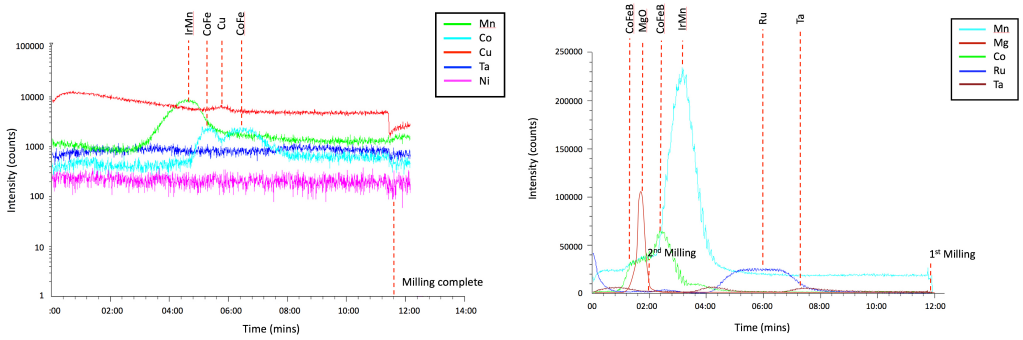



Figure 2.31: EPD scan taken during ion-milling of (a) GMR multi-layer stack and (b) TMR GMR multi-layer stack indicating the individual layers

### 2.7.7 *Patterning lift-off*

Lift-off is an alternative technique to etching processes like ion milling and is used if the material is sensitive to etch damage. The lift-off process starts by defining the resist mask on a substrate and then depositing the thin film on top. The sample is then placed in a resist stripping solution that will remove the resist layer and all the material placed on it. The quality of the lift-off depends on the resist type used. The lift-off process is used in steps of my GMR and TMR sensor fabrication, were $SiO_2$ is deposited for insulation or a Ta / Cu bilayer for top contact, see procedures in Appendix B. For effective lift off, Microposit 1165 remover (N-methyl-2- pyrrolidinone) is used and sample is kept in remover at 80°C in ultrasonic bath for approximately 1 hour. Figure 2.32 shows the used for steps for ultraviolet lithography patterning.

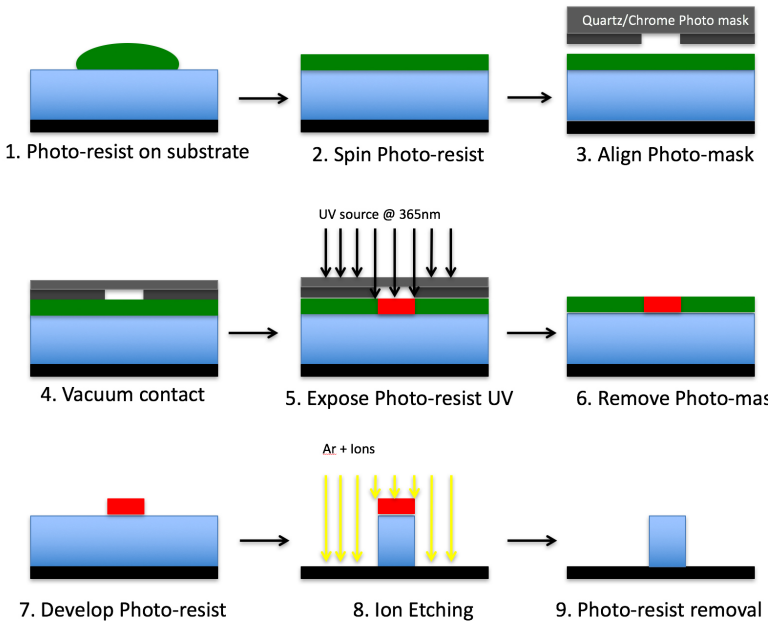



Figure 2.32: Steps for ultraviolet lithography patterning

## 2.8 DEVICE FABRICATION

This section outlines the design and fabrication process for the GMR and TMR Sensors, the full procedures are detailed in Appendix B. Figure 2.6 shows the multilayer thin film stack configurations used for both the GMR and TMR sensors, which were deposited using the Shamrock sputtering deposition system. A number of design iterations of the GMR and TMR sensor were developed, the fabrication process is common for all sensor iterations.

| Type | Multilayer stack (thickness in nm) |
|---|---|
| GMR Top pinned | $SiO_2$/Ta (5)/$Ni_{80}Fe_{20}$ (3)/$Co_{90}Fe_{10}$ (5)/Cu (2.9)/$Co_{90}Fe_{10}$ (3.5)/$Ir_{22}Mn_{78}$ (10)/Ta (5) |
| TMR Bottom pinned (SAF) | $SiO_2$/Ta (5)/Ru (30)/Ta (5)/$Ni_{80}Fe_{20}$ (5)/$Ir_{22}Mn_{78}$ (10) /$Co_{90}Fe_{10}$ (2.5)/Ru (0.9)/ $Co_{40}Fe_{40}B_{20}$ (3)/MgO (t)/ $Co_{40}Fe_{40}B_{20}$ (3)/ Ta (5)/Ru (5) |

Table 2.6: Multilayer stack configurations

### 2.8.1 *Giant magnetoresistance sensor fabrication*

GMR sensors were fabricated with multiple contacts to form a gradiometer in CIP configuration. The sensor was designed with the pinned layer set perpendicular to the free layer (crossed anisotropy). The sensors were patterned into micron-sized junctions on glass substrates. The first mask design encompassed four GMR sensors configured in two sets of two YOKE shape sensors forming gradiometers and alignment marks for the second layer overlay alignment during fabrication shown in Figure 2.33 (a). The second mask design provided the top electrode for the sensor as shown in Figure 2.33 (b). The top electrode mask was designed to allow the sensor to fit into both the microfluidic channel and the sensor interface. The two masks set were fabricated using the Heidelberg DWL 66FS lithography system.

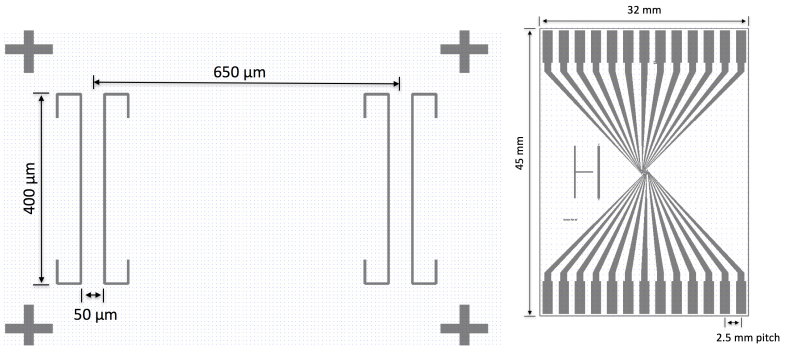



Figure 2.33: (a) 1st mask with YOKE sensors & alignment marks (b) 2nd mask sensor top electrode

### 2.8.2 *Step 1: Deposition of thin-film metal layers*

Thin-film metal layers were deposited onto glass substrates type Nexterion Glass D 44 mm x 33 mm x 170 um, supplied by VWR International.

1. Glass substrates are cleaned using Piranha cleaning procedure detailed in Appendix B

2. Substrates loaded into Shamrock sputtering tool Chamber A and layer sequence deposition in 6 - 10 mT field (see Appendix 8.2.3)

3. Free layers deposited first Ta (5)/NiFe (3)/CoFe (5)/Cu (2.9)
4. Substrate rotated 90řºand then fixed layers deposited CoFe (3.5)/IrMn (10)/Ta (5) setting the sensor exchange bias

### 2.8.3 *Step 2: YOKE sensor & alignment mark patterning*

1. Shipley 1813 positive photoresist is spun on the full GMR stack (Spinning parameters: 5000 rpm (~1.2 μm) for 45 s)
2. Resist pre-baked at 115ºC for 2 mins
3. Photoresist is exposed for 6 s (~112 mJ/cm$^2$) with 1st mask using the OAI mask aligner
4. The sample is developed in MF 319 developer for 50 - 60 s
5. Samples are Argon ion-milled in the Millatron at an angle of 85ºC down to the $SiO_2$ substrate (approx. 15 mins at 400 W RF power)
6. 30 nm of $SiO_2$ is deposited in Chamber B
7. Lift-off of the photoresist & $SiO_2$ is performed in Microposit 1165 remover (N-methyl-2-pyrrolidone) using an ultrasonic bath at 80º for 30 mins.

Figure 2.34(a) shows an optical image of the YOKE sensors & alignment marks after the 1st mask pattering.

### 2.8.4 *Step 3: Top electrode patterning*

1. Shipley 1813 positive photoresist is spun on this sample (Spinning parameters: 5000 rpm (~ 1.2 μm) for 45 s)
2. Resist is pre-baked at 115ºC for 2 mins
3. Photoresist exposed for 6 s with the second GMR top-electrode mask using the OAI mask aligner

4. Photoresist is developed in MF 319 developer for 50 - 60 s
5. Ta (5 nm)/Cu (50 nm) bilayer is sputtered as top contact on the resist defined areas
6. Lift off is performed in acetone in the ultrasonic bath
7. Sensor is then cut to correct dimensions using Disco DAD3220 Wafer Dicer

Figure 2.34 (b) shows an optical image of the top electrodes after the 2nd mask pattering.

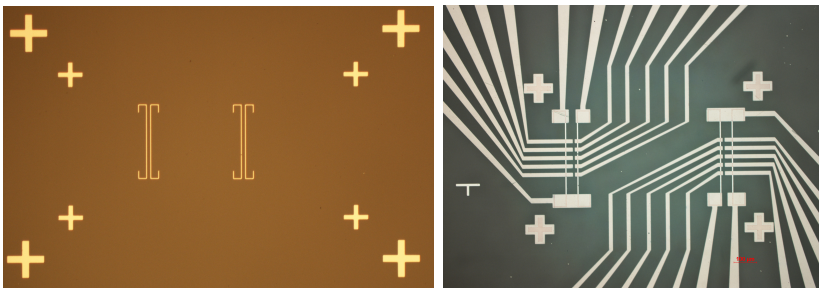


Figure 2.34: (a) Optical image of the YOKE sensors & alignment marks after the 1st mask pattering (b) Optical image of the top electrodes after the 2nd mask pattering

### 2.8.5 *Tunneling magnetoresistance sensor fabrication*

The TMR sensors were patterned onto Silicon wafer substrates into YOKE shaped junctions. The pinned layer was set perpendicular to the free layer using a post annealing process. The TMR sensors are fabricated using a three-step mask lithography process. The first lithography process exposes the bottom electrode and YOKE shape using UV lithography (S1813 positive photoresist), the substrate is then ion-milled. An insulator $SiO_2$ 50 nm is then deposited. The second lithography process exposes the yoke-junction, again using UV lithography (Negative resist ma-N1420). The substrate is ion-milled down to just below the MgO layer. A second $SiO_2$ 40 nm insulator layer is then deposited. The $SiO_2$ insulates the sensor from the top contacts. The third lithography process patterns the top-electrodes (using S1813 positive resist). Ti5/Cu60 top electrodes are then deposited.

### 2.8.6 *Step 1: Deposition of thin-film metal layers*

Thin-film metal layers were deposited onto a thermally oxidised silicon wafer at room temperature.

1. Deposition of bottom electrode layer in Shamrock chamber A sequence thickness in nm Ta (5)/Ru (30)/Ta (5)/NiFe (5)/IrMn (10)/CoFe (2.5)/Ru (0.9)/
2. Substrates transferred to chamber B and deposition of barrier junction CoFeB (3)/MgO (2)/CoFeB (3)
3. Substrates transferred to chamber A and deposition of capping layer /Ta (5)/Ru (5)

### 2.8.7 *Step 2: YOKE sensor bottom electrode & alignment mark patterning*

1. Shipley 1813 positive photoresist is spun on the full TMR stack (Spinning parameters: 3000 rpm (~1.2 μm) for 45 s).
2. Resist pre-baked at 115 °C for 2 mins
3. Photoresist is exposed for 6 s (~112 mJ/cm2) with 1st TMR mask using the OAI mask aligner
4. Sample developed in MF 319 developer for 50 seconds
5. Sample Argon-ion milled at an angle of 80 degrees down to the $SiO_2$ substrate (approx. 25 mins at 400 W RF power)
6. 70 nm of $SiO_2$ is deposited in Chamber B
7. Lift-off of the photoresist & $SiO_2$ is performed in Microposit 1165 remover using an ultrasonic bath at 80°C for 30 mins.

### 2.8.8 *Step 3: Junction area definition*

1. mn-N1420 negative photoresist is spun on the sample (Spinning parameters: 3000 rpm (~ 2 μm) for 45 s)
2. Resist is pre-baked at 115°C for 1 min
3. Photoresist exposed for 6 s (~ 112 mJ/cm$^2$) with TMR mask 2 using the OAI mask aligner
4. Resist is post-baked at 115°C for 1 min
5. Sample is developed in ma-D 533 developer for 40 - 60 seconds
6. Sample ion-milled at 80°C down to bottom FM electrode just below the MgO layer (approx. 10 mins at 400 W RF power)
7. $SiO_2$ (~ 50 nm) is sputtered on the etched samples in order to insulate the top and bottom contact
8. Lift-off of the photoresist & $SiO_2$ is performed in Microposit 1165 remover using an ultrasonic bath at 80°C for 30 mins.

Figure 2.35 (a) shows an optical image of the TMR sensor bottom electrode & alignment marks after the 1st mask pattering and TMR sensor junction after the 2nd mask pattering

### 2.8.9 *Step 4: Top electrode patterning*

1. Shipley 1813 positive photoresist is spun on sample (Spinning parameters: 5000 rpm (~ 1.2 μm) for 45 s)
2. Resist is pre-baked at 115°C for 2 mins
3. Photoresist exposed for 6 seconds by using TMR mask 3 using the OAI mask aligner

4. Photoresist is developed in MF 319 developer for 50 - 60 seconds. e. Ta (5 nm)/Cu (50 nm) bilayer is sputtered as top contact on the resist defined areas

5. Lift off is performed in acetone in the ultrasonic bath

6. Sensor is then cut to correct dimensions using Disco DAD3220 Wafer Dicer

Figure 2.35(b) shows an optical image of the TMR YOKE sensor with top electrode after the 3rd mask pattering process.

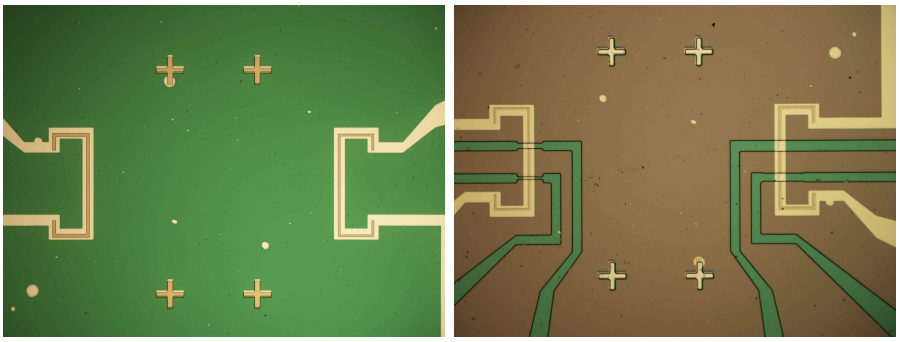


Figure 2.35: (a) Optical image of the TMR sensor bottom electrode & alignment marks after the 1st mask pattering and TMR sensor junction after the 2nd mask pattering (b) TMR sensor with top electrode after the 3rd mask pattering

### 2.8.10 *Step 5: Annealing*

High vacuum post-annealing was then performed at 350°C (1st anneal) for 1 hour in an applied magnetic field of 800 mT and then at 150°C (second anneal) for 1 hour. The first annealing step at high temperature sets the exchange bias of the bottom-pinned ferromagnetic layers perpendicular to the long arm of the yoke and induces the crystallisation of CoFeB at the MgO interfaces, which is necessary for a high TMR ratio. The second anneal at 150°C with the applied magnetic field parallel to the long arm of the yoke is aimed at resetting the easy axis of the top-free layer.

# 3

# GIANT MAGNETORESISTANCE SENSORS & TUNNELING MAGNETORESISTANCE SENSORS

## 3.1 INTRODUCTION

This chapter discusses the GMR sensor characterisation results including sensor resistance measurements of junctions, magnetoresistance measurements and noise measurements. The TMR sensor characterisation results include, magnetoresistance measurements and noise measurements.

## 3.2 GIANT MAGNETORESISTANCE SENSORS CHARACTERISATION

The characterisation of the GMR Bio-sensor included optical microscope and SEM images during the fabrication process, resistance measurements of junctions, magnetoresistance measurements and noise measurments. The magnetoresistance measurements were carried out on both un-patterned and patterned multi-layer thin film GMR samples using a four-point probe technique. The procedure used to measure the magnetoresistance of the sensor is discussed in Chaper 2 Section 2.5.1 and used a computer controlled Keithley 2400 source meter, power supply and electro-magnet. Figure 3.1 shows a schematic of the magnetoresistance technique. A DC current of 1 mA is applied in plane to the GMR thin film stack and the voltage response measured is as a function of the magnetic field. The field is applied in the parallel direction to the pinned layer direction with a strength ranging from - 200 mT to + 200 mT. The GMR sensors were fabricated as discussed in Chaper 2 Section 2.8.1 and were a top-pinned with a crossed anisotropy and had a thin film layer sequence thickness in nm Ta (5)/NiFe (3)/CoFe (5)/Cu (2.9)/CoFe (3.5)/IrMn (10)/Ta (5). The top-pinned deposition for the GMR has been shown to be

a more stable configuration with regard to the exchange bias. This allows the crossed anisotropy exchange bias to be set during the deposition process in an applied field. A bottom pinned deposition requires a post-annealing process to set the exchange bias.

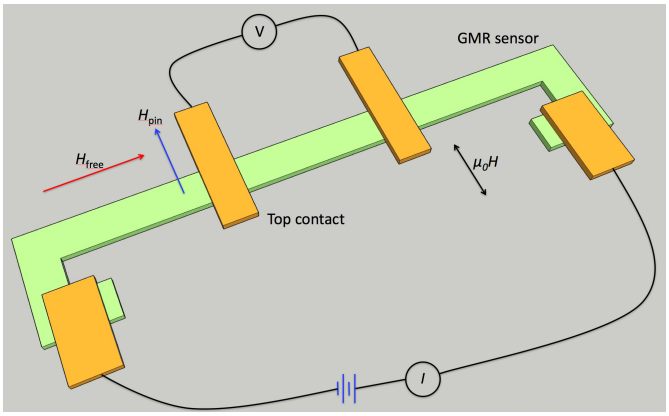



Figure 3.1: Schematic of the GMR sensor magnetoresistance measurement technique

### 3.2.1 *Magnetoresistance response of GMR sensors*

The magnetoresistance of the GMR multi-layer thin films is measured before the sensor is patterened. This is to ensure that the thin film has a GMR response and that the calibration of the metal targets was correct during deposition. Figure 3.2 shows the magnetoresistance response of the GMR thin film before patterning. It is useful to check that magnetoresistance is present in the thinfilm, it ensures that the calibrations of the metal targets used were correct, which is important before a number of samples are deposited.

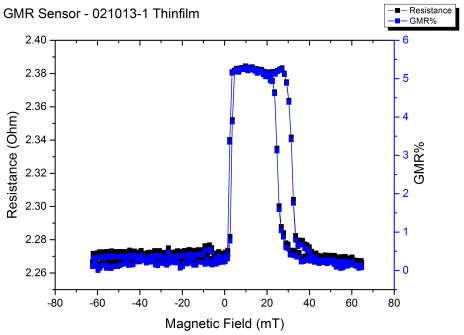



Figure 3.2: Magnetoresistance response of GMR thin film before the sensor was patterned

When the sensors are patterned, the sensors GMR magnetoresistance ratio is measured. The GMR sensorwas designed to encompase 4 Yoke shape sensors in total, labelled 1, 2, 3, and 4 as shown in Figure 3.3 (a). Current is applied to each of the sensors between Pad 1$(-I)$ and Pad 7 $(+I)$ or 8 $(+I)$. The measured sensor response is taken between respective pads as detailed in Figure 3.3 (b).

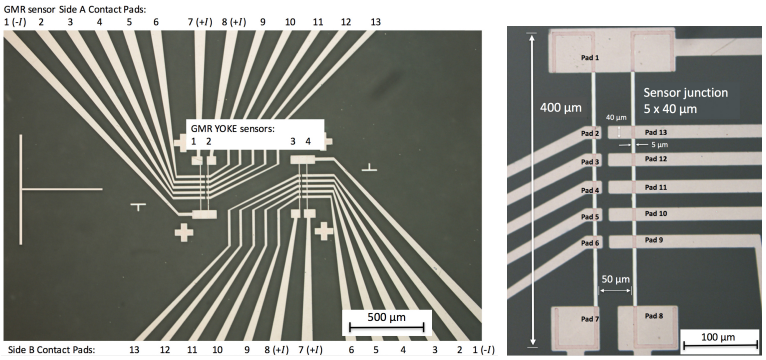



Figure 3.3: (a) Optical microscope image of the sensor GMR Bio-sensor pad layout and (b) contact pads along the sensors element

2-wire resistance measurements were carried out on each GMR sensor after the fabrication was complete. This ensures that that the correct resistance is measured between each of the sensor contact pads, and gives an indication that the sensor is at least electrically functional. Table 3.1 details the resistance measurements from one of the GMR sensors. Appendix 8.8.1 details additional resistance measurements from GMR sensors.

| Sensor | Side | Pads | Resistance (Ω) | Side | Pads | Resistance (Ω) |
|---|---|---|---|---|---|---|
| 090210 | A | 1-7 | 1009 | B | 1-7 | 1025 |
| | | 1-8 | 1036 | | 1-8 | 1022 |
| | | 1-2 | 611 | | 1-2 | 613 |
| | | 2-3 | 429 | | 2-3 | 444.3 |
| | | 3-4 | 390 | | 3-4 | 392 |
| | | 4-5 | 352 | | 4-5 | 395 |
| | | 5-6 | 341 | | 5-6 | 442 |
| | | 6-7 | 458 | | 6-7 | 481 |
| | | 7-8 | 1662 | | 7-8 | 1651 |
| | | 8-9 | 479 | | 8-9 | 514 |
| | | 9-10 | 404 | | 9-10 | 430 |
| | | 10-11 | 1772 | | 10-11 | 472 |
| | | 11-12 | 1837 | | 11-12 | 540 |
| | | 12-13 | 606 | | 12-13 | 1090 |

Table 3.1: GMR sensor two wire resistance measurements across contact pads

The magnetoresistance measurements were carried out on the patterned GMR Bio-sensors using a four-point probe technique across all sensor junctions in order to ensure the sensor had a good linear GMR % response, as well as ensuring that the sensor was centered around the zero field and had a good sensitivity. A DC current of 1 mA was applied in plane to the GMR sensor and the resistance response measured as a function of the magnetic field. The field is applied in the parallel direction to the pinned layer direction with a strength ranging from -200 mT to 200 mT (major loop) to -60 mT to 60 mT (minor loop). Figure 3.4 shows the major loop magnetoresistance measurements taken on GMR Bio-sensor 7245 across two of the sensor juctions. The sensors measured a GMR ratio of 7.9 %.

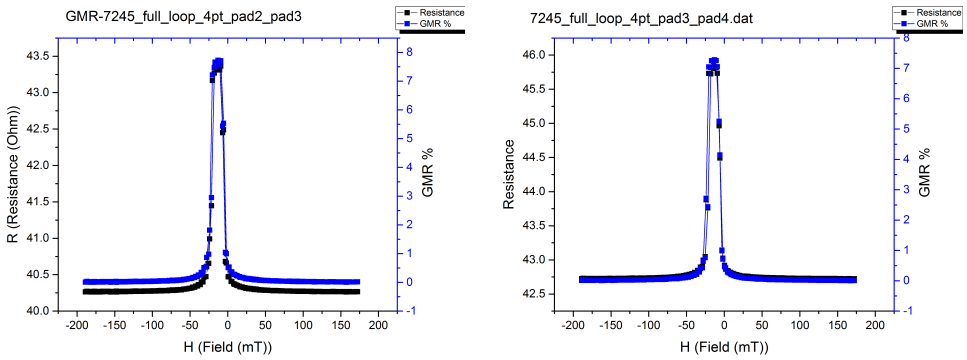



Figure 3.4: Major loop magneto-resistance measurements GMR Bio-sensor 7245

Figure 3.5 shows the minor loop magnetoresistance measurements taken from GMR Bio-sensor number 7245 across two of the sensor juctions. The maximum magnetoresistance is 7.9% with a sensitivity of 0.8%/mT. When the magnetic field is applied parallel to the pinned layer, the free layer magnetization follows the applied field faster than the pinned layer magnetization due to its smaller coercivity. Since the pinned layer magnetization is pinned only in one direction, the magnetoresistance increases when the free layer magnetization and pinned layer magnetization are anti-parallel and decreases when both the magnetizations are parallel. The characterization results verify the magnetic behaviour expected from a spin valve type GMR sensor. The sensors show a sensitivity of ~ 0.8 %/mT and the linear response.

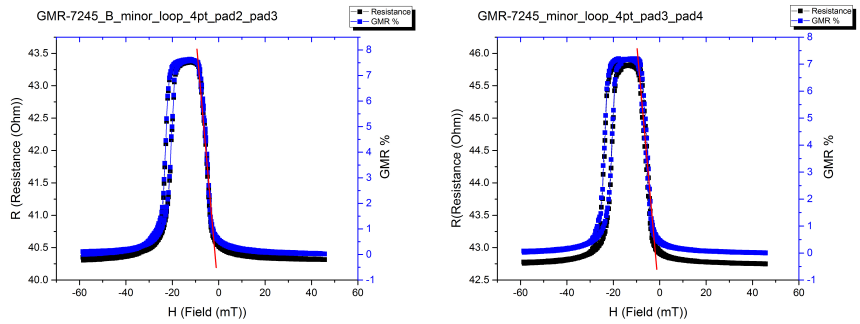



Figure 3.5: Minor loop magneto-resistance measurements GMR Bio-sensor 7245 showing magnetoresistance response & sensitivity

Figure 3.6 shows the minor loop in more detail. The magnetoresistance measurements were taken on GMR Bio-sensor 7245 across some of the sensor juctions. The sensors show a good linear responce across all GMR junctions.

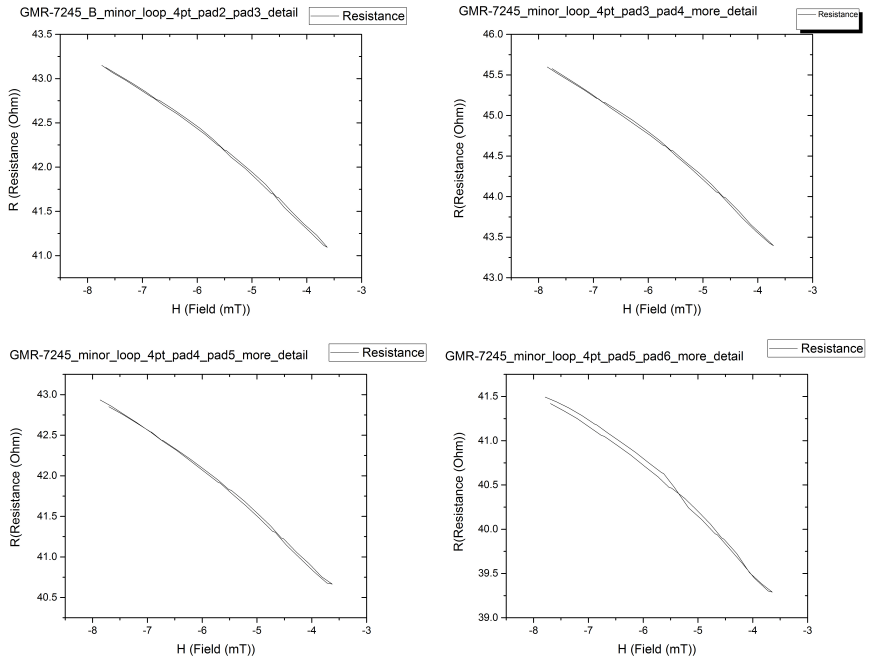



Figure 3.6: Minor loop magneto-resistance measurements for GMR Bio-sensor 7245 showing linerised response

A number of factors can affect the magnetoresistance response from the sensor. These include the sensors exchange bias not been correctly set or poor lithography processes during the sensor fabrication. Figure 3.7 (a) highlights a poor magnetoresistance response from GMR sensor 290813-2 were the exchange bias was not set correctly. This was possibly due to insufficient field strenght produced by the permanent magnet, which is used in the

deposition chamber. Figure 3.7 (b) shows the same sensor after a post anneal at 250°C, the exchange bias has been reset and the magnetoresistance response has improved.

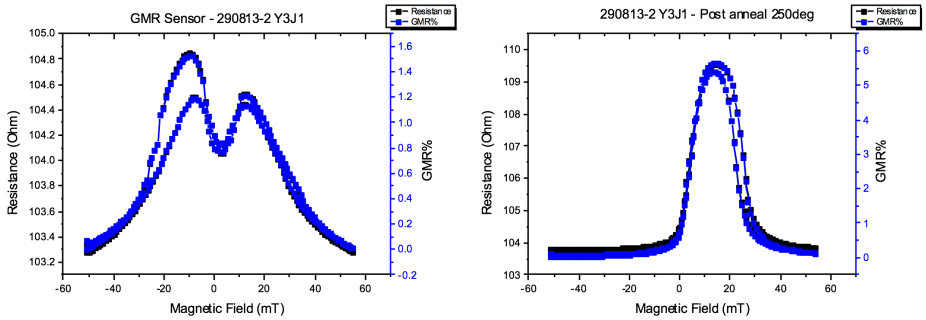



Figure 3.7: GMR sensor 290813-2 (a) exchange bias not set (b) after a post anneal at 250°C

### 3.2.2 *Magnetoresistance response of GMR Gradiometer sensors*

During a later iteration the GMR sensor was configured as a gradiometer. The first mask was redesigned reducing the spacing between GMR sensors from 50 µm to 20 µm. The top-electrode mask was redesigned to provide connections for the gradiometer configuration. Figure 3.8 shows an optical image of the gradiometer layout.

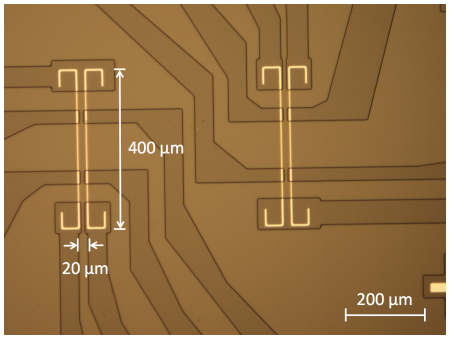



Figure 3.8: GMR Biosensor Gradiometer

Figure 3.9 shows the major and minor loop magnetoresistance measurement for the GMR gradiometer. The sensor measured a GMR ratio of 5.9 % and a sensitivity of ~ 0.8 %/mT with a linear response.

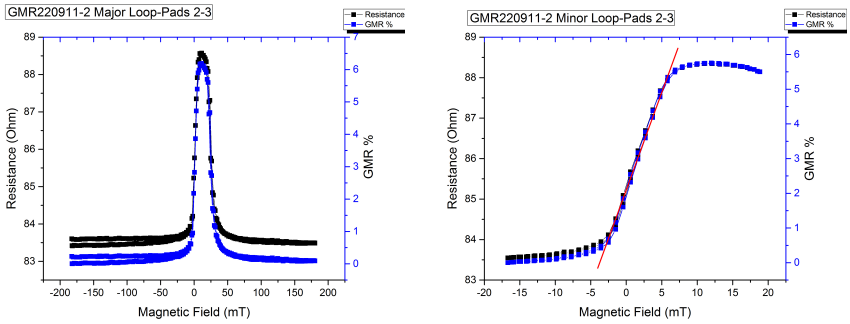



Figure 3.9: Major and minor loop magneto-resistance measurement GMR Bio-sensor Graiometer 220911-2

### 3.2.3 *Magnetoresistance response of GMR Gradiometer for focused flow sensors*

During the final nanowire detection experiments using the gradiometer the focused flow microfluidic channel was used. The focused flow channel allows for a variable controlled channel flow width of 100 µm. In a final iteration of the gradiometer the sensor was redesigned to better match the aspect ratio of the nanowires used in the detection experiments, which was 10 µm and better suit the microfluidic focus flow width of 100 µm. The optimisation included reducing the YOKE sensor length from 400 µm to 200 µm and reducing distance between the gradiometer Yoke sensor pair from 20 µm to 10 µm. A new set of photo-masks were prepared and the sensors are fabricated into a gradiometer using a two-mask lithography process as discussed in Chapter 2 Section 2.8. An optical image of the GMR Bio-sensor gradiometer for focus flow is shown in Figure 3.10, which details the revised YOKE gradiometer sensor pairs and the top electrode.

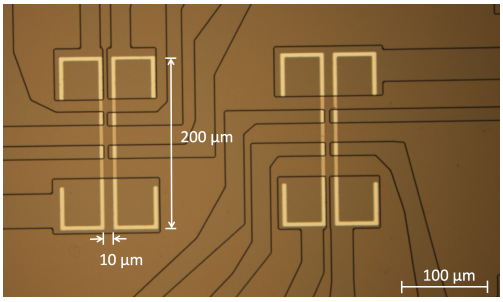



Figure 3.10: Optical image of the GMR Bio-sensor gradiometer for focus flow detailing revised YOKE gradiometer sensor pairs & top electrode

Figure 3.11 shows the major loop magnetoresistance measurements for the GMR gradiometer for focused flow sensor. The sensor measured a GMR ratio of 5.8 %, a sensitivity of ~ 0.8 %/mT and a linear response.

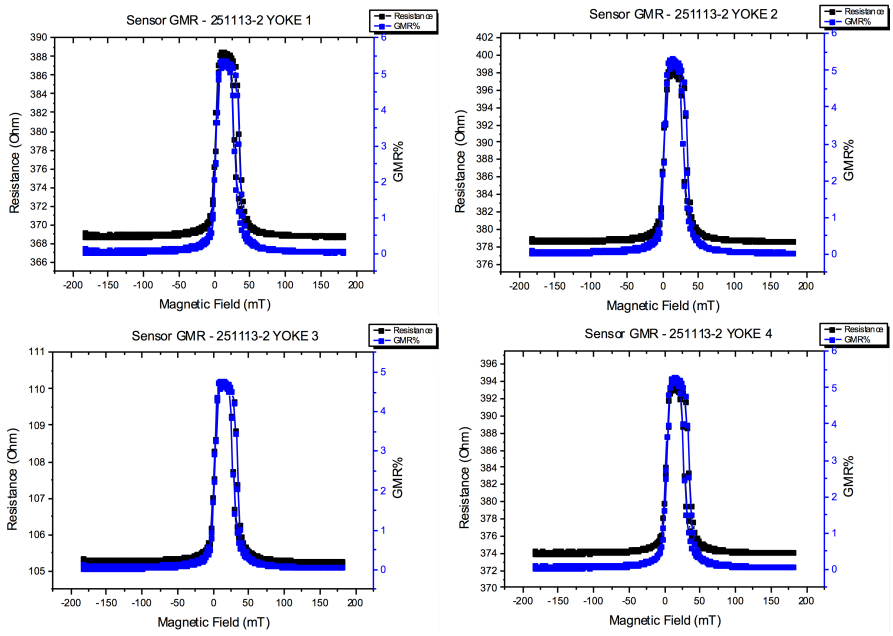



Figure 3.11: Major loop magneto-resistance measurement across each YOKE sensor of Gradiometer GMR Gradiometer Bio-sensor

### 3.2.4 *GMR sensor noise measurements*

The detection of the nanowire stray field as it passes across the sensor depends on a number of factors. These include the standoff distance that seperates the nanowire from the sensors, the sensors magnetoresistive response and sensitivity and the background noise generated. The noise has a number of contributions including electronic noise from the detection system and other sources, the interferences caused by the biological fluids such as blood samples flowing in the microfulic channel and also the noise generated from the magnetic sensor. There are a number of contributions to the sensors noise as discussed in Chapter 1 Section 1.8.

Noise measurements were carried out on the GMR sensor using the experimental noise measurement setup discussed in Chapter 2 Section 2.6.1. The sensor is connected to both the current source and ballast resistor and is placed in a PC controlled variable

electromagnet. The noise spectrum of the sensor response is amplified to provide an overall gain of $1 \times 10^4$. The sensor response is fed into a data acquisition card for PC controle via a labview interface. Figure 3.12 shows the result of normalized noise and GMR plotted as a function of magnetic field for the GMR sensor. The GMR sensor had a response of magnetoresistive response of 7.3% and a sensitivity of 0.8 %/mT.

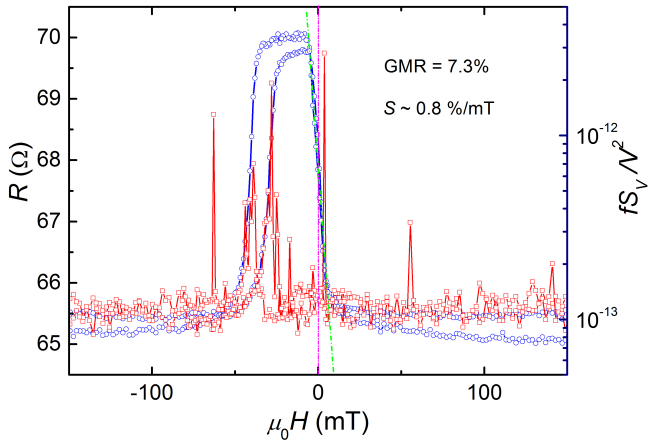



Figure 3.12: Normalized noise & GMR plotted as a function of magnetic field for GMR sensor

The noise power spectral density measured as a function of frequency for the GMR sensor is shown in Figure 3.13. The measured result shows the result of 1/f noise at low frequency and the white noise contribution at higher frequencies.

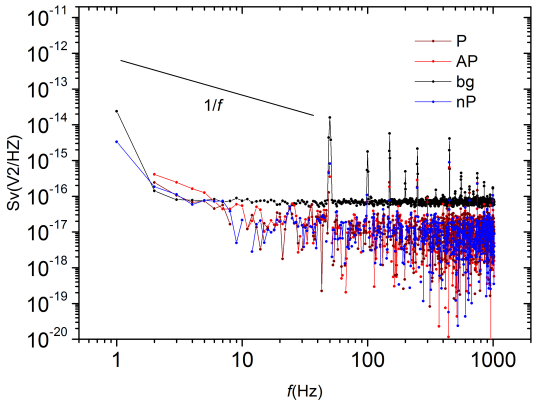



Figure 3.13: 1/f noise power spectral density as a function of frequency for the YOKE shape GMR sensor

Figure 3.14 shows the noise dependency of the GMR sensor to field. The GMR sensor produced a detectivity of 13.5 nT/√Hz at 10 Hz.

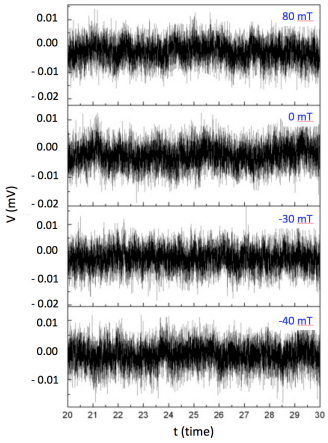



Figure 3.14: Noise dependency of the YOKE shape GMR sensor to field

YOKE shape GMR sensors were sucessfully fabricated on a glass substrate to facilitate optical analysis of the nanowires. The sensors provided a good linear GMR response of 7.3%, with a sensitivity of 0.8%/mT and a noise level field detectivity of 13.5nT/$\sqrt{\text{Hz}}$ @ 10Hz. These sensors were suitable for the application for the detection of magnetic nanowires flowing in the microfluidic channel.

### 3.2.5 *GMR YOKE shape micro-magnetic simulation*

A micro-magnetic simulation of the YOKE shape GMR tri-layer using OOMMF was carried out by our group. This was carried out to ensure that sensor long arm of the YOKE had a stable magnetic domain structure. Figure 3.15 shows the magnetic configuration of the YOKE sensor after the external field is decrease to zero.



Figure 3.15: Magnetic configuration of the YOKE sensor after the external field is decrease to zero

The magnetic domains are confined to the edges, providing a stable magnetic domain structure in the sensor long arm of the YOKE, reducing the noise associated with macroscopic domain wall motion reported by Pannetier et al [111]. From the simulations the vortex like domain states are moved to the corner of the active region, they show a confused magnetisation direction, which is a factor for the $1/f$ noise contribution. The stable magnetic domain structure lies along the sensors long arm of the YOKE, which is were the top electrodes are placed for the sensor measurments.

### 3.2.6 *Conclusions*

YOKE shape GMR sensors were sucessfully fabricated on a glass substrate to facilitate optical analysis of the nanowires. The sensors provided a good linear GMR response of 7.3%, with a sensitivity of 0.8%/mT and a noise level field detectivity of 13.5nT/$\sqrt{\text{Hz}}$ @ 10Hz. These sensors were suitable for the application for the detection of magnetic nanowires flowing in the microfluidic channel.

## 3.3 TUNNELING MAGNETORESISTANCE SENSORS CHARACTERISATION

Due to their large resistance change and high TMR ratio, TMR sensors were investigated as an alternative option to the GMR sensor. There were a number of iterations, until an

optimum design was selected for nanowire detection experiments. This section discusses the characterisation of the different TMR sensor iterations that were developed. The characterisation of the TMR sensor was similar to the GMR sensor and included optical microscope and SEM imaging, magnetoresistance measurements and noise measurements. The magnetoresistance measurements were carried out on both un-patterned and patterned multi-layer thin film TMR samples using a two-point probe technique discussed in Chaper 2 Section 2.5.1. Figure 3.16 shows a schematic of the magnetoresistance measurement technique. A DC current is applied in plane to the TMR thin film stack and the voltage response measured as a function of the magnetic field. The field was applied in the parallel direction to the pinned layer direction with a strength ranging from -200 mT to 200 mT. The TMR sensors were fabricated as discussed in Chaper 2 Section 2.8.5 and were an in-plane bottom-pinned with a crossed anisotropy multi-layer stack and had a thin film layer sequence thickness in nm Ta (5)/Ru (30)/Ta (5)/NiFe (5)/IrMn (10)/CoFe (2.5)/Ru (0.9)/ CoFeB (3)/MgO (2)/CoFeB (3)/Ta (5)/Ru (5).

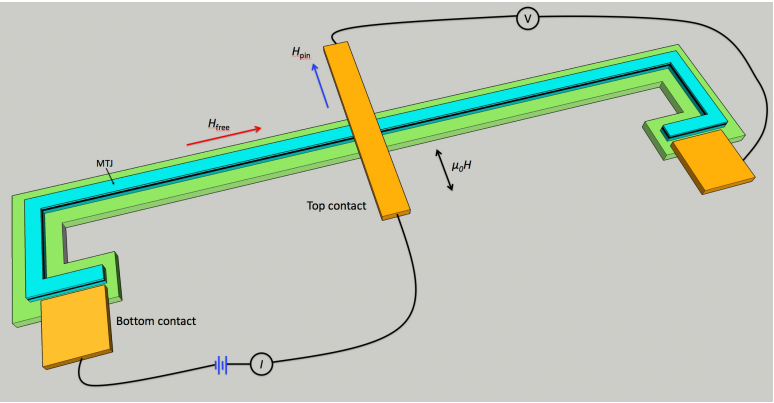



Figure 3.16: Schematic of the TMR sensor magnetoresistance measurement technique

### 3.3.1 *Tunneling magnetoresistance magnetoresistance measurement*

The magnetoresistance of the TMR multi-layer thin film was measured before the sensor is patterened, to ensure that the thin film had an MR response and that the calibration of the metal targets was correct during deposition. Figure 3.17 shows the initial data from TMR thin film stack on Si wafer substrate. The sample was annealed at 350°C as per the procedure outined in Chaper 2 Section 2.5.2.

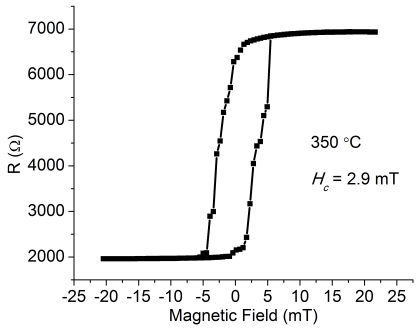



Figure 3.17: Initial data from TMR thin film stack before pattering annealed 350°C

### 3.3.2 *Tunneling magnetoresistance sensors 1st iteration development & characterisation*

The first TMR sensor design encorporated eight Yoke sensors (Y1 to Y8). The 1st lithography step provides the bottom electrode. Sensors Y1 to Y4 had a width of 5 µm and sensors Y5 to Y8 were 10 µm. The 2nd lithography step introduced gaps along the length of the YOKE sensors, which formed the sensor junctions (J1, J2 & J3). The width of the junction gaps ranged from 2 µm, 5 µm, 7 µm & 10 µm in respective sensors. The final lithography step applied the top electrode, which had a width of 40 µm. Figure 3.18 shows the design layout indicating the sensor reference numbers and dimensions.

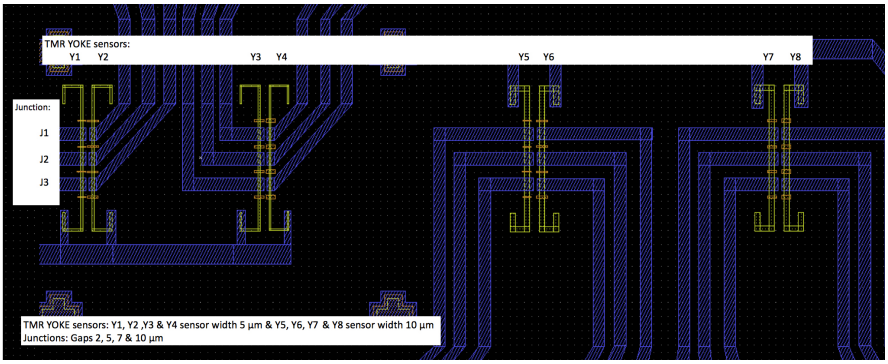



Figure 3.18: 1$^{ST}$ TMR sensor design indicating the sensor reference numbers and dimensions

An optical microscope image of the fabricated TMR sensor detailing the two YOKE sensors, junction gaps and top electrode is shown in Figure 3.19.

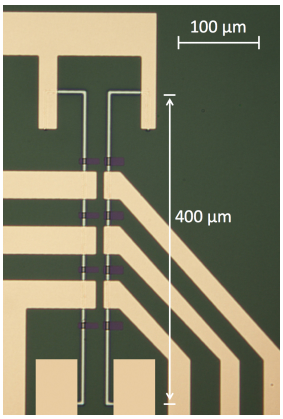



Figure 3.19: Optical microscope image of the TMR sensor detailing YOKE sensor, junction gaps and top contacts

SEM images and FMR measurements were taken of the TMR sensor to confirm the structure of the sensor. Figure 3.20(a) shows an SEM image of the bottom electrode, junction gap and top electrode. Figure 3.20(b) shows an AFM measurement detailing the top electrode and junction gaps. The sensor was annealed at 350 °C as per the procedure outined in Chaper 2 Section 2.5.2.

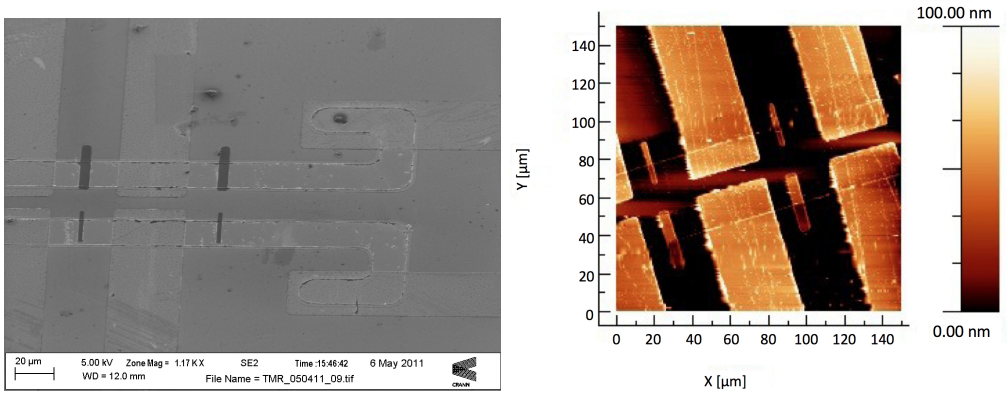



Figure 3.20: (a) SEM image of TMR sensor (b) AFM measurement of sensor and junction gaps

Figure 3.21(a) shows the measured magnetoresistance response (major loop) for one of the sensor junctions. The TMR ratio measured 24 %, which is low for an MTJ CoFeB/MgO/CoFeB barrier, which has expected TMR ratios in the order of 100%. Figure 3.21(b) shows the magnetoresistance response (minor loop). The measured TMR response also show hysteresis in the response.

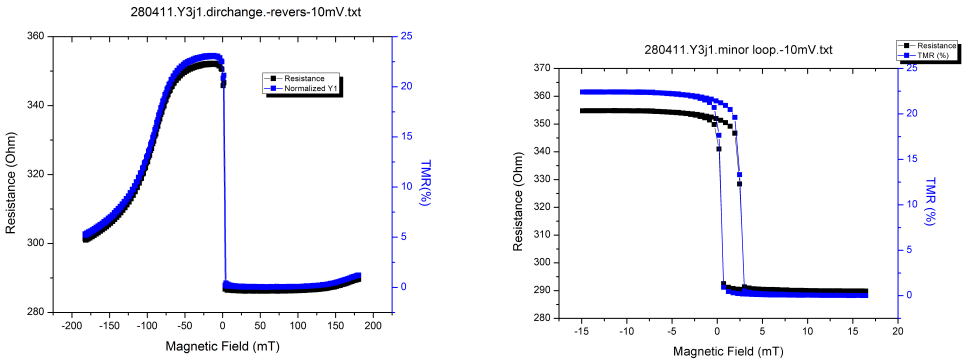



Figure 3.21: (b) TMR sensor 280411 magnetoresistance response major loop (b) magnetoresistance response minor loop

Table 3.2 lists the TMR ratio measured across each of the eight sensors from TMR sensor 280411, detailing the resistance measured and the product RA.

| Junction | Area $(\mu m)^2$ | Gap | Resistance (Ω) | RA $(\mu m)^2$* Ω) | TMR% |
|---|---|---|---|---|---|
| Y1J1 | 200 | 2 | ---- | ---- | ---- |
| Y2J1 | 200 | 5 | 260 | 52000 | 20 |
| Y3J1 | 200 | 7 | 286 | 57200 | 24 |
| Y4J3 | 200 | 10 | 170 | 34000 | 17 |
| Y5J1 | 400 | 2 | 653 | 261200 | 13 |
| Y6j1 | 400 | 5 | 830 | 332000 | 13.5 |
| Y7j1 | 400 | 7 | 816 | 326400 | 10.5 |
| Y8j3 | 400 | 10 | 839 | 335600 | 2.2 |

Table 3.2: TMR Sensor 280411 measured magnetoresistance response TMR% across eight YOKE sensors

Figure 3.22 shows the result of normalized noise and TMR plotted as a function of magnetic field for the YOKE shape TMR sensor 29041. The highest TMR ration measured was 20%.

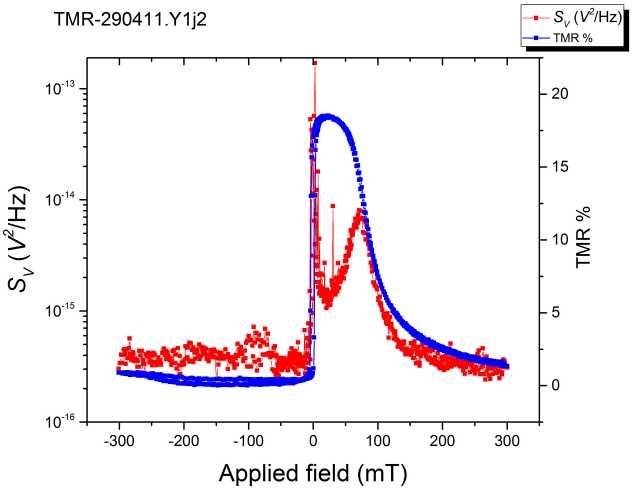



Figure 3.22: Normalized noise & TMR plotted as a function of magnetic field for TMR sensor 29041

The results from the first TMR sensor iteration show a low TMR ratio with a hysteretic response. The possible reasons for low TMR are that the resistance of bottom electrode is comparable with the junction resistance. Also the junction is large and there may be defects such as the edge of the junction shorting to the top electrode. A number of sensors were fabricated and characterised, these measurments are shown in Appendix 8.8.2.

## 3.4 TUNNELING MAGNETORESISTANCE SENSORS 2ND ITERATION CHARACTERISATION

A second TMR sensor mask-set was developed which encompassed a number of designs in the new mask set. The TMR ratio and noise response was measured for each design, were the optimum TMR sensor design was selected. A final mask set was then produced to allow the TMR sensor fit into the micro-fluidic channel for the nanowire detection experiments.

### 3.4.1 *TMR sensors Design 1 – Pillar*

The first design incorporated a rectangle pillar junction. Figure 3.23(a) shows the schematic design of the TMR pillar sensor. The long arm of the yoke, which provides the bottom electrode is 400 $\mu m$. This was designed to fit applications involving a microfluidic channel. TMR pillar junctions are patterned with the following sizes 4 * 4 $\mu m^2$; 4 * 12 $\mu m^2$; 4 * 20 $\mu m^2$ and 4 * 40 $\mu m^2$. The sensor was fabricated as per the procedure outlined in Chapter 2 Section 2.8.5. Figure 3.23(b) show an optical image of TMR pillar sensor showing bottom electrode, YOKE TMR junction & top electrode.

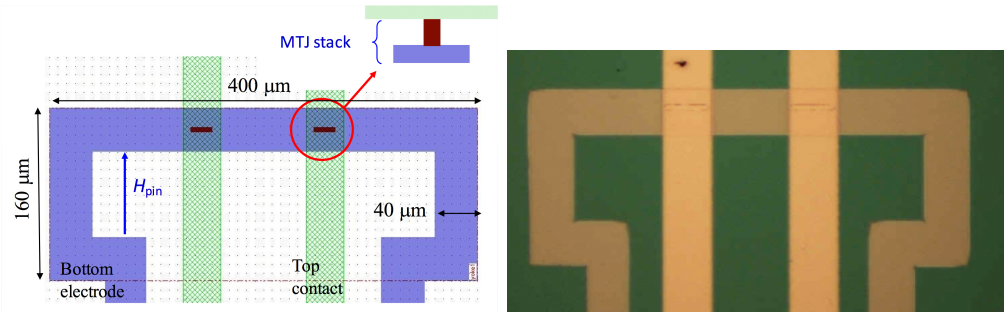



Figure 3.23: (a) Schematic of TMR pillar design (b) Optical image of TMR pillar sensor showing bottom electrode, YOKE TMR junction & top electrode

Following the fabrication the sensors were annealed at 350 °C for 1 hour. The post annealing process is used to set the exchange bias in the TMR sensors, were the free is set perpendicular to the pinned layer. The post annealing also assists in the crystallization of the CoFeB/MgO/CoFeB layers, which is necessary for high TMR ratios.

Figure 3.24 shows the measured magnetoresistance response across two pillar junctions for TMR sensor 080512. The sensors measured a TMR ratio of 190 %, which was closer to the expected response for this type of tunnel barrier. The high TMR ratio measured is closer to what we expect for a crystalline MTJ with a CoFeB/MgO/CoFeB barrier and indicates the high quality of the MgO barrier.

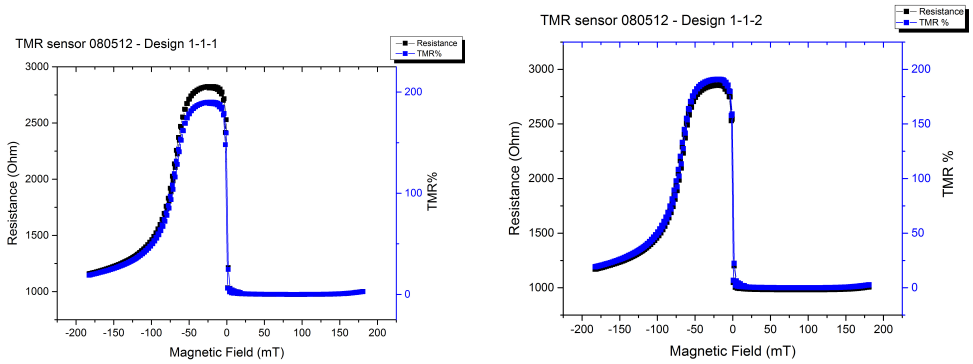



Figure 3.24: TMR Pillar sensor magnetoresistance measurements from two junctions after 1st anneal 350 °C

Table 3.3 lists the TMR ratio measured across each sensor on TMR Sensor 080512 detailing the resistance measured, product RA and TMR ratio after the post annealing at 350 °C for 1 hour. A high TMR ratio was measured across a number of junctions. Some sensor junctions show a decreased TMR ratio, this is likely due to defects in the junctions. Although the sensors produced a high TMR ratio, the TMR curve did not exhibit good linearity and showed hysteresis in the response.

| Sensor | Design | Junction | A (μm)² | R (Ω) | RA (μm)²*Ω) | TMR (%) |
|---|---|---|---|---|---|---|
| 080512 | Pillar | 1-1-1 | 4*4 | 975 | 15600 | 190 |
| | | 1-1-2 | 4*12 | 984 | 47232 | 180 |
| | | 1-2-1 | 4*20 | 2270 | 181600 | 140 |
| | | 1-2-2 | 4*40 | 3800 | 608000 | 190 |
| | | 1-3-1 | 4*40 | 4000 | 640000 | 55 |
| | | 1-3-2 | 4*40 | 6250 | 1000000 | 52 |

Table 3.3: TMR Pillar sensor detailing TMR junction product RA and measured TMR ratio (%) after 1st annealing 350 °C

### 3.4.2 *TMR sensors Design 2 – YOKE*

The second design incorporated a yoke junction. Figure 3.25(a) shows the schematic design of the yoke sensors. The long arm of the yoke, which provides the bottom electrode is 400 $\mu m$. TMR junctions are patterned into a yoke shape onto the bottom electrode. The junctions are patterned with the following sizes, width: 4 μm, 8 μm and 12 μm and

length: 400 µm. The sensing area is 4 × 40 µm$^2$, 4 × 30 µm$^2$ or 4 × 20 µm$^2$. The sensor was fabricated as per the procedure outlined in Chapter 2 Section 2.8.5. Figure 3.25(b) shows optical microscope image of the TMR yoke sensor showing bottom electrode, yoke TMR junction & top electrode.

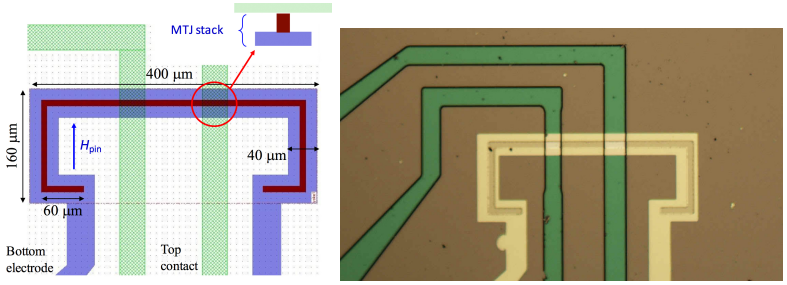



Figure 3.25: (a) Schematic design of the TMR YOKE sensor (b) Optical image of TMR YOKE sensor showing bottom electrode, YOKE TMR junction & top electrode

Following the fabrication the sensors were annealed at 350 °C for 1 hour. Figure 3.26 shows the measured magnetoresistance response across two of the yoke junctions for TMR sensor 240512. The sensors measured a TMR ratio of 225 %. The high TMR ratio indicates the high quality of the MgO barrier.

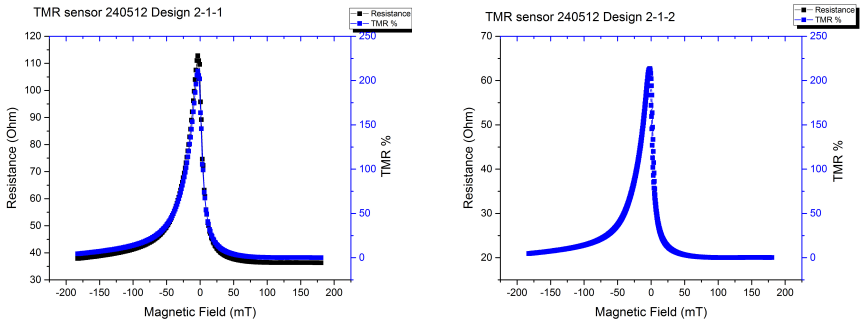



Figure 3.26: TMR YOKE sensor magnetoresistance measurements from two junctions after 1st anneal 350 °C

Table 3.4 lists the TMR ratio measured across yoke sensors for a number of TMR Sensors, detailing the resistance measured, product RA and TMR ratio after the post annealing at 350 °C for 1 hour. A high TMR ratio was measured across a number of junctions. Some sensor junctions show a decreased TMR ratio. This is likely due to defects in the junctions. Although the sensors produced a high TMR ratio, the TMR curve did not exhibit good linearity and showed hysteresis in the response.

| Sensor | Design | Junction | A (µm)² | R (Ω) | RA (µm)²*Ω) | TMR (%) |
|---|---|---|---|---|---|---|
| 060912 | Yoke | 2-1-1 | 4*40 | 1200 | 192000 | 160 |
| 050912 | Yoke | 2-1-1 | 4*40 | 130 | 20800 | 80 |
| | Yoke | 2-2-1 | 4*20 | 110 | 8800 | 75 |
| | Yoke | 2-2-2 | 4*30 | 130 | 15600 | 70 |
| | Yoke | 2-4-1 | 4*40 | 30 | 4800 | ----- |
| | Yoke | 2-4-2 | 4*50 | 10 | 2500 | ------ |
| 240512 | Yoke | 2-1-1 | 4*40 | 40 | 6400 | 225 |
| | Yoke | 2-1-2 | 4*80 | 20 | 6400 | 210 |
| | Yoke | 2-2-1 | 4*20 | 40 | 3200 | 180 |
| | Yoke | 2-2-2 | 4*30 | 30 | 3600 | 90 |
| | Yoke | 2-3-2 | 4*40 | 3 | 480 | 42 |
| | Yoke | 2-4-2 | 4*40 | 12 | 1920 | 150 |
| 070512 | Yoke | 2-1-1 | 4*20 | 985 | 78800 | 170 |
| | Yoke | 2-1-2 | 4*30 | 990 | 118800 | 190 |
| | Yoke | 2-2-1 | 4*40 | 998 | 159680 | 200 |
| | Yoke | 2-2-2 | 4*50 | 1005 | 201000 | 200 |
| 080512 | Yoke | 2-1-1 | 4*20 | 115 | 9200 | 84 |
| | Yoke | 2-1-2 | 4*30 | 80 | 9600 | 50 |
| | Yoke | 2-2-1 | 4*40 | 195 | 31200 | 37 |
| | Yoke | 2-3-2 | 4*50 | 260 | 5200 | 40 |
| | Yoke | 2-4-1 | 4*20 | 300 | 24000 | 30 |
| | Yoke | 2-4-2 | 4*30 | 300 | 36000 | 35 |

Table 3.4: TMR YOKE sensors detailing TMR junction product RA and measured TMR ratio (%) after 1st annealing 350ř$C$

Although a high TMR was obtained after the first annealing process, which indicates high quality of the MgO barrier, the TMR curves exhibit hysteresis and have poor linearity. This was because the orientation of the free layer magnetization set by annealing process and the shape anisotropy is insufficient to realize the crossed anisotropy configuration needed for the sensors. To acheive a linear response a second annealing process at a lower temperature of 110 °C was used. This resets the magnetization of the free layer along the long arm of the yoke. A linear response is acheived, but we get a loss in the TMR ratio.

The magnetoresistance response for a yoke sensor (sensing area of 4 × 40 $\mu m^2$) is shown in Figure 3.27. A TMR ratio of 190 % was measured after the first annealing process at 350 °C for 1 hour. A second annealing process was carrid out at 110 °C for 1 hour. There was a reduction in the TMR response, the TMR ratio measured 130%, showed a good linear response with no hysteresis. The sensitivity 27%/mT and the product RA ~ 1040 Ω µ$m^2$. This provided near-perpendicular configuration of the

two ferromagnetic electrodes, set by a two-step annealing process together with shape anisotropy.

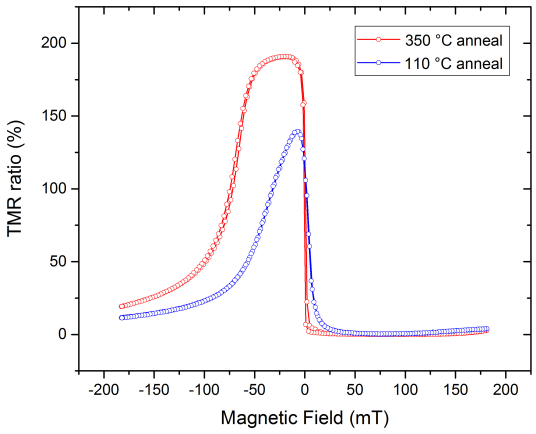



Figure 3.27: TMR yoke sensor magnetoresistance response result after 1st annealing at 350°C and 2nd annealing at 110°C showing linear TMR response

Figure 3.28 shows the minor loop magnetoresistance response of the TMR yoke sensor after the 2nd annealing process. Highlighting linear response with no hysteresis.

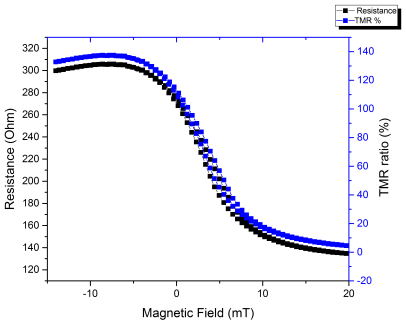



Figure 3.28: TMR YOKE sensor junction magnetoresistance result after second anneal major & minor loops showing linear TMR response

### 3.4.3 *TMR yoke sensor noise measurements*

Noise measurements were carried out on the TMR yoke sensor using the experimental noise measurement setup discussed in Chapter 2 Section 2.6.1. Figure 3.29 shows the result of normalized noise and TMR plotted as a function of magnetic field for the

TMR yoke sensor. The sensor measured a TMR ratio 125 % and sensitivity ~ 26 %/mT, product RA ~ 1040 Ω $\mu m^2$.

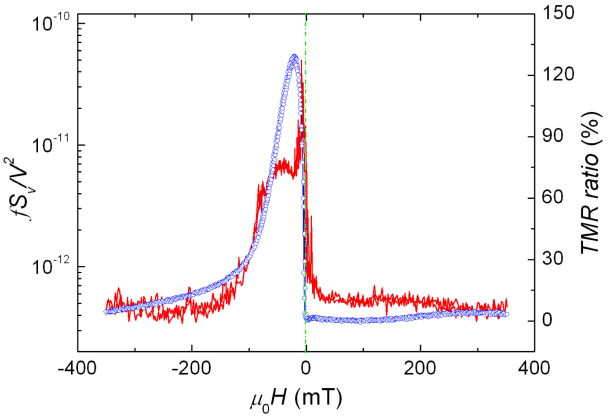



Figure 3.29: TMR YOKE sensor Normalized noise & TMR plotted as a function of magnetic field

The noise power spectral density measured as a function of frequency for the TMR yoke sensor is shown in Figure 3.30. The measured result shows the result of 1/f noise at low frequency and the white noise contribution at higher frequencies. The $1/f$ noise dominates at low frequencies and is larger compared to GMR sensors.

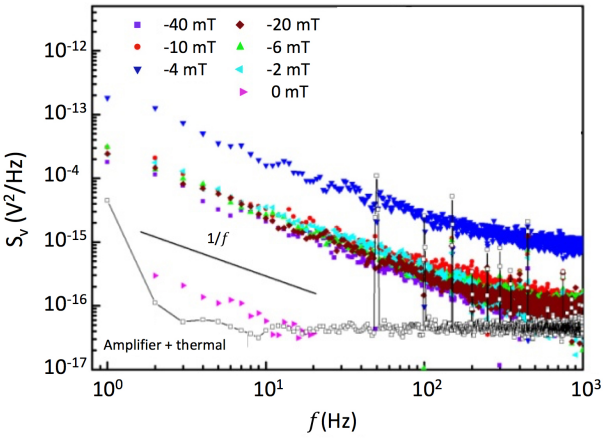



Figure 3.30: TMR YOKE sensor 1/f noise power spectral density as a function of frequency

Figure 3.31 shows the noise dependency of the TMR yoke sensor to field. The TMR yoke sensor produced a detectivity of 4.6 nT/√Hz at 10 Hz.

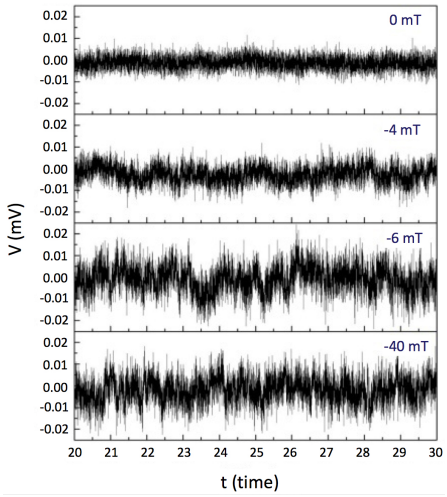



Figure 3.31: Figure shows the noise dependency of the YOKE shape TMR sensor to field

### 3.4.4 *TMR sensors Design 3 – Small YOKE*

The third design incorporated a small yoke junction. Figure 3.32 (a) shows the schematic design of the small yoke sensor. The long arm of the yoke, which provides the bottom electrode is 400 $\mu m$. TMR junctions are patterned into a small yoke shape onto the bottom electrode. The junctions are patterned with the following sizes, width: 4 μm and length: 40 μm and 80 μm. The sensor was fabricated as per the procedure outlined in Chapter 2 Section 2.8.5. Figure 3.32 (b) shows optical microscope image of the TMR small yoke sensor showing bottom electrode, yoke TMR junction & top electrode.

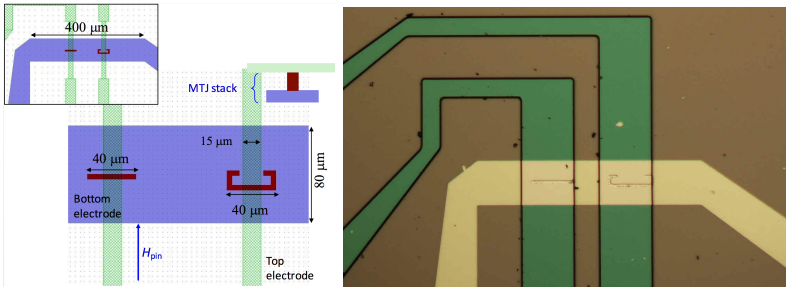



Figure 3.32: Schematic design of the TMR small YOKE sensor

Following the fabrication the sensors were annealed at 350 °C for 1 hour. Figure 3.33 shows the measured magnetoresistance response across two of the yoke junctions for

TMR sensor 070512. The sensors measured a TMR ratio of 190% and 180%. The high TMR ratio indicates the high quality of the MgO barrier.

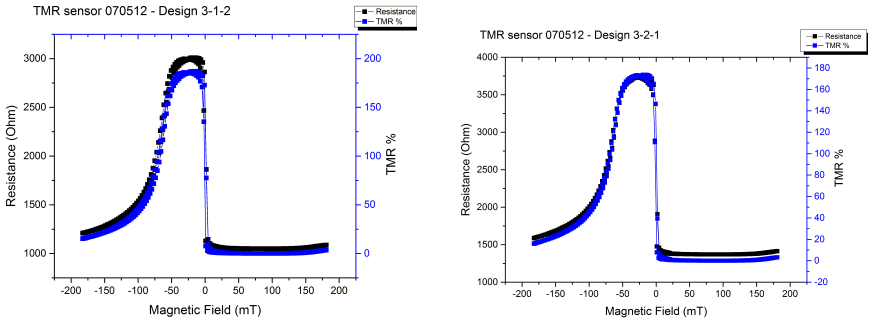



Figure 3.33: TMR small YOKE sensor magnetoresistance measurements from two junctions after 1st anneal 350 °C

Table 3.5 lists the TMR ratio measured across yoke sensors for a number of TMR small yoke sensors, detailing the resistance measured, product RA and TMR ratio after the post annealing at 350 °C for 1 hour.

| Sensor | Design | Junction | A (μm)² | R (Ω) | RA (μm)²*Ω) | TMR (%) |
|---|---|---|---|---|---|---|
| | Small Yoke | 3-1-1 | 4*80 | 992 | 317440 | 210 |
| | | 3-1-2 | 4*80 | 996 | 318720 | 180 |
| | | 3-2-1 | 4*80 | 1200 | 384000 | 200 |
| | | 3-2-2 | 4*80 | 874 | 279680 | 210 |
| 070512 | Small Yoke | 3-1-1 | ------ | ----- | ------ | ------- |
| | | 3-1-2 | 4*80 | 996 | 318720 | 180 |
| | | 3-2-1 | 4*80 | 1200 | 384000 | 200 |
| | | 3-2-2 | 4*80 | 874 | 279680 | 210 |
| | Small Yoke | 3-1-1 | 4*80 | 5000 | 1600000 | 52 |
| | | 3-3-1 | 4*80 | 6250 | 2000000 | 42 |
| | | 3-3-2 | 4*80 | 1050 | 336000 | 12 |

Table 3.5: TMR small YOKE sensors detailing TMR junction product RA and measured TMR ratio (%) after 1st annealing 350ř$C$

The magnetoresistance response for a small yoke sensor is shown in Figure 3.34. A TMR ratio of 180 % was measured after the first annealing process at 350 °C for 1 hour. A second annealing process was carried out at 110 °C for 1 hour.

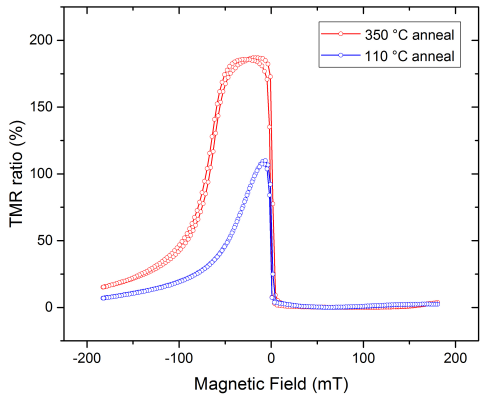



Figure 3.34: TMR small YOKE sensor junction magnetoresistance result after first and second anneal showing linear TMR response

There was a reduction in the TMR response, the TMR ratio measured 110%, showed a good linear response with no hysteresis. The sensitivity ~ 28 %/mT with RA ~ 3.6 * $10^5$ Ω µ$m^2$. This provided near-perpendicular configuration of the two ferromagnetic electrodes, set by a two-step annealing process together with shape anisotropy.

### 3.4.5 *TMR small yoke sensor noise measurements*

Noise measurements were carried out on the TMR small yoke sensor. Figure 3.35 shows the result of normalized noise and TMR plotted as a function of magnetic field.

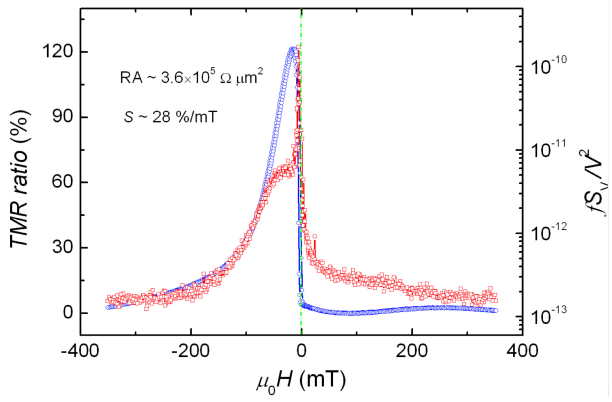



Figure 3.35: TMR small YOKE sensor Normalized noise & TMR plotted as a function of magnetic field

The sensor measured a TMR ratio 120 % and sensitivity ~ 28 %/mT, product RA ~ 3.6 * $10^5$ Ω $\mu m^2$.

The noise power spectral density measured as a function of frequency for the TMR small yoke sensor is shown in Figure 3.36. The measured result shows the result of 1/f noise at low frequency and the white noise contribution at higher frequencies. The $1/f$ noise dominates at low frequencies and is larger compared to GMR sensors.

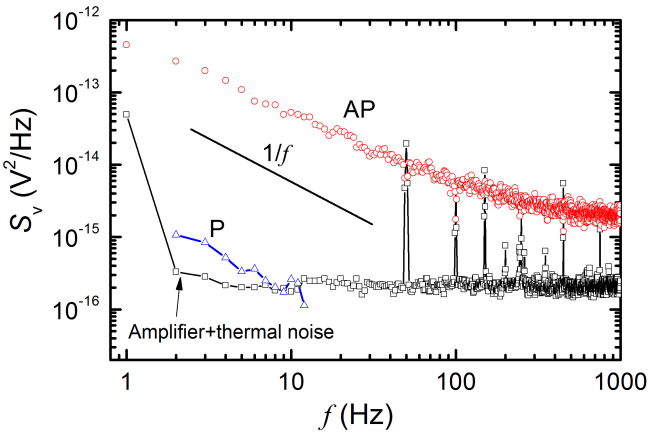



Figure 3.36: TMR small YOKE sensor 1/f noise power spectral density as a function of frequency

The TMR small yoke sensor produced a detectivity of 8.6 nT/√Hz at 10 Hz.

### 3.4.6 *Final TMR sensor layout for Micro-fluidic Channel*

After selection of optimum TMR yoke design the sensor layout footprint was revised to facilitate fitting inot the micro-fluidic chip and allowing the sensor to fit into the annealing chamber.

## 3.5 SUMMARY

A YOKE shape TMR sensor based on an MgO barrier magnetic tunnel junction was also sucessfully fabricated as an alternate sensor option. The sensor provided a good linear TMR response of 130% with field detectivity 4.8nT/√Hz at 10Hz [112]. The optimum

design was incorporated into a new mask set designed to fit into the microfluidic channel. Table 3.6 shows a summary of the sensors produced.

| Design | Resistance (Ω) | Area ($mm^2$) | RA (Ω $mm^2$) | MR | Sensitivity (%/mT) | Detectivity $(S_B)^{0.5}$ $(nT/(Hz)^{0.5})$ |
|---|---|---|---|---|---|---|
| TMR YOKE | 6.2 | 4 x 40 | 988 | 129 | 24 | 4.6 @10Hz |
| | 8.6 | 4 x 30 | 1032 | 119 | 23 | 7.4 @10Hz |
| | 8.3 | 4 x 20 | 667 | 122 | 27 | 4.8 @10Hz |
| TMR Small yoke | 1150 | 4 x 80 | $3.6 \times 10^5$ | 121 | 28 | 8.6 @10Hz |
| TMR Pillar | 4080 | 4 x 4 | $6.5 \times 10^4$ | 210 | 26 | 90 @10Hz |
| GMR YOKE (CIP) | 65.5 | 5 x 50 | | 7.3 | 0.8 | 13.5 @10Hz |

Table 3.6: Summary and comparison between detectivities at 10 Hz for different types of sensors

## 3.6 SENSOR PASSIVATION LAYER

The final and one of the most critical process during the sensor fabrication was the application of a passivation layer to protect the powered sensor during nanowire detection experiments from Di water and biological reagents flowing in the microfluidic channel. A number of passivation layers had been explored throughout the course of my study, these are summarised in Table 3.7.

| Material | Thickness | Duration | Discussion |
|---|---|---|---|
| $Si_3N_4$ | 150 nm | 10 min/ok | RF sputtered Silicon Nitride provided good passivation for the sensor with optimum thickness for nanowire detection experiments |
| $SiO_2$ | 700 nm | 50 sec/Fail | Provided reasonable passivation for the sensor, but failed after 50 seconds |
| $SiO_2$ | 1 µm | 1 min/ok | Provided good passivation for the sensor. But increased nanowire separation from sensor |
| SiO | 300 nm | 30 sec/Fail | Sensor failed in solution after 30 seconds |
| ALN (nitride) | 200nm | 30 sec/Fail | Sensor failed in solution after 30 seconds |
| ALN (nitride) | 300nm | 50 sec/Fail | Sensor failed in solution after 50 seconds |
| $ALO_X$ | 300nm | 50 sec/Fail | Sensor failed in solution after 50 seconds |
| $ALO_X$ | 600nm | 1 min/Fail | Sensor failed in solution after 60 seconds |
| PMMA | 300nm | 10 sec/Fail | Sensor failed in solution after 10 seconds |
| PMMA | 600nm | 20 sec/Fail | Sensor failed in solution after 20 seconds |

Table 3.7: Summary of passivation's layers investigated

The passivation layers included $SiO_2$ and pulsed dc Aluminium nitride at various thicknesses. Both materials adhered well to the sensor glass substrate and to the sensor top contacts in nm Ta 5/Cu 60. However the sensors failed during experimental work where the Di water leached through the passivation layers and shorted the sensor as shown in Figure 3.37GMR sensor passivated $SiO_2$ 600 nm failed during nanowire detection experiment3.37.

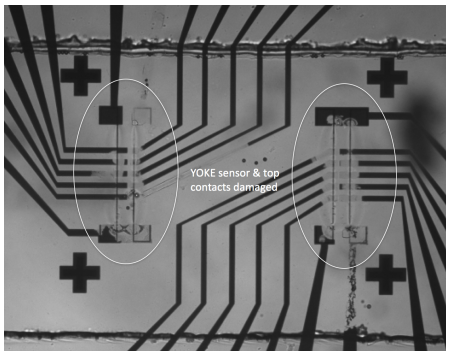



Figure 3.37: GMR sensor passivated $SiO_2$ 600 nm failed during nanowire detection experiment

A passivation layer was required that would last at a minimum for the duration of a nanowire detection experiment ~1 minute. But preferably longer to allow the sensor to be

used in multiple experiments and considering the fabrication work required to produce the sensor. Also reducing the thickness passivation is a critical factor to improving the magnitude of the detected signal response during the nanowire detection experiments. The response of the detected signal is inversely proportional to the distance between the nanowire and the sensor, which is determined by the thickness of the passivation layer and the various heights that the nanowire flows within the microfluidic channel. The magnetic stray field of the nanowire will decrease by approximately 70 % as the height above the sensor increases from 0.2 µm to 1 µm. The passivation layer thickness needs to be in the order of 100 nm above the GMR sensing area.

### 3.6.1 *RF sputtered Silicon Nitride (*$Si_3N_4$*)*

RF sputtered Silicon Nitride ($Si_3N_4$) was investigated as a possible option. Successfully reported by Chinthaka P. Gooneratne et al using 200nm of $Si_3N_4$ over a GMR sensor [64] and M.A. Signore et al [76]. We successfully deposited silicon nitride ($Si_3N_4$) thin films by reactive RF magnetron sputtering at room temperature in (Ar + N2) atmosphere on glass (silica) substrates for the characterization. Figure 3.38 shows the RF magnetron sputtering setup for Silicon nitride ($Si_3N_4$) thin films.

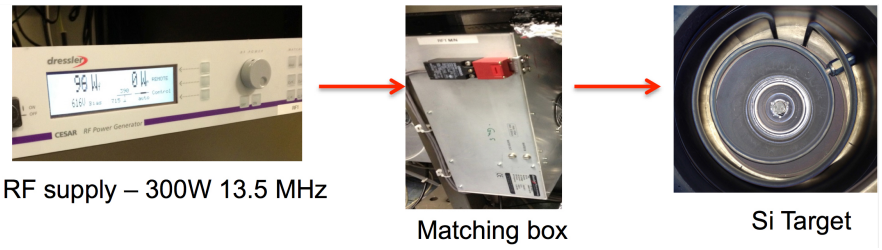



Figure 3.38: RF magnetron sputtering setup for Silicon nitride ($Si_3N_4$) thin films

The Radio Frequency (RF) technique as discussed in Chapter 2 Section 2.2.2, comprises of a Dressler Cesar 136 RF power supply 300W 13.5MHz, which was operated at 150W. This is connected to the magnetron through a capacitor and matching impedance circuit to the target to create a plasma. The target used was a silicon disk (99.99%) placed in Shamrock sputtering tool chamber A. Ar and N2 gases were introduced into the sputtering chamber via two separate mass flow controllers. The substrate sample holder

was 7 cm distant from the target and it was in rotation 44 rpm during the film growth. A series of calibrations at various power and gas ratio conditions were carried out to ascertain the optimum $Si_3N_4$ layer outlined in Table 3.8.

| Sample | Couple | Pwr (W) | Bias (V) | Ar (sccm) | N2 (sccm) | Time (Sec) | Notes - |
|---|---|---|---|---|---|---|---|
| 080514-1 | Coil | 100 | 638 | 25 | 0 | 1800 | Pwr: 96, Ar: 25.6, N2: 0.1, CG: 0.003 |
| 080514-2 | Coil | 100 | 638 | 25 | 5 | 1800 | Pwr: 97, Ar: 25.7, N2: 5.1-6.5, CG: 0.003 |
| 080514-3 | Coil | 100 | 638 | 25 | 7 | 1800 | Pwr: 97, Ar: 25.6, N2: 5.3 – 9.2, CG: 0.003 |
| 080514-4 | Direct | 200 | 230 | 25 | 0 | 1800 | Pwr: 197, Ar: 25.1, N2: 0.1, CG: 0.008 |
| 080514-5 | Direct | 200 | 216 | 25 | 5 | 1800 | Pwr: 97, Ar: 25.6, N2: 0.1, CG: 0.01<br>Bias 155 V after process complete |
| 080514-6 | Direct | 200 | 180 | 25 | 7 | 1800 | Pwr: 97, Ar: 25.6, N2: 0.1, CG: 0.001<br>Bias 140 V after process complete |

Table 3.8: $Si_3N_4$ calibrations various power & gas ratio conditions

An $Si_3N_4$ optimum calibration was carried out using RF power 150W, Argon 25 sccm and Nitrogen 7 sccm. The calibration details are shown in Table 3.9.

| Power (W) | Bias (V) | $N_2$ : Ar (sccm) | Deposition (Sec) | Thickness (nm) | Deposition rate (ºA/s) | Roughness (nm) |
|---|---|---|---|---|---|---|
| 150W | 260 | 25 : 7 | 7200 | 34.2 | 0.04752 | 0.6217 |

Table 3.9: Optimum $Si_3N_4$calibration

X-ray powder Reflexivity (XRR) waw carried out to determine the sputtered $Si_3N_4$ layer deposition rate, thickness and roughness. Figure 3.39 shows the XRR measurement of the $Si_3N_4$ layer and the model fitting using WINGIXA software.

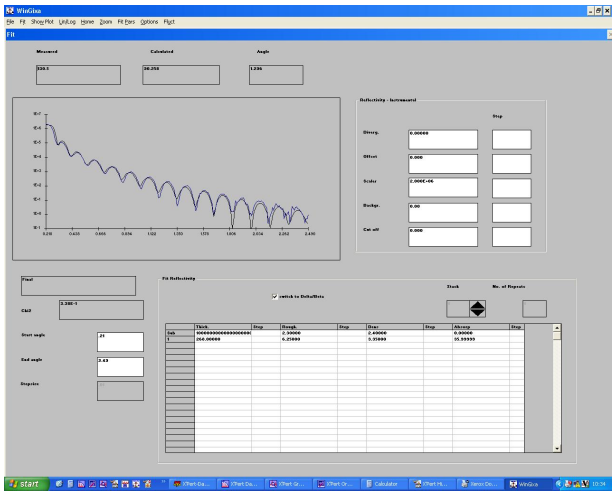


Figure 3.39: $Si_3N_4$calibration XRR fitting

X-ray powder Diffraction (XRD) was also carried out to provide structural information on the $Si_3N_4$ layer. The measured result showed a non-crystalline structure to the $Si_3N_4$ layer as shwon in Figure 3.40.

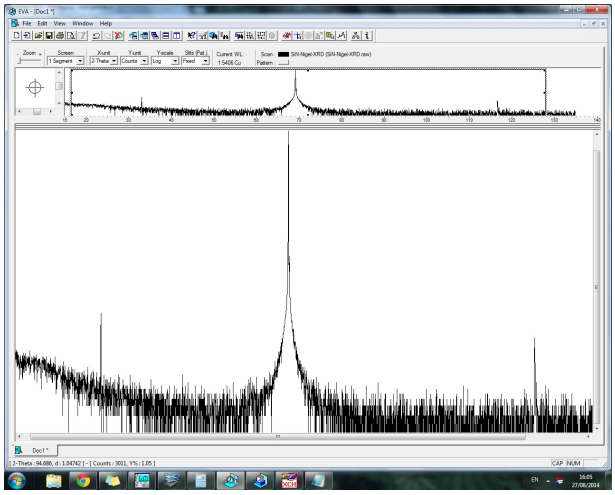


Figure 3.40: $Si_3N_4$ calibration XRD scan showing no crystalline structure

During the sputtering process the bias voltage (Bias v) was monitored. During the reactive sputtering using the Si target, the reactive gas N2 was added to the deposition chamber to react with the sputtered material depositing a compound in this case $Si_3N_4$. Figure 3.41(a) shows $Si_3N_4$ thin film layer 150 nm thickness deposited on a GMR sensor. One hour depositions were carried out with 10 minute burn-in process. The $Si_3N_4$ is transparent in appearance and adhered well to the GMR sensor. The continuity test showed good electrical insulation. The sensor tested successfully as a passivation layer to

protect GMR sensor during fluidics applications. Figure 3.41 (b) shows $Si_3N_4$ thin film layer 150nm with no burn-in process during the deposition, which causes the formation of compound material from the reactive gas on the substrate, also on the target surface (target poisoning), results in a decrease in the bias voltage and results in a mostly Si layer deposited on the sensor substrate.

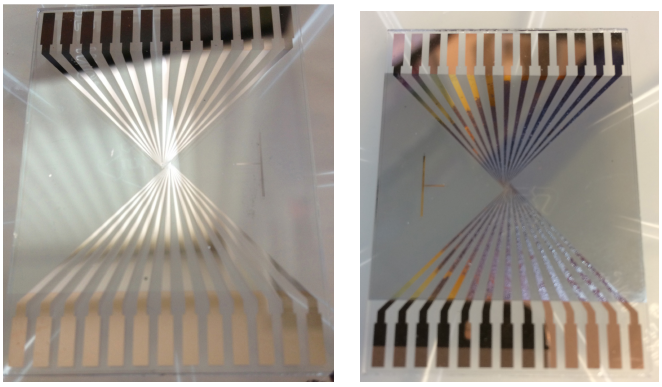


Figure 3.41: (a) $Si_3N_4$ 150nm deposition GMR sensor (b) $Si_3N_4$ deposition no burn-in process

## 3.7 CONCLUSIONS

In conclusion, YOKE shape GMR spin-valve sensors were sucessfully fabricated on a glass substrate to facilitate optical analysis of the nanowires. The sensors provided a good linear GMR response of 7.3%, with a sensitivity of 0.8%/mT and a noise level field detectivity 13.5nT/√Hz @ 10Hz. These sensors were suitable for application of the detection of magnetic nanowires flowing in the microfluidic channel. A YOKE shape TMR sensor based on an MgO barrier magnetic tunnel junction was also sucessfully fabricated as an alternate sensor option. The sensor provided a good linear TMR response of 130% with field detectivity 4.8nT/√Hz at 10Hz. RF sputtered $Si_3N_4$ was sucessfully deposited on GMR sensors with a thinkness of 150 nm for use as a passivation layer.

# 4

# NANOWIRE FABRICATION AND CHARACTERISATION

## 4.1 INTRODUCTION

Chapter 4 discusses the fabrication of magnetic nanowires, both single segment magnetic nanowires and two magnetic segmented nanowires that were used for investigation in my experiments for the detection of magnetic nanowires using the magnetoresistive sensors. Over the course of the research project a number of nanowire single metal compositions were investigated including Co , CoFe, CoNi and multi-segmented magnetic nanowires CoFe-Cu-CoFe and CoNi-Cu-CoNi.

## 4.2 NANOWIRES

The main goal of this work was to fabricate suitable magnetic nanowires, including multi-segmented magnetic nanowires using the porous anodic aluminium oxide (AAO) membrane template electrodeposition process discussed in Chapter 2 Section 2.3. In order to achieve this goal it was necessary to develop robust procedures for preparing single-metal nanowires and multi-segmented magnetic nanowires with a controlled distribution of length using existing optimised fabrication procedures. Over the course of the research project a number of nanowire single metal compositions were investigated including Co, CoFe, CoNi and multi-segmented magnetic nanowires CoFe-Cu-CoFe and CoNi-Cu-CoNi. Both one-segment (single metal) and multi-segment magnetic nanowires with a controlled distribution of length fabricated using a bottom-up approach for template electro-deposition, a summary of nanowires investigated is shown in Table 4.1. The analysis and characterisation of the nanowires was carried out using SEM & TEM to ensure that the nanowires had good separation and morphology and in order to

characterize the magnetic properties of the nanowires, a Superconducting Quantum Interference Device (SQUID) magnetometer was used.

| Type | Diameter (nm) | Length (μ) |
|---|---|---|
| Co | 200 | 5, 10, 20 |
| CoFe/Cu/CoFe | 200 | 10 |
| CoNi | 200 | 10 |
| CoNi/Cu/CoNi | 200 | 10 |

Table 4.1: Summary of Nanowires investigated

### 4.2.1 *Estimation of nanowire per AAO membrane*

Calculations were carried out to estimate the number of nanowires that each porous anodic aluminium oxide (AAO) membrane could produce. This information would be useful in the nanowire detection experiments when estimating the amount of nanowires been dispensed. The specifications of the AAO membrane are listed in Table 4.2.

| Membrane # 6809-6022 | Sample Ø mm | Pore size (nm) | Thickness (μm) |
|---|---|---|---|
| Whatman Anodisc 25 0.2μm 25mm Circle | 16 | 200 | 55 |

Table 4.2: AAO membrane specifications

The number of nanowires per membrane was calculated using hexagon geometry, Figure 4.1 shows an illustration of nanowires per membrane using hexagon geometry.

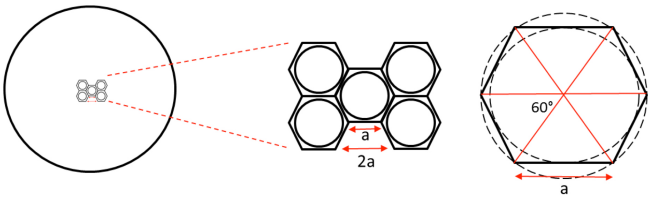



Figure 4.1: Illustration nanowires per membrane using hexagon geometry

Table 4.3 lists the parameters used for the hexagon geometry calculation of nanowires per membrane.

| Parameters | |
|---|---|
| Diameter of membrane | 16 mm |
| Diameter of pour size | 200 nm |
| $a = 2 \times Pour\ radius\ \tan\left(\frac{180}{n}\right)$ | 115 nm |
| n | Number of sides |
| ID: Interspatial distance = 2a | 2a = 230 nm |
| | |
| $A_m$ | Area of membrane |
| $A_n$ | Area of pour size including alumina |
| $N_{nw}$ | Number of nanowire per membrane |

Table 4.3: Parameters for hexagon geometry calculation of nanowires per membrane

$$A_m = \pi R^2 = 2.01 \times 10^{-4} \tag{4.1}$$

$$A_n = \frac{3\sqrt{3}}{2}\frac{ID^2}{2} = 2.60 \times \frac{(230 \times 10^{-9})^2}{2} = 6.877 \times 10^{-14} \tag{4.2}$$

$$N_{nw} = \frac{(8 \times 10^{-3})^2\pi}{6.877 \times 10^{-14}} = \frac{2.01 \times 10^{-4}\pi}{6.87788 \times 10^{-14}} = 2922.8 \times 10^6 \tag{4.3}$$

The AAO membrane does not have perfectly formed pores. During the deposition process not all of the pores produce nanowires. This can be seen looking at the SEM image shown in Figure 4.2 which shows a cross section of the nanowires in the membrane. A number cross sectional images of the nanowires in the membrane were inspected. On average 10% of the pores in the AAO membrane are not filled during the nanowire deposition process.

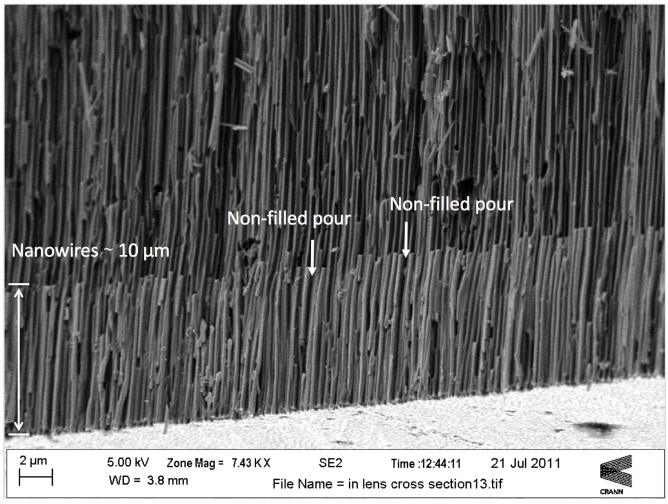



Figure 4.2: SEM image cross section of nanowires in the membrane

Also removing the nanowires from the AAO is difficult. The process as detailed in Chapter 2 Section 2.3.2, requires continual monitoring for each respective batch of nanowires. Not all nanowires are fully released from the AAO membrane.

In the nanowire detection experiments the sample weight for each sample that was dispensed was measured. The experimental conditions were kept the same so a comparison could be made between each respective experiment with regard to the approximate number of nanowires dispensed, see nanowire experiment preparation procedure Appendix 8 Section 8.7.10 for additional information.

## 4.3 SIGNAL MAGNETIC SEGMENT – COBALT (CO) NANOWIRES

To prepare Cobalt (Co) nanowires the electrodeposition cell is filled with the cobalt solution (0.5 molar) and connected to the potentiostat as per the electrodeposition process discussed in Chapter 2 Section 2.3. Details of the Cobalt solution prepared is listed in Table 4.4.

| Solution | Composition | Weight | Molar |
|---|---|---|---|
| Cobalt (Co) | $CoSO_4 xH_2O$ (Cobalt Sulfate Heptahydrate) | 25.299g | 0.5 |
| | NaCl (Sodium Chloride) | 0.643 g | |
| | $H_3BO_3$ (Boric Acid) | 4.946 g | |

Table 4.4: Cobalt (Co) solution

The potentiostat coreware software of the potentiostate is set with an over potential of -1.0 V, the time duration of the applied potential determines the length of the wires deposited. Cobalt wires were grown at 5 μm, 10 μm & 20 μm lengths, Table 4.5 details the cobalt nanowire deposition conditions.

| Nanowire length | Metal | Potential (Volt) | Charge (Q) | Time (min) |
|---|---|---|---|---|
| 5um | Co | -1 | 18 | 20 |
| 10um | Co | -1 | 38 | 40 |
| 20um | Co | -1 | 48 | 60 |

Table 4.5: Cobalt nanowire depositions

After deposition process is complete the nanowires are then released from the membrane using the procedure as discussed in Chapter 2 Section 2.3.2. Firstly the gold layer is removed from the membrane using a polishing process. The wires are released by dissolving the membrane in sodium hydroxide (NaOH) at a set temperature for a period of time. This process is critical to produce wires with good surface structure producing wires that are well dispersed. The full procedures for the preparation of the Cobalt solution, electrodeposition process and dissolving the nanowies from the AAO membrane are detailed in Appendix E.

### 4.3.1 *Cobalt nanowire characterisation*

To characterize the magnetic properties of magnetic nanowires in membrane, a Superconducting Quantum Interference Device (SQUID) Magnetometer, type Quantum Design MPMS 5XL was used as detailed in Chapter 2 Section 2.5.3. Cobalt nanowire samples still in AAO membrane were cut into 3 x 2.5 $mm^2$ sizes to allow them to fit into the SQUID sample holder (plastic straw). Figure 4.3 shows the magnetisation curve measured for the cobalt sample. From the magnetisation curve for Co, the remanent magnetic moment $m_r$ per measured sample, $m_r(per\,measured\,sample) = 0.93 \times 10^{-6}\mathrm{Am}^2$.

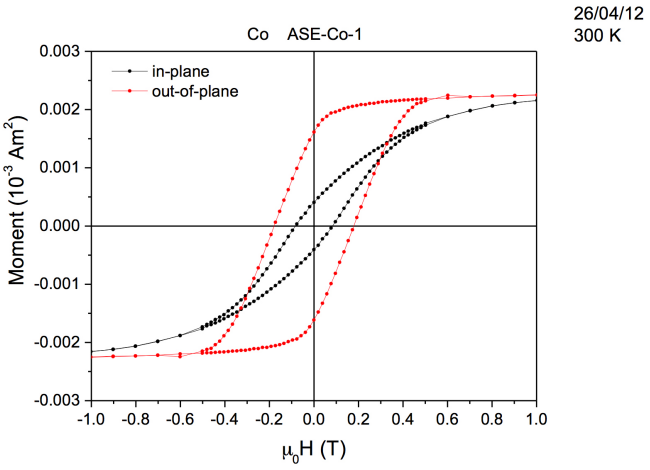



Figure 4.3: Cobalt magnetisation hysteresis loop measured using SQUID

SEM analysis was carried out on cobalt nanowires in membrane and also when the nanowires had been released from the membrane using the Carl Zeiss Ultra Field Emission SEM. The SEM analysis was used to determine the length of the nanowires in membrane and adjust the deposition rates accordingly, perform element analysis using EDX to ensure the composition is correct. Figure 4.4 shows a cross section image of the cobalt wires in the membrane

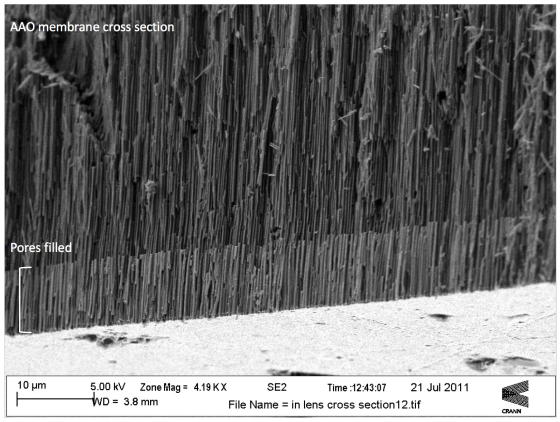



Figure 4.4: SEM image of Cobalt nanowires in membrane

The SEM analysis was also used to ensure that the nanowires had been fully released from the membrane and all the alumina has been removed during the dissolving process and the nanowires had good separation and morphology. The following images shown in Figure 4.5 show images of the cobalt wires after they had been dissolved from membrane.

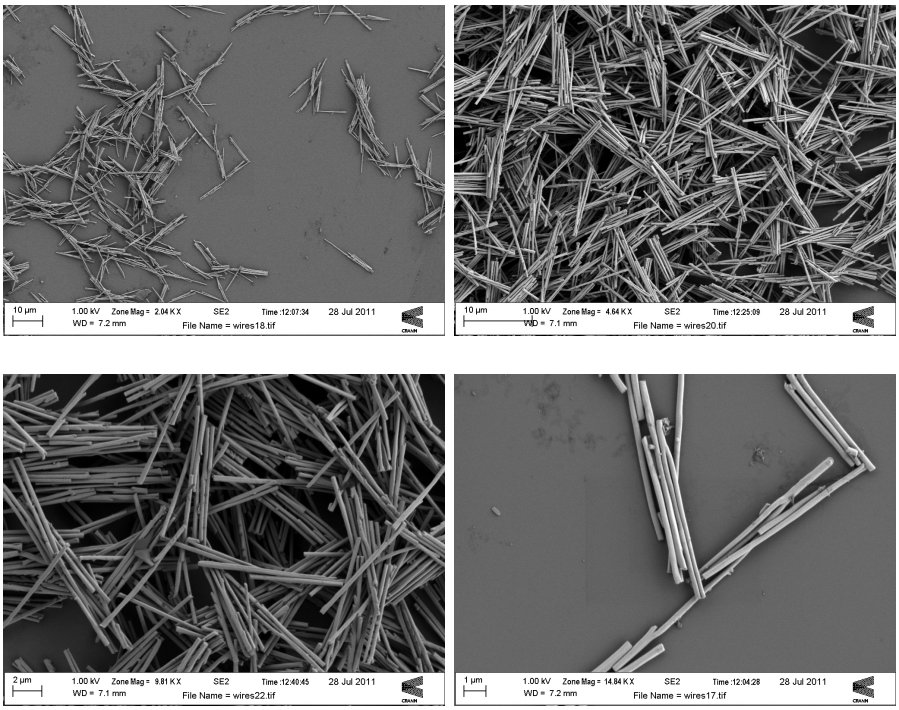



Figure 4.5: Cobalt wires after being dissolved from membrane

The Cobalt nanowires showed good morphology and resonable separation from the membrane, although still some bunching of nanowires.

## 4.4 TWO MAGNETIC SEGMENT COFE-CU-COFE NANOWIRES

Cobalt Iron (CoFe) magnetic nanowires separated by a Copper (Cu) nonmagnetic segment were produced for as multi-segmented nanowires (CoFe-Cu-CoFe) for detection experiments.

To produce the nanowires, firstly the CoFe solution (0.3 molar) and Cu solution (0.1 molar) are prepared as detailed in Table 4.6.

| Solution | | Weight | Molar |
|---|---|---|---|
| Cobalt Iron (CoFe) | L-Ascorbic acid | 1.0g | |
| | CoSo4 | 8.41g | 0.5 |
| | FeSO4 | 8.57g | 0.5 |
| | H3B03 | 2.0g | 0.12 |
| | | | |
| Copper (Cu) | Cu | 0.5 g | 3 |
| | Cu | 0.5 g | 3 |

Table 4.6: CoFe and Cu solutions

CoFe-Cu-CoFe nanowires are produced as per the electrodeposition process discussed in Chapter 2 Section 2.3. The 1st magnetic segment (CoFe) is prepared with the potentiostate Coreware software set to -0.95 volt, the time duration of the applied potential determines the length of the wires produced in the alumina membrane. To achieve a wires length of 3 to 4 µm the time duration was set to 1500 seconds. The total charge (Q) in coulombs passed is monitored by the potentiostat and the deposition plot saved. When the process is complete the excess CoFe solution is removed from the electrodeposition cell using a pipette, the cell is gently rinsed with Di water. The non-magnetic segment (Cu) is prepared with the potentiostate coreware software set to -0.95 volt for a time duration of 800 seconds to achieve a length of 3 to 4 µm. When complete the excess Cu solution is removed and 2nd magnetic segment (CoFe) is prepared. Table 4.7 details the process used to produce CoFe-Cu-CoFe nanowires.

| Sequence | Metal | Potential (V) | Charge (Q) | Time (Sec) |
|---|---|---|---|---|
| 1st magnetic segment | CoFe | -0.95 | 15 | 1500 |
| Non-magnetic segment | Cu | -0.95 | 8 | 800 |
| 2nd magnetic segment | CoFe | -0.95 | 15 | |

Table 4.7: Process to produce two magnetic segment CoFe-Cu-CoFe nanowires

After deposition the nanowires are then released from the membrane using sodium hydroxide (NaOH) at a set temperature for a period of time using the procedure as discussed in Chapter 2 Section 2.3.2. The full procedures for the preparation of the CoFe and Cu solution, the electrodeposition process and dissolving the nanowies from the AAO membrane are detailed in Appendix E.

### 4.4.1 *CoFe-Cu-CoFe nanowire characterisation*

To characterize the magnetic properties of magnetic nanowires in membrane, the CoFe samples were cut into 3 mm x 2.5 $mm^2$ sizes and placed into the SQUID. Figure 4.6 shows the magnetisation curve measured for the CoFe sample. From the magnetisation curve for CoFe, the remanent magnetic moment $m_r$ per measured sample, $m_r(per\,measured\,sample) = 2.5 \times 10^{-6} \mathrm{Am}^2$.

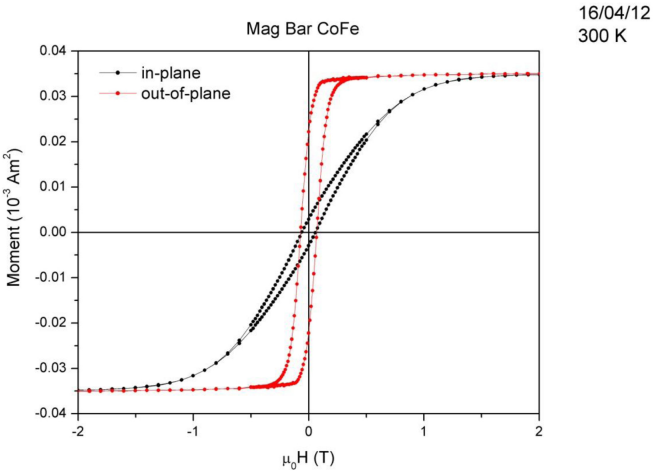



Figure 4.6: Hysteresis loop of CoFe nanowires

SEM analysis was carried out on CoFe-Cu-CoFe nanowires in membrane to determine the length of the nanowires in membrane and adjust the deposition rates accordingly. Figure 4.7 shows images of the CoFe-Cu-CoFe nanowires in membrane.

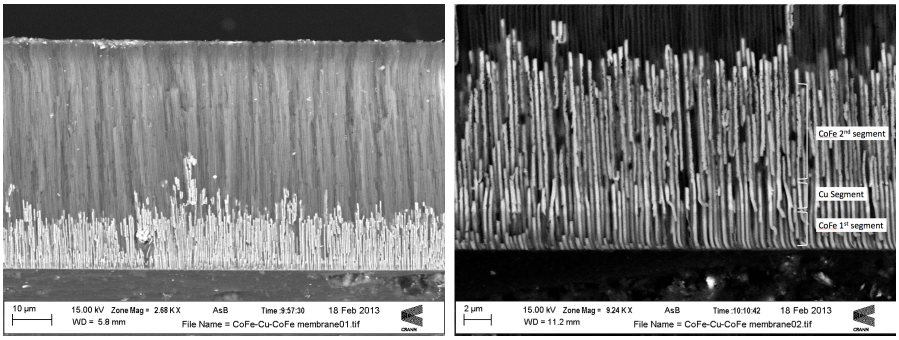



Figure 4.7: CoFe-Cu-CoFe nanowires in membrane indicating segments

SEM analysis was also carried out when the nanowires had been dissolved from the AAO membrane as shown in Figure 4.8 to ensure they had been fully released from the membrane. The SEM images showed some separation of the CoFe-Cu-CoFe nanowires, were the alumina appeared to be fully removed during the dissolving process.

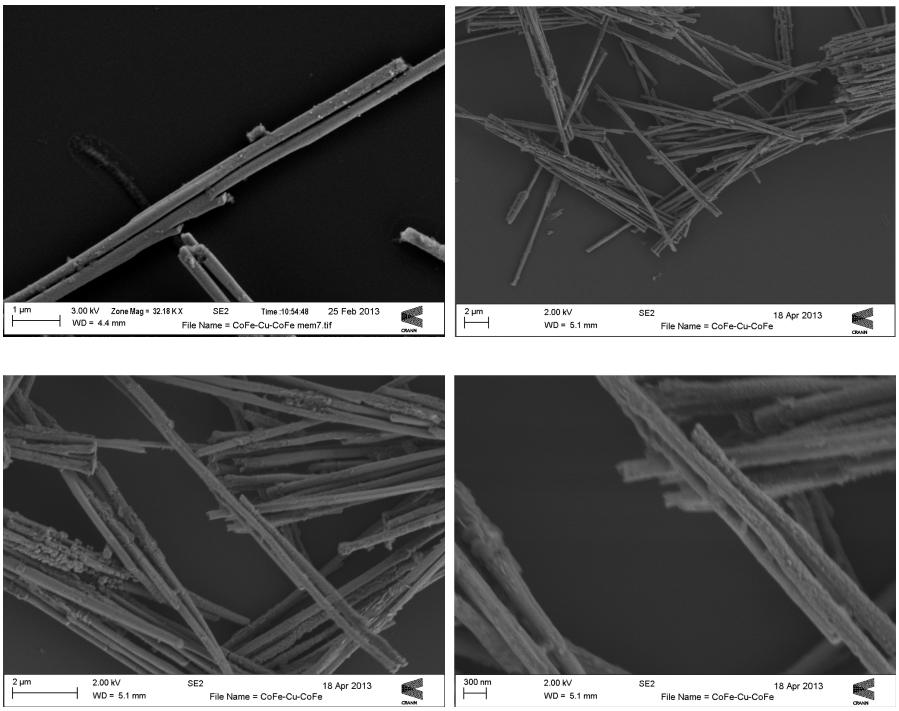



Figure 4.8: CoFe-Cu-CoFe nanowires after being dissolved from membrane

But in a high percentage of CoFe-Cu-CoFe nanowires there was an issue with nanowires bunched together and alumina still present.

An EDX line scan was carried out to ensure the composition of each segment was correct. Figure 4.9 shows the EDX line scan plot of CoFe-Cu-CoFe nanowires showing transistion between the magnetic and non-magnetic segments.

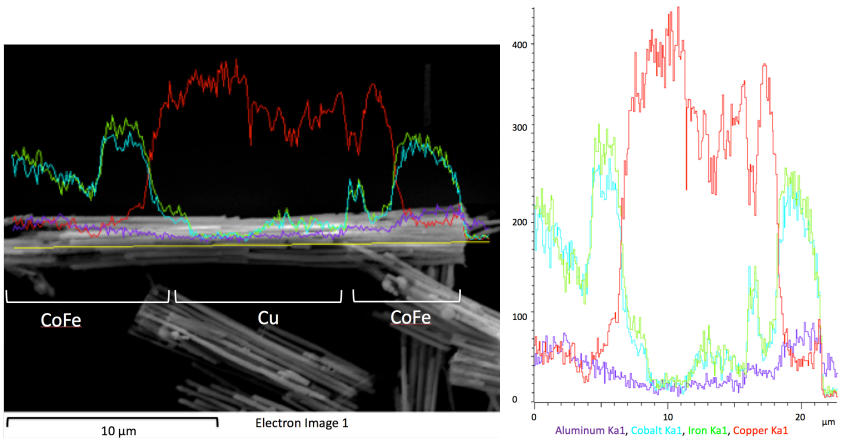



Figure 4.9: EDX line scan plot of CoFe-Cu-CoFe nanowires showing transitions of segments

There were issues with the morphology and structure of the CoFe nanowire segment when dissolving alumina from membrane. This is highlighted in Figure 4.10 which shows

the alumina still present and also the poor structure at the transition between the CoFe segment and the Cu segment.

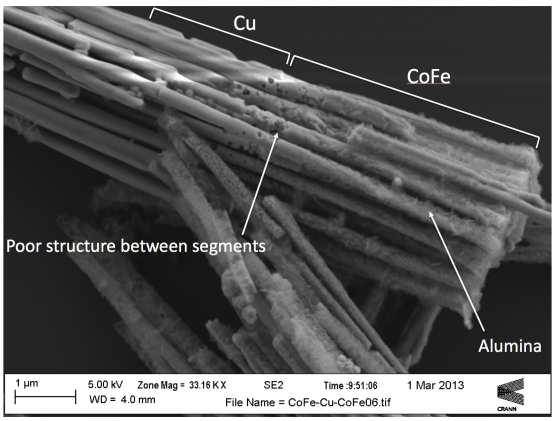



Figure 4.10: Issue dissolving alumina from the CoFe segment

The process used to dissolve the nanowires was modified till a more optimum process was realised. This involved varying the temperature of the NaOH and the time duration in which the membrane was dissolved.

Figure 4.11 shows the TEM analysis for CoFe-Cu-CoFe, which have been dissolved from membrane in NaOH solution at 45 $^{o}$C for 5mins. The TEM image shows that the alumina had not been fully removed. This was confirmed in the EDX scan, which shows the alumina peak present.

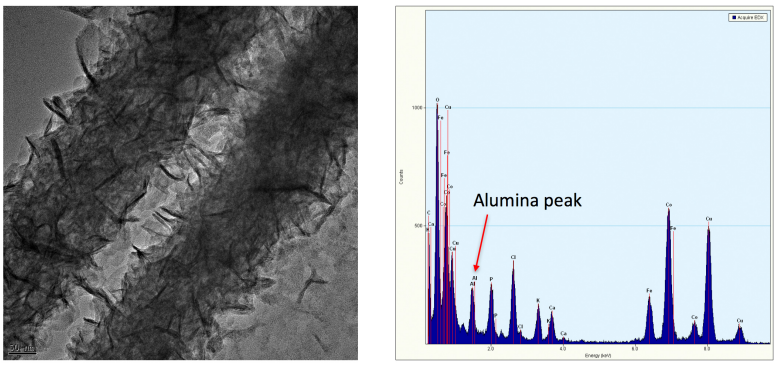



Figure 4.11: NaOH at 45 $^{o}$C for 5mins (a) TEM of CoFe-Cu-CoFe wires showing alumina present and (b) EDX scan showing showing alumina peak

Figure 4.12 shows the TEM analysis for CoFe-Cu-CoFe, which have been dissolved from membrane in NaOH solution at 45 $^{o}$C for 8 mins. The TEM image and EDX scan shows that the alumina has been removed. But the nanowires are degraded due to the NaOH.

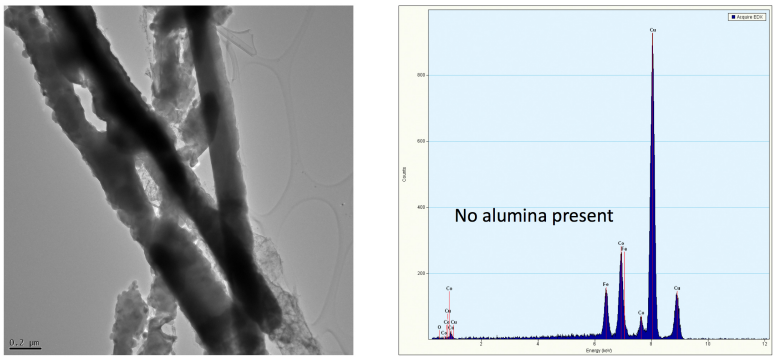



Figure 4.12: NaOH at 45 °C for 8 mins (a) TEM of CoFe-Cu-CoFe wires showing no alumina present and (b) EDX scan showing no showing alumina peak

The compromise was to reduce dissolving time to 7min and increase the temperature to 60 °C Overall, it was difficult to produce CoFe-Cu-CoFe nanowires that were well separated and showed good morphology and structure with all the alumina removed.

## 4.5 SIGNAL SEGMENT CONI & MULTI-SEGMENT CONI-CU-CONI NANOWIRES

Due to the issues with CoFe morphology and structure and dissolving alumina from membrane, Cobalt nickel (CoNi) was investigated as an alternative for both single segment magnetic nanowires and multi-segment nanowires.

Cobalt nickel (CoNi) single segment magnetic nanowires and CoNi-Cu-CoNi multi-segment nanowires were grown with a total length of 10 μm. Table 4.8, lists the solutions for CoNi 0.3 molar, CoNiCu interlayer that was used to assist the adhesion between the CoNi segment and the Cu segment and finally the Cu solution.

| Solution | Vol (cc) | Composition | Weight (g) | Molarity |
|---|---|---|---|---|
| CoNi 0.65M:0.35M | 50 | NaCl | 0.146 | |
| | | $CoSo_4$ | 9.13 | 0.65 |
| | | $NiSo_4$ | 4.83 | 0.36 |
| | | $H_3Bo_3$ | 0.37 | 0.12 |
| CoNiCu Interlayer | | CoNi | 0.63% | |
| | | Cu | 0.37% | |
| Cu | 10 | CuSo4 | 2.54 | 1 |

Table 4.8: CoNi, CoNiCu interlayer and solution Cu solution

Both CoNi single segment nanowires and CoNi-Cu-CoNi multi-segment nanowires are produced as per the electrodeposition process discussed in Chapter 2 Section 2.3. The 1st CoNi segment is prepared with the potentiostate coreware software set to -0.95 volt for a time duration of 2500 seconds. The interlayer CoNiCu solution is then applied, a two step voltage potential is applied at -0.7 Volt for 5 seconds and -0.6 Volt for 5 seconds. The interlayer assisted the adhesion between the two segments. The non-magnetic segment is then applied, this is achieved using a three-step voltage potential process, -0.4 Volt for 3 seconds, -0.3 Volt for 70 seconds and -0.2 Volt for 600 seconds. The 2nd CoNi magnetic nanowire segment is then applied at -0.9 Volt for 2500 seconds. The deposition sequence for CoNi nanowires and CoNi-Cu-CoNi segmented nanowires is shown in Table 4.9. This was achieved after a number of iterations and optimisation of the process.

| Sequence | Metal | Potential | Charge (Q) | Length (µm) | Time (sec) |
|---|---|---|---|---|---|
| 1st magnetic segment | CoNi | -0.9v | 15 | 3.5 | 2500 |
| Interlayer | CoNiCu | -0.7 | | | 5 |
| | | -0.6 | | | 5 |
| Non-magnetic segment | Cu | -0.4 | 14 | 3 | 3 |
| | | -0.2 | | | 70 |
| | | -0.2 | | | 600 |
| 2nd magnetic segment | CoNi | -0.9v | 15 | 3.5 | 2500 |

Table 4.9: Deposition sequence for CoNi-Cu-CoNi segmented nanowires

Table 4.10 highlight the conditions used for the growth of some of the batches of CoNi nanowires. Details of the CoNi-Cu-CoNi nanowire batches produced are listed in Appendix E.

| Sample | Segment | Type | Pot (V) | Time (Sec) | I (mA) | Charge (Q) | Length (µm) | OCP (V) | Mag (T) |
|---|---|---|---|---|---|---|---|---|---|
| 091215-1 | CoNi | | -0.9 | 5000 | 6.0 | 31 | 7 | 0.12 | 1.2 |
| 091215-2 | CoNi | | -0.9 | 5000 | 6.0 | 31 | 7 | 0.12 | 1.2 |
| 101215-1 | CoNi | | -0.9 | 7500 | 6.2 | 45 | 12 | 0.12 | 1.2 |
| 101215-2 | CoNi | | -0.9 | 7500 | 6.2 | 45 | 12 | 0.12 | 1.2 |
| 111215-1 | CoNi | | -0.9 | 2500 | 6.8 | 18 | 3 | 0.12 | 1.2 |
| 111215-2 | CoNi | | -0.9 | 2500 | 6.8 | 18 | 3 | 0.12 | 1.2 |
| 101215 | CoNi | | -0.9 | 7500 | 6.2 | 45 | 12 | 0.18 | 1.2 |
| 120116 | CoNi | | -0.9 | 6000 | 8.0 | 40 | 10 | 0.12 | 1.2 |
| 130116 | CoNi | | -0.9 | 6000 | 7.8 | 40 | 10 | 0.20 | 1.2 |
| 130116-1 | CoNi | | -0.9 | 3000 | 5.5 | 25 | 5 | 0.20 | 1.2 |
| 130116-2 | CoNi | | -0.9 | 3000 | 6.0 | 25 | 5 | 0.20 | 1.2 |
| 210116 | CoNi | | -0.9 | 6000 | 6.5 | 40 | 10 | 0.20 | 1.2 |
| | | | | | | | | | |

Table 4.10: CoNi deposition conditions

The full procedures for the preparation of the CoNi nanowire solutions, electrodeposition process and disolving the nanowies from the AAO membrane is detailed in Appendix E.

### 4.5.1 *CoNi-Cu-CoNi nanowire characterization*

To characterize the magnetic properties of magnetic nanowires in membrane, the CoNi samples were cut into 3 mm x 2.5 mm$^2$ sizes and placed into the SQUID. Figure 4.13 shows the magnetisation curve measured for the CoNi sample. From the magnetisation curve for CoNi, the remanent magnetic moment $m_r$ per measured sample, $m_r(per\,measured\,sample) = 1 \times 10^{-6}\mathrm{Am}^2$.

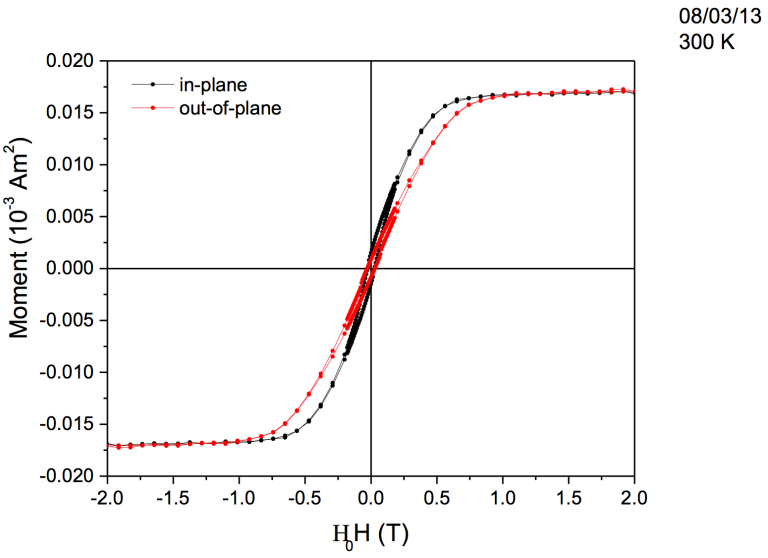



Figure 4.13: CoNi magnetisation hysteresis loop measured using SQUID

The SEM analysis was carried out on CoNi nanowires in membrane and also when the nanowires had been released from the membrane. The SEM analysis was used to determine the length of the nanowires in membrane and adjust the deposition rates accordingly. Element analysis using EDX was carried out to ensure the composition is correct. Figure 4.14 shows images of the CoNi single segment nanowires separated from membrane. The images showed good morphology and resonable separation from the membrane.

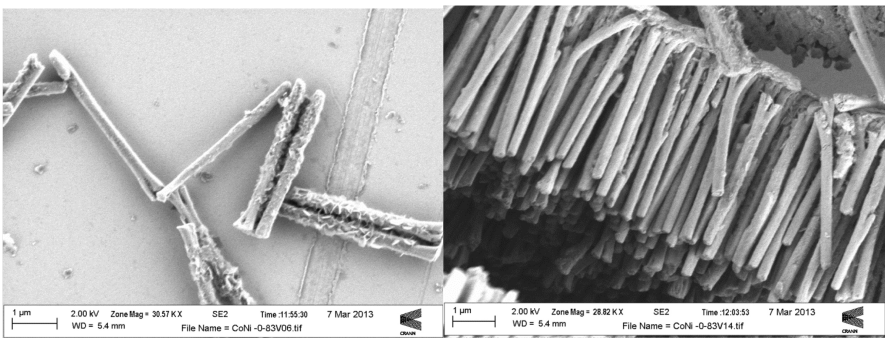



Figure 4.14: SEM images of CoNi single segment nanowires

Figure 4.15 shows the SEM images of the two magnetic segment CoNi-Cu-CoNi nanowires dissolved from membrane. The images showed good morphology and resonable separation from the membrane. Althought still breakages between the magnetic segment and non-magnetic segment.

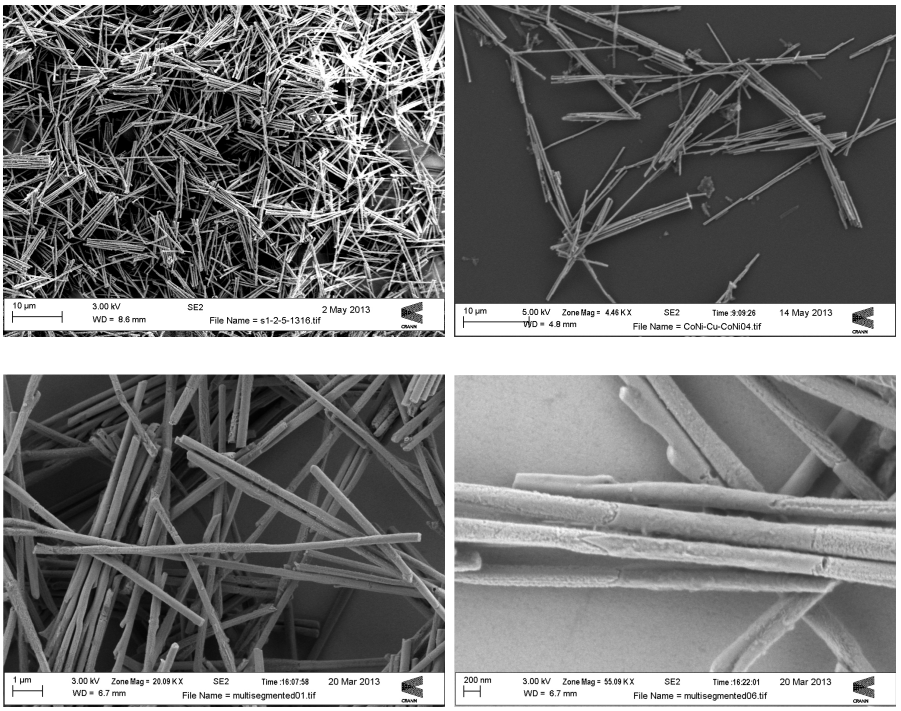



Figure 4.15: SEM images of CoNi-Cu-CoNi segmented nanowires

An EDX line scan shown in Figure 4.16 for multi-segmented nanowires was carried out to identify each segment element, a clear transition between the magnetic and non-magnetic segments.

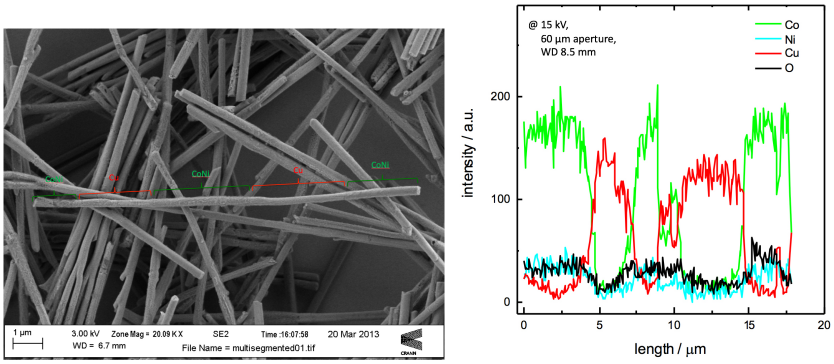



Figure 4.16: EDX line scan of CoNi-Cu-CoNi nanowires

The alumina appears to be removed more successfully from the CoNi nanowires. The use of the interlayer in the two-magnetic segment nanowires as helped the adhesion between segments and they are overall, uniform and well-defined. Althought still breakages between the magnetic segment and non-magnetic segment.

## 4.6 CONCLUSIONS

A number of nanowires were investigated throughout the study. Single segment cobalt nanowires were sucessfully fabricated with a robust procedure, which allowed them to be used for initial nanowire detection experiments.

The two magnetic segment CoFe-Cu-CoFe nanowires were produced to act as magnetic barcodes used during the nanowire detection experiments. Observation through SEM analysis showed a percentage of the nanowires produced after dissolving from the membrane had a porous morphology in the CoFe segment, and a weak adhesion between the CoFe and Cu segment interface.

Both single segment cobalt nickel (CoNi) nanowires and two magnetic segment nanowires using CoNi segments separated by a copper (Cu) non-magnetic spacer layer (CoNi -Cu-CoNi) were produced, providing suitable nanowires for the detection experiments for both single segment nanowire detection and two magnetic segment (barcode) detection using GMR sensors.

# 5

# DETECTION OF MAGNETIC NANOWIRES USING SINGLE SENSOR CONFIGURATION DETECTION SYSTEM

## 5.1 INTRODUCTION

This chapter discusses the principles for magnetic nanowire detection using a single magnetoresistive sensor. Based on the magnetisation curves measured for each of the magnetic nanowires that were used during my experimental work, calculations and model simulations were carried out to ascertain the expected response from the magnetic nanowire at various distances above the sensor. Also calculations were carried out to determine the velocity of a nanowire flowing in the microfluidic channel and the expected nanowire response time. This chapter also outlines the design, development and characterisation of the detection systems used for the detection of magnetic nanowires using GMR sensors and TMR sensors in single sensor configuration. Throughout the study a number of iterations of the nanowire detection system were developed to improve the signal to noise ratio and the detection of nanowires. Following this work a series of experiments were carried out towards the detection of magnetic nanowires.

## 5.2 MAGNETIC NANOWIRE DETECTION

The magnetic nanowires produce magnetic stray fields. When in close proximity, the stray field can be detected by the magnetoresistive sensor GMR or TMR. Calculations were carried out to provide an indication of the expected experimental signal response with regard to its magnetic magnitude response and time response. Figure 5.1 shows a schematic of nanowire at height ($z$) above the magnetoresistive sensor.

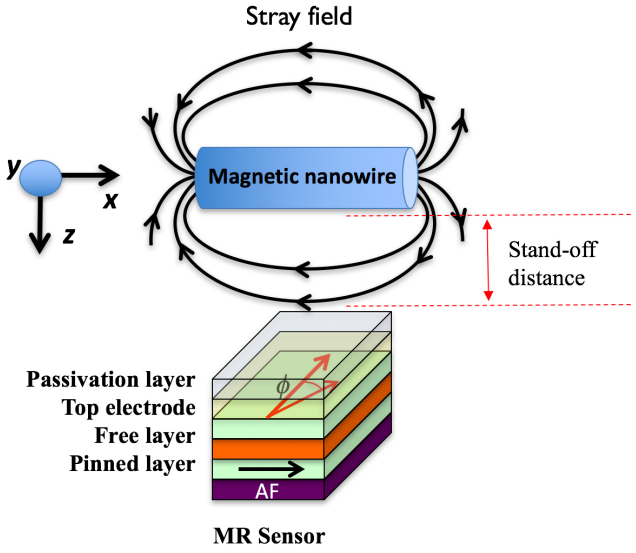



Figure 5.1: Schematic of nanowire at height ($z$) above the magnetoresistive sensor

The distance that separates the nanowire from the sensor determines the intensity of the magnetic field detected from the nanowire and is an important parameter to consider with respect to the detection of the magnetic stray fields and the sensitivity [113][114][115]. The vertical offset distance that separates the nanowire from the sensor is a result of both the thickness of the passivation layer, which covers the sensor and also the various heights that the nanowires flow within the microfluidic channel over the sensor. The passivation layer insulates and protects the magnetoresistive sensor during nanowire detection experiments from Di water and biological reagents flowing in the microfluidic channel which can be corrosive and conducting. A number of passivation layers had been explored throughout the course of my study, which are summarised in Chapter 3 Section 3.6 Table 3.11. $SiO_2$ with a thickness of 1 µm, was the principle passivation layer used for the nanowire detection experiments outined in this chapter using a single sensor configuration. Any passivation layer variation will be noted. Cobalt, Cobalt Iron ($Co_{50}Fe_{50}$) and Cobalt Nickel ($Co_{65}Ni_{35}$) were the principle nanowires used in the detection experiments. The nanowires varied in length from 5 µm to 40 µm and had a diameter ~ 200 nm. The type of nanowire and it's characteristics will be noted in each experiment accordingly. The model simulation that was used to simulate the response of a nanowire at various heights above the sensor, considers each nanowire as

a single domain and a magnetic dipole. The magnetic stray field produced by a single nanowire flowing along the sensitive direction of the sensor (x-direction) is given by,

$$B_X = \frac{\mu_0 m}{4\pi(z^3)} \tag{5.1}$$

Where $m$ is the magnetic moment, $\mu_0$ is the permeability of free space ($4\pi \times 10^{-7}$) and $z$ is the separation distance between the GMR sensor and the magnetic nanowire.

Magnetic field calculations and model response simulations based on the magnetisation curves measured for Cobalt, Cobalt Iron ($Co_{50}Fe_{50}$) and Cobalt Nickel ($Co_{65}Ni_{35}$) nanowires were carried out to determine the expected response of the respective nanowire at various heights above the sensor. This information would provide an indication of the expected response from the nanowire detection experiments, see Appendix C Section 8.4 to 8.6 for full calculation details.

## 5.3 MAGNETIC FIELD CALCULATION FOR COBALT NANOWIRES

The magnetisation curve as measured in Chapter 4 Section 4.3.3 for Cobalt (Co) is shown in Figure 5.2. From the magnetisation curve we can determine the in-plane remanent magnetic moment $m_r$ per measured sample. This will allow us to calculate the magnetic moment $m_r$ per nanowire.

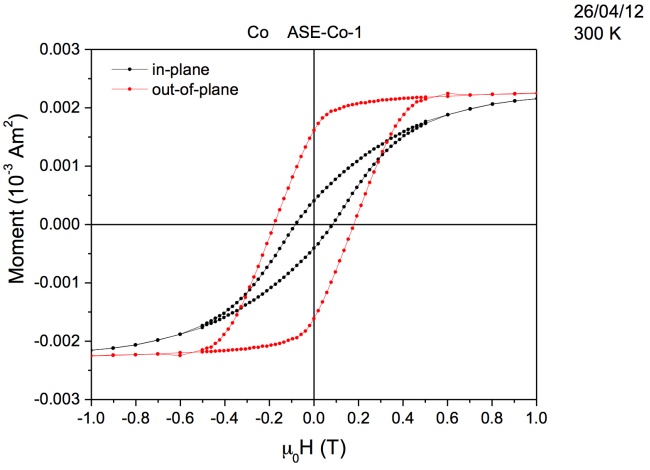



Figure 5.2: Magnetisation curve for measured for Cobalt (Co) magnetic nanowire sample

From the magnetisation curve for Co, the remanent magnetic moment $m_r$ per measured sample, $m_r(per\,measured\,sample) = 0.93 \times 10^{-6}\mathrm{Am}^2$. Table 5.1 shows the measured sample weight for the Co nanowires and the nanowire characteristics. As the nanowire sample is in membrane, the weight of the Co nanowire sample was determined by averaging a number of Co samples and then subtracting the weight of the AAO membrane, see Appendix C for AAO membrane and nanowire sample weights. The Co nanowires have a lenght 10 µm and diameter 200 nm. The Co density 8860 kg/m$^3$value is taken from the bulk physical properties.

| Co sample | |
|---|---|
| Sample weight | 102 µg |
| Nanowire length $l$ | 10 µm |
| Nanowire diameter $d$ | 200 nm |
| Density $\rho$ | 8860 kg/m$^3$ |

Table 5.1: Cobalt nanowire sample details

From the magnetisation curve the remanent Magnetisation $M_r$ per measured sample is,

$$M_r(measured\,sample) = \frac{m_r}{sample\,weight} = \frac{0.95 \times 10^{-6}}{102 \times 10^{-6}} = 9.314\,\frac{\mathrm{Am}^2}{\mathrm{kg}} \tag{5.2}$$

The nanowire volume $V_{nw}$,

$$V_{nw} = \frac{\pi \times (d)^2}{4} = \frac{\pi \times (200 \times 10^{-9})^2}{4} = 10 \times 10^{-6} = 0.314\,\mu m^3 \tag{5.3}$$

The remanent magnetic moment $m_r$per nanowire is,

$$m_r(per\,nanowire) = M_r \times V_{nw} \times \rho = 2.604 \times 10^{-14}\mathrm{Am}^2 \tag{5.4}$$

Taking the saturation value from the magnetisation curve measured for $Co$, the saturation magnetic moment $m_s$ per nanowire is $4 \times 10^{-13}\mathrm{Am}^2$. This gives $m_r/m_s = 6.51\%$. The nanowires saturation field response $B_s$ is 1.6 Tesla.

The therotical calculated saturation magnetisation for Co $M_s = 1450\,\mathrm{kA/m}$ and the corresponding saturation flux density$B_s = 1.82\,\mathrm{Tesla}$ see Appendix C Section 8.3.2.

### 5.3.1 *Stray field response of Cobalt nanowire at distances from the magnetoresistive sensor*

The field response $B_r$ in Tesla of Co nanowires at heights $(z)$ from the magnetoresistive sensor was calculated from the following expression,

$$B_r = \frac{\mu_0 m}{4\pi(z^3)} \tag{5.5}$$

Where $\mu_0 = 4\pi \times 10^{-7}$is the permeability of free space and $m_r$ is the remanent magnetic moment per nanowire. The magnitude of the response at heights $(z)$ will provide an indication of the experimental signal response magnitude of the magnetic nanowire as it flows across the sensor. The microfluidic channel used for my experimental work had a height of 30 µm. From the calculation in Eq.53, a Co nanowire traveling at a channel height $(z)$ of 6 µm should have a magnitude field response in the order of 12 µT.

$$B_r = \frac{4\pi \times 10^{-7} \times 2.604 \times 10^{-14}\mathrm{Am}^2}{4\pi} \times \frac{1}{(6\,^{-}\mathrm{m})^3} = 12.056\,\mu T \tag{5.6}$$

Table 5.2 shows the field calculation of a Co nanowire at various heights in the microfluidic channel, which is based on the remanent magnetic moment $m_r$calculated per nanowire.

| Cobalt (Co) | Channel height (µm) | Field response (µT) |
|---|---|---|
| Length 10 µm | 4 | 40.69 |
| Diameter 200 nm | 6 | 12.056 |
| | 8 | 5.086 |
| | 10 | 2.604 |
| | 14 | 0.949 |
| | 18 | 0.447 |
| | 25 | 0.167 |
| | 30 | 0.096 |

Table 5.2: Field calculation of a Co nanowire at various heights in the microfluidic channel

In the nanowire detection experiments using a single sensor configuration as outlined in this Chapter the background noise measured 0.451 volt. This corresponded to a field equivalent noise of ~ 11.5 µT. Therefore the nanowires would need to flow at a height of less than 8 µm in the microfluiduc channel before there is any signal detection of nanowires.

The response of the Co nanowire at various heights ($z$) above the sensor was also modelled using Manifest, which is a finite element and surface charge magnetics package. The nanowire parameters lenght, diameter and magnetic moment $m_r$ are entered into the cylinder model and the response at distance ($z$) from the nanowire is calculated. Figure 5.3 shows the response of the nanowire above the sensor.

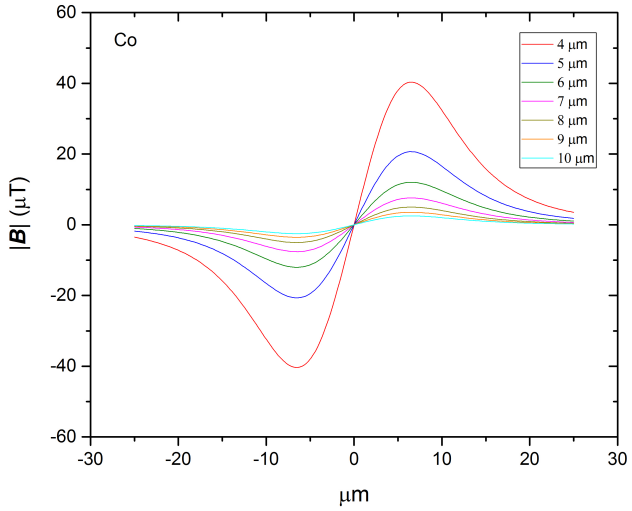



Figure 5.3: Model response of Co nano-wires at different heights z above the sensor

The shape of the modeled response is consistent with what we would expect for a magnetic nanowire dipole field. The cylinder dipole field is anisotropic, with twice the magnitude at the axical to the broadside and the magnitude falls off as $z^3$, where z is the distance from the dipole. From the modeled response of the Co nanowire, as the height increases the field magnitude response decreases by $z^3$.

## 5.4 MAGNETIC FIELD CALCULATION FOR $CO_{50}FE_{50}$ NANOWIRES

The magnetisation curve for $Co_{50}Fe_{50}$ measured in Chapter 4 Section 4.3.4 Figure 4.6, had a remanent magnetic moment $m_r$ per measured sample, $m_r(permeasuredsample) = 2.5 \times 10^{-6}\text{Am}^2$. Table 5.3 shows the measured sample weight for the $Co_{50}Fe_{50}$ nanowires and the nanowire characteristics, see Appendix C Section 8.3.1 for AAO membrane and nanowire sample weights Table 8.11. The $Co_{50}Fe_{50}$ nanowires have a lenngth 10 μm and diameter 200 nm. The $Co_{50}Fe_{50}$ density 8387 kg/m$^3$value is calculated from the bulk physical properties.

| $Co_{50}Fe_{50}$ sample | |
|---|---|
| Sample weight | 175 μg |
| Nanowire length $l$ | 10 μm |
| Nanowire diameter $d$ | 200 nm |
| Density $\rho$ | 8387 kg/m$^3$ |

Table 5.3: $Co_{50}Fe_{50}$ nanowire sample details

From the magnetisation curve the remanent Magnetisation $M_r$ per measured sample is,

$$M_r(measured\,sample) = \frac{m_r}{sample\,weight} = \frac{2.4 \times 10^{-6}}{175 \times 10^{-6}} = 14.28\,\frac{\text{Am}^2}{kg} \tag{5.7}$$

The nanowire volume $V_{nw}$,

$$V_{nw} = \frac{\pi \times (d)^2}{4} = \frac{\pi \times (200 \times 10^{-9})^2}{4} = 10 \times 10^{-6} = 0.314\,\mu m^3 \tag{5.8}$$

The remanent magnetic moment $m_r$per nanowire is,

$$m_r(per\,nanowire) = M_r \times V_{nw} \times \rho = 3.764 \times 10^{-14}\text{Am}^2 \tag{5.9}$$

Taking the saturation value from the magnetisation curve measured for $Co_{50}Fe_{50}$, the saturation magnetic moment $m_s$ per nanowire is $4.5 \times 10^{-13} Am^2$. This gives $m_r/m_s = 8.365\%$. The nanowires saturation field response $B_s$ is 1.8 Tesla.

The therotical calculated saturation magnetisation for Co $M_s = 1599\,kA/m$ and the corresponding saturation flux density$B_s = 2.00$ Tesla see Appendix C Section 8.5.

### 5.4.1 *Stray field response of $Co_{50}Fe_{50}$nanowires at distances from the magnetoresistive sensor*

The field response $B_r$ in Tesla of$Co_{50}Fe_{50}$ nanowires at distances ($z$) from the magnetoresistive sensor can be determined from Eq 5.1. From the calculation in Eq 5.10, a $Co_{50}Fe_{50}$ nanowire traveling at a channel height (z) of 6.5 µm should have a magnetude field response of 12.056 µT.

$$B_r = \frac{4\pi \times 10^{-7} \times 2.604 \times 10^{-14} Am^2}{4\pi} \times \frac{1}{(6.5\mu m)^3} = 12\,\mu T \tag{5.10}$$

Table 5.4 shows the field calculation of a $Co_{50}Fe_{50}$ nanowire at various heights in the microfluidic channel, which is based on the remanent magnetic moment $m_r$ calculated per nanowire.

| $Co_{50}Fe_{50}$ | Channel height (µm) | Field response (µT) |
|---|---|---|
| Length 10 µm<br>Diameter 200 nm | 4 | 49.602 |
| | 6 | 14.697 |
| | 8 | 6.200 |
| | 10 | 3.175 |
| | 14 | 3.175 |
| | 18 | 1.157 |
| | 25 | 0.203 |
| | 30 | 0.118 |

Table 5.4: Field calculation of a Co50Fe50 nanowire at various heights in the microfluidic channel.

In the nanowire detection experiments using a single sensor configuration as outlined in this Chapter the background noise measured at 0.451 V, this corresponds to field equivalent noise of ~ 11.5 µT. Therefore the nanowires would need to flow at a height of less than 7 µm in the microfluidic channel before there is any signal detection of nanowires. The response of the $Co_{50}Fe_{50}$ nanowire at various heights ($z$) above the sensor was also modelled using Manifest as shown in Figure 5.4.

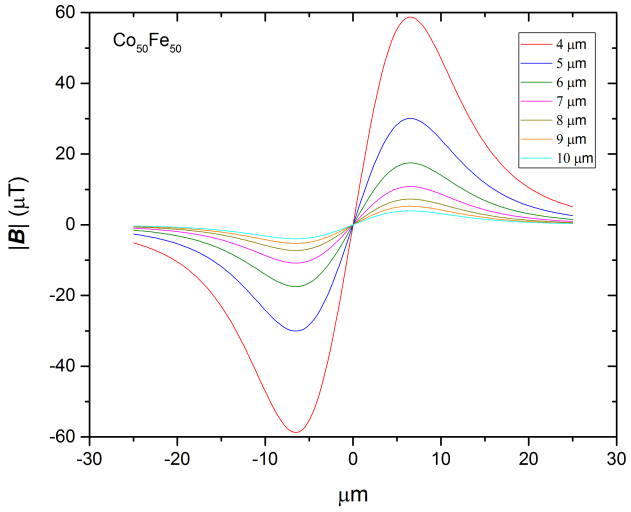



Figure 5.4: Model response of CoFe nanowire at different heights$z$ above the sensor

From the modeled response of the $Co_{50}Fe_{50}$ nanowire, as the height increases the field magnitude response decreases by $z^3$.

## 5.5 MAGNETIC FIELD CALCULATION FOR FOR co65ni35 NANOWIRES

The magnetisation curve for $Co_{65}Ni_{35}$ measured in Chapter 4 Section 4.3.4 Figure 4.13, had a remanent magnetic moment $m_r$ per measured sample, $m_r(permeasuredsample) = 1 \times 10^{-6}\text{Am}^2$. Table 5.5 shows the measured sample weight for the $Co_{65}Ni_{35}$ nanowires and the nanowire characteristics, see Appendix C Section 8.3.1 for AAO membrane and nanowire sample weights Table 8.11. The $Co_{65}Ni_{35}$ nanowires have a lenght 10 µm and diameter 200 nm. The $Co_{65}Ni_{35}$ density 8903 kg/m$^3$value is calculated from the bulk physical properties.

| $Co_{65}Ni_{35}$ sample | |
|---|---|
| Sample weight | 120 µg |
| Nanowire length $l$ | 10 µm |
| Nanowire diameter $d$ | 200 nm |
| Density $\rho$ | 8903 kg/m$^3$ |

Table 5.5: $Co_{65}Ni_{35}$ nanowire sample details

From the magnetisation curve the remanent Magnetisation $M_r$ per measured sample is,

$$M_r(measured\,sample) = \frac{m_r}{sample\,weight} = \frac{1 \times 10^{-6}}{120 \times 10^{-6}} = 8.333\,\frac{\mathrm{Am}^2}{kg} \tag{5.11}$$

The nanowire volume $V_{nw}$,

$$V_{nw} = \frac{\pi \times (d)^2}{4} = \frac{\pi \times (200 \times 10^{-9})^2}{4} = 10 \times 10^{-6} = 0.314\,\mu m^3 \tag{5.12}$$

The remanent magnetic moment $m_r$per nanowire is,

$$m_r(per\,nanowire) = M_r \times V_{nw} \times \rho = 2.331 \times 10^{-14}\mathrm{Am}^2 \tag{5.13}$$

Taking the saturation value from the magnetisation curve measured for $Co_{65}Ni_{35}$, the saturation magnetic moment$m_s$per nanowire is$3.496 \times 10^{-13}\mathrm{Am}^2$. This gives $m_r/m_s =$ 7.172%. The nano-wires saturation field response $B_s$ is 1.3 Tesla.

The therotical calculated saturation magnetisation for $Co_{65}Ni_{35}$ $M_s = 1120\,\mathrm{kA/m}$ and the corresponding saturation flux density$B_s = 1.4\,\mathrm{Tesla}$ see Appendix C Section 8.6.1.

### 5.5.1 *Stray field response of* $Co_{65}Ni_{35}$ *nanowires at distances from the magnetoresistive sensor*

The field response $B_r$ in Tesla of$Co_{65}Ni_{35}$ nanowires at distances ($z$) from the magnetoresistive sensor can be determined from Eq 5.1. From the calculation in Eq.61, a $Co_{65}Ni_{35}$ nanowire traveling at a channel height (z) of 5.8 µm should have a magnitude field response of 12 µT.

$$B_r = \frac{4\pi \times 10^{-7} \times 2.604 \times 10^{-14} Am^2}{4\pi} \times \frac{1}{(5.8\mu m)^3} = 12\,\mu T \tag{5.14}$$

Table 5.6 shows the field calculation of a $Co_{65}Ni_{35}$ nanowire at various heights in the microfluidic channel, which is based on the remanent magnetic moment $m_r$ calculated per nanowire.

| $Co_{65}Ni_{35}$ | Channel height (µm) | Field response (µT) |
|---|---|---|
| Length 10 µm<br>Diameter 200 nm | 4 | 36.419 |
| | 6 | 10.791 |
| | 8 | 4.552 |
| | 10 | 2.331 |
| | 14 | 0.849 |
| | 18 | 0.4 |
| | 25 | 0.149 |
| | 30 | 0.086 |

Table 5.6: Field calculation of a $Co_{65}Ni_{35}$ nanowire at various heights in the microfluidic channel

In the nanowire detection experiments using a single sensor configuration as outlined in this Chapter the background noise measured 0.51 V, this corresponded to field equivalent noise of ~ 11.5 µT. Therefore the nanowires would need to flow at a height of less than 5.5 µm in the microfluiduc channel before there is any signal detection of nanowires. The response of the $Co_{65}Ni_{35}$ nanowire at various heights ($z$) above the sensor was also modelled using Manifest is shown in Figure 5.5.

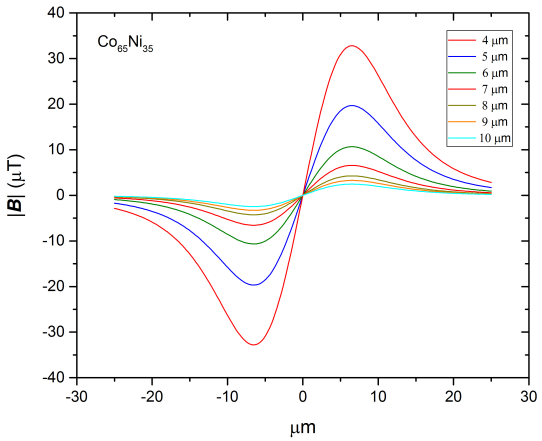



Figure 5.5: Model response of $Co_{65}Ni_{35}$ nano-wires in membrane at different heights$z$ above the sensor

The modeled response of the $Co_{65}Ni_{35}$ nanowire, as the height increases the field magnitude response decreases by $z^3$.

### 5.5.2 *Stray field model for a uniformly magnetised $Co_{65}Ni_{35}$ cylinder*

The magnetic field for a uniformly magnetised cylinder was also modelled using a routine written in Mathcad. The magnetic cylinder model allows us to calculate the model response for a uniformly magnetised nanowire (cylinder) and view the magnetic dipole field line direction and intensity at distance z from the nanowire. The routine allows us to enter the nanowire length, diameter and field ($Br$). Figure 5.6 show the model response for the magnetic dipole field lines and intensity for a magnetic nanowire

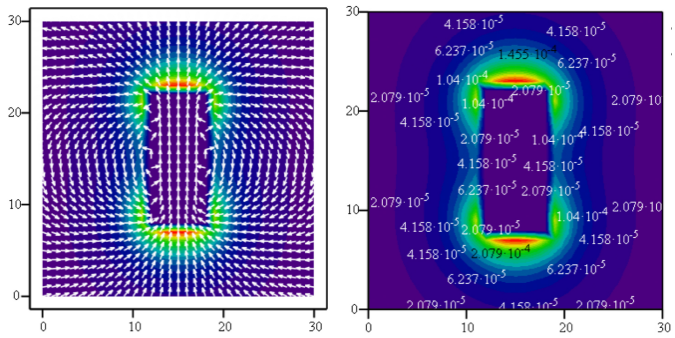



Figure 5.6: Response of nanowire magnetic dipole showing field lines and magnitude

## 5.6 VELOCITY OF MAGNETIC NANOWIRES FLOWING IN MICROFLUIDIC CHANNEL

To determine the response time of the nanowire traveling across the sensor at different velocities through the microfluidic channel calculations were carried out. Figure 5.7 shows an illustration of a nanowire traveling across the sensor in the microfluidic channel.

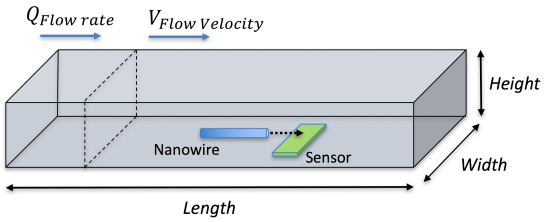



Figure 5.7: Illustration of nanowire traveling across the sensor in the microfluidic channel

During the nanowire detection experiments a syringe displacement pump was used to dispense nanowires across the sensor. Table 5.7 details the microfluidic chip channel

geometries, with the cross sectional area calculations for each of the microfluidic chip, sensor and nanowire parameters.

| Item | Parameters |
|---|---|
| Microfluidic pump | Volumetric flow rates 100nl - 20µl/minute using 100µl syringe<br>Shear stress range is 0.5 – 20 dyne/cm$^2$<br>Velocity range 10µm/s to 10cm/s |
| Microfluidic chip | Geometry: Rectangular, Length: 14 mm and Width: 600 µm<br>Height: 30 µm, $A_{Cross\ sectional\ area} = 30 \times 10^{-6} \times 600 \times 10^{-6} = 1.8 \times 10^{-8}$<br>Height: 60 µm, $A_{Cross\ sectional\ area} = 60 \times 10^{-6} \times 600 \times 10^{-6} = 3.6 \times 10^{-8}$<br>Height: 120 µm, $A_{Cross\ sectional\ area} = 120 \times 10^{-6} \times 600 \times 10^{-6} = 7.2 \times 10^{-8}$ |
| Nanowire length | 5 µm, 10 µm, 20 µm |
| Sensor width | 5 µm |
| Distance between sensors | 50 µm or 10 µm |

Table 5.7: Microfluidic pump parameters, channel geometries, sensor and nanowire details

The velocity of nanowire flowing in the microfluidic channel is determined by the flow rate over the microfluidic channel cross sectional area given by,

$$V_{Flow\ velocoty} = \frac{Q_{Flow\ rate}}{A_{Cross\ sectional\ area}} \tag{5.15}$$

Calculations were carried out based on the microfluidic pump flow rates to determine the fluidic velocity in each microfluidic chip. Table 5.8 details the fluid velocities per pump flow rate for the microfluidic chip with height 30 µm, which was the principle microfluidic chip used for experimental work.

| Microfluidic chip height: 30 µm | | | | | |
|---|---|---|---|---|---|
| Flow rate (nl/s) | Sheer stress (Dyne/cm$^2$) | Volume dispensed (µl) | Pressure (psi) | Reynolds number | Velocity (mm/s) |
| 14.4 | 0.1 | 0.37 | 0.015 | 0.045 (laminar) | 0.8 |
| 28.8 | 0.2 | 0.60 | 0.03 | 0.091 (laminar) | 1.6 |
| 43.2 | 0.3 | 0.896 | 0.05 | 0.137 (laminar) | 2.4 |
| 100.8 | 0.7 | 1.051 | 0.102 | 0.320 (laminar) | 5.6 |
| 144.0 | 1.0 | 1.301 | 0.155 | 0.457 (laminar) | 8.0 |
| 200.0 | 1.4 | 1.605 | 0.215 | 0.634 (laminar) | 11.1 |
| 270.0 | 1.6 | 1.701 | 0.291 | 0.857 (laminar) | 15.0 |
| 311.6 | 1.7 | 1.752 | 0.362 | 1.068 (laminar) | 18.70 |
| 400.0 | 1.8 | 1.810 | 0.431 | 1.269 (laminar) | 22.2 |
| 600.0 | 2.0 | 2.620 | 0.646 | 1.904 (laminar) | 33.3 |

Table 5.8: Microfluidic pump settings with flow velocity rates for microfluidic chip height: 30 µm

Table 5.9 details the fluid velocities per pump flow rate for the microfluidic chips with height 60 µm and 120µm respectively.

| Microfluidic chip height: 60 µm | | | |
|---|---|---|---|
| Flow rate (nl/s) | Pressure (psi) | Reynolds number | Velocity (mm/s) |
| 14.4 | 0.002 | 0.043 (laminar) | 0.4 |
| 28.8 | 0.004 | 0.087 (laminar) | 0.8 |
| 43.2 | 0.006 | 0.130 (laminar) | 1.2 |
| 100.8 | 0.014 | 0.305 (laminar) | 2.8 |
| 144.0 | 0.021 | 0.436 (laminar) | 4.0 |
| 200.0 | 0.029 | 0.606 (laminar) | 5.5 |
| 270.0 | 0.039 | 0.818 (laminar) | 7.5 |
| 311.6 | 0.046 | 0.943 (laminar) | 9.35 |
| 400.0 | 0.059 | 1.210 (laminar) | 11.1 |
| 600.0 | 0.087 | 1.818 (laminar) | 16.65 |

| Microfluidic chip height: 120 µm | | | |
|---|---|---|---|
| Flow rate (nl/s) | Pressure (psi) | Reynolds number | Velocity (mm/s) |
| 14.4 | 0.0003 | 0.040 (laminar) | 0.20 |
| 28.8 | 0.0006 | 0.080 (laminar) | 0.40 |
| 43.2 | 0.001 | 0.120 (laminar) | 0.60 |
| 100.8 | 0.002 | 0.280 (laminar) | 1.40 |
| 144.0 | 0.003 | 0.400 (laminar) | 2.00 |
| 200.0 | 0.0043 | 0.555 (laminar) | 2.77 |
| 270.0 | 0.0059 | 0.750 (laminar) | 3.75 |
| 311.6 | 0.0068 | 0.865 (laminar) | 4.32 |
| 400.0 | 0.0087 | 1.111 (laminar) | 5.55 |
| 600.0 | 0.013 | 1.666 (laminar) | 8.33 |

Table 5.9: Microfluidic pump settings with flow velocity rates for microfluidic chip height- 60 µm and 120 µm

### 5.6.1 *Estimation of nanowire response time*

Calculations were carried out to determine the expected response time of a detected nanowire flowing in the microfluidic channel at velocities. Figure 5.8 shows a schematic of nanowire response time flowing across the sensor.

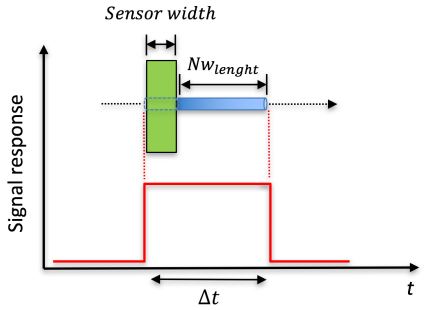



Figure 5.8: Schematic of nanowire response time

For example a nanowire 10 µm in length, traveling in the microfluidic chip with height 30 µm and width 600 µm across a sensor of 5 µm width at a velocity of 0.8 mm/s will have a response time,

$$Nw_{response\,time} = \frac{Nw_{length} + Sensor\,width}{Velocity} = \frac{15 \times 10^{-6}}{0.8 \times 10^{-3}} = 18.75\,\text{ms} \tag{5.16}$$

Table 5.10 details the nanowire response times $Nw_{response\,time}$at different velocities for different nanowire lengths using a microfluidic chip height: 30 µm.

| Microfluidic chip height: 30 µm | | | | |
|---|---|---|---|---|
| Parameters | Velocity (mm/s) | Nanowire 5 µm Response time (ms) | Nanowire 10 µm Response time (ms) | Nanowire 20 µm Response time (ms) |
| Nanowire length 5 µm, 10 µm & 20 µm<br>Sensor width 5 µm | 0.8 | 12.5 | 18.75 | 31.25 |
| | 1.6 | 6.25 | 9.37 | 15.62 |
| | 2.4 | 4.16 | 6.25 | 10.41 |
| | 5.6 | 1.78 | 2.67 | 4.462 |
| | 8.0 | 1.25 | 1.87 | 3.125 |
| | 11.1 | 0.90 | 1.36 | 2.225 |
| | 15.0 | 0.66 | 1.00 | 1.666 |
| | 18.75 | 0.533 | 0.80 | 1.333 |
| | 22.2 | 0.450 | 0.67 | 1.112 |
| | 33.3 | 0.300 | 0.45 | 0.750 |

Table 5.10: Nanowire response times at different velocities for different nanowire lengths using a microfluidic chip height: 30 µm

## 5.7 FIRST ITERATION OF THE NANOWIRE DETECTION SYSTEM

Following the nanowire calculations with regard to its expected magnetic magnitude response and the time response as the nanowire passes over the magnetoresistive sensor, a detection system was designed to allow detection of the nanowire stray field as it passes across the magnetoresistive sensor. Figure 5.9 shows a schematic diagram highlighing in red the design components in the first iteration nanowire detection system.

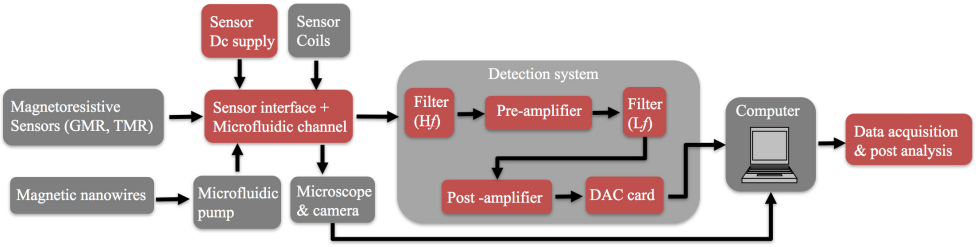



Figure 5.9: Schematic diagram highlighing design components in the first iteration nanowwire detection system

The system comprised of a sensor interface and microfluidic channel, sensor current supply, the detection system incorporated an amplifier and filter stage, this connected to a PC with data acquisition software via a data acquisition board. Figure 5.10 shows the first iteration of nanowire detection system showing sensor interface, in-house built pre-amplifier stage, Stanford Research SR560 post amplifier stage and a Keithley KUSB-3116 data acquisition board.

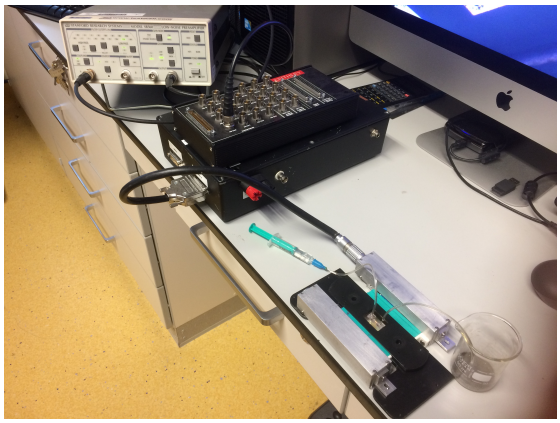


Figure 5.10: First iteration of nanowire detection system showing sensor interface, pre-amplifier, SR560 post amplifier and data acquisition board

### 5.7.1 *Sensor current supply*

The current circuit used to supply the GMR sensor comprised of LM234 10 mA programable current source, which was supplied using a + 15 Volt DC voltage supply Caltex BPS4000. Figure 5.11 shows the current circuit design, which was set at 2 mA. The current noise produced by the LM234 when utilized as an active load in an amplifier is 12 dB. The circuit supplies current to the two YOKE GMR sensors. Two current circuits were built for sensor side A and B respectivily.

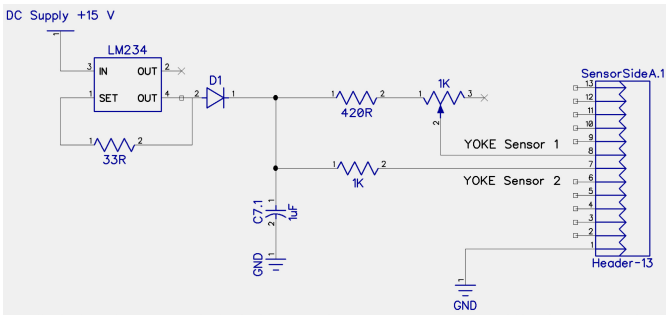



Figure 5.11: Single sensor configuration current suppy

### 5.7.2 *Sensor interface & microfluidic channel*

The sensor interface allowed placement of the GMR sensor and fitting of the microfluidic chip into a basic frame to allow placement under a standard microscope. The GMR

sensor was slotted into a 2.5 mm pitch edge connector, with electrical connections to the amplifier stage. The frame allows fitting of the microfluidic chip and sensor under a microscope as shown the Figure 5.12.

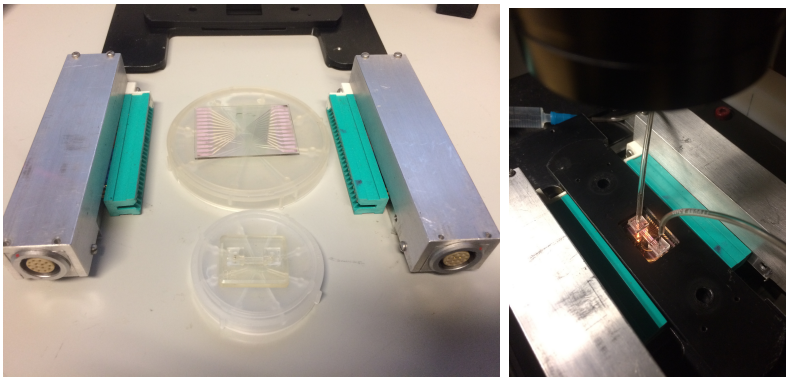


Figure 5.12: (a) Sensor & microfluidic chip interface and (b) placement under microscope

The microfluidic chips were supplied by a company called Cellix. They are a plastic chip with a Polydimethylsiloxane (PDMS) channel. The Microfluidic single channel design shown in figure 5.13 has a channel dimensions length 14 mm, width 600 µm and heights 120 µm, 60 µm and 30µm as detailed in Table 5.7. The external dimensions are 23 mm x 18.7 mm.

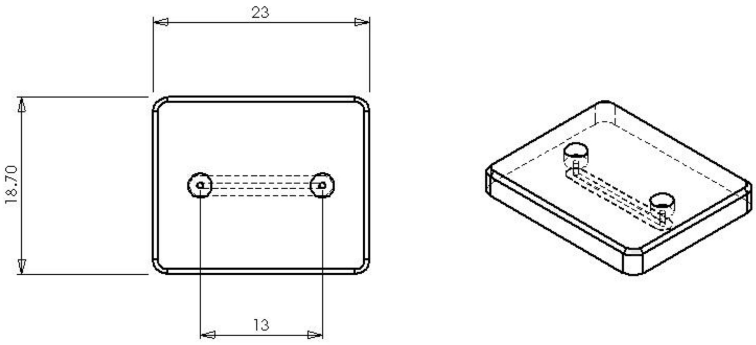



Figure 5.13: Microfluidic chip single channel design

### 5.7.3 *Detection system*

In order to measure the small signals arising from the flowing nanowires, a two stage signal amplifying and filter system was implemented. The first stage pre-amplifier used a very low noise amplifier type INA103, which has a noise level of $1\text{nV}/\sqrt{\text{Hz}}$. The amplifier

gain was set to 100 (40 dB) and incorporated a high pass filter at 70 Hz as shown in Figure 5.14. The high pass filter was used to reduce the signal noise level by blocking any DC to 70 Hz signals, such as 50 Hz generated by electrical mains supplies. Each of the pre-amplifiers were connected to the sensing elements along the length of the YOKE GMR sensor. A total of sixteen amplifiers were implemented, eight on each sensor side A and B respectively.

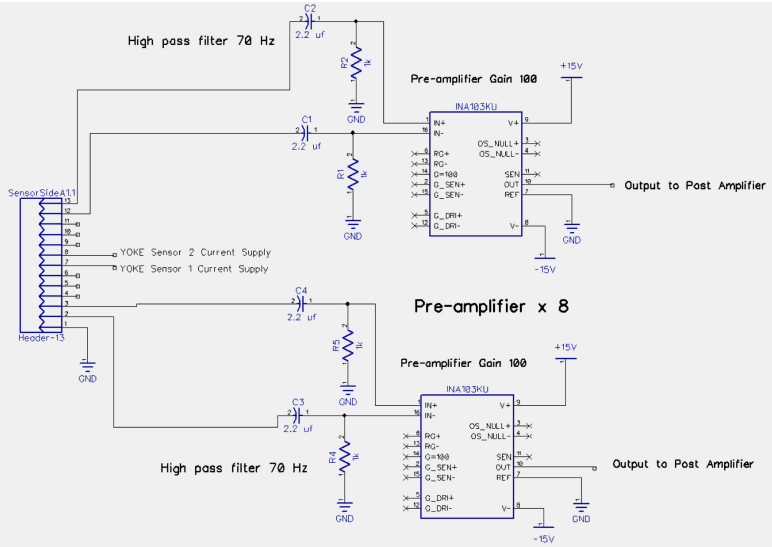



Figure 5.14: Single sensor configuration pre-amplifier stage side A

For the initial detection system design work and nanowire detection experiments the post-amplifer was a commercial Stanford Research amplifier type SR560 as shown in Figure 5.10. The SR560 amplifier provides variable gain selection from 1 to 50,000 and variable LPF and HPF filter selection 0.03 Hz to 1 MHz, this allowed for the optimum selection of the post amplifier gain and low pass filter. The SR560 has a noise level of $4\text{nV}/\sqrt{\text{Hz}}$ at 1 kHz. The post-amplifier then connects to a Keithley data acquisition card type KUSB-3116. The Keithley KUSB-3116 is a 16 bit DAC with sample rate of 500 kS/s, it provides 16 channels with a 2 µs sample interval. The noise level is 0.4 LSB rms, which is 61.2 µVrms.

### 5.7.4 *Sensor and system noise calculations and measurements*

The system noise measurements were carried out with various post-amplifier gains applied using the Stanford Research amplifier type SR560 as shown in Figure 5.15. The filter set at HPF 30 Hz and LPF 30 KHz.

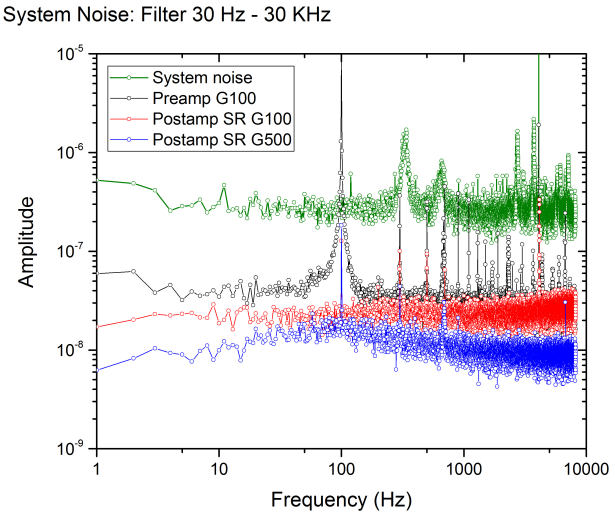



Figure 5.15: System noise measurements with various post-amplifier gains applied using Stanford Research amplifier type SR560

From the noise measurements taken at various gains, an optimum gain was selected the post-amplifier at 100 (40 dB) using the Stanford Research amplifier. Including the pre-amplifier gain of 100 (40 dB), this provided an overall system gain of 10,000 (80 db) in the amplifier stage. Figure 5.16 shows the noise considerations at various band-pass filtering using the Stanford Research amplifier type SR560.

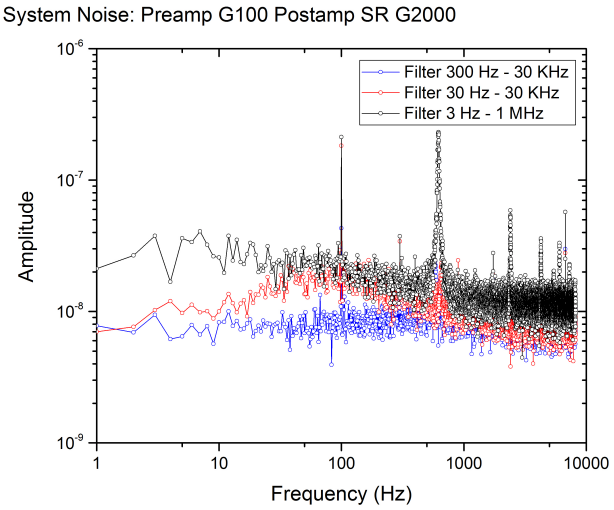



Figure 5.16: System noise considerations at various band-pass filtering using Stanford Research post-amplifier type SR560

Filtering considerations were made based on the noise measurements shown in Figure 5.16. A 70 Hz high-pass filter was implemented in the pre-amplifier blocking all signals from DC to 70 Hz, and 75 KHz low-pass filter was set on the post amplifier using the Stanford Research amplifier. The detected signals from the post-amplifier are connected into a Keithley data acquisition module and data is then recorded using Lab-view customised software.

A schematic showing the detection system band-pass filtering on the noise power spectral density for a GMR sensor is detailed in Figure 5.17. Highlighted in green is the band-pass filter implemented into the detection system, which provides an overall gain of 10,000. The low frequency noise contributions are filtered out up to 70 Hz and the high frequency noise contributions after 75 KHz are filtered out. The sensor noise witnin the bandpass of the filters is

$$\sqrt{1 \times 10^{-17} \frac{V^2}{\sqrt{Hz}}} = 3.162 \frac{\text{nV}}{\sqrt{\text{Hz}}} \tag{5.17}$$

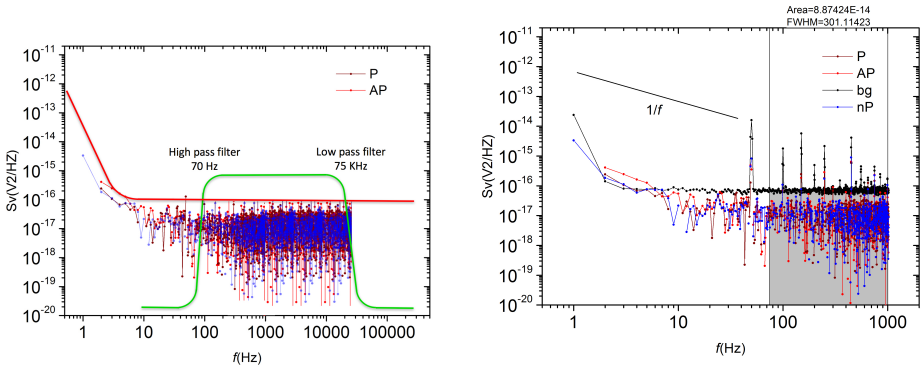



Figure 5.17: Schematic detection system band-pass filtering on the noise power spectral density for the GMR sensor

The first stage of the detection system after the high pass filter (70 Hz) is a very low noise ($1\text{nV}/\sqrt{\text{Hz}}$) preamplifier type INA103 (Gain 100). The INA103 datasheet provides the noise spectral density plots that can be used for low resistance (<1kOhm) noise measurments shown in Figure 5.18. The preamplifier voltage noise within the bandpass of the filters is

$$\left(1.8\frac{\text{nV}}{\sqrt{\text{Hz}}}\right)^2 = 0.324\times10^{-17}\frac{\text{V}^2}{\text{Hz}} \tag{5.18}$$

The preamplifier current noise within the bandpass filter is

$$2\frac{\text{pA}}{\sqrt{\text{Hz}}}\times 200\Omega = 0.4\frac{\text{nV}}{\sqrt{\text{Hz}}} \tag{5.19}$$

or

$$\left(2\frac{\text{pA}}{\sqrt{\text{Hz}}}\times 200\Omega\right)^2 = 0.016\times10^{-17}\frac{\text{V}^2}{\text{Hz}} \tag{5.20}$$

The combined noise for the sensor and the preamplifier is,

$$\sqrt{1.3\times10^{-17}\frac{\text{V}^2}{\sqrt{\text{Hz}}}} = 3.606\frac{\text{nV}}{\sqrt{\text{Hz}}} \tag{5.21}$$

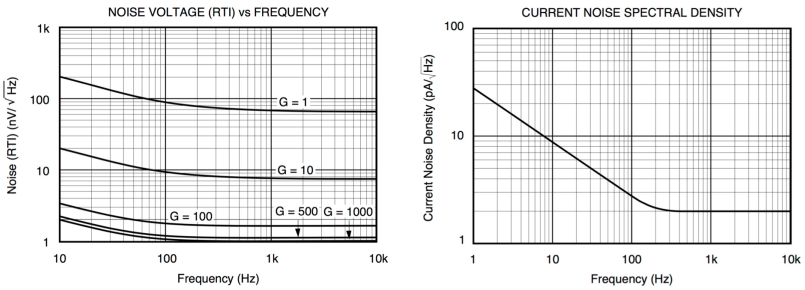



Figure 5.18: INA103 voltage and current noise spectral density

The second stage of the detection system is the low pass filter (75 KHz) and the post-amplifier (Gain 100). This connects to the data acquistion card, which was a Keithly 3116, which is a 16-bit DAC card with 2 LSB noise. The noise contribution from the 16-bit DAC card is

$$\frac{2}{2^{16}} \times 10\text{V} = 0.305\,\text{mV} \tag{5.22}$$

These are the principle noise contributions from the sensor through the detection system chain.

### 5.7.5 *Data acquisition*

The detected signals from the Keithley 16-bit DAC card are connected to a PC via USB for data acquisition. A Lab-view routine was designed, which provides functionality to record the signal detection data and save it to a data file for post analysis Figure 5.19 shows the Lab-view interface window and block diagram of the program file. The routine allows a selection of up to 16 channels, setting of sample rate, all channels can be viewed in real time. The recorded signal responses are saved into a data file for post analysis.

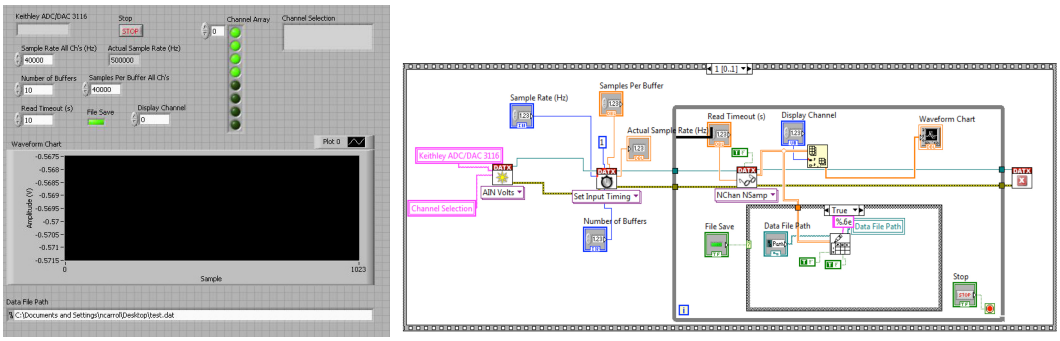



Figure 5.19: Lab-view interface and block diagram

### 5.7.6 *Pulse Height Amplification routine for post data analysis*

Pulse Height Amplification (PHA) routine was written in Math-Lab software to provide de-noising and improvements to the signal-to-noise ratio of the captured datasets and also to provide post statistical analysis of the captured datasets from the nanowire detection experiments. The PHA software comprises of two sections. The first pre-conditioning section provides model fitting of the captured nanowire detected responce, this provides parametric de-noising of the captured signal response, reducing the background noise by a factor. Figure 5.20(a) shows an example of a model fitting (blue line) of the captured nanowire detected responce (red dots). The second PHA section locates all actual nanowire detected events, integrates each signal response. The upper and lower threshold can be adjusted to exclude the noise contribution as shown in Figure 5.20(b) dashed green line. Each detected signal is then extracted as a signal amplitude as shown in Figure 5.20(c). This allows for post statistical analysis of the extracted nanowire detected events.

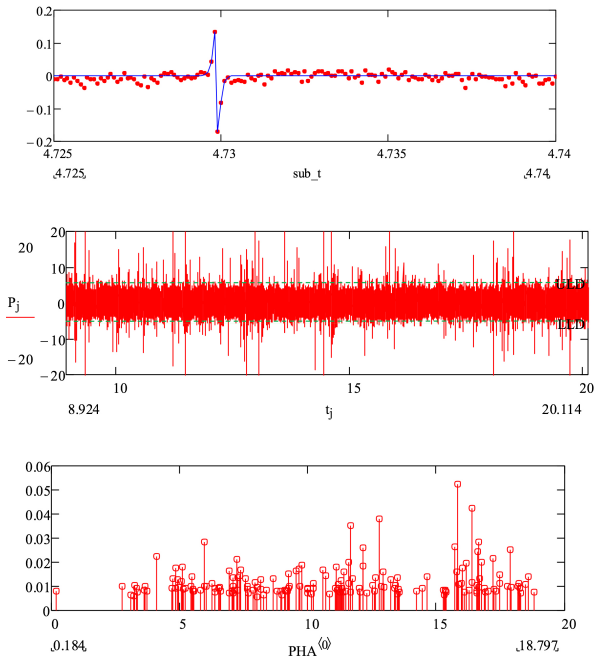



Figure 5.20: Figure (a) PHA model fitting (blue line) of the captured nanowire detected responce (red dots), (c) upper and lower threshold set and (c) PHA detected events extracted a signal amplitudes

## 5.8 NANOWIRE DETECTION EXPERIMENTS

Using the detecion system discribed in Section 5.7, initial nanowire detection experiments were carried to ascertain if we could detect the magnetic nanowire stray field as it passed across the GMR sensor.

Firstly a series of noise measurements were carried out. The detection system was configured with an overall gain of 10,000 (80 dB) in the pre and post amplifier stage, with a high-pass filter 70 Hz and a low-pass filter 100 KHz. Figure 5.21 (a) shows the eletrical configuration for the GMR sensor.

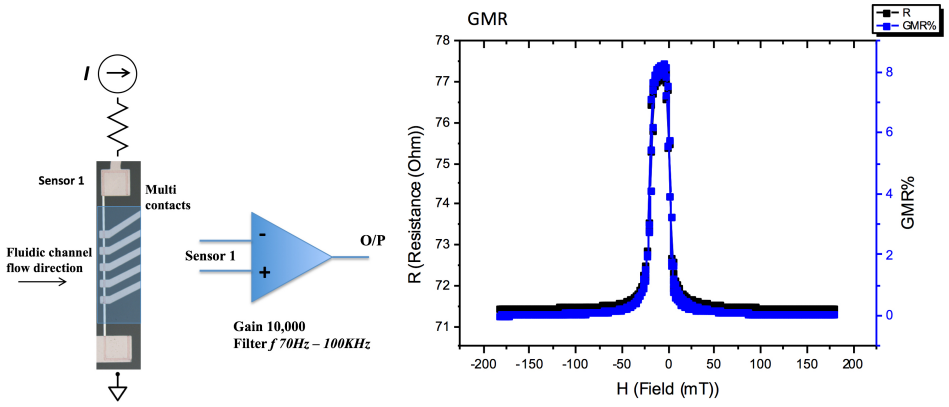



Figure 5.21: (a) GMR sensor experimental single sensor configuration and (b) GMR sensor used in the experiment magnetoresistance response measurment

In this configuration the GMR sensor is placed into the sensor interface and microfluidic channel. A current of 2 mA is applied directly across the GMR sensor and the background noise response measured from two of the multi-contacts along the length of the sensor. The GMR sensor has a length of 400 µm and width 5 µm as detailed in Figure 8.18in (Chapter.3 Section 3.2.1). The sensor used in the experiment measured a magnetoresistance ratio of 8.2 % and had a linear response and sensitivity of 0.8%/mT as shown in Figure 5.21 (b). The sensor was passivated with $SiO_2$ 900 nm to protect it from microfluidics during the experiment. The measured signal response is in volts, a calibration field factor is applied to show the response in magnetic field.

### 5.8.1 *Sensor magnetic field Calibration*

Each GMR and TMR sensor is calibrated with regard to the detection system and allows for the correct magnetic field scale to be applied, for noise measurments and nanowire detection experiments. The calibration is performed using the experimental set up shown in Figure 5.22.

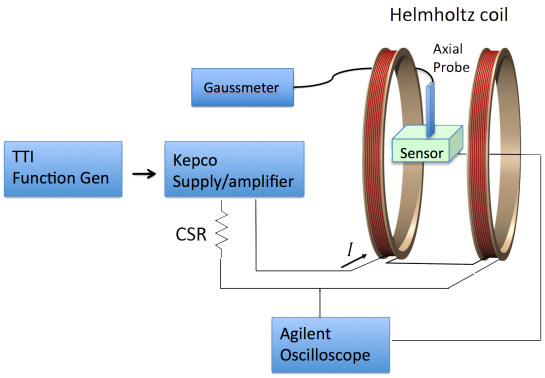



Figure 5.22: Sensor field calibration configuration

The GMR or TMR sensor is placed in a pair of standard laboratory Helmholtz coils, the coils had 320 turns, a diameter of 12.5 cm and a distance between the coils of 20 cm. The Helmholtz coils ensure a uniform field is produced across the sensor. Using the function generator type TTI TG315 and a bipolar operational amplifier type Kepco BOP 20-10, a variable field range is generated by the Helmholtz coils. The response of the Helmholtz coils is monitored via the current sensing resistor (CSR) 0.45 ohm and an oscilloscope. The field response of the sensor is measured using an oscilloscope and the sensitivity is determined by the Coil response/Sensor response. A gauss meter with an axial probe is used to measure the magnetic field. Table 5.11 lists typical sensor calibration conditions measured.

| **Calibration conditions: Single sensor configuration** | |
|---|---|
| Function generator | 128 Hz @ 1.5 mV pk-pk |
| Bipolar amplifier | -10 V @ -0.6 Amp |
| | |
| $\mathcal{U}_{csr}$ (Coil response) | 40.00 $mV\ pk-pk$ (CSR-current sensing resistor) |
| $\mathcal{U}_{amp}$ (Sensor response) | 2.5 $V\ pk-pk$ |
| $\mathcal{U}_{csr}bias$ | 400.7$mV\ pk-pk$ |
| | |
| Field calibration bias | 398.7 $mV$ = 1.9 mT (Optimum bias) |
| $Cal_{field}$ | $\frac{1.9\ mT}{V}$ |
| $Cal_{amp}$ (Cal constant) | $\frac{\mathcal{U}_{amp}}{\mathcal{U}_{csr}V\ .\ Cal_{field}} = 32.89\ V/mT$ |

Table 5.11: Calibration conditions measured for single sensor configuration

### 5.8.2 *Noise measurements*

Noise measurment of the detection system and the sensor response were carried out. Figure 5.23 (a) shows the background noise response recorded with no deionised water flowing through the fluidic channel, the noise measured 0.423 Vdc at a gain of 10,000. With the calibration field constant applied, this measured at ~ 10.7 μT.

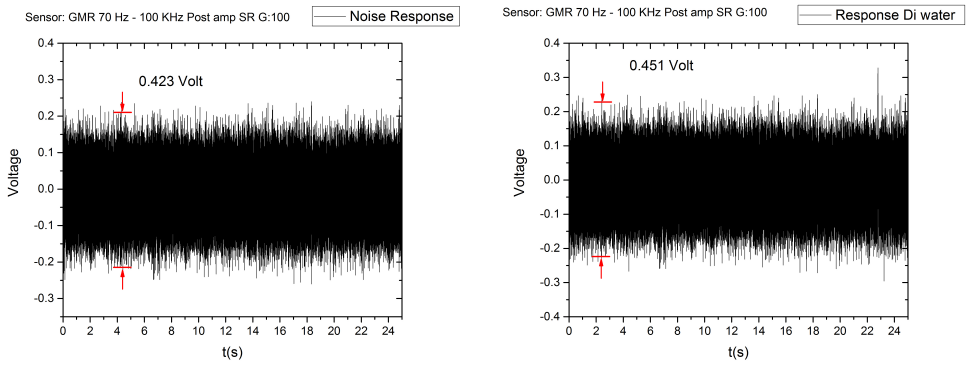



Figure 5.23: (a) background noise response recorded from GMR sensor with no deionised water flowing (b) background noise response recorded from sensor with deionised water flowing

The noise measurments were repeated with deionised water flowing through the microfluidic channel, Figure 5.23(b) shows the background noise response recorded with deionised water flowing through the fluidic channel, the noise measured 0.451 Vdc. With the calibration field constant applied this measures at ~ 11.5 μT. The background noise measured is a combination of environmental noise, the electronic noise from the detection system and the sensor. There is also noise contribution when the deionised water is flowing through the channel across the sensor.

### 5.8.3 *Nanowire detection experiments - Cobalt (Co) nanowires*

In the initial detection experiments, nanowires were injected into the microfluidic channel using a hand syringe. The GMR sensor was calibrated with regard to the detection system and allows for the correct magnetic magnitude scale to be applied during experiments. Details of Co nanowires Batch: 03261108 used in the experiment are detailed in Table

5.12. The Cobalt nanowires were deposited at an over potential of -1 Vdc, for a duration of 6000 seconds at 5.8 mA as outline in (Chaper 4 Section 4.3.1).

| Sample | Segment | Type | Pot (V) | Time (Sec) | Current (mA) | Charge (Q) | Length (µm) |
|---|---|---|---|---|---|---|---|
| 03261108 | Co | | -1 | 6000 | 5.8 | 65 | 40 |

Table 5.12: Co nanowire sample deposition conditions

Table 5.13 shows the conditions used to dissolve the nanowires from the membrane. To dissolve the nanowires from the membrane they were placed in a solution of NaOH 1 molar at 60 $^{o}$C for a duration of 7 minutes. The sample was visually checked periodically every one minute period. A final sonication process for 20 seconds separates the nanowires. To remove the NaOH solution, the nanowires are rinsed in de-ionised water a number of times using a centrifuge at 2900 rpm as outline in (Chaper 4 Section 4.3.1).

| Sample | Type | Solution (1molar) | Temp ($^{0}$C) | Method | Weight (g) |
|---|---|---|---|---|---|
| 03261108 | Co | NaOH | 60 | 7 mins NaOH & Sonication 20 sec<br>Rinse in DI water centrifuge 2900 rpm | 0.0140021 |

Table 5.13: Co nanowire sample dissolving conditions

To confirm the dispersion and length of the nanowires in the sample, images were taken of each sample batch using both the SEM and microscope. Figure 5.24 (a) shows the SEM image of Co nanowires sample 03261108. The nanowires varied in length 10 µm up to 30 µm.

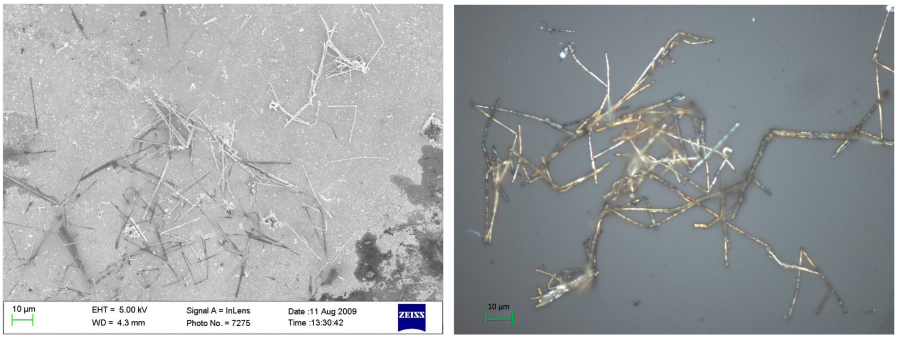



Figure 5.24: (a) SEM image of Co nanowires sample 03261108 (b) Microscope inspection image of Co nanowires prior to dispensing

The inspection image of nanowires prior to dispensing shown in Figure 5.24(b) showed reasonable separation of nanowires and also bunching of nanowires.

The Co nanowires length 30 µm were injected across the GMR sensor at velocities using a hand syringe. The detected response of the Co nanowires sample 03261108 flowing across the sensor is shown in Figure 5.25.

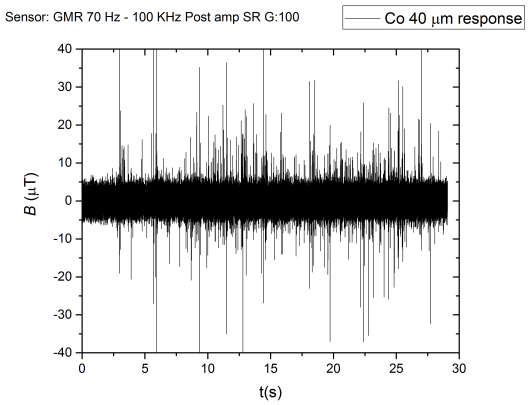



Figure 5.25: Response of Co nanowires sample 03261108 flowing across sensor

The nanowires are dispensed after the first 3 seconds and stopped after a 27 second time period. During the time period when nano-wires are dispensed, detected responses are recorded. The detected responses varied in amplitude from 15 µT to 60 µT . Figure 5.26 highlights in detail some of the detected events from the Co nano-wires sample 03261108.

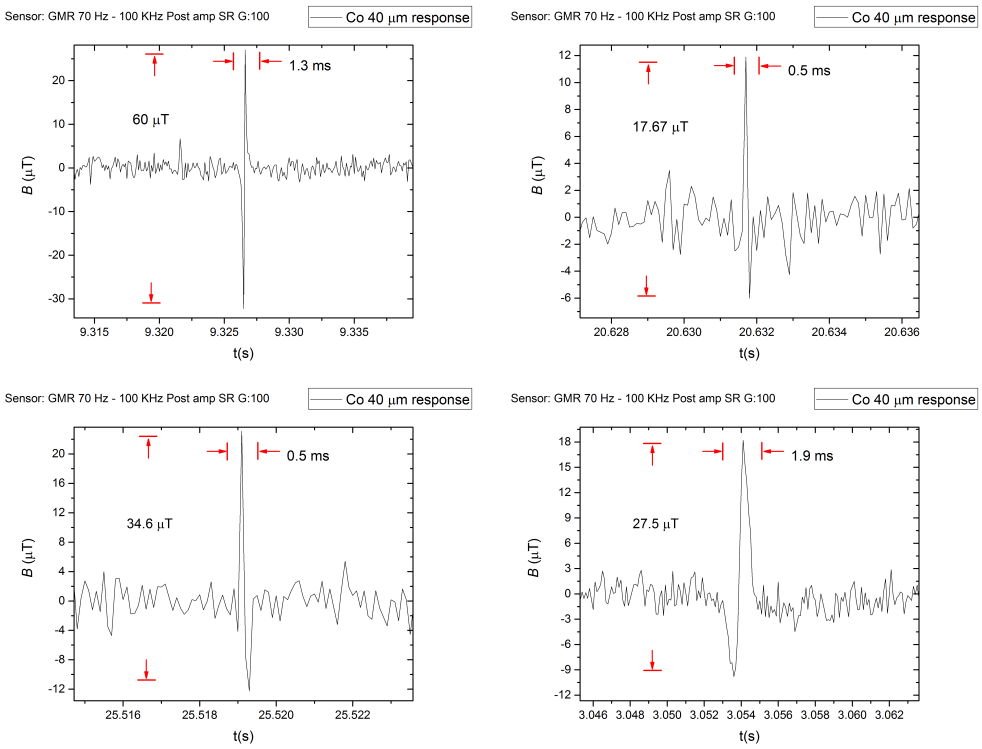



Figure 5.26: Detected events of Co nano-wires sample 03261108 flowing across sensor

Looking at the detected events from the Co nano-wires sample 03261108 highlighted in Figure 5.26, the shape of the detected responses are consistent with what we would expect for the detection of a magnetic nanowire dipole field as incidated in the Co nanowire modelled response detailed in Figure 5.3. The detected nanowires vary in amplitude, indicating the nanowires are traveling at different heights within the microfluidic channel. The detected events with higher amplitude indicate that a number of nanowires are bunched or clumped together as they travel across the sensor. There is also an indication that nanowires are traveling in different orientations and angles as they pass over the GMR sensor, as we see variations in the detected polarity response magnetudes and also different polarity directions. The variance in time response of the nanowires is mainly due to the fact that the wires were dispensed using a hand syringe in these initial experiments. From the variation in nanowire response times the nanowires are flowing at velocities of between 8 to 40 mm/s within the channel as detailed in Table 5.10 in Section 5.6.1. A post statistical analysis was carried out on the captured data using the Pulse height amplification (PHA) routine as discussed in Section 5.7.5. The PHA provides parametric de-noising of the captured signal response and extracts all

detected events as a single amplitude. Figure 5.27 shows the PHA model fitting with the experimental detected response.

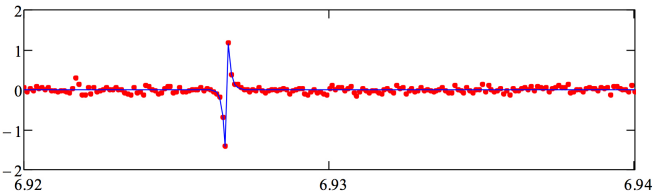



Figure 5.27: Co nano-wires sample 03261108 model fitting to experimental data

The PHA suppressed the background noise by a factor of 1.48. The PHA locates all actual nanowire detected events, integrates each signal response and extracts it as a signal amplitude. Figure 5.28 shows a plot of detected nanowire events during the experiment extracted as single amplitudes. The upper and lower threshold was adjusted to exclude the noise contribution.

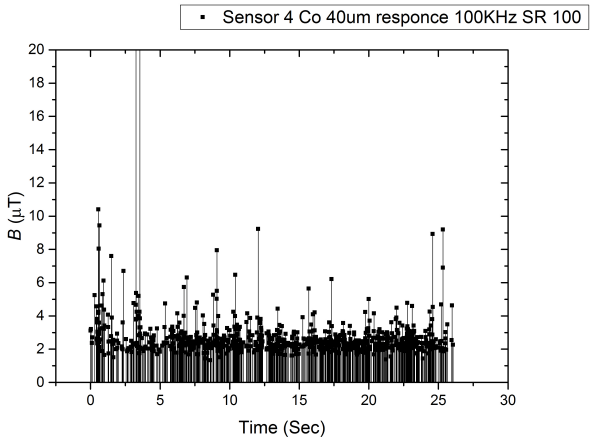



Figure 5.28: Detected nanowire events during the experiment extracted as single amplitudes post PHA

A post statistical analysis of the extracted nanowire detected events are shown in the bar chart in Figure 5.29. The bar chart shows the number of detected nanowire events per field. The total count of nanowires detected was 986. The field of the nanowires detected were in the range of 3 to 10 µT after the PHA.

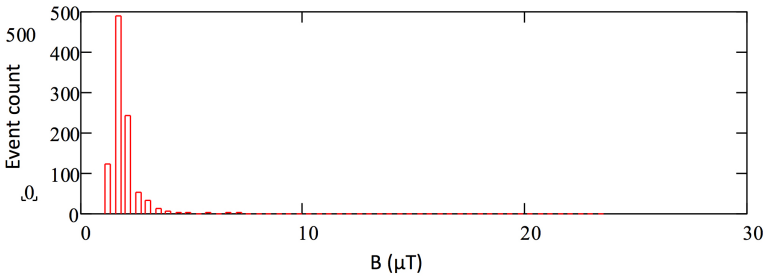



Figure 5.29: Number of detected nanowire events per field for CoNi 03261108

Comparing this to the modelled response of Co nano-wires 10 µm length at different heights ($z$) above the sensor detailed in Figure 5.3 Section 5.3.1, the majority of nanowires are traveling in the order of 7 to 11 µm in the microfluidic channel. The microfluidic channel used in the experimet had a height of 30 µm. This experiment was repeated a number of times with regard to noise measurements and nanowire detection. Table 5.4 summarises the results

| Parameters | Response time (ms) | Velocity (mm/s) | Noise before PHA (µT) | PHA Noise suppression | PHA Nanowire count | Detected field range after PHA (µT) |
|---|---|---|---|---|---|---|
| Nanowire type: Cobalt | 0.5 – 2.4 | 12 – 40 | 11.345 | 1.048 | 986 | 3 - 25 |
| Length: 40 µm | 0.6 – 2.4 | 12 – 40 | 12.30 | 1.010 | 838 | 2.5 - 30 |
| Dispensed: Hand syringe | 0.5 – 2.0 | 13 – 40 | 11.105 | 1.560 | 510 | 4 - 15 |
| Microfluidic channel: Height 30 µm | 0.4 – 3.0 | 13 – 45 | 12.600 | 1.930 | 620 | 3.5 - 50 |
| Sensor: GMR | 0.8 – 1.8 | 8 – 40 | 12.020 | 1.060 | 480 | 5 - 45 |
| | 0.6 – 1.8 | 14 – 35 | 11.505 | 1.082 | 705 | 4 - 20 |

Table 5.14: Summary of initial nanowire detection experiments

Following the initial nanowire detecion experiments a number of developments were implemented to better optimise the nanowire detection results. Firstly there were issues with the sensor interface, it was difficult to fit the sensor into the edge connector without damaging the sensor top-contacts. Secondly it was difficult to fit, align and seal the microfluidic chip over the sensor. Thirdly the implementation of a multi-channel post-amplifier to replace the Stanford Research amplifier. Finally the use of a microfluidic pump to dispense nano-wires across the sensor at a controlled flow rate and a microscope camera to monitor the flow of nanowires during detection experiments.

## 5.9 SECOND ITERATION OF THE NANOWIRE DETECTION SYSTEM

Following the initial nanowire detecion experiments a number of developments were implemented to the overall detection system to better optimise the detection of nanowires.

Figure 5.30 shows a schematic diagram highlighing in red the design components developed in the second iteration nano-wire detection system.

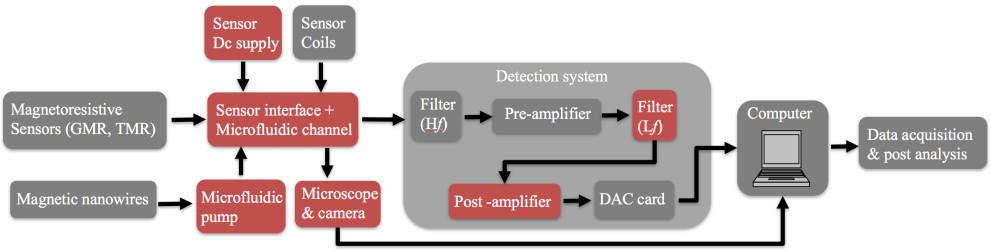



Figure 5.30: Schematic diagram highlighing design component changes in the second iteration nano-wire detection system

A new sensor interface was designed in house to address issues of damaged sensor contacts and also alignment/sealing issues with the microfluidic chip over the sensor. A multi-channel post-amplifier with gain of 100 and low pass filter 100 KHz was implemented. Finaly a microfluidic pump was used to dispense nanowires across the sensor at a controlled flow rate and a microscope camera to monitor the flow of nanowires during detection experiments. Figure 5.31 (a) shows the shows the second iteration of nanowire detection system showing sensor interface, in-house built pre and post amplifier stage, microfluidic pump, microscope and camera.

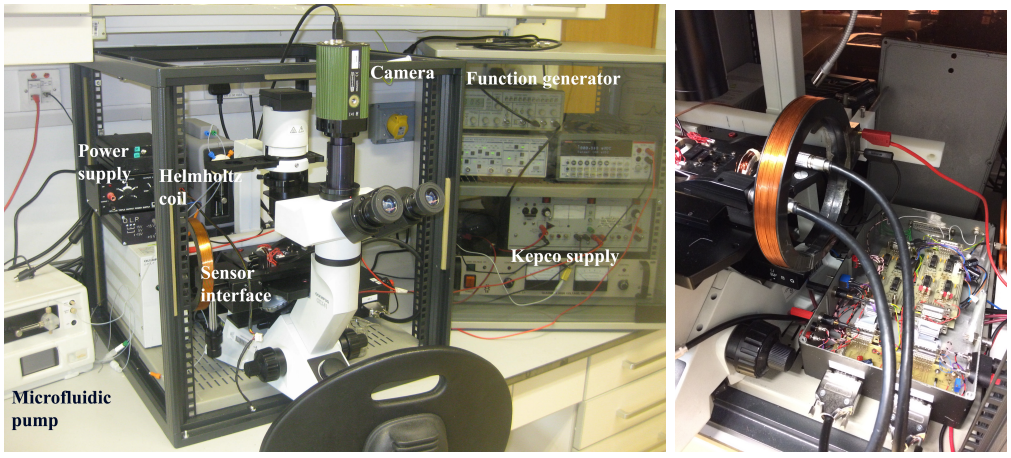



Figure 5.31: (a) Second iteration nano-wire detection system (b) Detection system showing amplifier stage & Sensor interface

Also shown are the function generator, bipolar operational amplifier (Kepco) and standard laboratory Helmholtz coils, which are used for the sensor magnetic field calibration as discussed in Section 5.8.1.

### 5.9.1 *Sensor interface*

The sensor interface allows optimum connection to the electronic detection system, it provides electrical connections to the GMR and TMR sensors and facilitates the microfluidic channel placement and alignment over the sensor area. The interface was designed in-house using solid works CAD package shown in Figure 5.32.

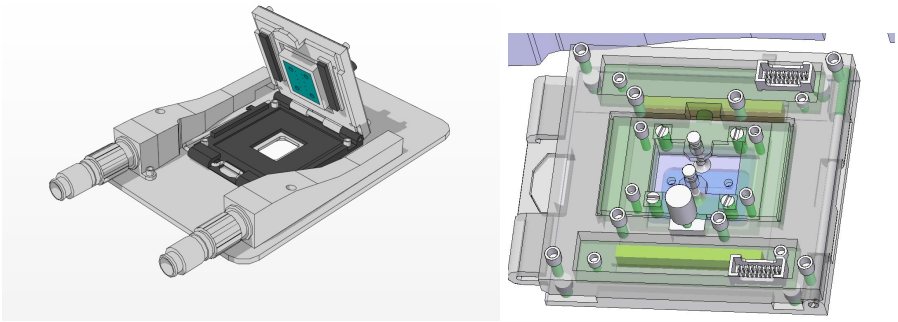


Figure 5.32: Sensor interface design

The interface was also fabricated in-house shown in Figure 5.33, opens to allow both the sensor and the microfluidic chip to be easily placed and secured in one step. Multi-connections to the sensor were provided using electrical pogo-pin connectors via a pcb interface board. The connections provide the current supply to the sensor and reading back the detected signals. The cables from the sensor interface to the detection system were shielded and in configured in cross over pairs to reduce noise. The interface also incorporated adjustments to align the microfluidic channel over the sensor and ensure an optimum seal between the sensor and channel preventing any fluid leaks and to fit into a standard microscope for inspection and recording via camera during the nanowire detection experiments.

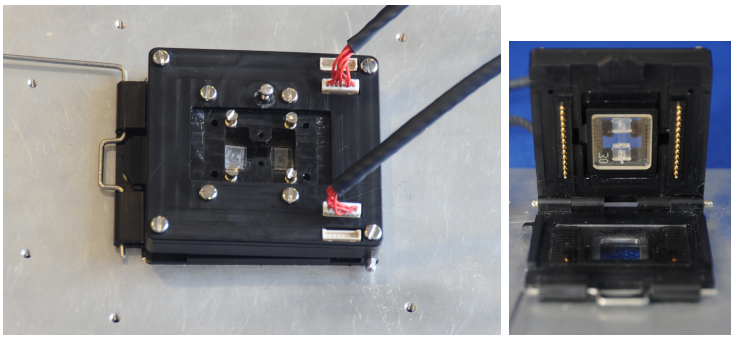


Figure 5.33: Sensor interface

### 5.9.2 *Low pass filter and post amplifier*

Following optimum selection of the post amplifier gain and low pass filter using the Stanford Research amplifier, a 16 channel post-amplifier and low pass filter was designed and implemented in-house. The post-amplifiers encorporated a low noise amplifier type OP470, which has noise level of $5nV/\sqrt{Hz}$. It was designed with a low pass second order butterworth filter set at 100 kHz, with the amplifier gain set to 100. The low-pass filter would remove any frequency noise above 100 kHz that may affect the detected signal response.

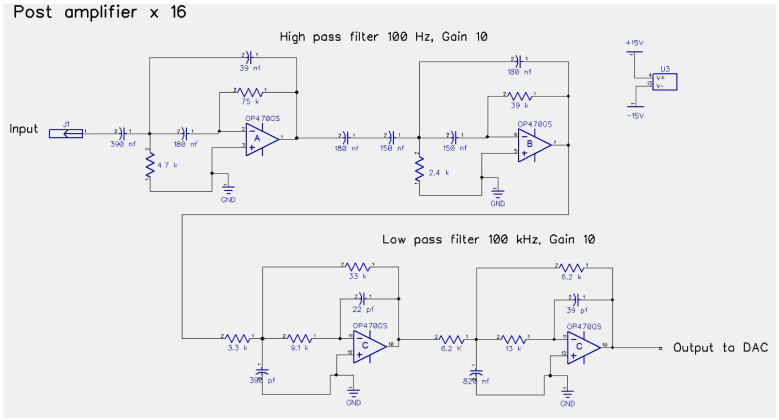



Figure 5.34: Single sensor post-amplifier side A

The pre and post amplifiers in the detection system were powered using a +/- 15 DC voltage (Caltex BPS4000). The overall amplifier section in the detection system provides a gain of 10,000 (80dB) and a bandwidth of HP$f$ 70 Hz – LP$f$ 100 kHz.

### 5.9.3 *Microfluidic pump*

The microfluidic pump used to dispense the nanowires was supplied by a company called Cellix. Specifications of the microfluidic pump Type: Mirus SP 1.0 Nano-pump are detailed in Table 5.7in Section 5.6. The flow profile dispense the nanowires is configured using the Mirus Venaflux software as shown in Figure 5.35(a). The software allows for the pump initialisation, setting the microfluidic channel geometry and washout of microfludic channel and connections. Figure 5.35(b) shows the microfluidic pump connected to the sensor interface.

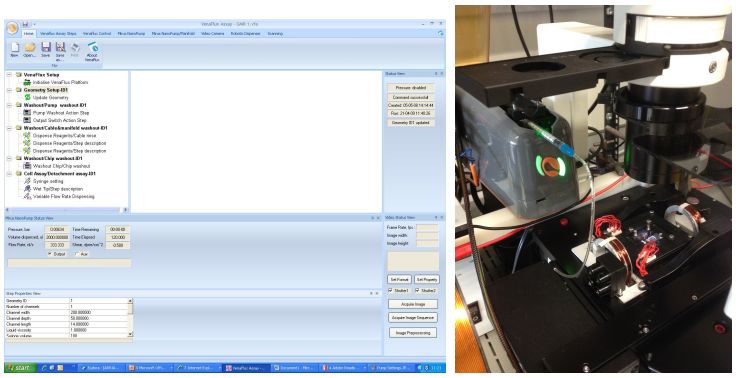


Figure 5.35: (a) Mirus Venaflux software interface window and (b) Microfluidic pump connected to the sensor interface

### 5.9.4 *Microscope and camera*

The microscope used was an Olympus CKX41, which 4X, 10X, 20X and 40X objective lens. The camera used was a QImaging QIClick ccd 12-bit camera, which has a high-resolution 1.4-million-pixel sensor and provides 10fps full resolution at 12-bits as shown in Figure 5.31.

## 5.10 NANOWIRE DETECTION EXPERIMENTS - SECOND ITERATION OF THE DETECTION SYSTEM

Nanowire detection experiments were carried out using the second iteration of the detection system. The GMR sensor was configured as detailed in Figure 5.21 (a) and

used the same experiment procedure as detailed in Section 5.8. A 2 mA current supply was applied directly across the GMR sensor and the background noise response measured from two of the multi-contacts along the length of the sensor. The sensor used in the experiment measured a magnetoresistance ratio of 7.9 % and had a linear response and sensitivity of 0.8% mV/mT as shown in Figure 5.36. The sensor was passivated with SiO2 900 nm. The sensor was calibrated to show the response in magnetic field as per the procedure outined in Section 5.8.1.

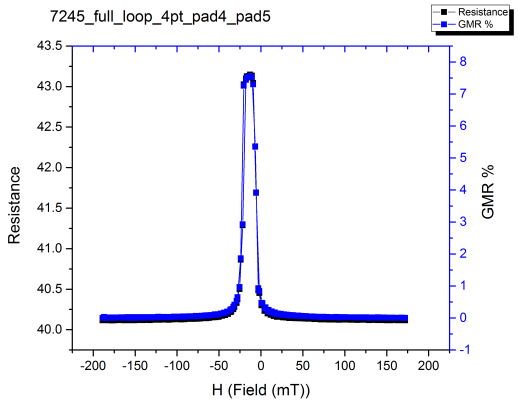



Figure 5.36: GMR sensor used in the experiment magnetoresistance response measurment

### 5.10.1 *Noise measurements*

The background noise response recorded measured 0.15 Vdc at a gain of 10,000 (80 dB), as shown in Figure 5.37. With the calibration field constant applied this measures at ~ 5 μT.

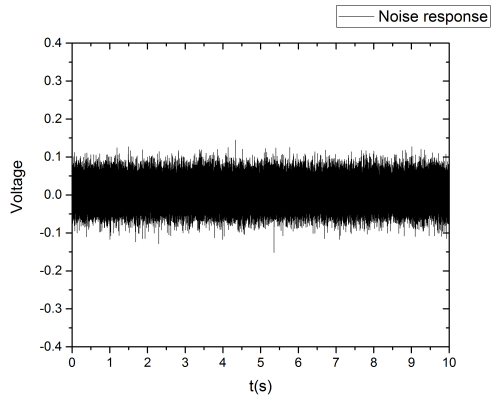



Figure 5.37: 2nd iteration detection system noise respnse

### 5.10.2 *Nanowire detection experiment - Cobalt (Co) nanowires*

Co nanowires Batch: 03261108 as details in Table 5.12 were dispenced into the microfluidic channel using the Mirus pump at velocity of 15 mm/s. The nanowire batch as detailed in Figure 5.24 (a) and (b), varied in length from 10 µm up to 30 µm and showed reasonable separation of nanowires and also bunching of nanowires. The detected response of the Co nanowires flowing across the sensor at velocity of 15 mm/s is shown in Figure (a) 5.38.

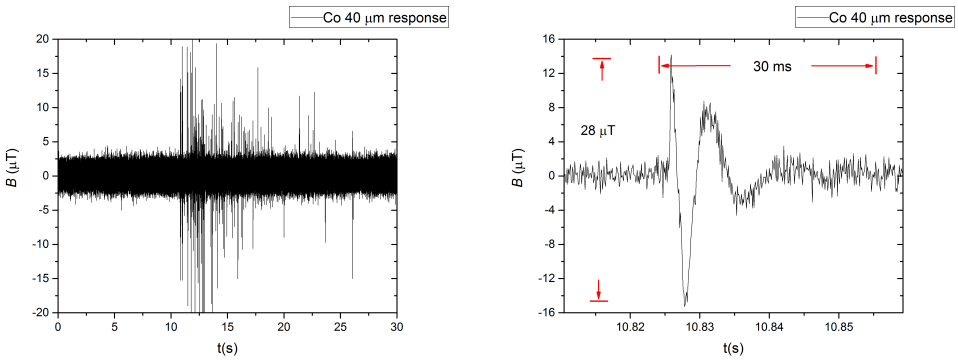



Figure 5.38: (a) Response of Co nanowire using 2nd iteration detection system (b) Detected event in details from the Co nano-wires sample 03261108

The nanowires are dispensed after the first 10 seconds and stopped after a 28 second time period. The detected responses varied in amplitude from 5 µT to 35 µT. Figure 5.38 (b) highlights in detail one of the detected events from the Co nanowires sample 03261108. Two principle points were observed from the results of the detected events in comparision to the initial nanowire detection experiments, which used the Stanford Research SR560 post amplifier. Firstly the backgroud noise had reduced by a factor of two from 0.451 Vdc (~ 10 µT) to 0.2 Vdc (~ 2.5 µT). Secondly the response time of the detected events, which was in the order of 30 ms and shape of the shape of the detected event. A decay/under damped oscillation was observed for each detected event. As the nanowires are flowing at a velocity of 15 mm/s per second within the microfluidic channel, for a 10 µm nanowire traveling a across a 5 µm sensor width the expected response time should be in the order of 1 ms as detailed in Table 5.10 in Section 5.6.1 A post statistical analysis was carried out on the captured data using the Pulse height

amplification (PHA) routine as discussed in Section 5.7.5. Figure 5.39 shows the PHA model fitting with the experimental detected response.

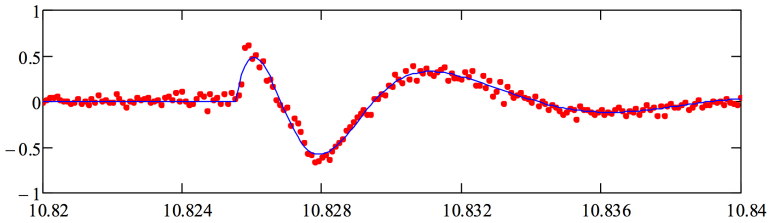



Figure 5.39: Co nano-wires sample 03261108 PHA model fitting to experimental data using 2nd iteration detection system

Figure 5.40 shows a plot of detected nanowire events during the experiment extracted as single amplitudes using the PHA.

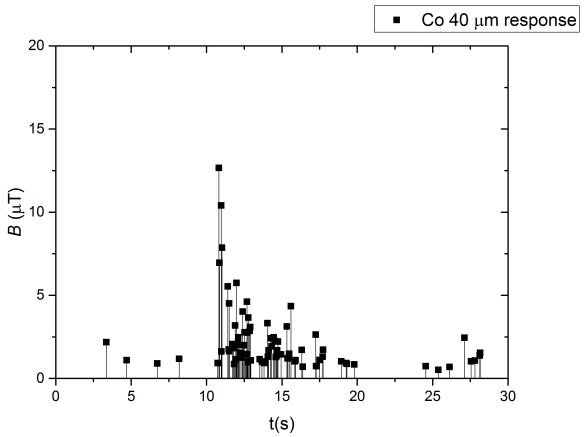



Figure 5.40: Detected nanowire events during the experiment extracted as single amplitudes from the 2nd iteration detection system

A post statistical analysis of the extracted nanowire detected events are shown in the bar chart in Figure 5.41 . The bar chart shows the number of detected nanowire events per field. The total count of nanowires detected was 89. The nanowires detected range was in the order of 2 to 12 µT post PHA.

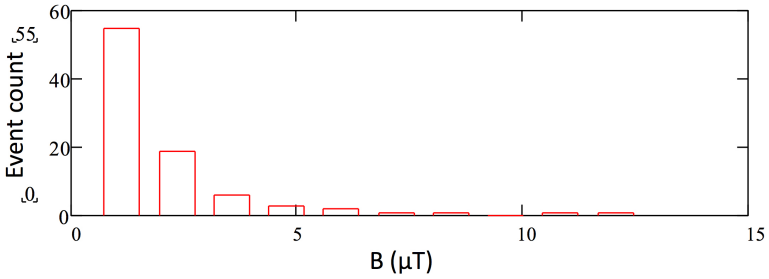



Figure 5.41: Number of detected nanowire events per field for CoNi 03261108 in 2nd iteration detection system

The number of detected nanowire events was low in comparision to the initial nanowire detection experiments, which was in the order of 900. The detection system was investigated as a possible reason for the low detected nanowire count and the long response time of the detected nanowire. The response of the high pass filter in the pre-amplifier stageand the low pass filter in the post-amplifier stage were measured as shown in Figure 5.42 (a) and (b). An issue was identified in the post-amplifier's low pass filter response. The filter was designed as a LPF 100 kHz, the actual measured response was 2.5 kHz. this clipping of the filter response, which effectly causes a much narrower bandpass filter would account for both the reduction in the measured backgroud noise and also the long response time of the detected nanowire events with the observed oscillation decay, possibly casused by loading from the post-amplifier.

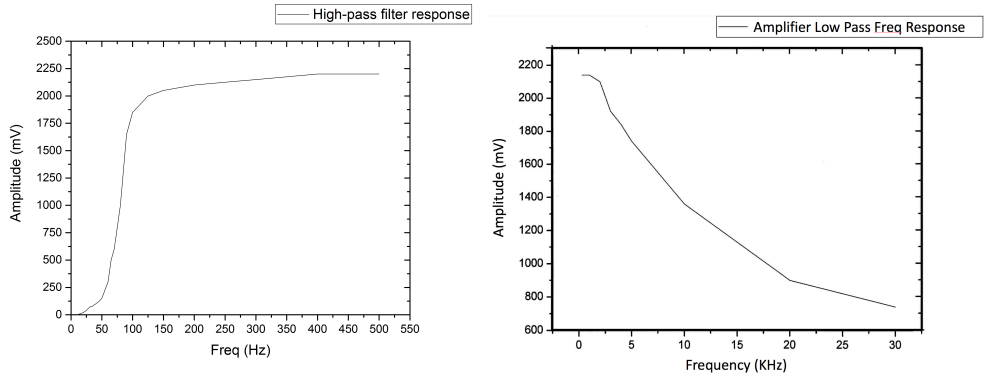



Figure 5.42: (a) Pre-amplifier high pass filter response and (b) Post-amplifier low pass filter response

Following this the post-amplifier and low pass filter was redesigned. The new design encorporated a low noise amplifier type OP-270, which has noise level of $5nV/\sqrt{Hz}$. It

was designed with a low pass first order filter set at 75 kHz. The amplifier gain set to 100. The measured response of the 75 kHz LPF is shown in Figure 5.43.

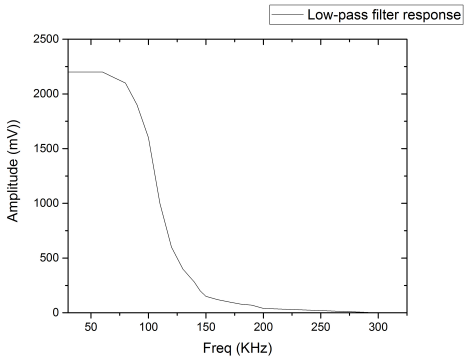



Figure 5.43: Post-amplifier low pass filter corrected response

### 5.10.3 *Nanowire detection experiments using second iteration detection system - Noise measurements*

Nanowire detection experiments were carried out using the corrected post-amplifier and low pass filter. The GMR sensor was configured as detailed in Figure 5.21 (a) and used the same experiment procedure as detailed in Section 5.8. A 3 mA current supply was applied directly across the GMR sensor and the background noise response measured from two of the multi-contacts along the length of the sensor.

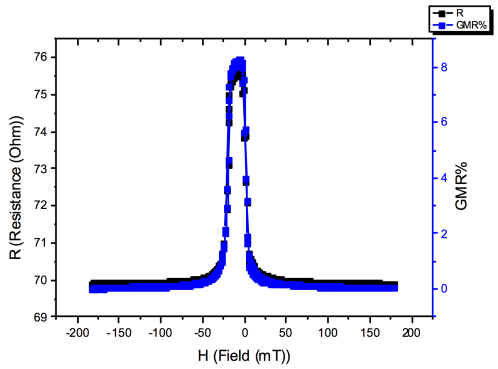



Figure 5.44: GMR sensor magnetoresistive curve

The sensor used in the experiment measured a magnetoresistance ratio of 7.8 % and had a linear response and sensitivity of 0.9%/mT as shown in Figure 5.44. The sensor

was passivated with $Si0_2$ 900 nm. The sensor was calibrated to show the response in magnetic field as per the procedure outined in Sesntion 5.8.1.

### 5.10.4 *Noise measurements*

The background noise response recorded measured 0.45 Vdc at a gain of 10,000, as shown in Figure 5.45 . With the calibration field constant applied this measured at 12.12 µT.

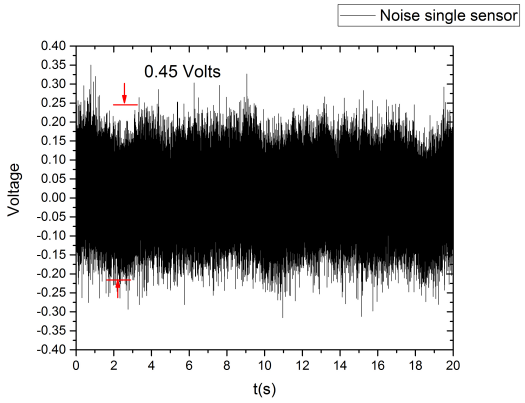



Figure 5.45: Noise response of a GMR sensor in single sensor configuration

### 5.10.5 *CoNi Nanowire detection experiments in single GMR sensor configuration*

Nanowire detection experiments were carried out using CoNi nanowires, which had an average length of 12 µm. The Mirus microfluidic pump was used to dispenced the nanowires into the microfluidic channel, the channel geometry used had a width 600 µm, height 30 µm & length 14mm. Details of the CoNi nanowires Batch: 070513 are shown in Table 5.15. The CoNi nanowires were deposited at an over potential of -0.9 Vdc, for a duration of 7500 seconds at 6.2 mA as outlined in the procedure in Chaper 4 Section 4.4.

| Sample | Segment | Type | Pot (V) | Time (Sec) | I (mA) | Charge (Q) | Length (um) | OCP (V) | Mag (T) |
|---|---|---|---|---|---|---|---|---|---|
| 070513 | CoNi | | -0.9 | 7500 | 6.2 | 45 | 12 | 0.12 | 1.2 |

Table 5.15: CoNi nanowire sample deposition conditions

Table 5.16 shows the conditions used to dissolve the nanowires from membrane. To dissolve the nanowires form the membrane they were placed in a solution of Na0H 1 molar at 70 °C for a duration of 11 minutes. The sample was visually checked periodically every few minutes period, with sonication process of 10 seconds. To remove the NaOH solution, the nanowires are rinsed in de-ionised water a number of times using a magnet as outlined in the procedure in Chaper 4 Section 4.4.

| Sample | Type | Solution (1molar) | Temp ($^0$C) | Method | Weight (g) |
|---|---|---|---|---|---|
| 070513 | CoNi | Na0H | 70 | Min 3/sonication 10sec, Min 5/ sonication 10sec, Min 11/ sonication 10sec, stop, Rinse in DI water x 6 using magnet | 0.0933 |

Table 5.16: CoNi nanowire sample condition used to dissolve from membrane

The inspection image of nanowires prior to dispensing is shown in Figure 5.46. The nanowires were reasonably well separated wires but still some clumping and attachment of wires.

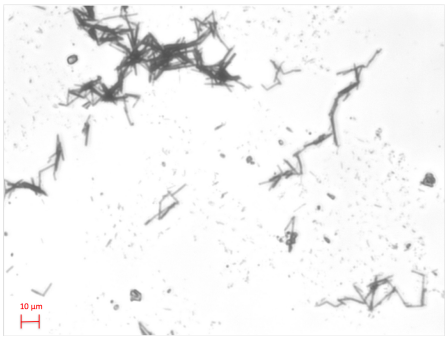



Figure 5.46: Image of nanowire before dispensing

For the experiment 0.3 µg of CoNi nanowires, which approximates to ~ 6,500 nanowires as per the nanowire experiment preparation procedure detailied Appendix 8 Section 8.7.10, are were dispensed across the sensor at a velocity of 15 mm/s. The detected response of the CoNi 070513 nanowires flowing across the sensor is shown in Figure 5.47.

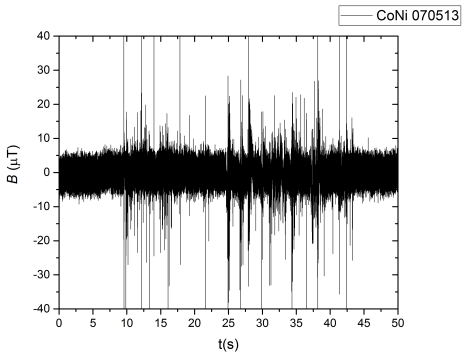



Figure 5.47: Response of CoNi 070513 nano-wires flowing across sensor

The CoNi nanowires are dispensed after the first 10 seconds and stopped after 45 second time period. During the time period when nanowires are dispensed the detected responses are recorded. The detected responses varied in amplitude from 10 µT to 90 µT. Figure 5.48 highlights in details some of the detected events from the CoNi nanowire detection experiment.

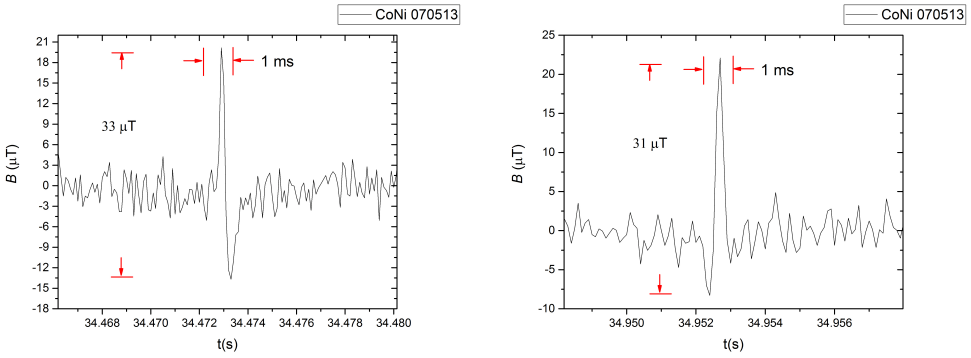



Figure 5.48: Response of CoNi 070513 wires detailing detected events

Looking at the detected events of the CoNi nanowire sample shown in Figure 5.48, the shape of the detected responses are consistent with what we would expect for the detection of a magnetic nanowire dipole field as incidated in the CoNi nanowire modelled response detailed in Figure 5.5. As the nanowires are flowing at a velocity of 15 mm per second within the microfluidic channel, for a 10 µm nanowire traveling a across a 5 µm sensor width the expected response time is in the order of 1 ms as detailed in Table 5.10 in Section 5.6.1. There are a number of detected events with a response time of 1 ms. The issue with the post amplifier low pass filter has been resolved, were we don't see this

damped oscillation response from the detected nanowire. Here the nanowire response are comparable to the initial nanowire detection experiments, which used the Stanford Research SR560 post amplifier. The detected nanowires vary in amplitude, indicating the nanowires are traveling at different heights within the microfluidic channel. The nanowires are also traveling in different orientations and angles as they pass over the GMR sensor, as we see variations in the detected polarity response magnetudes and also different polarity directions.

A number of the detected events have magnitude responses ranging from 60 µT to 120 µT with response times of 3 ms to 4 ms as shown in Figure 5.49.

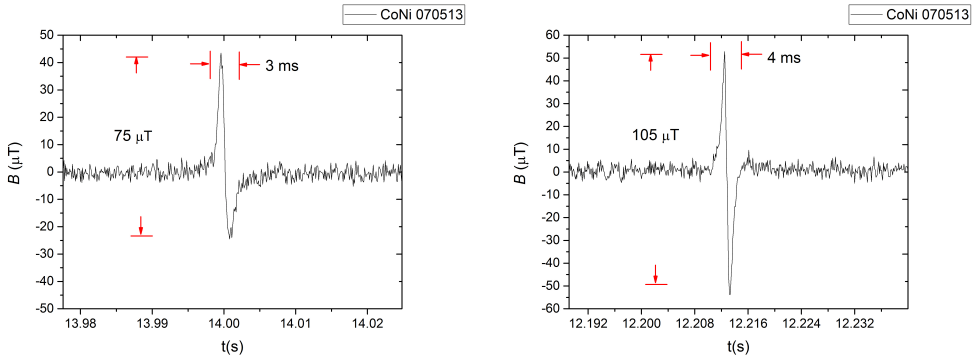



Figure 5.49: Response of CoNi 070513 wires detailing detected events with longer response time

The magnitude and time response of the detected signals are too large for single nanowire detection and most probably indicating the detection of a number of nanowires possibly bunched together. This is confirmed with a optical camera capture during the experiment Figure 5.50 which shows bunching of nanowires as they travel through the microfluidic channel.

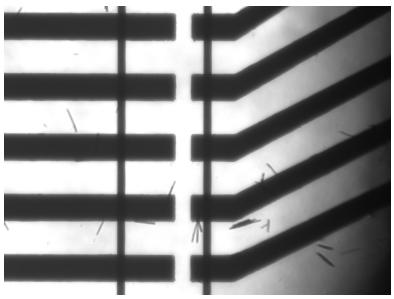


Figure 5.50: Nano-wires flowing in channel

A post statistical analysis was carried out on the captured data using the Pulse height amplification (PHA) routine as discussed in Section 5.7.5. Figure 5.51 shows the PHA model fitting with the experimental detected response, this allows all detected events to be identified.

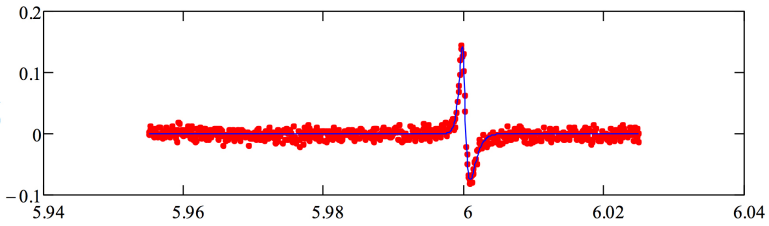



Figure 5.51: CoNi nano-wires sample 070513 model fitting to experimental data

After the PHA, the background noise from experiment using the CoNi 070513 nanowires was suppressed by a factor of 3.747. The PHA locates all actual nanowire detected events, integrates each signal response and extracts it as a signal amplitude. Figure 5.52 shows a plot of detected nanowire events extracted as single amplitudes. The upper and lower threshold was adjusted to exclude the noise contribution

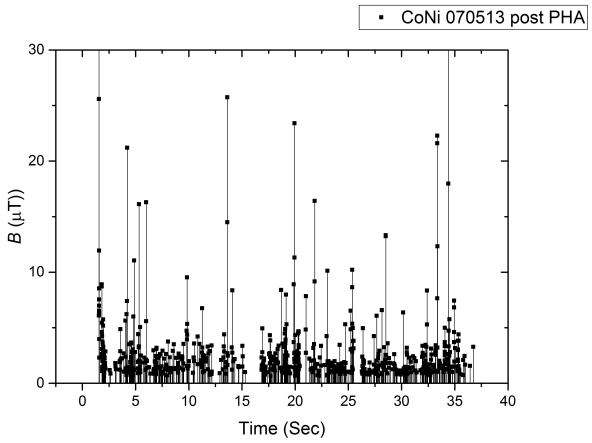



Figure 5.52: Detected nanowire events for CoNi batch 070513 during the experiment extracted as single amplitudes post PHA

A post statistical analysis of the extracted nanowire detected events shown in Figure 5.53 shows the number of detected nanowire events per field. The total count of nanowires detected was 665. The field of the nanowires detected were in the range of 2 to 52 μT after the PHA.

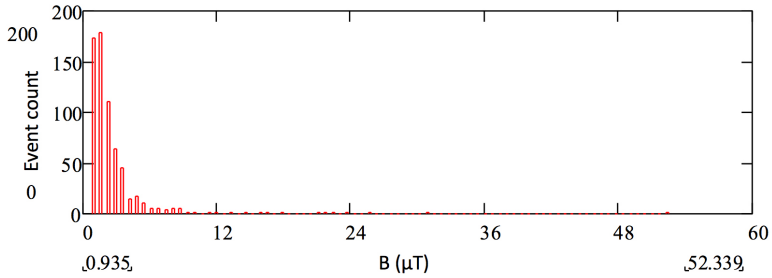



Figure 5.53: Number of detected nanowire events per field for CoNi 070513

Comparing this to the modelled response of CoNi nanowires 10 µm length at different heights ($z$) above the sensor shown in Figure 5.5, the majority of nanowires are traveling at a height in the order of 11 µm in the microfluiduc channel. The experiment was repeated a number of times using different GMR sensors and nanowire batches, with regard to noise measurements and nanowire detection. Table 5.17summarises the results of CoNi nanowire detection experiments using GMR sensor in 2nd iteration detection system.

| Parameters | Response time (ms) | Velocity (mm/s) | Noise before PHA (µT) | PHA Noise suppression | PHA Nanowire count | Detected field range after PHA (µT) |
|---|---|---|---|---|---|---|
| Nanowire type: $Co_{65}Ni_{35}$ | 1.2 – 3.5 | 15 | 12.12 | 3.747 | 665 | 2 - 52 |
| Length: 10 µm | 1 – 4 | 15 | 12.00 | 3.65 | 729 | 3 - 60 |
| Dispensed: Microfluidic pump | 1.2 – 3.5 | 15 | 11.98 | 2.50 | 690 | 4 - 55 |
| Microfluidic channel: Height 30 µm | 1 – 3 | 15 | 11.80 | 2.85 | 750 | 3.5 - 65 |
| Sensor: GMR | 0.9 – 3.5 | 15 | 12.20 | 3.10 | 625 | 4 - 30 |
| | 1 – 3.5 | 15 | 12.10 | 3.50 | 701 | 3 - 50 |

Table 5.17: Summary of CoNi nanowire detection experiments using GMR sensor in 2nd iteration detection system

In conclusion the number of nanowires detected is lower than the amount of nanowires dispenced, which should be ~ in the order of thousands. This is due to a number of factors. Firstly the majority of the detected nanowire events that are within the expected time response of 1 ms are just above the measured background noise level. The background noise needs to be reduced in order to clearly detect individual single magnetic nanowires flowing within the microfluidic channel. The detected signals with large response magnitudes, which have response times in the order of 3 ms to 4 ms are too large for single nanowire detection and are indicating the detection of a number of nanowires bunched together. Also other factors that effect the number of nanowires detected are, the width of the microfluidic channel is 600 µm and the length of the GMR sensor is 400 µm so a precentage of nanowires are not traveling across the sensor. Also a

large number of nanowires adhere to the tubing that is used in the microfluidic pump system to pickup and dispence the nanowires into the microfluidic channel.

## 5.11 NANOWIRE DETECTION EXPERIMENTS USING TMR SENSORS

Following the nanowire detecion experiments using the GMR sensor, detecion experiments were carried out using a TMR sensor. The TMR sensor was developed as a possible alternative to the GMR sensor due to its large magnetoresistance TMR ratio, and would this high TMR ratio provide an improvement over the GMR sensor with regard to the magnitude of the signal detection.

Using the second iteration detecion system discribed in Section 5.9 with the corrected post amplifier, the TMR sensor was setup in a single sensor configuration as shown in Figure 5.54 (a). The form-factor of the TMR sensors are restricted due to the annealing chamber size, therefore the TMR sensors are hardwired onto a blank top-contact connector to allowing fitting into the sensor interface and microfluidic channel as shown in Figure 5.54 (b).

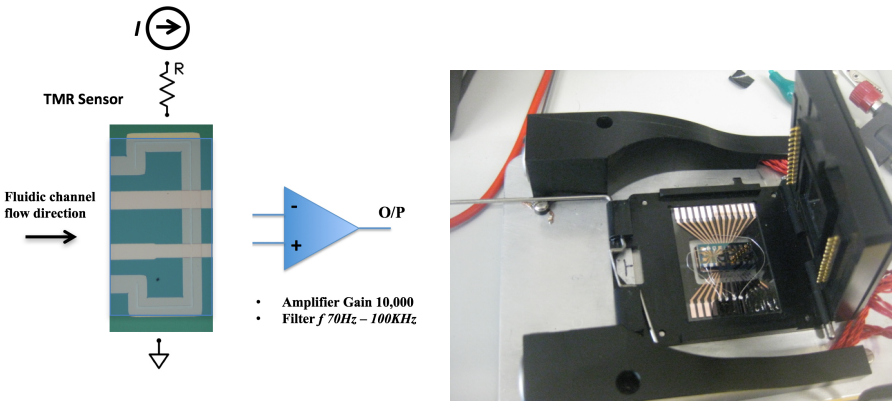



Figure 5.54: (a) TMR single sensor configuration and (b) TMR sensor interface connection

### 5.11.1 *TMR current circuit*

The TMR sensors were powered using a REF200 variable 100 μA current source, which has a noise level $20pA/\sqrt{Hz}$ at 10 KHz. The current circuit was powered using a + 15 Volt DC voltage supply.

### 5.11.2 *Noise measurements using TMR sensors*

Nanowire detection experiments were carried out using the same experiment procedure as detailed in Section 5.8. A 100 μA current supply was applied directly across the TMR sensor and the background noise response measured from the two contacts along the length of the sensor. The TMR sensor used in the experiment was a bottom-pinned MTJ stack configuration with an MgO thickness of 2.5 nm and was patterned into a yoke shape. The sensor magnetoresistive response measured a ratio of 130% TMR as shown in Figure 5.55 with a sensitivity of 27 %/mT and the product RA was 1040 $\mu m^2\Omega$. The sensor was passivated with $Si0_2$ 900 nm to protect it from microfluidics during the experiment. The sensor was calibrated to show the response in magnetic field as per the procedure outined in Sesntion 5.8.1.

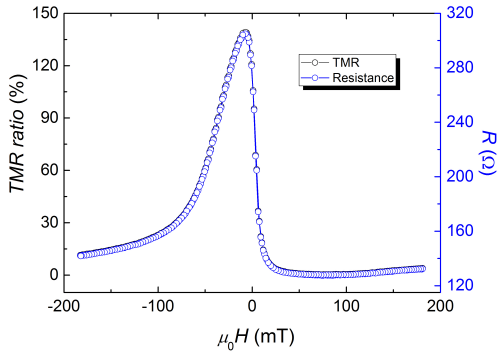



Figure 5.55: TMR YOKE sensor junction magnetoresistance curve

### 5.11.3 *Noise measurements*

The background noise response recorded measured 0.50Vdc at a gain of 10,000, as shown in Figure 5.56. With the calibration field constant applied this measured at 12.85 μT.

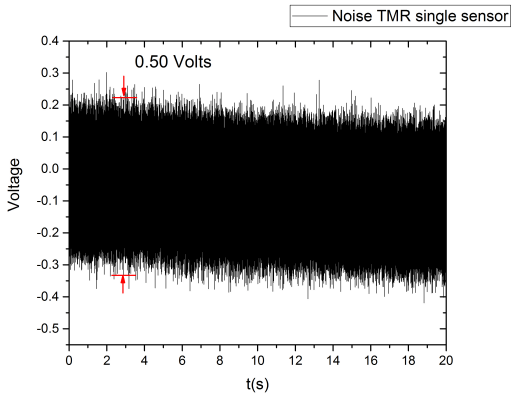



Figure 5.56: Background noise response recorded for TMR single sensor configuration

### 5.11.4 *CoFe Nanowire detection experiment using TMR sensors in single sensor configuration*

Nanowire detection experiments were carried out using CoFe nanowires, which had an average length of 10 µm. The Mirus microfluidic pump was used to dispenced the nanowires into the microfluidic channel, the channel geometry used had a width 600 µm, height 30 µm & length 14 mm. Details of the CoFe nanowires Batch: 111112 are shown in Table 5.18. The CoFe nanowires were deposited at an over potential of -0.95 Vdc, for a duration of 4000 seconds as outlined in the procedure in Chaper 4 Section 4.3.4.

| Sample | Type | Pot (V) | Time (Sec) | Charge (Q) | Length (µm) |
|---|---|---|---|---|---|
| 111112 | CoFe | -0.95 | 4000 | 39 | 10 |

Table 5.18: CoFe 111112 nanowire sample deposition conditions

Table 5.19 shows the conditions used to dissolve the nanowires from membrane. To dissolve the nanowires form the membrane they were placed in a solution of NaOH 1 molar at 45 ºC for a duration of 8 minutes. The sample was visually checked periodically every few minutes period, with a sonication process of 5 seconds. The NaOH is removed from the solution by rinsing the nanowires in de-ionised water a number of times using centrifuge at 2900 rpm as outlined in the procedure in Chaper 4 Section 4.3.

| Sample | Type | Solution (1molar) | Temp ($^0$C) | Method | Weight (g) |
|---|---|---|---|---|---|
| 111112 | CoFe | NaOH | 45 | 5 – 8 mins NaOH & Sonication 5 sec<br>Rinse in DI water centrifuge 2900 rpm | 0.0150130 |

Table 5.19: CoFe 111112 nanowire sample condition used to dissolve from membrane

For the experiment 0.3 µg of CoNi nanowires, which approximates to ~ 6,500 nanowires (detailed in the nanowire experiment preparation procedure Appendix Section 8.7.10), were dispensed across the sensor at a velocity of 15 mm/s. The detected response of the CoFe nanowires flowing across the sensor is shown in Figure 5.57.

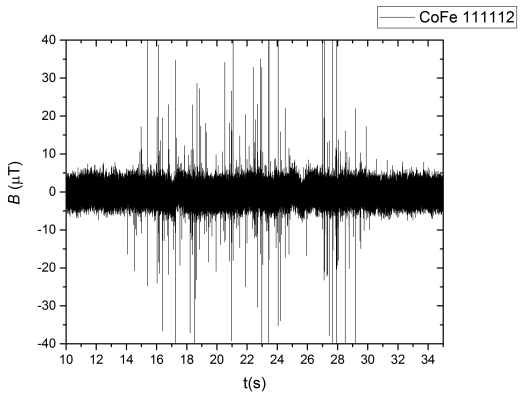



Figure 5.57: Response of CoFe 111112 nano-wires flowing across TMR sensor

The CoFe nanowires are dispensed after the first 14 seconds and stopped after 30 second time period. During the time period when nano-wires are dispensed detected responses are recorded from the TMR sensor. The detected responses varied in amplitude from 10 µT to 100 µT. Figure 5.58 highlights in details some of the detected events from the detection experiment.

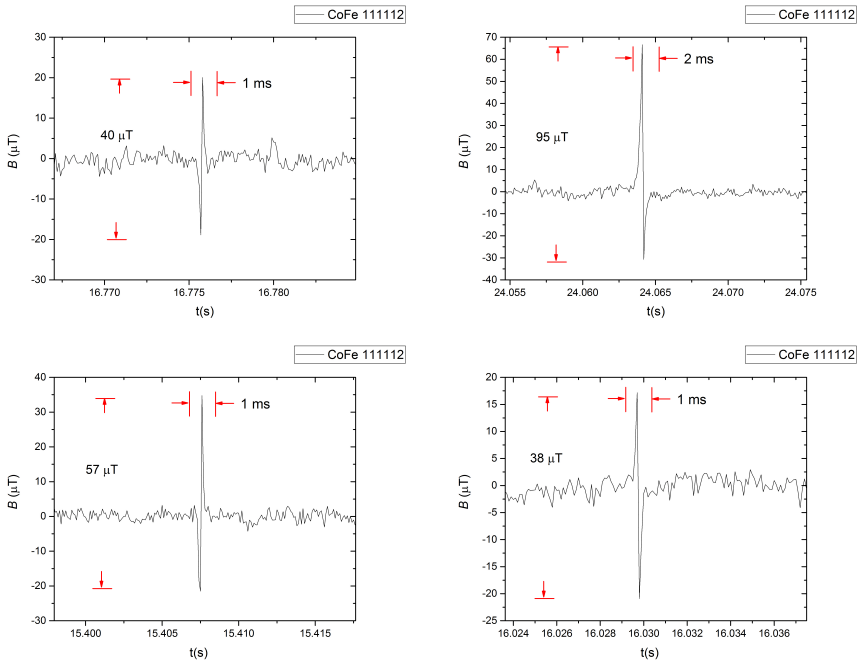



Figure 5.58: Response of CoFe 111112 nano-wires detailing detected events

The detected responses are consistent with what we would expect for the detection of a magnetic nanowire dipole field as incidated in the CoFe nanowire modelled response detailed in Figure 5.4. A number of the detected events have a response time of 1 ms as highlighted in Figure 5.58, which is a consistent response as nanowires are flowing at a velocity of 15 mm per second within the microfluidic channel, for a 10 µm nanowire traveling a across a 5 µm sensor (width) the expected response time is in the order of 1 ms. Simular to the GMR detection experiments the detected nanowires vary in amplitude, indicating the nanowires are traveling at different heights within the microfluidic channel. The nanowires are also traveling in different orientations and angles as they pass over the GMR sensor, as we see variations in the detected polarity response magnitudes and also different polarity directions. A post statistical analysis was carried out on the captured data using the Pulse height amplification (PHA) routine as discussed in Section 5.7.5 . Figure 5.59 shows the model fitting with experimental results using the PHA.

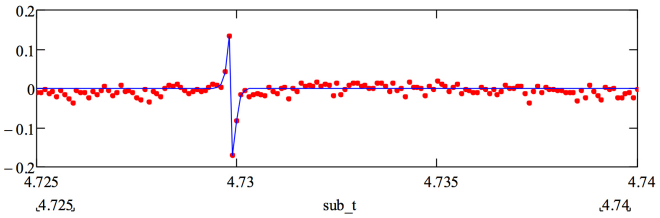



Figure 5.59: CoFe nano-wires sample 111112 model fitting to experimental data

After the PHA, the background noise from experiment using the CoFe batch: 111112 nanowires was suppressed by a factor of 1.436. The PHA locates all actual nanowire detected events, integrates each signal response and extracts it as a signal amplitude. Figure 5.60 shows a plot of detected nanowire events during the experiment extracted as single amplitudes. The upper and lower threshold was adjusted to exclude the noise contribution

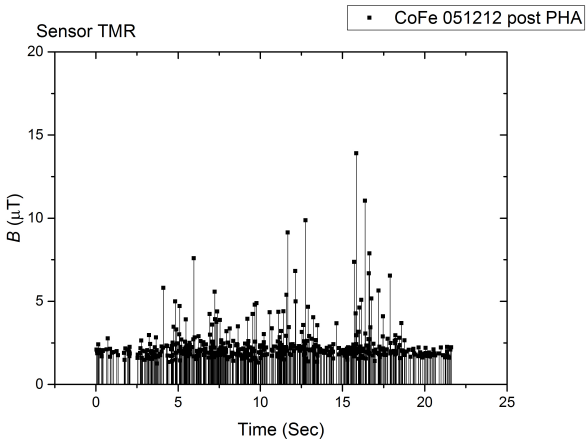



Figure 5.60: Detected nanowire events for CoNi batch 070513 during the experiment extracted as single amplitudes post PHA

A post statistical analysis of the extracted nanowire detected events shown in Figure 5.61 shows the number of detected nanowire events per field. The total count of nanowires detected was 383. The field of the nanowires detected were in the range of 2.5 to 15 µT after the PHA.

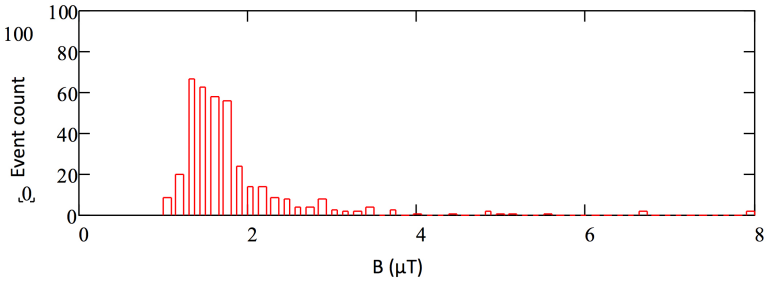



Figure 5.61: Number of detected nanowire events per field for CoFe 111112

Comparing this to the modelled response of CoFe nanowires 10 µm length at different heights $z$ above the sensor shown in Figure 5.61 the majority of nanowires are traveling at a height in the order of 10 µm in the microfluiduc channel. The experiment was repeated a number of times using different GMR sensors and nanowire batches, with regard to noise measurements and nanowire detection. Table 5.20 summarises the results of CoFe nanowire detection experiments using TMR sensor in 2nd iteration detection system. The number of nanowires detected is lower than the amount of nanowires dispenced, which should be ~ in the order of thousands.

| Parameters | Response time (ms) | Velocity (mm/s) | Noise before PHA (μT) | PHA Noise suppression | PHA Nanowire count | Detected field range after PHA (μT) |
|---|---|---|---|---|---|---|
| Nanowire type: $Co_{50}Fe_{50}$ | 1.0 – 2.0 | 15 | 12.854 | 1.436 | 383 | 2 - 20 |
| Length: 10 µm | 1.2 – 2.0 | 15 | 12.905 | 2.265 | 280 | 2 - 25 |
| Dispensed: Microfluidic pump | | | | | | |
| Microfluidic channel: Height 30 µm | | | | | | |
| Sensor: TMR | | | | | | |

Table 5.20: Summary of CoFe nanowire detection experiments using TMR sensor in 2nd iteration detection system

## 5.12 CONCLUSIONS

Following the series of nanowire detection experiments using a GMR sensor, the background noise measured using the GMR sensor was in the order of 11.5 µT (0.45 Vdc post amplification). This is too high for the detection of single individual nano-wires. In order to detect single wires we need to be in a noise range of at least 10 dB lower in the order of 5 µT. The number of nanowires detected is lower than the amount of nanowires dispenced, which should be ~ in the order of thousands for bot the GMR and TMR sensor.

The background noise measurement using the TMR sensor was comparable to the GMR sensor. Comparably the TMR sensor presents a number of additional difficulties over the GMR sensor. Firstly the TMR sensor is more difficult to fabricate requiring an additional lithography step for the TMR sensor junction, with additional processes to implement this such as $Si0_2$ deposition layer and Argon ion-milling. This effects the yeild rate of usable sensors produced. Secondly the TMR sensors are sensitive to large supply current sensor. Finaly the TMR sensor is much more susceptible to damage during the handling process, were the TMR sensor needs to be hard wired the onto a blank top-contact chip, to allows it to fit into the sensor interface and microfludidic channel. A decision was made to focus on development of the GMR sensor.

# 6

# DETECTION OF MAGNETIC NANOWIRES USING GRADIOMETER SENSOR CONFIGURATION

## 6.1 INTRODUCTION

Following the nanowire detection experiments discussed in Chapter 5 using the GMR and TMR sensors in a single sensor configuration, the focus was to reduce the background noise sufficiently and increase our signal to noise ratio for the detection of single segment magnetic nanowires and investigate the detection of multi-segmented magnetic nanowires using GMR sensors. This chapter discusses the development of the gradiometer configuration for noise reduction and the final optimised gradiometer configuration with integrated electronic detection system. This chapter also discusses the nanowire detection experiments carried out on the respective gradiometer systems and the nanowire detection experiments on two magnetic segment nanowires.

## 6.2 GRADIOMETER NANOWIRE DETECTION SYSTEM

A number of areas were focused on in order to increase our signal to noise ratio for the detection of single segment magnetic nanowires and investigate the detection of multi-segmented magnetic nanowires using GMR sensors. Figure 6.1 shows a schematic diagram highlighing in red the design components developed in the gradiometer nanowire detection system.

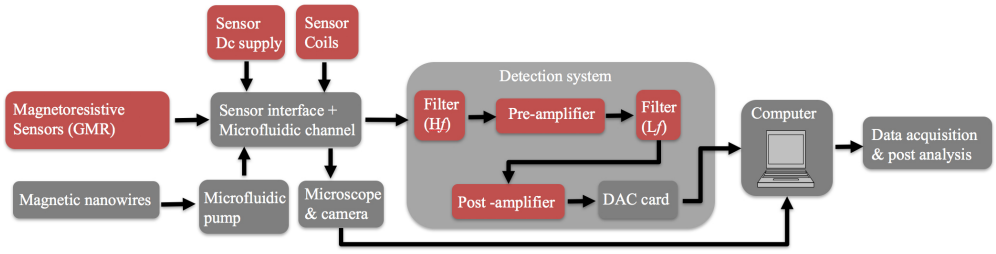



Figure 6.1: Schematic diagram highlighing design component changes in the gradiometer nanowire detection system

Firstly the GMR sensors were reconfigured in a gradiometer pair for noise cancelation. Secondly the layout of the GMR sensor was redesigned, the first UV mask was redesigned reducing the spacing between GMR sensors from 50 μm to 20 μm and the top electrode mask was redesigned to provide connections for the gradiometer configuration. The detection system preamplifier and post-amplifier were redesigned to accommodate gradiometer configuration. The current supply circuit was redesigned. The thickness of the sensor passivation layer was reduced from 900 nm to 150 nm using RF sputtered Silicon Nitride ($Si_3N_4$) as discussed in Chapter 3 section 3.5.1. Finally the standard laboratory Helmholtz coils, which ensure a uniform field is produced across the sensor, were replaced with two pairs of Helmholtz coils, which were built in-house and intrgrated mechanically into the sensor interface frame. This provides two advantages, firstly by mechanicaly intergrating the Helmholtz coils into the sensor interface frame we reduce microphonic pickup as the coils will resonate in-phase with the sensor interface. Secondly reducing the size of the coils, increases the resonant frequency in the order of 10's of KHz, this moves resonant frequency noise contribution further up the bandwidth and away from my operational frequency. The first Helmholtz coil pair was used to balance the gradiometer resposne by applying small bias field to the sensor in the order of 2 - 4 mT. The second Helmholtz coil pair was use to carry out the field calibration. The coils have a diameter of 50 mm and width of 3 mm, they have 50 turns. The distance between the coils is 90 mm.

### 6.2.1 *Gradiometer configuration*

The gradiometer reduces the measured background noise, bringing it closer to the intrinsic noise levels of the sensor by canceling the extrinsic noise. The extrinsic noise contributions can have a number of sources including large mains transformers, pulsed switch power supplies or fluorescent lighting. These noise contributions can be considered in far-field i.e. their is a spatial separation distance. The gradiometer picks up these high spatial frequencies, and see's them as a homogenous field (in-phase) and cancels the contributions accordingly through the differential amplifier. An illustration of the gradiometer concept is shown in Figure 6.2.

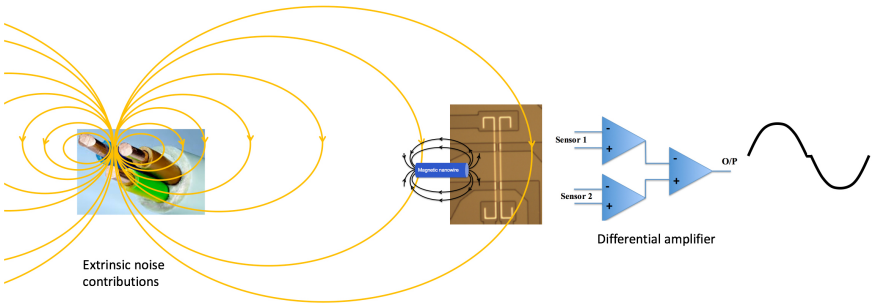



Figure 6.2: Illustration of the gradiometer concept

The gradiometer then neglects the low spatial frequencies of the field produced by the passing magnetic nanowire, which has a non-homogeneous field. In effect the gradiometer provides spatial localization to the local source namely the passing nanowire, and acts as a high-pass spatial filter. The output response of the gradiometer is also asymetric.

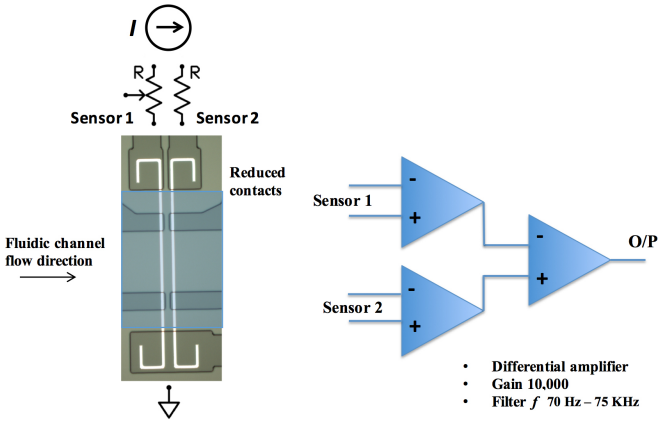



Figure 6.3: Gradiometer configuration using GMR sensors

The measured output signal from the gradiometer is taken from the difference between the signals measured from GMR Sensor 1 and GMR Sensor 2, which form the gradiometer pair as shown in Figure 6.3. The measured signals measured from each sensor connect into a differential amplifier configuration. Configuring the sensors in this way allows for the cancelation extrinsic far-field noise contributions and thus reducing the background noise closer to the intrinsic noise level.

The GMR sensor was redesigned for the gradiometer configuration. The 1st mask was redesigned, reducing the spacing between GMR sensors from 50 μm to 20 μm. The 2nd mask, which facilitates the top electrodes was redesigned to provide connections for the gradiometer configuration. The top electrode mask provides connections for the current supply and for signal detection on each of the two GMR YOKE sensors that form the gradiometer pair, as discussed in Chapter 3 Section 3.2.2. The overall GMR sensor layout accommodates two gradiometer pairs, which are designated side A & B in the schematic layout.

### 6.2.2 *Detection system for gradiometer*

The differential amplifier stage in the detection system comprises of two preamplifiers, which connect into a single post amplifier for each respective gradiometer. The pre-amplifiers were redesigned to accommodate two connections from each GMR YOKE sensor (Sensor 1 and Sensor 2). The pre-amplifiers were INA103 instrumental amplifiers with a gain set to 100 (40 dB) and incorporated a high-pass first order filter Dc to 70 Hz. . Figure 6.4 shows the schematic diagram of the pre-amplifier stage for the first gradiometer pair labeled Sensor Side A, with the second gradiometer pair labeled Sensor Side B.

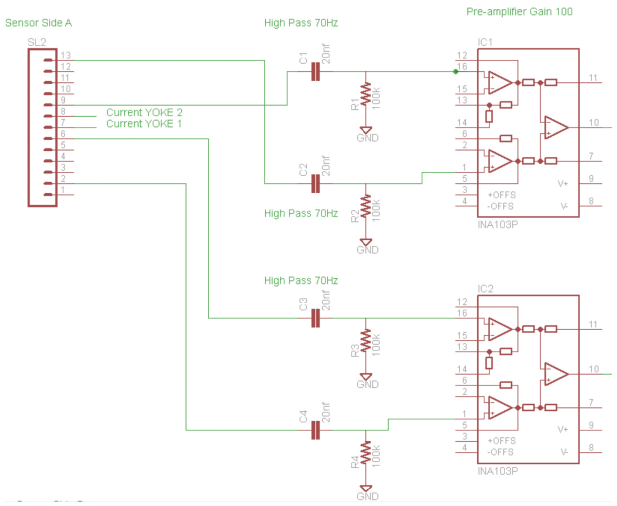



Figure 6.4: Gradiometer pre amplifier stage side A

The post-amplifier section of each gradiometer comprises of a low noise precision operational amplifier type OPA658. The OPA658 are wide-band, low power current feed-back amplifiers with a low level noise of $3.2nV/\sqrt{Hz}$ at 100 kHz and were designed with a low pass second order Butterworth filter 75 kHz and the gain was set to 100 (40dB). Figure 6.5 shows the schematic diagram of the post-amplifier. The output signal from the post amplifier in the gradiometer configuration is the difference in the signal detected between the two GMR YOKE sensors, which form the gradiometer pair.

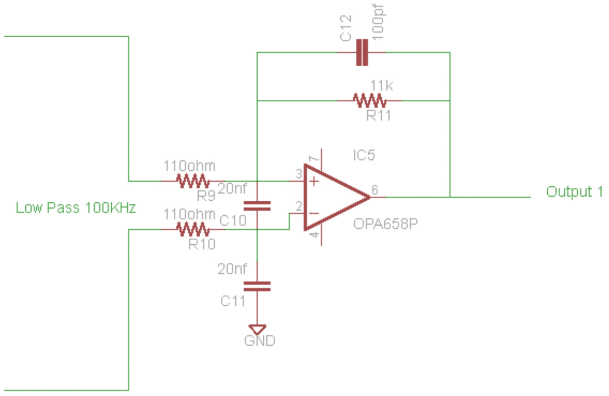



Figure 6.5: Gradiometer post amplifier stage side A

### 6.2.3 *Current circuit for graidometer*

In order to maximise the signal cancelation between the two GMR sensors in the gradiometer pair and improve our signal to noise ratio, the current circuit was designed, which provided balancing of the current supply into each of the two GMR YOKE sensors. The current circuit encompassed an LT3092234 adjustable low noise 10 mA current source, powered using a + 15 Volt DC voltage supply. In this circuit design the current is now supplied to each of the two GMR YOKE sensors that form the gradiometer pair. Given slight variations in resistance between the two GMR YOKE sensors, which can be due to fabrication and depositions variations, the current circuit was designed to allow balancing the current supply into each GMR YOKE sensor using the variable potentiometer R19. This provides balancing of up to 50% variation.

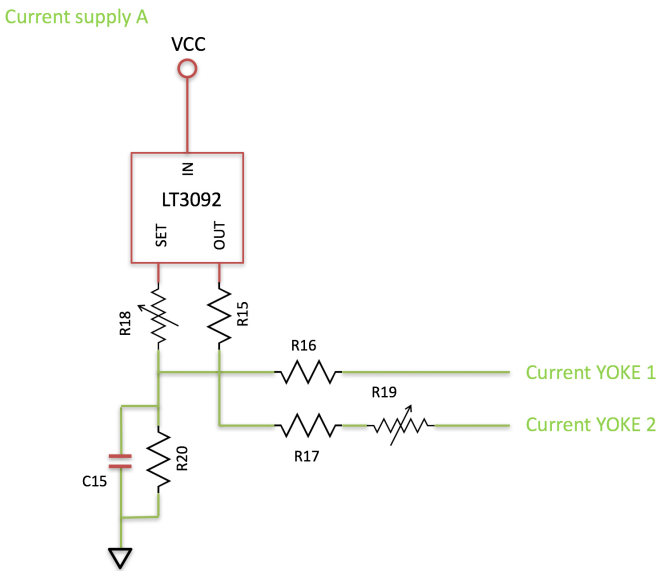



Figure 6.6: Gradiometer current supply side A

## 6.3 BALANCED GRADIOMETER RESPONSE

This section describes the procedure carried out to balance the two GMR YOKE sensors that form the gradiometer pair. The balance procedure is critical for noise cancelation and relies on each of the sensors in the gradiometer pair having a good linear magnetoresistance response that are comparably matched. The current circuit

was designed to allow for up to 50% balancing correction between both sensors. The balancing procedure is carried out for each respective gradiometer sensor pair prior to the nanowire detection experiments. A schematic of gradiometer balance setup is shown in Figure 6.7.

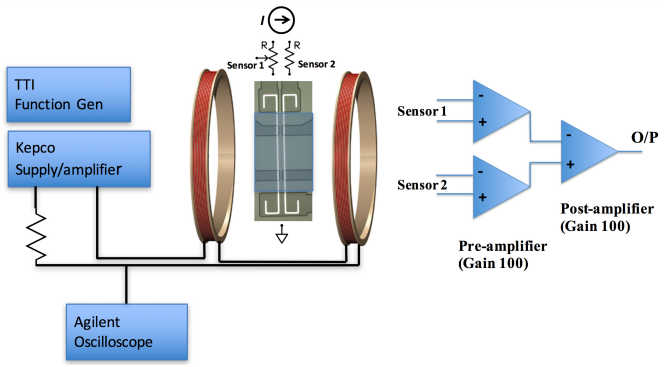



Figure 6.7: Schematic of gradiometer balance procedure

A supply of 4 mA is applied to the gradiometer sensor. The sensor is placed in the centre of the Helmholtz coil pair, which is connected to a TTI function generator and Kepco bidirectional amplifier. As mentioned balancing and noise cancelation relies on each of the sensors in the gradiometer pair having a good linear magnetoresistance response that are comparably matched, Figure 6.8 shows the magnetoresistive response of two sensors in the gradiometer pair for GMR sensor number: GMR-061115. The magnetoresistance response measured 5.2 % respectively and each sensor had a good linear response comparable matched which allows for optimum balancing and noise cancelation.

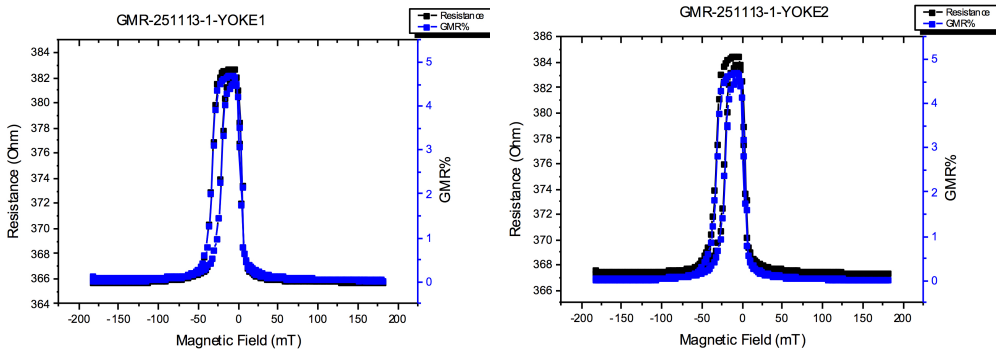



Figure 6.8: GMR-061115 magnetoresistive response of sensor 1 & 2

To balance the gradiometer response, a bias signal is applied via the TTI function generator at 120 Hz/2.2 V pk-pk into a Kepco bidirectional amplifier which was set to -19 V/0.6 Amp to the Helmholtz coil pair. Figure 6.9 details the measured response of the gradiometers using an oscilloscope. The oscilloscope trace shown in yellow (Oscilloscope channel 1), shows the bias signal applied to the Helmholtz coils which measured at 120 Hz 240 mV. Using a gauss-meter placed at the sensor area centre of Helmholtz coils, the field measured 1.8 mT.

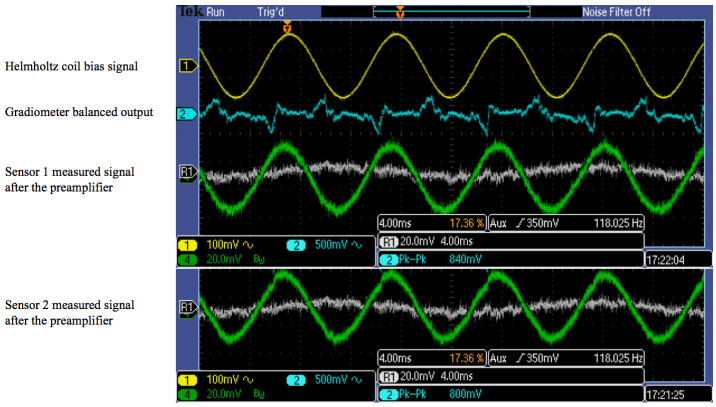



Figure 6.9: Measured result of balanced gradiometer; trace 1 (yellow) applied bias signal, traces 4 (green) sensor 1 & 2 response after the preamplifier stage and trace 2 (blue) the overall balanced Gradiometer output response after the post-amplifier

The two trace's shown in green (Oscilloscope channel 4) show the measured response to the applied bias signal from the Sensors 1 and 2 of the gradiometer after the preamplifier stage which has a gain of 100. Using the variable potentiometer R19 in the current circuit the measured signals from Sensors 1 and 2 can be balanced or best matched. For noise or signal cancelation both of the measured signals from Sensor 1 and 2 need to be in-phase as shown in Figure 6.9. The balanced signals from Sensors 1 and 2 after the preamplifier measured at 60 mV and 56 mV respectively. The trace shown in blue (Oscilloscope channel 2) shows the overall balanced gradiometer output response after the post-amplifier with an overall gain of 10,000. The balanced output from the gradiometer measured 820 mV (In-phase) and 11.6V (Out of phase) providing a ratio 15:1.

### 6.3.1 *Gradiometer sensor field Calibration*

The gradiometer sensor was calibrated to show the response in magnetic field as per the procedure outined in Chapter 5 Section 5.8.1. Using the function generator type TTI TG315 and bipolar operational amplifier type Kepco BOP 20-10 a variable field range is applied to the in-house Helmholtz coil pair, which is placed at the sensor interface. The response of the Helmholtz coil is monitored via the current sensing resistor (CSR) 0.45 ohm and an oscilloscope. The field response of the sensor is measured using an oscilloscope and the sensitivity is determined by the Coil response/Sensor response. A gauss meter with an axial probe is used to measure the magnetic field. Table 6.1 details the gradiometer sensor calibration conditions measured.

| **Calibration: Gradiometer sensor configuration** | |
|---|---|
| $\mathcal{U}_{csr}$ (Coil response) | 9.98 $mV\ pk-pk$ (CSR-current sensing resistor) |
| $\mathcal{U}_{amp}$ (Sensor response) | 8.10 $V\ pk-pk$ |
| $\mathcal{U}_{csr}bias$ | 576.70 $mV\ pk-pk$ |
| | |
| Field calibration bias | 1.80 mT (Optimum bias) |
| | |
| $Cal_{amp}$ (Cal constant) | $\frac{Sensor\ response\ Volt \times Coil\ response\ Volt}{Coil\ response\ Volt\ max \times Bias\ mT} = \frac{4.671\,V}{0.01796} = 260.07\,V/mT$ |
| $\mathcal{U}_{Sensor\ cal\ factor}$ | $\frac{1}{260.07\,V/mT} = 38\ \mu T/V$ |

Table 6.1: Calibration conditions measured for Gradiometer sensor configuration

### 6.3.2 *Gradiometer noise measurements*

Noise measurment of the detection system and the balanced gradiometer sensor response were carried out. Figure 6.10 (a) shows the background noise response recorded with no deionised water flowing through the fluidic channel, the noise measured 0.145 Vdc at a gain of 10,000. With the calibration field constant applied, this measured at 3.5 μT. This provides a factor of 3 improvement over the noise measured using the single sensor configuration.

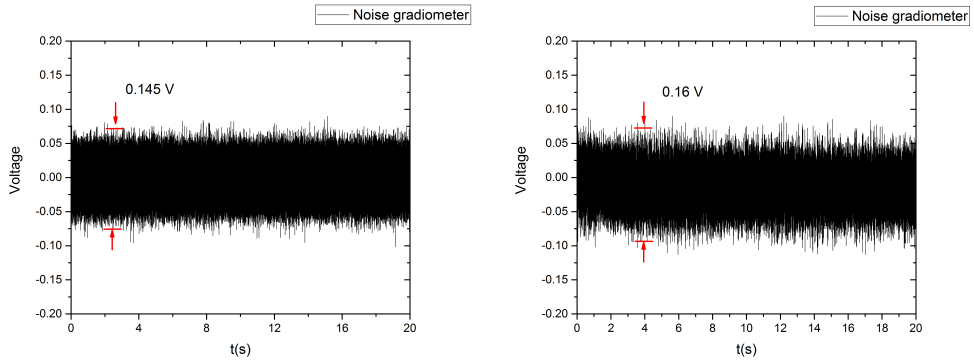



Figure 6.10: a) background noise response recorded from balanced gradiometer sensor GMR-061115 with no deionised water flowing (b) background noise response recorded fromgradiometer sensor with deionised water flowing

The noise measurments were repeated with deionised water flowing through the microfluidic channel. Figure 6.10 (b) shows the background noise response recorded with deionised water flowing through the fluidic channel. The noise measured was 0.16 Vdc. With the calibration field constant applied, this measured at 3.9 μT. The background noise measured is a combination of environmental noise, the electronic noise from the detection system and the sensor. There is also noise contribution when the deionised water is flowing through the channel across the sensor.

## 6.4 NANOWIRE DETECTION EXPERIMENTS USING THE GRADIOMETER CONFIGURATION

A number of nanowire detection experiments were carried out to determine the improvement using the gradiometer configuration. The microfluidic channel has a geometry of width 600 μm, height 30 μm & length 14 mm. The nanowires are injected into the channel using a controlled syringe micro-pump “Miros” from the company Cellix.

### 6.4.1 *CoNi Nanowire detection using the gradiometer configuration - Batch 091213-1*

Details of CoNi nanowires Batch: 091213-1 used in the experiment are detailed in Table 6.2. The CoNi nanowires were deposited at an over potential of -0.9 Vdc, for a duration

of 5000 seconds at 6.0 mA producing a nanowire length of 9 μm as outline in Chaper 4 Section 4.5.

| Sample | Segment | Type | Pot (V) | Time (Sec) | Current (mA) | Charge (Q) | Length (um) | OCP (V) | Mag (T) |
|---|---|---|---|---|---|---|---|---|---|
| 091213-1 | CoNi | | -0.9 | 5000 | 6.0 | 31 | 9 | 0.12 | 1.2 |

Table 6.2: 091213-1 CoNi nanowire sample deposition conditions

Table 6.3 shows the conditions used to dissolve the nanowires from the membrane. To dissolve the nanowires from the membrane they were placed in a solution of NaOH 1 molar at 70 $^{o}$C for a duration of 11 minutes. The sample was visually checked periodically every few minutes, with sonication process of 10 seconds. To removed the NaOH solution, the nanowires were rinsed in deionised water a number of times. This was acheived by placing a permanent magnet next to the sample, which hold the sample in place while the NaOH solution is removed.

| Sample | Type | Solution (1molar) | Temp ($^{o}$C) | Method | Weight (g) |
|---|---|---|---|---|---|
| 091213-1 | CoNi | NaOH | 70 | Min 3/sonication 10sec, Min 5/ sonication 10sec, Min 11/ sonication 10sec, stop, Rinse in DI water x 6 using magnet | 0.0933 |

Table 6.3: 091213-1 CoNi nanowire sample condition used to dissolve from membrane

The microscope inspection image of the nanowires prior to dispensing is shown in Figure 6.11. This showed reasonably well separated nano-wires, but still some bunching of nanowires. For the nanowire detection experimnents I found that the microscope image can be taken quickly compared to an SEM image and it provides a good indication of the dispersion of the nanowires before they are dispenced across the sensor.

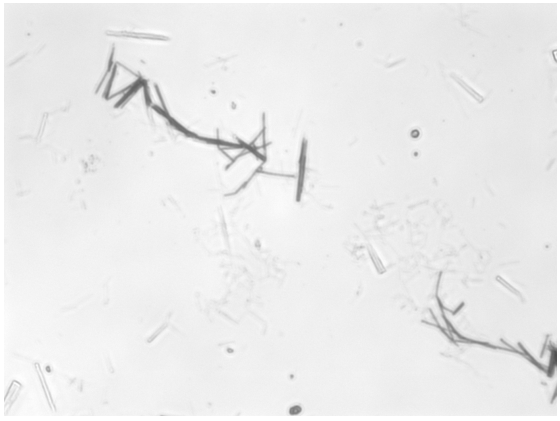


Figure 6.11: Microscope image of CoNi nano-wires batch: 091213-1 before dispensing

For the experiment 0.31 µg of CoNi nanowires, which approximates to ~ 7,200 nanowires as per the nanowire experiment preparation procedure detailied Appendix 8 Section 8.7.10, are were dispensed across the sensor at a velocity of 20 mm/s. Gradiometer GMR sensors used in the experiment measured a magnetoresistance of 5.2% with a linear response and a sensitivity of 0.9%/mT as detailed in Figure 6.8. The sensor was passivated using $Si_3N_4$ with a thinkness of 150 nm to protect it from microfluidics during the experiment. The detected response of the CoNi nanowires batch SM319 (091213-1) flowing across the sensor is shown in Figure 6.12. The CoNi nanowires are dispensed after the first 10 seconds and stopped after 35 second time period. During the time period when nanowires are dispensed. the detected responses are recorded.

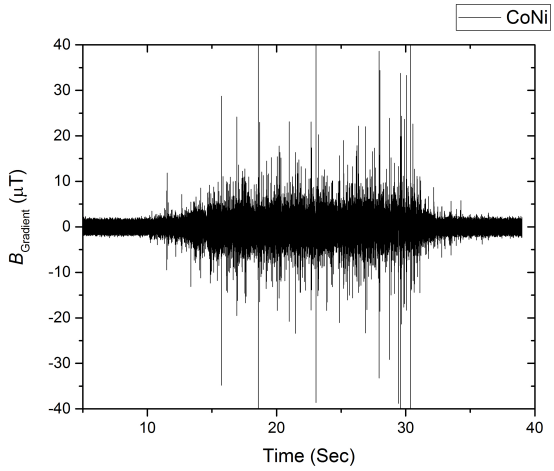



Figure 6.12: Response of CoNi SM319 (091213) wires flowing across gradiometer sensor

Figure 6.13 highlights in details some of the detected events from the CoNi nanowire detection experiment. The magnitude of the detected signals range from 10 µT to 70 µT with a response times of 0.5 ms to 0.7 ms.

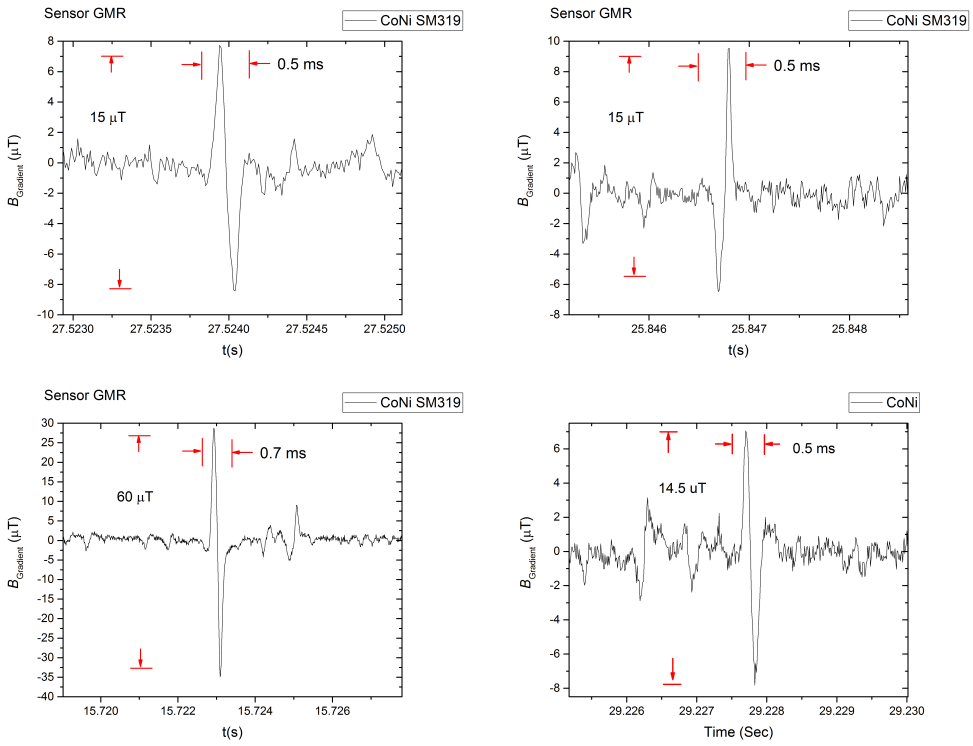



Figure 6.13: Response of CoNi SM319 wires detailing detected events

As the nanowires are flowing at a velocity of 20 mm per second within the microfluidic channel, for a 10 µm nanowire traveling a across a 5 µm sensor width the expected response time is in the order of 0.65 ms as detailed in Table 5.10 in Chaper 5 Section 5.6.1. There are a number of detected events with response times of 0.5 ms to 0.7 ms. The detected nanowires vary in amplitude with the same time response, indicating the nanowires are traveling at different heights within the microfluidic channel. The nanowires are also traveling in different orientations and angles as they pass over the gradiometer sensor, as we see variations in the detected polarity response magnitudes and also different polarity directions. This is also indicated in the optical camera image shown in Figure 6.14, which shows nanowires traveling in different orientations and angles as they pass over the gradiometer sensor.

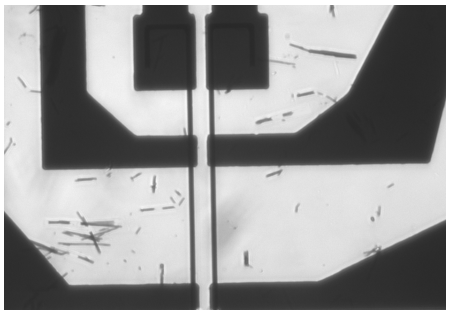


Figure 6.14: CoNi single segment nanowires flowing across gradiometer in microfluidic channel

A post statistical analysis was carried out on the captured data using the Pulse height amplification (PHA) routine as discussed in Section 5.7.5. The PHA provides parametric de-noising of the captured signal response and extracts all detected events as a single amplitude. Figure 6.15 shows the PHA model fitting with the experimental detected response.

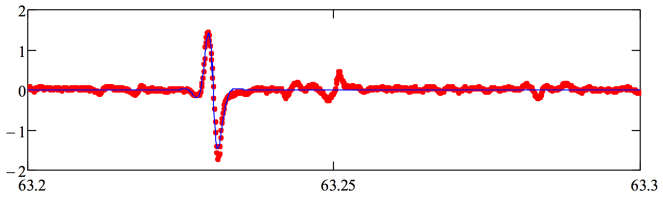



Figure 6.15: CoNi nano-wires sample SM319 (091213) model fitting to experimental data

The PHA suppressed the background noise by a factor of 2.098. The PHA locates all actual nanowire detected events, integrates each signal response and extracts it as a signal amplitude. Figure 6.16 shows a plot of detected nanowire events during the experiment extracted as single amplitudes. The upper and lower threshold was adjusted to exclude the noise contribution.

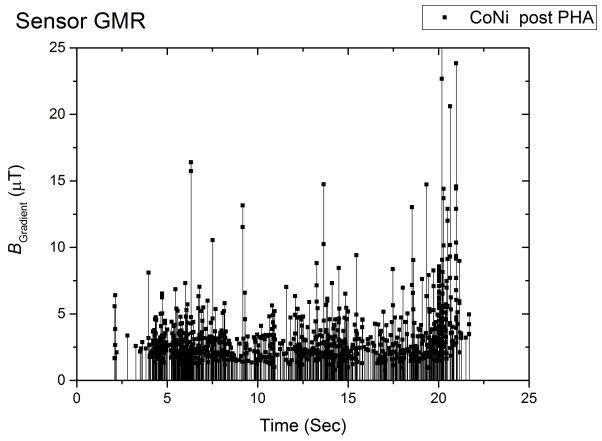



Figure 6.16: Detected nanowire events for CoNi batch SM319 (091213) during the experiment extracted as single amplitudes post PHA

A post statistical analysis of the extracted nanowire detected events are shown in the bar chart in Figure 6.17. The bar chart shows the number of detected nanowire events per field. The total count of nanowires detected was 1500. The field of the nanowires detected were in the range of 2 to 35 µT after the PHA.

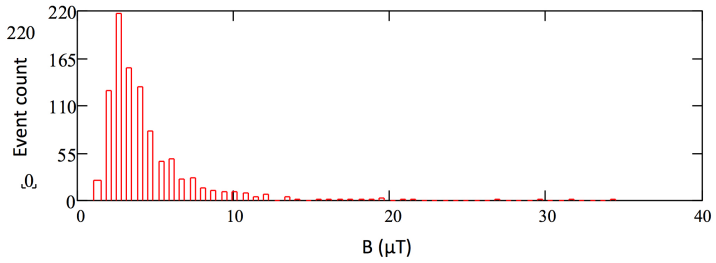



Figure 6.17: Number of detected nanowire events per field for CoNi batch SM319 (091213)

Comparing this to the modelled response of CoNi nanowires at different heights $z$ above the sensor as shown in Figure 5.5, the majority of nanowires are traveling at a height in the order of 8 µm in the microfluiduc channel. There is a significant increase in the number of number of nanowires detected ~ 1500 using the Gradiometer configuration compared to the single sensor configuration, which was ~ 600 nanowires

### 6.4.2 *CoNi Nanowire detection using the gradiometer configuration - Batch SM319G9 (091213-2)*

The gradiometer GMR sensors used in the experiment measured a magnetoresistance of 5.3% with a linear response and a sensitivity of 1%/mT. The sensor was passivated using $Si_3N_4$ with a thickness of 150 nm to protect it from microfluidics during the experiment. The background noise response recorded for the balanced gradiometer sensor measured at 0.132 Vdc. With the calibration field constant applied, this measured at 3.2 μT.

Details of CoNi nano-wires batch: SM319 (091213-2) used in the experiment are detailed in Table 6.4. The CoNi nanowires were deposited at an over potential of -0.9 Vdc, for a duration of 5000 seconds at 6.1 mA producing a nano-wires length of 9 μm as outline in Chaper 4 Section 4.5.

| Sample | Segment | Type | Pot (V) | Time (Sec) | Current (mA) | Charge (Q) | Length (um) | OCP (V) | Mag (T) |
|---|---|---|---|---|---|---|---|---|---|
| 091213-2 | CoNi | | -0.9 | 5000 | 6.1 | 31 | 9 | 0.11 | 1.2 |

Table 6.4: CoNi (SM319G4) 091213-2 deposition conditions

Table 6.5shows the conditions used to dissolve the nanowires from membrane using the same method as discussed in the pervious experiment.

| Sample | Type | Solution (1molar) | Temp ($^0$C) | Method | Weight (g) |
|---|---|---|---|---|---|
| 091213-2 | CoNi | Na0H | 70 | Min 3/sonication 10sec, Min 5/ sonication 10sec, Min 11/ sonication 10sec, stop, Rinse in DI water x 6 using magnet | 0.0946 |

Table 6.5: CoNi (SM319G4) 091213-2 conditions used to dissolve from membrane

For the experiment 0.17 μg of CoNi nanowires, which approximates to ~ 3,900 nanowires as per the nanowire experiment preparation procedure detailied Appendix 8 Section 8.7.10, are were dispensed across the sensor at a velocity of 10 mm/s. The detected response of the CoNi nanowires batch SM319 (091213-2) flowing across the sensor is shown in Figure 6.18. During the time period when nanowires are dispensed. the detected responses are recorded.

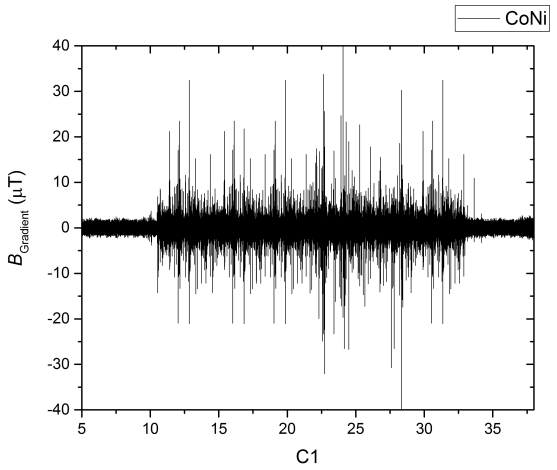



Figure 6.18: Response of CoNi SM319 (091213-2) wires flowing across gradiometer sensor

Figure 6.19 highlights in detail some of the detected events from the CoNi nanowire batch 091213-2 detection experiment. The magnitude of the detected signals range from 10 µT to 50 µT with a response times of 1.5 ms to 2 ms.

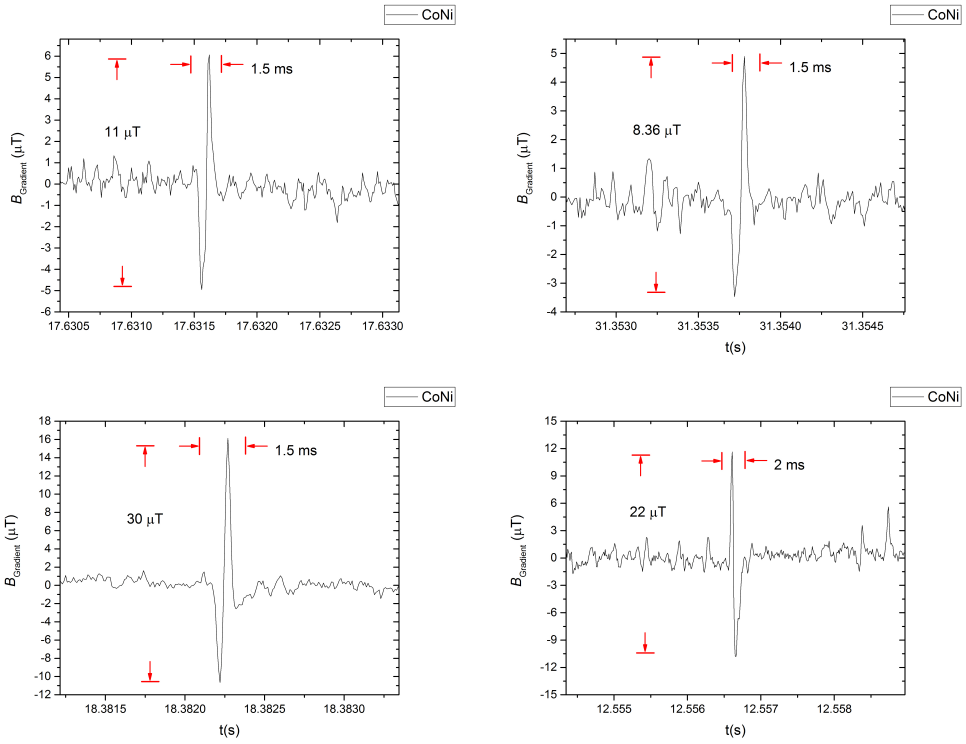



Figure 6.19: Response of CoNi SM319 (091213-2) wires detailing detected events

The nanowires are flowing at a velocity of 10 mm/s within the microfluidic channel. For a 10 µm nanowire traveling a across a 5 µm sensor (width) the expected response

time is in the order of 1.5 ms. There are a number of detected events with response times of 1.5 ms to 2 ms. The detected nanowires vary in amplitude with the same time response, indicating the nanowires are traveling at different heights within the microfluidic channel. The nanowires are also traveling in different orientations and angles as they pass over the gradiometer sensor, as we see variations in the detected polarity response magnetudes and also different polarity directions. This is also incidacted in the optical camera image shown in Figure 6.20 , which shows nanowires traveling in different orientations and angles as they pass over the gradiometer sensor.

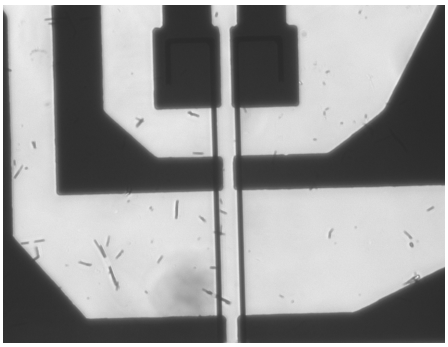


Figure 6.20: CoNi single segment nanowires flowing across gradiometer in microfluidic channel

A post statistical analysis was carried out on the captured data using the Pulse height amplification (PHA) routine as discussed in Section 5.7.5. Figure 6.21 shows the PHA model fitting with the experimental detected response.

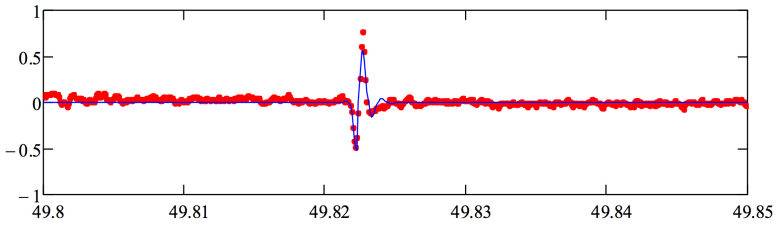



Figure 6.21: CoNi nano-wires sample SM319 (091213-2) model fitting to experimental data

The PHA suppressed the background noise by a factor of 1.753. Figure 6.22 shows a plot of detected nanowire events during the experiment extracted as single amplitudes. The upper and lower threshold was adjusted to exclude the noise contribution.

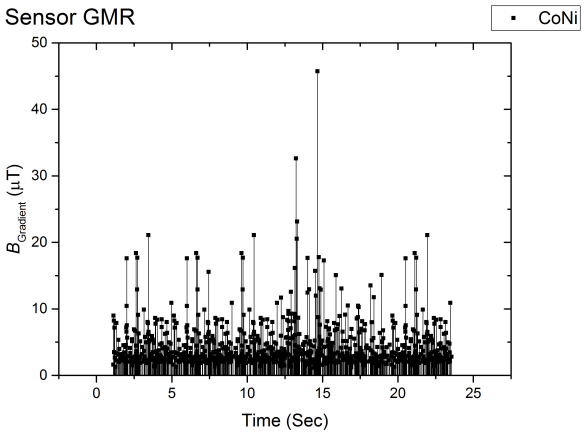



Figure 6.22: Detected nanowire events for CoNi batch SM319 (091213-2) during the experiment extracted as single amplitudes post PHA

A post statistical analysis of the extracted nanowire detected events are shown in the bar chart in Figure 6.23. The bar chart shows the number of detected nanowire events per field. The total count of nanowires detected was 980. The field of the nanowires detected were in the range of 2 to 46 μT after the PHA. Again the there is an increase in the number of number of nanowires detected ~ 1000 using the Gradiometer configuration compared to the single sensor configuration, which was ~ 600 nanowires.

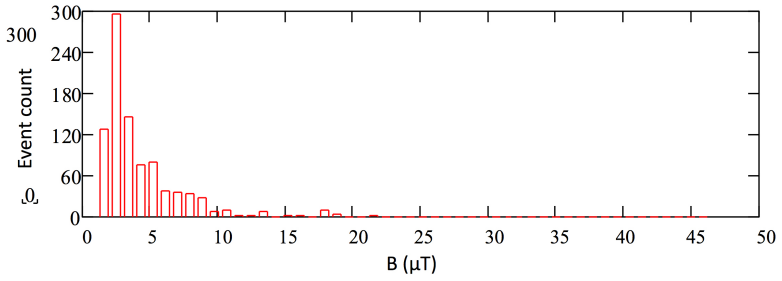



Figure 6.23: Number of detected nanowire events per field for CoNi batch SM319 (091213-2)

Comparing this to the modelled response of CoNi nanowires 10 μm length at different heights $z$ above the sensor shown in Figure 5.5, the majority of nanowires are traveling at a height in the order of 10 μm in the microfluiduc channel. Table 6.6 summaries the results of the CoNi nanowire detection experiments using the gradiometer. The gradiometer has improved the signal to noise by factor of 3 over the single sensor configuration, putting us in the range for the detection of single segment magnetic nanowires. The number of nanowires detected has increased by a factor of almost 2 compared to the single sensor

configuration detection experiments. Nanowire detection experiments were carried out towards the detection of two magnetic segment nanowires using CoNi-Cu-CoNi.

| Parameters | Response time (ms) | Velocity (mm/s) | Noise before PHA (μT) | PHA Noise suppression | PHA Nanowire count | Detected field range after PHA (μT) |
|---|---|---|---|---|---|---|
| Nanowire type: $Co_{65}Ni_{35}$ | 0.5 – 0.7 | 20 | 3.5 | 2.098 | 1500 | 2 - 35 |
| Length: 9 μm | 1.5 – 2.0 | 10 | 3.2 | 1.753 | 980 | 2 - 46 |
| Dispensed: Microfluidic pump | 1 – 1.2 | 15 | 3.9 | 1.801 | 1120 | 2.5 - 42 |
| Microfluidic channel: Height 30 μm | | | | | | |
| Sensor: Gradiometer GMR | | | | | | |

Table 6.6: Summary of CoNi nanowire detection experiments using gradiometer

### 6.4.3 *CoNi-Cu-CoNi Nanowire detection using the gradiometer configuration - Batch 211013-3*

The gradiometer GMR sensors used in the experiment measured a magnetoresistance of 5.2% with a linear response and a sensitivity of 0.9%/mT. The sensor was passivated using $Si_3N_4$ with a thickness of 150 nm to protect it from microfluidics during the experiment. The background noise response recorded for the balanced gradiometer sensor measured at 0.169 Vdc. With the calibration field constant applied, this measured at 4.1 μT.

Details of CoNi-Cu-CoNi nanowires batch: 211013-3 used in the experiment are detailed in Table 6.7. The first CoNi nanowire segment was deposited with an over potential of -0.9 Vdc, for a duration of 2500 seconds at 6.5 mA producing a segment length of 3.5 μm. The interlayer was then deposited to assist adhesion. The non-magnetic layer Cu was then deposited with an over potential of -0.2 Vdc, for a duration of 600 seconds at 11 mA producing a segment length of 4 μm. The second CoNi nanowire segment was deposited with an over potential of -0.9 Vdc, for a duration of 2500 seconds at 6.0 mA producing a segment length of 3.5 μm.

| Sample | Segment | Type | Pot (V) | Time (Sec) | I (mA) | Charge (Q) | Length (μm) | OCP (V) | Mag (T) |
|---|---|---|---|---|---|---|---|---|---|
| 211013-3 | CoNi | 1st mag seg | -0.9 | 2500 | 6.5 | 15 | 3.5 | 0.15 | 1.2 |
| CoNiCuCoNi | CoNiCu | Interlayer | -0.7 | 3 | 40 | | | | |
| | | | -0.6 | 3 | 20 | | | | |
| | Cu | Spacer | -0.4 | 3 | 15 | | | | |
| | | | -0.2 | 600 | 11 | 20 | 4 | | |
| | CoNi | 2nd mag seg | -0.9 | 2500 | 6.0 | 15 | 3.5 | | |

Table 6.7: CoNi-Cu-CoNi 210113-3 deposition conditions

Table 6.8 shows the conditions used to dissolve the nanowires from membrane using the same method as discussed in the pervious experiment.

| Sample | Type | Solution (1molar) | Temp ($^0$C) | Method | Weight (g) |
|---|---|---|---|---|---|
| 211013-3 | CoNi-Cu-CoNi | Na0H | 70 | Min 4/sonication 10sec, Min 8/ sonication 10sec, Min 10 stop, Rinse in DI water x 6 using magnet | 0.09200 |

Table 6.8: CoNi-Cu-CoNi 210113-3 conditions used to dissolve from membrane

The microscope inspection image of the nanowires prior to dispensing as shown in Figure 6.24. This showed a percentage of well separated nanowires. A number of the segments within the CoNi-Cu-CoNi nanowires are broken. Also a number of nanowires are not fully dissolved from the AAO alumina membrane.

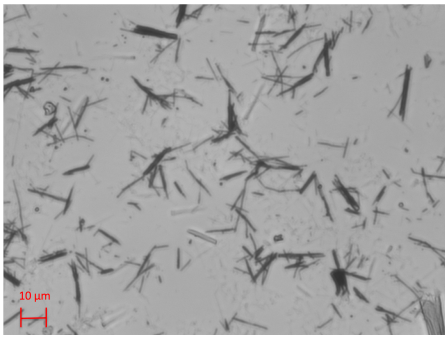



Figure 6.24: CoNiCuCoNi 211013-3 microscope image-2

For the experiment 0.3 µg of CoNi nanowires, which approximates to ~ 6,625 nanowires as per the nanowire experiment preparation procedure detailied Appendix 8 Section 8.7.10, are were dispensed across the sensor at a velocity of 15 mm/s. The detected response of the CoNi-Cu-CoNi nanowires batch: 211013-3 flowing across the sensor is shown in Figure 6.25. The CoNi nanowires are dispensed after the first 5 seconds and stopped after 30 second time period. During the time period when nanowires are dispensed. the detected responses are recorded.

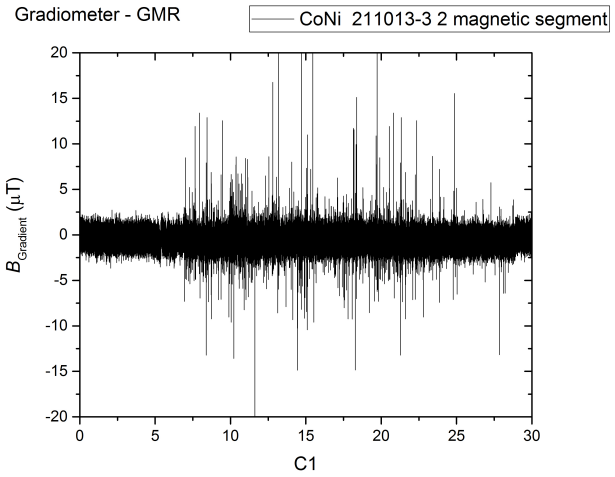



Figure 6.25: Response of CoNi-Cu-CoNi 211013-3 nano-wires flowing across gradiometer sensor

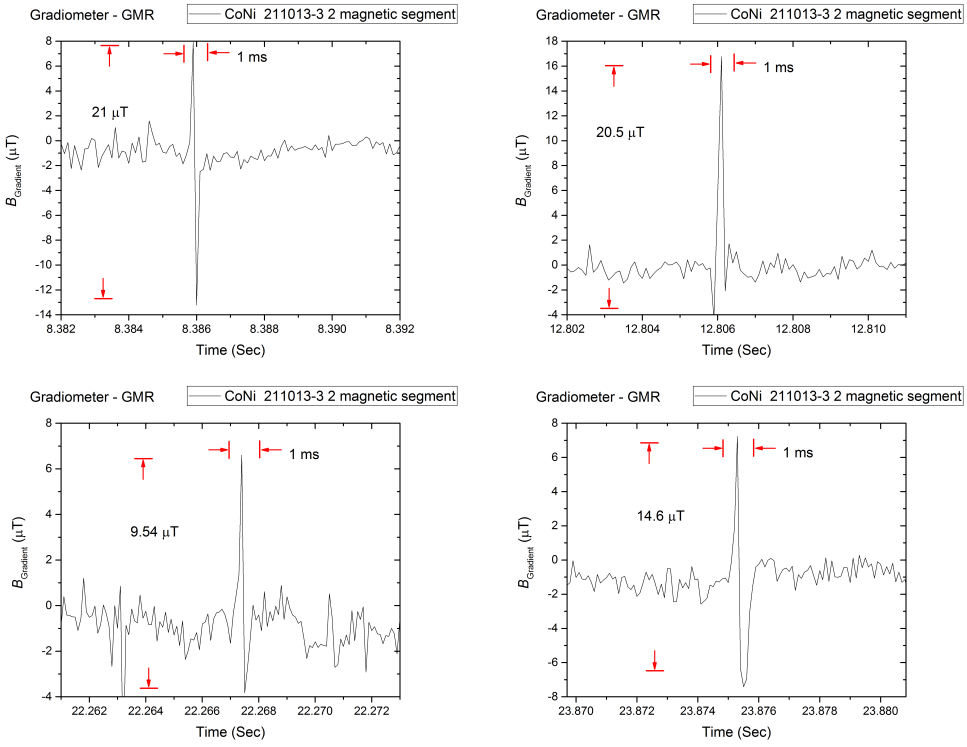



Figure 6.26: Response of CoNi-Cu-Coni 211013-3 nanowires detailing detected events

Figure 6.26 highlights in detail some of the detected events from the CoNi-Cu-CoNi detection experiment. The magnitude of the detected signals range from 6 µT to 30 µT with a response times of 1 ms.

The nanowires are flowing at a velocity of 15 mm per second within the microfluidic channel. For a 10 µm nanowire traveling a across a 5 µm sensor (width) the expected

response time is in the order of 1 ms. There are a number of detected events with response times of 1 ms. The detected nanowires vary in amplitude with the same time response, indicating the nanowires are traveling at different heights within the microfluidic channel. The nanowires are also traveling in different orientations and angles as they pass over the gradiometer sensor, as we see variations in the detected polarity response magnetudes and also different polarity directions. There is no evidence of the detection of the non-magnetic segment within the CoNi-Cu-CoNi nanowires. The response is simular to the response for a single segment CoNi nanowire, with a linear transition between the axial positions of the magnetic dipole response.

A post statistical analysis was carried out on the captured data using the Pulse height amplification (PHA) routine. Figure 6.27 shows the PHA model fitting with the experimental detected response.

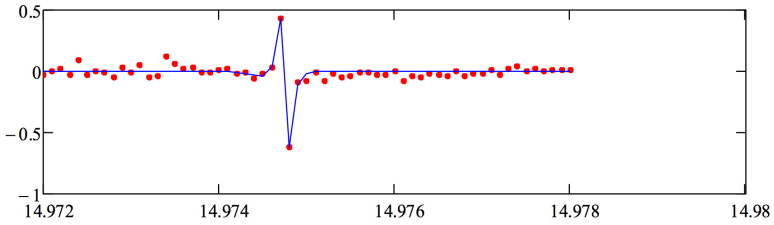



Figure 6.27: CoNi-Cu-CoNi nano-wires sample 211013-3 model fitting to experimental data

The PHA suppressed the background noise by a factor of 1.201. Figure 6.28 shows a plot of detected nanowire events during the experiment extracted as single amplitudes. The upper and lower threshold was adjusted to exclude the noise contribution.

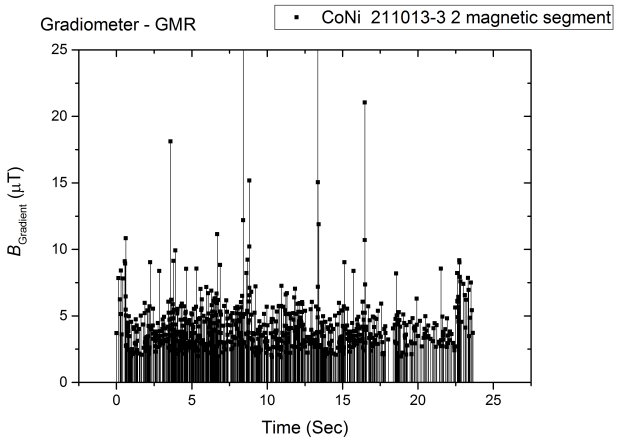



Figure 6.28: Detected nanowire events for CoNi-Cu-CoNi 211013-3 during the experiment extracted as single amplitudes post PHA

A post statistical analysis of the extracted nanowire detected events are shown in the bar chart in Figure 6.29. The bar chart shows the number of detected nanowire events per field. The total count of nanowires detected was 915. The field of the nanowires detected were in the range of 2 to 27 µT after the PHA.

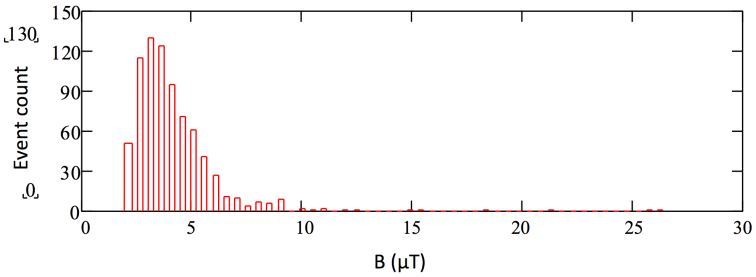



Figure 6.29: Number of detected nanowire events per field for CoNi-Cu-CoNi 211013-3

Comparing this to the modelled response of CoNi nanowires shown in Figure 5.5, the majority of nanowires are traveling at a height in the order of 7 to 10 µm in the microfluiduc channel. The experiment was repeated using another batch CoNi-Cu-CoNi nanowires and gradiometer.

### 6.4.4 *CoNi-Cu-CoNi Nanowire detection using the gradiometer configuration - Batch 211013-4*

The gradiometer GMR sensors used in the experiment measured a magnetoresistance of 5.2% with a linear response and a sensitivity of 0.9%/mT. The sensor was passivated using $Si_3N_4$ with a thickness of 150 nm to protect it from microfluidics during the experiment. The background noise response recorded for the balanced gradiometer sensor measured at 0.15 Vdc. With the calibration field constant applied, this measured at 3.8 μT. Details of CoNi-Cu-CoNi nanowires batch: 211013-4 used in the experiment are detailed in Table 6.9.

| Sample | Segment | Type | Pot (V) | Time (Sec) | I (mA) | Charge (Q) | Length (μm) | OCP (V) | Mag (T) |
|---|---|---|---|---|---|---|---|---|---|
| 211013-4 CoNiCuCoNi | CoNi | 1st mag seg | -0.9 | 2500 | 6.3 | 15 | 3.3 | 0.14 | 1.2 |
| | CoNiCu | Interlayer | -0.7 | 3 | 40 | | | | |
| | | | -0.6 | 3 | 20 | | | | |
| | Cu | Spacer | -0.4 | 3 | 15 | | | | |
| | | | -0.2 | 600 | 11 | 20 | 4 | | |
| | CoNi | 2nd mag seg | -0.9 | 2500 | 6.2 | 15 | 3.4 | | |

Table 6.9: CoNi-Cu-CoNi 210113-4 deposition conditions

Table 6.10 shows the conditions used to dissolve the nanowires from membrane using the same method as discussed in the pervious experiment.

| Sample | Type | Solution (1molar) | Temp ($^0$C) | Method | Weight (g) |
|---|---|---|---|---|---|
| 211013-4 | CoNi-Cu-CoNi | Na0H | 70 | Min 4/sonication 10sec, Min 8/ sonication 10sec, Min 10 stop, Rinse in DI water x 6 using magnet | 0.09210 |

Table 6.10: CoNi-Cu-CoNi 210113-4 conditions used to dissolve from membrane

For the experiment 0.3 μg of CoNi nanowires, which approximates to ~ 6,625 nanowires as per the nanowire experiment preparation procedure detailied Appendix 8 Section 8.7.10, are were dispensed across the sensor at a velocity of 15 mm/s. The detected response of the CoNi-Cu-CoNi nanowires batch: 211013-4 flowing across the sensor is shown in Figure 6.30. The CoNi nanowires are dispensed after the first 7 seconds and stopped after 30 second time period. During the time period when nanowires are dispensed. the detected responses are recorded.

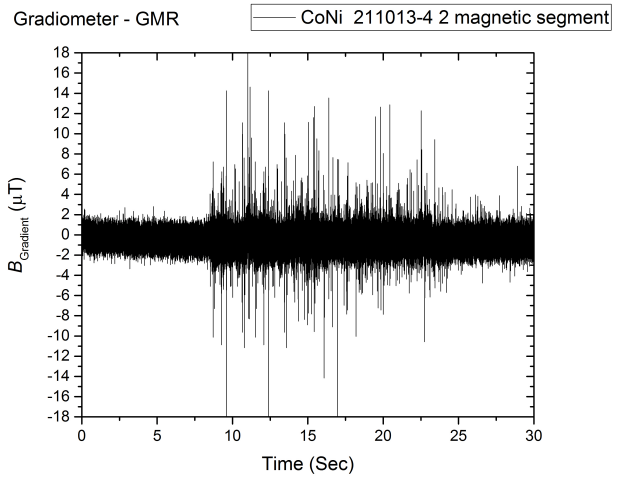



Figure 6.30: Response of CoNi-Cu-CoNi 211013-4 nano-wires flowing across gradiometer sensor

Figure 6.31 highlights in detail some of the detected events from the CoNi-Cu-CoNi detection experiment. The magnitude of the detected signals range from 8 μT to 32 μT with a response times of 1 ms to 1.5 ms.

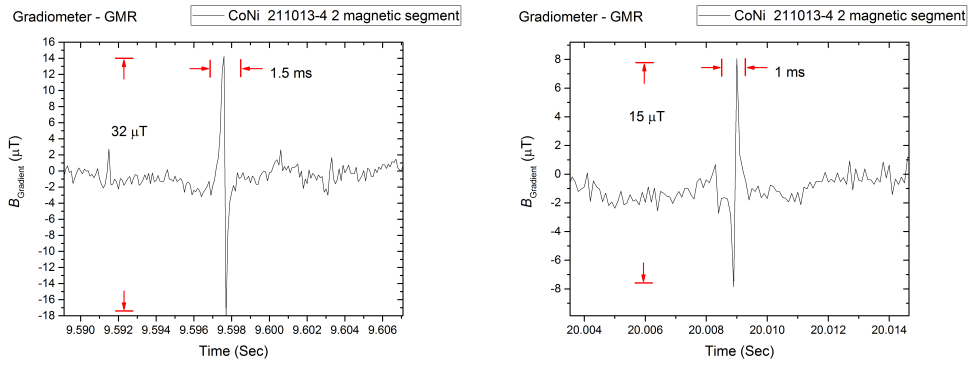



Figure 6.31: Response of CoNi-Cu-Coni 211013-4 nano-wires detailing detected events

There is no evidence of the detection of the non-magnetic segment within the CoNi-Cu-CoNi nanowires. The response is simular to the response for a single segment CoNi nanowire, with a linear transition between the axial positions of the magnetic dipole response. A post statistical analysis was carried out on the captured data using the Pulse height amplification (PHA) routine. Figure 6.32 shows the PHA model fitting with the experimental detected response.

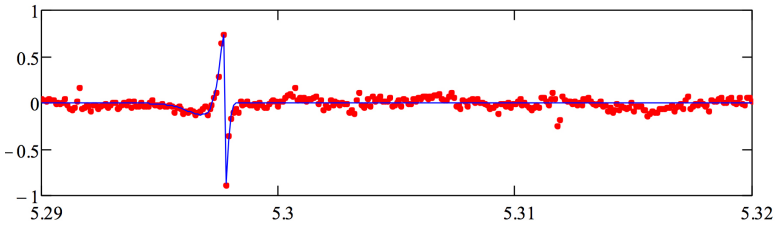



Figure 6.32: CoNi-Cu-CoNi nano-wires sample 211013-4 model fitting to experimental data

The PHA suppressed the background noise by a factor of 2.04. Figure 6.33 shows a plot of detected nanowire events during the experiment extracted as single amplitudes. The upper and lower threshold was adjusted to exclude the noise contribution.

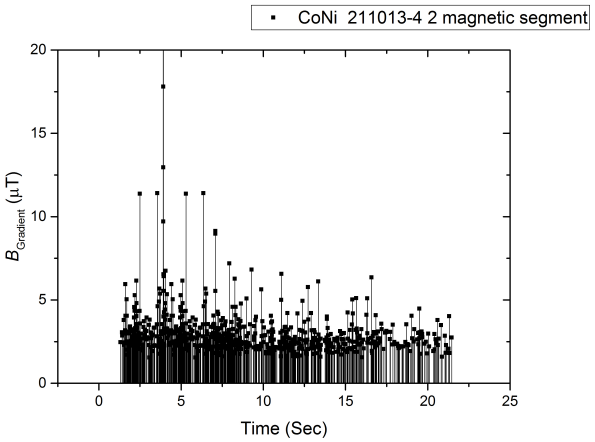



Figure 6.33: Detected nanowire events for CoNi-Cu-CoNi 211013-4 during the experiment extracted as single amplitudes post PHA

A post statistical analysis of the extracted nanowire detected events are shown in the bar chart in Figure 6.34. The bar chart shows the number of detected nanowire events per field. The total count of nanowires detected was 810. The field of the nanowires detected were in the range of 2 to 28 μT after the PHA.

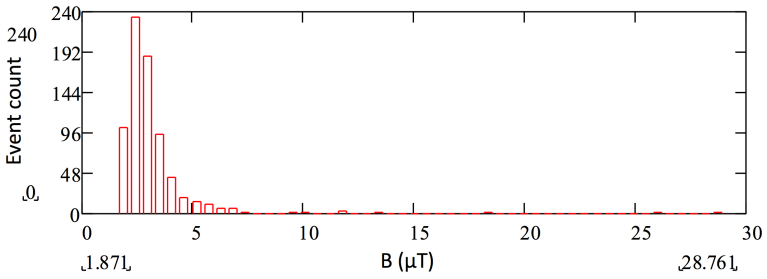



Figure 6.34: Number of detected nanowire events per field for CoNi-Cu-CoNi 211013-4

Comparing this to the modelled response of CoNi nanowires shown in Figure 5.5, the majority of nanowires are traveling at a height in the order of 7 to 10 µm in the microfluiduc channel. There is good detection of the CoNi-Cu-CoNi nanowires with an increase in the number of number of nanowires detected compared to the single sensor configuration. There is no evidence of the detection of the non-magnetic segment within the CoNi-Cu-CoNi nanowires. Table 6.11 summaries the results of the CoNi-Cu-CoNi nanowire detection experiments using the gradiometer.

| Parameters | Response time (ms) | Velocity (mm/s) | Noise before PHA (µT) | PHA Noise suppression | PHA Nanowire count | Detected field range after PHA (µT) |
|---|---|---|---|---|---|---|
| Nanowire type: CoNi-Cu-CoNi<br>Length: 12 µm<br>Dispensed: Microfluidic pump<br>Microfluidic channel: Height 30 µm<br>Sensor: Gradiometer GMR | 1 | 15 | 4.1 | 1.201 | 915 | 2 - 27 |
| | 1 – 1.5 | 15 | 3.8 | 2.04 | 810 | 2 - 28 |

Table 6.11: Summary of CoNi-Cu-CoNi nanowire detection experiments using gradiometer

### 6.4.5 *Conclusions*

Configuring two GMR sensors as gradiometer has increased signal to noise by factor of 3, puttings us in the range for the detection of single segment magnetic nanowires. Following the nanowire experiments on single segment CoNi nanowires, the number of detected nanowires has increased, which is a result of the reduction of the background noise from the balanced gradiometer configuration. From the first experiments for the detection of two magnetic segment nano-wires CoNi-Cu-CoNi there are detection of nanowires, however there is no detection of the non-magnetic segment within the two magnetic segment nanowires.

To provide further improvements to the signal to noise ratio a number of areas were focused on. These included a redesign of the gradiometer sensor to better match the aspect ratio of the nanowire to the gradiometer for focused flow. Integration of the complete electronic detection system into a revised sensor interface. Integration of coils into the revised sensor interface.

## 6.5 FINAL OPTIMISATION OF THE GRADIOMETER FOR NANOWIRE DETECTION

Configuring the GMR sensors as gradiometer has been advantageous providing a factor of 3 increase in the signal-to-noise ratio. A number of area were focused on to optimise the gradiometer. Figure shows a schematic diagram highlighing in red the design components developed in the optimisation of the gradiometer nanowire detection system.

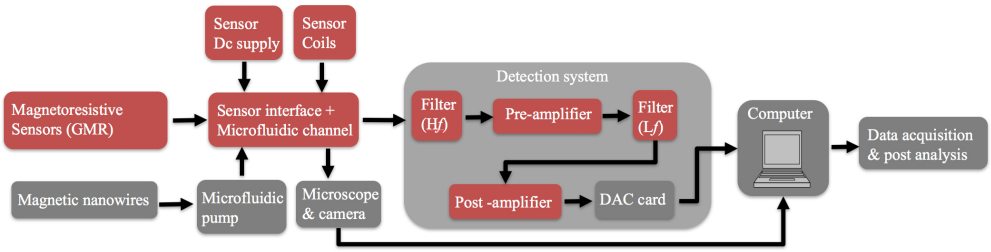



Figure 6.35: Schematic diagram highlighing design component changes in the optimised gradiometer nanowire detection system

Firstly the gradiometer sensor was redesigned to better match the aspect ratio of the nanowire to the gradiometer for focused flow. Secondly theelectronic detection system was integration into a revised sensor interface. Finally integration of Helmholtz coils and shielding.

### 6.5.1 *Gradiometer sensor design for focused flow*

The gradiometer sensor was redesigned to better match the aspect ratio of the nanowire to the gradiometer using the focus flow microfluidic channel. The focus flow microfluidic channel allows for a variable controlled channel flow in the order of 100 µm. The redesign included reducing the YOKE sensor length from 400 µm to 200 µm and reducing distance between the gradiometer Yoke sensor pair from 20 µm to 10 µm as discussed in Chapter 3 Section 3.2.3. The focused flow channel design is shown in Figure 6.36. The channel has dimensions width 800 µm x height 30 µm and length 14 mm. The external dimensions are 27 mm x 19.7 mm. It has an adhesive bottom layer which fixes to the sensor. The focused flow requires a second microfluidic pump, one for the main sheet flow and the second to

achieve the focused flow in the channel. The focused flow channel was configured as per the procedure detailied in Appendix 8 Section 8.7.11.

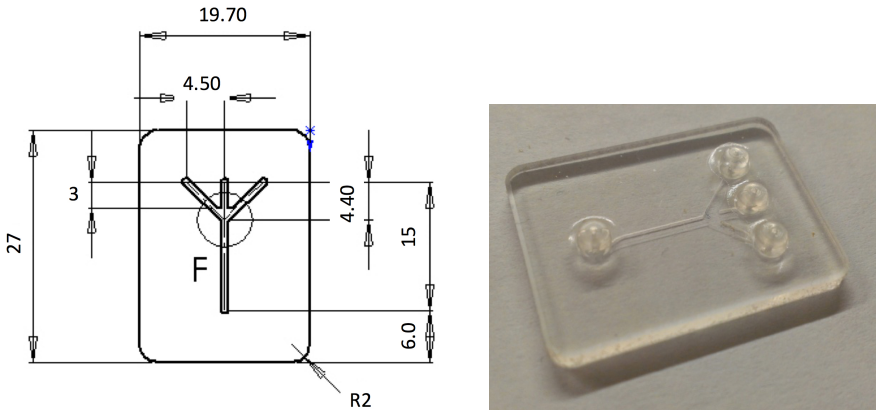



Figure 6.36: Focused Flow channel design and device

### 6.5.2 *Detection system integration into the sensor interface*

Integrating the electronics a revised sensor interface would enable the pre-amplifiers to be placed closer to the gradiometer sensor reducing cable length and assist in the noise reduction. Also it would allow for easier integration of miniature bias/calibration coils and shielding.

The detection system electronics layout was redesigned to incorporate all the differential pre-amplifiers and post-amplifiers for the two gradiometer sensor pairs labeled Sensor side A and B. Figure 6.37 shows the schematic of the integrated detection system. The overall gain of the amplification system was set at 10,000 (80dB). The high pass filter (70 Hz) was impedance matched to the pre-amplifier. The post amplifier was replaced with an INA103 and incorporated at low pass filter (75 KHz). The current circuit allow for adjustment and balance of the current supplies to each respective sensor. The new design incorporated test points, which allowed the phase response of the sensor to be checked, also adjustment of the sensor phase response. This is used in the gradiometer balancing process.

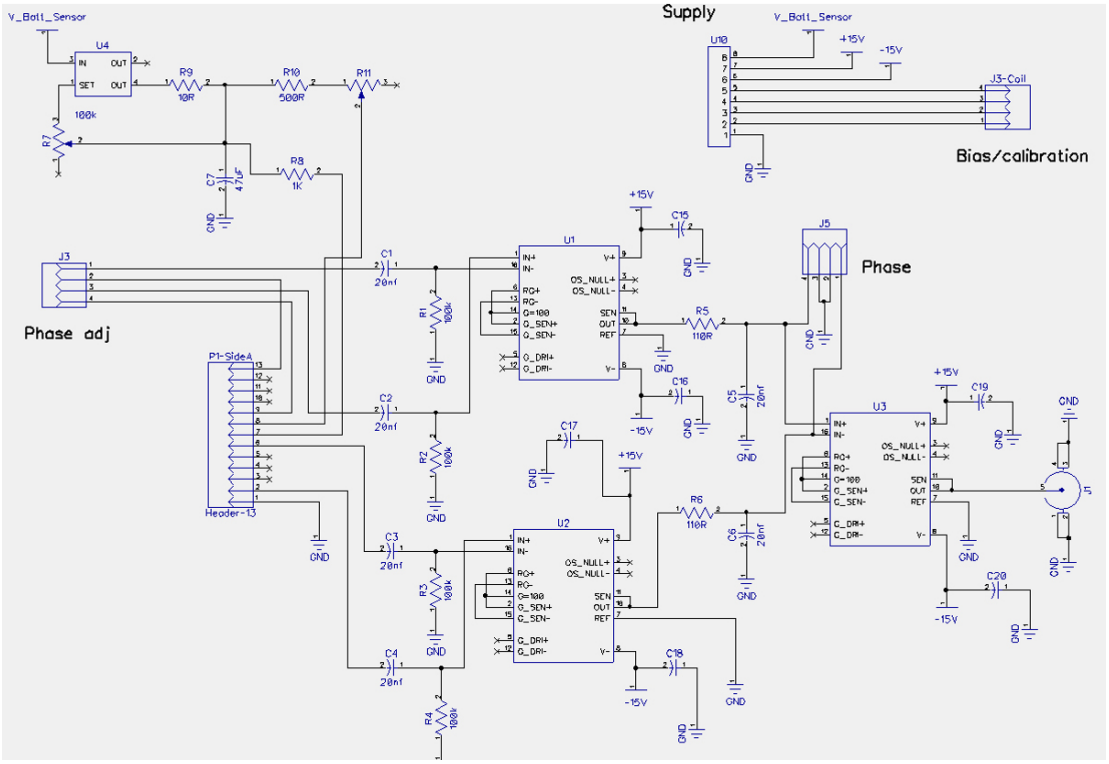



Figure 6.37: Revised schematic for optimised gradiometer

The sensor interface was redesigned to allow the new integrated electronic design layout and the miniature bias/calibration Helmholtz coils to fit. Figure 6.38(a) shows the final optimised gradiometer which fits under a standard microscope (b) with the top shielding cover in place. The phase check test points and adjustments are indicated. The optimised gradiometer is powered by a battery pack via the main input connector, which also provides connections for the Helmholtz coils. There are two output SMA connections for the respective gradiometer sensor side A and B.

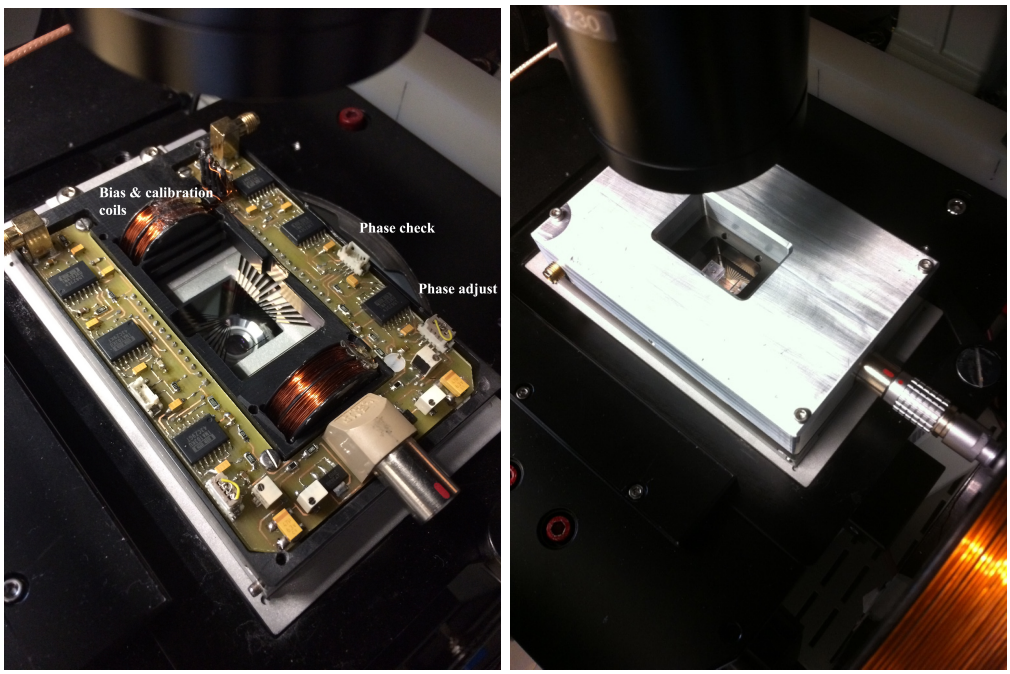



Figure 6.38: Revised gradiometer & fitted with shield under microscope

The two pairs Helmholtz coils integrated into the chip carrier allow firstly for a small bias field to be applied to the sensor in the order of 2 mT, which will better optimise the sensitivity of the sensor. Secondly the sensor response can be calibrated using the second gradient Helmholtz coil. The coils are diameter 26 mm and width 5 mm, they have 450 turns and measured 12.4 ohm. The distance between the coils is 50 mm.

### 6.5.3 *Balanced optimised gradiometer response*

The optimised gradiometer was balanced as per the procedure discussed in Section 6.3. Figure 6.39 shows the magnetoresistive response of two sensors in the gradiometer pair for GMR sensor. The magneto-resistance response measured 5.5% respectively and each sensor had a good linear response comparably matched which allows for optimum balancing and noise cancelation.

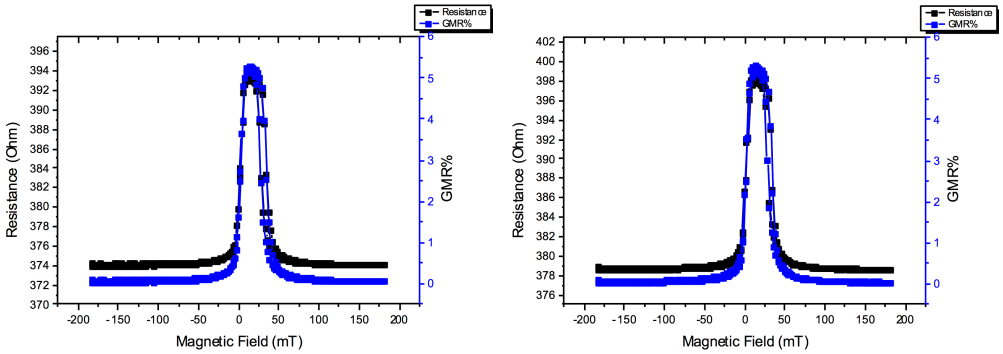



Figure 6.39: GMR- magnetoresistive response of Gradiometer Sensor 1 & 2

To balance the gradiometer response, a bias signal is applied via the TTI function generator at 125 Hz/2.2 V pk-pk into a Kepco bidirectional amplifier which was set to -18 V/0.7 Amp to the Helmholtz coil pair. Figure 6.40 details the measured response of the gradiometers using an oscilloscope. The oscilloscope trace shown in yellow (Oscilloscope channel 1), shows the bias signal applied to the Helmholtz coils which measured at 125 Hz 240 mV. Using a gauss-meter placed at the sensor area centre of Helmholtz coils, the field measured 1.6 mT.

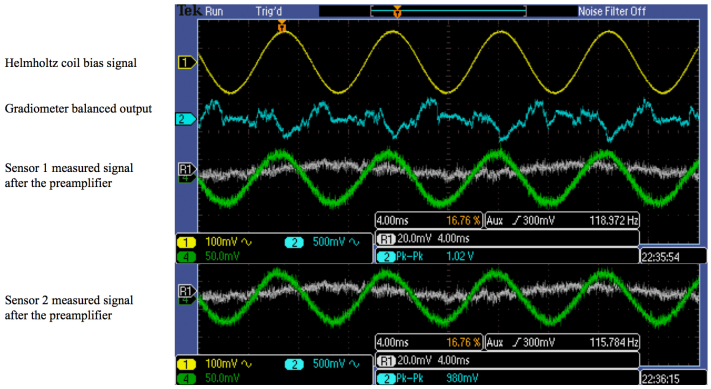



Figure 6.40: Measured result of balanced optimised gradiometer; trace 1 (yellow) applied bias signal, traces 4 (green) sensor 1 & 2 response after the preamplifier stage and trace 2 (blue) the overall balanced Gradiometer output response after the post-amplifier

The two trace's shown in green (Oscilloscope channel 4) show the measured response to the applied bias signal from the Sensors 1 and 2 of the gradiometer after the preamplifier stag,e which has a gain of 100. Using the variable potentiometer R19 in the current circuit the measured signals from Sensors 1 and 2 can be balanced or best matched. For noise or signal cancelation, both of the measured signals from Sensor 1 and 2 need to be in-phase. The balanced signals from sensors 1 and 2, after the preamplifier measured

at 120 mV and 100 mV respectively. The trace shown in blue (Oscilloscope channel 2) shows the overall balanced Gradiometer output response after the post-amplifier with an overall gain of 10,000. The balanced output from the gradiometer measured 980 mV (In-phase) and 22 V (Out of phase) providing a ratio 22:1.

### 6.5.4 *Optimised gradiometer field calibration*

The optimised gradiometer sensor was calibrated to show the response in magnetic field as per the procedure outined in Chapter 5 Section 5.8.1. Table 6.12 details the gradiometer sensor calibration conditions measured.

| **Calibration: Gradiometer focus flow sensor configuration** | |
|---|---|
| $\mathcal{U}_{csr}$ (Coil response) | 9.50 $mV\ pk-pk$ (CSR-current sensing resistor) |
| $\mathcal{U}_{amp}$ (Sensor response) | 8.50 $V\ pk-pk$ |
| $\mathcal{U}_{csr}bias$ | 519.17 $mV\ pk-pk$ |
| | |
| Field calibration bias | 1.60 mT (Optimum bias) |
| | |
| $Cal_{amp}$ (Cal constant) | $\frac{Sensor\ response\ Volt \times Coil\ response\ Volt}{Coil\ response\ Volt\ max \times Bias\ mT} = 123.6\ V/mT$ |
| $\mathcal{U}_{Sensor\ cal\ factor}$ | $\frac{1}{338.4\ V/mT} = 28\ \mu T/V$ |

Table 6.12: Calibration conditions measured for Gradiometer focus flow sensor configuration

### 6.5.5 *Optimised gradiometer noise measurement*

Noise measurment of the balanced optimised gradiometer sensor response were carried out. Figure 6.41 (a) shows the background noise response recorded with no deionised water flowing through the fluidic channel, the noise measured 0.095 Vdc at a gain of 10,000. With the calibration field constant applied, this measured at 2.5 μT. This provides a further improvement over the noise measured using the gradiometer configuration by a factor of 1.4. Figure 6.41 (b) shows the background noise response recorded with deionised water flowing through the fluidic channel, the noise measured 0.1 Vdc. With the calibration field constant applied, this measured at 2.6 μT.

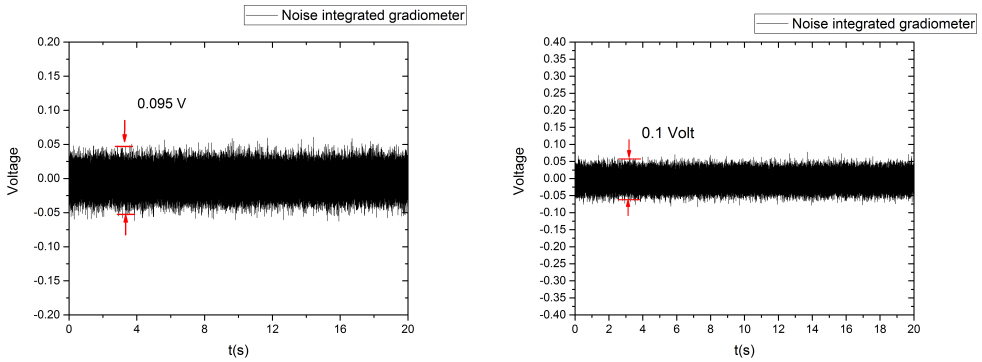



Figure 6.41: (a) background noise response measured in optimised gradiometer sensor configuration GMR-081215 (b) background noise response measured with deionised water flowing

The optimised gradiometer reduces the background by a factor of 4.5 over the single sensor configuration. The overall improvement in the background noise is highlighted in Figure 6.42 which shows the noise comparison between the single sensor configuration and the optimised gradiometer configuration.

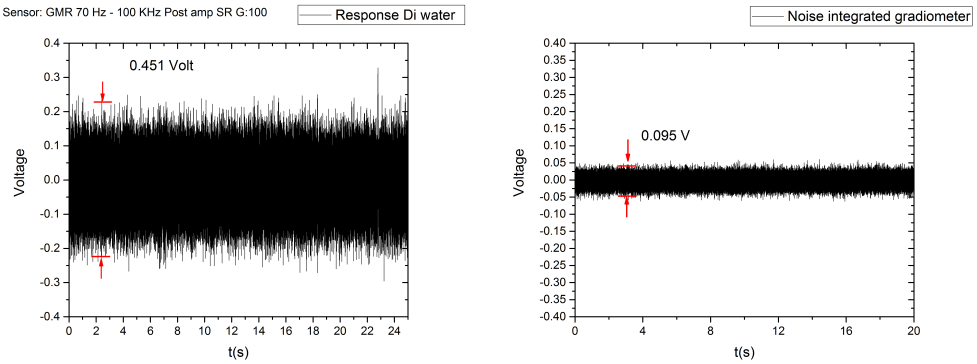



Figure 6.42: Background noise comparison between single sensor configuration and optimised gradiometer configuration

Ultimately the noise cancelation and improved signal to noise ratio completely relies on each of the GMR sensors in the gradiometer pair having a good linear magnetoresistance response that are comparably matched. Large variations in the gradiometer sensor pair will lead to a higher background noise.

## 6.6 NANOWIRE DETECTION EXPERIMENTS USING OPTIMISED GRADIOMETER CONFIGURATION

A number of nanowire detection experiments were carried out to determine the improvement using the optimised gradiometer configuration. The focused flow channel has a geometry of width 800µm, height 30 µm & length 14mm. The nanowires are injected into the channel using a controlled syringe micro-pump "Miros".

### 6.6.1 *CoNi Nanowire detection using the optimised gradiometer - 101215-1*

The balanced optimised gradiometer discussed in Section 6.2.3 was used for the nanowire detection experiment The sensor was passivated with $Si_3N_4$ 150 nm to protect it from microfluidics during the experiment. Details of CoNi nanowires batch: 101215 used in the experiment are detailed in Table 6.43.

| Sample | Segment | Type | Pot (V) | Time (Sec) | I (mA) | Charge (Q) | Length (um) | OCP (V) | Mag (T) |
|---|---|---|---|---|---|---|---|---|---|
| 101215-1 | CoNi | | -0.9 | 5500 | 7.8 | 38 | 8 | 0.11 | 1.2 |

Figure 6.43: 101215-1 CoNi nanowire sample deposition conditions

Table 6.44 shows the conditions used to dissolve the nano-wires from membrane.

| Sample | Type | Solution (1molar) | Temp ($^0$C) | Method | Weight (g) |
|---|---|---|---|---|---|
| 101215 | CoNi | Na0H | 70 | Min 3/sonication 10sec, Min 5/ sonication 10sec, Min 11/ sonication 10sec, stop, Rinse in DI water x 6 using magnet | 0.0933 |

Figure 6.44: 101215-1 CoNi nanowire sample condition used to dissolve from membrane

The microscope inspection image of the nanowires prior to dispensing as shown in Figure 6.45. This showed better separation of nanowires, but still some bunching together.

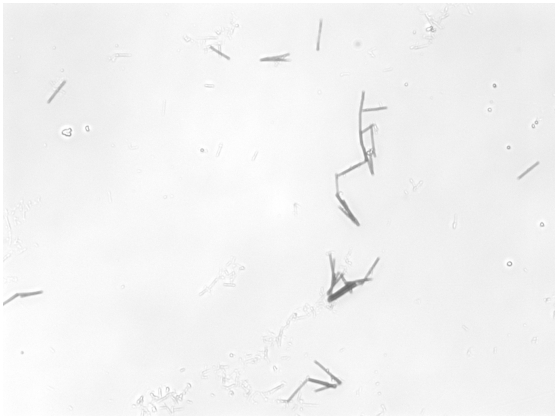


Figure 6.45: Image of nanowire batch 101215 CoNi before dispensing

For the experiment 0.06 µg of CoNi nanowires, which approximates to ~ 1,400 nanowires as per the nanowire experiment preparation procedure detailied Appendix 8 Section 8.7.10, are were dispensed across the sensor at a velocity of 20 mm/s. The detected response of the CoNi nanowires batch: 101215 flowing across the sensor is shown in Figure 6.46 . The CoNi nanowires are dispensed after the first 10 seconds and stopped after 20 second time period. During the time period when nanowires are dispensed. The detected responses are recorded.

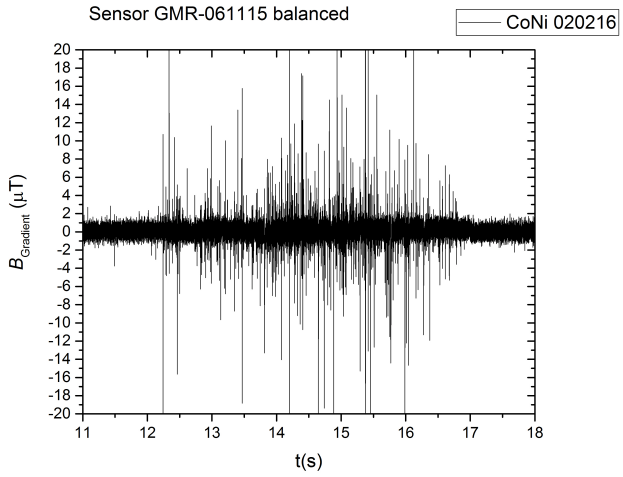



Figure 6.46: Detected response of the CoNi nano-wires flowing across optimised gradiometer sensor

Figure 6.47 highlights in details some of the detected events. The magnitude of the detected signals range from 4 µT to 40 µT with a response times of 0.6 ms to 0.8 ms.

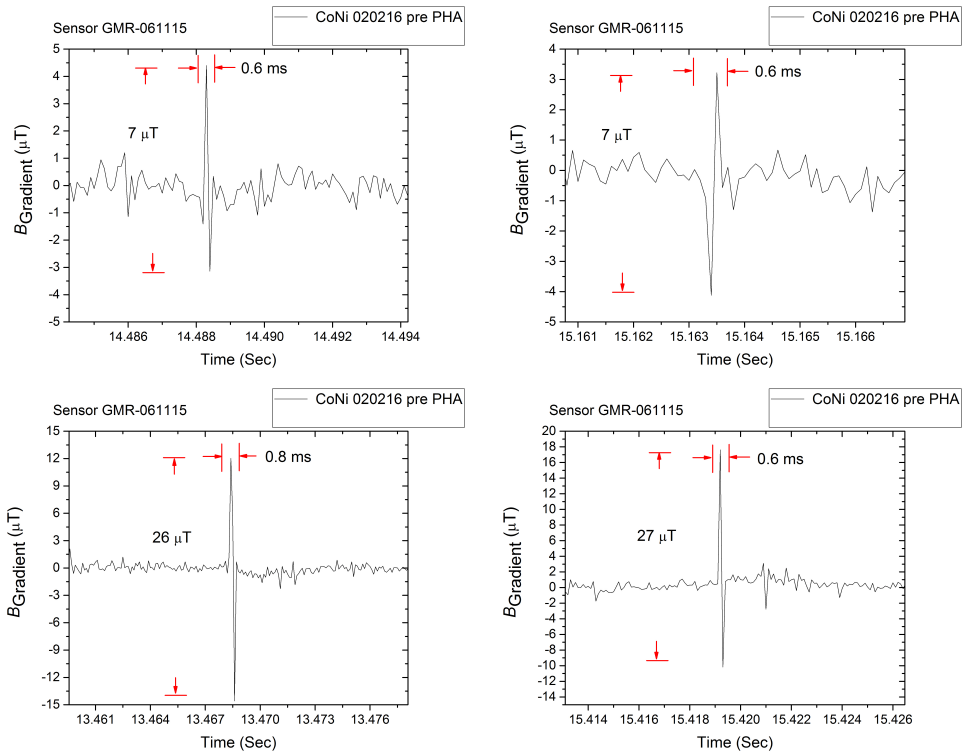



Figure 6.47: Detected events of CoNi batch 101215 wire flowing across sensor

The nanowires are flowing at a velocity of 20 mm per second within the microfluidic channel. For a 10 µm nanowire traveling a across a 5 µm sensor (width) the expected response time is in the order of 0.6 ms. There are a number of detected events with response times of 0.6 ms. The detected nanowires vary in amplitude with the same time response, indicating the nanowires are traveling at different heights within the microfluidic channel. The nanowires are also traveling in different orientations and angles as they pass over the gradiometer sensor, as we see variations in the detected polarity response magnetudes and also different polarity directions. This is also incidacted in the optical camera image shown in Figure 6.48, which shows nanowires traveling in different orientations and angles as they pass over the optimised gradiometer sensor.

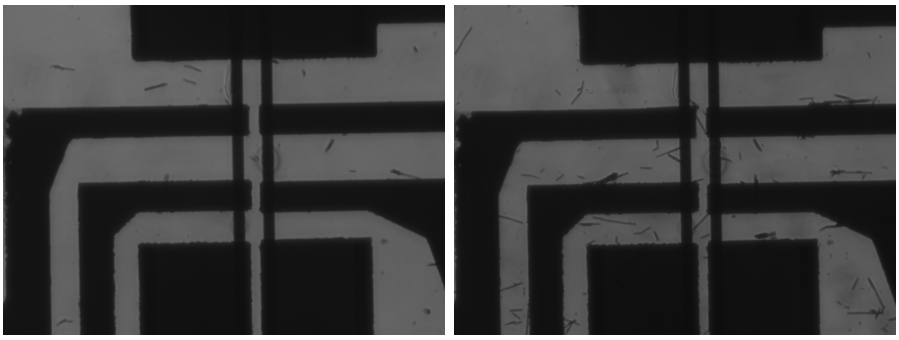


Figure 6.48: CoNi batch 101215 single segment nano-wires flowing across GMR sensor gradiometer configuration focus flow microfluidic channel

A post statistical analysis was carried out on the captured data using the Pulse height amplification (PHA) routine. Figure 6.49 shows the PHA model fitting with the experimental detected response.

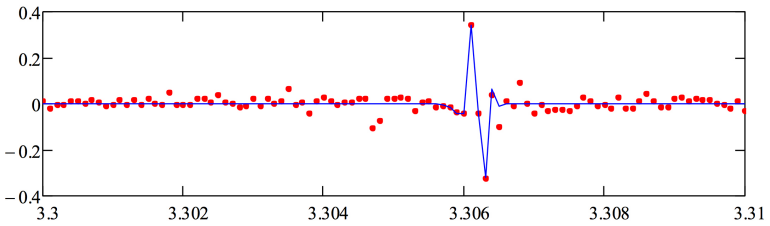



Figure 6.49: CoNi batch 101215 model fitting to experimental data

The PHA suppressed the background noise by a factor of 1.892. Figure 6.50shows a plot of detected nanowire events during the experiment extracted as single amplitudes. The upper and lower threshold was adjusted to exclude the noise contribution.

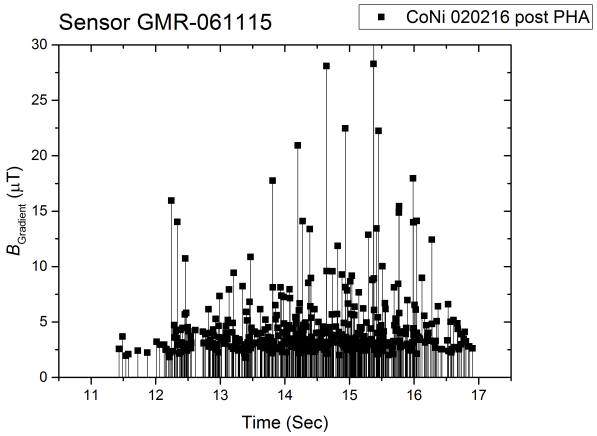



Figure 6.50: Detected nanowire events CoNi batch 101215 during the experiment extracted as signal amplitudes post PHA

A post statistical analysis of the extracted nanowire detected events are shown in the bar chart in Figure 6.51 . The bar chart shows the number of detected nanowire events per field. The total count of nanowires detected was 480. The field of the nanowires detected were in the range of 2 to 28 µT after the PHA.

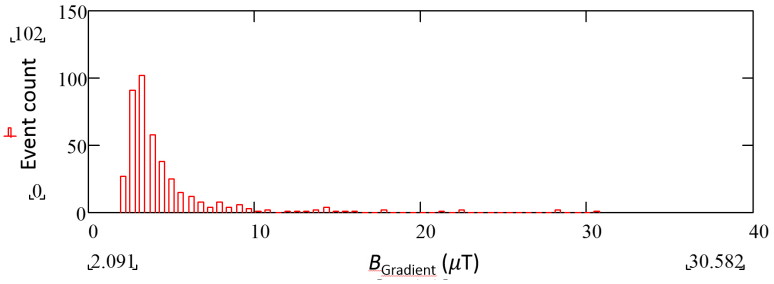



Figure 6.51: Number of detected nanowire events per field for CoNi batch 101215

Comparing this to the modelled response of CoNi nanowires shown in Figure 5.5, the majority of nanowires are traveling at a height in the order of 7 to 10 µm in the microfluiduc channel.

### 6.6.2 *CoNi Nanowire detection using the optimised gradiometer - Batch 130116*

The balanced optimised gradiometer discussed in Section 6.2.3 was used for the nanowire detection experiment. The sensor was passivated with $Si_3N_4$ 150 nm to protect it from microfluidics during the experiment. Details of CoNi nanowire batch: 130116 used in the experiment are detailed in Table 6.13.

| Sample | Segment | Type | Pot (V) | Time (Sec) | Current (mA) | Charge (Q) | Length (um) | OCP (V) | Mag (T) |
|---|---|---|---|---|---|---|---|---|---|
| 130116 | CoNi | | -0.9 | 5000 | 6.2 | 31 | 9 | 0.10 | 1.2 |

Table 6.13: 130116 CoNi nanowire sample deposition conditions

Table 6.14 shows the conditions used to dissolve the nanowires from membrane.

| Sample | Type | Solution (1molar) | Temp ($^0$C) | Method | Weight (g) |
|---|---|---|---|---|---|
| 130116 | CoNi | NaOH | 70 | Min 3/sonication 10 sec, Min 6/ sonication 10 sec, Min 11/ sonication 10 sec, stop, Rinse in DI water x 6 using magnet | 0.0946 |

Table 6.14: 130116 CoNi nanowire sample condition used to dissolve from membrane

For the experiment 0.05 µg of CoNi nanowires, which approximates to ~ 1,100 nanowires as per the nanowire experiment preparation procedure detailied Appendix 8 Section 8.7.10, are were dispensed across the sensor at a velocity of 15 mm/s. The detected response of the CoNi nanowires batch: 130116 flowing across the sensor is shown in Figure 6.52.

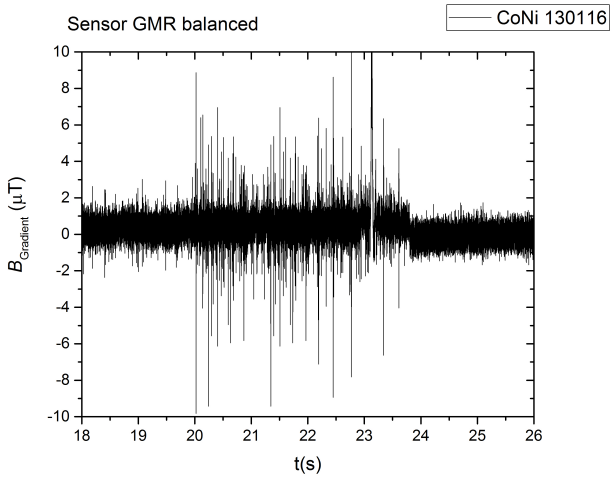



Figure 6.52: Detected response of the CoNi 130116 nano-wires flowing across optimised gradiometer sensor

Figure 6.53 highlight in details some of the detected events. The magnitude of the detected signals range from 4 µT to 18 µT with a response times of 0.5 ms to 1 ms.

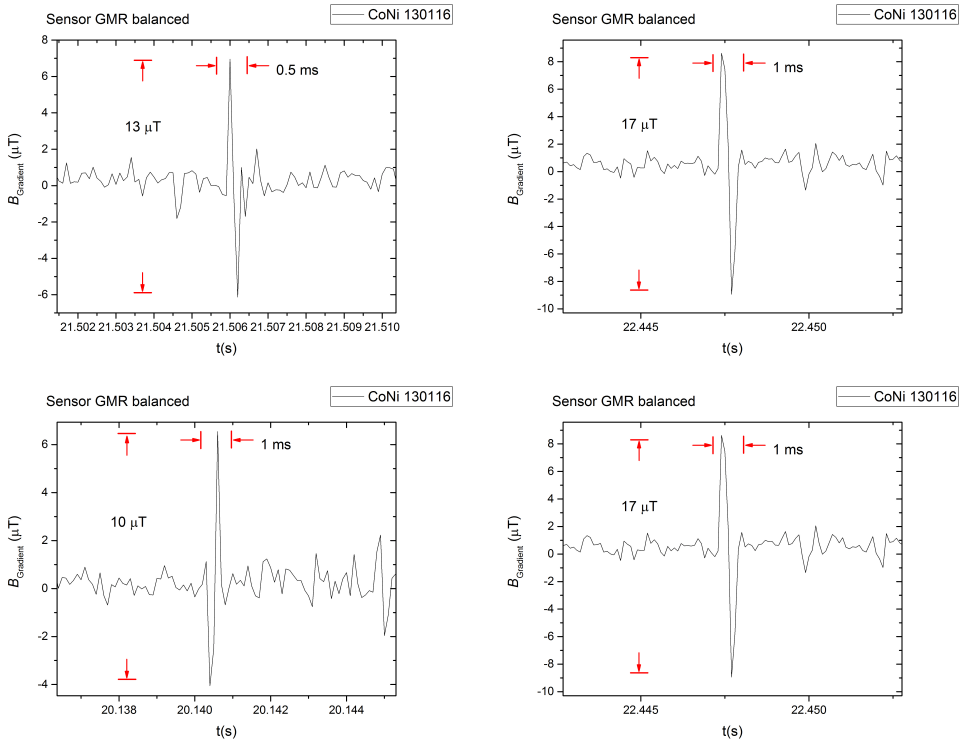



Figure 6.53: Detected events of CoNi batch 130116 wire flowing across sensor

There are a number of detected events with response times of 1 ms, which is expected for a flow velocity rate of 15 mm/s. The detected nanowires vary in amplitude with the same time response, indicating the nanowires are traveling at different heights within the microfluidic channel. The nanowires are also traveling in different orientations and angles as they pass over the gradiometer sensor, as we see variations in the detected polarity response magnetudes and also different polarity directions. This is also incidacted in the optical camera image shown in Figure 6.54, which shows nanowires traveling in different orientations and angles as they pass over the optimised gradiometer sensor.

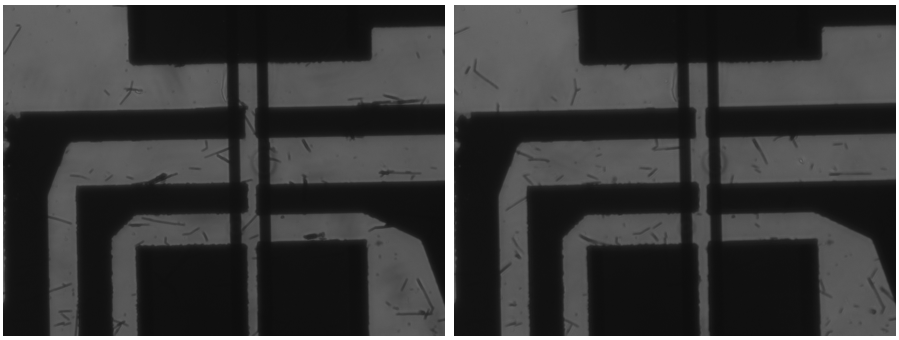


Figure 6.54: CoNi batch 130116 single segment nano-wires flowing across GMR sensor gradiometer configuration focus flow microfluidic channel

A post statistical analysis was carried out on the captured data using the Pulse Height Amplifier (PHA) routine. The PHA suppressed the background noise by a factor of 1.510. Figure 6.55shows a plot of detected nanowire events during the experiment extracted as single amplitudes. The upper and lower threshold was adjusted to exclude the noise contribution.

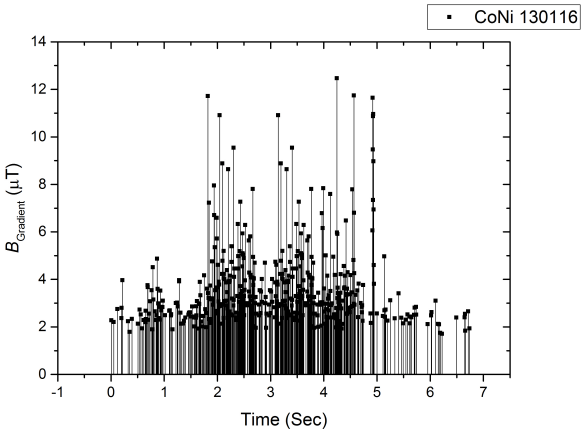



Figure 6.55: Detected nanowire events CoNi batch 130116 during the experiment extracted as signal amplitudes post PHA

A post statistical analysis of the extracted nanowire detected events are shown in the bar chart in Figure 6.56. The bar chart shows the number of detected nanowire events per field. The total count of nanowires detected was 460. The field of the nanowires detected were in the range of 2 to 13 µT after the PHA.

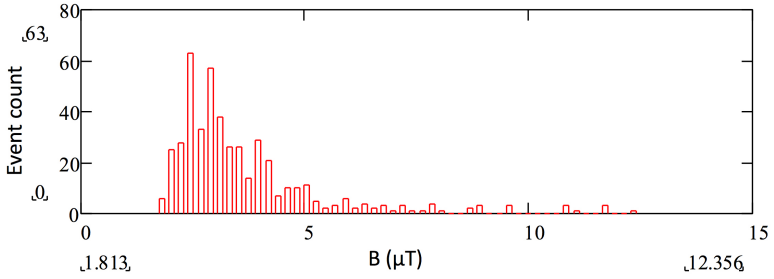



Figure 6.56: Number of detected nanowire events per field for CoNi batch 130116

Comparing this to the modelled response of CoNi nanowires shown in Figure 5.5, the majority of nanowires are traveling at a height in the order 10 µm in the microfluiduc channel. The optimisation of the gradiometer has provided a further noise reduction factor of 1.4 over the first gradiometer configuration. There is consistant detection of

nanowires comparable with the first gradiometer configuration. Table 6.60 shows a summary of CoNi nanowire detection experiments using the optimised gradiometer. Nanowire detection experiments were carried out towards the detection if two magnetic segment nanowires using CoNi-Cu-CoNi.

| Parameters | Response time (ms) | Velocity (mm/s) | Noise before PHA (μT) | PHA Noise suppression | PHA Nanowire count | Detected field range after PHA (μT) |
|---|---|---|---|---|---|---|
| Nanowire type: $Co_{65}Ni_{35}$ | 0.6 – 0.8 | 20 | 2.6 | 1.892 | 480 | 2 - 28 |
| Length: 8 μm | 0.5 – 1.0 | 15 | 2.6 | 1.510 | 460 | 2 - 13 |
| Dispensed: Microfluidic pump | | | | | | |
| Microfluidic channel: Height 30 μm | | | | | | |
| Sensor: Gradiometer GMR | | | | | | |

Table 6.15: Summary of CoNi nanowire detection experiments using the optimised gradiometer

### 6.6.3 *CoNi-Cu-CoNi Nanowire detection using the optimised gradiometer configuration - Batch 071215*

The gradiometer GMR sensors used in the experiment measured a magnetoresistance of 5.2% with a linear response and a sensitivity of 0.9%/mT. The sensor was passivated using $Si_3N_4$ with a thickness of 150 nm to protect it from microfluidics during the experiment. The background noise response recorded for the balanced gradiometer sensor measured at 0.11 Vdc. With the calibration field constant applied, this measured at 2.7 μT. Details of CoNi-Cu-CoNi nanowires batch: batch: 071215 used in the experiment are detailed in Table 6.16.

| Sample | Segment | Type | Pot (V) | Time (Sec) | I (mA) | Charge (Q) | Length (μm) | OCP (V) | Mag (T) |
|---|---|---|---|---|---|---|---|---|---|
| 071215 CoNiCuCoNi | CoNi | 1st mag seg | -0.9 | 2500 | 6.0 | 15 | 3 | 0.12 | 1.2 |
| | CoNiCu | Interlayer | -0.7 | 3 | 40 | | | | |
| | | | -0.6 | 3 | 20 | | | | |
| | Cu | Spacer | -0.4 | 3 | 15 | | | | |
| | | | -0.2 | 600 | 11 | 20 | 3.5 | | |
| | CoNi | 2nd mag seg | -0.9 | 2500 | 6.1 | 15 | 3 | | |

Table 6.16: 071215 CoNi-Cu-CoNi nanowire sample deposition conditions

Table 6.17 shows the conditions used to dissolve the nano-wires from membrane.

| Sample | Type | Solution (1molar) | Temp ($^0$C) | Method | Weight (g) |
|---|---|---|---|---|---|
| 071215 | CoNi-Cu-CoNi | Na0H | 70 | Min 4/sonication 10 sec, Min 8/ sonication 10 sec, Min 10 stop, Rinse in DI water x 6 using magnet | 0.0913 |

Table 6.17: 071215 CoNi-Cu-CoNi nanowire sample condition used to dissolve from membrane

For the experiment 0.05 µg of CoNi nanowires, which approximates to ~ 1,100 nanowires as per the nanowire experiment preparation procedure detailied Appendix 8 Section 8.7.10, are were dispensed across the sensor at a velocity of 15 mm/s. The detected response of the CoNi nanowires batch: 071215 flowing across the sensor is shown in Figure 6.57.

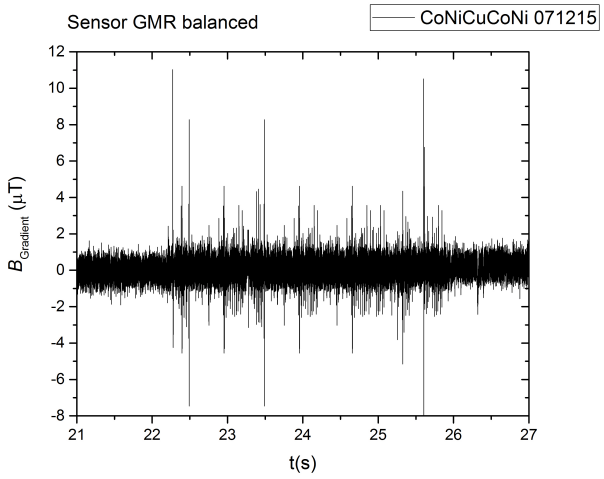



Figure 6.57: Detected response of the CoNi-Cu-CoNi 071215 nano-wires flowing across optimised gradiometer sensor

Figure 6.58 highlight in details some of the detected events. The magnitude of the detected signals range from 4 µT to 18 µT with a response times 1 ms.

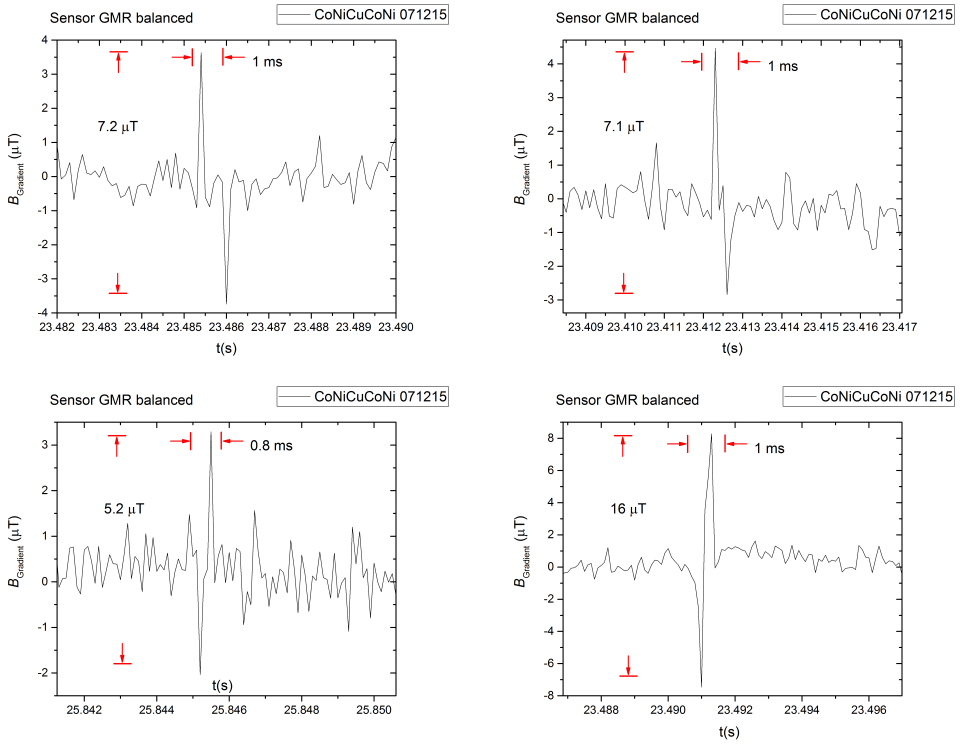



Figure 6.58: Detected events of CoNi-Cu-CoNi batch 071215 wire flowing across sensor

The magnitude and time response time of the detected signal indicate detection of individual nanowires. A number of detected events the transition between the axial positions of the nanowires dipole field is non-linear, compared to the response of a single segment CoNi response with is always linear. Suggesting possible detection of the non-magnetic segment within the CoNi-Cu-CoNi nanowires.

But this detected response was not prevalent for all detect events during the experiment, as shown in Figure 6.59.

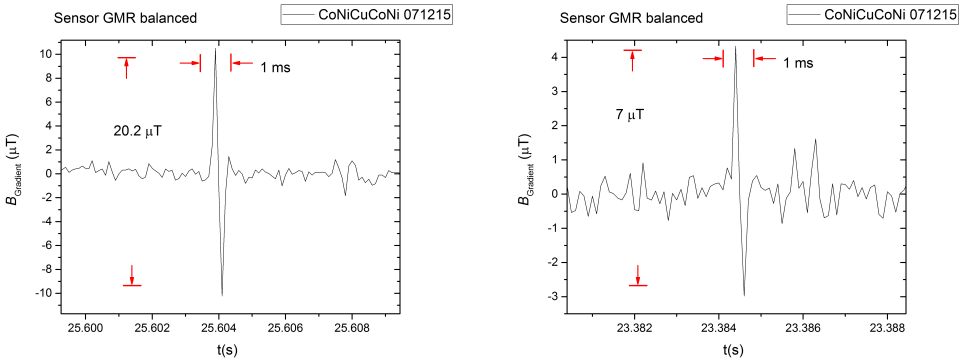



Figure 6.59: More detected events of CoNi-Cu-CoNi batch 071215 wire flowing across sensor

A post statistical analysis was carried out on the captured data using the Pulse Height Amplifier (PHA) routine. The PHA suppressed the background noise by a factor of 2.310. Figure 6.60 shows a plot of detected nanowire events during the experiment extracted as single amplitudes. The upper and lower threshold was adjusted to exclude the noise contribution.

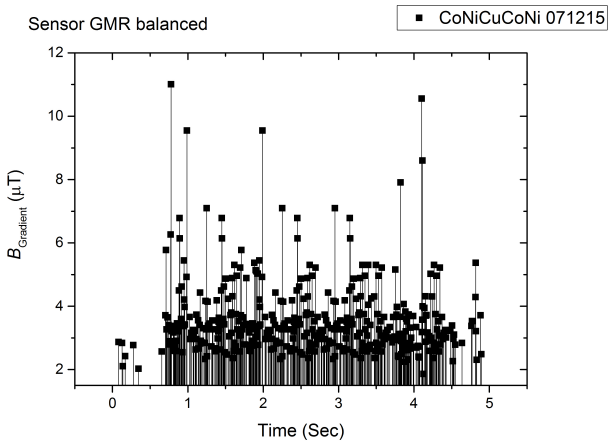



Figure 6.60: Detected nanowire events CoNi-Cu-CoNi batch 071215 during the experiment extracted as signal amplitudes post PHA

A post statistical analysis of the extracted nanowire detected events are shown in the bar chart in Figure 6.61. The bar chart shows the number of detected nanowire events per field. The total count of nanowires detected was 401. The field of the nanowires detected were in the range of 2 to 10 µT after the PHA.

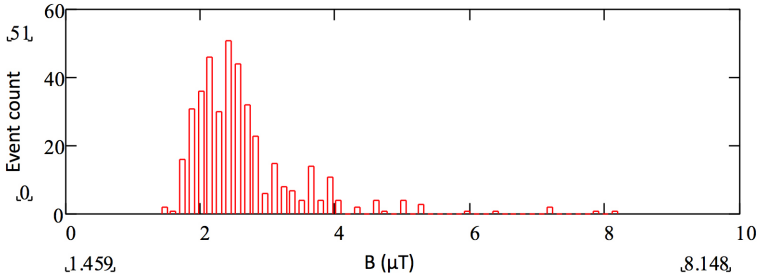



Figure 6.61: Number of detected nanowire events per field for CoNi-Cu-CoNi batch 071215

Comparing this to the modelled response of CoNi nanowires shown in Figure 5.5, the majority of nanowires are traveling at a height in the order 10 µm in the microfluiduc channel. A number of detected events the transition between the axial positions of the nanowires dipole field is non-linear, compared to the response of a single segment CoNi

response with is always linear. Suggesting possible detection of the non-magnetic segment within the CoNi-Cu-CoNi nano-wires. But this detected response was not prevalent for all detect events during the experiment. Table shows a summary of CoNi-Cu-CoNi nanowire detection experiments using the optimised gradiometer.

| Parameters | Response time (ms) | Velocity (mm/s) | Noise before PHA (μT) | PHA Noise suppression | PHA Nanowire count | Detected field range after PHA (μT) |
|---|---|---|---|---|---|---|
| Nanowire type: CoNi-Cu-CoNi | 0.8 – 1 | 15 | 2.7 | 2.310 | 401 | 2 - 10 |
| Length: 10 μm | 0.8 – 1 | 15 | 2.5 | 1.820 | 450 | 2 - 20 |
| Dispensed: Microfluidic pump | | | | | | |
| Microfluidic channel: Height 30 μm | | | | | | |
| Sensor: Gradiometer GMR | | | | | | |

Table 6.18: Summary of CoNi-Cu-CoNi nanowire detection experiments using the optimised gradiometer

## 6.7 CONCLUSIONS

The optimisation of the gradiometer including the integration of detection system electronics, impedance matching of the high pass filters to pre-amplifiers, integration of Helmholtz coils bias coils and shielding and also the optimisation of the gradiometer sensor configuration for focus flow with optimum sensor balancing has provided an improvement to the background noise by a factor of 4.5 over the noise measured using the single sensor configuration. Configuring the two sensors in a gradiometer pair has been very successful in reducing the background noise sufficiently for the detection of single segment magnetic nanowires.

The final detection experiments of the two-magnetic-segment nanowires indicated detection of the non-magnetic segment in some of the detected events. The final optimized gradiometer with focused flow allows for a higher probability of individual nanowires to flow across the sensor. This detected response was not prevalent for all detected events during the experiment and not repeatable over a number of CoNi-Cu-CoNi two magnetic segment detection experiments. The issues are mainly nanowire related. Firstly it is difficult to separate the two magnetic segment nanowires from the membrane, while keeping the segmented nanowire integrity. There are breakages within the segments, clumping of nanowires still in alumina membrane. The situation is further complicated by the fact that the two magnetic segment nanowires are effectively frequency doubling

and the nanowires adhere together. It is difficult to successfully pass a two-magnetic segment nanowires across the gradiometer and to ultimately differentiate them from single segment magnetic nanowires. This leads to a low probability for detection of multi-segmented nanowire using this scheme, which is time and amplitude dependent.

# 7

# CONCLUSIONS AND FUTURE WORK

## 7.1 CONCLUSIONS

YOKE shape GMR spin-valve sensors were successfully fabricated on a glass substrate to facilitate optical analysis of the nanowires. The sensors provided a good linear GMR response of 7.3%, with a sensitivity of 0.8%/mT and a noise level field detectivity 13.5nT/$\sqrt{Hz}$ @ 10Hz. These sensors were suitable for application of the detection of magnetic nanowires flowing in the microfluidic channel. A YOKE shape TMR sensor based on an MgO barrier magnetic tunnel junction was also successfully fabricated as an alternate sensor option. The sensor provided a good linear TMR response of 130% with field detectivity 4.8nT/$\sqrt{Hz}$ at 10Hz. A number of nanowires were investigated throughout the study. Both single segment cobalt nickel (CoNi) nanowires and two magnetic segment nanowires using CoNi segments separated by a copper (Cu) non-magnetic spacer layer (CoNi -Cu-CoNi) were produced, providing suitable nanowires for the detection experiments using GMR sensors. Throughout the study a number of iterations of the nanowire detection system have been developed to improve the signal to noise ratio and the detection of nanowires. From the first iteration using a single sensor configuration, which achieved nanowire detection but we observed a high background noise compared to the detected signal. Configuring two GMR sensors as gradiometer increased the signal to noise by factor of 4.5 and puts us in the range for the detection of single segment magnetic nanowires. Reducing the thickness of the sensor passivation layer to 150 nm using RF sputtered $Si_3N_4$, and final optimisation of gradiometer including, integration of the detection electronics, bias/calibration coils and shielding. Redesigning the GMR gradiometer sensor to better match the aspect ratio of the nanowire length and better suit the microfluidic focus flow channel, optimisation of gradiometer including, integration of the detection electronics, impedance matching

the filter to the preamplifier, integration of the bias/calibration coils and shielding. Has provided further improvements to the signal-to-noise ratio and brought us to the point were we are more within the range for the detection of single individual nanowires.

The final nanowire experiments re-confirm the detection of the short single metal magnetic nanowires. The final detection experiments of the two-magnetic-segment nanowires indicate detection of the non-magnetic segment within the two-magnetic-segment nanowires in some of the detected events. The optimized gradiometer with focused flow allows for a higher probability of individual nanowires to flow across the sensor. This detected response was not prevalent for all detected events during the experiment and not repeatable over a number of two-magnetic-segment nanowire detection experiments. The issues are mainly nanowire related. Firstly it is difficult to separate the two magnetic segment nanowires from the membrane, while keeping the segmented nanowire integrity. There are breakages within the segments, clumping of nanowires still in alumina membrane. It is difficult to successfully pass a two-magnetic segment nanowires across the gradiometer and to ultimately differentiate them from single segment magnetic nanowires. This leads to a low probability for detection of multi-segmented nanowire using this scheme, which is time and amplitude dependent.

Although there cannot be reliable detection of multi-segmented nanowires, the detection of short nanowires is completely reliable with respect to orientation or the height at which they flow in the microfluidic channel. The final iteration of the test bed provides flow cytometry counting using suitable functionalized nanowires. If commercial this would provide a cost effective and reliable in-vitro in-field diagnostic method applicable to applications such as early cancer detection.

## 7.2 FUTURE WORK

An alternate approach towards the detection of multi-segmented nanowires could be frequency-dispersive using the spin-valve sensor configured as a resonant detector in the form of a spin torque oscillator. This approach will allow detection of single segment nanowires via a shift in the devices resonant frequency. It will also allow detection

of multi-segmented nanowires by tuning the individual segments with in the multi-segmented nanowires via different composition ratios and shape anisotropy. Thereby producing a unique resonant signature for each multi-segmented nanowire.

Spin torque oscillators (STO) are broadband microwave signal generators sensitive to external fields. Using GMR or TMR magnetoresistance trilayer stack configurations, these devices will be fabricated as nano-pillars with diameter on the order of 100 nm. A direct current excites and controls the dynamic magnetic response via the spin transfer torque effect. They can be used as resonant detectors through the application of a.c. microwave frequency. Typically the STO devices require high TMR% ratio's, incorporating a perpendicular free layer with low product RA.

Measurements with the STO resonant detectors is potentially the only way to increase detection bandwidth, without dramatic microfluidic problems. Work is well underway on a working process for the fabrication and testing of spin torque oscillator-based resonant detectors. Appendix A discusses in detail the work to date including the basis of spin torque diode device, a literary review of the latest work in this area and my current developments on the implementation of the device.

# REFERENCES


[1] J. M. D. Coey. *Magnetism and Magnetic Materials*. Cambridge University Press, 2010.

[2] Coehoorn. R. Magnetic multilayers and giant magnetoresistance. *Springer Series in Surface Sciences*, 37:65–127, 2000.

[3] Donald R. Uhlmann W. David Kingery, H. K. Bowen. *Introduction to Ceramics, 2nd Edition*. Wiley, 1976.

[4] O. H.Wyatt and D. Dew-Hughes. *Metals Ceramics Polymers*. Cambridge University Press, 1974.

[5] C. D. Graham B. D. Cullity. *Introduction to Magnetic Materials, 2nd Edition*. Wiley-IEEE Press, 2008.

[6] K. Honda and S. Kaya. Magnetisation of single crystals of iron. *Science*, 1926.

[7] S. Kaya. On the magnetisation of single crystals of nickel. *Science*, 1927.

[8] S. Kaya. Magnetisation of single crystals of cobalt. *Science*, 1928.

[9] S. Yuasa and D. Djayaprawira. Giant tunnel magnetoresistance in magnetic tunnel junctions with a crystalline mgo (001) barrier. *Journal of Physics D: Applied Physics*, 40(21), 2007.

[10] M. Pannetier, C. Fermon, G.L Goff, J. Simola, and E Kerr. Femtotesla magnetic field measurement with magnetoresistive sensors. *Science*, 304(1648 - 1650):5677, 2004.

[11] Guanxiong Li, Vikram Joshi, Robert L. White, Shan X. Wang, and Jennifer T. Kemp. Detection of single micron-sized magnetic bead and magnetic nanoparticles using spin valve sensors for biological applications. *Journal of Applied Physics*, 93(10):7557 – 7559, 2003.

[12] Guanxiong Li, Shouheng Sun, Robert J. Wilson, Robert L. White, Nader Pourmand, and Shan X. Wang. Spin valve sensors for ultrasensitive detection of superparamagnetic nanoparticles for biological applications. *ens Actuators A Phys*, 126(1):98 106, 2006.

[13] J. Loureiro, R. Ferreira, and S. Cardoso. Toward a magnetoresistive chip cytometer: Integrated detection of magnetic beads flowing at cm/s velocities in microfluidic channels. *APPLIED PHYSICS LETTERS*, 95(034104):3, 2009.

[14] Fernandes. A Duarte. C Cardoso. F Bexiga. R Cardoso.S Freitas.P. Lab-on-chip cytometry based on magnetoresistive sensors for bacteria detection in milk. *sensors*, 2014.

[15] M. N. Baibich, J. M. Broto, A. Fert, F. Nguyen Van Dau, F. Petroff, P. Etienne, G. Creuzet, A. Friederich, and J. Chazelas. Giant magnetoresistance of (001)fe/(001)cr magnetic superlattices. *PHYSICAL REVIEW LETTERS*, 61(21):2472 –75, 1988.

[16] G. Binasch, P. Grunberg, F. Saurenbach, and W. Zinn. Enhanced magnetoresistance in layered magnetic structures with antiferromagnetic interlayer exchange. *Phys Rev B*, 39(7):4828, 1989.

[17] H. Ohno. Making nonmagnetic semiconductors ferromagnetic. *Science*, 281(5379):951–956, 1998.

[18] S. A. Wolf, D. D. Awschalom, R. A. Buhrman, J. M. Daughton, S. von Molnár, M. L. Roukes, A. Y. Chtchelkanova, and D. M. Treger. Spintronics: A spin-based electronics vision for the future. *Science*, 294(5546):1488–1495, 2001.

[19] A. Fert, A. Barthélémy, J. Ben Youssef, J.-P. Contour, V. Cros, J.M. De Teresa, A. Hamzic, J.M. George, G. Faini, J. Grollier, H. JaffrÃšs, H. Le Gall, F. Montaigne, F. Pailloux, and F. Petroff. Review of recent results on spin polarized tunneling and magnetic switching by spin injection. *Materials Science & Engineering B*, 84(1-2):1 – 9, 2001.

[20] I. A. Campbell, A. Fert, and R. Pomeroy. Evidence for two current conduction iron. *Philosophical Magazine*, 15(137):977–983, 1967.

[21] A. Fert and I. A. Campbell. Two-current conduction in nickel. *Phys. Rev. Lett.*, 21:1190–1192, Oct 1968.

[22] P. Grünberg, R. Schreiber, Y. Pang, M. B. Brodsky, and H. Sowers. Layered magnetic structures: Evidence for antiferromagnetic coupling of fe layers across cr interlayers. *Phys. Rev. Lett.*, 57:2442–2445, Nov 1986.

[23] N. F. Mott. The resistance and thermoelectric properties of the transition metals. *Proceedings of the Royal Society of London A: Mathematical, Physical and Engineering Sciences*, 156(888):368–382, 1936.

[24] J. S. Moodera, Lisa R. Kinder, Terrilyn M. Wong, and R. Meservey. Large magnetoresistance at room temperature in ferromagnetic thin film tunnel junctions. *Physical Review Letters*, 74(16):3273–3276, 1995. PRL.

[25] T. Miyazaki and N. Tezuka. Giant magnetic tunneling effect in fe/al2o3/fe junction. 139(3):231–234, 1995.

[26] S. Tehrani, E. Chen, M. Durlam, M. DeHerrera, J. M. Slaughter, J. Shi, and G. Kerszykowski. High density submicron magnetoresistive random access memory (invited). *Journal of Applied Physics*, 85(8):5822–5827, 1999.

[27] S. Ikeda, J. Hayakawa, Y. M. Lee, F. Matsukura, Y. Ohno, T. Hanyu, and H. Ohno. Magnetic tunnel junctions for spintronic memories and beyond. *IEEE Transactions on Electron Devices*, 54(5):991–1002, May 2007.

[28] S. S. P. Parkin, K. P. Roche, M. G. Samant, P. M. Rice, R. B. Beyers, R. E. Scheuerlein, E. J. O Sullivan, S. L. Brown, J. Bucchigano, D. W. Abraham, Yu Lu, M. Rooks, P. L. Trouilloud, R. A. Wanner, and W. J. Gallagher. Exchange-biased magnetic tunnel junctions and application to nonvolatile magnetic random access memory (invited). *Journal of Applied Physics*, 85(8):5828–5833, 1999.

[29] E. Yu. Tsymbal and D. G. Pettifor. Spin-polarized electron tunneling across a disordered insulator. *Phys. Rev. B*, 58:432–437, Jul 1998.

[30] E. Yu. Tsymbal and D. G. Pettifor. The influence of impurities within the barrier on tunneling magnetoresistance. *Journal of Applied Physics*, 85(8):5801–5803, 1999.

[31] Manish Sharma, Shan X. Wang, and Janice H. Nickel. Inversion of spin polarization and tunneling magnetoresistance in spin-dependent tunneling junctions. *Phys. Rev. Lett.*, 82:616–619, Jan 1999.

[32] P. LeClair, H. J. M. Swagten, J. T. Kohlhepp, R. J. M. van de Veerdonk, and W. J. M. de Jonge. Apparent spin polarization decay in cu-dusted Co/al$_2O_3$/Co tunnel junctions. *Phys. Rev. Lett.*, 84:2933–2936, Mar 2000.

[33] Jose Maria De Teresa, Agnès Barthélémy, Albert Fert, Jean Pierre Contour, François Montaigne, and Pierre Seneor. Role of metal-oxide interface in determining the spin polarization of magnetic tunnel junctions. *Science*, 286(5439):507–509, 1999.

[34] D. Bagrets, A. Bagrets, A. Vedyayev, and B. Dieny. Influence of s-d interfacial scattering on the magnetoresistance of magnetic tunnel junctions. *PA Journal*, 65(6):064430, 2002.

[35] J. M. MacLaren, X.-G. Zhang, W. H. Butler, and Xindong Wang. Layer kkr approach to bloch-wave transmission and reflection: Application to spin-dependent tunneling. *Phys. Rev. B*, 59:5470–5478, Feb 1999.

[36] W. H. Butler, X.-G. Zhang, T. C. Schulthess, and J. M. MacLaren. Spin-dependent tunneling conductance of Fe|MgO|Fe sandwiches. *Phys. Rev. B*, 63:054416, Jan 2001.

[37] J. Mathon and A. Umerski. Theory of tunneling magnetoresistance of an epitaxial fe/mgo/fe(001) junction. *Phys. Rev. B*, 63:220403, May 2001.

[38] William H Butler. Tunneling magnetoresistance from a symmetry filtering effect. *Science and Technology of Advanced Materials*, 9(1):014106, 2008.

[39] S.S.P. Parkin, C. Kaiser, A. PANCHULA, P.M. RICE, B. HUGHES, M. SAMANT, and S.H. YANG. Giant tunnelling magnetoresistance at room temperature with mgo (100) tunnel barriers. *Nature Materials*, 3(862 - 867), 2004.

[40] S. Yuasa and T. Nagahama. Giant room-temperature magnetoresistance in single-crystal fe/mgo/fe magnetic tunnel junctions. *Nature Materials*, 3:868, 2004.

[41] S. Ikeda, J. Hayakawa, Y. Ashizawa, Y. M. Lee, K. Miura, H. Hasegawa, M. Tsunoda, F. Matsukura, and H. Ohno. Tunnel magnetoresistance of 604diffusion in cofeb/mgo/cofeb pseudo-spin-valves annealed at high temperature. *Appl. Phys. Lett*, 93(082508):1 – 3, 2008.

[42] J.C. Slonczewski. Current-driven excitation of magnetic multilayers. *Journal of Magnetism and Magnetic Materials*, 159(1):L1 – L7, 1996.

[43] L. Berger. Emission of spin waves by a magnetic multilayer traversed by a current. *Phys. Rev. B*, 54:9353–9358, Oct 1996.

[44] G Rieger, K Ludwig, J. Hauch, and W. Clemens. Gmr sensors for contactless position detection. *Elsevier - Sensors and Actuators A: Physical*, 91:7 – 11, 2001.

[45] E. Nagaev. Lanthanum manganites and other giant-magnetoresistance magnetic conductors. *Phys.-Usp*, 39(8):781, 1996.

[46] C. Tsang and R.E. Fontana. Magnetics of small magnetoresistive sensors. *JOURNAL OF APPLIED PHYSICS*, 55(6):2226 – 2231, 1984.

[47] P. P. Freitas, F. A. Cardoso, V. C. Martins, S. A. M. Martins, J. Loureir, J. Amaral, R. C. Chaves, S. Cardoso, L. P. Fonseca, A. M. Sebastia , M. Pannetier-Lecoeur, and C. Fermon. Spintronic platforms for biomedical applications. *RSC*, Lab Chip(12):546, 2012.

[48] M. Pannetier-Lecoeur, L. Parkkonen, N. Sergeeva-Chollet, H. Polovy, C. Fermon, and C. Fowley. Magnetocardiography with sensors based on giant magnetoresistance. *APPLIED PHYSICS LETTERS*, 98(15):3705, 2011.

[49] Matthew Sands Richard P. Feynman, Robert B. Leighton. *The Feynman Lectures on Physics*. Wesley, 1964.

[50] Carmen-Gabriela Stefanita. *Magnetism Basics and Applications*. Springer, 2012.

[51] Nolting Wolfgang Ramakanth Anupuru. *Quantum Theory of Magnetism*. Springer, 2009.

[52] Robert Resnick Robert Eisberg. *Quantum Physics of Atoms, Molecules, Solids, Nuclei, and Particles 2nd Edition*. Wiley, 1985.

[53] David J. Griffiths. *Introduction to Quantum Mechanics*. Pearson Education, 2004.

[54] Stancil Daniel Prabhakar Anil. *Spin Waves Theory and Applications*. Springer, 2009.

[55] N. F. Mott. The mechanical properties of metals. *Proceedings of the Physical Society. Section B*, 64(9):729, 1951.

[56] Abdesalem Houari and Mohamed A. Belkhir. Ab initio studies of magnetic properties of cobalt and tetracobalt nitride co4n. *Cond Mat Science*, 2015.

[57] G. A. Prinz. Stabilization of bcc co via epitaxial growth on gaas. *Phys. Rev. Lett.*, 54(10):1051–1054, March 1985.

[58] W. H. Meiklejohn and C. P. Bean. New magnetic anisotropy. *Physical Review*, 102(5):1413–1414, 1956. PR.

[59] W. H. Meiklejohn and C. P. Bean. New magnetic anisotropy. *Physical Review*, 105(3):904–913, 1957. PR.

[60] J. Nogue and I. Schuller. Exchange bias. *Journal of Magnetism and Magnetic Materials*, 192:203, 1999.

[61] W. Thomson. On the electro-dynamic qualities of metals. *Proc R Soc London*, 8:546, 1857.

[62] S Tumanski. *Thin Film Magnetoresistive Sensors (Series in Sensors)*. CRC Press, 2001.

[63] P. M. Tedrow and R. Meservey. Spin-dependent tunneling into ferromagnetic nickel. *Phys. Rev. Lett.*, 26:192–195, Jan 1971.

[64] Mary Beth Stearns. Simple explanation of tunneling spin-polarization of fe, co, ni and its alloys. *Journal of Magnetism and Magnetic Materials*, 5(2):167 – 171, 1977.

[65] M.N Baibich, J.M Broto, A. Fert, F.N.V. Dau, and F. Petroff. Giant magnetoresistance of (001)fe/(001)cr magnetic super- lattices. *Phys Rev Lett*, 61(21):2472, 1988.

[66] R K Nesbet. Giant magnetoresistance due to spin-dependent interface scattering. *Journal of Physics: Condensed Matter*, 6(31):L449, 1994.

[67] B Dieny. Classical theory of giant magnetoresistance in spin-valve multilayers: influence of thicknesses, number of periods, bulk and interfacial spin-dependent scattering. *J. Phys. Condens. Matler*, 4:8009 – 8020, 1992.

[68] B. L. Johnson and R. E. Camley. Theory of giant magnetoresistance effects in fe/cr multilayers: Spin-dependent scattering from impurities. *Phys. Rev. B*, 44:9997–10002, Nov 1991.

[69] Herman Bennett L. Watson R. E. *Magnetic Multilayers*. World Scientific, 1994.

[70] T. Valet and A. Fert. Theory of the perpendicular magnetoresistance in magnetic multilayers. *Phys. Rev. B*, 48:7099–7113, Sep 1993.

[71] Eric E. Fullerton, M. J. Conover, J. E. Mattson, C. H. Sowers, and S. D. Bader. 150% magnetoresistance in sputtered fe/cr(100) superlattices. *Applied Physics Letters*, 63(12):1699–1701, 1993.

[72] S. S. P. Parkin, R. Bhadra, and K. P. Roche. Oscillatory magnetic exchange coupling through thin copper layers. *Phys. Rev. Lett.*, 66:2152–2155, Apr 1991.

[73] W. H. Butler, X. G. Zhang, D. M. C. Nicholson, and J. M. MacLaren. Spin-dependent scattering and giant magnetoresistance. *Journal of Magnetism and Magnetic Materials*, 151(3):354–362, 1995.

[74] A Vedyayev, C Cowache, N Ryzhanova, and B Dieny. Quantum effects in the giant magnetoresistance of magnetic multilayered structures. *Journal of Physics: Condensed Matter*, 5(44):8289, 1993.

[75] C.B. Duke. Tunneling phenomena in solids. *Academic Press, New York*, 1969.

[76] J. C. Fisher and I. Giaever. Tunneling through thin insulating layers. *J. Appl. Phys.*, 32(172), 1961.

[77] John G. Simmons. Generalized formula for the electric tunnel effect between similar electrodes separated by a thin insulating film. *Journal of Applied Physics*, 34(6):1793–1803, June 1963.

[78] M. Julliere. Tunneling between ferromagnetic films. *Physics Letters*, 54A(3):225 – 226, 1975.

[79] J.S. Moodera, L.R. Kinder, T.M. Wong, and R. Meservey. Large magnetoresistance at room temperature in ferromagnetic thin- film tunnel junctions. *Phys Rev Lett*, 1995.

[80] Li Gao, Xin Jiang, See-Hun Yang, Philip M. Rice, Teya Topuria, and Stuart S. P. Parkin. Increased tunneling magnetoresistance using normally bcc cofe alloy electrodes made amorphous without glass forming additives. *Physical Review Letters*, 102(24):247205, 2009. PRL.

[81] Stuart S. P. Parkin, Christian Kaiser, Alex Panchula, Philip M. Rice, Brian Hughes, Mahesh Samant, and See-Hun Yang. Giant tunnelling magnetoresistance at room temperature with mgo (100) tunnel barriers. *Nat Mater*, 3(12):862–867, 2004. 10.1038/nmat1256.

[82] Y. M. Lee, J. Hayakawa, S. Ikeda, F. Matsukura, and H. Ohno. Effect of electrode composition on the tunnel magnetoresistance of pseudo-spin-valve magnetic tunnel junction with a mgo tunnel barrier. *Applied Physics Letters*, 90(21):212507, 2007.

[83] Jiang Lixian, Naganuma Hiroshi, Oogane Mikihiko, and Ando Yasuo. Large tunnel magnetoresistance of 1056based double barrier magnetic tunnel junction. *Applied Physics Express*, 2(8):083002, 2009.

[84] X-G Zhang and W H Butler. Band structure, evanescent states, and transport in spin tunnel junctions. *Journal of Physics: Condensed Matter*, 15(41):R1603, 2003.

[85] David D. Djayaprawira, Koji Tsunekawa, Motonobu Nagai, Hiroki Maehara, Shinji Yamagata, Naoki Watanabe, Shinji Yuasa, Yoshishige Suzuki, and Koji Ando. 230magnetic tunnel junctions. *Applied Physics Letters*, 86(9):092502, 2005.

[86] K. Tsunekawa M. Nagai H. Maehara. Cofeb/mgo/cofeb magnetic tunnel junctions with high tmr ratio and low junction resistance. *IEEE International,*, 2005.

[87] B Dieny and V.S. Speriosu. Giant magnetoresistive in soft ferromagnetic multilayers. *Phys. Rev. B*, 43(1):1297 – 1300, 1991.

[88] P.P. Freitas, R. Ferreira, S. Cardoso, and F. A. Cardoso. Magnetoresistive sensors. *19*, JOURNAL OF PHYSICS: CONDENSED MATTER(16):165221 – 21, 2007.

[89] S. S. P. Parkin, N. More, and K. P. Roche. Oscillations in exchange coupling and magnetoresistance in metallic superlattice structures: Co/ru, co/cr, and fe/cr. *Phys. Rev. Lett.*, 64(19):2304–2307, May 1990.

[90] B. Dieny, M. Li, S. H. Liao, C. Horng, and K. Ju. Quantitative interpretation of the magnetoresistive response (amplitude and shape) of spin valves with synthetic antiferromagnetic pinned layers. *Journal of Applied Physics*, 87(7):3415–3420, March 2000.

[91] Cardoso Susana Mukhopadhyay Subhas Chandra Reig, Candid. *Giant Magnetoresistance (GMR) Sensors*. Springer, 2013.

[92] C. Ren and X. Liu. Low-frequency magnetic noise in magnetic tunnel junctions. *Phys. Rev. B*, 69(104405):1 – 5, 2004.

[93] R Stearrett, W.G. Wang, L. R. Shah, J. Q. Xiao, and E. R. Nowak. Magnetic noise evolution in cofeb/mgo/cofeb tunnel junctions during annealing. *Appl. Phys. Lett.*, 97(243502):1 – 3, 2010.

[94] A. Krohn and C.W. Bohn. Electrodeposition of alloys: Present state of the art. *Electrodeposition and Surface Treatment*, 1(3):199 – 211, 1973.

[95] C.U. Chisholm. Cobalt-chromium coatings by electrodeposition: Review and initial experimental studies. *Electrodeposition and Surface Treatment*, 3(5):321 – 333, 1975.

[96] Larry R. Faulkner Allen J. Bard. *Electrochemical Methods: Fundamentals and Applications, 2nd Edition*. Wiley, 2001.

[97] H. Helmholtz. Studien ÃŒber electrische grenzschichten. *Annalen der Physik*, 243(7):337–382, 1879.

[98] Vladimir L. Shapovalov and Gerald Brezesinski. Breakdown of the gouy chapman model for highly charged langmuir monolayers counterion size effect. *The Journal of Physical Chemistry B*, 110(20):10032–10040, 2006. PMID: 16706462.

[99] O. Stern. Zur theorie der elektrolytischen doppelschicht. *Z. Elektrochem. Angew. Phys. Chem.*, 30:508–516, 1924. cited By 78.

[100] Hideki Masuda and Kenji Fukuda. Ordered metal nanohole arrays made by a two-step replication of honeycomb structures of anodic alumina. *Science*, 268(5216):1466–1468, 1995.

[101] Andreas Keilbach, James Moses, Ralf KÃ¶hn, Markus DÃ¶blinger, and Thomas Bein. Electrodeposition of copper and silver nanowires in hierarchical mesoporous silica/anodic alumina nanostructures. *Chemistry of Materials*, 22(19):5430–5436, 2010.

[102] N. Adeela, K. Maaz, U. Khan, S. Karim, M. Ahmad, M. Iqbal, S. Riaz, X.F. Han, and M. Maqbool. Fabrication and temperature dependent magnetic properties of nickel nanowires embedded in alumina templates. *Ceramics International*, 41(9 Part B):12081–12086, 2015.

[103] H. Zeng, R. Skomski, L. Menon, Y. Liu, S. Bandyopadhyay, and D. J. Sellmyer. Structure and magnetic properties of ferromagnetic nanowires in self-assembled arrays. *Phys. Rev. B*, 65:134426, Mar 2002.

[104] G. J. Strijkers, J. H. J. Dalderop, M. A. A. Broeksteeg, H. J. M. Swagten, and W. J. M. de Jonge. Structure and magnetization of arrays of electrodeposited co wires in anodic alumina. *Journal of Applied Physics*, 86(9):5141–5145, 1999.

[105] EV Sukovatitsina AV Ognev LA Chebotkevich SV Komogortsev AS Samardak F Nasirpouri M Nadi. Conversion of magnetic anisotropy in electrodeposited coni alloy nanowires. *Journal of Magnetism and Magnetic Materials*, 2015.

[106] M. S. Viqueira, N. Bajales, S. E. Urreta, and P. G. Bercoff. Magnetization mechanisms in ordered arrays of polycrystalline fe100 and co nanowires. *Journal of Applied Physics*, 117(20):204302, 2015.

[107] M. Darques, A. Bogaert, F. Elhoussine, S. Michotte, J. Medina, A. Encinas, and L. Piraux. Controlled growth of cocu nanowires and application to multilayered cocu/cu nanowires with selected anisotropy. *Journal of Physics D: Applied Physics*, 39:5025, 2006.

[108] Chinthaka P. Gooneratne, Ioanna Giouroudi, Cai Liang, and Jurgen Kosel. A giant magnetoresistance ring-sensor based microsystem for magnetic bead manipulation and detection. *J. Appl. Phys*, 109(07E517):3, 2011.

[109] J. Loureiro, P. Z. Andrade, S. Cardoso, C. L. da Silva, J. M. Cabral, and P. P. Freitas. Spintronic chip cytometer. *Journal of Applied Physics*, 109(7):07B311, 2011.

[110] B.W. Sheats, J.R. Smith. *Microlithography: science and technology.* New York: MARCEL DEKKER, INC., 1998.

[111] M. Pannetiera, C. Fermon, G.L. Goff, J. Simola, E. Kerr, and J.M.D. Coey. Noise in small magnetic systems applications to very sensitive magnetoresistive sensors. *Journal of Magnetism and Magnetic Materials*, 290:1158, 2004.

[112] J. Y. Chen and N. Carroll. Yoke-shaped mgo-barrier magnetic tunnel junction sensors. *APPLIED PHYSICS LETTERS*, 101(262402):4, 2012.

[113] Tobias Baier, Swati Mohanty, Klaus S. Drese, Federica Rampf, Jungtae Kim, and Friedhelm Schönfeld. Modelling immunomagnetic cell capture in cfd. *Microfluidics and Nanofluidics*, 7(2):205–216, Aug 2009.

[114] Y. C. Lim, A. Z. Kouzani, and W. Duan. Lab-on-a-chip: A component view. *Microsyst. Technol.*, 16(12):1995–2015, December 2010.

[115] Leslie Y. Yeo, Hsueh-Chia Chang, Peggy P. Y. Chan, and James R. Friend. Microfluidic devices for bioapplications. *Small*, 7(1):12–48, 2011.

[116] SI Kiselev, JC Sankey, IN Krivorotov, NC Emley, RJ Schoelkopf, RA Buhrman, and DC Ralph. Microwave oscillations of a nanomagnet driven by a spin-polarized current. *Nature*, 425(6956):380, September 2003.

[117] W. H. Rippard, M. R. Pufall, S. Kaka, S. E. Russek, and T. J. Silva. Direct-current induced dynamics in cofe/nife point contacts. *Phys. Rev. Lett.*, 92:027201, Jan 2004.

# 8

# APPENDIX

## 8.1 APPENDIX A - SPIN TORQUE DIODE DETECTOR

### 8.1.1 *Resonant detection using Spin Torque Diodes*

Spintronics is concerned with both the spin and charge of the electron, it encompasses a quite large range of applications based on the effects of giant magnetoresistance (GMR) and tunnel magnetoresistance (TMR). The devices are usually composed of two ferromagnetic layers separated by a non-magnetic spacer. Depending on the nature of the spacer, one considers two broad classes, GMR spin valves when the spacer is a normal metal layer, and TMR based on magnetic tunnel junctions when a spacer is an insulator. In these structures, one ferromagnetic layer is called the fixed or the reference layer, since its magnetization is pinned by magnetic coupling to an antiferromagnet, and the other is the free layer, the free layer magnetization can be switched to obtain either parallel or antiparallel alignment of the two magnetizations, which corresponds to two different resistance states of the device. Magnetoresistance has led to various applications such as field sensors, in particular read-heads for hard-disk or two-state devices like magnetic memory (MRAM). Spin transfer torque is concerned with the generation and utilisation of spin currents, specifically in the switching of magnetisation states and sustained precession of the magnetization states by the transfer of angular momentum. The manipulation of sustained magnetic precession has been of great research interest and focus over the last few years in the development of spin torque nano oscillators and spin torque diodes.

### 8.1.2 *Spin transfer torque introduction*

Spin transfer torque relates to the interaction of a spin polarized electronic current with the local magnetization: magnetic moment is transferred from the conduction electrons to the magnetization, resulting in a change of the magnetization orientation. In 1996, it was theoretically demonstrated both by Berger and Slonczewski that a spin polarized electronic current will transfer magnetic moment to the local magnetization of a ferromagnet. Shown experimentally the existence of spin transfer torque in 1998. This is illustrated in Figure 8.1.

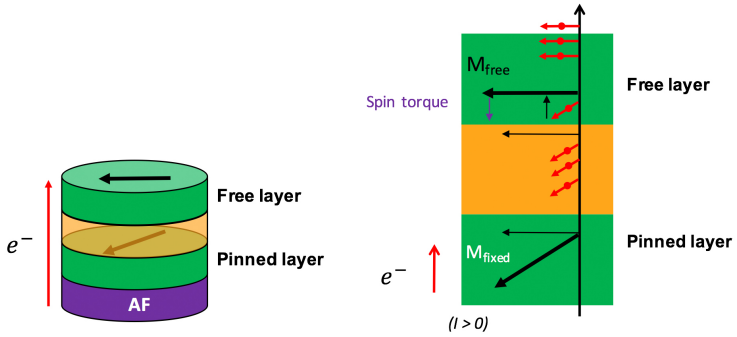



Figure 8.1: Schematic showing two ferromagnetic layers with different direction of magnetization

Spin transfer torque can induce steady-state precession or reversal of magnetization. Figure shows the magnetization dynamics associated with spin transfer torque. Spin transfer torque mechanism is explained considering the dynamics to be governed by the Landau-Lifshitz-Gilbert-Slonczewski equation, which is also shown in Figure. The first term gives the Larmor precession of the magnetisation about the effective field, here in the pression term, $m$ is a unit vector along the magnetisation direction, $\gamma$ is the gyromagnetic ratio, $H_{eff}$ is an effective magnetic field arising from an external field, exchange stiffness, dipole field and anisotropy field which is caused by the spin-orbit interaction.

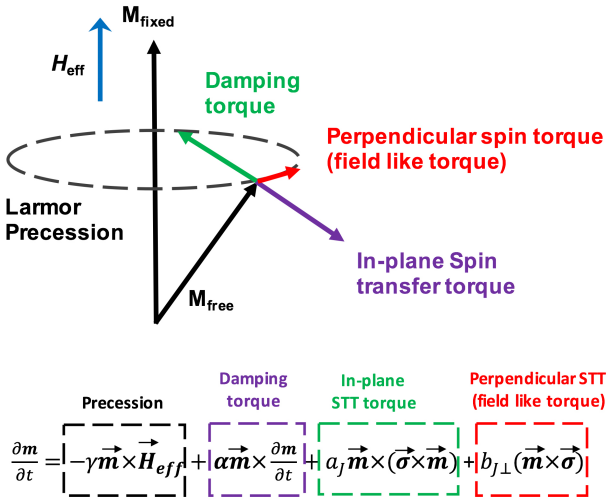



Figure 8.2: Illustration of the torques acting on the magnetisation during spin current injection. The spin transfer torque acts in the opposite direction to the damping and the field-like torque acts opposite the precession

The damping term gives the relaxation of the magnetisation towards $H_{eff}$ , here $\alpha$ is the Gilbert damping constant. The STT torque term, where $a_J$ is a coefficient of the spin torque and $\sigma$ is a unit vector in the direction of the injected electron spin, was first introduced by Slonczewski [42]and is essentially an anti-damping component. The field like torque term corresponds to the interaction between the magnetisation and the spin-polarised current, which gives rise to an effective field and associated torque as introduced by Zhang et al, here the component $b_J$ is a coefficient of the field like torque. Both $b_J$ and $a_J$are determined by geometric details of the materials in the configuration.

### 8.1.3 *Spin torque nano-oscillator*

Spin transfer torque has been tested on a large variety of devices and present the same essential characteristic. Ferromagnetic spinvalve tri-layer with a nanometric cross sectional area ~100 nm ∅. These can be a point contact or nano-pillar. The small cross-sectional area is necessary since spin transfer torque can only be observed for very large current density of the order of $10^6$to $10^8$ A $cm^{-2}$. Spectral measurements showed that spin transfer torque can induce a steady-state precession. The Spin torque nano oscillators are broadband microwave signal generators were direct current excites and controls a magnetodymanic response via spin transfer torque effect. The Spin torque

oscillators come in two different architectures, nano-pillars with diameter ~100 nm ∅. and nano-contacts were current enters an extended magnetic structure through a constriction. They can resonate frequencies of a few GHz [116][117].

The principle of operation of a spin torque nano oscillators are based on based on the effects of giant magnetoresistance (GMR) or tunnel magnetoresistance (TMR). The high current density is achieved through a nano-contact or a nano-pillar, which connects the spin torque nano oscillators to the rest of the integrated circuit. Figure 8.3 (a) shown the typical nano oscillator top-contact, which is based on an RF GSG probe form factor Figure 8.3(b) shows the nano oscillator pillar, which are ~100 nm ∅.

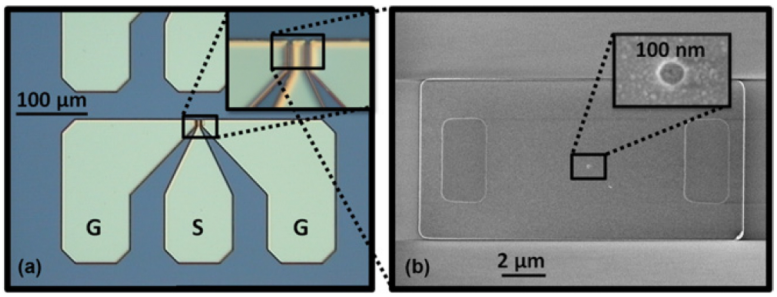



Figure 8.3: a) Typical nano oscillator top-contact, based on an RF GSG probe form factor (b) Nano oscillator pillar ~100 nm

Figure 8.4 shows a schematic for a GMR based spin torque nano oscillators using a point contact. Using an applied DC bias current spin wave resonance is excited in the free layer by a high current density. The RF voltage is achieved by the change in resistance from GMR as the free layer oscillates between parallel and antiparallel magnetisation with respect to the fixed layer. The frequency of the oscillation can be tuned by an applied field to effect the Larmor precession. The role of the fixed layer is to provide the spin transfer torque to match the damping of the precession of the magnetisation about the effective field.

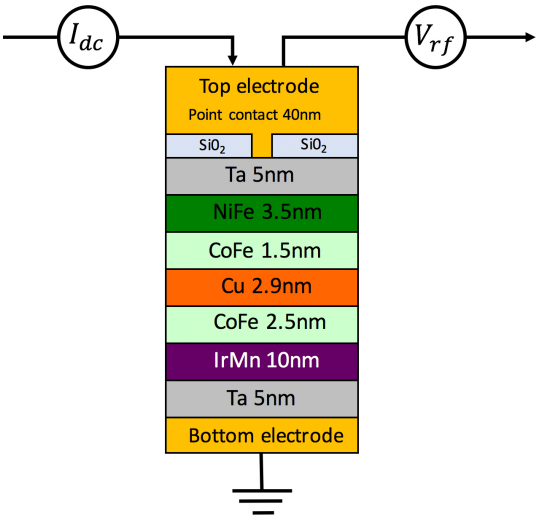



Figure 8.4: GMR based spin torque nano oscillator using point contact. Precession of the magnetisation of the free layer can generate frequency in the GHz range

Devices can be tuned by adjusting the amplitude of an applied field with respect to the devices coercive field $H_C$ . When the applied field $H < H_C$ to the coercive field, spin torque induces hysteretic switching between the two stable equilibrium positions. This is seen as a large & sharp resistance change and has applications in ST-MRAMS. Illustrated in Figure 8.5.

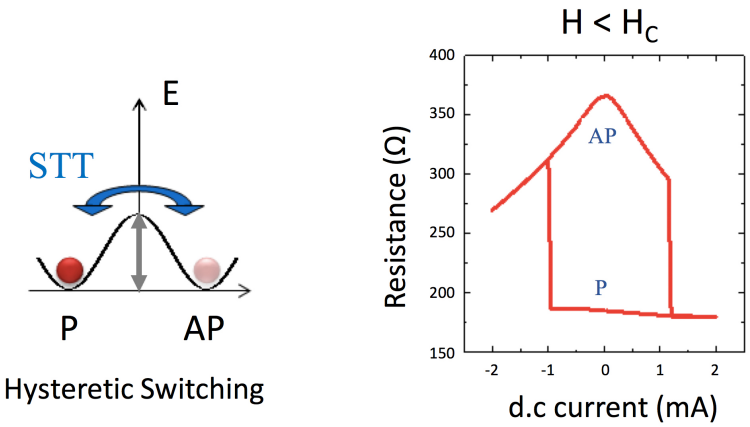



Figure 8.5: When H < Hc spin torque induces hysteretic switching between the two stable equilibrium positions

A sustained oscillation precession is achieved when $H > H_C$. the external field H is larger than the coercive field HC. With enough current to destabilize the parallel state the magnetisation enters a regime of spin-torque precession as shown in Figure 8.6.

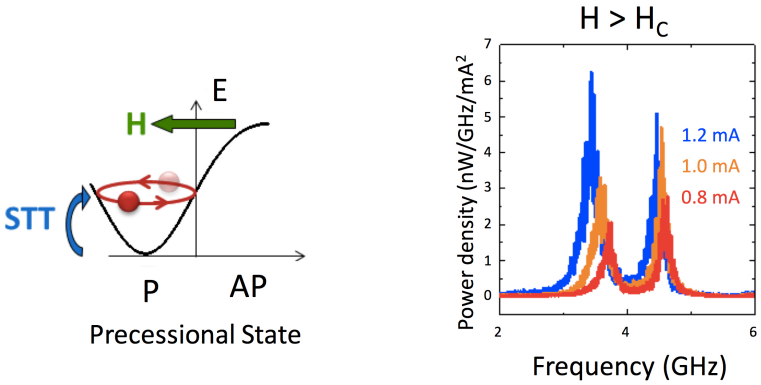



Figure 8.6: When H > HC magnetisation enters a regime of spin-torque precession

Commercial oscillators the benchmark oscillator output power is 0 dBm, in a 50 ohm system this is 1mW. Currently using a GMR spin-valve the output power is in the 100's of Pico watt range. The highest output power achieved in TMR MTJ based STOs using CoFeB/MgO/CoFeB nano-piller junction is just above 2μW. To achieve increased output power, high TMR ratio is required in MTJ nano-pillars with a low product RA.

### 8.1.4 *Spin-torque microwave detector – Spin-torque diode*

If the DC bias current is replaced using an AC current with a frequency (ω) close to the magnetization resonance frequency (ω0) of the device it induces large amplitude magnetization precessions. The resistance and current oscillate at the same frequency, which gives rise to a rectified d.c. voltage effect as illustrated in Figure.

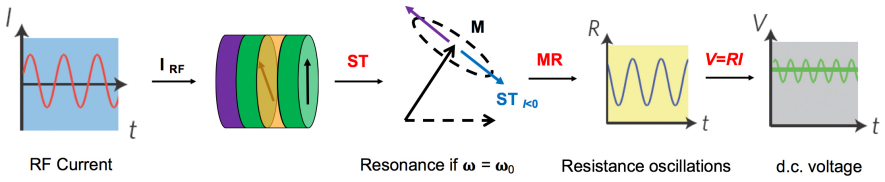



Figure 8.7: Schematic of spin-torque diode

These TMR MTJ based nanopillars called spin-torque diodes can act as a microwave resonant detectors. Utilizing the spin of electrons in addition to charge, these key emerging spintronic devices have the potential to overcome the theoretical performance limits of their semiconductor (Schottky) counterparts. To explain the physical mechanism

of spin torque diodes a comparison can be made to a p-n junction, as illustrated in Figure

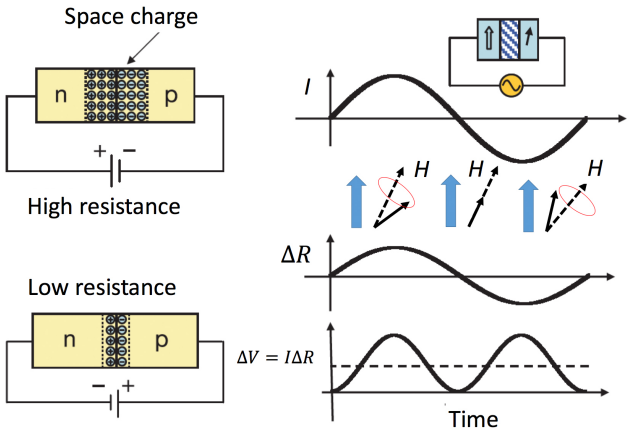



Figure 8.8: Physical mechanism of spin torque diode and comparison to a p-n junction

The p-n junction diode's high or low resistance state is determined by the direction of the current flow. For a Spin-torque diode, when an AC current with a frequency (ω) is applied it exerts a torque on the free-layer spin moment, this is indicated by the solid black arrow in Figure. As the AC current with a frequency ω nears the resonant frequency ω0 of the free-layer spin-moment, the spin is tilted towards the pinned-layer magnetization during the negative half of the frequency ω, which leads to a low resistance. During second half of the cycle the spin is tilted in the opposite direction, which leads to a high-resistance state. The difference in resistance during positive and negative produces dc voltage effect.

For both Spin torque oscillators and Spin torque diodes the research measurement technique all present the same essential configuration as illustrated in Figure. An electro magnet is used to provide a variable applied field. A bias tee enables both the injection of an rf signal via a signal generator to the nano-pillar and measurement of the rf detected response via a source meter and lock-in amplifier. Connection to the nano-pillar is via an RF GSG probe form factor.

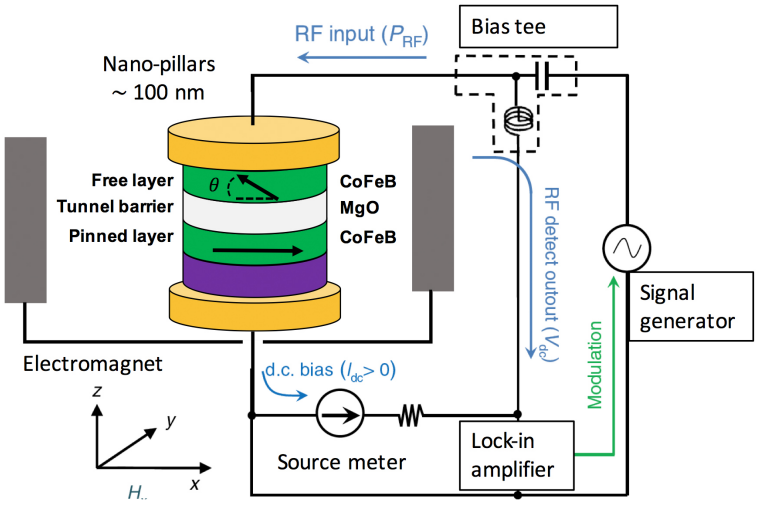



Figure 8.9: Schematic of Spin torque diode measurement configuration

### 8.1.5 *Literary review spin torque diodes*

Several groups show high detection sensitivities using MTJ nano-pillars, free layer with perpendicular magnetic anisotropy. The operating frequencies were 1–2 GHz [Ref]. Bin Fang et al (2016) [Ref] demonstrated a large spin-torque diode sensitivity 75,400 mV mW-1 at 1.2 GHz using low-input microwave powers at room temperature. This was achieved without an applied bias magnetic field. The device was an out of plane magnetic tunnel junction with a configuration in nanometers of PtMn (15)/Co70Fe30 (2.3)/Ru (0.85)/Co40Fe40B20 (2.4)/MgO (0.8)/ Co20Fe60B20. The device was patterened into an oval elliptical shape (150 nm – 60 nm) using e-beam and ion-milling. The TMR ratio measured 87.5 %, RA product parallel magnetization configuration was 4.5 Ωμm2. A perpendicularly magnetized free layer was induced by controlling the perpendicular magnetic anisotropy at the interface of the Co20Fe60B20 layer with the MgO layer. The magnetization configuration enables the device to excite large-amplitude magnetization precession under a small spin-torque. In addition, the CoFeB–MgO– CoFeB material combination ensures high TMR. These factors are key ingredients to enhance the sensitivity of the spin-torque diode. The applied RF current was modulated at a low frequency (10 kHz) to improve signal to noise ratio. The spin-torque microwave emission output voltage was simultaneously recorded via the bias tee and measured using a

spectrum analyzer and lock-in amplifier. This mechanism (injection-locking) provides a narrow bandwidth of 510 MHz to 540 MHz were the larger detection voltage is measured. Practical applications a frequency tunable RF detector with a high sensitivity at higher frequencies is desirable. Dhananjay et al (2016) [ref] demonstrated enhanced spin-torque diode sensitivity of 16mV/mW at high frequency of 9 GHz using parametric synchronization at 2f0. The device was an in-plane magnetic tunnel junction with a configuration in nanometers of IrMn(5)/CoFe(2.1)/Ru(0.81)/CoFe(1)/CoFeB (1.5)/MgO (1)/CoFeB (3.5). The device was patterened into a circular pillar with a diameter of 180 nm and measured a TMR ratio of 73 %. A field modulation spin torque ferromagnetic resonance technique (FM-STFMR) was used, to provide a better signal-to-noise ratio as well as a higher sensitivity. Synchronization with an external RF current is more efficient at 2f0, which is referred to as parametric synchronization. Table 8.1 summaries the development of spin-torque diodes over the past few year, indicating the increase in the spin torque diodes detection sensitivity and reduced requirement of an applied magnetic field.

| Ref | MTJ | TMR % | $H_{ext}$ (Normal) | $I_{dc}$ (mA) | Pillar (nm) | Detection sensitivity | RA ($\Omega\mu m^2$) | $I_c$ (mA) | $f_o$ (GHz) | $V_{max}$ ($\mu V$) |
|---|---|---|---|---|---|---|---|---|---|---|
| 2005 Tulapurkar | PtMn(15)/CoFe(2.5)/Ru(0.85)/CoFeB(3) /MgO(0.85)/CoFeB(3) | 100 | $30^0$ | 1 | Elliptical 200 _100 | 1.4mV $mW^{-1}$ | | -0.55 | 1.8 | 50 |
| 2010 Ishibashi | PtMn(15)/CoFe(2.5)/Ru(0.85)/$Co_{60}Fe_{20}B_{20}$(3)/MgO(1.2)/$Co_{16}Fe_{64}B_{20}$(2)/cap | 105 | $5^0$ | | Elliptical 100 _150 | 170mV/$mW^{-1}$ | 2.1 | | | 180 |
| 2014 Miwa, S | PtMn(15)/$Co_{70}Fe_{30}$(2.5)/Ru(0.85)/$Co_{60}Fe_{20}B_{20}$(3)/MgO(1)/$Fe_{80}B_{20}$(2)/MgO (1)/Ta(5)/cap/(Perpendicular free layer) | 86 | $10^0$ | | Circle 120 | 12,000mVm$W^{-1}$ | 2.5 | -0.42 | 1.5 | 120 |
| 2016 Bin Fang | PtMn(15)/$Co_{70}Fe_{30}$(2.3)/Ru(0.85)/$Co_{40}Fe_{40}B_{20}$ (2.4)/MgO (0.8)/ $Co_{20}Fe_{60}B_{20}$ (Perpendicular free layer) | 87.5 | $0^0$ | | Elliptical 150_60 | 75,400mVm$W^{-1}$ | 4.5 | -0.25 | 1.2 | 754 |

Table 8.1: Summary of the development of spin-torque diodes

Sushruth et al (2017) demonstrated in a conference digest review resonant detection of super-paramagnetic micro-beads using vortex based spin-torque oscillator. d.c. current drives oscillations of the two vortices, via spin-torque, generating an RF resonance signal 325 MHz. The spin-torque oscillator oscillator based on the current-induced dynamics of two weakly coupled vortices that provide self-sustained oscillations of gyrotropic modes, each of them depending on the relative configuration of each vortex. The device was an in-plane magnetic tunnel junction with a CoFe/Ru/CoFeB SAF layer, MgO tunnel barrier thickness 1 nm and NiFe/Cu/NiFe spin valve. Patterend into a conic pillar wth a

diameter of 290 nm. The TMR ratio measured 70%. In the resonant detection experiment, super-paramagnetic beads with a diameter 1μm filled with iron oxide particles. The beads are placed on the device. Figure 8.10 (a) shows output signals from the resonant detector before with no beads applied (bare) and after the beads are applied (beads). This was obtained using an applied field of 248 mT. Figure 8.10 (b) shows resonance frequencies as a function of external magnetic field with and without beads.

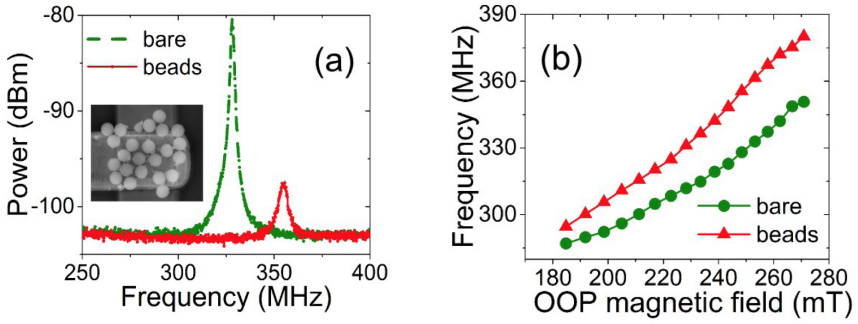



Figure 8.10: Figure (a) Output signals from the resonant detector before with (green) & after the beads applied (red). (b) shows resonance frequencies as a function of external magnetic field with and without beads

The results show a shift in the measured resonant frequency when the micro-beads are placed on the device. The resonant frequency is shifted by 30 MHz with a loss of -17 dB (22 μV rms – 2.2 μV rms @ 50 ohm)

### 8.1.6 *Conclusions*

The field of spin-orbit torque is truly a new and budding area of research. Some of the details about the phenomenon are effectively still under debate, such as the comparative roles of the local and non-local spin orbit torques. The value that spin-orbit torque offers in the promise of applied field free non-volatile memories and various other efficient integrated spin-based circuit elements is both intellectually exciting and commercially appealing and is likely to stimulate much research over the next few years. The area will likely see fast integration with consumer electronics owing to its generally simple device structure as compared to spin transfer torque based devices, specifically, in the limit of

small functioning active regions spin transfer torque requires two magnetic domains and spin-orbit torque requires only one.

### 8.1.7 *Electron Beam Lithography*

The Spin-torque diode device is typically fabricated using an MTJ spinvalve multi-film tri-layer with a nanometric cross sectional area ~100 nm ∅. Simular to the TMR sensor, the Spin-torque diode fabrication requires a three-step lithography process.

The UV photolithography process is limited by the diffraction limit in the order of the wavelength. The AOL mask aligner is capable of patterning up to dimensions of 2 um at 365nm wavelength. To fabricate a device, which has a nano-metric cross sectional area in the order of ~100 nm ∅ an alternative lithographic method is required. By using electron as an "exposure source", we can overcome the diffraction limit of optical lithography and the use of the electron beam to define lithographic patterns is known as electron beam lithography (EBL). Since De Broglie's calculations predicted that the wavelength $\lambda$ of a particle can be determined by $\lambda = h/(mv)$,were $h$ is the Planck's constant, m is the mass of the particle and v is the particle velocity, we can reduce the wavelength by increasing the velocity of the electron until the diffraction limit no longer matters.

EBL systems, can draw patterns in extremely small dimensions, they can generate a high-resolution electron beam with a large electric current on a nano-Ampere order that facilitates the high-speed drawing of fine patterns on the substrate. They also facilitate patter overlay, which is critical for devices that have multiple lithography steps and they are flexiable with regard to pattern change. Electron beam resist are usually polymer chains and exhibit physical or chemical change due to exposure to high energy electron beam. Electron beam resist, like optical resist, can also be differentiated into positive resist and negative resist. On exposure to the electron beam, the positive resist will break down into less complex fragments with a lower molecular weight, making the exposed area more soluble compared to the unexposed area. In comparison, the exposure of electron beam to a negative resist will result in a more complex chain, which will remain un-dissolved by the developer solution.

### 8.1.8 *Elionix 7700 e-Beam lithography system*

Our e-Beam lithography is an Elionix 7700 shown in Figure 8.11. This is a dedicated electron beam lithographical platform which utilizes a ZrO/W thermal field emission source, and an electron column normally operating at an acceleration voltage of 75 kV to write features in a variety of resists, on a variety of substrates. The laser interferometer-controlled stage and an assortment of chucks allow features to be written on substrates up to 6 inches in diameter, as well as on much smaller samples. Patterns to be written can be imported from AutoCAD "dxf" as well as Calma "gds" format, and can also be defined in the native CAD language used by the system. Writing field sizes range from 75 microns to 2.4 nm on a side. Maximum clock speed (1 / minimum delay) is 10 MHz.

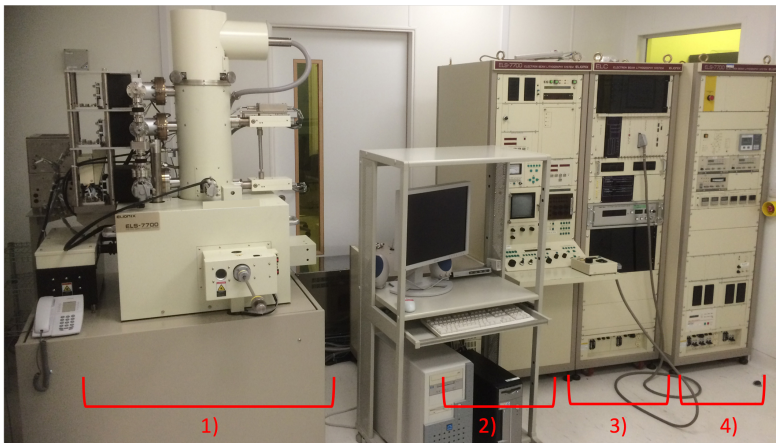



Figure 8.11: Elionix 7700 dedicated electron beam (e-Beam) lithography system

Table 8.2 details the main components of the Elionix system.

| Section | |
|---|---|
| 1: Main unit: | • Field emission gun<br>• Scanning beam column<br>• Main chamber & sample placement<br>• Deflection amplifiers<br>• OL & BL aperture – mesh-aperture, ⦰ 120µm , 60 µm & 30µm |
| 2: EOC rack: | • Beam condition setting & control<br>• Focus & Stigmation, aperture control & current meter<br>• CPU<br>• HV source |
| 3: ELC rack: | • Lithography pattern development (DAC's)<br>• Automatic stage control (interferometer) |
| 4: EVAC rack: | • Vacuum system & power supplies |

Table 8.2: Main components of the Elionix system

### 8.1.9 *Spin torque diode sensor fabrication*

The Spin torque diode sensor is patterned onto silicon wafer substrates into nano pillar junctions using a four-step EBL lithography process. The top electrode contact is designed to fit the RF GSG type probe for measurement.

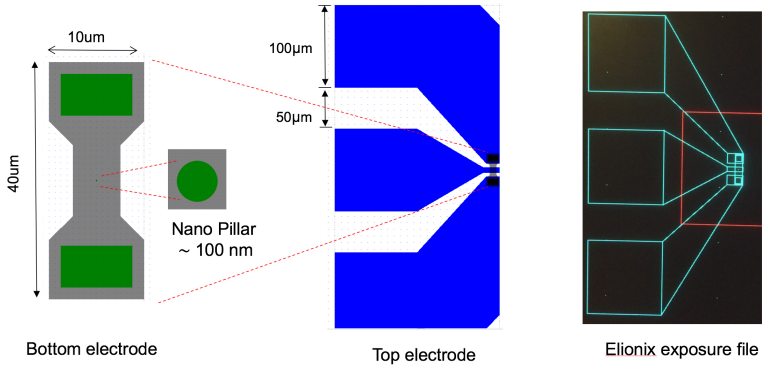



Figure 8.12: Schematic of the design of the Spin torque diode sensor detailing the bottom electrode, nano-pillar and top electrode and also an image of the Elionix process files for the respective exposure layers

The samples are diced into a 1 cm x 1 cm size using Disco DAD3220 Wafer Dicer to allows placement into the electro-magnet test bed. All lithography exposures are carried out using EBL files on the Elionix system, which allows for correct overlay alignment. Figure 8.12 shows a schematic of the design of the Spin torque diode sensor detailing the bottom electrode, nano-pillar and top electrode and also an image of the Elionix process files for the respective lithography exposure layer.

The Elionix system has a beam blank time of 1/10MHz, which is 100 ns. Exposure (dose) calculations were carried out for each lithography layer using the following expression,

$$D = \frac{tI}{\delta^2} \tag{8.1}$$

Where $I$ is the beam current, $t$ is the dwell time, $D$ is the area dose and$\delta$ is the step size. Elionix has a number of write field & dots per field options. Table8.3 details the Elionix exposure files for each of the lithography steps required to fabricate the Spin torque diode sensor and the optimum exposure times for each layer following exposure tests.

| File | Description | Resist | Write field (μm) | Dose (μC/cm²) | Dots | Beam Current (pA) | Dwell time (μs/dot) |
|---|---|---|---|---|---|---|---|
| Cross1.con | Alignment marks | PMMA-3 | 150 | 600 | 60,000 | 230 | 0.16 |
| L_shape.con | Location shape | PMMA-3 | 150 | 600 | 60,000 | 230 | 0.16 |
| Layer1.con | Bottom electrode | ma-N2403 | 150 | 600 | 60,000 | 230 | 0.16 |
| Layer2.con | Contact pads | ma-N2403 | 150 | 600 | 60,000 | 230 | 0.16 |
| Layer3.con | Pillar | ma-N2403 | 150 | 600 | 60,000 | 230 | 0.16 |
| Layer4.con | Top contacts | PMMA-3 | 600 | 600 | 60,000 | 230 | 2.608 |

Table 8.3: Elionix exposure files for each of the lithography steps and the optimum exposure times for each layer

Development has started on GMR multi-layer thin film stacks, these will be used for initial measurements and assist in producing a robust fabrication procedure. TMR multi-layer thin film stack configurations will then be explored. Figure 8.13details GMR and TMR multi-layer stack configurations that have been deposited using the Shamrock sputtering deposition system.

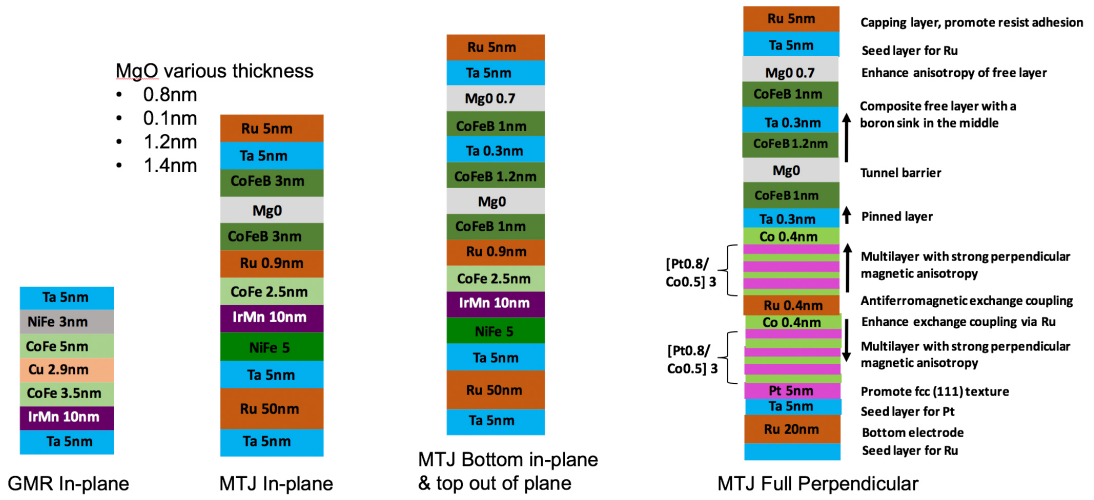



Figure 8.13: GMR and TMR multi-layer stack configurations deposited for Spin torque diode sensors

### 8.1.10 *Step 1: Expose alignment & registration marks for the overlay of each layer*

1. PMMA-3 EBL positive photoresist is spun on the full GMR stack. Spinning parameters: 3000 rpm for 50 s (Spin program 50 AL PMMA)
2. Resist pre-baked at 180oc for 3mins
3. Expose sample using EBL file (Cross1.con & L_shape.con)
4. Develop MIBK:IPA 1:3 for 50sec, wash IPA and spin dry

5. Ta (5 nm)/Cu (50 nm) bilayer is sputtered as top contact on the resist defined areas

6. Lift off is performed in acetone in the ultrasonic bath

Table 8.4 details the exposure (dose) time calculations and exposure conditions for the alignment & registration marks file on the Elionix system.

| Exposure | File | Description | Write field (µm) | Dose (µC/cm²) | Dots | Beam Current (pA) | Dwell time (µs/dot) |
|---|---|---|---|---|---|---|---|
| 1 | Cross1.con | Alignment marks | 150 | 600 | 60,000 | 230 | 0.16 |
| 1 | L_shape.con | Location shape | 150 | 600 | 60,000 | 230 | 0.16 |

Table 8.4: EBL exposure conditions for optical image alignment mark & registration marks

Figure 8.14 (a) shows an optical image alignment mark and Figure 8.14 (b) registration marks after the 1st EBL exposure.

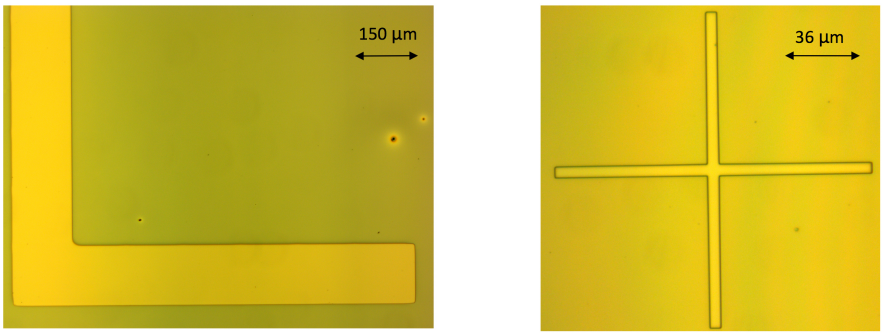



Figure 8.14: (a) shows an optical image alignment mark (b) registration marks after the 1st EBL exposure

### 8.1.11 *Step 2: Expose bottom electrode for Spin torque diode device*

1. ma-N2403 EBL negative photoresist is spun on sample. Spinning parameters: 3000 rpm for 30 s

2. Resist pre-baked at 90oc for 30 secs

3. Expose sample using EBL file (Layer 1.con)

4. Develop ma-D 532 for 30sec, wash Di water and spin dry

5. Sample Argon-ion milled at an angle of 80o down to the SiO2 substrate (approx. 25 mins at 400 W RF power)

6. SiO2 is deposited in Chamber B, 30 nm for GMR stack and 70 nm for TMR

7. Lift-off of the photoresist & SiO2 is performed in Microposit 1165 remover using an ultrasonic bath at 80oC for 30 mins

Table 8.5details the exposure (dose) time calculations and exposure conditions for the bottom electrode file on the Elionix system.

| Exposure | File | Description | Write field (µm) | Dose (µC/cm²) | Dots | Beam Current (pA) | Dwell time (µs/dot) |
|---|---|---|---|---|---|---|---|
| 2 | Layer1.con | Bottom electrode | 150 | 600 | 60,000 | 130 | 0.14 |

Table 8.5: Exposure (dose) time calculations and exposure conditions for the bottom electrode

Figure 8.15 (a) shows an SEM image of the bottom electrode at different exposure dwell times 0.1 to 0.29 µs/dot and Figure 8.15 (b) shows SEM image of bottom electrode after ion-milling, using optimum dwell times 0.14µs/dot as per calculation.

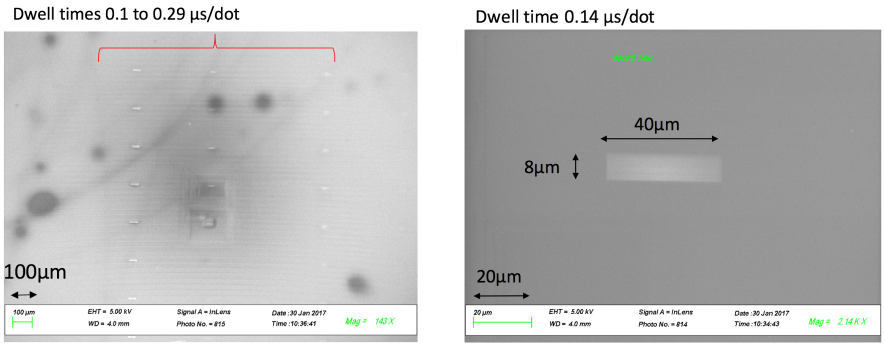



Figure 8.15: (a) SEM image of the bottom electrode at different exposure dwell times 0.1 to 0.29 µs/dot and (b) SEM image of bottom electrode after ion-milling, using optimum dwell time 0.14µs/dot

### 8.1.12 *Step 3: Expose junction pillars and contact pads*

1. ma-N2403 EBL negative photoresist is spun on sample. Spinning parameters: 3000 rpm for 30 s

2. Resist pre-baked at 90oc for 30 secs

3. Expose sample using EBL files (Layer 2.con & Layer 3.con)

4. Develop ma-D 532 for 30sec, wash Di water and spin dry

5. Sample Argon-ion milled at an angle of 80o down to bottom FM electrode just below the MgO layer (approx. 10 mins at 400 W RF power)

6. SiO2 is deposited in Chamber B is sputtered on the etched samples in order to insulate the top and bottom contact, ~ 10 nm for GMR stack and ~ 50 nm for TMR

7. Lift-off of the photoresist & SiO2 is performed in Microposit 1165 remover using an ultrasonic bath at 80oC for 30 mins

I was unable to expose the nano size junction pillar using the Elionix system, this to due to the fact that the beam current from the Elionix system was too low to expose this size feature. The field emission gun on the system is due its service. When this is complete facbrication work will continue.

### 8.1.13 *Step 4: Expose top electrode*

1. PMMA-3 EBL positive photoresist is spun on the full GMR stack. Spinning parameters: 3000 rpm for 50 s (Spin program 50 AL PMMA)

2. Resist pre-baked at 180oc for 3mins

3. Expose sample using EBL file (Layer 4.con)

4. Develop MIBK:IPA 1:3 for 50sec, wash IPA and spin dry

5. Ta (5 nm)/Cu (50 nm) bilayer is sputtered as top contact on the resist defined areas

6. Lift off is performed in acetone in the ultrasonic bath

Table 8.6 details the exposure (dose) time calculations and exposure conditions for the top electrode file on the Elionix system.

| Exposure | File | Description | Write field (µm) | Dose (µC/cm²) | Dots | Beam Current (pA) | Dwell time (µs/dot) |
|---|---|---|---|---|---|---|---|
| 4 | Layer4.con | Top contacts | 60 | 600 | 60,000 | 210 | 1.43 |

Table 8.6: Exposure (dose) time calculations and exposure conditions for the top electrode

Figure 8.16 (a) shows an SEM image of the top electrode at different exposure dwell times 0.2 to 0.3 µs/dot and Figure 8.16 (b) shows SEM image of top electrode after ion-milling, using optimum dwell times 0.14 µs/dot as per calculation.

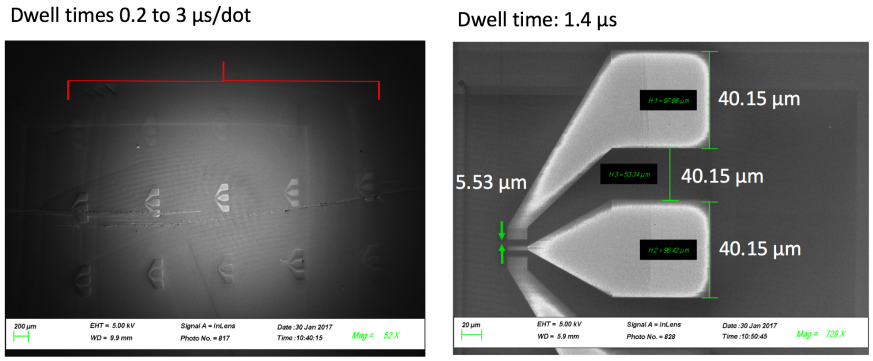



Figure 8.16: SEM image of the top electrode at different exposure dwell times 0.2 to 0.3 µs/dot and (b) SEM image of top electrode after ion-milling, using optimum dwell time 0.14 µs/dot

## 8.2 APPENDIX B - GMR AND TMR SENSOR FABRICATION PROCEDURE

### 8.2.1 *GMR sensor fabrication procedure*

In order to allow for magnetic and optical (via a microscope) detection of magnetic nanowires in a microfluidic channel, GMR sensors were fabricated with multiple contacts to form a gradiometer in CIP configuration. The sensor was designed with the pinned layer set perpendicular to the free layer (crossed anisotropy) as shown in Figure 8.17 , which illustrates the schematic of GMR Biosensor fabrication plan. The total thickness of the GMR stack 34.3 nm (~35nm). The sensors were patterened into micron-sized junctions on glass substrates, which allowed for transport and magnetoresistance measurements and noise measurments via the conventional four-point probe method.

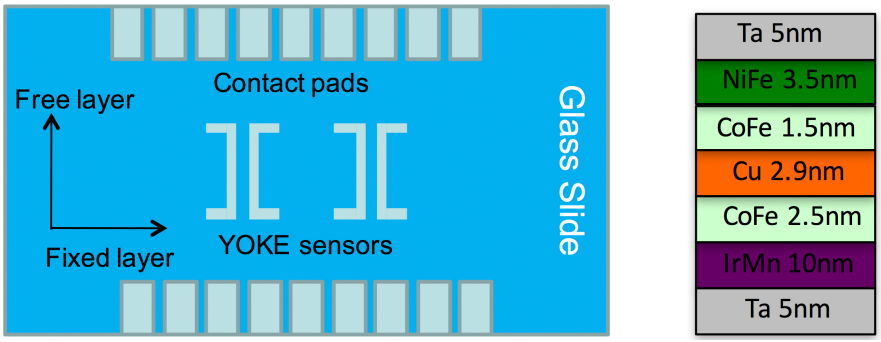



Figure 8.17: Schematic of GMR Biosensor fabrication plan

#### 8.2.1.1 *GMR Biosensor CAD design*

The layout design for the GMR sensor was carried out using layout editor software called CleWin 4.0. The first mask design encompassed four GMR sensors configured in two sets of two YOKE shape sensors forming gradiometers and alignment marks for the second layer overaly alignment during fabrication, Figure 8.18 shows the design layout for the first mask which encompassed four GMR sensors .

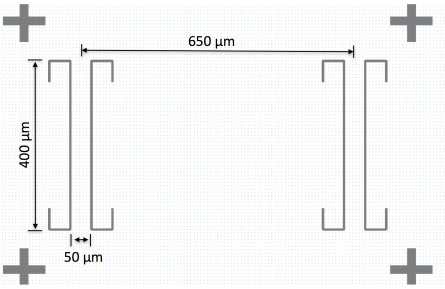



Figure 8.18: Mask 1 GMR Biosensor YOKE sensors

The second mask design provided the top contacts over the GMR sensors. It was designed as hown in Figure 8.19 to allow the GMR bio-sensor to fit into both the microfluidic channel and the sensor interface for nanowire detection.

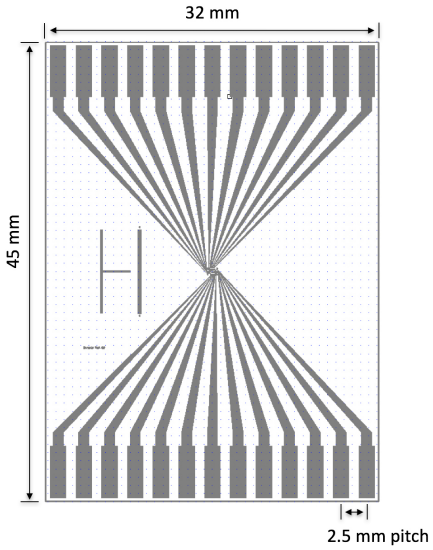



Figure 8.19: Mask 2 GMR Biosensor Top layer

#### 8.2.1.2 *Step 1: Deposition of thin-film metal layers*

Thin-film metal layers Thin-film metal layers where deposited onto glass substrates type Nexterion Glass D 44 mm x 33 mm x 170 um, supplied by VWR International

1. Glass substrates are cleaned using Piranha cleaning procedure (procedure detailed in Appendix B)

2. Substrates loaded into Shamrock sputtering tool Chamber A

3. Deposition layer sequence thickness in nm Ta (5)/NiFe (3)/CoFe (5)/Cu (2.9)/CoFe (3.5)/IrMn (10/Ta (5)

4. Layer sequence grown in magnetic field 6 mT

5. Free layers deposited first Ta (5)/NiFe (3)/CoFe (5)/Cu (2.9)

6. Substrated rotated 90ř and then fixed layers deposited CoFe (3.5)/IrMn (10)/Ta (5) setting the sensor exchange bias

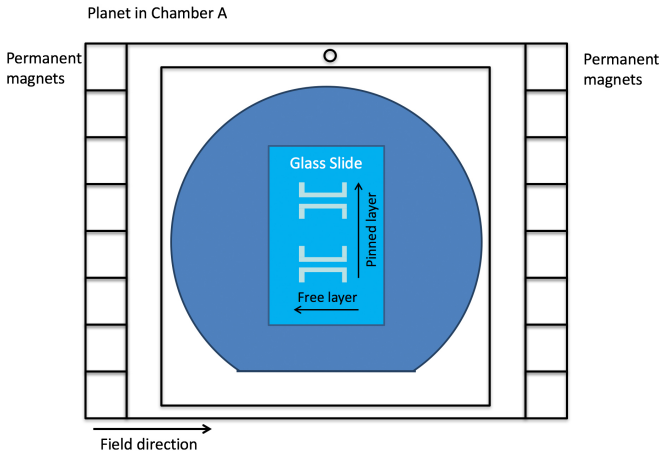



Figure 8.20: Substrate in Chamber A

#### 8.2.1.3 *Step 2: YOKE sensor & alignment mark patterning*

1. Shipley 1813 positive photoresist is spun on the full GMR stack (Spinning parameters: 5000 rpm (~1.2 μm) for 45 s)

2. Resist pre-baked at 115 °C for 2 mins

3. Photoresist is exposed for 6 s (~112 mJ/cm$^2$) with GMR mask 1 using the OAI mask aligner

4. Photoresist is developed in MF 319 developer for 50 - 60 s

5. Samples are loaded into our Millatron ion milling system and etched at an angle of 85ř down to the SiO2 substrate (approx. 15 mins at 400 W RF power)

6. 30 nm of $SiO_2$ is deposited in Chamber B

7. Lift-off of the photoresist & $SiO_2$ is performed in Microposit 1165 remover (N-methyl-2-pyrrolidone) using an ultrasonic bath at 80 °C for 30 mins.

Figure 8.21 shows an optical image of the GMR YOKE sensors and alignment marks after the first mask pattering.

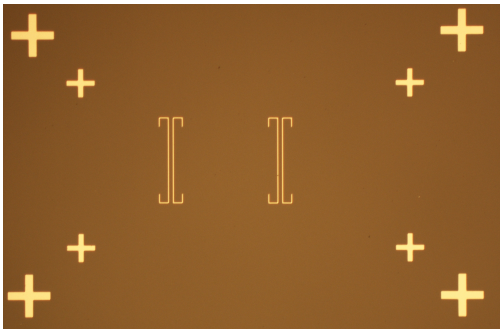


Figure 8.21: Optical image of the GMR YOKE sensors & alignment marks after the first mask pattering

#### 8.2.1.4 *Step 3: Top contact patterning*

1. Shipley 1813 positive photoresist is spun on this sample (Spinning parameters: 5000 rpm (~ 1.2 μm) for 45 s)
2. Resist is pre-baked at 115řC for 2 mins
3. Photoresist exposed for 6 s with the second GMR top-electrode mask using the OAI mask aligner
4. Photoresist is developed in MF 319 developer for 50 - 60 s
5. Ta (5 nm)/Cu (50 nm) bilayer is sputtered as top contact on the resist defined areas
6. Lift off is performed in acetone in the ultrasonic bath
7. Sensor is then cut to correct dimensions using Disco DAD3220 Wafer Dicer
8. Passivation layer (See procedure: $SiO_2$ Chamber B, ALN Chamber A, SiN Chamber A)

Figure 8.22 shows an optical image of the GMR Bio-sensor with top-contacts after the second mask pattering.

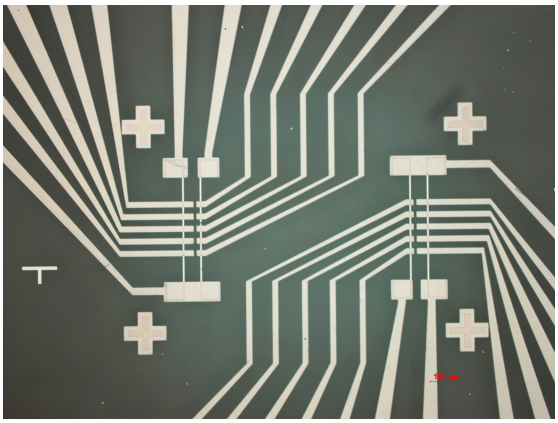


Figure 8.22: Image GMR YOKE sensors with top contacts

#### 8.2.1.5 *Procedure Piranha cleaning of glass substrates*

Piranha solution is a 3:1 mixture of sulphuric acid (H2SO4) and 30% hydrogen peroxide (H2O2), used to clean organic residues off substrates. Because the mixture is a strong oxidizer, it will remove most organic matter, and it will also hydroxylate most surfaces (add OH groups), making them extremely hydrophilic (water compatible).

1. Heat 3:1 $H_2S0_4$ : $H_20_2$solution at 100řC
2. Etch substrates in solution for 15 min and wash twice in separate beaker with Di water for 1 min
3. Place glass substrate on clean wipe and dry with Ni gun
4. Allow acid to cool down, and dispose of diluted acid in waste acid bottle as outlined in waste disposal procedure

### 8.2.2 *TMR sensor fabrication procedure*

Due to their large resistance change and high TMR ratio, TMR sensors were investigated as an alternative option to the GMR sensor. A number of design interations of the TMR sensor were developed, until an optimum design was selected for nanowire detection experiments. This section discusses the fabrication procedure for one of the sensor designs, which is common for all TMR sensor iterations. The sensors were patterened

onto Silicon wafer substrates into micron-sized junctions, which allowed for transport and magnetoresistance measurements and noise measurments via the conventional four-point probe method.

Microfabrication was achieved by a combination of UVlithography, Ar+ ion milling and lift-off. UV-lithography is performed in the CRANN Class-100 clean room using the OAI 800 CE (wavelength 365 nm) mask aligner. A set of photo-masks is used to transfer the sensor pattern onto the sputtered thin film. The design for the sensor patterns was done using layout editor software called CleWin 4.0. The photo-masks sets for each sensor were then fabricated using the Heidelberg DWL 66FS which is a laser lithography system for mask making. Each mask is chrome glass 4" x 4"x 1.5mm, the Heidelberg writes the sensor pattern onto the chrome glass and through development process the area of the chrome layer containing the sensor pattern is removed. The sputtered magnetic thin films are pattern into sensors by using the masks and UV lithography. The ultraviolet light modifies the chemical resistance of a polymer (photo-resist) and allows the exposed photo-resist to be dissolved in a solvent. Then through a process of Ion-milling the material layers that are not required are removed leaving only the required structure.

An MgO-based bottom-pinned TMR thin-film stack with a layer sequence thickness in nm Ta (5)/Ru (30)/Ta (5)/NiFe (5)/IrMn (10)/CoFe (2.5)/Ru (0.9)/CoFeB (3)/MgO (x)/CoFeB (3)/Ta (5)/Ru (5) (nanometers) is deposited onto a thermally-oxidized silicon wafer at room temperature. All metallic multilayers are grown by dc-magnetron sputtering methods and the MgO layers were grown by rf-sputtering from two MgO targets in a target-facing-target gun in the Shamrock sputtering tool. The yoke shaped MTJs are patterned by UV lithography and Ar ion-milling using a three-step mask lithography process. The first lithography process exposes the bottom electrode and YOKE shape using UV lithography (S1813 positive photoresist), the substrate is then ion-milled. An insulator SiO2 50nm is then deposited. The second lithography process exposes the yoke-junction, again using UV lithography (Negative resist ma-N1420). The substrate is ion-milled down to just below the MgO layer. A second SiO2 40nm insulator layer is then deposited. The SiO2 insulates the sensor from the top contacts. The third lithography process patterns the top-electrodes (using S1813 positive resist). Ti5/Cu60 top electrodes are then deposited.

#### 8.2.2.1 *Step 1: Deposition of thin-film metal layers*

Thin-film metal layers where deposited onto a thermally oxidized silicon wafer at room temperature.

1. Substrates loaded into Shamrock sputtering tool Chamber A
2. Deposition of bottom electrode layer sequence in nm thickness nm Ta (5)/Ru (30)/Ta (5)/NiFe (5)/IrMn (10)/CoFe (2.5)/Ru (0.9)/
3. Subtrates transferred to chamber B and deposition of barrier junction CoFeB (3)/MgO (2)/CoFeB (3)
4. Subtrates transferred to chamber A and deposition of capping layer /Ta (5)/Ru (5)

#### 8.2.2.2 *Step 2: YOKE sensor & alignment mark patterning*

1. Shipley 1813 positive photoresist is spun on the full TMR stack (Spinning parameters: 3000 rpm (~1.2 μm) for 45 s).
2. Resist pre-baked at 115řC for 2 mins
3. Photoresist is exposed for 6 s (~112 mJ/cm2) with TMR mask 1 using the OAI mask aligner
4. Photoresist is developed in MF 319 developer for 50 s
5. Samples are loaded into our Millatron ion milling system and etched at an angle of 80ř down to the $SiO_2$ substrate (approx. 25 mins at 400 W RF power)
6. 70 nm of $SiO_2$ is deposited in Chamber B
7. Lift-off of the photoresist & $SiO_2$ is performed in Microposit 1165 remover (N-methyl-2-pyrrolidone) using an ultrasonic bath at 80řC for 30 mins.

Figure 8.23 shows an optical image of the TMR YOKE sensor bottom electrode and alignment marks after the first mask pattering.

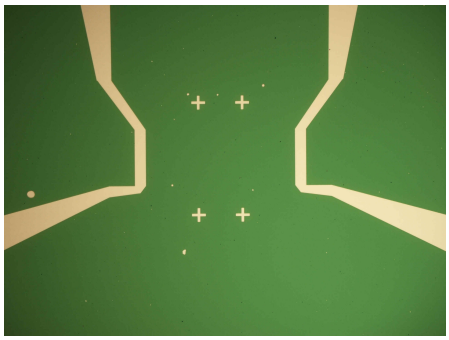


Figure 8.23: TMR YOKE sensor bottom electrode and alignment marks after the first mask pattering

#### 8.2.2.3 *Step 3: Junction area definition*

1. mn-N1420 negative photoresist is spun on the sample (Spinning parameters: 3000 rpm (~ 2 μm) for 45 s)
2. Resist is pre-baked at 115řC for 1 min
3. Photoresist exposed for 6 s (~ 112 mJ/cm2) with TMR mask 2 using the OAI mask aligner
4. Resist is post-baked at 115řC for 1 min
5. Photoresist is developed in ma-D 533 developer for 40 - 60 s
6. Samples then are loaded into our Millatron Ion Milling system and etched at 80ř down to bottom FM electrode just below the MgO layer (approx. 10 mins at 400 W RF power)
7. $SiO_2$ (~ 50 nm) is sputtered on the etched samples in order to insulate the top and bottom contact
8. Lift-off of the photoresist & $SiO_2$ is performed in Microposit 1165 remover (N-methyl-2-pyrrolidone) using an ultrasonic bath at 80ř for 30 mins.

Figure 8.24 shows an optical image of the TMR YOKE sensor junction after the second mask pattering.

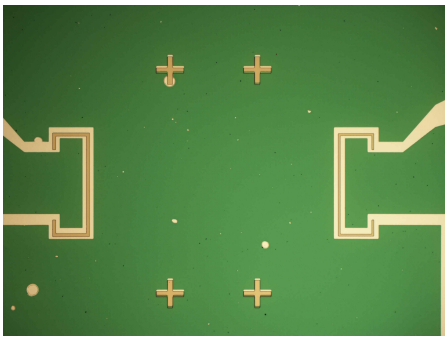


Figure 8.24: MR YOKE sensor junction after the second mask pattering

#### 8.2.2.4 *Step 4: Top contact patterning*

1. Shipley 1813 positive photoresist is spun on sample (Spinning parameters: 5000 rpm (~ 1.2 μm) for 45 s)
2. Resist is pre-baked at 115řC for 2 mins
3. Photoresist exposed for 6 s by using TMR mask 3 using the OAI mask aligner
4. Photoresist is developed in MF 319 developer for 50 - 60 s. e. Ta (5 nm)/Cu (50 nm) bilayer is sputtered as top contact on the resist defined areas
5. Lift off is performed in acetone in the ultrasonic bath
6. Sensor is then cut to correct dimensions using Disco DAD3220 Wafer Dicer

Figure 8.25 shows an optical image of the TMR YOKE sensor with top contacts after the third mask pattering.

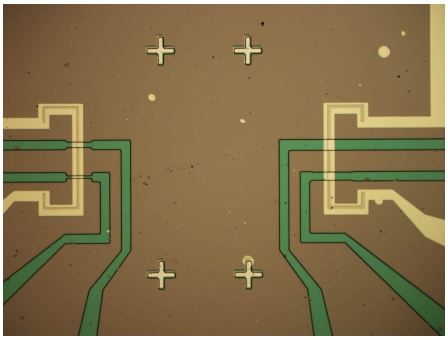
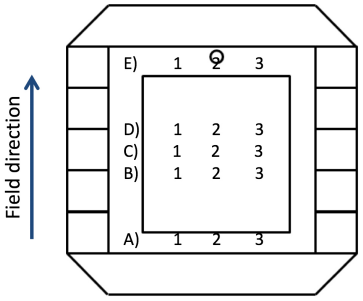


Figure 8.25: TMR YOKE sensor with top contacts after the third mask pattering

#### 8.2.2.5 *Step 5: Annealing*

High vacuum post-annealing was then performed at 350řC (1st anneal) for 1 hour in an applied magnetic field of 800 mT and then at 150řC (second anneal) for 1 hour. The first annealing step at high temperature sets the exchange bias of the bottom-pinned ferromagnetic layers perpendicular to the long arm of the yoke and induces the crystallization of CoFeB at the MgO interfaces, which is necessary for a high TMR ratio. The second anneal at 150ř$C$ with the applied magnetic field parallel to the long arm of the yoke is aimed at resetting the easy axis of the top-free layer. Measurements of magnetoresistance as a function of the direction of the applied field, indicate that the angle between the free and pinned layers is about 70ř.

### 8.2.3 *Shamrock Chamber A permanent magnet field measurments*




| | C2) mT |
|---|---|
| Planet 1 | 6.3 |
| Planet 2 | 6.6 |
| Planet 3 | 5.5 |
| Planet 4 | -6.0 |

Figure 8.26: Shamrock Chamber A permanent magnet field measurments

| | | A) mT | B) mT | C) mT | D) mT | E) mT |
|---|---|---|---|---|---|---|
| Planet 1 | 1 | 21.5 | 6.1 | 6.0 | 6.1 | 22.5 |
| | 2 | 22.5 | 6.3 | 6.3 | 6.2 | 21.8 |
| | 3 | 21.5 | 6.2 | 6.2 | 6.3 | 21.9 |
| | | | | | | |
| Planet 2 | 1 | 21.9 | 6.4 | 6.5 | 6.5 | 21.8 |
| | 2 | 21.8 | 6.4 | 6.6 | 6.4 | 22.0 |
| | 3 | 22.0 | 6.4 | 6.5 | 6.2 | 22.0 |
| | | | | | | |
| Planet 3 | 1 | 19.8 | 5.4 | 5.5 | 5.3 | 20.2 |
| | 2 | 20.0 | 5.2 | 5.5 | 5.4 | 20.0 |
| | 3 | 20.0 | 5.4 | 5.5 | 5.2 | 20.1 |
| | | | | | | |
| Planet 4 | 1 | -21.8 | -6.0 | -6.1 | -6.1 | -22.0 |
| | 2 | -22.0 | -6.1 | -6.0 | -6.0 | -22.1 |
| | 3 | -22.0 | -6.1 | -6.0 | -6.0 | -22.3 |

Table 8.7: Shamrock Chamber A permanent magnet field measurments in detail

## 8.3 APPENDIX C - AAO MEMBRANE AND NANOWIRE SAMPLE WEIGHTS

### 8.3.1 *Membrane and Nanowire sample weights*

| Membrane #6809-6022 | Sample Ø (mm) | Poresize (nm) | Thickness (µm) |
|---|---|---|---|
| Whatman Anodisc 25 | 16 | 200 | 55 |
| 0.2µm 25mm Circle | | | |

Table 8.8: Whatman Anodisc 25 details:

The yield weight of the $Co_{65}Ni_{35}$ nanowires that where produced from each membrane was measured using a laboratory high precision balance scales and averaged over a number of samples. Table shows the average sample weight yield in membrane for different lengths of $Co_{65}Ni_{35}$nanowires.

| Type: | Sample 1 (g) | Sample 2 (g) | Sample 3 (g) | Sample 4 (g) | Overall Avg (g) | Au avarage (g) | CoNi weight (Avg) |
|---|---|---|---|---|---|---|---|
| Membrane | 0.035638 | 0.035652 | 0.035681 | 0.035635 | 0.0356515 | | |
| Membrane/Au ~150nm | 0.037281 | 0.037284 | 0.037282 | 0.037286 | 0.03728325 | 0.00163175 | |
| Membrane/Au/CoNi Q40 | 0.051261 | 0.051268 | 0.05127 | 0.05126163 | 0.051265158 | | 0.013981908 |
| Membrane/Au/CoNi Q31 | 0.048698 | 0.048706 | 0.04871 | 0.048691 | 0.04870125 | | 0.011418 |
| Membrane/Au/CoNi 20 | 0.045151 | 0.045162 | 0.045158 | 0.045148 | 0.04515475 | | 0.0078715 |

Table 8.9: CoNi sample weight in complete membrane

| In membrane | Sample Avg (g) | NW Length (µm) |
|---|---|---|
| Au ~150nm | 0.00163175 | |
| CoNi Q40 | 0.013981908 | 15 |
| CoNi Q31 | 0.011418 | 10 |
| CoNi 20 | 0.0078715 | 5 |

Table 8.10: Nanowire length to deposition charge (Q)

| Type: SQUID sample size | Sample 1 (g) | Sample 2 (g) | Sample 3 (g) | Sample 4 (g) | Overall Average (g) | CoNi weight (g) |
|---|---|---|---|---|---|---|
| Membrane 5 x 5 mm | 0.001642 | 0.00165 | 0.001701 | 0.00161 | 0.00165075 | |
| CoNi Q31 Au removed | 0.001801 | 0.001801 | 0.001801 | 0.001801 | 0.001801 | 0.00015025 |

| Type: SQUID sample size | Sample 1 (g) | Sample 2 (g) | Sample 3 (g) | Sample 4 (g) | Overall Average (g) | CoNi weight (g) |
|---|---|---|---|---|---|---|
| Membrane 3 x 3 mm | 0.000664 | 0.000662 | 0.000665 | 0.000661 | 0.000663 | |
| CoNi Q31 Au removed | 0.000852 | 0.00085 | 0.000849 | 0.000848 | 0.00084975 | 0.00018675 |

| Type: SQUID sample size | Sample 1 (g) | Sample 2 (g) | Sample 3 (g) | Sample 4 (g) | Overall Average (g) | CoNi weight (g) |
|---|---|---|---|---|---|---|
| Membrane 2.5 x 2.5 mm | 0.000578 | 0.000579 | 0.000579 | 0.000578 | 0.0005785 | |
| CoNi Q31 Au removed | 0.000716 | 0.000714 | 0.000713 | 0.000713 | 0.000714 | 0.0001355 |

| Type: SQUID sample size | Sample 1 (g) | Sample 2 (g) | Sample 3 (g) | Sample 4 (g) | Overall Average (g) | CoNi weight (g) |
|---|---|---|---|---|---|---|
| Membrane 3 x 2.5 mm | 0.000616 | 0.000613 | 0.000618 | 0.000619 | 0.0006165 | |
| CoNi Q31 Au removed | 0.00074 | 0.000744 | 0.000739 | 0.00074 | 0.00074075 | 0.00012425 |

| Type: SQUID sample size | Sample 1 (g) | Sample 2 (g) | Sample 3 (g) | Sample 4 (g) | Overall Average (g) | CoNi weight (g) |
|---|---|---|---|---|---|---|
| Membrane 3 x 2.5 mm | 0.000615 | 0.000616 | 0.000617 | 0.000617 | 0.00061625 | |
| CoNi Q31 Au removed | 0.000739 | 0.000732 | 0.000738 | 0.000738 | 0.00073675 | 0.0001205 |

| Type: SQUID sample size | Sample 1 (g) | CoNi Sample (g) |
|---|---|---|
| Membrane 3 x 2.5 mm | 0.000617 | |
| CoNi Q31 Au removed | 0.000737 | 0.00012 |

| Type: SQUID sample size | Sample 1 (g) | Sample 2 (g) | Sample 3 (g) | Sample 4 (g) | Overall Average (g) | CoNi weight (g) |
|---|---|---|---|---|---|---|
| Membrane 3 x 2.5 mm | 0.000614 | 0.000615 | 0.000616 | 0.000618 | 0.00061575 | |
| Co Q31 Au removed | 0.000735 | 0.000733 | 0.000737 | 0.000737 | 0.0007355 | 0.00011975 |

| Type: SQUID sample size | Sample 1 (g) | Sample 2 (g) | Sample 3 (g) | Sample 4 (g) | Overall Average (g) | CoNi weight (g) |
|---|---|---|---|---|---|---|
| Membrane 3 x 2.5 mm | 0.000615 | 0.000612 | 0.000615 | 0.000614 | 0.000614 | |
| CoFe Q31 Au removed | 0.000785 | 0.00079 | 0.000792 | 0.00079 | 0.00078925 | 0.00017525 |

Table 8.11: Nanowire sample weight per SQUID sample size

## 8.4 APPENDIX D - NANOWIRE MAGNETIC FIELD CALCULATIONS

### 8.4.1 *Calculated field response of Cobalt nano-wires*

The calculated saturation magnetisation $M_s$ and the saturation flux density$B_s$ for Co is equal to the product of the net magnetic moment for each atom and the number of atoms present. For Cobalt the net magnetic moments per atom is 1.72 $\mu_B$. Where$\mu_B = 9.27 \times 10^{-24} Am^2$. The number of atoms per cubic meter is determined by,

$$N = \frac{\rho N_A}{A_{Ni}} \tag{8.2}$$

Where $\rho$ is the density, $A_{Ni}$ is the atomic weight and $N_A$is Avogadro's number

$$N = \frac{(8.86 \times 10^6 g/m^3) \times (6.023 \times 10^{23} atom/mol)}{58.93 g/mol} = 9.055 \times 10^{28} atoms/m^3 \quad (8.3)$$

The calculated saturation magnetisation $M_s = 1.72 \mu_B N = 1450\, kA/m$. The corresponding saturation flux density $B_s = \mu_0 M_S = 1.82\, Tesla$.

### 8.4.2 *Magnetic field calculation for Cobalt nano-wires*

The magnetisation curve as measured in Chapter 4 Section 4.3.3 for Cobalt (Co) is shown in Figure 8.27. From the magnetisation curve we can determine the in-plance remanent magnetic moment $m_r$ per measured sample. This will allow us to calculate the magnetic moment $m_r$ per nanowire.

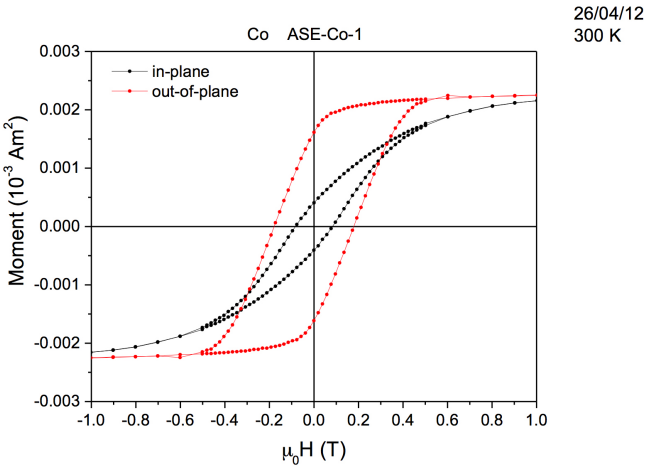



Figure 8.27: Magnetisation curve for measured for Cobalt (Co) magnetic nanowire sample

From the magnetisation curve for $Co$, the remanent magnetic moment $m_r$ per measured sample, $m_r(per\, measured\, sample) = 0.93 \times 10^{-6} Am^2$. Table 8.12 shows the measured sample weight for the $Co$ nanowires and the nanowire characteristics. As the nanowire sample is in membrane, the weight of the Co nano-wire sample was determined by averaging four Co samples and then subtracting the weight of the AAO membrane, see Appendix C for AAO membrane and nano-wire sample weights. The Co nano-wires have a lenght 10 μm and diameter 200 nm. The Co density 8860 kg/m$^3$value is taken from the bulk physical properties.

| Co sample | |
|---|---|
| Sample weight | 102 µg |
| Nanowire length $l$ | 10 µm |
| Nanowire diameter $d$ | 200 nm |
| Density $\rho$ | 8860 kg/m$^3$ |

Table 8.12: Cobalt nanowire sample details

From the magnetisation curve the remanent Magnetisation $M_r$ per measured sample is,

$$M_r(measured\,sample) = \frac{m_r}{sample\,weight} = \frac{0.95 \times 10^{-6}}{102 \times 10^{-6}} = 9.314 \frac{Am^2}{kg} \tag{8.4}$$

The nanowire volume $V_{nw}$,

$$V_{nw} = \frac{\pi \times (d)^2}{4} = \frac{\pi \times (200 \times 10^{-9})^2}{4} = 10 \times 10^{-6} = 0.314 \mu m^3 \tag{8.5}$$

The remanent magnetic moment $m_r$per nanowire is,

$$m_r(per\,nanowire) = M_r \times V_{nw} \times \rho = 2.604 \times 10^{-14} Am^2 \tag{8.6}$$

Taking the saturation value from the magnetisation curve measured for $Co$, the saturation magnetic moment $m_s$ per nanowire is $4 \times 10^{-13} Am^2$. This gives $m_r/m_s = 6.51\%$. The nano-wires saturation field response $B_s$ is 1.6 Tesla.

The therotical calculated saturation magnetisation for Co $M_s = 1450\,kA/m$ and the corresponding saturation flux density$B_s = 1.82\,Tesla$ see Appendix C Section 8.3.2.

#### 8.4.2.1 *Magnetic field response of Cobalt nano-wire at distances from the magnetoresistive sensor*

The field response $B_r$ in Tesla of Co nano-wires at heights $(z)$ from the magnetoresistive sensor was calculated from the following expression,

$$B_r = \frac{\mu_0 \times m}{4\pi(z^3)} \tag{8.7}$$

| Cobalt (Co) | Channel height (µm) | Field response (µT) |
|---|---|---|
| Length 10 µm | 4 | 40.69 |
| Diameter 200 nm | 6 | 12.056 |
| | 8 | 5.086 |
| | 10 | 2.604 |
| | 14 | 0.949 |
| | 18 | 0.447 |
| | 25 | 0.167 |
| | 30 | 0.096 |

Table 8.13: Field calculation of a Co nanowire at various heights in the microfluidic channel

Where $\mu_0 = 4\pi \times 10^{-7}$is the permeability of free space and $m_r$ is the remanent magnetic moment per nanowire. The magnitude of the response at heights $(z)$ will provide an indication of the experimental signal response magnetude of the magnetic nanowire as it flows across the sensor. The microfluidic channel used for my experimental work had a height of 30 µm. From the calculation in Eq.53, a Co nanowire traveling at a channel height (z) of 6 µm should have a magnetude field response of 12.056 µT.

$$B_r = \frac{4\pi \times 10^{-7} \times 2.604 \times 10^{-14} Am^2}{4\pi} \times \frac{1}{(6\mu m)^3} = 12.056\,\mu T \tag{8.8}$$

Table 8.13shows the field calculation of a Co nanowire at various heights in the microfluidic channel.

In the nano-wire detection experiments using a single sensor configuration as outlined in this Chapter the backgroupd noise measured 0.423 Volt at a gain of 10,000, which is 43 µV. This corresponded to field equivalent noise of ~ 10 µT. Therefore the nanowires would need to flow at a height of less than 6 µm in the microfluiduc channel before there is any signal detection of nanowires.

The response of the Co nanowire at various heights $(z)$ above the sensor was also modelled using Manifest, which is a finite element and surface charge magnetics package. The nano-wire parameters lenght, diameter and magnetic moment $m_r$ are entered into the cylinder model and the response at distance $(z)$ from the nano-wire is calculated. Figure 8.28 shows the response of the nano-wire above the sensor.

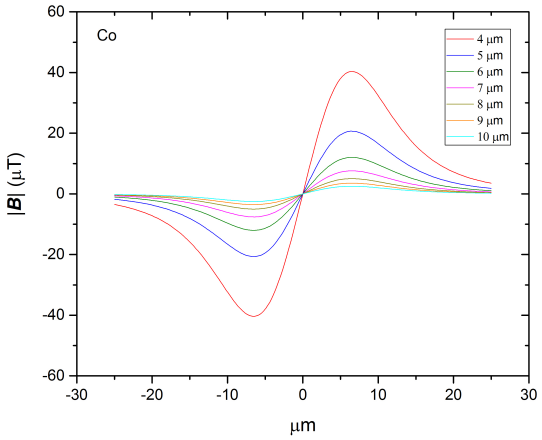



Figure 8.28: Model response of Co nano-wires at different heights z above the sensor

The shape of the modeled response is consistent with what we would expect for a magnetic nanowire dipole field. The cylinder dipole field is anisotropic, with twice the magnetude at the axical to the broadside and the magnetude falls off as $z^3$, were z is the distance from the dipole. From the nodeled response of the Co nano-wire, as the height increases the field magnitude response decreases by $z^3$.

## 8.5 MAGNETIC FIELD CALCULATION FOR FOR $CO_{50}FE_{50}$NANO-WIRES

The magnetisation curve as measured in Chapter 4 Section 4.3.4 for $Co_{50}Fe_{50}$ is shown in Figure 8.17. From the magnetisation curve we can determine the in-plance remanent magnetic moment $m_r$ per measured sample. This will allow us to calculate the magnetic moment $m_r$ per nanowire.

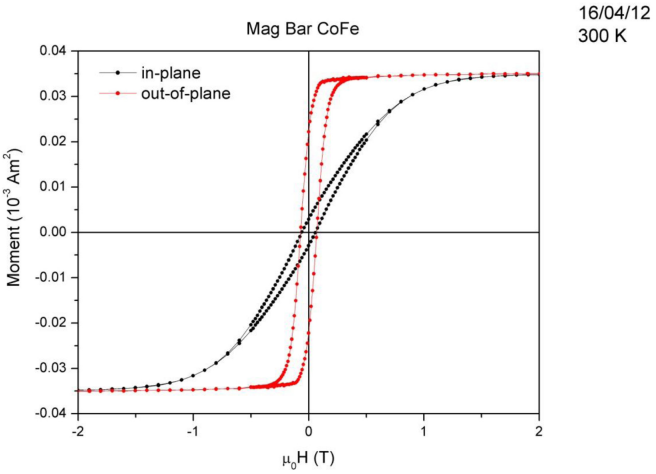



Figure 8.29: Magnetisation curve $Co_{50}Fe_{50}$

From the magnetisation curve for $Co_{50}Fe_{50}$, the remanent magnetic moment $m_r$ per measured sample, $m_r(permeasuredsample) = 2.5 \times 10^{-6} Am^2$. Table 8.14 shows the measured sample weight for the $Co_{50}Fe_{50}$ nanowires and the nanowire characteristics. As the nanowire sample is in membrane, the weight of the $Co_{50}Fe_{50}$ nano-wire sample was determined by averaging four $Co_{50}Fe_{50}$ samples and then subtracting the weight of the AAO membrane, see Appendix C Section 8.3.1 for AAO membrane and nano-wire sample weights. The $Co_{50}Fe_{50}$ nano-wires have a lenght 10 µm and diameter 200 nm. The $Co_{50}Fe_{50}$density 8387 kg/m$^3$value is calculated from the bulk physical properties.

| $Co_{50}Fe_{50}$ sample | |
|---|---|
| Sample weight | 175 µg |
| Nanowire length $l$ | 10 µm |
| Nanowire diameter $d$ | 200 nm |
| Density $\rho$ | 8387 kg/m$^3$ |

Table 8.14: $Co_{50}Fe_{50}$ nanowire sample details

From the magnetisation curve the remanent Magnetisation $M_r$ per measured sample is,

$$M_r(measured\,sample) = \frac{m_r Am^2}{sample\,weight} = \frac{2.4 \times 10^{-6} Am^2}{175 \times 10^{-6} g} = 14.28 \frac{Am^2}{kg} \tag{8.9}$$

The nanowire volume $V_{nw}$,

$$V_{nw} = \frac{\pi \times (d)^2}{4} = \frac{\pi \times (200 \times 10^{-9})^2}{4} = 10 \times 10^{-6} = 0.314 \mu m^3 \tag{8.10}$$

The remanent magnetic moment $m_r$per nanowire is,

$$m_r(per\, nanowire) = M_r \times V_{nw} \times \rho = 3.764 \times 10^{-14} Am^2 \tag{8.11}$$

Taking the saturation value from the magnetisation curve measured for $Co_{50}Fe_{50}$, the saturation magnetic moment $m_s$ per nanowire is $4.5 \times 10^{-13} Am^2$. This gives $m_r/m_s = 8.365\%$. The nano-wires saturation field response $B_s$ is 1.8 Tesla.

### 8.5.1 *Calculated field response of $Co_{50}Fe_{50}$ nano-wires*

The calculated saturation magnetisation $M_s$ and the saturation flux density$B_s$ for $Co_{50}Fe_{50}$ is equal to the product of the net magnetic moment for each atom and the number of atoms present. For Cobalt the net magnetic moments per atom is 1.72 $\mu_B$and for Iron the net magnetic moments per atom is 2.22 $\mu_B$. Where$\mu_B = 9.27 \times 10^{-24} Am^2$. The number of atoms per cubic meter is determined by,

$$N = \frac{\rho N_A}{A_{Ni}} \tag{8.12}$$

Where $\rho$ is the density, $A_{Ni}$ is the atomic weight and $N_A$is Avogadro's number. For Fe this calculates as,

$$N = \frac{(7.874 \times 10^6 g/m^3) \times (6.023 \times 10^{23} atom/mol)}{55.85 g/mol} = 8.498 \times 10^{28} atoms/m^3 \tag{8.13}$$

The calculated saturation magnetisation for Fe $M_s = 1.72 \mu_B N = 1748\, kA/m$. The corresponding saturation flux density for Fe $B_s = \mu_0 M_S = 2.19\, Tesla$. For Co the calculated saturation magnetisation $= 1450\, kA/m$. The corresponding saturation flux density for Fe $B_s = 1.82\, Tesla$. So for $Co_{50}Fe_{50}$ the magnetic saturation,$M_s = 1599\, kA/m$, the corresponding saturation flux density, $B_s = 2.00\, Tesla$.

### 8.5.2 *Magnetic field response of Cobalt nano-wires at distances from the magnetoresistive sensor*

The field response $B_r$ in Tesla of$Co_{50}Fe_{50}$ nano-wires at distances $(z)$ from the magnetoresistive sensor can be determined using the following expression,

$$B_r = \frac{\mu_0 \times m}{4\pi(z^3)} \tag{8.14}$$

Where $\mu_0 = 4\pi \times 10^{-7}$is the permeability of free space and$m_r$is the remanent magnetic moment per nanowire. The magnitude of the response at distances $(z)$ will provide an indication of the experimental signal response from the magnetic nanowire as if flows across the sensor. The microfluidic channel used for my experimental work had a height of 30 µm. From the calculation in Eq.58, a $Co_{50}Fe_{50}$ nanowire traveling at a channel height (z) of 6 µm should have a magnetude field response of 12.056 µT.

$$B_r = \frac{4\pi \times 10^{-7} \times 2.604 \times 10^{-14} Am^2}{4\pi} \times \frac{1}{(6.5\mu m)^3} = 12\,\mu T \tag{8.15}$$

Table 8.15 shows the field calculation of a $Co_{50}Fe_{50}$ nanowire at various heights in the microfluidic channel.

| $Co_{50}Fe_{50}$ | Channel height (µm) | Field response (µT) |
|---|---|---|
| Length 10 µm<br>Diameter 200 nm | 4 | 49.602 |
| | 6 | 14.697 |
| | 8 | 6.200 |
| | 10 | 3.175 |
| | 14 | 3.175 |
| | 18 | 1.157 |
| | 25 | 0.203 |
| | 30 | 0.118 |

Table 8.15: Field calculation of a Co50Fe50 nanowire at various heights in the microfluidic channel.

In the nano-wire detection experiments using a single sensor configuration as outlined in this Chapter the backgroupd noise measured 0.423 Volt at a gain of 10,000, which is 43 µV. This corresponded to field equivalent noise of ~ 10 µT. Therefore the nanowires would need to flow at a height of less than 6.5 µm in the microfluiduc channel before there is any signal detection of nanowires.

The response of the $Co_{50}Fe_{50}$ nanowire at various heights ($z$) above the sensor was also modelled using Manifest, which is a finite element and surface charge magnetics package. The nano-wire parameters lenght, diameter and magnetic moment $m_r$ are entered into the cylinder model and the response at distance ($z$) from the nano-wire is calculated. Figure 8.30 shows the response of the nano-wire above the sensor.

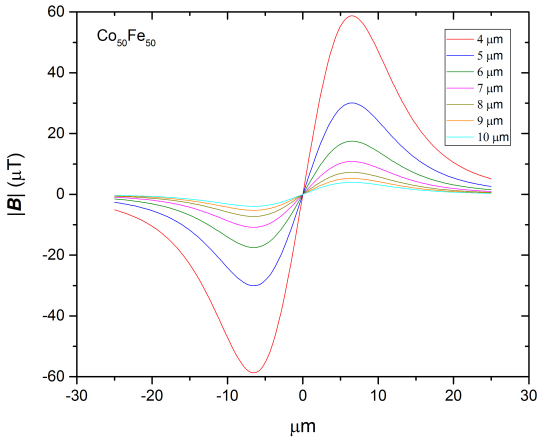



Figure 8.30: Model response of CoFe nanowire at different heights$z$ above the sensor

The shape of the modeled response is consistent with what we would expect for a magnetic nanowire dipole field. The cylinder dipole field is anisotropic, with twice the magnetude at the axical to the broadside and the magnetude falls off as $z^3$, were z is the distance from the dipole. From the nodeled response of the Co nano-wire, as the height increases the field magnitude response decreases by $z^3$.

## 8.6 MAGNETIC FIELD CALCULATION FOR FOR $co_{65}ni_{35}$ NANO-WIRES

The magnetisation curve as measured in Chapter 4 Section 4.3.4 for $Co_{65}Ni_{35}$ is shown in Figure 8.31. From the magnetisation curve we can determine the in-plance remanent magnetic moment $m_r$ per measured sample. This will allow us to calculate the magnetic moment $m_r$ per nanowire.

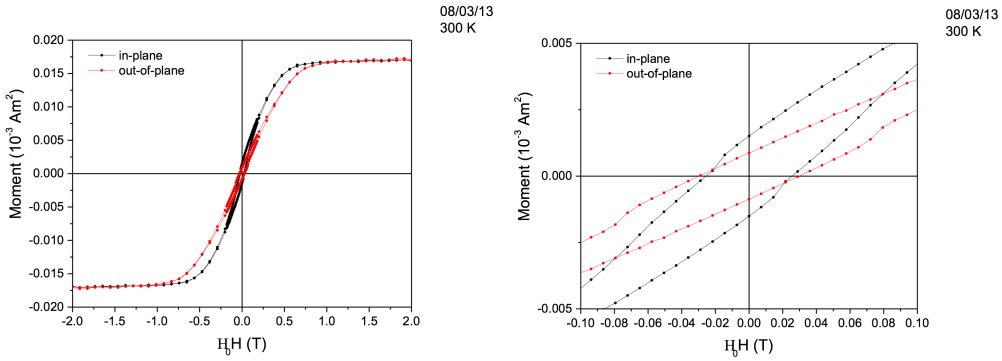



Figure 8.31: Magnetisation curve for $Co_{65}Ni_{35}$ nanowires in membrane

From the magnetisation curve for $Co_{65}Ni_{35}$, the remanent magnetic moment $m_r$ per measured sample, $m_r(permeasuredsample) = 1 \times 10^{-6} Am^2$. Table 8.16 shows the measured sample weight for the $Co_{65}Ni_{35}$ nanowires and the nanowire characteristics. As the nanowire sample is in membrane, the weight of the $Co_{65}Ni_{35}$ nano-wire sample was determined by averaging four $Co_{65}Ni_{35}$ samples and then subtracting the weight of the AAO membrane, see Appendix C Section 8.3.1 for AAO membrane and nano-wire sample weights. The $Co_{65}Ni_{35}$ nano-wires have a lenght 10 μm and diameter 200 nm. The $Co_{65}Ni_{35}$ density 8903 kg/m$^3$value is calculated from the bulk physical properties.

| $Co_{65}Ni_{35}$ sample | |
|---|---|
| Sample weight | 120 μg |
| Nanowire length $l$ | 10 μm |
| Nanowire diameter $d$ | 200 nm |
| Density $\rho$ | 8903 kg/m$^3$ |

Table 8.16: $Co_{65}Ni_{35}$ nanowire sample details

From the magnetisation curve the remanent Magnetisation $M_r$ per measured sample is,

$$M_r(measured\,sample) = \frac{m_r Am^2}{sample\,weight} = \frac{1 \times 10^{-6} Am^2}{120 \times 10^{-6} g} = 8.333 \frac{Am^2}{kg} \tag{8.16}$$

The nanowire volume $V_{nw}$,

$$V_{nw} = \frac{\pi \times (d)^2}{4} = \frac{\pi \times (200 \times 10^{-9})^2}{4} = 10 \times 10^{-6} = 0.314 \mu m^3 \tag{8.17}$$

The remanent magnetic moment $m_r$per nanowire is,

$$m_r(per\,nanowire) = M_r \times V_{nw} \times \rho = 2.331 \times 10^{-14} Am^2 \tag{8.18}$$

Taking the saturation value from the magnetisation curve measured for $Co_{65}Ni_{35}$, the saturation magnetic moment$m_s$per nanowire is$3.496 \times 10^{-13} Am^2$. This gives $m_r/m_s =$ 7.172%. The nano-wires saturation field response $B_s$ is 1.3 Tesla.

### 8.6.1 *Calculated field response of $Co_{65}Ni_{35}$ nano-wires*

The calculated saturation magnetisation $M_s$ and the saturation flux density$B_s$ for $Co_{65}Ni_{35}$ is equal to the product of the net magnetic moment for each atom and the number of atoms present. For Cobalt the net magnetic moments per atom is 1.72 $\mu_B$and for Nickel the net magnetic moments per atom is 1.72 $\mu_B$. Where$\mu_B = 9.27 \times 10^{-24} Am^2$. The number of atoms per cubic meter is determined by,

$$N = \frac{\rho N_A}{A_{Ni}} \tag{8.19}$$

Where $\rho$ is the density, $A_{Ni}$ is the atomic weight and $N_A$is Avogadro's number. For Nickel this calculates as,

$$N = \frac{(8.90 \times 10^6 g/m^3) \times (6.023 \times 10^{23} atom/mol)}{58.71 g/mol} = 9.13 \times 10^{28} atoms/m^3 \tag{8.20}$$

The calculated saturation magnetisation for Nickel $M_s = 1.72\mu_B N = 510\,kA/m$. The corresponding saturation flux density for Nickel $B_s = \mu_0 M_S = 0.64\,Tesla$. For Co the calculated saturation magnetisation $= 1450\,kA/m$. The corresponding saturation flux density for Fe $B_s = 1.82\,Tesla$. So for $Co_{65}Ni_{35}$ the magnetic saturation,$M_s = 1120\,kA/m$, the corresponding saturation flux density, $B_s = 1.4\,Tesla$.

| $Co_{65}Ni_{35}$ | Channel height (µm) | Field response (µT) |
|---|---|---|
| Length 10 µm | 4 | 36.419 |
| Diameter 200 nm | 6 | 10.791 |
| | 8 | 4.552 |
| | 10 | 2.331 |
| | 14 | 0.849 |
| | 18 | 0.4 |
| | 25 | 0.149 |
| | 30 | 0.086 |

Table 8.17: Field calculation of a Co65Ni35 nanowire at various heights in the microfluidic channel

### 8.6.2 *Magnetic field response of $Co_{65}Ni_{35}$ nano-wires at distances from the magnetoresistive sensor*

The field response $B_r$ in Tesla of$Co_{65}Ni_{35}$ nano-wires at distances $(z)$ from the magnetoresistive sensor can be determined using the following expression,

$$B_r = \frac{\mu_0 \times m}{4\pi(z^3)} \tag{8.21}$$

Where $\mu_0 = 4\pi \times 10^{-7}$is the permeability of free space and$m_r$is the remanent magnetic moment per nanowire. The magnitude of the response at distances $(z)$ will provide an indication of the experimental signal response from the magnetic nanowire as if flows across the sensor. The microfluidic channel used for my experimental work had a height of 30 µm. From the calculation in Eq.65, a $Co_{65}Ni_{35}$ nanowire traveling at a channel height (z) of 5.8 µm should have a magnetude field response of 12 µT.

$$B_r = \frac{4\pi \times 10^{-7} \times 2.604 \times 10^{-14} Am^2}{4\pi} \times \frac{1}{(5.8\mu m)^3} = 12\,\mu T \tag{8.22}$$

Table 8.17 shows the field calculation of a $Co_{65}Ni_{35}$ nanowire at various heights in the microfluidic channel.

In the nano-wire detection experiments using a single sensor configuration as outlined in this Chapter the backgroupd noise measured 0.423 Volt at a gain of 10,000, which is 43 µV. This corresponded to field equivalent noise of ~ 10 µT. Therefore the nanowires would need to flow at a height of less than 5.8 µm in the microfluiduc channel before there is any signal detection of nanowires.

The response of the $Co_{65}Ni_{35}$ nanowire at various heights ($z$) above the sensor was also modelled using Manifest, which is a finite element and surface charge magnetics package. The nano-wire parameters lenght, diameter and magnetic moment $m_r$ are entered into the cylinder model and the response at distance ($z$) from the nano-wire is calculated. Figure 8.32 shows the response of the nano-wire above the sensor.

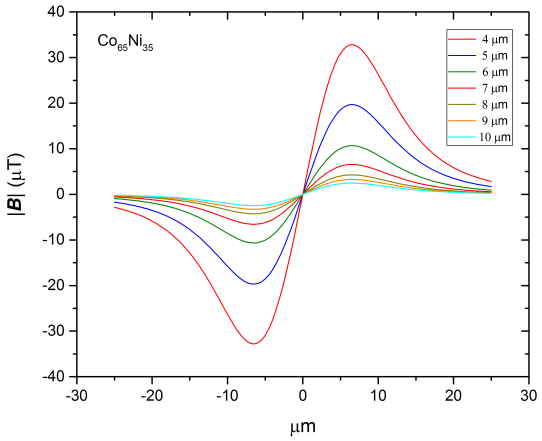



Figure 8.32: Model response of $Co_{65}Ni_{35}$ nano-wires in membrane at different heights$z$ above the sensor

The shape of the modeled response is consistent with what we would expect for a magnetic nanowire dipole field. The cylinder dipole field is anisotropic, with twice the magnetude at the axical to the broadside and the magnetude falls off as $z^3$, were z is the distance from the dipole. From the nodeled response of the $Co_{65}Ni_{35}$ nano-wire, as the height increases the field magnitude response decreases by $z^3$.

## 8.7 APPENDIX E - NANOWIRE FABRICATION PROCEDURES

### 8.7.1 *Cobalt (Co) solution procedure:*

- Use volumetric cylinder to measure 60 ml of Di water. Add the Di water to a beaker. (Do not add the full 100 ml because saturation occurs in the solution)

- Place a large plastic dish on weighing scale and measure the Boric acid. Add the Boric acid to the beaker and stir magnetically. This is done because Boric acid is highly concentrated and takes the longest time to dissolve
- Place a large plastic dish on weighing scale and measure the Cobalt Sulfate Heptahydrate
- Place a small plastic dish on weighing scale and measure the Sodium Chloride
- Add the Cobalt Sulfate Heptahydrate and the Sodium Chloride to the beaker
- Stir for 15 minutes
- Add 20 ml of DI water
- Stir for 15 minutes
- Add 20 ml of Di water
- Stir until solution is completely dissolved

### 8.7.2 *Cobalt (Co) Electrodeposition procedure:*

A commercial potentiostat (Solatron SI 1280B) is used to grow the wires potentiostatically. A small glass cell is designed to hold one membrane as the cathode against an O-ring.

- Clean equipment and rinse in DI water
- Attach lead to sputtered gold on membrane surface using silver paint
- Place membrane in seal and tighten clip. Solution will leak if clip is unevenly tightened. Over tightening will result in a cracked membrane.
- Add Co solution to cylinder
- Remove reference electrode from KCl solution, rinse with DI water. (This electrode is calibrated and marked accordingly). The position of the RE in the cell is critical
- Attach the counter electrode

- Position the electrode and attach the RE, CE and WE wires accordingly
- An over potential of 1.0 V is used. Depending on length required, the deposition may continue for 30 – 60 minutes. The total charge passed is monitored by the potentiostat.
- Solatron software setup - Open folder /name, Double click 'Potentiostatic'; insert a new filename (date) and set the potential, Select measure up to start test, select Graphic – To view plots and overlay different plots

### 8.7.3 *Cobalt (Co) nanowire removal from membrane procedure:*

After deposition the nanowires are then released from the membrane. Firstly the gold layer is removed from the membrane using a polishing process. The membrane is then dissolved to remove the alumina and so releasing the wires. This process is critical to produce wires with good surface structure producing wires that are well dispersed. The wires are released by dissolving the membrane in sodium hydroxide (NaOH) at a set temperature for a period of time. 1 molar of NaOH is prepared by dissolving 4g of NaOH into 100ml of DI water. The membrane is placed into a beaker of 10ml of the NaOH solution at 60oC for 7 minuets. When the alumina has been dissolved the sample is then placed in an ultrasonic bath for 20 seconds to separate the wires. The NaOH solution is removed by centrifuging the solution at 2900 rpm for 3 min. The NaOH solution is removed leaving the pellet of nanowires. The centrifuging process is repeated six times using DI water to ensure that the NaOH has been fully removed. The pH of the solution should measure around 7 (pH~7) indicating that there is no effective NaOH left around wires. The wires should now be well separated, unbroken with the alumina removed.

Procedure

Wires are liberated from the membrane by dissolving the membrane in NaOH.

- Place membrane in a 100 ml beaker. (The gold backing is first polished off with backing paper)

- Add a 1M NaOH solution to a beaker and heat on a hotplate to 30°C. Use a thermometer to monitor the temperature
- Place the beaker in a larger beaker of DI water and place in sonic bath
- Sonicate for 7-10 minutes. The timing is critical
- Shake well each minute
- Look for a rapid rapid color change in solution from clear to murky yellow
- When the membrane is dissolved, hold wires using magnet and remove NaOH using pipette
- Add DI water and sonicate for 10 seconds. Dispose of pipette
- Using the magnet and a new pipette, remove DI water
- Repeat the following rinsing steps 10 times - Add DI water, Sonicate for 10 seconds, Shake well, Remove DI water
- Label jar (Date, Type, Potential, Charge)
- Seal jar in parafilm and place in the sonic bath for 1 hour

### 8.7.4 *CoFe & Cu solution procedure*

The CoFe solution detailed in Table 4.6 is prepared using 8.41g CoSO4.7H2O (Cobalt-Sulfate) with 8.57g FeSO4.7H2O (IronSulfate), 2g Boric Acid and 1g L-Ascorbic acid in 100ml Di water. 50 ml of DI water was added to a 100 ml beaker and all of the powders are added. The solution is stirred until completely dissolved, the remaining 50ml if DI water is then added. This produces 100 ml of the CoFe 0.3 Molar solution. The Cu solution is prepared using 0.5 g of Copper Sulfate (CuSO4.5H2O) mixed in 100ml DI water.

Preparation procedure for CoFe solution

1. Put a plastic spoon in the all 4 containers, they are usually beside glove-box in P5. You can realize them through the spoons

2. Put all the powders in a Beaker and add around 50 milli-liter of water and put it on the stirrer and let it dissolve

3. Put the solution in a 100 milliliter Volumetric Flax and add DI water until the solution volume reaches 100 milliliter

4. This produces 100 milliliter of the CoFe 0.3 Molar

Preparation procedure for Cu solution

1. Take 2.5 gram of Copper Sulfate )CuSO4.5H2O)

2. Dissolve the powder same as above in 100 milliliter of DI water

3. This produces 100 millilitres of the 0.1M Cu solution

### 8.7.5 *CoFe-Cu-CoFe nanowire electrodepositon procedure*

Prepare Wathman membrane with gold sputtered on back and make a connection with the silver wire and silver paintSet-up glass deposition cell with reference electrode and platinum electrode Set-up Solatron potentiostate,

Turn on the potentiostat —-> open the CoreWare software on the Desktop—-> go to insert experiment —-> potentiostatic mode.

1. Set voltage on -0.95 V

2. Select "VS. Reference Electrode"

3. Set time on 1500 seconds

4. Connect the RED alligator to Platinum electrode

5. Connect the WHITE alligator to the reference electrode

6. Connect the GREEN alligator to the membrane

7. Pour prepared solution of CoFe to the cell and run the experiment and wait for the 1500 seconds to be finished ( This the first CoFe segment)

8. When this is complete, remove the excess solution and pour in the Copper solution
9. The Cu segment requires voltage set to -0.95 V and run for 800 seconds (This produces Cu Segment)
10. When this is complete, remove the excess Cu solution and again pour CoFe solution
11. Repart steps 1 – 7 this will produce the Run the second CoFe Segment
12. In each step carried out name the file and save it
13. Repeat the process as many segments as required

### 8.7.6 *CoNi-Cu-CoNi solution procedure*

1. CoNi 0.3 molar solution as per Table 8.18
2. 50ml of DI water is added to a 100 ml beaker and all of the powders are added.
3. The solution is stirred until completely dissolved
4. The remaining 50ml of DI water is then added
5. CoNiCu interlayer solution with a ratio of CoNi 0.63% : Cu 0.37%
6. Cu solution as per Table 8.18
7. 0.5 g of Copper Sulfate (CuSO4.5H2O) mixed in 100ml DI water

| Solution | Vol (cc) | Composition | Weight (g) | Molarity |
|---|---|---|---|---|
| CoNi 0.65M:0.35M | 50 | NaCl | 0.146 | |
| | | $CoSo_4$ | 9.13 | 0.65 |
| | | $NiSo_4$ | 4.83 | 0.36 |
| | | $H_3Bo_3$ | 0.37 | 0.12 |
| CoNiCu Interlayer | | CoNi | 0.63% | |
| | | Cu | 0.37% | |
| Cu | 10 | CuSo4 | 2.54 | 1 |

Table 8.18: CoNi, CoNiCu interlayer and solution Cu solution

### 8.7.7 *CoNi-Cu-CoNi electrodepositon procedure*

| Sequence | Metal | Potential | Charge (Q) | Length (μm) | Time (sec) |
|---|---|---|---|---|---|
| 1st magnetic segment | CoNi | -0.9v | 15 | 3.5 | 2500 |
| Interlayer | CoNiCu | -0.7 | | | 5 |
| | | -0.6 | | | 5 |
| Non-magnetic segment | Cu | -0.4 | 14 | 3 | 3 |
| | | -0.2 | | | 70 |
| | | -0.2 | | | 600 |
| 2nd magnetic segment | CoNi | -0.9v | 15 | 3.5 | 2500 |

Table 8.19: Deposition sequence for CoNi-Cu-CoNi segmented nanowires

### 8.7.8 *Growth conditions of some of the CoNi and CoNi-Cu-CoNi nanowire batches produced*

Table 8.20 and 8.21 highlight the conditions used for the growth of some of the CoNi and CoNi-Cu-CoNi nanowire batches produced.

| Sample | Segment | Type | Pot (V) | Time (Sec) | I (mA) | Charge (Q) | Length (μm) | OCP (V) | Mag (T) |
|---|---|---|---|---|---|---|---|---|---|
| 091215-1 | CoNi | | -0.9 | 5000 | 6.0 | 31 | 7 | 0.12 | 1.2 |
| 091215-2 | CoNi | | -0.9 | 5000 | 6.0 | 31 | 7 | 0.12 | 1.2 |
| 101215-1 | CoNi | | -0.9 | 7500 | 6.2 | 45 | 12 | 0.12 | 1.2 |
| 101215-2 | CoNi | | -0.9 | 7500 | 6.2 | 45 | 12 | 0.12 | 1.2 |
| 111215-1 | CoNi | | -0.9 | 2500 | 6.8 | 18 | 3 | 0.12 | 1.2 |
| 111215-2 | CoNi | | -0.9 | 2500 | 6.8 | 18 | 3 | 0.12 | 1.2 |
| 101215 | CoNi | | -0.9 | 7500 | 6.2 | 45 | 12 | 0.18 | 1.2 |
| 120116 | CoNi | | -0.9 | 6000 | 8.0 | 40 | 10 | 0.12 | 1.2 |
| 130116 | CoNi | | -0.9 | 6000 | 7.8 | 40 | 10 | 0.20 | 1.2 |
| 130116-1 | CoNi | | -0.9 | 3000 | 5.5 | 25 | 5 | 0.20 | 1.2 |
| 130116-2 | CoNi | | -0.9 | 3000 | 6.0 | 25 | 5 | 0.20 | 1.2 |
| 210116 | CoNi | | -0.9 | 6000 | 6.5 | 40 | 10 | 0.20 | 1.2 |
| | | | | | | | | | |

Table 8.20: CoNi deposition conditions

| Sample | Segment | Type | Pot (V) | Time (Sec) | I (mA) | Charge (Q) | Length (µm) | OCP (V) | Mag (T) |
|---|---|---|---|---|---|---|---|---|---|
| 231115-1 | CoNi | 1st mag seg | -0.9 | 6000 | 9 | 40 | 10 | 0.18 | 1.2 |
| CoNiCuCoNi | CoNiCu | Interlayer | -0.7 | 3 | 35 | | | | |
| | | | -0.6 | 3 | 30 | | | | |
| | Cu | Spacer | -0.4 | 3 | 25 | | | | |
| | | | -0.2 | 600 | 14 | 20 | 5 | | |
| | CoNi | 2nd mag seg | -0.9 | 6000 | 11 | 40 | 10 | | |
| | | | | | | | | | |
| 231115-2 | CoNi | 1st mag seg | -0.9 | 6000 | 6.8 | 40 | 10 | 0.18 | 1.2 |
| CoNiCuCoNi | CoNiCu | Interlayer | -0.7 | 3 | | | | | |
| | | | -0.6 | 3 | | | | | |
| | Cu | Spacer | -0.4 | | | | | | |
| | | | -0.2 | 600 | | 20 | 5 | | |
| | CoNi | 2nd mag seg | -0.9 | 6000 | 7.0 | 50 | 10 | | |
| | | | | | | | | | |
| 081215-1 | CoNi | 1st mag seg | -0.9 | 5000 | 6.0 | 30 | 7 | 0.12 | 1.2 |
| CoNiCuCoNi | CoNiCu | Interlayer | -0.7 | 3 | 6.8 | | | | |
| | | | -0.6 | 3 | 2.5 | | | | |
| | Cu | Spacer | -0.4 | 3 | 18 | | | | |
| | | | -0.2 | 600 | 11 | 20 | 5 | | |
| | CoNi | 2nd mag seg | -0.9 | 5000 | 6.8 | 30 | 7 | | |
| | | | | | | | | | |
| 081215-1 | CoNi | 1st mag seg | -0.9 | 5000 | 6.8 | 31 | 7 | 0.12 | 1.2 |
| CoNiCuCoNi | CoNiCu | Interlayer | -0.7 | 3 | 6.8 | | | | |
| | | | -0.6 | 3 | 2.5 | | | | |
| | Cu | Spacer | -0.4 | 3 | 18 | | | | |
| | | | -0.2 | 600 | 11 | 20 | 5 | | |
| | | | | | | | | | |
| | | | | | | | | | |
| | CoNi | 2nd mag seg | -0.9 | 5000 | 6.8 | 31 | 7 | | |
| | | | | | | | | | |
| 181215 | CoNi | 1st mag seg | -0.9 | 2500 | 6.5 | 15 | 3.5 | 0.12 | 1.2 |
| CoNiCuCoNi | CoNiCu | Interlayer | -0.7 | 3 | 40 | | | | |
| | | | -0.6 | 3 | 20 | | | | |
| | Cu | Spacer | -0.4 | 3 | 15 | | | | |
| | | | -0.2 | 600 | 11 | 20 | 5 | | |
| | CoNi | 2nd mag seg | -0.9 | 2500 | 6.0 | 15 | 3.5 | | |

Table 8.21: CoNi-Cu-CoNi deposition conditions

### 8.7.9 *CoNi & CoNi-Cu-CoNi nanowires seperation from membrane*

After deposition wires are then released from the membrane. Similar to the process described in section firstly the gold layer is removed from the membrane using a polishing process, the membrane is then dissolved to remove the alumina and so releasing the wires using sodium hydroxide (NaOH) at a set temperature for a period of time. NaOH 1 molar was prepared by dissolving 4g of NaOH into 100ml of DI water. The CoNi membrane is placed into a beaker of 10ml of the NaOH solution at 700C. A process of sonication and inspection every 2 – 3 minuits as detailed in Table 8.22 is used to remove the alumina from the membrane. When complete the NaOH solution is removed

to stop the reaction by using a magnet to hold the nanowires and the NaOH removed. The nanowires are washed six times in DI water to removed any NaOH solution. This process is critical to produce wires with good surface structure producing wires that are well dispersed and requires constant visual inspection for each respective nanowire batch produced.

| Sample | Type | Solution (1molar) | Temp (°C) | Method | Weight (g) |
|---|---|---|---|---|---|
| 071215 | CoNi-Cu-CoNi | Na0H | 70 | Min 4/sonication 10sec, Min 8/ sonication 10sec, Min 10 stop, Rinse in DI water x 6 using magnet | 0.0913 |
| 081215 | CoNi-Cu-CoNi | Na0H | 70 | Min 4/sonication 10sec, Min 8/ sonication 10sec, Min 10 stop, Rinse in DI water x 6 using magnet | 0.0930 |
| 101215 | CoNi | Na0H | 70 | Min 3/sonication 10sec, Min 5/ sonication 10sec, Min 11/ sonication 10sec, stop, Rinse in DI water x 6 using magnet | 0.0933 |
| 101215 | CoNi | Na0H | 70 | Min 5/sonication 10sec, Min 8/ sonication 10sec, Min 11/ sonication 10sec, stop Min 12, Rinse in DI water x 6 using magnet | 0.0932 |
| 111215 | CoNi | Na0H | 70 | Min 3/sonication 10sec, Min 5/ sonication 10sec, Min 11/ sonication 10sec, stop, Rinse in DI water x 6 using magnet | 0.0940 |
| 120116 | CoNi | Na0H | 70 | Min 2/sonication 10sec, Min 4/ sonication 10sec, Min 6/ sonication 10sec, Min 8/ sonication 10sec stop Min 9, Rinse in DI water x 6 using magnet | 0.0980 |
| 130116 | CoNi-Cu-CoNi | Na0H | 70 | Min 5/sonication 5sec, Min 8/ sonication 5sec, Stop Min 10 Rinse in DI water x 6 using magnet | 0.0931 |

Table 8.22: Conditions of samples separation from membrane

### 8.7.10 *Nanowire experiment preparation procedure*

This section outlines the method used to prepare nanowires for the nanowire detection experiments and also estimate the volume of nanowires dispensed during the experiments. The average weight of CoNi nanowires lenght 10 µm, that is produced in each membrane is ~ 11.42 mg. This is based on full membrane weight measuments as detailed in Appendix 8.3 Section 8.3.1 Table 8.9. On average 10% of the membrane pours are not filled during the deposition process. The approimate number of nanowires produced per full membrane is $\sim 2630.52 \times 10^6$.

When the nanowires are removed from the AAO membrane as per the procedure outlined in Chapter 2 Section 2.3.2. The nanowire sample is then dried and the weight

measured. Table 8.23 shows the weight measured for a number of nanowire samples and the estimate number of nanowires.

| Type: | Sample weight (mg) | ~ Number of nanowires |
|---|---|---|
| CoNi ~ 10 µm | 0.0071 | 1.6241E+09 |
| | 0.0070 | 1.6009E+09 |
| | 0.0072 | 1.6572E+09 |
| | 0.0069 | 1.5783E+09 |
| | 0.0070 | 1.6009E+09 |
| | 0.0071 | 1.6241E+09 |
| | 0.0074 | 1.6925E+09 |
| | 0.0072 | 1.6572E+09 |
| | 0.0068 | 1.5554E+09 |
| | 0.0070 | 1.6009E+09 |
| | 0.0072 | 1.6572E+09 |
| | 0.0071 | 1.6241E+08 |
| Average: | 0.0072 | 1.6572E+09 |

Table 8.23: CoNi measured sample weight after dissolving from the AAO membrane

Procedure

In preparation for each nanowire detection experiment, the nanowire sample is suspended in 10 ml of deionised water (beaker 1), as shown in Figure. Based on a average sample weight 72 µg, the approimate number of nanowires produced per sample is ~ $1.657 \times 10^9$.

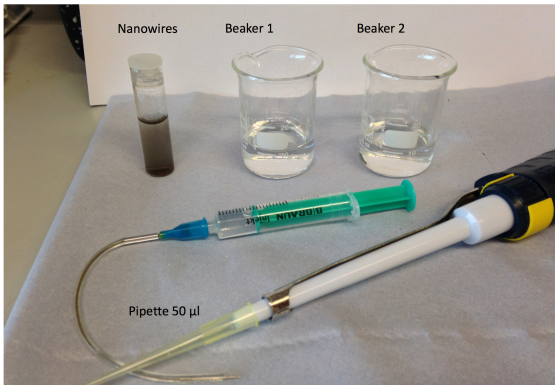



Figure 8.33: Nanowire preparation

50 µl of this sample is then removed using a pipette and suspended in 10 ml of deionised water (Beaker 2). This is a sample weight of ~ 360 µg, the approimate number of nanowires now suspended in 10 ml of deionised water is ~ $8.286 \times 10^6$.

During the experiment 8 µl of the 10 ml sample from Beaker 2 are dispensed through the microfluidic channel. This is a sample weight of ~ 0.3 µg, the approimate number of nanowires dispensed through the microfluidic channel is ~ 6625, detailed in Table which shows nanowire estimates per volume dispensed.

| 50 µl suspended in Beaker 2 (10 ml) | | | | | | |
|---|---|---|---|---|---|---|
| Sample weight | Nanowires | Volume dispensed | Sample weight dispensed | Nanowires dispensed | Velocity (mm/s) | Time (Sec) |
| ~ 360 µg | ~ $8.286 \times 10^6$ | 30 µl | ~ 1 µg | ~ 24855 | 15 | |
| | | 20 µl | ~ 0.75 µg | ~ 16910 | 15 | |
| | | 10 µl | ~ 0.35 µg | ~ 8285 | 15 | |
| | | 8 µl | ~ 0.3 µg | ~ 6625 | 15 | 30 |
| | | 8.7 µl | ~ 0.31 µg | ~ 7200 | 20 | 25 |
| | | 4.7 µl | ~ 0.17 µg | ~ 3895 | 10 | 25 |
| 25 µl suspended in Beaker 2 (10 ml) | | | | | | |
| ~ 180 µg | ~ $4.143 \times 10^6$ | 3.5 µl | ~ 0.06 µg | ~ 1450 | 20 | 10 |
| | | 2.7 µl | ~ 0.05 µg | ~ 1118 | 15 | 10 |

Table 8.24: Nanowire estimates per volume dispensed

This is very much an approximation and used as a rough guide towards the expected count of nanowires detected. What is important is that in the nanowire detection experiments the sample weight for each sample that was dispenced was measured amd and also the experimental conditions were kept the same so a comparison could be made between each respective experiment with regard to nanowire count.

### 8.7.11 *Focused flow channel was configuration*

Focused flow or hydrodynamic flow requires two microfluidic pumps, one for dispensing the sample and one for the sheath flow. This requires compiling two flow protocols using Venaflux assay software. The procedure includes initializing the pumps and camera, priming the tube, pickup sample and dispense drop to avoid bubble entrapment. Figure 8.34shows a schematic of Focused flow cell junction.

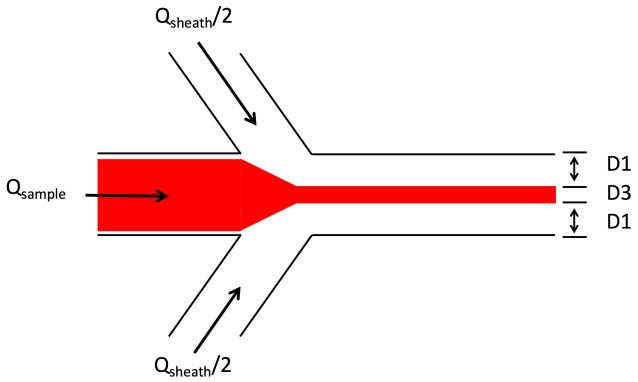



Figure 8.34: Schematic of Focused flow cell junction

The compression factor of the sample flow is estimated as the ratio between sample flow rate QSample and the flow rate of the sheath sample QSheath, which is determined by

$$\frac{(D_1 + D_2)}{D_3} = \frac{Q_{Sheath}}{Q_{Sample}} = Ratio \tag{8.23}$$

$$D_1 + D_2 = R \times D_3 \tag{8.24}$$

$$D_1 + D_2 + D_3 = W \tag{8.25}$$

$W$ is the width of the focused flow stream,

$$D_3 = \frac{W}{1 + R} \tag{8.26}$$

For my experiment the channel overall width is 800 μm and height 30 μm. The focused flow width is 100 μm. Table 8.25summarises the calculations for the focused flow channel flow rates.

| D3 μm | D1 = D2 μm | Ratio | Channel area $m^2$ | $Q_{Sample}$ nl/s | $Q_{Sheath}$ nl/s | Velocity mm/s |
|---|---|---|---|---|---|---|
| 100 | 350 | 7 | $0.3 \times 10^{-8}$ | 450 | 3150 | 15 |
| | | | | 600 | 4200 | 20 |

Table 8.25: Calculations for the focused flow channel flow rates

## 8.8 APPENDIX F - GMR AND TMR SENSOR MAGNETORESISTANCE RESPONSE

### 8.8.1 *GMR sensor additional resistance measurments*

Figure 8.26shows GMR sensor two wire resistance measurements across contact pads for a number of sensors.

| Sensor | Side | Pads | Resistance (ohms) | Side | Pads | Resistance (ohms) | Sensor | Side | Pads | Resistance (ohms) | Side | Pads | Resistance (ohms) | Sensor | Side | Pads | Resistance (ohms) | Side | Pads | Resistance (ohms) |
|---|---|---|---|---|---|---|---|---|---|---|---|---|---|---|---|---|---|---|---|---|
| 240310 | A | 1-7 | 1816 | B | 1-7 | 1873 | 070210 | A | 1-7 | 1050 | B | 1-7 | OL | 090210 | A | 1-7 | 1009 | B | 1-7 | 1025 |
| | | 1-8 | 1522 | | 1-8 | 1860 | | | 1-8 | 1050 | | 1-8 | 1052 | | | 1-8 | 1036 | | 1-8 | 1022 |
| | | 1-2 | 2311 | | 1-2 | 1625 | | | 1-2 | 600 | | 1-2 | 582 | | | 1-2 | 611 | | 1-2 | 613 |
| | | 2-3 | 1555 | | 2-3 | 1234 | | | 2-3 | 405 | | 2-3 | 471 | | | 2-3 | 429 | | 2-3 | 444.3 |
| | | 3-4 | 1157 | | 3-4 | 1055 | | | 3-4 | 370 | | 3-4 | OL | | | 3-4 | 390 | | 3-4 | 392 |
| | | 4-5 | 988 | | 4-5 | 947 | | | 4-5 | 340 | | 4-5 | OL | | | 4-5 | 352 | | 4-5 | 395 |
| | | 5-6 | 883 | | 5-6 | 948 | | | 5-6 | 332 | | 5-6 | OL | | | 5-6 | 341 | | 5-6 | 442 |
| | | 6-7 | 937 | | 6-7 | 963 | | | 6-7 | 450 | | 6-7 | OL | | | 6-7 | 458 | | 6-7 | 481 |
| | | 7-8 | 2666 | | 7-8 | 2165 | | | 7-8 | 1700 | | 7-8 | OL | | | 7-8 | 1662 | | 7-8 | 1651 |
| | | 8-9 | 1017 | | 8-9 | 1072 | | | 8-9 | 430 | | 8-9 | 500 | | | 8-9 | 479 | | 8-9 | 514 |
| | | 9-10 | 1153 | | 9-10 | 1223 | | | 9-10 | 387 | | 9-10 | 388 | | | 9-10 | 404 | | 9-10 | 430 |
| | | 10-11 | 1718 | | 10-11 | 1421 | | | 10-11 | 438 | | 10-11 | 442 | | | 10-11 | 1772 | | 10-11 | 472 |
| | | 11-12 | 1553 | | 11-12 | 1632 | | | 11-12 | 500 | | 11-12 | 500 | | | 11-12 | 1837 | | 11-12 | 540 |
| | | 12-13 | 2031 | | 12-13 | 1986 | | | 12-13 | 565 | | 12-13 | 570 | | | 12-13 | 606 | | 12-13 | 1090 |
| | | | | | | | | | | | | | | | | | | | | |

Table 8.26: GMR sensor two wire resistance measurements across contact pads for a number of sensors

### 8.8.2 *GMR sensor additional magnetoresistance measurments*

Figure 8.35 shows the minor loop magneto-resistance measurements taken on GMR Bio-sensor 7244 between pads 2 - 3 and along the lenght of the YOKE snesor between pads 2 - 6.

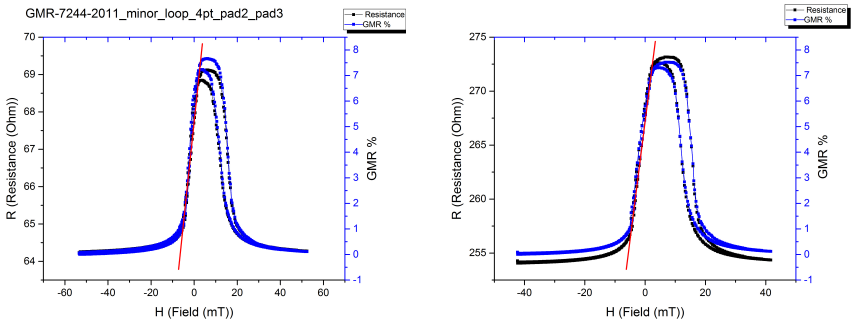



Figure 8.35: Minor loop magneto-resistance measurement GMR Bio-sensor 7244 Pad 2 - 3 & Pad 2 - 6

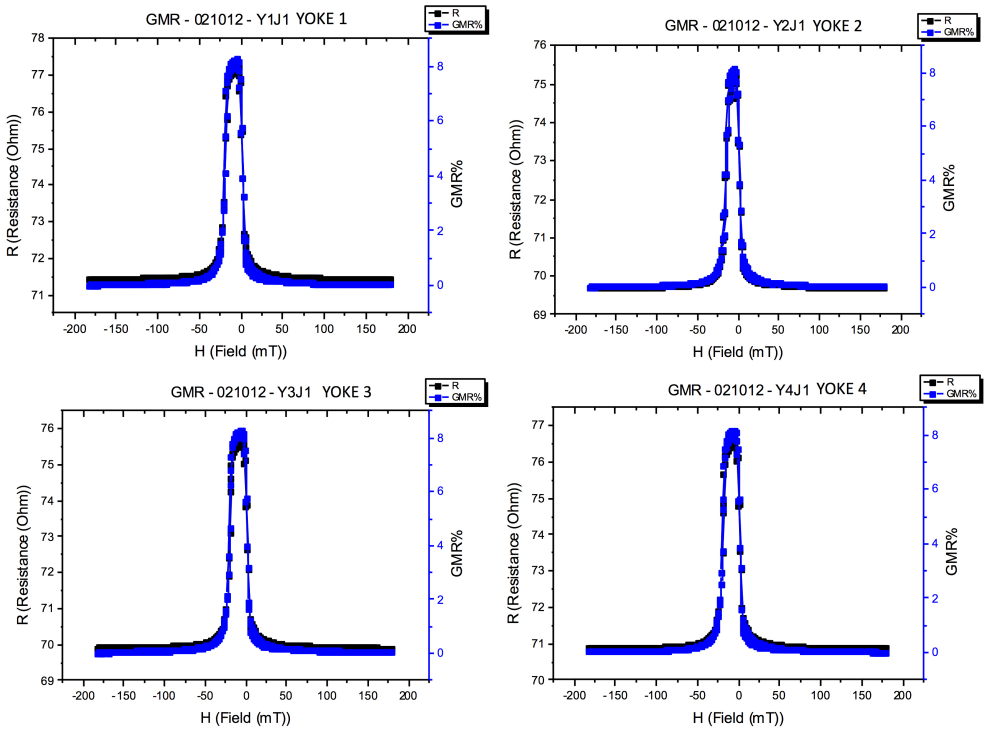



Figure 8.36: Major loop magneto-resistance measurement across each YOKE sensor of Gradiometer GMR Gradiometer Bio-sensor 021012

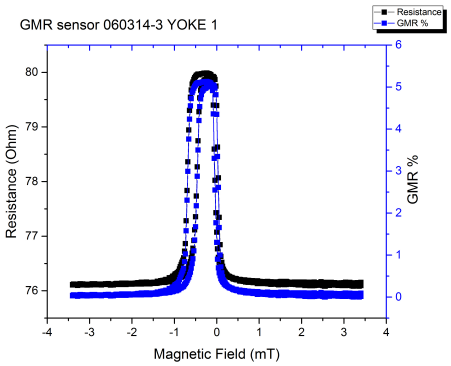



Figure 8.37: Minor loop magneto-resistance measurements GMR Bio-sensor showing magnetoresistance response & sensitivity

### 8.8.3 *1st TMR sensor additional magnetoresistance measurments*

8.38shows the measured magnetoresistance response major and minor loops across YOKE sensor Y5 of TMR sensor 300511. The sensor was patterened without the 2nd

lithtography step and has no gaps inserted along the YOKE sensor. The sensor showed a TMR ratio of 14 % and the minor loop response shows hysterices.

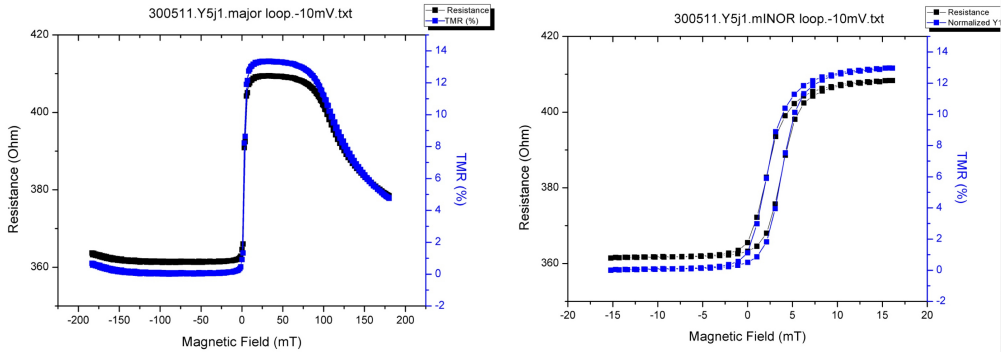



Figure 8.38: TMR Sensor 300511 magnetoresistance response with no gaps in Yoke sensor

Table 8.27shows some of the juctions measured on TMR Sensor 300511 detailing the resistance measured, product RA and TMR ratio.

| Junction | Area $(\mu m)^2$ | No Gap | Resistance (Ω) | RA $(\mu m)^4$* Ω) | TMR% |
|---|---|---|---|---|---|
| Y5J1 | 4000 | | 361 | 1444000 | 14 |
| Y5J2 | 4000 | | 549 | 2196000 | 13 |
| Y5J3 | 4000 | | 637 | 2548000 | 13 |
| Y6j1 | 4000 | | 623 | 2492000 | 10 |
| Y6j2 | 4000 | | 651 | 2604000 | 12 |
| Y6j3 | 4000 | | 679 | 2716000 | 12 |
| Y7j1 | 4000 | | 623 | 2492000 | 10 |
| Y7j2 | 4000 | | 619 | 2476000 | 11 |
| Y7j3 | 4000 | | 658 | 2632000 | 12 |

Table 8.27: TMR Sensor 300511 magnetoresistance response with no gaps in Yoke sensor

TMR sensor where fabricated including the 2nd lithtography step, where junction gaps are ion-milled along the YOKE sensor.

Figure 8.39shows the TMR ratio measured along each juction of YOKE sensor Y5 for TMR Sensor 280411.

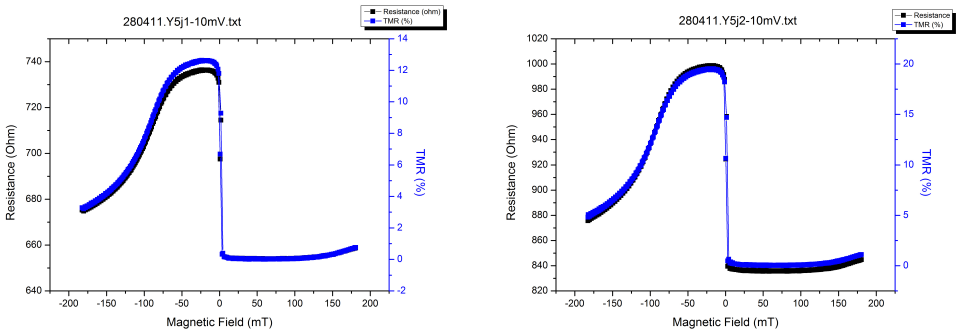



Figure 8.39: TMR Sensor 280411 TMR ratio measured along each juction of YOKE sensor Y5

Table 8.28shows the TMR ratio measured measured along each juction of YOKE sensor Y5 for TMR Sensor 280411 detailing the resistance measured, product RA and TMR ratio.

| Junction | Area $(\mu m)^2$ | Gap | Resistance (Ω) | RA $(\mu m)^2$* Ω) | TMR% |
|---|---|---|---|---|---|
| J5J1 | 400 | 2 | 653 | 261200 | 13 |
| J5J2 | 400 | 2 | 1075 | 430000 | 20 |
| J5J3 | 400 | 2 | 900 | 360000 | 22 |

Table 8.28: TMR Sensor 280411 measured magnetoresistance response along each juction of YOKE sensor Y5

Figure 8.40shows the measured magnetoresistance response major loop across YOKE sensor Y5 and Y6 for TMR sensor 290411, highlighting the heighest TMR ratio measured of 35 %.

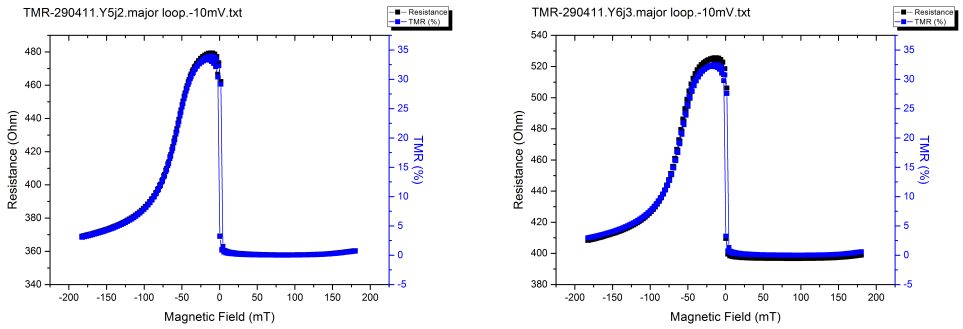



Figure 8.40: TMR sensor 290411 magnetoresistance response major loop across YOKE sensor Y5 and Y6

Table 8.29shows the TMR ratio measured across each of the eight YOKE sensors and junctions 1 for TMR Sensor 290411 detailing the resistance measured, product RA and TMR ratio.

| Junction | Area $(\mu m)^2$ | Gap | Resistance (Ω) | RA $(\mu m)^2$* Ω) | TMR% |
|---|---|---|---|---|---|
| Y1J1 | 200 | 2 | 332 | 66400 | 4 |
| Y1J2 | 200 | 2 | 299 | 59800 | 3.5 |
| Y1J3 | 200 | 2 | 355 | 71000 | 10 |
| Y2J1 | 200 | 5 | 361 | 72200 | 22 |
| Y2J2 | 200 | 5 | 326 | 65200 | 11 |
| Y2J3 | 200 | 5 | 334 | 66800 | 14 |
| Y3J1 | 200 | 7 | 376 | 75200 | 27 |
| Y3J2 | 200 | 7 | 382 | 76400 | 27 |
| Y3J3 | 200 | 7 | 387 | 75600 | 17 |
| Y4J1 | 200 | 10 | 180 | 36000 | 14 |
| Y4J2 | 200 | 10 | 460 | 92000 | 16 |
| Y4J3 | 200 | 10 | 411 | 82200 | 18 |
| Y5J1 | 400 | 2 | 219 | 87600 | 10 |
| Y5J2 | 400 | 2 | 358 | 143200 | 34 |
| Y5J3 | 400 | 2 | 374 | 149600 | 35 |
| Y6j1 | 400 | 5 | 391 | 156400 | 36 |
| Y6j2 | 400 | 5 | 374 | 149600 | 23 |
| Y6j3 | 400 | 5 | 397 | 158800 | 34 |
| Y7j1 | 400 | 7 | 382 | 152800 | 21 |
| Y7j2 | 400 | 7 | 412 | 164800 | 30 |
| Y7j3 | 400 | 7 | 312 | 124800 | 32 |
| Y8j1 | 400 | 10 | 315 | 126000 | 22 |
| Y8j2 | 400 | 10 | 298 | 119200 | 23 |
| Y8j3 | 400 | 10 | 451 | 180400 | 30 |

Table 8.29: TMR Sensor 29041 TMR ratio measured across each of the eight YOKE sensors and junctions

## 8.9 APPENDIX G - MAGNETO-FLUORESCENCE PROTOTYPE SYSTEM

The magnetic nanowire detection system was part of an overall platform, which included a fluorescent sensor system. This was in collaboration with the project partner companies Cellix and Radisions as part of an FP7 project. The project aimed to investigate magnetic sensors and fluorescent sensor technologies with the aim to develop a portable and cost-effective flow cytometry platform for applications such as early detection of cancer cells. Figure 8.41 shows a schematic of the project concept for the magneto-fluorescence prototype system.

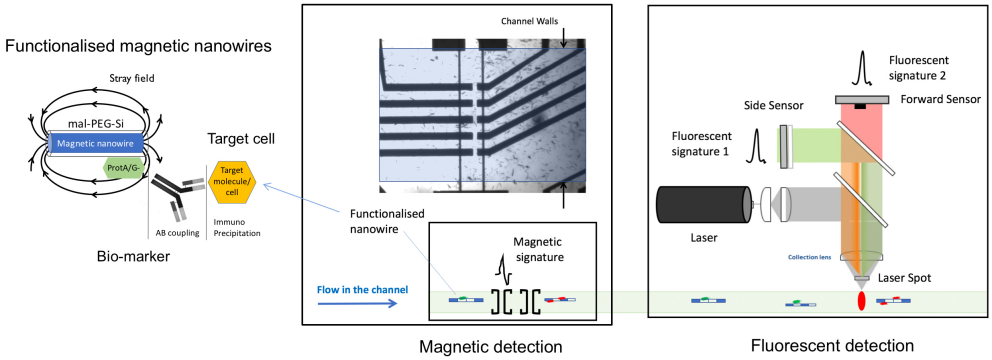



Figure 8.41: Design of magneto-fluorescence prototype system

Towards the end of the project both systems were integrated to complete the final project deliverable. The overall system platform showed a good maturity level with user-friendly procedure and protocol setup. I went to Reims (France) and presented at the NAMDIATREAM final review meeting. I successful demonstrated magnetic nanowire detection. It provided a good opportunity for the review board to look at the magnetic sensors and detection system. Figure 8.42 shows the integrated Magneto-fluorescence prototype system. The fluorescent sensor system developed was based on the FACSCANTO flow cytometry platform from BD biosciences.

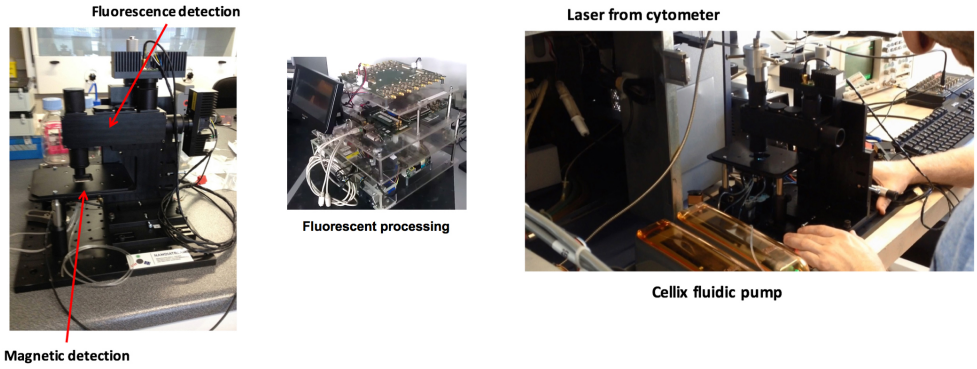



Figure 8.42: Integrated Magneto-fluorescence prototype system

Side and forward sensors measure light scattered by the cells at right angles to the laser beam (side scatter, SS) and light scattered in a forward direction (forward scatter, FS). Filters coated onto substrate and mounted onto sensors. A band-pass filter to block the laser light & only measure the fluorescence. Fluorophore (FITC) excited a 488nm laser. Fluorophore chemical that when illuminated by light of one wavelength (normally

a laser), emits light at a longer wavelength. Figure shows details of the sensor, filter and fluorescence emission profiles.

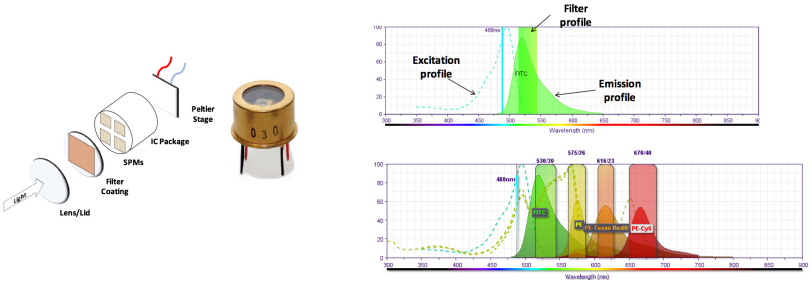



Figure 8.43: Sensor, filter and fluorescence emission profiles

The magnetic nanowires were functionalised to allow specific cell targeting bio-markers to be attached, this work was carried out by TCD medicine and chemistry departments. The nanowires were conjugated with HER2 cell surface receptor antibody examined in breast & lung cancer cell lines. The functionalized wires were used to detect recombinant sErbB2 using confocal microscopy & fluorescent cytometry. They are functionalized using the following mechanism as illustrated in Figure 8.44. The nanowires functionalised with Protein G' by amino-maleimide. Protein G' is an immunoglobin binding protein which binds to IgG. IgG then binds to cancer targeting antibodies HER2. This is then binds to IgG-FITC fluorescent antibodies for flow sensing

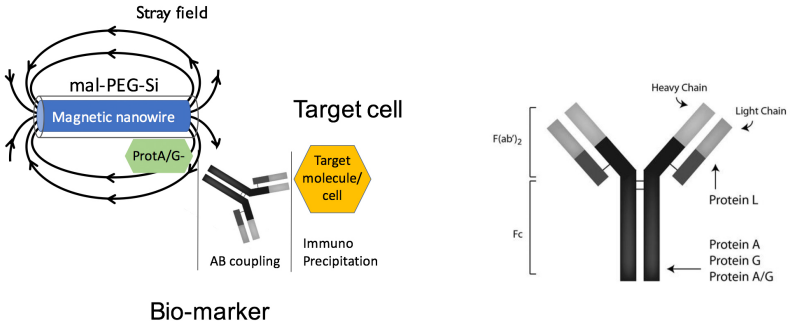



Figure 8.44: Nanowire functionalized mechanism

Functionalised (Herceptin) nanowires used to capture recombinant sErbB2 (cell), followed by a fluorescently labelled detection antibody (Anti-ErbB2). Figure 8.45 shows the results.

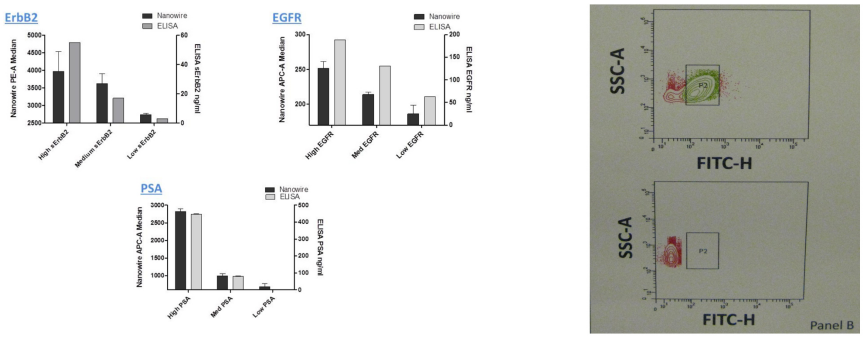



Figure 8.45: Fluorescence intensity from nanowires measured using confocal microscopy and flow cytometry. The mean fluorescence intensity was increased in the presence of the target, compared to a control

In the presence of the target sErbB2, the fluorescence intensity increases, indicating capture of the target on the wire. The flow cytometry and mean fluorescence intensity was increased in the presence of the target, compared to a control.